

EISSN 1305-3612

# DIR

## Diagnostic and Interventional Radiology

**TSR**  
1924  
TURKISH SOCIETY  
OF RADIOLOGY

[dirjournal.org](http://dirjournal.org)

VOLUME 29  
ISSUE 1  
JANUARY 2023

**Editor in Chief**


Mehmet Ruhi Onur, MD

*Department of Radiology, Hacettepe University Faculty of Medicine, Ankara, Turkey*

ORCID ID: 0000-0003-1732-7862


**Section Editors and Scientific Editorial Board**

**Abdominal Imaging**

İlkay S. İdilman, MD 

*Department of Radiology, Hacettepe University Faculty of Medicine, Ankara, Turkey*

ORCID ID: 0000-0002-1913-2404

Sonay Aydın, MD 

*Department of Radiology, Erzincan Binali Yıldırım University Faculty of Medicine, Erzincan, Turkey*

ORCID ID: 0000-0002-3812-6333


**Artificial Intelligence and Informatics**

Burak Koçak, MD 

*Department of Radiology, University of Health Sciences, Başakşehir Çam and Sakura City Hospital, İstanbul, Turkey*

ORCID ID: 0000-0002-7307-396X


**Breast Imaging**

Füsun Taşkın, MD 

*Department of Radiology, Acıbadem University Faculty of Medicine, İstanbul, Turkey*

ORCID ID: 0000-0001-7985-3660


**Chest and Cardiovascular Imaging**

Furkan Ufuk, MD 

*Department of Radiology, Pamukkale University Faculty of Medicine, Denizli, Turkey*

ORCID ID: 0000-0002-8614-5387


**Hybrid Imaging and Nuclear Medicine**

Evrin Bengi Türkbey, MD 

*Radiology and Imaging Sciences, Clinical Center, National Institutes of Health Bethesda, Maryland, United States*


ORCID ID: 0000-0002-5216-3528

**Interventional Radiology**

Barbaros Çil, MD, FCIRES 

*Department of Radiology, Koç University School of Medicine, İstanbul, Turkey*


ORCID ID: 0000-0003-1079-0088

Bahri Üstünsöz, MD 

*Department of Radiology, LSUHSC (Louisiana State University Health Science Center) School of Medicine, New Orleans, United States*

ORCID ID: 0000-0003-4308-6708


**Musculoskeletal Imaging**

Zeynep Maraş Özdemir, MD 

*Department of Radiology, İnönü University Faculty of Medicine, Malatya, Turkey*

ORCID ID: 0000-0003-1085-8978

**Neuroradiology**

Gülgün Yılmaz Ovalı, MD 

*Department of Radiology, Celal Bayar University Faculty of Medicine, Manisa, Turkey*


ORCID ID: 0000-0001-8433-5622

Erkan Gökçe, MD 

*Department of Radiology, Tokat Gaziosmanpaşa University Faculty of Medicine, Tokat, Turkey*


ORCID ID: 0000-0003-3947-2972

**Pediatric Radiology**

Meltem Ceyhan Bilgici, MD 

*Department of Radiology, 19 Mayıs University Faculty of Medicine, Samsun, Turkey*

ORCID ID: 0000-0002-0133-0234

Evrin Özmen, MD 

*Department of Radiology, Koç University Hospital, İstanbul, Turkey*

ORCID ID: 0000-0003-3100-4197


**Publication Coordinator**

Şükrü Mehmet Ertürk, MD 

*Department of Radiology, İstanbul University, İstanbul Faculty of Medicine, İstanbul, Turkey*

ORCID ID: 0000-0003-4086-675X

**Biostatistical Consultant**

İlker Ercan, PhD 

*Department of Biostatistics, Uludağ University School of Medicine, Bursa, Turkey*

ORCID ID: 0000-0002-2382-290X

**Publication Services**

Galenos Publishing, İstanbul, TR

**Past Editors**

**Editors in Chief**

Mustafa Seçil, MD (2016-2022)

Nevzat Karabulut, MD (2011-2016)

Üstün Aydingöz, MD (2010-2011)

Okan Akhan, MD (2001-2010)

Ferhun Balkancı, MD (1999-2001)

Aytekin Besim, MD (1994-1999)\*

\* Dr. Aytekin Besim actually served as the General Coordinator. His work in this capacity, however, was in effect that of an Editor in Chief.

**Editors**

Ayşenur Cila, MD (2001-2002)

Suat Kemal Aytaç, MD (1997-2001)

Erhan Ilgıt, MD (1994-2001)

Okan Akhan, MD (1994-2001)

Ferhun Balkancı, MD (1994-2000)

Serdar Akyar, MD (1994-1997)

**Section Editors**

Section Editorship was established in 2002 at the tenure of Dr Okan Akhan, Editor in Chief.

**Abdominal Imaging**

Bengi Gürses, MD (2020-2023)

Mehmet Ruhi Onur, MD (2016-2022)

Barış Türkbey, MD (2014-2020)

Mustafa N. Özmen, MD (2012-2018)

Murat Acar, MD (2015-2016)

Mustafa Seçil, MD (2011-2016)

Ahmet Tuncay Turgut, MD (2011)

Deniz Akata, MD (2007-2011)

Ayşe Erden, MD (2002-2011)

Okan Akhan, MD (2002-2010)

Hakan Özdemir, MD (2002-2010)

**Artificial Intelligence and Informatics**

Bariş Türkbey, MD (2020-2023)

**Breast Imaging**

Mustafa Erkin Arıbal, MD (2016-2023)

Sibel Kul (2015-2018)

Ayşenur Oktay, MD (2009-2014)

Ayşegül Özdemir, MD (2004-2009)

**Cardiovascular Imaging**

Uğur Bozlar, MD (2016-2023)

Muşturay Karçaaltıncaba, MD (2007-2010)

Mecit Kantarcı (2010-2016)

**Chest Imaging**

Nevzat Karabulut, MD (2010-2014)

Çetin Atasoy, MD (2007-2010)

Macit Arıyürek, MD (2002-2007)

Figen Demirkazık, MD, (2014-2018)

**General Radiology**

Ersin Öztürk, MD (2014-2017)

Utku Şenol, MD (2010-2013)

Oğuz Dicle, MD (2007-2010)

**Interventional Radiology**

Cüneyt Aytekin, MD (2016-2023)

Bora Peynircioğlu, MD (2012-2015)

Levent Oğuzkurt, MD (2011-2014)

Fatih Boyvat, MD (2007-2010)

İsmail Oran, MD (2015-2019)

**Musculoskeletal Imaging**

Hatice Tuba Sanal, MD (2016-2023)

Fatih Kantarcı, MD (2014-2016)

Ayşenur Oktay, MD (2011-2013)

Üstün Aydıngöz, MD (2002-2011)

Berna Dirim Mete (2016-2017)

**Neuroradiology and Head & Neck Imaging**

Kubilay Aydın, MD (2016-2023)

Nafi Aygün, MD (2016-2023)

Kader Karlı Oğuz, MD (2011-2015)

Süleyman Men, MD (2007-2013)

Muhteşem Ağıldere, MD (2002-2011)

**Nuclear Medicine**

A. Cahid Civelek, MD (2016-2023)

Oktay Sarı, MD (2015)

Akın Yıldız, MD (2011-2014)

**Pediatric Radiology**

Korgün Koral, MD (2016-2023)

Murat Kocaoğlu, MD (2016-2023)

Ensar Yekeler, MD (2014-2016)

Suat Fitöz, MD (2007-2013)

Diagnostic and Interventional Radiology (Diagn Interv Radiol) is a bimonthly periodical of the Turkish Society of Radiology and the content of the journal is available at <https://www.dirjournal.org/>. It is peer-reviewed and adheres to the highest ethical and editorial standards. The editors of the journal endorse the Editorial Policy Statements Approved by the Council of Science Editors Board of Directors ([www.councilscienceeditors.org/services/draft\\_approved.cfm](http://www.councilscienceeditors.org/services/draft_approved.cfm)). The journal is in compliance with the Recommendations for the Conduct, Reporting, Editing and Publication of Scholarly Work in Medical Journals published by the International Committee of Medical Journal Editors (updated May 2022, [www.icmje.org](http://www.icmje.org)).

First ten volumes of Diagnostic and Interventional Radiology have been published in Turkish under the name of Tanısal ve Girişimsel Radyoloji (Index Medicus® abbreviation: Tani Girişim Radyol), the current title's exact Turkish translation.

Diagnostic and Interventional Radiology is an open access publication, and the journal's publication model is based on Budapest Open Access Initiative (BOAI) declaration. All published content is available online, free of charge at <https://www.dirjournal.org/>. Authors retain the copyright of their published work in Diagnostic and Interventional Radiology. The journal's content is licensed under a Creative Commons Attribution-NonCommercial (CC BY-NC) 4.0 International License which permits third parties to share and adapt the content for non-commercial purposes by giving the appropriate credit to the original work.

Diagnostic and Interventional Radiology is indexed in **Pubmed/Medline, Pubmed Central, Web of Science, TUBITAK ULAKBIM TR Index, HINARI, EMBASE, CINAHL, Scopus, Gale and CNKI.**

**Contact Information**

Diagnostic and Interventional Radiology Turkish Society of Radiology

Hoşdere Cad., Güzelkent Sok., Çankaya Evleri, F/2, 06540

Ankara, Turkey

E-mail: [info@dirjournal.org](mailto:info@dirjournal.org)

Phone: +90 (312) 442 36 53 Fax: +90 (312) 442 36 54

**Publisher Contact**

Address: Molla Gürani Mah. Kaçamak Sk.

No: 21/1 34093 İstanbul, Turkey

Phone: +90 (530) 177 30 97

E-mail: [info@galenos.com.tr](mailto:info@galenos.com.tr)/[yayin@galenos.com.tr](mailto:yayin@galenos.com.tr)

Web: [www.galenos.com.tr](http://www.galenos.com.tr) **Publisher Certificate Number: 14521**

**Online Publication Date: January 2023**

EISSN 1305-3612

International scientific journal published bimonthly.



## Instructions to Authors

Diagnostic and Interventional Radiology (Diagn Interv Radiol) is a medium for disseminating scientific information based on research, clinical experience, and observations pertaining to diagnostic and interventional radiology. The journal is the double-blind peer-reviewed, bimonthly, open-access publication organ of the Turkish Society of Radiology and its publication language is English. Diagnostic and Interventional Radiology is currently indexed by Science Citation Index Expanded, PubMed MEDLINE, PubMed Central, TUBITAK ULAKBIM TR Index, HINARI, EMBASE, CINAHL, Scopus, Gale and CNKI.

The journal is a medium for original articles, reviews, pictorial essays, technical notes related to all fields of diagnostic and interventional radiology.

The editorial and publication process of the Diagnostic and Interventional Radiology are shaped in accordance with the guidelines of the International Committee of Medical Journal Editors (ICMJE), World Association of Medical Editors (WAME), Council of Science Editors (CSE), Committee on Publication Ethics (COPE), European Association of Science Editors (EASE), and National Information Standards Organization (NISO). The journal is in conformity with the Principles of Transparency and Best Practice in Scholarly Publishing.

### Authorship

Each individual listed as an author should fulfill the authorship criteria recommended by the International Committee of Medical Journal Editors (ICMJE - [www.icmje.org](http://www.icmje.org)). To be listed as an author, an individual should have made substantial contributions to all four categories established by the ICMJE: (a) conception and design, or acquisition of data, or analysis and interpretation of data, (b) drafting the article or revising it critically for important intellectual content, (c) final approval of the version to be published, and (d) agreement to be accountable for all aspects of the work in ensuring that questions related to the accuracy or integrity of any part of the work are appropriately investigated and resolved. Individuals who contributed to the preparation of the manuscript but do not fulfill the authorship criteria should be acknowledged in an acknowledgements section, which should be included in the title page of the manuscript. If the editorial board suspects a case of "gift authorship", the submission will be rejected without further review.

### Ethical standards

For studies involving human or animal participants, the authors should indicate whether the procedures followed were in accordance with the ethical standards of the responsible committee on human and animal experimentation (institutional or regional) and with the Helsinki Declaration). Application or approval number/year of the study should also be provided. The editorial board will act in accordance with COPE guidelines if an ethical misconduct is suspected.

It is the authors' responsibility to carefully protect the patients' anonymity and to verify that any experimental investigation with human subjects reported in the submission was performed with informed consent and following all the guidelines for experimental investigation with human subjects required by the institution(s) with which all the authors are affiliated with. For photographs that may reveal the identity of the patients, signed releases of the patient or of his/her legal representative should be enclosed.

Prospective human studies require both an ethics committee approval and informed consent by participants. Retrospective studies require an ethics committee approval with waiver of informed consent. Authors may be required to document such approval.

All submissions are screened by a similarity detection software (iThenticate by CrossCheck). Manuscripts with an overall similarity index of greater than 20%, or duplication rate at or higher than 5% with a single source are returned back to authors without further evaluation along with the similarity report.

In the event of alleged or suspected research misconduct, e.g., plagiarism, citation manipulation, and data falsification/fabrication, the Editorial Board will follow and act in accordance with COPE guidelines.

### Withdrawal Policy

Articles may be withdrawn under certain circumstances.

The article will be withdrawn if it;

- violates professional ethical codes,
- is subject to a legal dispute,
- has multiple submissions,
- includes fake claims of authorship, plagiarism, misleading data, and false data that may pose a severe health risk.

The editorial board will follow the principles set by COPE (Committee on Publication Ethics) in case of an article withdrawal.

### Manuscript Preparation

The manuscripts should be prepared in accordance with ICMJE-Recommendations for the Conduct, Reporting, Editing, and Publication of Scholarly Work in Medical Journals (updated in May 2022 - <https://www.icmje.org/recommendations/>).

Original Investigations and Reviews should be presented in accordance with the following guidelines: randomized study – CONSORT, observational study – STROBE, study on diagnostic accuracy – STARD, systematic reviews and meta-analysis PRISMA, nonrandomized behavioral and public health intervention studies – TREND.

Diagnostic and Interventional Radiology will only evaluate manuscripts submitted via the journal's self-explanatory online manuscript submission and evaluation system available at [mc04.manuscriptcentral.com/dir](http://mc04.manuscriptcentral.com/dir). Evaluation process of submitted manuscripts takes 4 weeks on average.

Manuscripts are evaluated and published on the understanding that they are original contributions, and do not contain data that have been published elsewhere or are under consideration by another journal. Authors are required to make a full statement at the time of submission about all prior reports and submissions that might be considered duplicate or redundant publication, and mention any previously published abstracts for meeting presentations that contain partial or similar material in the cover letter. They must reference any similar previous publications in the manuscript.

Authors must obtain written permission from the copyright owner to reproduce previously published figures, tables, or any other material in both print and electronic formats and present it during submission. The original source should be cited within the references and below the reprinted material.

**Cover letter:** A cover letter must be provided with all manuscripts. This letter may be used to emphasize the importance of the study. The authors should briefly state the existing knowledge relevant to the study and the contributions their study make to the existing knowledge. The correspondent author should also include a statement in the cover letter declaring that he/she accepts to undertake all the responsibility for authorship during the submission and review stages of the manuscript.

## *Instructions to Authors*

**Title page:** A separate title page should be submitted with all manuscripts and should include the title of the manuscript, name(s), affiliation(s), and major degree(s) of the author(s). The name, address, telephone (including the mobile phone number) and fax numbers and e-mail address of the corresponding author should be clearly listed. Grant information and other sources of support should also be included. Individuals who contributed to the preparation of the manuscript but do not fulfill the authorship criteria should also be acknowledged in the title page. Manuscripts should not be signed by more than 6 authors unless they are multicenter or multidisciplinary studies.

### **Main document**

**Abstract:** All submissions (except for Letters to the Editor) should be accompanied by an abstract limited to 400 words. A structured abstract is only required with original articles and it should include the following subheadings: PURPOSE, METHODS, RESULTS, CONCLUSION.

**Main points:** Each submission should be accompanied by 3 to 5 “main points”, which should emphasize the most striking results of the study and highlight the message that is intended to be conveyed to the readers. As these main points would be targeting radiology residents, experts and residents of other fields of medicine, as well as radiology experts, they should be kept as plain and simple as possible. These points should be constructed in a way that provides the readers with a general overview of the article and enables them to have a general idea about the article.

The main points should be listed at the end of the main text, above the reference list.

**Example:** Liu S, Xu X, Cheng Q, et al. Simple quantitative measurement based on DWI to objectively judge DWI-FLAIR mismatch in a canine stroke model. *Diagn Interv Radiol* 2015; 21:348–354.

- The relative diffusion-weighted imaging signal intensity (rDWI) of ischemic lesions might be helpful to identify the status of fluid attenuated inversion recovery (FLAIR) imaging in acute ischemic stroke.
- The relative apparent diffusion coefficient (rADC) value appears not useful to identify the status of FLAIR imaging in the acute period.
- Based on our embolic canine model, rDWI increased gradually in the acute period, while the rADC kept stable, which might explain why rDWI is helpful to identify the status of FLAIR imaging, while rADC is not.

### **Main text**

#### **Original Articles**

Original articles should provide new information based on original research. The main text should be structured with Introduction, Methods, Results, and Discussion subheadings. The number of cited references should not exceed 50 and the main text should be limited to 4500 words. Number of tables included in an original article should be limited to 4 and the number of figures should be limited to 7 (or a total of 15 figure parts).

#### **Introduction**

State briefly the nature and purpose of the work, quoting the relevant literature.

#### **Methods**

Include the details of clinical and technical procedures.

### **Research ethics standards compliance**

All manuscripts dealing with human subjects must contain a statement indicating that the study was approved by the Institutional Review Board or a comparable formal research ethics review committee. If none is present at your institution, there should be a statement that the research was performed according to the Declaration of Helsinki principles ([www.wma.net/e/policy/b3.htm](http://www.wma.net/e/policy/b3.htm)). There should also be a statement about whether informed consent was obtained from research subjects.

### **Results**

Present these clearly, concisely, and without comment. Statistical analysis results should also be provided in this section to support conclusions when available.

### **Discussion**

Explain your results and relate them to those of other authors; define their significance for clinical practice. Limitations, drawbacks, or shortcomings of the study should also be stated in the discussion section before the conclusion paragraph. In the last paragraph, a strong conclusion should be written.

### **Review Articles**

Review articles are scientific analyses of recent developments on a specific topic as reported in the literature. No new information is described, and no opinions or personal experiences are expressed. Reviews include only the highlights on a subject. Main text should be limited to 4000 words and the number of cited references should not exceed 75. Number of tables included in a review article should be limited to 4 and the number of figures should be limited to 15 (or a total of 30 figure parts).

### **Pictorial Essay**

This is a continuing medical education exercise with the teaching message in the figures and their legends. Text should include a brief abstract; there may be as many as 30 figure parts. No new information is included. The value of the paper turns on the quality of the illustrations. Authors can submit dynamic images (e.g. video files) or include supplemental image files for online presentation that further illustrate the educational purpose of the essay. Maximums: Pages of text – 4 (1,500 words); References – 20; Figures – 15 or total of 30 images; No table Main text should be limited to 1500 words and the number of cited references should not exceed 15.

### **Technical Notes**

Technical note is a brief description of a specific technique, procedure, modification of a technique, or new equipment of interest to radiologists. It should include a brief introduction followed by Technique section for case reports or Methods section for case series, and Discussion is limited to the specific message, including the uses of the technique, equipment, or software. Literature reviews and lengthy descriptions of cases are not appropriate.

Main text should be limited to 1500 words and the number of cited references should not exceed 8. Number of tables included in a technical note should be limited to 4 and the number of figures should be limited to 3 (or a total of 6 figure parts).

### Letter to the Editor and Reply

Letters to the Editor and Replies should offer objective and constructive criticism of published articles within last 6 months. Letters may also discuss matters of general interest to radiologists and may include images. Material being submitted or published elsewhere should not be duplicated in letters.

Main text should be limited to 500 words and the number of cited references should not exceed 6. No tables should be included and the number of figures should be limited to 2 (or a total of 4 figure parts).

### Recommendations for Manuscripts:

Type of manuscript	Word limit	Abstract word limit	Reference limit	Author limit	Table limit	Figure limit
Original Article	4500	400 (Structured)	50	6*	4	7 or total of 15 images
Review Article	4000	200	75	5	4	15 or total of 24 images
Pictorial Essay	1500	400	20	5	1	15 figures or total of 30 figure parts
Technical Note	1500	200	8	5	2	3 figures or total of 6 figure parts
Letter	500	N/A	6	4	No tables	2 figures or total of 4 figure parts

\*Manuscripts should not be signed by more than 6 authors unless they are multicenter or multidisciplinary studies.

\*\*Considering the specific condition of the manuscript, minor flexibilities may be applied for the recommendations upon the decision of Editor-in-Chief or the Section Editors.

### References

Both in-text citations and the references must be prepared according to the AMA Manual of style.

While citing publications, preference should be given to the latest, most up-to-date publications. Authors are responsible for the accuracy of references. If an ahead-of-print publication is cited, the DOI number should be provided. Journal titles should be abbreviated in accordance with the journal abbreviations in Index Medicus/MEDLINE/PubMed. When there are six or fewer authors, all authors should be listed. If there are seven or more authors, the first three authors should be listed followed by "et al." In the main text of the manuscript, references should be cited in superscript after punctuation. The reference styles for different types of publications are presented in the following examples.

**Journal Article:** Economopoulos KJ, Brockmeier SF. Rotator cuff tears in overhead athletes. *Clin Sports Med.* 2012;31(4):675-692.

**Book Section:** Fikremariam D, Serafini M. Multidisciplinary approach to pain management. In: Vadivelu N, Urman RD, Hines RL, eds. *Essentials of Pain Management.* New York, NY: Springer New York; 2011:17-28.

**Books with a Single Author:** Patterson JW. *Weedon's Skin Pathology.* 4th ed. Churchill Livingstone; 2016.

**Editor(s) as Author:** Etzel RA, Balk SJ, eds. *Pediatric Environmental Health.* American Academy of Pediatrics; 2011.

**Conference Proceedings:** Morales M, Zhou X. Health practices of immigrant women: indigenous knowledge in an urban environment. Paper presented at: 78th Association for Information Science and Technology Annual Meeting; November 6-10; 2015; St Louis, MO. Accessed March 15, 2016. <https://www.asist.org/files/meetings/am15/proceedings/openpage15.html>

**Thesis:** Maiti N. Association Between Behaviours, Health Characteristics and Injuries Among Adolescents in the United States. Dissertation. Palo Alto University; 2010.

**Online Journal Articles:** Tamburini S, Shen N, Chih Wu H, Clemente KC. The microbiome in early life: implications for health outcomes. *Nat Med.* Published online July 7, 2016. doi:10.1038/nm4142

**Epub Ahead of Print Articles: Websites:** International Society for Infectious Diseases. ProMed-mail. Accessed February 10, 2016. <http://www.promedmail.org>

### Tables

Tables should be included in the main document and should be presented after the reference list. Tables should be numbered consecutively in the order they are referred to within the main text. A descriptive title should be provided for all tables and the titles should be placed above the tables. Abbreviations used in the tables should be defined below by footnotes (even if they are defined within the main text). Tables should be created using the "insert table" command of the word processing software and they should be arranged clearly to provide an easy reading. Data presented in the tables should not be a repetition of the data presented within the main text but should be supporting the main text.

### Figures and figure legends

Figures, graphics, and photographs should be submitted as separate files (in TIFF or JPEG format) through the submission system. The files should not be embedded in a Word document or the main document. When there are figure subunits, the subunits should not be merged to form a single image. Each subunit should be submitted separately through the submission system. Images should not be labelled (a, b, c, etc.) to indicate figure subunits. Thick and thin arrows, arrowheads, stars, asterisks, abbreviations and similar marks can be used on the images to support figure legends. Like the rest of the submission, the figures too should be blind. Any information within the images that may indicate the institution or the patient should be removed.

Figure legends should be listed at the end of the main document.

### General

All acronyms and abbreviations used in the manuscript should be defined at first use, both in the abstract and in the main text. The abbreviation should be provided in parenthesis following the definition.

Statistical analysis should be performed in accordance with guidelines on reporting statistics in medical journals (Altman DG, Gore SM, Gardner MJ, Pocock SJ. Statistical guidelines for contributors to medical journals. *Br Med J* 1983; 7; 1489-1493.). Information on the statistical analysis process of the study should be provided within the main text.

When a drug, product, hardware, or software mentioned within the main text product information, the name and producer of the product should be provided in parenthesis in the following format: "Discovery St PET/CT scanner (GE Healthcare)."

## Instructions to Authors

All references, tables, and figures should be referred to within the main text and they should be numbered consecutively in the order they are referred to within the main text.

### Initial evaluation and Peer review process

Manuscripts submitted to Diagnostic and Interventional Radiology will first go through a technical evaluation process where the editorial office staff will ensure that the manuscript is prepared and submitted in accordance with the journal's guidelines. Submissions that do not conform to the journal's guidelines will be returned to the submitting author with technical correction requests.

All submissions are screened by a similarity detection software (iThenticate by CrossCheck), and those with an overall similarity index of greater than 20%, or duplication rate at or higher than 5% with a single source are returned back to authors without further evaluation along with the similarity report.

Manuscripts meeting the requirements mentioned in journal's guideline will go under the review process. The initial review will be performed by Editor-in-Chief and the Section Editor, which include the evaluation of the manuscript for its originality, importance of the findings, scientific merit, interest to readers and compliance with the policy of the journal in force. Manuscripts with insufficient priority for publication are not sent out for further review and rejected promptly at this level to allow the authors to submit their work elsewhere without delay.

Manuscripts that pass through the initial review are sent to peer review, which is performed in a blinded manner by at least two external and independent reviewers. During the review process, all original articles are evaluated by at least one senior consultant of statistics for proper handling and consistency of data, and use of correct statistical method. The Section Editor and / or Editor-in-Chief are the final authority in the decision-making process for all submissions.

### Revisions

When submitting a revised version of a paper, the author must submit a detailed "Response to reviewers" that states point by point how each issue raised by the reviewers has been covered and where it can be found (each reviewer's comment followed by the author's reply and line numbers where the changes have been made) as well as an annotated copy, and a clear copy of the main document.

Revised manuscripts must be submitted within 30 days from the date of the decision letter. If the revised version of the manuscript is not submitted within the allocated time, the revision option will be automatically cancelled by the submission system. If the submitting author(s) believe that additional time is required, they should request an extension before the initial 30-day period is over.

### Proofs and DOI Number

Accepted manuscripts are copy-edited for grammar, punctuation, and format by professional language editors. Following the copyediting process, the authors will be asked to review and approve the changes made during the

process. Authors will be contacted for a second time after the layout process and will be asked to review and approve the PDF proof of their article for publication. Once the production process of a manuscript is completed it is published online on the journal's webpage as an ahead-of-print publication before it is included in its scheduled issue.

### Publication Fee Policy

Diagnostic and Interventional Radiology (DIR) applies an Article Processing Charge (APCs) for only accepted articles. No fees are requested from the authors during submission and evaluation process. All manuscripts must be submitted via Manuscript Manager.

An APC fee of and local taxes will be applied depending on the article type (see Table 1)

Review	\$ 1250
Original Article	\$ 1000
Pictorial Essay	\$ 750
Technical Note	

**Table 1. Article Types and Fees**

The APCs will be accepted through the link that will be sent to the corresponding author of each article via the online article system. In the next step, the authors will be receiving a receipt of their payment.

\*Please note that the Article Processing Charge (APC) will not affect neither the editorial and peer-review process nor the priority of the manuscripts by no means. All submissions will be evaluated by the Editorial Board and the external reviewers in terms of scientific quality and ethical standards.

### Refund Policy:

Returning the article to the author; Diagnostic and Interventional Radiology (DIR) will refund the submission fees with a coupon code if the article is returned to the author. Using this code, authors can use the submission fees of different articles without making a new payment.

### Article Retraction:

Infringements of publication/research ethics, such as multiple submissions, bogus claims of authorship, plagiarism, and fraudulent use of data could lead to article retraction.

A retraction statement titled "Retraction: [article title]" must be signed by the authors and/or the editor. The original article is marked as retracted but a PDF version remains available to readers, and the retraction statement is linked to the original published paper.

## Contents

### ABDOMINAL IMAGING

1 **Original Article.** Cine magnetic resonance urography as a new approach for postoperative evaluation of the reconstructed upper urinary tract: a multicenter study. *Xinfei Li, Zhihua Li, Xiang Wang, Weijie Zhu, Mingming Ma, Peng Zhang, Hongjian Zhu, He Wang, Xuesong Li, Liqun Zhou*

9 **Review.** Urethrocytography: a guide for urological surgery?. *Patrícia S. Freitas, Ana S. Alves, Paulo S. Correia, João L. Dias*

18 **Pictorial Essay.** Ovarian dysgerminoma: clues to the radiological diagnosis. *Sofia Amante, Ana Félix, Teresa Margarida Cunha*

24 **Technical Note.** Length of the healthy and pathological small intestine in patients with Crohn's disease: calculations using computed tomography and magnetic resonance enterography. *Laura Maria Minordi, Luigi Larosa, Maria Gabriella Brizi, Alessandro Armuzzi, Riccardo Manfredi*

29 **Original Article.** Analysis of interreader agreement in structured reports of pelvic multiparametric magnetic resonance imaging using the METastasis Reporting and Data System for Prostate Cancer guidelines. *Xiang Liu, Tingting Xie, Zhaonan Sun, Ying Guo, Xiaodong Zhang, Xiaoying Wang*

### ARTIFICIAL INTELLIGENCE AND INFORMATICS

40 **Review.** Artificial intelligence in diagnostic ultrasonography. *Oğuz Dicle*

46 **Original Article.** A snapshot of teleradiology practice in Turkey: the results of a survey among radiologists. *Oğuz Dicle, Utku Şenol, Mustafa Nasuh Özmen, Üstün Aydıngöz*

### BREAST IMAGING

53 **Original Article.** Radiological and clinicopathological findings of breast cancer during the COVID-19 pandemic: a comparative study with the pre-pandemic era. *Merve Gürsoy, Özge Aslan, Ayşenur Oktay Alfatlı, Osman Zekioglu, Berk Göktepe*

59 **Pictorial Essay.** Multimodality imaging and histopathology of metaplastic breast cancer. *Hakkı Çelik, Işıl Başara Akın, Merih Güray Durak, Pınar Balcı*

### CARDIOVASCULAR IMAGING

68 **Pictorial Essay.** Cross-sectional imaging findings of cardiac outpouchings. *Furkan Ufuk, Tuncay Hazırolan*

### CHEST IMAGING

80 **Pictorial Essay.** Drug-induced lung disease: a brief update for radiologists. *Furkan Ufuk, Selen Bayraktaroğlu, Ayşe Rüksan Ütebey*

91 **Original Article.** Chest computed tomography radiomics to predict the outcome for patients with COVID-19 at an early stage. *Shan Wu, Ranying Zhang, Xinjian Wan, Ting Yao, Qingwei Zhang, Xiaohua Chen, Xiaohong Fan*

103 **Original Article.** Long-term lung perfusion changes related to COVID-19: a dual energy computed tomography study. *Sonay Aydın, Erdal Karavaş, Edhem Ünver, Düzgün Can Şenbil, Mecit Kantarcı*

109 **Original Article.** Peritumoral imaging features of thymic epithelial tumors for the prediction of transcapsular invasion: beyond intratumoral analysis. *Jongmin Park, Byunggeon Park, Jihoon Hong, Jung Guen Cha, Kyung Min Shin, Jaehee Lee, An Na Seo, Young Woo Do, Won Kee Lee, Jae-Kwang Lim*

### EMERGENCY RADIOLOGY

117 **Pictorial Essay.** The spectrum of computed tomography findings in blunt trauma of the subclavian/axillary artery: a pictorial essay. *Emanuele Barabino, Diego Ivaldi, Giulia Pittaluga, Arianna Nivolli, Matteo Arnò, Paolo Gazzo*

### INTERVENTIONAL RADIOLOGY

128 **Original Article.** Optimized visualization of focal liver lesions and vascular structures in real-time T1-weighted gradient echo sequences for magnetic resonance-guided liver procedures. *Vanessa Franziska Schmidt, Olaf Dietrich, Philipp Maximilian Kazmierczak, Max Seidensticker, Jens Ricke, Marco Armbruster*

138 **Review.** Catheters in vascular interventional radiology: an illustrated review. *Vineeta Ojha, Sreenivasa Narayana Raju, Amit Deshpande, Kartik P. Ganga, Sanjeev Kumar*



## Contents

**146 Review.** A comprehensive review of transvenous obliteration techniques in the management of gastric varices. *Irfan Masood, Amin Moshksar, Brian Wong, Hasan Khan, Arsalan Saleem*

**155 Original Article.** CT-guided microcoil localization for scapula-blocked pulmonary nodules using penetrating lung puncture before video-assisted thoracic surgery. *Ye Tian, Jianli An, Zibo Zou, Yanchao Dong, Jingpeng Wu, Zhuo Chen, Hongtao Niu*

**161 Original Article.** Prediction of common hepatic artery catheter insertion based on celiac trunk morphology. *Atsushi Saiga, Hajime Yokota, Akira Akutsu, Yoshihiko Ooka, Yoshihiro Kubota, Takeshi Wada, Jun Koizumi, Takashi Uno*

**167 Technical Note.** Percutaneous cryoablation of follicular thyroid carcinoma metastasis to the pancreas. *Saim Yilmaz, Hatice Arıöz Habibi*

**170 Original Article.** Selective arterial embolization of renal angiomyolipoma: comparing ethanol–lipiodol emulsion and polyvinyl alcohol particles as embolic agents. *Long Jin, Ho Jong Chun, Jung Suk Oh, Byung Gil Choi, Hae Gyu Lee, Il Jung Kim*

### MODALITY-BASED (UC, CT, MRI, PET-CT) IMAGING

**175 Original Article.** Advanced virtual monoenergetic imaging algorithm for lower extremity computed tomography angiography: effects on image quality, artifacts, and peripheral

arterial disease evaluation. *Jung Han Hwang, Jin Mo Kang, Suyoung Park, So Hyun Park, Jeong Ho Kim, Ki Hyun Lee, Ji Hoon Shin, Seong Yong Pak*

**183 Original Article.** Role of T2 mapping of magnetic resonance imaging in the differentiation of endometrial cancer and benign endometrial lesions. *Han Xu, Jie Zhang, Yuqing Han, Qingwei Liu, Jinlai Liu, Xianshun Yuan, Jiamei Li, Jinye Li, Ximing Wang*

### NUCLEAR MEDICINE AND MOLECULAR IMAGING

**190 Original Article.** A computer program to assess the bone scan index for Tc-99m hydroxymethylene diphosphonate: evaluation of jaw pathologies of patients with bone metastases using SPECT/CT. *Ruri Ogawa, Ichiro Ogura*

### UNSPECIFIED

**195 Original Article.** Sacral injury and influencing factors after ultrasonic ablation of uterine fibroids  $\leq 30$  mm from the sacrum. *An-Qi Zheng, Jin-Yun Chen, Zhi-Bo Xiao, Rong Zhang, Jin Bai*

### CARDIOVASCULAR IMAGING

**202 Letter to the Editor.** Questions about “Intra-atrial right coronary artery on dual-source CT”. *Furkan Ufuk*



# Cine magnetic resonance urography as a new approach for postoperative evaluation of the reconstructed upper urinary tract: a multicenter study

Xinfei Li\*

Zhихua Li\*

Xiang Wang

Weijie Zhu

Mingming Ma

Peng Zhang

Hongjian Zhu

He Wang

Xuesong Li

Liqun Zhou

\*Xinfei Li and Zhихua Li contribute equally to this paper.

From the Department of Urology (X.L. ✉ lixinfei@pku.edu.cn, Z.L., X.W., W.Z., Xu.L., L.Z.), Peking University First Hospital, Institute of Urology, National Urological Cancer Center, Beijing, China; Department of Radiology, (M.M., H.W.), Peking University First Hospital, Beijing, China; Clinic of Urology (P.Z.), Emergency General Hospital, Beijing, China; Clinic of Urology (H.Z.), Beijing Jiangong Hospital, Beijing, China.

Received 22 April 2021; revision requested 21 May 2021; last revision received 22 November 2021; accepted 09 December 2021.



Epub: 17.01.2023

Publication date: 31.01.2023

DOI: 10.5152/dir.2022.21418

## PURPOSE

To evaluate the feasibility and usefulness of cine magnetic resonance urography (cine MRU) as a novel postoperative examination after upper urinary tract reconstruction surgery.

## METHODS

Ninety-six patients underwent cine MRU for postoperative evaluation between August 2015 and August 2020. The morphological observations included regular peristalsis, anastomosis, urine flow signals, and reflux. The quantitative evaluations included luminal diameter, peristaltic amplitude, contraction ratio, peristaltic waves, and ureteric jets. The surgical outcomes were classified as success, gray area, or failure by combining the results of cine MRU, symptoms, and the degree of hydronephrosis.

## RESULTS

There was no obvious stenosis of the anastomosis in 83 patients (86.46%). Regular peristalsis of the ureter and signals of urination was observed in 85 (88.54%) and 84 patients (87.50%), respectively. In addition, three patients (3.13%) showed urine reflux. The patients in both the success group and the gray area group showed significantly different creatinine levels (success  $86.2 \pm 22.3 \mu\text{mol/L}$  vs. failure  $110.7 \pm 8.2 \mu\text{mol/L}$ ,  $P = 0.016$ ; gray area  $81.0 \pm 20.0 \mu\text{mol/L}$  vs. failure  $110.7 \pm 8.2 \mu\text{mol/L}$ ,  $P = 0.009$ ) and estimated glomerular filtration rate (success:  $88.5 \pm 23.1 \text{ mL/min}\cdot 1.73 \text{ m}^2$ , failure:  $61.6 \pm 14.1 \text{ mL/min}\cdot 1.73 \text{ m}^2$ ,  $P = 0.014$ ; gray area:  $94.7 \pm 24.6 \text{ mL/min}\cdot 1.73 \text{ m}^2$ , failure:  $61.6 \pm 14.1 \text{ mL/min}\cdot 1.73 \text{ m}^2$ ,  $P = 0.007$ ) compared to those in the failure group. The ipsilateral split renal function was  $33.6 \pm 15.0$ ,  $24.5 \pm 13.4$ , and  $20.1 \pm 0.4 \text{ mL/min}$  in the success, gray area, and failure groups, respectively ( $P = 0.354$ ).

## CONCLUSION

Cine MRU demonstrates the morphology and function of the reconstructed upper urinary tract. The results of cine MRU can be used to evaluate the surgical effect, providing guidance for further treatment.

## KEYWORDS

Cine MRU, magnetic resonance imaging, reconstructive surgery, ureter, ureteric stricture

Ureteral stenosis can lead to hydronephrosis, recurrent urinary tract infections, or deterioration of renal function. Surgical management mainly focuses on solving the problem of lumen obstruction. However, ineffective peristalsis or no peristalsis of the ureter may still exist after reconstruction surgeries.<sup>1</sup> Moreover, a wide ureter often needs a relatively long time to recover. Because existing follow-up examinations are static assessments, it is difficult to assess the function of the ureter and distinguish between physiological and pathological dilatation.

Cine magnetic resonance imaging (cine MRI), which captures a number of sequential images over a short period of time, enables the dynamic evaluation of an organ's function.<sup>2</sup> Recent advances in cine MRI techniques allow visualization of peristaltic movement directly and clearly, thus making it a useful tool in the fields of cardiology, obstetrics, gynecology, and gastroenterology.<sup>2-6</sup> Urine is a natural contrast agent, and the ureter anatomy is well visualized by the cine MRI method in T2-weighted images.<sup>7</sup> However, the role of cine magnetic resonance urography (cine MRU) in the postoperative evaluation of the reconstructed upper urinary tract has not yet been reported. The purpose of the present study is to evaluate the feasibility and usefulness of cine MRU as a novel postoperative examination after upper urinary tract reconstruction surgery.

## Methods

### Patients

A total of 692 patients underwent surgical treatment for ureteral strictures between August 2015 and August 2020. Out of this number, 96 patients underwent cine MRU for postoperative evaluation. The inclusion criteria included patients who received surgical treatment for ureteral stenosis and volunteered to undergo cine MRU for postoperative evaluation. The exclusion criteria were as follows: (1) no surgery was performed or surgery was intolerable; (2) ureteral stents or nephrostomy tubes had not been removed; (3) patients refused to undergo cine MRU; or (4) patients were unable to cooperate, resulting in failure of the MRU examination or blurred images. Data regarding patient characteristics, symptoms, degree of hydronephrosis, renal function, surgical strategies, and complications were collected. This study was approved by our ethics committee (no: 2020-SR-283) and performed in accordance with the ethical standards of the 1964 Declaration of Helsinki and its subsequent amendments.

#### Main points

- Cine magnetic resonance urography (cine MRU) displays both the morphology and function of the postoperative upper urinary tract.
- The results of cine MRU can be used to evaluate the surgical effect.
- Cine MRU provides guidance for further treatment in patients who undergo upper urinary tract reconstruction surgery.

Written informed consent was obtained from all patients in the study.

### Protocol

All cine MRUs were performed using a 3-T system with a phased-array torso surface coil (Signa Excite TM; GE Medical Systems, Milwaukee, WI, USA). The reconstructed upper urinary tract was identified using a coronal localizer. Static T2-weighted HASTE sequence images, which covered the entire upper urinary tract, were obtained. Using HASTE sequences, the following parameters were applied: field of view = 36 × 36 cm, repetition time = 800 ms, flip angle = 80°, section thickness = 70 mm, matrix = 512, temporal resolution = 0.5 seconds, scan time = 1 second, and time interval = 13 seconds. A series of 30 consecutive specific coronal images was obtained to form a cine loop within a scan time of 407 s.

### Image analysis and data sampling

Image analysis was performed by two experienced radiologists using a Picture Archiving and Communication System workstation. Morphological evaluation was performed first by considering the following factors: (1) whether the upper urinary tract was dilated; (2) whether the peristalsis of the reconstructed upper urinary tract was regular and effective; (3) whether the anastomosis was narrow; (4) whether the urine flow signal was unobstructed; and (5) whether reflux existed. Further quantitative measurements taken included luminal diameter, amplitude, contraction ratio, and ureteric jet frequency. When the radiologists had disagreements on morphological evaluation, discussions took place to reach a consensus. For the quantitative measurements, we took an average of the evaluation results as reported by the two radiologists.

### Follow up

Patient follow-ups were managed at 1, 3, 6, and 12 months after surgical treatment, then at least once every 6 months. The patients regularly received symptom evaluation, physical examinations, routine urine tests, blood tests [including serum creatinine, estimated glomerular filtration rate (eGFR), electrolytes, and blood gas analysis only for the ileal ureter], and ultrasound at each visit. Cine MRU, renal scintigraphy, and diuretic renograms were performed 3–6 months after the surgery. Surgical success was defined as relief of symptoms and improved/stable hydronephrosis.

### Statistical analysis

The surgical outcomes were classified into three categories as follows: success (unobstructed anastomosis and regular peristalsis in cine MRU, relieved symptoms, and improved/stable hydronephrosis), gray area (abnormalities in cine MRU but relief of symptoms, and improved/stable hydronephrosis), and failure (abnormalities in cine MRU, no relief of symptoms, and deteriorated hydronephrosis). All analyses were performed using SPSS Statistics version 24.0 (IBM Corporation). Normally distributed continuous variables were presented by mean ± standard deviation, non-normally distributed continuous variables were presented by median (minimum to maximum), and categorical variables were presented by frequency and percentage. The Kolmogorov–Smirnov test was used to check whether variables had normal distribution. The frequency of categorical variables was compared using chi-square tests. The Fisher–Freeman–Halton test was used when there was a problem with expected count. Differences among the three subgroups were analyzed by either One-Way analysis of variance for normally distributed variables or a Kruskal–Wallis test for non-normally distributed variables, and statistical significance was further subjected to Bonferroni post-hoc analysis. Positive coincidence rate, negative coincidence rate, and Cohen's  $\kappa$  coefficient were calculated to evaluate the concordance of morphological evaluation between the two radiologists. A weighted  $\kappa$  value was used if more than two raters were considered. To analyze the reliability of the normally distributed continuous variables, the intraclass correlation coefficient (ICC) was calculated with the Two-Way random, absolute agreement, and single measures method. Linear regression analysis using the enter method was used to examine the effects of age, body mass index, preoperative creatinine, luminal diameter, peristaltic amplitude, and ureteric jet frequency on postoperative split renal function. A two-sided  $P < 0.050$  was considered statistically significant.

## Results

A total of 96 patients completed cine MRU after upper urinary tract reconstruction, and the mean age of the patients was 38.0 ± 13.8 years. The reconstructive strategies included ileal ureter (n = 38, 39.58%), pyeloplasty (n = 21, 21.88%), ureteroneocystostomy (n = 9, 9.38%), Boari flap (n = 7, 7.29%), balloon dilation (n = 6, 6.25%), lingual mucosal ureteroplasty (n = 5, 5.21%), appendiceal uret-

eroplasty (n = 3, 3.13%), endoureterotomy (n = 4, 4.17%), ureteroureterostomy (n = 1, 1.04%), ureterolysis (n = 1, 1.04%), and kidney autotransplantation (n = 1, 1.04%). The characteristics and comparisons in the success, gray, and failure groups are shown in Table 1.

Figure 1 shows the cine MRU imaging of the reconstructed upper urinary tract after different surgical strategies (see Supplementary Videos 1-10 for the video results). The positive coincidence rate, negative coincidence rate, and the Cohen's  $\kappa$  coefficient values are shown in Table 2 for the evaluation of anastomotic stenosis, regular peristalsis, ureteral jet, and reflux. The ICC of diameter and amplitude were 0.999 [95% confidence interval (CI) (0.615–1.000),  $P < 0.001$ ] and 0.996 [95% CI (0.898–0.999),  $P < 0.001$ ], respectively. The weighted  $\kappa$  value of the frequency of ureteral jets was 0.958 [95% CI (0.923–0.992),  $P < 0.001$ ]. There was no obvious stenosis

of the anastomosis in 83 patients (86.46%). Regular peristalsis of the ureter and urination signals were observed in 85 (88.54%) and 84 patients (87.50%), respectively. In addition, three patients (3.13%) had urine reflux when asked to urinate. The specific parameters of cine MRU according to different surgical strategies are shown in Supplementary Table 1. Linear regression analysis showed that diameter ( $P = 0.153$ ), amplitude ( $P = 0.565$ ), and frequency of ureteric jet ( $P = 0.220$ ) cannot predict the postoperative split renal function (Table 3 and Supplementary Table 2).

The patients in both the success and gray area groups showed significantly different creatinine levels (success:  $86.2 \pm 22.3 \mu\text{mol/L}$  vs. failure:  $110.7 \pm 8.2 \mu\text{mol/L}$ ,  $P = 0.016$ ; gray area  $81.0 \pm 20.0 \mu\text{mol/L}$  vs. failure:  $110.7 \pm 8.2 \mu\text{mol/L}$ ,  $P = 0.009$ ) and eGFR (success  $88.5 \pm 23.1 \text{ mL/min}\cdot 1.73 \text{ m}^2$  vs. failure:  $61.6 \pm 14.1 \text{ mL/min}\cdot 1.73 \text{ m}^2$ ,  $P = 0.014$ ; gray area:  $94.7 \pm 24.6 \text{ mL/min}\cdot 1.73 \text{ m}^2$  vs. failure:  $61.6 \pm$

$14.1 \text{ mL/min}\cdot 1.73 \text{ m}^2$ ,  $P = 0.007$ ) compared to those in the failure group. The ipsilateral split renal function was  $33.6 \pm 15.0$ ,  $24.5 \pm 13.4$ , and  $20.1 \pm 0.4 \text{ mL/min}$  in the success, gray area, and failure groups respectively, without significant differences ( $P = 0.354$ ) (Table 4).

## Discussion

The transportation of urine depends on the peristalsis of the ureter and hydrostatic pressure of the upper urinary tract.<sup>8</sup> Some pathological conditions have been highlighted as interfering with ureter contraction and triggering dysfunction.<sup>1</sup> Since the effects of long-term hydrostatic expansion and surgical operations on the smooth muscle of the ureter cannot be ignored, postoperative evaluation for the reconstructed upper urinary tract should provide more information to clarify the entire urination process.<sup>9</sup>

**Table 1.** Baseline characteristics of patients and comparisons in different groups

	Success	Gray area	Failure	P value
n	83 (86.46%)	8 (8.33%)	5 (5.21%)	
<b>Gender</b>				1.000
Male	39 (46.99%)	4 (50.00%)	2 (40.00%)	
Female	44 (53.01%)	4 (50.00%)	3 (60.00%)	
Age (years)	$38.0 \pm 13.4$	$36.5 \pm 21.4$	$40.2 \pm 6.6$	0.897
BMI (kg/m <sup>2</sup> )	$22.8 \pm 4.4$	$20.6 \pm 3.0$	$24.0 \pm 2.9$	0.391
<b>Side</b>				0.336
Left	40 (48.19%)	3 (37.50%)	1 (20.00%)	
Right	34 (40.96%)	4 (50.00%)	2 (40.00%)	
Bilateral	9 (10.84%)	1 (12.50%)	2 (40.00%)	
<b>Location</b>				-
Upper	37 (44.58%)	2 (25.00%)	2 (40.00%)	
Middle	9 (10.84%)	0 (0%)	2 (40.00%)	
Lower	31 (37.35%)	6 (75.00%)	1 (20.00%)	
Multiple	1 (1.20%)	0 (0%)	0 (0%)	
Unknown	5 (6.02%)	0 (0%)	0 (0%)	
Stricture length (cm)	$8.5 (0.5-30.0)$	$1.1 (1.0-5.0)$	$10.0 (5.0-21.0)$	0.081
<b>Symptoms</b>				-
Flank pain	31 (37.35%)	2 (25.00%)	1 (20.00%)	
Fever	7 (8.43%)	0 (0%)	0 (0%)	
Nausea or vomit	3 (3.61%)	2 (25.00%)	1 (20.00%)	
Hematuria	4 (4.82%)	0 (0%)	0 (0%)	
Abdominal pain	4 (4.82%)	0 (0%)	0 (0%)	
Anasarca	1 (1.20%)	0 (0%)	0 (0%)	
Asymptomatic	33 (39.76%)	4 (50.00%)	3 (60.00%)	
Preoperative creatinine ( $\mu\text{mol/L}$ )	$81.8 \pm 25.6$	$92.9 \pm 47.9$	$108.5 \pm 22.4$	0.079
Preoperative ipsilateral split renal function (mL/min)	$32.1 \pm 17.1$	$43.0 \pm 15.6$	$30.0 \pm 15.6$	0.663

BMI, body mass index.

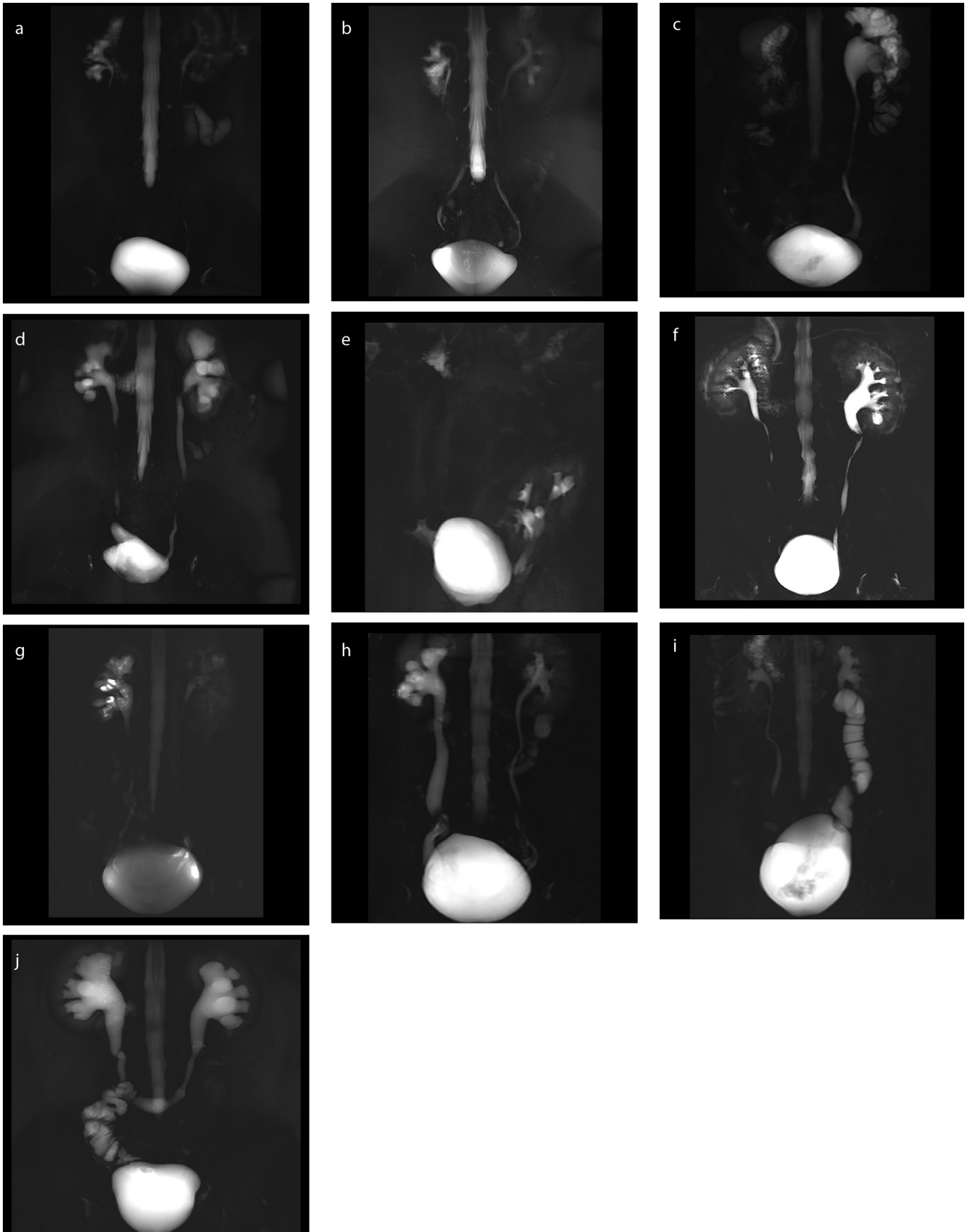


**Figure 1.** Cine magnetic resonance urography imaging of reconstructed upper urinary tract after different surgical strategies. (a) Ureteroureostomy, (b) ureteroneocystostomy, (c) pyeloplasty, (d) Boari flap, (e) kidney autotransplantation, (f) lingual mucosa graft ureteroplasty, (g) appendiceal ureteroplasty, (h) megaureter, (i) ileal ureter, (j) bilateral ileal ureter

**Table 2.** Consistency analysis of the morphological evaluation in cine magnetic resonance urography between two radiologists

	Positive coincidence rate	Negative coincidence rate	$\kappa$ value	<i>P</i> value
Anastomotic stenosis	0.988	0.923	0.911	<0.001
Regular peristalsis	1.000	0.909	0.947	<0.001
Ureteral jet	1.000	1.000	1.000	<0.001
Reflux	1.000	1.000	1.000	<0.001

**Table 3.** Linear regression analysis of postoperative ipsilateral split renal function

	$\beta$	95% CI	Adjusted R square	<i>P</i> value*
Age (years)	-0.274	-0.653–0.105	0.035	0.151
BMI (kg/m <sup>2</sup> )	-0.770	-2.110–0.570	0.004	0.248
Preoperative creatinine ( $\mu$ mol/L)	-0.195	-0.373–0.018	0.112	0.032
Diameter (mm)	-0.641	-1.537–0.255	0.045	0.153
Amplitude (mm)	-0.209	-0.932–0.513	0.005	0.565
Jet	1.635	-1.040–4.310	0.021	0.220

\*The *P* values of the regression model and the coefficient are the same for simple linear regression.  $\beta$ , unstandardized regression coefficient; CI, confidence interval; BMI, body mass index.

**Table 4.** The postoperative creatinine, eGFR, and split renal function in the success, gray area, and failure groups

	Creatinine ( $\mu$ mol/L)	eGFR (mL/min·1.73 m <sup>2</sup> )	Ipsilateral split renal function (mL/min)
Success	86.2 ± 22.3	88.5 ± 23.1	33.6 ± 15.0
Gray	81.0 ± 20.0	94.7 ± 24.6	24.5 ± 13.4
Failure	110.7 ± 8.2	61.6 ± 14.1	20.1 ± 0.4
<i>P</i> value			
Overall	0.016	0.007	0.354
Success vs. failure	0.016	0.014	-
Gray vs. failure	0.009	0.007	-
Success vs. gray	0.613	0.564	-

eGFR, estimated glomerular filtration rate.

The diameter of the normal ureter is 1–6 mm.<sup>10,11</sup> In our study, the average diameter of the ureter lumen after the operation was larger than normal. The reconstructed upper urinary tract often fails to fully return to normal. However, we found that diameter and peristaltic amplitude were not significantly correlated with postoperative renal function as long as the anastomosis was not narrowed. Routine postoperative examinations only evaluate the degree of upper urinary tract dilatation and do not truly reflect the patient's recovery.<sup>12</sup> Therefore, it is necessary to consider the morphology and quantitative information of the dilated reconstructive upper urinary tract.

Cine MRU provides high-contrast-resolution images with detailed information to demonstrate the general morphology of the postoperative upper urinary tract, including not only peristalsis but also the presence of fixed stenoses.<sup>13</sup> Dynamic images showed that ureteral stenosis disappeared and that

urine could pass smoothly in a small portion of patients who had suspected anastomotic stenosis, which may have been due to pseudolumen stenosis caused by postoperative inflammation and thickening of the wall. In addition, our results showed that the fixed stenosis had an impact on the recovery of postoperative renal function. Therefore, stenosis captured by cine MRU images requires further treatment to protect renal function.

A previous study has confirmed that urine flow and ureteric jets could be visualized in cine MRU as low-signal waves.<sup>13</sup> Observation of the urine jet is strong evidence that the reconstructed upper urinary tract is capable of transporting urine, and it is also prevents complete ureteral obstruction.<sup>14,15</sup> Moreover, the ureteric jet is affected by the diameter and contraction of the ureter.<sup>16</sup> The frequency of ureteric jets also changed accordingly. For unilateral ureteral surgery, the ureteric jets of the contralateral ureter can be used as a reference.

The definition of successful reconstruction in previous studies mainly relied on the relief of symptoms and the relief of obstruction, as is shown in images.<sup>17</sup> Tseng et al.<sup>18</sup> evaluated the success of ureteral reconstruction, where they reduced overestimation of the success rate by a trifecta outcome, which was defined as reserved renal function, no progression of hydronephrosis, and no long-term stent placement. However, the evaluation criteria were relatively subjective.

In the present study, surgical outcomes were divided into success, gray area, and failure categories, combining the results of cine MRU, symptoms, and the degree of hydronephrosis. The creatinine levels and eGFRs of patients were significantly worse in the failure group compared to the success and gray area groups. The split renal function gradually decreased in the success, gray area, and failure groups, but there were no statistically significant differences. We considered that the sample size was not large

enough to reach significant results. Therefore, we proposed that patients in the failure group should receive surgical treatment again to save ipsilateral renal function, while those in the gray area should receive active surveillance, which helps identify abnormalities and determine subsequent strategies. Regular follow-up was sufficient for patients who were evaluated as having a successful outcome.

For the upper urinary tract without hydronephrosis, cine MRU is not recommended for postoperative follow-up. The ureter is long, tortuous, and has a thin lumen. Compared to the heart and uterus, the target is smaller and the variation is greater.<sup>19</sup> It is not easy to obtain a complete upper urinary tract image in the coronal position. In this study, patients with an unclear or not developed ureter had symptom relief and normal renal function during follow-up. Therefore, we recommend using the ultrasound results as the basis for further performance of cine MRU.

There were some limitations to our study. First, the index evaluation of cine MRU needed to be done manually. It is difficult to avoid visual differences between different observers. In addition, the quantitative method of analysis was time-consuming. Second, it is important to determine the quantitative criteria to further standardize the evaluation of cine MRU.<sup>20</sup> Third, the quantitative measurement of urine flow and velocity would help in further understanding the upper urinary tract urination function. At present, it has been reported that four-dimensional flow MR is useful in the cardiovascular field,<sup>21</sup> and additional studies should focus on this issue. Finally, the patients included in this study had different severities of preoperative hydronephrosis and different treatment modalities were adopted, which may lead to bias. Therefore, larger sample sizes are needed in the future.

In conclusion, cine MRU allows for an innovative view of the excretion process of urine. Dynamic images demonstrate the morphology and function of the postoperative upper urinary tract. The results of cine MRU can be used to evaluate the surgical effect by classi-

fying surgical results into success, gray area, or failure categories, thereby providing guidance for further treatment. For non-dilated ureters, the effect of cine MRU is poor.

### Conflict of interest disclosure

The authors declared no conflicts of interest.

## References

1. Whitaker RH. Some observations and theories on the wide ureter and hydronephrosis. *Br J Urol.* 1975;47(4):377-385. [\[CrossRef\]](#)
2. Soares DM, Junior HW, Bittencourt LK, Lopes FPPL, de Oliveira MAP. The role of cine MR imaging in the assessment of uterine function. *Arch Gynecol Obstet.* 2019;300(3):545-553. [\[CrossRef\]](#)
3. Curtis AD, Cheng HM. Primer and historical review on rapid cardiac CINE MRI. *J Magn Reson Imaging.* 2022;55(2):373-388. [\[CrossRef\]](#)
4. Liu S, Zhang Q, Yin C, et al. Optimized approach to cine MRI of uterine peristalsis. *J Magn Reson Imaging.* 2016;44(6):1397-1404. [\[CrossRef\]](#)
5. Hoad C, Clarke C, Marciani L, Graves MJ, Corsetti M. Will MRI of gastrointestinal function parallel the clinical success of cine cardiac MRI? *Br J Radiol.* 2019;92(1093):20180433. [\[CrossRef\]](#)
6. de Jonge CS, Smout AJPM, Nederveen AJ, Stoker J. Evaluation of gastrointestinal motility with MRI: advances, challenges and opportunities. *Neurogastroenterol Motil.* 2018;30(1). [\[CrossRef\]](#)
7. Abreu-Gomez J, Udare A, Shanbhogue KP, Schieda N. Update on MR urography (MRU): technique and clinical applications. *Abdom Radiol (NY).* 2019;44(12):3800-3810. [\[CrossRef\]](#)
8. Vahidi B, Fatouree N. A numerical simulation of peristaltic motion in the ureter using fluid structure interactions. *Annu Int Conf IEEE Eng Med Biol Soc.* 2007;2007:1168-1171. [\[CrossRef\]](#)
9. Osman F, Romics I, Nyirády P, Monos E, Nádasy GL. Ureteral motility. *Acta Physiol Hung.* 2009;96(4):407-426. [\[CrossRef\]](#)
10. Zelenko N, Coll D, Rosenfeld AT, Smith RC. Normal ureter size on unenhanced helical CT. *AJR Am J Roentgenol.* 2004;182(4):1039-1041. [\[CrossRef\]](#)

11. Potenta SE, D'Agostino R, Sternberg KM, Tatsumi K, Perusse K. CT Urography for Evaluation of the Ureter. *Radiographics.* 2015;35(3):709-726. [\[CrossRef\]](#)
12. Farrugia MK, Whitaker RH. The search for the definition, etiology, and effective diagnosis of upper urinary tract obstruction: the Whitaker test then and now. *J Pediatr Urol.* 2019;15(1):18-26. [\[CrossRef\]](#)
13. Zhu WJ, Ma MM, Zheng MM, et al. Cine magnetic resonance urography for postoperative evaluation of reconstructive urinary tract after ileal ureter substitution: initial experience. *Clin Radiol.* 2020;75(6):480.e1-480.e9. [\[CrossRef\]](#)
14. de Bessa J Jr, Dénes FT, Chammas MC, et al. Diagnostic accuracy of color Doppler sonographic study of the ureteric jets in evaluation of hydronephrosis. *J Pediatr Urol.* 2008;4(2):113-117. [\[CrossRef\]](#)
15. Lojindarat S, Suwikrom S, Puangsa-art S. Postoperative color Doppler sonography of the ureteral jets to detect ureteral patency in laparoscopic hysterectomy. *J Med Assoc Thai.* 2011;94(10):1169-1174. [\[CrossRef\]](#)
16. Cvitković Kuzmić A, Brkljčić B, Rados M, Galesić K. Doppler visualization of ureteric jets in unilateral hydronephrosis in children and adolescents. *Eur J Radiol.* 2001;39(3):209-214. [\[CrossRef\]](#)
17. Lee M, Lee Z, Koster H, et al. Intermediate-term outcomes after robotic ureteral reconstruction for long-segment ( $\geq 4$  centimeters) strictures in the proximal ureter: a multi-institutional experience. *Investig Clin Urol.* 2021;62(1):65-71. [\[CrossRef\]](#)
18. Tseng CS, Tai TE, Hong CH, et al. Trifecta outcome of ureteral reconstruction in iatrogenic injury and non-iatrogenic ureteral lesions: a 10-year experience at a tertiary referral center. *World J Urol.* 2019;37(9):1949-1957. [\[CrossRef\]](#)
19. Motola JA, Shahon RS, Smith AD. Anatomy of the ureter. *Urol Clin North Am.* 1988;15(3):295-299. [\[CrossRef\]](#)
20. Reiter U, Reiter C, Kräuter C, Nizhnikava V, Fuchsjaeger MH, Reiter G. Quantitative clinical cardiac magnetic resonance imaging. *Rofo.* 2020;192(3):246-256. [\[CrossRef\]](#)
21. Azarine A, Garçon P, Stansal A, et al. Four-dimensional Flow MRI: principles and cardiovascular applications. *Radiographics.* 2019;39(3):632-648. [\[CrossRef\]](#)

---

**Supplementary Video 1.** Cine magnetic resonance urography imaging after ureterouretostomy

<https://www.youtube.com/shorts/oPRtOb-aJdY>

**Supplementary Video 2.** Cine magnetic resonance urography imaging after ureteroneocystostomy

<https://www.youtube.com/shorts/xWGUvFDfo0>

**Supplementary Video 3.** Cine magnetic resonance urography imaging after pyeloplasty

<https://www.youtube.com/shorts/udUPge8w2nQ>

**Supplementary Video 4.** Cine magnetic resonance urography imaging after Boari flap

<https://www.youtube.com/shorts/GcaSR-DmHys>

**Supplementary Video 5.** Cine magnetic resonance urography imaging after kidney autotransplantation

<https://www.youtube.com/shorts/MYWhO5oihs>

**Supplementary Video 6.** Cine magnetic resonance urography imaging after lingual mucosa graft ureteroplasty

<https://www.youtube.com/shorts/ueQl1XyT9Y4>

**Supplementary Video 7.** Cine magnetic resonance urography imaging after appendiceal ureteroplasty

<https://www.youtube.com/shorts/PklzrLPNa4>

**Supplementary Video 8.** Cine magnetic resonance urography imaging after megaureter

<https://www.youtube.com/shorts/etjvoPvj5YQ>

**Supplementary Video 9.** Cine magnetic resonance urography imaging after ileal ureter

<https://www.youtube.com/shorts/ImMePNKj2A>

**Supplementary Video 10.** Cine magnetic resonance urography imaging after bilateral ileal ureter

[https://www.youtube.com/shorts/CxA\\_Se3fbeY](https://www.youtube.com/shorts/CxA_Se3fbeY)



**Supplementary Table 1.** Detailed information of morphology and quantification in cine MRU

Surgery	Ureter		Dilation		Calyces	Regular peristalsis	Unobstructed anastomosis	Urine jet	Reflux	Diameter (mm)	Amplitude (mm)	Contraction ratio	Urine jet frequency
	Ureter	Pelvis	Pelvis	Ureter									
Pyeloplasty	-	21 (100%)	21 (100%)	11 (52.38%)	21 (100%)	21 (100%)	17 (80.95%)	0 (0%)	4.18 (1.54–7.69)	3.65 (2.07–4.90)	0.301 (0.161–0.540)	4 (0–11)	
Ureteroureterostomy	0 (0%)	1 (100%)	1 (100%)	1 (100%)	1 (100%)	1 (100%)	1 (100%)	0 (0%)	-	2.00	1.00		
Ureteroneocystostomy	6 (66.67%)	9 (100%)	9 (100%)	8 (88.89%)	9 (100%)	9 (100%)	6 (66.67%)	2 (22.22%)	5.47 (2.74–9.73)	3.94 (3.22–5.74)	0.419 (0.371–0.540)	2 (0–4)	
Boari flap	5 (71.43%)	6 (85.71%)	6 (85.71%)	7 (100%)	5 (71.43%)	5 (71.43%)	7 (100%)	0 (0%)	7.32 (3.34–25.57)	5.44 (4.23–6.37)	0.430 (0.406–0.620)	3.5 (1–5)	
Lingual mucosal graft	0 (0%)	5 (100%)	5 (100%)	4 (80.00%)	5 (100%)	5 (100%)	3 (60.00%)	0 (0%)	5.58 (3.87–6.19)	-	-	2 (0–3)	
Appendiceal graft	3 (100%)	3 (100%)	3 (100%)	3 (100%)	3 (100%)	3 (100%)	3 (100%)	0 (0%)	11.77 (5.90–20.12)	-	-	2 (0–2)	
Megaureter	4 (100%)	4 (100%)	4 (100%)	4 (100%)	2 (50.00%)	2 (50.00%)	3 (75.00%)	0 (0%)	12.5 (10.67–15.13)	5.08 (2.57–5.29)	0.346 (0.238–0.528)	5 (0–6)	
Ileal ureter	12 (31.58%)	38 (100%)	38 (100%)	37 (97.37%)	32 (84.21%)	32 (84.21%)	37 (97.37%)	0 (0%)	17.81 (8.01–29.56)	9.77 (4.87–19.90)	0.628 (0.508–790)	3 (0–7)	
Balloon dilation	3 (50.00%)	6 (100%)	6 (100%)	6 (100%)	4 (66.67%)	4 (66.67%)	5 (83.3%)	1 (100%)	5.59 (4.57–16.37)	-	-	4 (0–6)	
Autologous kidney transplantation	1 (100%)	1 (100%)	1 (100%)	1 (100%)	0 (0%)	0 (0%)	1 (100%)	0 (0%)	7.47	1.24	0.166	4	
Adhesion lysis	0 (0%)	0 (0%)	0 (0%)	1 (100%)	1 (100%)	1 (100%)	1 (100%)	0 (0%)	-	-	-	3	

Cine MRU, cine magnetic resonance urography.

**Supplementary Table 2.** The linear regression model with postoperative renal function as the dependent variable using entry method

	$\beta$	95% CI	P value (coefficient)	adjusted R square	P value (model)
Age (years)	-0.142	-0.743–0.458	0.615		
BMI (kg/m <sup>2</sup> )	-0.553	-2.505–1.400	0.549		
Preoperative creatinine ( $\mu$ mol/L)	-0.195	-0.474–0.085	0.155		
Diameter (mm)	-0.765	-2.963–1.432	0.462	0.005	0.459
Amplitude (mm)	0.762	-3.136–4.659	0.678		
Jet	1.738	-2.053–5.528	0.338		

$\beta$ , unstandardized regression coefficient; CI, confidence interval; BMI, body mass index.



# Urethrocytography: a guide for urological surgery?

Patrícia S. Freitas

Ana S. Alves

Paulo S. Correia

João L. Dias

## ABSTRACT

Urethrocytography remains the gold-standard technique for urethral pathology diagnosis. Nowadays, of the various indications for performing urethrocytography, the most common is due to a clinical suspicion of urethral stricture. Due to the high prevalence of strictures and their substantial impact on a patient's quality of life, the examination must allow the location, exclusion of multifocality, and assessment of the extent of the stricture to influence surgical planning. This article intends to demonstrate that the radiologist's role, by performing and interpreting the modality of urethrocytography, influences and is crucial for the urologic therapeutic decision and that the patients who were submitted to reconstruction by urethroplasty had a better success rate. The authors aim to review the radiological anatomy of the male urethra, discuss the modalities of choice for imaging the urethra (retrograde urethrocytography and voiding cystourethrocytography), provide an overview of the different indications for performing the study, examine the different etiologies for urethral strictures, understand the relevance of the different appearances of urethral pathology, and identify the surgical options, especially in the treatment of urethral strictures. Simultaneously, the study exposes cases of urethral trauma, fistulas, diverticulum, and congenital abnormalities.

## KEYWORDS

Male urethra, radiology, surgery, urethral stenosis, urethrocytography, urology

Compared to the female urethra, the male urethra is more prone to develop pathology.<sup>1,2</sup> Urethral stricture is the most common pathological condition. Due to its high occurrence, radiologists must understand the urethral anatomy and typical clinical presentation of the underlying disease besides recognizing its imaging findings. Urethrogram techniques such as retrograde urethrocytography (RUG) and voiding cystourethrocytography (VCUG) are the modalities of choice for imaging the urethra. Given that most urethral strictures need urological intervention, it is also important to understand the most common surgical procedures and their possible complications. An adequate interpretation of the urethrogram, describing the stricture caliber, extension, and location, is crucial and largely influences the urological surgical approach.

## Normal anatomy of the male urethra

The male urethra is a narrow fibromuscular tube that measures about 17.5–20 cm in length and is anatomically separated by the urogenital diaphragm into two sections: the anterior and posterior urethra.<sup>3,4</sup> The urethra begins at the internal urethral orifice in the trigone of the bladder and opens in the fossa navicularis at the external urethral meatus.

The anterior urethra is conventionally divided into the penile and bulbar urethra. The bulbar urethra, being entirely internal, originates at the inferior aspect of the urogenital diaphragm and terminates at the penoscrotal junction.<sup>4</sup> Proximal to the dilated portion, the bulbar urethra assumes a conical shape at the bulbomembranous junction. The penile (or pendulous) part is entirely external and extends from the penoscrotal junction to the external meatus at the penile glands.<sup>3</sup> The periurethral Littre glands lie parallel to the dorsal aspect of the anterior urethra.

From the Department of Radiology (P.S.F. ✉ patriciafreitas958@gmail.com, A.S.A., P.S.C., J.L.D.), Centro Hospitalar Universitário de Lisboa Central, Lisbon, Portugal; Department of Radiology (J.L.D.) Hospital CUF Tejo, Lisbon, Portugal.

Received 26 June 2021; revision requested 26 July 2021; last revision received 2 September 2021; accepted 4 October 2021.



Epub: 21.12.2022

Publication date: 31.01.2023

DOI: 10.5152/dir.2022.21640

The posterior urethra is also divided into two segments: the prostatic and membranous urethra. The prostatic urethra is approximately 3.5 cm long; in its posterior wall, the so-called urethral crest continues into the verumontanum, where the prostatic utricle lies.<sup>3</sup> Distal and lateral to the utricle, the orifices of the prostatic or ejaculatory ducts appear. The prostatic urethra then tapers toward the membranous urethra, the narrowest part of the urethra, which measures approximately 1–1.5 cm long, and ends in the inferior aspect of the urogenital diaphragm. The Cowper glands lie within the urogenital diaphragm, lateral to the membranous urethra, and their ducts empty into the bulbar urethra.<sup>3</sup>

The external sphincter is a striated voluntary muscle located within the urogenital diaphragm and is responsible for active continence.

## Radiological anatomy of the male urethra

RUG is a diagnostic procedure based on the retrograde injection of iodinated contrast media through the urethral meatus. The anterior urethra is better evaluated in retrograde studies, which allows better repletion. In contrast, VCUG is useful for the posterior urethra study. In this technique, the bladder neck opens widely during urination, permitting the identification of normal permeability and distension of the posterior urethra (Figure 1). Additionally, VCUG can help detect bladder abnormalities and is also an indication for studying vesicoureteral reflux.

## Technical procedure

Less invasive than urethroscopy, urethrocystography is frequently requested by urologists to evaluate strictures and decide

the need for surgery and its appropriate approach. It is also requested as the follow-up to surgical procedures such as urethrotomy and urethroplasty.

Table 1 summarizes the material that should be used during the urethrocystography procedure. Although some authors preconized the use of a Foley catheter, it is also a valid option to inject the iodinated contrast directly into the urethral meatus.<sup>3,5</sup> During the procedure, five basic steps should be followed: patient preparation, RUG, cystography, VCUG, and a post-voiding study. Table 2 describes them in detail. Also, some tips and tricks to accomplish a successful examination when faced with RUG difficulties are listed in Table 3.

If the urethral meatus shows a severe stricture, meatotomy, or hypospadias, the conventional method with balloon filling in the tip of the catheter is not useful. Instead, a thinner cannula attached to the syringe should be used, or the contrast could be injected directly into the meatus.

Strictures that resist contrast progression may expel the Foley catheter, and excessive distension of the catheter balloon may tear the mucosa. This statement may be particu-

larly important for patients medicated with anticoagulants or antiaggregants.

The clamp method is a new technique popular in some European hospitals and does not use syringes or the conventional Foley catheter with balloon inflation.<sup>6</sup> This method consists of drip infusion and external compression with a ring and uses a thin pre-lubricated catheter (6-Fr), which is described in more detail in Table 3.<sup>6</sup> A prospective study concluded that this is a simple, effective, and well-tolerated procedure.<sup>6</sup>

## Indications, contraindications, and cautions

In accordance with the practice parameters of the American College of Radiology, the current indications for performing a RUG are urethral strictures (suspicion, follow-up, or pre- or post-surgery), pelvic trauma, urethral diverticula, bladder outlet or urethral obstruction, hematuria, recurrent urinary tract infection (UTI), diminished urinary stream, incomplete voiding, urethral foreign bodies, tumors, fistulae or false passages, post-operative urethral injury, and congenital abnormalities.<sup>7</sup> The indications for VCUG are the same, plus the vesicoureteral reflux; bladder morphology, capacity,

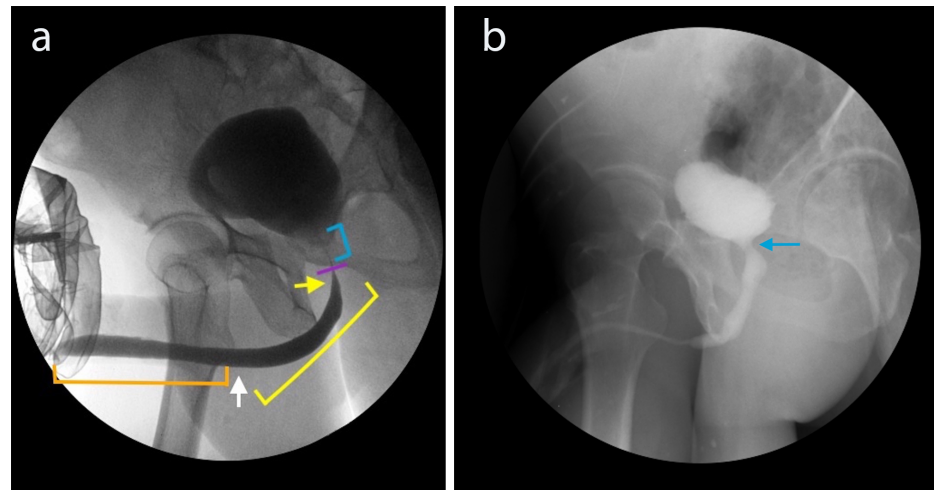


**Figure 1.** RUG (a) and VCUG (b) images show penile urethra (orange bracket, a); penoscrotal junction (white arrow, a); bulbar urethra (yellow bracket, a); bulbomembranous junction assuming conical shape (yellow arrow, a); membranous urethra (purple line, a); prostatic urethra (blue bracket, a) and bladder neck opening (blue arrow, b). RUG, retrograde urethrocystography; VCUG, voiding cystourethrography.

### Main points

- Urethral stricture is a high-prevalence pathology and substantially impacts patients' quality of life.
- Urethrocystography remains the gold-standard technique for urethral pathology diagnosis.
- Urethral dilatation and internal urethrotomy have equivalent long-term success rates, which are significantly lower when compared to the urethroplasty surgical rates.
- The radiologist's role, by performing and interpreting the modality of urethrocystography, influences the urologic therapeutic decision.

**Table 1.** List of the material needed in the radiology department to perform a urethrocystography

Sterile gloves	12-Fr / 14-Fr Foley catheter (100% silicone) (optional)
Lead gloves	Sterile field with a hole
Iodinated contrast water-soluble (ex. Iohexol)	Sterile cup
Physiological saline (NaCl)	Sterile compresses
Distilled water	Lidocaine 2% (ex: lidonostrum)
Bladder syringe 100 mL	Urinal
Syringe 5 mL (optional)	Catheter clamp (optional)

and injury; incontinence; and unexplained intraperitoneal fluid after surgery or trauma.<sup>7</sup>

No absolute contraindications are found in the medical literature for these exams. However, a few relative contraindications are consensual: pregnancy, UTI (antibiotic prophylaxis should be considered in patients with a history of UTI; if an active infection exists, postponing the exam is advised), recent instrumentation, and iodinated contrast allergy, especially if there has been ex-

travasation of contrast from the urethra or bladder.<sup>7</sup>

Complications due to contrast media are rare. Despite that, there might be complications related to the technique, like urethral trauma, intravasation of contrast, and hematuria.

Although it is rare, there might be a few indications for female urethrography. These generally include urethral diverticulum, urethral strictures, and urethral trauma.<sup>1,8</sup> The

latter is one of the most common etiologies because of obstetrical complications.<sup>1,2,8</sup>

## Artifacts and other pitfalls

Several artifacts may occur during the procedure. Radiologists should recognize these findings and not mistake them for pathology.

The kinking artifact occurs due to incorrect positioning by mild or incomplete traction of the penis gland (Figure 2). Filling defects

**Table 2.** Urethrocytography protocol. Description of the five basic steps that should be performed during the procedure

<b>1. Patient preparation</b>	<ul style="list-style-type: none"> <li>- Explain the procedure and the potential discomfort/pain;</li> <li>- Ask the patient to micturate before the examination;</li> <li>- Take a preliminary radiograph (AP view with the center focused just below the pubic bone and also a supine oblique view);</li> <li>- Place the patient in a supine, right posterior oblique position (35°–45°), with the right knee flexed under the extended left leg;</li> <li>- Retract the foreskin for physiological saline cleaning;</li> <li>- Sterile field placement.</li> </ul>
<b>2. RUG</b>	<ul style="list-style-type: none"> <li>- Protect your hands with lead gloves and then put on sterilization gloves.</li> <li>- Prepare the bladder syringe with 100 mL of iodinated contrast diluted in physiological saline (60% + 40%, respectively);</li> <li>- Inject iodinated contrast directly into the urethral meatus. Use your left hand as a clamp by holding the penile gland. With your right hand, introduce the syringe tip into the urethral meatus and inject the contrast media until the patient achieves the voiding sensation. This less invasive method may prevent urethral trauma; however, it might occasionally cause significant contrast media extravasation and lead to more hand radiation exposure. Due to these reasons, you may opt for a different technique, such as the Foley catheter;</li> <li>- Put a small amount of local anesthetic (lidocaine 2%) at the tip of the catheter (some authors do not recommend lubricating the catheter, as it may increase the risk of expulsion);</li> <li>- Place the catheter tip in the fossa navicularis (approximately 2 cm);</li> <li>- Inflate the catheter balloon with 2 cc of distilled water or air;</li> <li>- Moderate traction is required to elongate the urethra, and pressure is applied over the glans to avoid expulsion of the catheter*;</li> <li>- Contrast material is instilled slowly;</li> <li>- Record the anterior urethra distension and the bladder filling;</li> <li>- Clamp the catheter and remove the syringe; then fill in the syringe again with contrast and adjust it to the catheter posteriorly; remove the clamp;</li> <li>- When the patient mentions the need to urinate, we clamp the system, deflate the balloon and remove the catheter.</li> </ul>
<b>3. Cystography</b>	<ul style="list-style-type: none"> <li>- AP and lateral projections radiographs (initial bladder volume).</li> </ul>
<b>4. VCUG</b>	<ul style="list-style-type: none"> <li>- Place the patient in the orthostatic and left-posterior-oblique position (35°–45°);</li> <li>- Fluoroscopy at the moment of voiding.</li> </ul>
<b>5. Post-voiding study</b>	<ul style="list-style-type: none"> <li>- AP and lateral radiographs to document post-void residue volume or a unique AP radiograph to document the absence of residue.</li> </ul>

\*Adequate distention and urethral traction are the keys to preventing overlap, foreshortening, or underestimating strictures; RUG, retrograde urethrocytography; VCUG, voiding cystourethrography; AP, anteroposterior.

**Table 3.** Tips and tricks

RUG and VCUG difficulty	Tips and tricks
<b>Urethral meatus' stricture</b>	<ul style="list-style-type: none"> <li>- If you do not feel comfortable injecting iodinated contrast directly into the urethral meatus with a syringe or if the Foley catheter may be too large, use an infant feeding tube (usually 5-Fr, 8-Fr, or 10-Fr depending on the stenosis degree) or an HSG catheter (5-Fr or 7-Fr with balloon)</li> </ul>
<b>Catheter balloon slipping out</b>	<ul style="list-style-type: none"> <li>- You may use the clamp method: a clamp device connected to a balloon-less catheter and a drip infusion system. The catheter (6-Fr pre-lubricated) is coupled to the device and connected to the infusion system to be purged. The catheter is then inserted into the urethral meatus, and the device is moved in a more proximal direction. The clamp ring will surround the balanoprepuical sulcus, and you must tighten the band to apply external compression. After the preparation, you may open the infusion system and check that there is no extravasation of contrast material so that the RUG can begin.<sup>6</sup></li> <li>- This can also be avoided by externally compressing the penile gland and the catheter balloon with the examiner's hand.</li> </ul>
<b>Female urethrography</b>	<p>Although it is very rarely necessary to evaluate the female urethra, in this case, you may use the:</p> <ul style="list-style-type: none"> <li>- Midori catheter</li> <li>- HSG catheter (5-Fr)</li> <li>- Rubber bulb of the Knutsson clamp (if available).</li> </ul>

RUG, retrograde urethrocytography; VCUG, voiding cystourethrography; HSG, hysterosalpingography.

mostly happen when the Foley catheter is not correctly purged, and an air bubble enters the urethra, which may simulate a urethral stone (Figure 3); however, most of the time, these artifacts are transitory and disappear during the fluoroscopic study. A non-pathological filling defect can also be found in the prostatic urethra caused by a normal anatomical structure, like the verumontanum (Figure 4). The contraction of the constrictor nudae muscle may appear as an anterior indentation in the proximal bulbar urethra, which should not be reported as a focal stricture (Figure 4). The posterior urethra should not be seen as a pathological tapering in the RUG, since it only distends while voiding.

Some normal structures, like Littre glands and Cowper glands and ducts, may be opacified in the urethrogram (Figure 5). Despite being normal, their appearance can be related

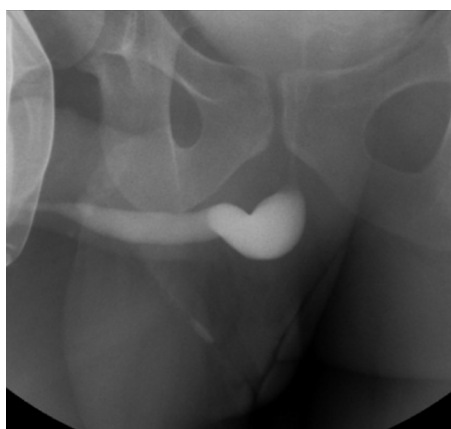
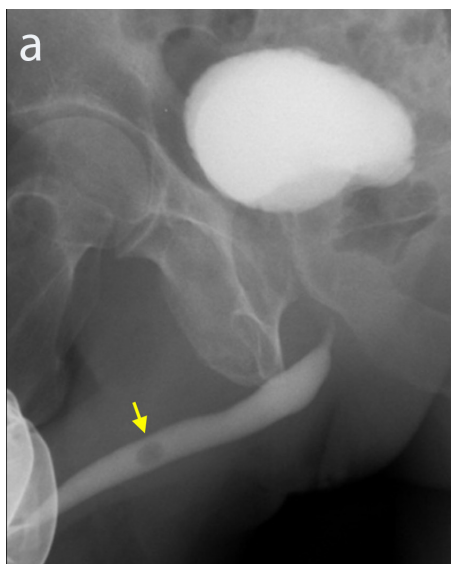


**Figure 2.** RUG demonstrating incomplete traction of the penis gland leading to a kinking artifact. RUG, retrograde urethrocytography.



to pathologies, like strictures or inflammation. The other structures that can be opacified are prostatic ducts and seminal vesicles (Figure 5). It is important to recognize and be aware of the anatomic location of these structures since they may simulate a fistula pathway.

Other artifacts may appear due to extracorporeal extravasation of the contrast material. Similar linear extra-urethral opacifications may be seen due to contrast intravasation into regional vessels (Figure 6). It may be understood as a complication due to high resistance during the contrast administration.

## Urethral pathology

### A. Strictures

Pathology of the male urethra is a common problem and can substantially affect patients' quality of life. It is more common in older adults (>50 years) and usually presents as strictures.<sup>9</sup>

Most patients with a urethral stricture usually show clinically chronic obstructive voiding symptoms. Some may relate the symptoms to a cause, such as a history of prior instrumentation, infection, or injury. However, the etiology of some strictures remains unknown due to the time delay between the symptoms and the causal event.<sup>10</sup>

#### A. 1- Stricture classification

##### A. 1.1- Based on etiology

The main etiologies of strictures are idiopathic, iatrogenic, inflammatory, traumatic,

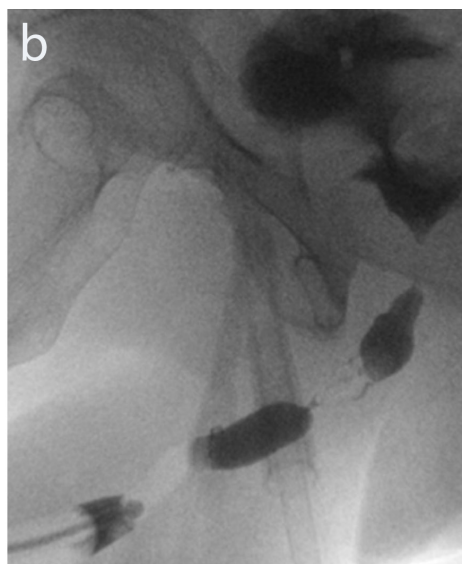


**Figure 3.** RUG (a) and inverted RUG (b) showing transitory filling defects caused by air bubbles artifacts due to an incorrectly purged Foley catheter, which may mimic a urethral stone (yellow arrow, a). RUG, retrograde urethrocytography.

and tumoral.<sup>11</sup> **Iatrogenic strictures** are responsible for approximately 45% of all urethral strictures and usually involve a fixed and narrow location.<sup>9,10,12</sup> They occur mostly in the membranous urethra but also at the penoscrotal junction. The main iatrogenic causes are post-radiotherapy and instrumentation, such as trans-urethral resections, prolonged catheterization, cystoscopy, and hypospadias repair.<sup>10,12</sup> Regarding **idiopathic causes**, there are clinical features that point to strictures being triggered by unrecognized repetitive minor perineal trauma.<sup>13</sup> **Inflammatory stricture** usually involves the proximal bulbar urethra; it may result from infectious urethritis, non-specific urethritis, or Balanitis xerotica obliterans (BXO). **Traumatic strictures** generally involve the bulbomembranous junction and develop rapidly. Usually, they affect short segments and are related to pelvic trauma.<sup>14</sup> Despite the fact that urethral stricture disease may increase the risk of urethral neoplasia by more than 50%, tumoral stricture remains the rarest cause.<sup>9</sup>

However, the etiology varies by population and study. According to Verla et al.<sup>15</sup>, the classification can also be presented as idiopathic, iatrogenic, external trauma, infection, and lichen sclerosus. A multicenter study published in 2013 showed that urethral strictures in the USA and Italy are more iatrogenic rather than caused by external trauma when compared to India (35% vs. 16% and 16% vs. 36%, respectively).<sup>16</sup> Additionally, developing countries face primarily infectious strictures, while in the Western world, one of the most important strictures is iatrogenic.<sup>10,16,17</sup> Concerning the pediatric population, the common causes of urethral stricture are traumatic (36.9%), iatrogenic (31.8%), and idiopathic (28.7%).<sup>18</sup> Congenital strictures, such as congenital bulbar stricture (Cobb's collar), are a very rare entity and are still a subject of controversy.<sup>18</sup>

##### A. 1.2- Based on location

The vast majority of strictures are anterior, especially at the bulbar urethra. They typically result from fibrous scarring due to the proliferation of fibroblasts and collagen, which reduces the urethral width, and are commonly related to spongiofibrosis.<sup>3</sup> On the other hand, the posterior urethra stricture usually results from an obliterative process caused by trauma, surgery, or other iatrogenic procedures such as pelvic radiation.<sup>19</sup>

The main etiologies of **penile urethral strictures** are inflammatory (40%) and iatrogenic (40%). Traumatic and idiopathic ori-

gin account for less incidence (5% and 15%, respectively).<sup>19,20</sup> BXO is the genital form of lichen sclerosus. It usually presents as white plaques on the glans and the foreskin; it is a

chronic inflammatory condition dominated by atrophic rather than proliferative fibrosis.<sup>20</sup> BXO can lead to the distal urethra and meatal stricture, being more severe when it

reaches the penile urethra (Figure 7). Other infectious and inflammatory causes can be due to gonococcal urethritis, nongonococcal urethritis (*Chlamydia trachomatis*), and condyloma and tuberculosis, which are very rare. The iatrogenic causes usually result from post-reconstructive hypospadias surgery, post-urethral instrumentation, and traumatic catheter insertion.<sup>10,11</sup>

The etiology of **bulbar urethral stricture** is idiopathic (40%), iatrogenic (35%), post-traumatic (15%), and inflammatory (10%).<sup>19,20</sup> Generally, post-traumatic bulbar strictures are short in length and classically as a result of a straddle injury (Figure 8). Iatrogenic strictures are common; if occurring after traumatic catheter insertion or prolonged catheter exposure, the bulbar–penile transition is the most frequent site affected. However, if they happen after transurethral resection of the prostate (TURP), then the bulbomembranous transition is the most probable site to be injured. The idiopathic strictures are usually short and occur in young men, mostly at the proximal portion.<sup>20</sup> The infectious etiologies are rare; however, a classic etiological agent is *Gonococcal urethritis*, which is generally responsible for long-segment and irregular strictures (Figure 8).<sup>3,20</sup> It is important to recognize if the stricture extends to the membranous urethra, so the external urinary sphincter is not damaged during surgery.

One of the most common causes of **membranous urethral stricture** is iatrogenic, post-TURP. Due to its location, the associated fibrosis compromises the sphincter function. When there is significant pelvic trauma, the membranous urethral stricture may result from distraction injuries (obliterative stricture).<sup>14</sup>

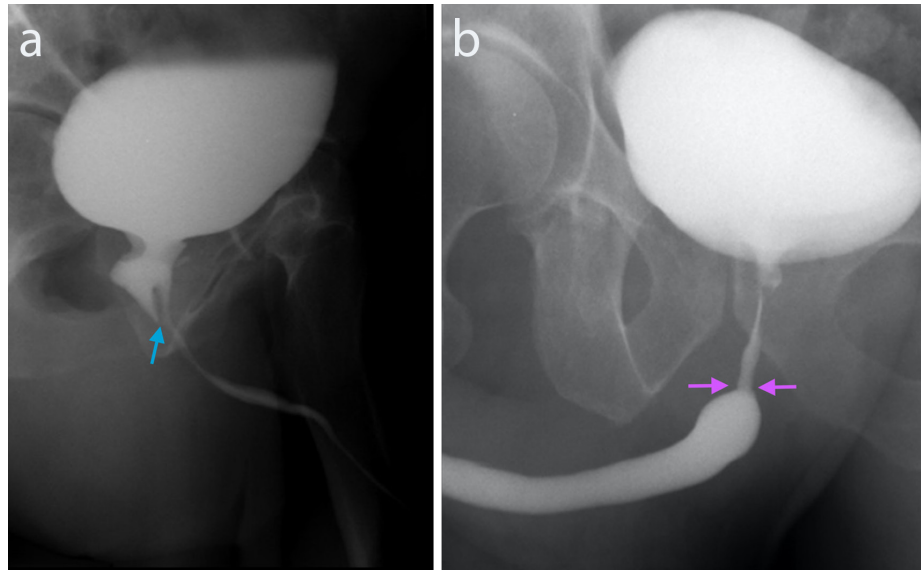


**Figure 4.** (a, b) RUG showing non-pathological filling defects in the prostatic urethra caused by a normal anatomical structure. Verumontanum as a filling defect (blue arrow, a) and normal tapering of the transition of the bulbar urethra to the posterior urethra due to the contraction of the constrictor nudae muscle (purple arrows, b). This must not be reported as a focal stricture since the posterior urethra only distends properly in the VCUG. VCUG, voiding cystourethrography.

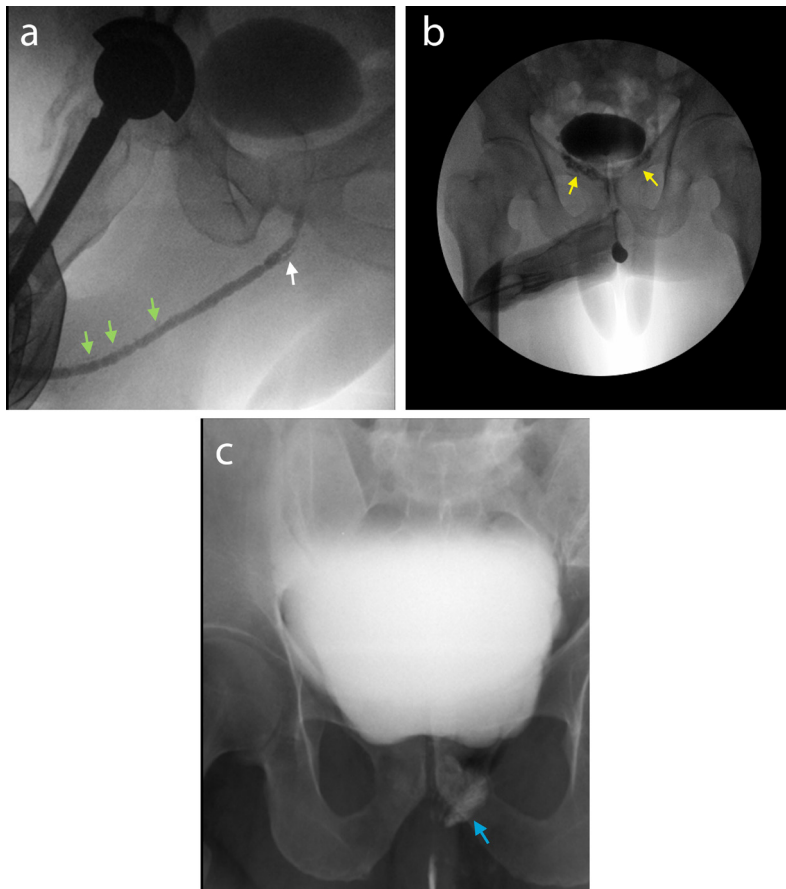


**Figure 5.** (a–c) RUG (a, b) and VCUG (c) show opacified Littre glands (green arrows, a) and opacified Cowper gland (white arrow a), contrast reflux to seminal vesicles (yellow arrows, b) and opacified left prostatic duct (blue arrow, c). RUG, retrograde urethrography; VCUG, voiding cystourethrography.

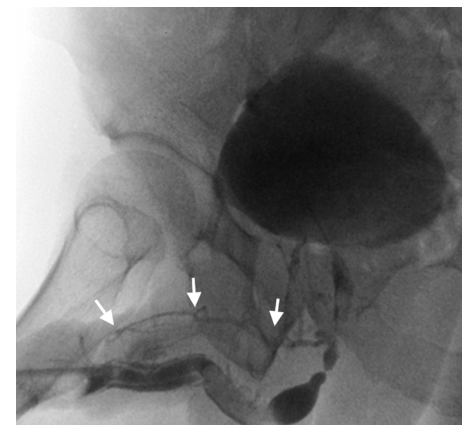


**Figure 6.** RUG shows opacification of the venous system due to high resistance during the urethrogram study (white arrows). RUG, retrograde urethrography.

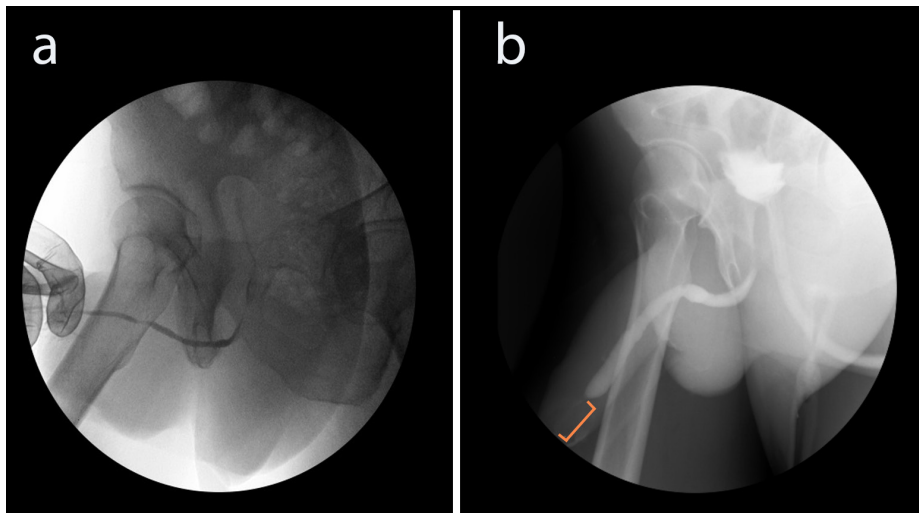


**Figure 7.** (a, b) Two different patients with balanitis xerotica obliterans. The urethrogram shows a filiform anterior urethra due to multiple strictures (a) and a long-segment penile urethra stricture (orange bracket, b). Both patients were proposed for BMG urethroplasty. BMG, buccal mucosal graft.

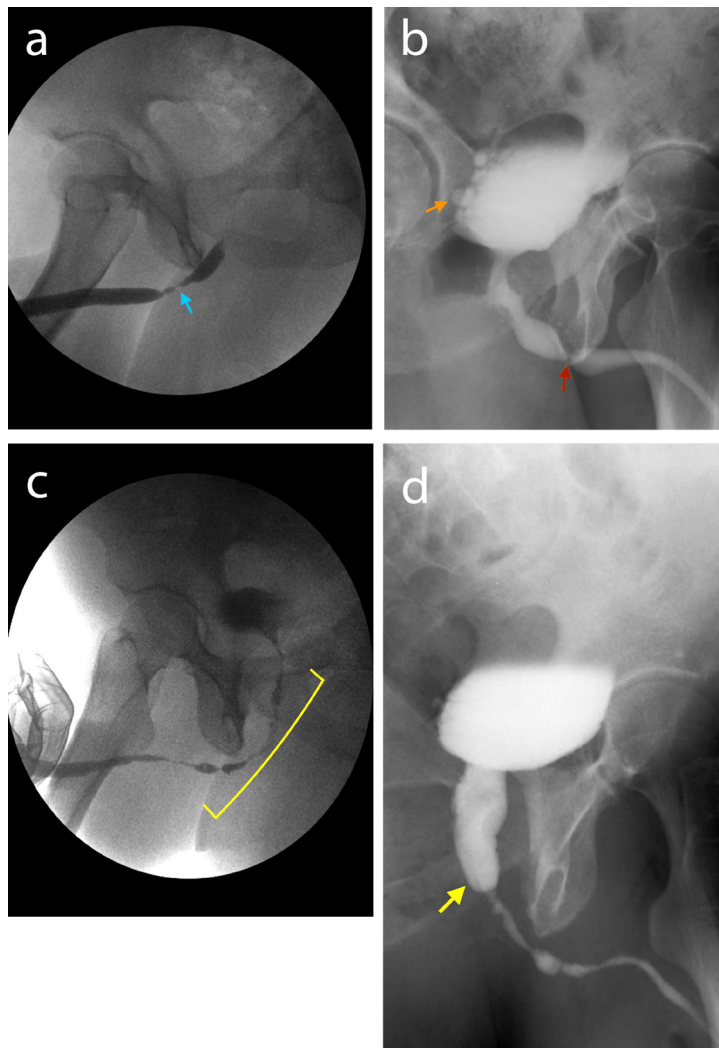


**Figure 8.** Bulbar urethral strictures demonstrated in RUG (a, c) and VCUG (b, d). RUG shows proximal bulbar stricture resulting from a straddle injury in a 45-year-old patient with a post-pelvic trauma status (blue arrow, a). VCUG reveals ring stricture of the proximal bulbar urethra (red arrow, b), causing dilatation of the upstream segments in a patient with gonococcal urethritis. Bladder diverticula (orange arrow, b). Long-segment and irregular bulbar stricture in a 72-year-old patient with a clinical history of previous urethritis (yellow bracket, c). The enlarged caliber of the prostatic urethra (yellow arrow, d) due to the high pressure of the long-segment bulbar stricture. RUG, retrograde urethrocytography; VCUG, voiding cystourethrography.

**Prostatic urethral strictures** usually occur after prostatic treatment (prostatectomy, brachytherapy, or cryotherapy). Strictures of the bladder neck may occur post-TURP.<sup>20</sup>

#### A. 1.3- Based on length and caliber

Usually, there are short-segment strictures, long-segment strictures, multiple strictures, and obliterative strictures. Using Devine's method, urethral strictures can be classified by RUG and sonourethrogram (SUG) as mild, moderate, and severe according to the reduction in the caliber of the urethral lumen (<33%, 33%–50%, and >50%, respectively).<sup>21,22</sup> This is calculated by comparing the caliber of the maximum point of the stricture with the normal urethral caliber outside the stenotic segment length. Focal strictures were also classified into three groups: short, intermediate, and long (<1 cm, 1–2.5 cm, and >2.5–6 cm, respectively).<sup>21,22</sup>

#### A. 2- Stricture complications

Studies have shown that the natural history of untreated urethral stricture disease can lead to complications such as a thick-walled trabeculated bladder (85%), acute urinary retention (60%), prostatitis (50%), epididymal-orchitis (25%), hydronephrosis (20%), peri-urethral abscess (15%), and stones (10%).<sup>9,10</sup> As previously stated, a permanent urethral stricture increases the risk of malignancy by 50%.<sup>9</sup>

#### A. 3- Stricture treatment options

Treatment options for strictures depend on multiple factors. This section explains the different surgical techniques and elucidates the best treatment options for each urethral stricture location.

##### A.3.1- Surgical techniques

###### A.3.1.1- Minimally invasive procedures

The minimally invasive procedures include **urethral dilatation** and **internal urethrotomy (IU)**, the latter showing higher success rates for bulbar strictures <1.5 cm in length. Some studies, such as Steenkamp et al.,<sup>23,24</sup> have shown no difference between these two procedures regarding recurrence rates. They also concluded that both methods are less effective with longer strictures. IU is performed by making a transurethral incision to release the scar tissue, which allows healing by secondary intention at a larger caliber (Figure 9); it has shown a success rate of 8%–80% and a long-term success rate of 20%–30%.<sup>19,25,26</sup>

The minimally invasive procedures show a high risk of recurrence, especially if there is a long segment stricture (80% chance of recurrence if the stricture segment is >4 cm) or multiple strictures.<sup>19</sup> The risk is also greatest at the penile or membranous ure-

thra and if long-length spongiofibrosis is associated. A UTI at the time of the procedure and previous urethral procedures can also contribute to the recurrence.

### A. 3.1.2- Reconstructive surgery

Reconstructive surgery of the urethra shows better long-term success rates, estimated at 85%–90%, and is the most effective method for the definitive correction of urethral stricture.<sup>27,28</sup> It is mostly performed in two ways, end-to-end anastomotic urethroplasty and graft urethroplasties. However, a perineal urethrostomy can also be carried out if there are severe or panurethral strictures, primarily those with BXO or recurrent strictures after hypospadias repairs.<sup>29</sup>

**End-to-end anastomotic urethroplasty** consists of stricture excision followed by anastomotic suturing of the urethral ends; it usually has few complications and has been traditionally used for bulbar strictures <2 cm in length.<sup>30</sup> It is not recommended for penile strictures.

Moreover, **graft urethroplasty** is the gold standard for definitive correction; the procedure consists of a urethrotomy of the stricture with posterior defect closure with a buccal mucosal graft (BMG).<sup>20</sup> This is an effective procedure for strictures longer than two centimeters.

### A. 3.2- Treatment options based on location

Depending on the urethral stricture location, there are specific indications for which treatment is selected. So, it is important to document the precise location of the stricture because it will influence the surgeon's decision.

**Penile urethral stricture:** Usually, it is treated with graft urethroplasty. The patch can be either a penile skin flap or BMG. However, if it is a complicated stricture with suspected lichen sclerosus, urethroplasty using penile skin as a graft should not be used because of the stricture's high recurrence rate.<sup>29</sup> Urethral dilatation or IU can be the initial treatment for meatus or fossa navicularis stricture.

**Bulbar urethral stricture:** For uncomplicated short-segment bulbar strictures, end-to-end anastomotic urethroplasty or minimally invasive procedures are the treatment options. However, if there are long-segment or recurrent short-segment strictures, the treatment of choice is graft urethroplasty.<sup>29</sup>

**Posterior urethral stricture:** In case of complete posterior urethral disruption by pelvic fracture, a bulbomembranous anastomotic urethroplasty should be carried out.<sup>29</sup> However, if the membranous stricture

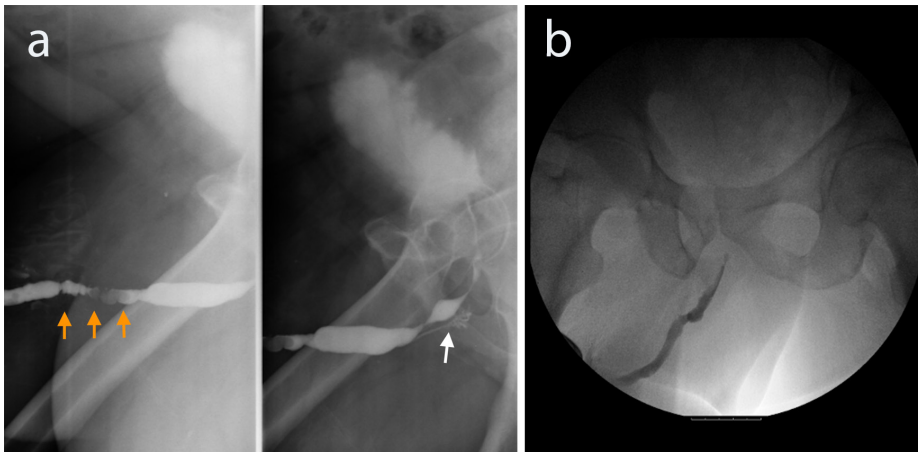


**Figure 9.** Anterior urethral strictures before (a) and after (b) treatment. The 72-year-old patient shows in the RUG multiple ring strictures of the anterior urethra (orange arrow, a) with a Cowper gland opacification due to high pressure (white arrow, a). Three years later, the patient underwent IU, and the RUG showed a favorable evolution of the previous strictures (b). IU, internal urethrotomy; RUG, retrograde urethrocytography.

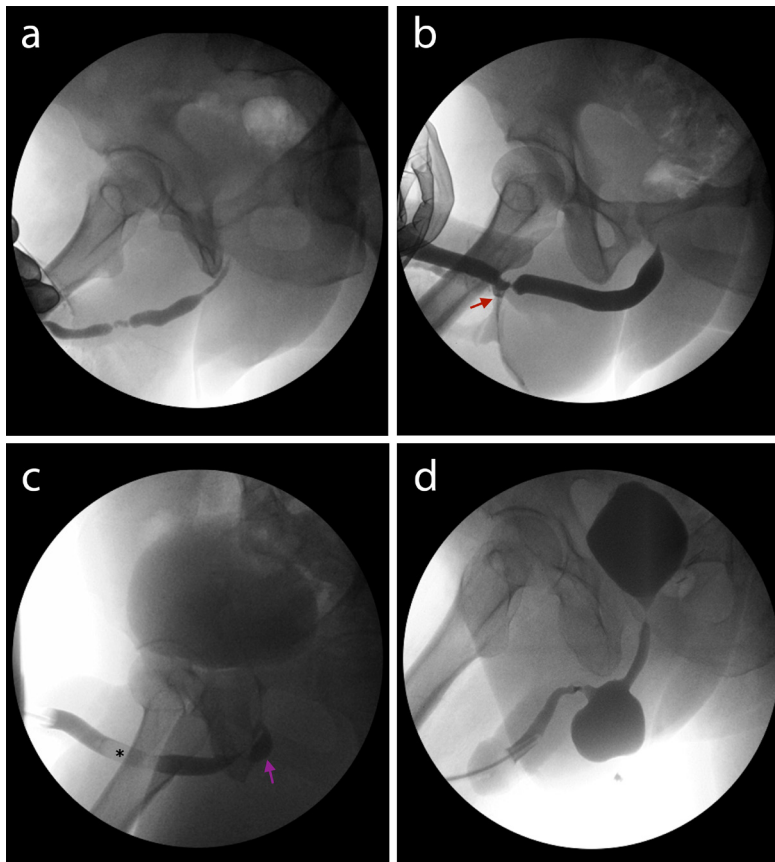


**Figure 10.** RUG showing post-operative complications in four different patients. Recurrent penile urethra stricture in a patient who has already undergone five IUs (a). Penile urethral trauma already submitted to urethroplasty; as a post-surgery complication, a urethral fistula developed at the healing wound (red arrow, b). Post-urethroplasty diverticulum (purple arrow, c); air bubble artifact (\*, c). Status post-artificial urinary sphincter, showing a diverticular image upstream of the stenotic segment (29 × 30 mm), which communicates with the penile urethra, suggestive of a pre-stenotic diverticulum (d). RUG, retrograde urethrocytography; IU, internal urethrotomy.



is secondary to TURP, a urethral dilatation is preferred to preserve the sphincter. Prostatic strictures are uncommon and technically very challenging to treat.

After reconstructive surgery, to allow adequate healing of the tissues without urine exposure, surgeons insert a transurethral catheter and remove it after 7–21 days.<sup>31</sup> Most urethroplasty centers use peri-catheter RUG to evaluate the appropriate time for catheter removal. This technique consists of placing a small-caliber tube (e.g., feeding tube 5-Fr) in the urethral meatus next to the transurethral catheter and injecting contrast alongside the catheter.<sup>31</sup> Although it is not a mandatory routine technique, it may have a crucial role in difficult cases, such as tension anastomoses or when redoing procedures. It will prevent the risk of infection, radiation exposure, and extra cost.<sup>31</sup>

#### A. 4- Post-operative complications

Post-urethroplasty complications are rare.<sup>19</sup> These include urine leaks, post-voiding dribble, UTIs, fistula development, urethral diverticulum, and stricture recurrence (Figure 10). The complications include incontinence, chordee, erectile and ejaculatory dysfunction, and necrosis of the penile skin. However, some studies have shown that after one year of surgical reconstruction, there is no difference in erectile function compared to that preoperatively.<sup>32,33</sup> Harvest site complications might also include pain, oral numbness, and mouth tightness. Recurrent strictures in patients who have already been submitted to urethroplasty are generally treated with IU alone, demonstrating better long-term success rates.<sup>34,35</sup>

#### B. Other urethral pathologies

The urethra is susceptible to trauma because of its relation to the pubic bones and puboprostatic ligaments. Injury to the posterior urethra occurs in 3%–25% of patients with pelvic fractures.<sup>14,36</sup> The posterior urethral trauma usually happens after a crushing force, and the anterior urethra injury generally occurs after a straddling injury.<sup>37</sup> Rarely there might be a penile fracture or a penetrating injury (Figure 11). The Goldman system proposes the classification of urethral injuries for urethrography.

There are also congenital urethral abnormalities (Figure 12). In this category, urethral duplication, megalourethra, posterior urethral valves, congenital urethral stenosis, urethral diverticulum, epispadias, and hypospadias stand out.<sup>38</sup>

Male urethral tumors are a rare condition and represent less than 1% of all urologic cancers in those aged >50 years.<sup>3</sup>

### Complementary techniques

As an additional method, some authors believe that detecting an anterior urethral stricture in RUG indicates retrograde sonourethrography (RSUG).<sup>39</sup> This comes with the fact that RSUG visualizes the peri-urethral tissues and surrounding spongiofibrosis and measures the stenosis more accurately.<sup>39</sup> However, a study has also shown that by considering the radiographic magnification and the application of correct measurement methods, RUG does not underestimate stricture length.<sup>21</sup>

Computed tomography (CT) RUG may be useful in evaluating traumatic urethral injuries and periurethral fistulas.<sup>40,41</sup> A study published

in 2021 on CT-RUG using the clamp method reported no pain in 81% of patients and showed that this technique had better diagnostic efficacy in cases of periurethral fistula, urethral stent, previous urethroplasty, and urethral lithiasis compared to RUG and RSUG.<sup>42</sup>

Recent articles have shown the utility of magnetic resonance imaging (MRI) in urethral stricture disease. This technique can detect spongiofibrosis, reducing the limitation of the subjective SUG examination and giving detailed information about periurethral tissue and anatomic relationships.<sup>43</sup>

### Conclusion

Urethral stricture is a high-prevalence pathology that substantially impacts a patient's quality of life.

Urethrocytography is the standard technique to detect urethral pathology and influences therapeutic decisions. Sometimes the urethrogram study may be complemented with ultrasound, MRI, or CT, which better defines the peri-urethral and adjacent organs.

Urethral stricture treatment depends on multiple factors. Both minimally invasive procedures have equivalent long-term success rates that are significantly lower when compared to urethroplasty surgical rates.

The radiologist's involvement is crucial in the urethrocytography interpretation, initial description, and eventual need for additional diagnostic strategy, demonstrating a consequent impact on the decision of the proper urologic surgical approach.



Figure 11. A 40-year-old man with a bulbar urethral fracture after trauma (orange arrow).

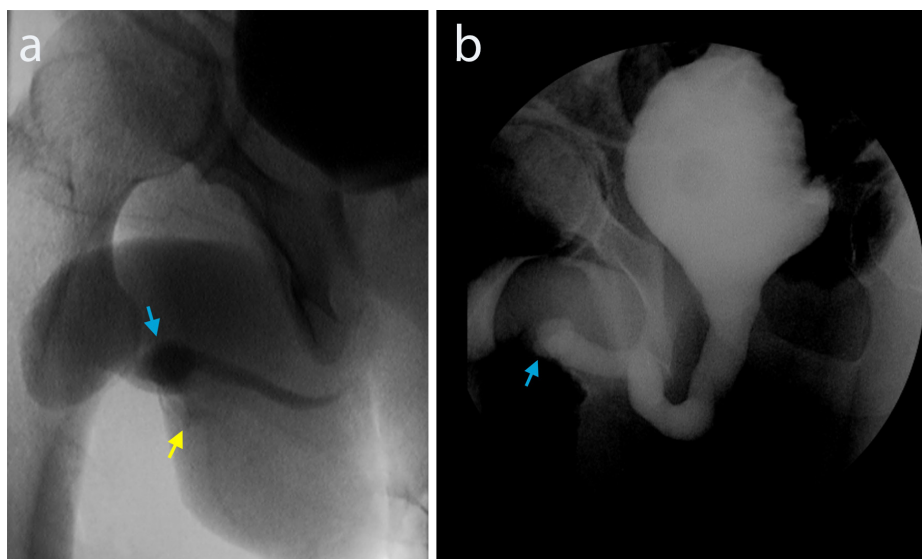


Figure 12. (a, b) Status post-hypospadias surgery. Dilatation of terminal urethra (blue arrow, a and b) and ventral penile fistula (yellow arrow, a).

## Conflict of interest disclosure

The authors declared no conflicts of interest.

## References

1. Patel DN, Fok CS, Webster GD, Anger JT. Female urethral injuries associated with pelvic fracture: a systematic review of the literature. *BJU Int.* 2017;120(6):766-773. [CrossRef]
2. Waterloos M, Verla W. Female urethroplasty: a practical guide emphasizing diagnosis and surgical treatment of female urethral stricture disease. *Biomed Res Int.* 2019;2019:6715257. [CrossRef]
3. Kawashima A, Sandler CM, Wasserman NF, LeRoy AJ, King BF Jr, Goldman SM. Imaging of urethral disease: a pictorial review. *Radiographics.* 2004;24 Suppl 1:S195-S216. [CrossRef]
4. Eaton J, Richenberg J. Imaging of the urethra: Current status. *Imaging.* 2005;17(2):139-149. [CrossRef]
5. Sandler CM, Corriere JN Jr. Urethrography in the diagnosis of acute urethral injuries. *Urol Clin North Am.* 1989;16(2):283-289. [CrossRef]
6. Berná-Mestre JD, Berná-Serna JD, Aparicio-Mesón M, Canteras-Jordana M. Urethrography in men: conventional technique versus clamp method. *Radiology.* 2009;252(1):240-246. [CrossRef]
7. American College of Radiology. ACR-SAR practice parameter for the performance of adult cystography and urethrography; 1992. Revised 2020. [CrossRef]
8. El-Nashar SA, Singh R, Bacon MM, et al. Female urethral diverticulum: presentation, diagnosis, and predictors of outcomes after Surgery. *Female Pelvic Med Reconstr Surg.* 2016;22(6):447-452. [CrossRef]
9. Flanagan JC, Batz R, Nordeck SM, Lemack GE, Brewington C. Urethrography for assessment of the Adult Male Urethra: RadioGraphics Fundamentals | Online Presentation. *Radiographics.* 2018;38(3):831-832. [CrossRef]
10. Lumen N, Hoebeke P, Willemsen P, De Troyer B, Pieters R, Oosterlinck W. Etiology of urethral stricture disease in the 21st century. *J Urol.* 2009;182(3):983-987. [CrossRef]
11. Wessells H, Angermeier KW, Elliott S, et al. Male urethral stricture: American Urological Association Guideline. *J Urol.* 2017;197(1):182-190. [CrossRef]
12. Fenton AS, Morey AF, Aviles R, Garcia CR. Anterior urethral strictures: etiology and characteristics. *Urology.* 2005;65(6):1055-1058. [CrossRef]
13. Viers BR, Pagliara TJ, Rew CA, et al. Characteristics of idiopathic urethral strictures: a link to remote perineal trauma? *Urology.* 2017;110:228-233. [CrossRef]
14. Ingram MD, Watson SG, Skippage PL, Patel U. Urethral injuries after pelvic trauma: evaluation with urethrography. *Radiographics.* 2008;28(6):1631-1643. [CrossRef]
15. Verla W, Oosterlinck W, Spinoit AF, Waterloos M. A comprehensive review emphasizing anatomy, etiology, diagnosis, and treatment of male urethral stricture disease. *Biomed Res Int.* 2019;2019:9046430. [CrossRef]
16. Stein DM, Thum DJ, Barbagli G, et al. A geographic analysis of male urethral stricture aetiology and location. *BJU Int.* 2013;112(6):830-834. [CrossRef]
17. Fall B, Sow Y, Mansouri I, et al. Etiology and current clinical characteristics of male urethral stricture disease: experience from a public teaching hospital in Senegal. *Int Urol Nephrol.* 2011;43(4):969-974. [CrossRef]
18. Ansari MS, Yadav P, Srivastava A, Kapoor R, Ashwin Shekar P. Etiology and characteristics of pediatric urethral strictures in a developing country in the 21st century. *J Pediatr Urol.* 2019;15(4):403.e1-403.e8. [CrossRef]
19. Hampson LA, McAninch JW, Breyer BN. Male urethral strictures and their management. *Nat Rev Urol.* 2014;11(1):43-50. [CrossRef]
20. Mundy AR, Andrich DE. Urethral strictures. *BJU Int.* 2011;107(1):6-26. [CrossRef]
21. Babnik Peskar D, Visnar Perovic A. Comparison of radiographic and sonographic urethrography for assessing urethral strictures. *Eur Radiol.* 2004;14(1):137-144. [CrossRef]
22. Devine CJ Jr. Surgery of the urethra. In: Wals PC, Gittes RF, Perlmutter AD, Stamey TA eds. *Campbell's urology*, 5th edn. Saunders, Philadelphia; 1986:2860-2863. [CrossRef]
23. Steenkamp JW, Heyns CF, de Kock ML. Internal urethrotomy versus dilation as treatment for male urethral strictures: a prospective, randomized comparison. *J Urol.* 1997;157(1):98-101. [CrossRef]
24. Steenkamp JW, Heyns CF, de Kock ML. Out-patient treatment for male urethral strictures—dilatation versus internal urethrotomy. *S Afr J Surg.* 1997;35(3):125-130. [CrossRef]
25. Pansadoro V, Emiliozzi P. Internal urethrotomy in the management of anterior urethral strictures: long-term followup. *J Urol.* 1996;156(1):73-75. [CrossRef]
26. Santucci RA, McAninch JW. Actuarial success rate of open urethral stricture repair in 369 patient open repairs, compared to 210 DIV or dilation. AUA meeting. 2001. [CrossRef]
27. Wong SS, Aboumarzouk OM, Narahari R, O'Riordan A, Pickard R. Simple urethral dilatation, endoscopic urethrotomy, and urethroplasty for urethral stricture disease in adult men. *Cochrane Database Syst Rev.* 2012;12:CD006934. [CrossRef]
28. Naudé AM, Heyns CF. What is the place of internal urethrotomy in the treatment of urethral stricture disease? *Nat Clin Pract Urol.* 2005;2(11):538-545. [CrossRef]
29. Dugi DD 3rd, Simhan J, Morey AF. Urethroplasty for stricture disease: contemporary techniques and outcomes. *Urology.* 2016;89:12-18. [CrossRef]
30. Jordan GH, McCammon KA. Surgery of the penis and urethra. Vol. 1, (Elsevier Saunders, Oxford, 2012;956-1000. [CrossRef]
31. Haider A, Mahmud SM. Pericatheter urethrogram after anastomotic urethroplasty: Is it a must? *Pak J Med Sci.* 2018;34(5):1191-1194. [CrossRef]
32. Erickson BA, Wysock JS, McVary KT, Gonzalez CM. Erectile function, sexual drive, and ejaculatory function after reconstructive surgery for anterior urethral stricture disease. *BJU Int.* 2007;99(3):607-611. [CrossRef]
33. Xie H, Xu YM, Xu XL, Sa YL, Wu DL, Zhang XC. Evaluation of erectile function after urethral reconstruction: a prospective study. *Asian J Androl.* 2009;11(2):209-214. [CrossRef]
34. Santucci RA, Mario LA, McAninch JW. Anastomotic urethroplasty for bulbar urethral stricture: analysis of 168 patients. *J Urol.* 2002;167(4):1715-1719. [CrossRef]
35. Morey AF, Kizer WS. Proximal bulbar urethroplasty via extended anastomotic approach—what are the limits? *J Urol.* 2006;175(6):2145-2149; discussion 2149. [CrossRef]
36. Patel U. Lower urinary tract trauma. In: Patel U, Rickards D, eds. *Imaging and urodynamics of the lower urinary tract.* London, England: Taylor & Francis, 2005:115-121. [CrossRef]
37. Goldman SM, Sandler CM, Corriere JN Jr, McGuire EJ. Blunt urethral trauma: a unified, anatomical mechanical classification. *J Urol.* 1997;157(1):85-89. [CrossRef]
38. Kim B, Kawashima A, LeRoy AJ. Imaging of the male urethra. *Semin Ultrasound CT MR.* 2007;28(4):258-273. [CrossRef]
39. Berná-Mestre JD, Balmaceda T, Martínez D, et al. Optimisation of sonourethrography: the clamp method. *Eur Radiol.* 2018;28(5):1961-1968. [CrossRef]
40. Theisen KM, Kadow BT, Rusilko PJ. Three-dimensional imaging of urethral stricture disease and urethral pathology for operative planning. *Curr Urol Rep.* 2016;17(8):54. [CrossRef]
41. Lv XG, Peng XF, Feng C, Xu YM, Shen YL. The application of CT voiding urethrography in the evaluation of urethral stricture associated with fistula: a preliminary report. *Int Urol Nephrol.* 2016;48(8):1267-1273. [CrossRef]
42. Berná-Mestre JDD, Guzmán-Aroca F, Puerta-Sales A, et al. A new technique for computed-tomography urethrography in males: the clamp method. *Appl Sci.* 2021;11(3):1006. [CrossRef]
43. Frankiewicz M, Markiet K, Krukowski J, Szurowska E, Matuszewski M. MRI in patients with urethral stricture: a systematic review. *Diagn Interv Radiol.* 2021;27(1):134-146. [CrossRef]



# Ovarian dysgerminoma: clues to the radiological diagnosis

Sofia Amante   
Ana Félix   
Teresa Margarida Cunha 

## ABSTRACT

Ovarian dysgerminoma (OD) is a rare germ cell tumor accounting for 1%–2% of all malignant ovarian tumors and is generally associated with a good prognosis. The condition is more frequent in young women and can arise in dysgenetic gonads that contain gonadoblastomas. While the definitive diagnosis of OD is only possible histologically, certain radiological features can provide facilitating clues. A large, unilateral, solid, lobulated ovarian tumor with markedly enhancing septa should raise the suspicion of OD in young women. Serum lactate dehydrogenase is characteristically elevated in this tumor type and can complement its diagnosis and postoperative follow-up; however, it is a nonspecific marker. Moreover, knowing the mimickers of OD is essential to optimizing the radiological image interpretation and allowing for adequate management and timely treatment. Therefore, in this article, the radiological and clinical-pathologic features of ODs were reviewed to allow radiologists to become familiarized with them and narrow the diagnostic possibilities when facing this type of tumor.

## KEYWORDS

Computed tomography, magnetic resonance imaging, ovarian dysgerminoma, radiology, ultrasound

Ovarian tumors are divided into epithelial neoplasms, mesenchymal neoplasms, sex cord-stromal tumors, and germ cell tumors.<sup>1</sup> According to the 2020 World Health Organization Classification of Tumors, ovarian germ cell tumors include mature and immature teratoma, dysgerminoma, yolk sac tumors (YSTs), embryonal carcinoma, non-gestational choriocarcinoma, mixed germ cell tumors, monodermal teratomas and somatic type, and germ cell-sex cord-stromal tumors.<sup>1</sup> Ovarian dysgerminoma (OD) is a rare malignant tumor that derives from primordial germ cells and constitutes the female equivalent of testicular seminoma.<sup>1-9</sup> This type of tumor accounts for 1%–2% of malignant ovarian tumors and constitutes the most common ovarian malignant germ cell neoplasm, with an incidence rate of 32.8%–37.5%.<sup>1-10</sup>

While OD can occur at any age, females in their second to third decades of life are the most affected, and 15%–20% are diagnosed during pregnancy or post-childbirth.<sup>4-9</sup> However, the pathogenesis is still not well understood. The attendant theories suggest that OD can emerge from gonadoblastomas associated with gonadal dysgenesis or directly from primordial germ cells with spontaneous *KIT* gene mutations.<sup>5,6,10</sup> In rare cases, gonadoblastomas can arise in females without chromosomal abnormalities or gonadal dysgenesis.<sup>10</sup> In contrast to other germ cell tumors, OD can occur in both ovaries in 10%–15% of cases,<sup>1-3</sup> while the right ovary is generally the most affected, largely due to its slower differentiation.<sup>2</sup> While most patients are symptomatic, presenting a palpable pelvic or abdominal mass, OD may be present in asymptomatic women.<sup>6,8</sup> Menstrual disorders, abdominal enlargement and severe pain, explained by torsion, hemorrhage, or tumor rupture, are among the attendant complaints.<sup>2-6</sup>

High lactate dehydrogenase (LDH) levels are often associated with OD and can be used to complement the diagnosis and assist in postoperative follow-ups; however, this presents a non-specific laboratory finding.<sup>2-6,8-12</sup> In 3%–5% of cases, OD also contains syncytiotrophoblastic cells, which produce low quantities of human chorionic gonadotropin.<sup>1,4-7</sup> This feature can be responsible for endocrine abnormalities and for stimulating pregnancy.<sup>5,6</sup>

From the Department of Radiology, (S.A. ✉ sofia.ma.1990@gmail.com), Hospital do Divino Espírito Santo de Ponta Delgada; (T.M.C.), Instituto Português de Oncologia de Lisboa Francisco Gentil, Lisbon, Portugal; Department of Pathology, (A.F.) Instituto Português de Oncologia de Lisboa Francisco Gentil; NOVA Medical School - Universidade NOVA de Lisboa, Lisbon, Portugal

Received 22 March 2021; revision requested 27 April 2021; last revision received 2 September 2021; accepted 4 October 2021



Epub: 21.12.2022

Publication date: 31.01.2023

DOI: 10.5152/dir.2022.21317

You may cite this article as: Amante S, Félix A, Cunha TM. Ovarian dysgerminoma: clues to the radiological diagnosis. *Diagn Interv Radiol.* 2023;29(1):18-23.

Generally speaking, OD spreads late, typically through the lymph system (28% of cases).<sup>4</sup> Peritoneal implantation occurs when tumor rupture is present.<sup>4</sup> This malignancy generally has an excellent prognosis, with almost 100% at the five-year survival rate, even when chemotherapy is needed.<sup>1-6</sup> Furthermore, around 75% of ODs are detected at an early stage, with surgery the main treatment option.<sup>8,9</sup>

Studies have reported that OD imaging reveals a large, multilobulated mass, predominantly solid, with lobules divided by fibrovascular septa.<sup>6-10</sup> While various radiological clues can help in diagnosing OD, accurate preoperative diagnosis using radiologic findings alone remains a challenge. Nonetheless, radiologists must be aware of this tumor's main characteristics, both in terms of the different imaging methods and the attendant pathology and markers, to reduce the differential diagnosis. This article thus reviews the imaging appearance of OD using a multimodal approach and explores its differential diagnoses.

## Morphology and histopathology

Macroscopically, ODs are large, solid, multinodular tumors, which appear fleshy, yellow, or cream-colored (Figure 1).<sup>4-6</sup> Areas of necrosis, hemorrhage, and cystic degeneration may occur,<sup>1,4-6</sup> while calcifications can also be seen in dysgerminomas, typically with a speckled or spotted pattern.<sup>1,2</sup> Grossly visible calcifications only occur in dysgerminomas arising from a pre-existing gonadoblastoma with calcifications described as mottled or punctate. However, calcifications may also be detected in dysgerminomas without an underlying recognizable gonadoblastoma.<sup>2</sup>

Microscopically, ODs are generally composed of round cell nests separated by thin fibrous septa infiltrated by lymphocytes (Figure 1).<sup>1,4-6</sup> Tumor cells are large and polygonal in shape with clear or eosinophilic cytoplasm containing a large central nucleus.<sup>1,4-6</sup> Mitoses are often abundant.<sup>4-6</sup> Immunohistochemically, OD can be positive for octamer-binding transcription factor 4, Sal-like protein 4, LIN28, NANOG, KIT (CD117) and D2-40, and negative for epithelial membrane antigen, CD30 and GPC3, while cytokeratins may be focally positive.<sup>1</sup>

## Radiological findings

### Ultrasound

On ultrasound imaging, OD frequently appears as a solid mass without specific features.<sup>3</sup> In most cases, it consists of a mul-

tilobulated tumor with smooth contours, well-defined borders, and heterogeneous echogenicity, characterized by prominent fibrovascular septa.<sup>4-6</sup> Necrosis, hemorrhagic areas, and speckled calcifications may also be depicted (Figure 1).<sup>2-5</sup> Under color or power Doppler ultrasound imaging, OD is highly vascularized, revealing a prominent flow in the septa (Figures 1-3).<sup>4-6</sup>

### Computed tomography (CT)

While the classic septa of OD are generally thin, in the presence of stromal edema, they can become thickened or amorphous with low attenuation on CT examination (Figure 3).<sup>2</sup> Due to their fibrous content, septa frequently demonstrate avid enhancement on contrast-enhanced CT imaging (Figure 3).<sup>2-5</sup> Moreover, hyperdense and speckled calcifications have been observed in this type

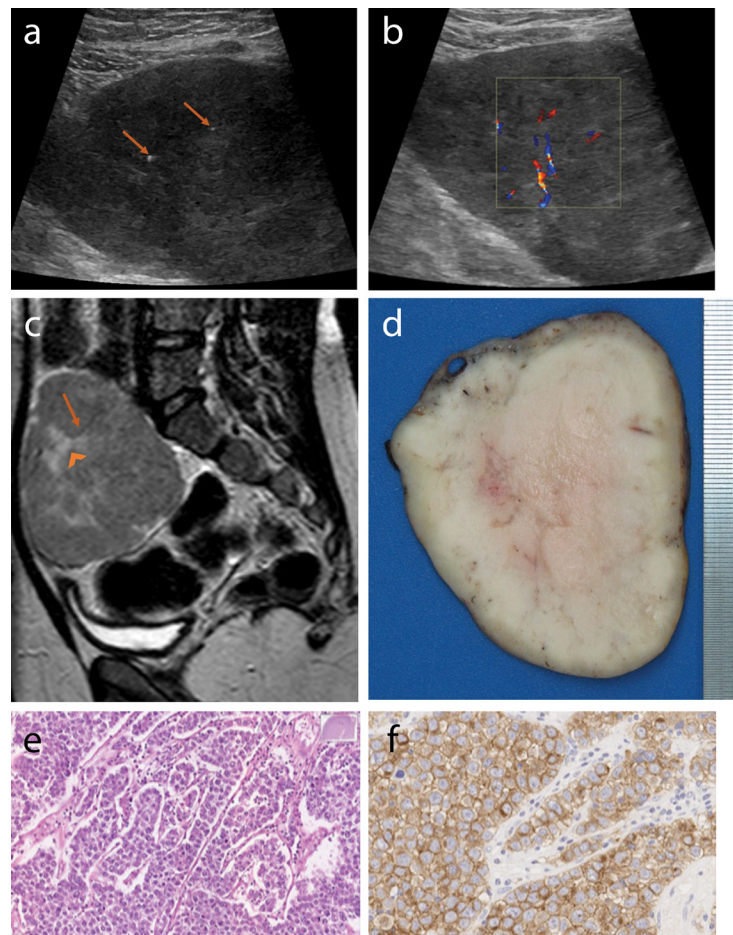


**Figure 1.** An eight-year-old female patient with Mayer-Rokitansky-Küster-Hauser syndrome was diagnosed with left ovarian dysgerminoma. Transabdominal pelvic ultrasound images (a, b) showing a heterogeneous, predominantly hypoechoic solid tumor with some scattered calcifications (*thin arrows*, a). Note the fibrovascular septa blood flow on the color Doppler study (b). Sagittal T2WI (c) showing a large pelvic tumor with intermediate-SI and prominent septa with linear low-SI vessels (arrow) and high-SI edematous component (arrowhead). The section surface of the left adnexal specimen (d) shows a solid and capsulated cream-colored tumor. Hematoxylin and eosin staining of the dysgerminoma (e) reveals uniform large cells with empty nuclei and prominent nucleoli separated by fibrous septa with some lymphocytes. Anti-CD117 staining (f) reveals all cells stained in the cytoplasm and cell membrane; septa with disperse lymphocytes are negative. T2WI, T2-weighted imaging; SI, signal intensity.

### Main points

- Ovarian dysgerminoma (OD) is a rare germ cell tumor with good prognosis that affects young females.
- Imaging can provide clues for the diagnosis of OD, revealing a large, predominantly solid, and multilobulated lesion with fibrovascular septa, which typically have low signal intensity on T2-weighted images without edema and marked enhancement on contrast-enhanced images.
- The condition typically presents with non-specific elevated serum lactate dehydrogenase levels.
- The main treatment for OD is surgery that often allows for fertility preservation.

of tumor, as well as in its retroperitoneal spread.<sup>2,7,9</sup> The nonspecific “ovarian vascular pedicle” sign was also identified in large ODs (Figure 3), which provides a clue for ovarian origin, allowing for narrowing the differential diagnosis.<sup>2</sup> Recently, Tsuboyama et al.<sup>10</sup> described the presence of central vessels that converge from the septa as a possible OD characteristic, while further studies are needed in this regard.<sup>10</sup>

### Magnetic resonance imaging (MRI)

On MRI, OD manifests as a large, multilobulated, predominantly solid tumor with heterogeneous signal intensity (SI) and prominent fibrovascular septa.<sup>6-10</sup> Generally, it mainly has low- or intermediate-SI relative to muscle on T1-weighted imaging (T1WI) and intermediate-SI on T2-weighted imaging (T2WI) (Figures 2, 4).<sup>2,4</sup> On T2WI, tumoral septa typically appear as thin lines with low- or intermediate-SI, while on T1WI, they are difficult to grasp, commonly presenting low-SI (Figures 2, 4).<sup>2,5</sup> When edematous changes are present, the septa may become thickened with high-SI on T2WI (Figure 1).<sup>2,4</sup> Depending on the degree of edema, they can be classified into thin non-edematous, thin edematous, thick edematous, and map-shaped edematous septa, which are predominant in large tumors.<sup>2</sup> Notably, 50% of ODs display more than one type of septa.<sup>2</sup> Large tumors generally exhibit heterogeneous SI, partly caused by necrosis or hemorrhage (Figures 2, 4).<sup>2,7</sup> Necrosis and hemorrhage do not enhance after contrast administration and exhibit high-SI on T2WI, while on T1WI, necrosis has low-SI and hemorrhage high-SI.

Following gadolinium administration, OD generally enhances less than normal myometrium and its septa demonstrate intense enhancement with mild or no enhancement of the edematous component (Figures 2, 4).<sup>2,5</sup> According to its malignancy and increased cellularity, OD is also associated with diffusion restriction, exhibiting high-SI on diffusion-weighted imaging (DWI) and low apparent diffusion coefficient (ADC) values (Figure 2).<sup>2,9</sup> Zhao et al.<sup>2</sup> reported a mean ADC value of  $0.830 \pm 0.154 \times 10^{-3} \text{ mm}^2/\text{s}$  for OD; however, further studies are needed.

Thus, when facing a large, predominantly solid, multilobulated ovarian mass, with diffusion restriction and prominent septa, which characteristically demonstrates low-SI on T1WI and avid enhancement following contrast administration, the diagnosis of dysgerminoma in young women with elevated serum LDH values should be considered. The

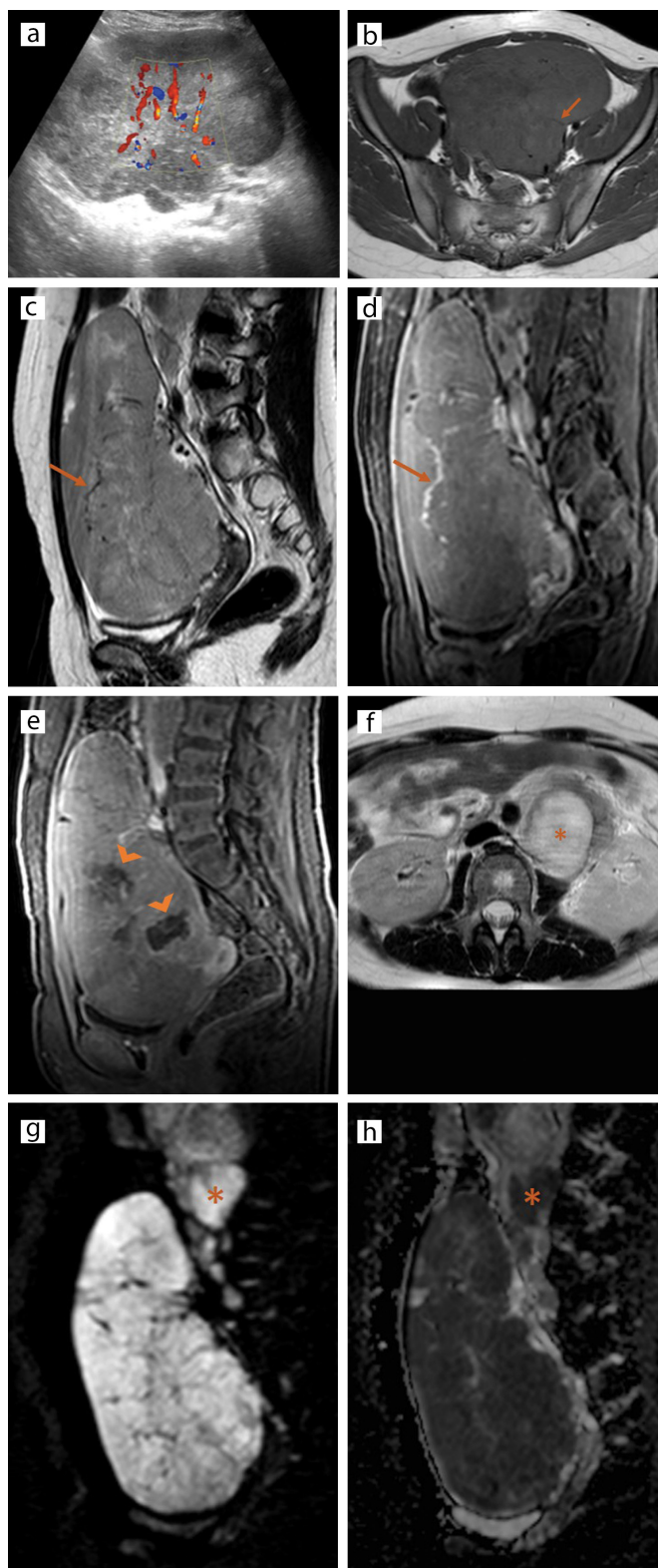


**Figure 2.** A 12-year-old female patient was diagnosed with left ovarian dysgerminoma and lymphatic dissemination. Transabdominal pelvic color Doppler ultrasound imaging (a) revealing a solid multilobulated tumor with heterogeneous echogenicity and marked vascularization. Axial T1WI (b) sagittal T2WI (c) and sagittal contrast-enhanced T1WI (d) revealing a large lobulated solid mass, divided into lobules by septa, which have low-SI on T1 and T2WI and avidly enhance following gadolinium administration (thin arrows, b-d). Sagittal gadolinium-enhanced image (e): note the lower enhancement of the tumor compared to myometrium and the presence of concomitant areas of necrosis (arrowheads). Axial T2WI (f) revealing left para-aortic adenopathy (asterisk). Pelvic tumor and adenopathy (asterisks, g, h) clearly show diffusion restriction, with high-SI on DWI ( $b = 1000 \text{ s/mm}^2$ ) (g) and low ADC values (h) (tumor ADC value:  $0.76 \text{ mm}^2/\text{s}$ ; adenopathy ADC value:  $0.68 \text{ mm}^2/\text{s}$ ). T1WI, T1-weighted imaging; T2WI, T2-weighted imaging; SI, signal intensity; ADC, apparent diffusion coefficient; DWI, diffusion-weighted imaging.

best imaging method for assessing these radiologic features is the MRI method, which allows for an accurate characterization of OD fibrovascular septa and for evaluating the behavior of the lesion in DWI examinations. While these findings are not specific to OD, when integrated with appropriate clinic and laboratory markers, they can help narrow the differential diagnosis.

### Differential diagnosis

Differentiating dysgerminoma from other lesions and reaching a timely diagnosis is essential since it influences the treatment that can allow fertility to be preserved.<sup>2-4, 8-10</sup> Nevertheless, a differential diagnosis of OD can be challenging since some mimicking tumors may have nonspecific radiological features. In a young patient with an ovarian mass, radiological studies associated with clinical and laboratory parameters can be helpful in differentiating OD from granulosa cell tumors (GCT) (juvenile type), YST, Sertoli-Leydig tumors (SLT), and immature teratoma.<sup>9</sup> Furthermore, OD should also be differentiated from lymphoma, which can occur at a young age, as well as from benign

tumors, such as sclerosing stromal tumors, ovarian fibroma, and subserosal uterine leiomyoma.

Juvenile GCT is an estrogen-producing tumor that typically presents with isosexual pseudoprecocity and menstrual alterations. On MRI, a sponge-like appearance (multiple cystic lesions within a solid mass) can be observed, which is not typical of OD (Figure 5).<sup>3,13</sup> Meanwhile, YST and SLT are generally unilateral lesions with non-specific radiological features.<sup>9,13</sup> Unlike OD, YST is usually associated with high alpha-fetoprotein values and SLT occurs with androgenic symptoms of virilization in 33% of cases.<sup>9,13</sup> Small areas of fat are important to distinguishing an immature teratoma from OD (Figure 6).<sup>9</sup>

Primary ovarian lymphoma without lymph nodes or bone marrow involvement is extremely rare and may be difficult to distinguish from OD.<sup>9</sup> The condition tends to appear as a bilateral, solid and large homogeneous mass, which enhances mildly and uniformly following contrast administration, without calcifications or ascites (Figure 7).<sup>14</sup> Studies have reported that ovarian lymphoma can course with septal

structures with high-SI on T2WI and preserved ovarian follicles at its periphery.<sup>15</sup> These features can be useful diagnostic clues and help in differentiating OD, which generally presents low-SI septa on T2WI and with no peripheral follicles; however, the differential diagnosis can be difficult when OD reveals edematous septa.

While sclerosing stromal tumors occur predominantly in young women, much like OD, these tumors can be differentiated through their enhancement pattern. Sclerosing stromal tumors characteristically present avid and early peripheral contrast enhancement with centripetal progression, a pattern unassociated with OD (Figure 8).<sup>5,7,12</sup> Fibroma is the most frequent benign solid ovarian tumor, is uncommon at a young age and, unlike OD, is characterized by markedly low-SI on T2WI (Figure 9).<sup>13</sup> Cellular fibroma may have high-SI areas on T2WI, but septa are unusual.<sup>13</sup> Lastly, subserosal uterine leiomyomas should also be distinguished from OD. This type of tumor characteristically projects outward from uterine subserosa and reveals low to intermediate-SI on T1WI compared with myometrium and low-SI on T2WI. The presence of the bridging vessel sign on MRI (flow voids in the uterine feeding branches) reveals their uterine origin and can be a useful marker.<sup>7</sup>

### Conclusion

OD is a rare germ cell tumor that can be challenging to diagnose. While diagnosis is only possible histologically, various radiological features should lead to its hypothesis, namely, the presence of a large, solid, and lobulated tumor with markedly enhancing septa in a young woman. The knowledge of the pathology, symptoms, and markers of OD is also essential to optimizing the radiological interpretation and enabling timely treatment and appropriate follow-ups. As such, radiologists must be familiarized with the characteristics of OD since they can be the first to suspect its presence.

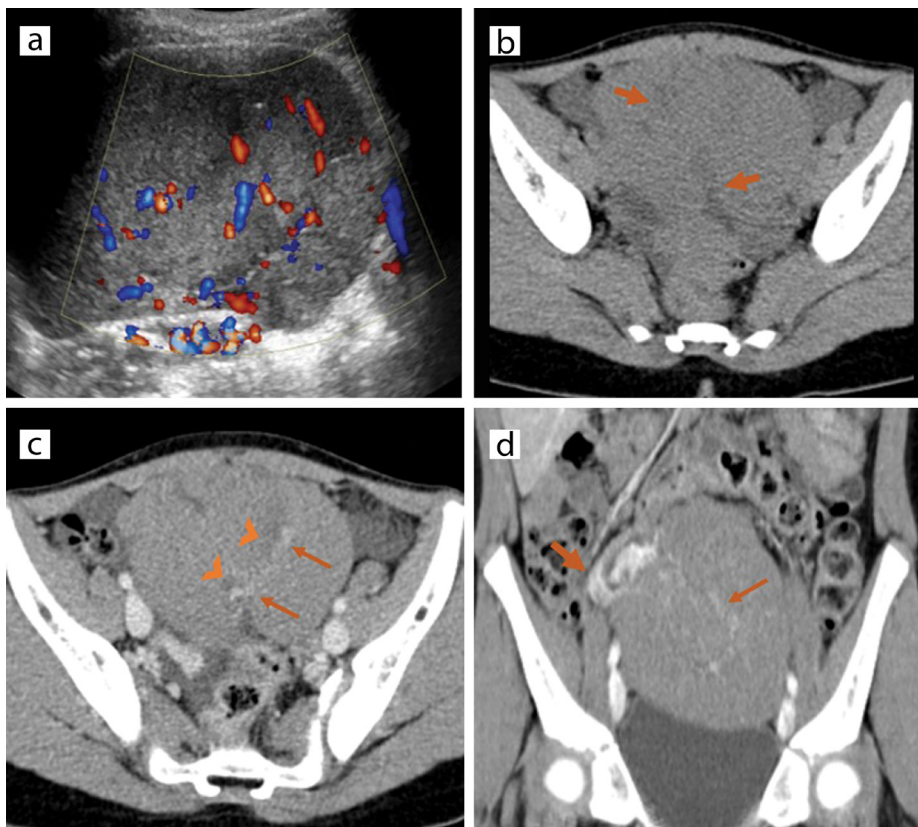


**Figure 3.** A 10-year-old female patient was diagnosed with right ovarian dysgerminoma. Transabdominal color Doppler US image (a) showing a solid mass with heterogeneous echogenicity and richly vascularized septa. Axial pre-contrast (b) and axial and coronal contrast-enhanced CT images (c, d) revealing a solid pelvic tumor with thick hypoattenuating septa (thick arrows, b) with enhancing vessels (thin arrows, c, d) and edematous non-enhancing components (arrowheads, c). Note the “ovarian vascular pedicle” sign, with enlarged right ovarian vein (thick arrow, d). CT, computed tomography.

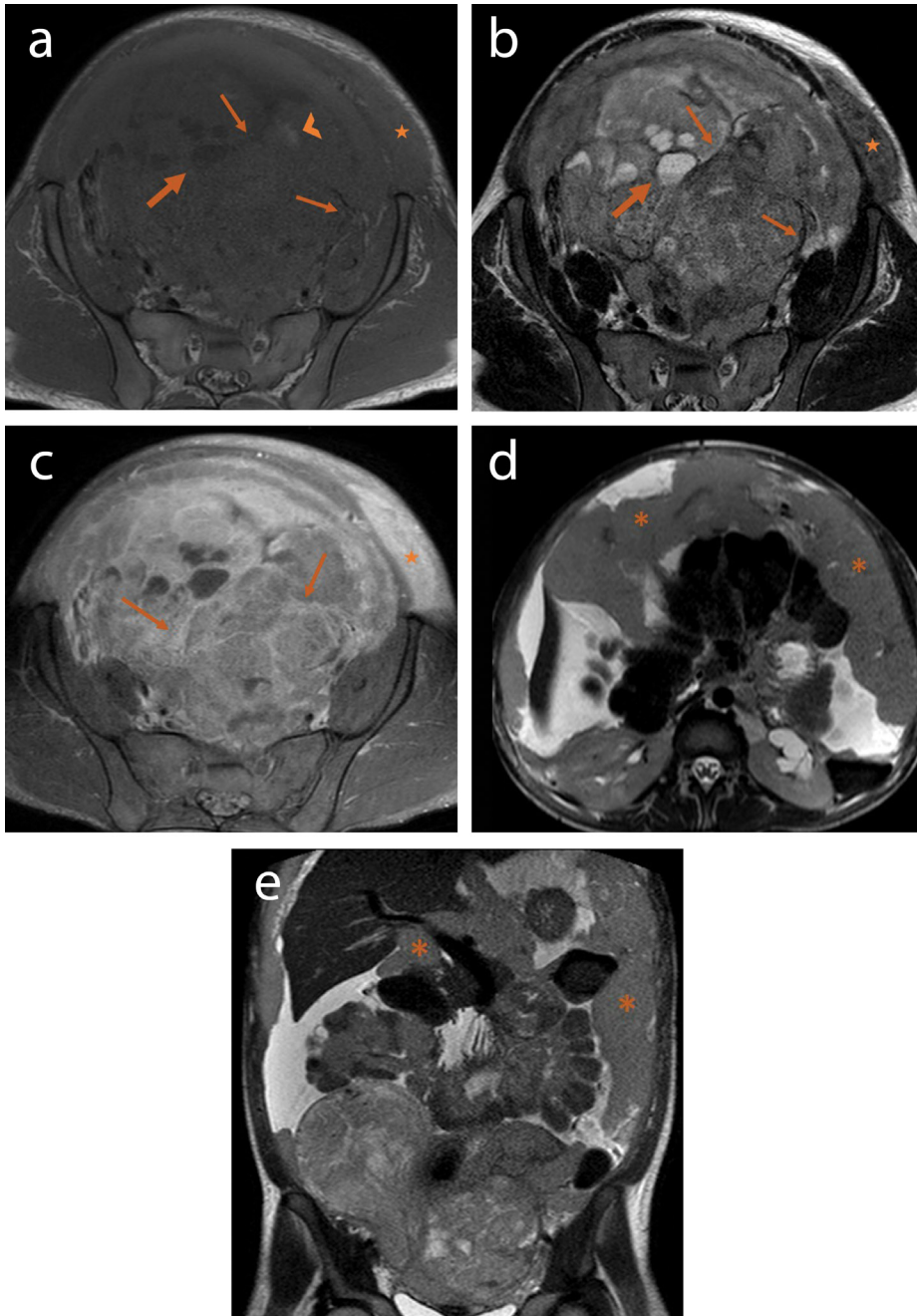


**Figure 4.** A 22-year-old female was diagnosed with bilateral ovarian dysgerminoma and peritoneal and lymphatic dissemination. Axial T1WI (a) and axial T2WI (b) show large, multilobulated, heterogeneous bilateral tumor, with septa of low-SI on T1WI and T2WI (thin arrows, a, b), some of them associated with edematous component. Hemorrhagic areas with high-SI on T1WI are observed (arrowhead, a), as well as multiple cystic areas, low-SI on T1WI and high-SI on T2WI (thick arrows, a, b). Axial gadolinium-enhanced image (c) revealing heterogeneous contrast enhancement of the tumor, with several enhancing and thickened septa (thin arrows). Axial and coronal T2WI (d, e) also reveal exuberant peritoneal metastases (asterisks). Note the presence of metastases in the left abdominal wall, anterior to the abdominal wall muscles, which were externalized through the entrance port of diagnostic laparoscopic surgery (stars, a, b, e). T1WI, T1-weighted imaging; T2WI, T2-weighted imaging; SI, signal intensity.

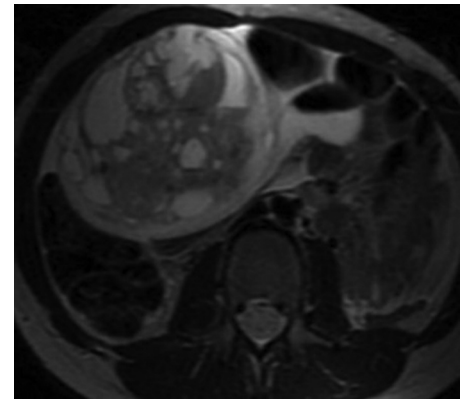


**Figure 5.** Axial T2WI showing a large right ovarian tumor, with a sponge-like appearance compatible with an ovarian juvenile granulosa cell tumor. T2WI, T2-weighted imaging.

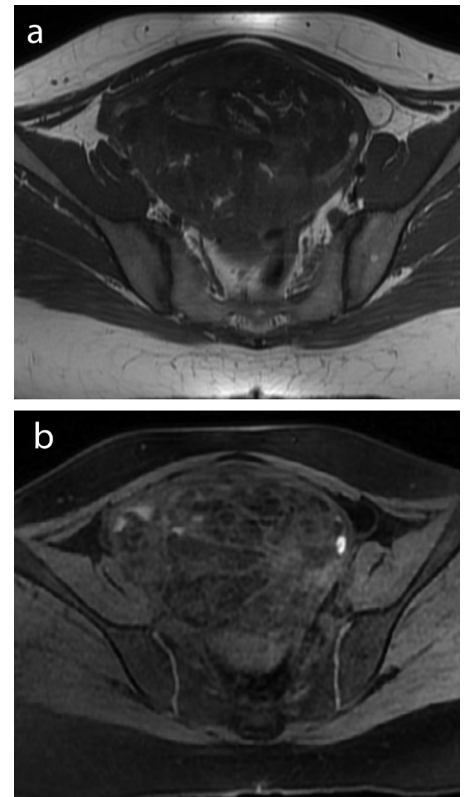


**Figure 6.** Axial T1WI (a) and fat-suppressed T1WI (b) revealing a large immature teratoma of the right ovary with small areas of fat. T1WI, T1-weighted imaging.

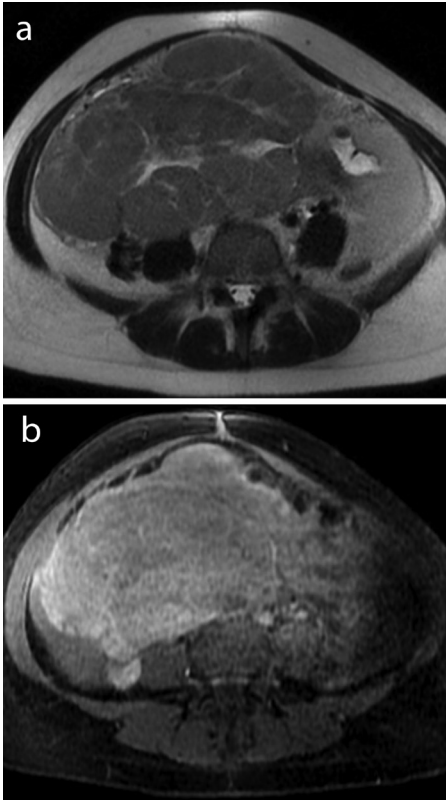


**Figure 7.** Axial T2WI (a) and gadolinium-enhanced image (b) revealing a bilateral primary ovarian B-cell lymphoma with high-SI septa on T2WI and progressive and homogeneous enhancement. T2WI, T2-weighted imaging; SI, signal intensity.

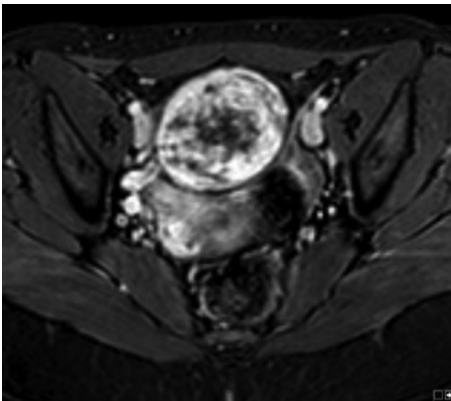


**Figure 8.** Axial gadolinium-enhanced image revealing a right ovarian sclerosing stromal tumor with avid and early peripheral contrast enhancement.

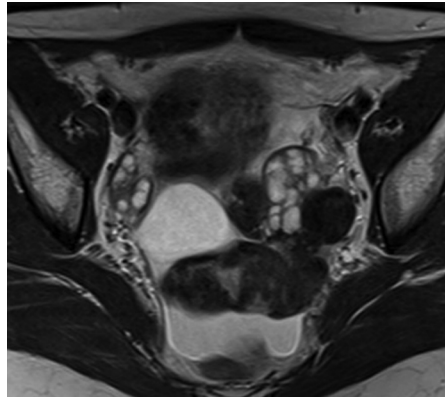


**Figure 9.** Axial T2WI revealing a left ovarian fibroma with markedly low-SI. T2WI, T2-weighted imaging; SI, signal intensity.

#### Conflict of interest disclosure

The authors declared no conflicts of interest.

#### References

- Cheung AN, Ellenson LH, Gilks CB, et al. Tumours of the ovary. In: WHO Classification of Tumours: Female Genital Tumours. 5th ed. International Agency for Research on Cancer, 2020:119-144. [\[CrossRef\]](#)
- Zhao S, Sun F, Bao L, et al. Pure dysgerminoma of the ovary: CT and MRI features with pathological correlation in 13 tumors. *J Ovarian Res.* 2020;13(1):71. [\[CrossRef\]](#)
- Hanafy AK, Mujtaba B, Yedururi S, et al. Imaging in pediatric ovarian tumors. *Abdom Radiol (NY).* 2020;45:520-536. [\[CrossRef\]](#)
- Shaaban AM, Rezvani M, Elsayes KM, et al. Ovarian malignant germ cell tumors: Cellular classification and clinical and imaging features. *Radiographics.* 2014;34(3):777-801. [\[CrossRef\]](#)
- Heo SH, Kim JW, Shin SS, et al. Review of ovarian tumors in children and adolescents: Radiologic-pathologic correlation. *Radiographics.* 2014;34(7):2039-2055. [\[CrossRef\]](#)
- Guerrero S, Testa AC, Timmerman D, et al. Imaging of gynecological disease (6): Clinical and ultrasound characteristics of ovarian dysgerminoma. *Ultrasound Obstet Gynecol.* 2011;37(5):596-602. [\[CrossRef\]](#)
- Jung SE, Lee JM, Rha SE, Byun JY, Jung JI, Hahn ST. CT and MR imaging of ovarian tumors with emphasis on differential diagnosis. *Radiographics.* 2002;22(6):1305-1325. [\[CrossRef\]](#)
- Kilic C, Cakir C, Yuksel D, et al. Ovarian dysgerminoma: a tertiary center experience. *J Adolesc Young Adult Oncol.* 2020;10(3):303-308. [\[CrossRef\]](#)
- Forstner R. CT and MRI in Ovarian Carcinoma. In: Forstner R, Cunha TM, Hamm B, eds. CT and MRI in Ovarian Carcinoma. 2nd ed. Springer: Cham; 2017:287-323. [\[CrossRef\]](#)
- Tsuboyama T, Hori Y, Hori M, et al. Imaging findings of ovarian dysgerminoma with emphasis on multiplicity and vascular architecture: pathogenic implications. *Abdom Radiol (NY).* 2018;43(7):1515-1523. [\[CrossRef\]](#)
- Miyazaki N, Kobayashi Y, Nishigaya Y, Momomura M, Matsumoto H, Iwashita M. Burkitt lymphoma of the ovary: A case report and literature review. *J Obstet Gynaecol Res.* 2013;39(8):1363-1366. [\[CrossRef\]](#)
- Horta M, Cunha TM. Tumores malignos não epiteliais do ovário. In: Ramos I, Ventura SR, eds. Imagem Em Oncologia Médica. 1st ed. Lidel: 2017:256-267. [\[CrossRef\]](#)
- Horta M, Cunha TM. Sex cord-stromal tumors of the ovary: a comprehensive review and update for radiologists. *Diagn Interv Radiol.* 2015;21(4):277-286. [\[CrossRef\]](#)
- Slonimsky E, Korach J, Perri T, Davidson T, Apter S, Inbar Y. Gynecological lymphoma: a case series and review of the literature. *J Comput Assist Tomogr.* 2018;42(3):435-440. [\[CrossRef\]](#)
- Tanaka YO, Yamada K, Oki A, Yoshikawa H, Minami M. Magnetic resonance imaging findings of small round cell tumors of the ovary: a report of 5 cases with literature review. *J Comput Assist Tomogr.* 2006;30(1):12-17. [\[CrossRef\]](#)





# Length of the healthy and pathological small intestine in patients with Crohn's disease: calculations using computed tomography and magnetic resonance enterography

Laura Maria Minordi

Luigi Larosa

Maria Gabriella Brizi

Alessandro Armuzzi

Riccardo Manfredi

## ABSTRACT

Many patients with Crohn's disease (CD) require surgical intervention during their lifetime. A correct preoperative assessment of the intestinal length is necessary to predict and quickly treat postoperative nutritional disorders. The aim of this paper is to explain the method used in our hospital to measure intestinal length in patients with CD and its usefulness for making the correct therapeutic decision. Vessel analysis software is used to measure small bowel length through computed tomography enterography (CTE) or magnetic resonance enterography (MRE). The method permits two-dimensional and three-dimensional curved multiplanar reconstructions and allows each loop to be stretched using a point-by-point identification of the intestinal lumen. Subsequently, the software allows the creation of a virtual image, on which the intestinal length is measured linearly. This methodology was tested on three patients; patients 1 and 3 were examined using CTE, and patient 2 was examined using MRE. The outcomes were discussed at a multidisciplinary team meeting (MDT). As a result, surgical ileocolic resection was recommended for patient 1 and medical therapy for patients 2 and 3. Intestinal length measurements have proved vital during MDTs for making appropriate therapeutic decisions.

## KEYWORDS

Bowel, Crohn's disease, CT, inflammatory bowel disease, MR enterography

Many patients with ileocolic Crohn's disease (CD) require one or more surgical interventions during their lifetime. In these patients, the indication for surgery is based on various criteria, such as the presence of stricturing or perforating disease, risk for postoperative recurrence, grade of inflammatory activity, and length of the intestinal loops involved. If the bowel resection is too extensive and residual small intestine is less than 75 cm, the patient may suffer from short bowel syndrome.<sup>1</sup>

The exact length of the small intestine remains controversial in the literature, and its measurement depends on the techniques used. In addition, some studies have reported that the length of the small bowel appears to be variable, depending on the age, sex, weight, and height of the patient.<sup>2,3</sup> A study by Regan et al.<sup>4</sup> found that stenosis in patients with CD can occur because of the increased contractile activity of fibroblasts at the level of the extracellular matrix, appreciable both in healthy areas and in macroscopically inflamed regions. For this reason, patients with CD have a shorter bowel than that of the normal population.<sup>2,3</sup>

In this paper, we describe a method for measuring intestinal loops through computed tomography enterography (CTE) or magnetic resonance enterography (MRE) using vessel analysis software. The method enables two-dimensional (2D) and three-dimensional (3D) curved multiplanar reconstructions (MPRs) and allows each loop to be stretched. Subsequently, the software creates a virtual image through which intestinal length can be measured linearly. This method has been used successfully in the evaluation of patients with acute diverticulitis,

From the UOC Radiologia Addomino-Pelvica, Dipartimento di Diagnostica per immagini, Radioterapia Oncologica ed Ematologia (L.L.M. ✉ lauramaria.minordi@policlinicogemelli.it, L.L., G.B., R.M.), Fondazione Policlinico Universitario Agostino Gemelli, IRCCS, Roma, Italia; Università Cattolica del sacro Cuore, Roma, Italia (G.B., R.M.); Unit of Gastroenterology (A.A), Fondazione Policlinico Universitario Agostino Gemelli IRCCS, Roma, Italia.

Received 13 September 2021; revision requested 31 October 2021; last revision received 10 December 2021; accepted 27 December 2021.



Epub: 05.01.2023

Publication date: 31.01.2023

DOI: 10.5152/dir.2022.21968

You may cite this article as: Minordi LM, Larosa L, Brizi MG, Armuzzi A, Manfredi R. Length of the healthy and pathological small intestine in patients with Crohn's disease: calculations using computed tomography and magnetic resonance enterography. *Diagn Interv Radiol.* 2023;29(1):24-28.

revealing a correlation between the lengths of colon involved, considered as a percentage of the entire colon, and the need for a patient to be hospitalized.<sup>5</sup> The same method can be used to measure the intestinal length in patients with CD in many clinical situations, particularly when it is necessary to plan a surgical intervention in patients who have already undergone intestinal resection to avoid short bowel syndrome.<sup>1</sup>

## Technique

In our hospital, MRE and CTE are performed after the oral administration of a polyethylene glycol solution (PEG). We administer 1.5–2.0 L of PEG in doses of 100 mL starting 35 min before the MR and CT examinations.

When a patient has a known diagnosis of CD, we perform CTE only after the injection of an iodinated contrast medium. The CT technical parameters are presented in Table 1.

In MRE, the sequences are performed before and after the intravenous administration of a paramagnetic contrast medium: a single-shot T2-weighted and balanced steady-state-free precession sequence, T2-weighted fat-suppressed sequence, multiphase 3D T1-weighted fat-suppressed postcontrast image sequence, and diffusion-weighted imaging (values usually 0–800 or 0–600 s/mm<sup>2</sup>) sequence. The MR parameters are set out in Table 2.

The imaging criteria for CD diagnosis are summarized in Table 3.

The CT and MR examinations are revised using postprocessing technologies such as MPR, and a specific postprocessing 2D and 3D software (Vue PACS Carestream) is applied to these images. We select the series of images for the reconstruction using the “view as” button and then select “vessel analysis”. In this way, we obtain 3D and 2D reconstructions in axial, coronal, and sagittal planes. Using the manual protocol, we create a virtual image that makes the intestine tubular through the point-by-point identification of the intestinal lumen distended through PEG. On the image thus obtained, we can perform the necessary measurements to evaluate the patient using a linear measurement.

The time needed to perform the measurements is variable. Based on our calculations, between 20 and 30 min is required for each measurement, to which the time necessary to view the images and draft the report must be added.

Indications for surgical resection or the modification/confirmation of medical therapy are discussed in a multidisciplinary team meeting (MDT), held in our department once a week, in which radiologists, gastroenterologists, surgeons, and pathologists participate.

### Case 1

Patient 1 is a 74-year-old man with known CD treated through medical therapy. He was hospitalized for persistent abdominal pain and serotonin fever (>38°C), but his symptoms did not respond to medical therapy. His bowel movements were regular, and there was only one incident of vomiting. At admission, his blood tests were normal except for C-reactive protein (CRP) values (19.8 mg/L; normal values <5.0). The patient underwent CTE (Figure 1), and the results were discussed

in the MDT. The MDT decision was to perform intestinal resection, with the intestine measured during ileocolonic resection using a radiological measurement.

### Case 2

Patient 2 is a 43-year-old woman with known stenosing CD treated through medical therapy. She was hospitalized for worsening abdominal pain with constipation. Blood tests: normocytic anemia (hemoglobin: 10.4 g/dL; normal values 12.0–15.0), erythrocyte sedimentation rate (ESR): 43 mm (normal values 0–20), CRP: 6 mg/L (normal values <5.0). During hospitalization, the treatments were effective, and her condition continued to improve.

Subsequently, MRE was performed (Figure 2), and the results were discussed in the MDT. The MDT decision was to continue medical therapy.

### Case 3

Patient 3 is a 36-year-old man with known CD treated through medical therapy. He was experiencing severe pain following diarrhea (about 2–4 discharges per day). He had also experienced weight loss of approximately 5–6 kg in the previous 2 months.

In the endoscopic examination, the ileocecal valve appeared substenotic and was covered by edematous and bleeding mucosa, and a single ulcer was detected. The mucosa of the ileum also appeared edematous and sensitive to bleeding with ulcers.

Blood tests on admission to the hospital were normal except for CRP (20.3 mg/L; normal values <5.0) and ESR (30 mm; normal values 0–20).

### Main points

- Many patients with ileocolic Crohn's disease require one or more surgical interventions during their lifetime. In these patients, the indication for surgery is based on various criteria, such as the presence of stricturing or perforating disease, risk of postoperative recurrence, grade of inflammatory activity, and length of the intestinal loops involved.
- If the bowel resection is too extensive and residual small intestine is less than 75 cm, the patient may suffer from short bowel syndrome.
- The preoperative assessment of intestinal length is useful for predicting and quickly treating postoperative nutritional disorders.
- We recommend that vessel analysis software be employed for measuring the small bowel loops using computed tomography and magnetic resonance enterography.

**Table 1.** Computed tomography parameters

Type of CT scanner	64-row spiral CT
Slice thickness	1.5 mm
Interval	1.25 mm
Automated tube current modulation	(200–700 mA)
Pitch	0.969 mm/rot
Rotation time	0.9 s
Modality of intravenous injection of iodinated contrast medium	100–130 mL of iodinated contrast agent is administered in two separate and consecutive boluses: the first bolus at a rate of 1.5 mL/s (1/3 of the total amount of iodinated contrast agent given to the patient), the second bolus at a rate of 3 mL/s (the remaining 2/3 of the total amount of iodinated contrast agent given to the patient). The images are acquired 75 s after intravenous injection. This modality of administration allows an arterial and portal study of the abdomen in a single scan.

CT, computed tomography; mm, millimeters; mA, milliamperere; s, second.

Table 2. Magnetic resonance parameters					
Sequence details	T1 Gradient echo	T2 Gradient echo	T2 Spin echo	T2 fat-saturated Spin echo	DWI
Pulse sequence	FSPGR	FIESTA	SSFSE	SSFSE	EPI
Patient position	Supine				
Anatomical coverage	From the top of the liver dome to pubic symphysis				
RF coil	Phased array (multi-channel RF coil)	Phased array (multi-channel RF coil)	Phased array (multi-channel RF coil)	Phased array (multi-channel RF coil)	Phased array (multi-channel RF coil)
Breath-hold during MR examination/respiratory gating	Yes (single or multiple)	Yes (single or multiple)	Yes (single or multiple)	Yes (single or multiple)	Respiratory triggering
Plane	Axial/coronal	Axial/coronal	Axial/coronal	Axial/coronal	Axial/coronal
TR, ms	Short/minimum	Short/minimum	Long (optimal)	Long (optimal)	Long (optimal)
TE, ms	Minimum	Minimum	60–100 (optimal)	100	60
Flip angle (degrees)	>70 (or optimal)	>45 (or optimal)	180 (or optimal)	180 (or optimal)	<90 (or optimal)
NEX	>1 (or optimal)	>1 (or optimal)	>1 (or optimal)	>1 (or optimal)	>1 (or optimal)
Slice thickness, mm	4 (3D acquisition) 6–7 (2D acquisition)	6–7	6–7	5	6
Slice gap, mm	0.5–1	0.5–1	0.5–1	1	1
Matrix	256 256 or site optimal	256 256 or site optimal	256 256 or site optimal	320 224 or site optimal	320 224 or site optimal
Slice acquisition order	Interleaved/sequential	Interleaved/sequential	Interleaved/sequential	Interleaved/sequential	Interleaved/sequential
FOV (cm)	22–48 (or optimal to cover all anatomy)	22–48 (or optimal to cover all anatomy)	22–48 (or optimal to cover all anatomy)	22–48 (or optimal to cover all anatomy)	22–48 (or optimal to cover all anatomy)
b value	-	-	-	-	600–800

MR, magnetic resonance; DWI, diffusion-weighted imaging; RF, radiofrequency; TR, repetition time; TE, echo time; NEX, number of excitations; mm, millimeters; cm, centimeters; FOV, field of view; FSPGR, fast-spoiled gradient echo; FIESTA, fast imaging employing steady-state acquisition; SSFSE, single-shot fast-spin echo; EPI, echo-planar imaging.

Table 3. Imaging criteria for the diagnosis of Crohn's disease	
Mural thickening	Wall thickness more than 3 mm
Bowel wall edema	In CT scans: hypodensity of submucosal layer In MR imaging: wall hyperintense signal compared with skeletal muscle on T2-weighted sequences
Mucosal ulcers	Deep depressions in the mucosal surface
Bowel wall enhancement	Stratified in active inflammatory subtype: intense enhancement of the mucosa and serosa and hypodensity (CT) or low signal intensity (MR) of submucosa Homogeneous in fibro-stenotic subtype
Engorgement of vasa recta	Hyperemia of the near mesentery
Perienteric stranding	Loss of the normal sharp interface between the bowel wall and mesentery
Fibrofatty proliferation	Excess of mesenteric fat
Stenosis (fibrostenotic subtype)	Upstream dilatation with loop caliber greater than 3 cm
Fistula (fistulizing/perforating subtype)	Communication with a near structure (e.g., enteroenteric, enterocolic, enterocutaneous, enterovesicular fistulas)
Abscess	Capsulated fluid collection near pathological loop; it could contain air
Lymph node enlargement	Short diameter greater than 1 cm

CT, computed tomography; MR, magnetic resonance.

The patient underwent CTE to determine the appropriate treatment (Figure 3), and the results were discussed in the MDT. The MDT decision was to not perform surgical therapy because of the high risk of short bowel syndrome and to continue medical therapy.

## Discussion

Previously, the measurement of the length of the small intestine was performed using a barium X-ray.<sup>3</sup> Currently, the calculation of the length of the intestine is conducted through MRE or CTE, using vascular imaging software,<sup>6</sup> 2D MPR,<sup>7</sup> or an automatic calculation method.<sup>8</sup>

In our hospital, two gastrointestinal radiologists use the method described here to measure intestinal length (both small bowel and colon) in all patients with CD, especially in patients with extensive alteration of the small bowel who must undergo surgery. Coronal and sagittal MPR using CTE or coronal and axial images from MRE do not allow the small bowel to be visualized in its longitu-

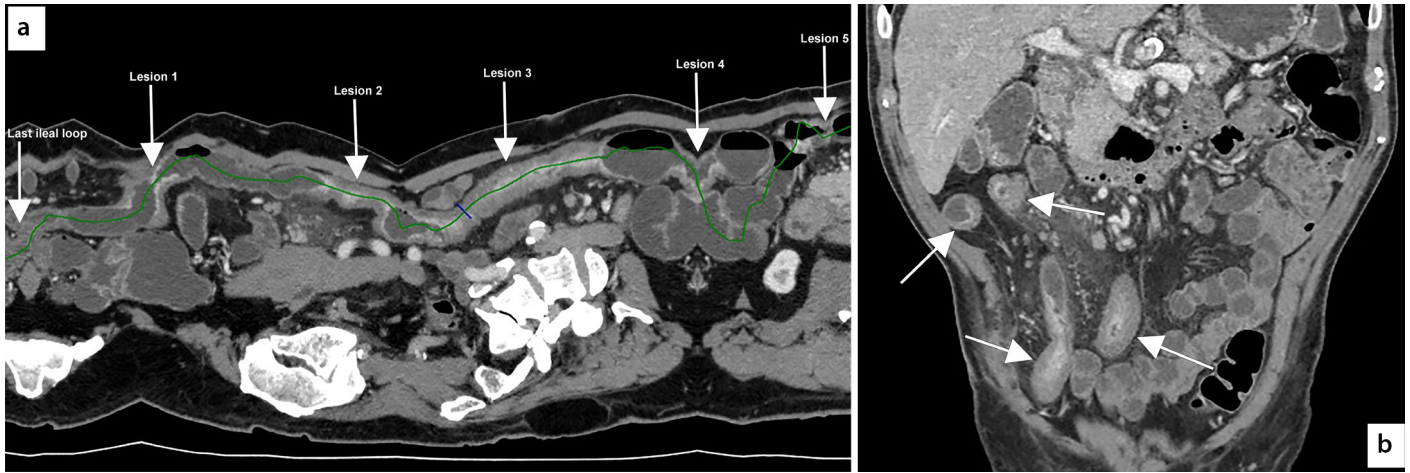


**Figure 1.** Computed tomography enterography (a) reveals extensive small bowel alteration affecting the last 80 cm of the ileum, characterized by the presence of multiple thick-walled and reduced-caliber tracts alternating with normal or increased caliber tracts, which are also represented in the reconstructions obtained through vessel analysis. In this reconstruction, it is possible to accurately assess the overall extent of the disease and each lesion. Last ileal loop: length of 45 mm, lesion 1: 32 mm, lesion 2: 54 mm, lesion 3: 130 mm, lesion 4: 32 mm, lesion 5: 40 mm. Lesions 2 and 3 exhibit increased density of the perivisceral adipose tissue. Between lesions 3 and 4 and between lesions 4 and 5, the loops are dilated (maximum caliber: 35 mm). Multiplanar coronal reconstruction (b) does not allow the small bowel to be visualized in its longitudinal extension because of the long section of intestine affected by the pathology.

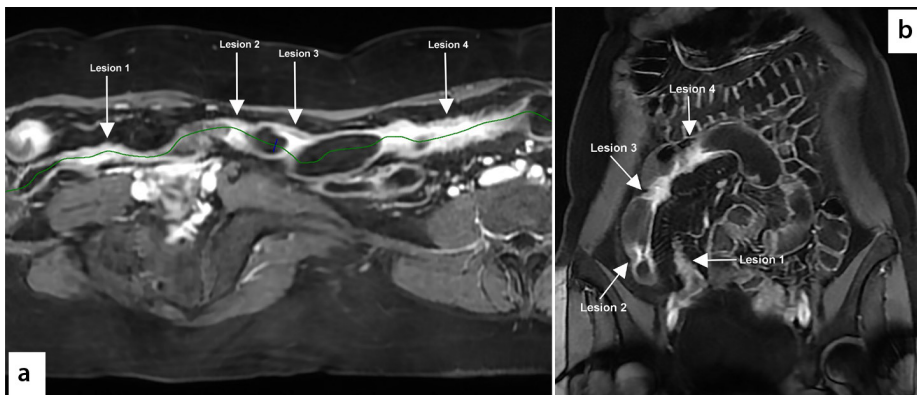


**Figure 2.** Magnetic resonance enterography (a) reveals small bowel alteration affecting the last 40 cm of the ileum, characterized by the presence of four thick-walled and reduced-caliber tracts, which are represented in the reconstructions obtained through vessel analysis. In this reconstruction, it is possible to accurately assess the overall extent of the disease and each lesion. Lesion 1: length of 70 mm, lesion 2: 10 mm, lesion 3: 14 mm, lesion 4: 100 mm. Coronal T1 image performed after the intravenous injection of gadolinium contrast medium (b) does not allow the small bowel to be visualized in its longitudinal extension because of the long section of intestine affected by the pathology; however, it was possible to measure the length of each pathological loop in the various planes.

nal extension if a long section of intestine is affected by the pathology. In this paper, we have described a method to measure intestinal length and presented three patients with CD.

Patient 1 had a diseased intestine less than a meter long and no response to medical therapy; he therefore underwent ileal resection surgery. After ileocolonic resection, the intestine measurement was consistent with the radiological measurement, and no

complications in the postsurgical course were identified. Patient 2 exhibited signs of disease activity, and the CT showed small bowel alteration affecting the last 40 cm of the ileum. He responded to medical therapy, and therefore, in the MDT, it was decided to continue with this course of treatment. Patient 3 had extensive bowel involvement with the consequent high risk of short bowel syndrome; it was therefore decided to continue medical therapy.

The technique described in this paper is used to calculate the length of both the small intestine and colon. The measurement was performed on the colon for diverticular disease.<sup>5</sup> In CD, it has greater practical utility for measuring the healthy or pathological small intestine to avoid performing an extensive resection that would lead to short bowel syndrome. Breathing artifacts do not hinder the measurement either in CT or MR.

If patients have fistulas, they are a candidate for bowel resection surgery, and the radiological support consists of measuring the length of the pathological small bowel loops, residual normal bowel, and distance of the fistula from the ileocecal valve or from the Treitz. In the case of stenosis, using this method enables the length of the stenosis to be measured. In addition, for stenosis or skip lesions, their distance from the ileocecal valve can be calculated, providing information that could be useful in cases of stricturoplastic therapy or the endoscopic dilation of the stenosis.

In conclusion, the vessel analysis method is easy to perform to measure the extent of the disease, and it is usually available in radiological departments. The measurements performed by us have always proved useful during MTDs for both clinicians and surgeons to make the correct therapeutic (medical or surgical) decision.

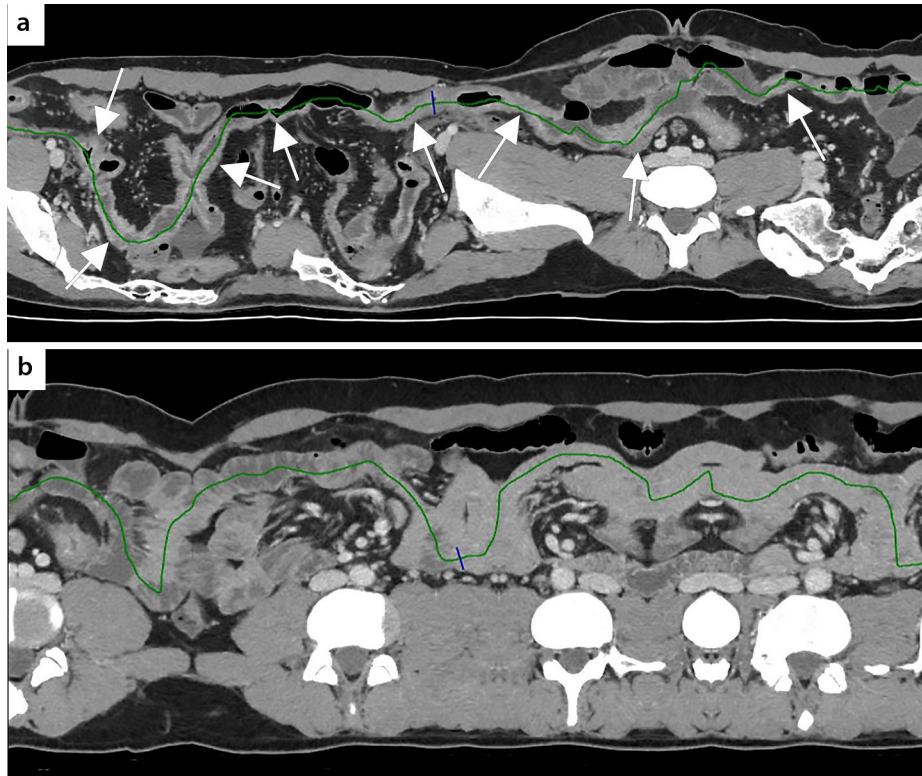


**Figure 3.** Computed tomography enterography reconstruction (a) reveals extensive alteration of the small loops, both the distal jejunum and ileum, including the last ileal loop and ileocecal valve, for at least 140 cm. The ileocecal valve is poorly identifiable. Immediately upstream, further ileal loops are observed with thickened walls (maximum thickness 10 mm) with an extension of approximately 30 cm and a lumen of reduced caliber (3 mm). The ileum upstream and distal jejunum have at least eight pathological tracts with thickened walls (maximum thickness 7 mm), with a longitudinal extension varying from 2 to 6 cm, and reduced caliber (residual lumen of 4 mm), alternating with tracts of normal or slightly increased caliber (maximum caliber: 25 mm). These alterations are also associated with hypervascularization, increased density of adipose tissue, and reactive lymph nodes in the mesentery. (b) At the request of the surgeon, the healthy intestine was measured and was approximately 70 cm.

### Conflict of interest disclosure

The authors declared no conflicts of interest.

### References

1. Limketkai BN, Parian AM, Shah ND, Colombel JF. Short bowel syndrome and intestinal failure in Crohn's disease. *Inflamm Bowel Dis.* 2016;22(5):1209-1218. [\[CrossRef\]](#)
2. Glehen O, Lifante JC, Vignal J, et al. Small bowel length in Crohn's disease. *Int J Colorectal Dis.* 2003;18(5):423-427. [\[CrossRef\]](#)
3. Shatari T, Clark MA, Lee JR, Keighley MR. Reliability of radiographic measurement of small intestinal length. *Colorectal Dis.* 2004;6(5):327-329. [\[CrossRef\]](#)
4. Regan MC, Flavin BM, Fitzpatrick JM, O'Connell PR. Stricture formation in Crohn's disease: the role of intestinal fibroblasts. *Ann Surg.* 2000;231(1):46-50. [\[CrossRef\]](#)
5. Minordi LM, Larosa L, Berté G, Pecere S, Manfredi R. CT of the acute colonic diverticulitis: a pictorial essay. *Diagn Interv Radiol.* 2020;26(6):546-551. [\[CrossRef\]](#)
6. Sinha R, Trivedi D, Murphy PD, Fallis S. Small-intestinal length measurement on MR enterography: comparison with in vivo surgical measurement. *AJR Am J Roentgenol.* 2014;203(3):274-279. [\[CrossRef\]](#)
7. Brouquet A, Rangheard AS, Ifergan J, et al. The accuracy of preoperative imaging in measuring the length of the ileocolic segment affected by Crohn's disease: a prospective cohort study. *Colorectal Dis.* 2017;19(5):437-445. [\[CrossRef\]](#)
8. Wilson NA, Park HS, Lee KS, Barron LK, Warner BW. A novel approach to calculating small intestine length based on magnetic resonance enterography. *J Am Coll Surg.* 2017;225(2):266-273.e1. [\[CrossRef\]](#)



# Analysis of interreader agreement in structured reports of pelvic multiparametric magnetic resonance imaging using the METastasis Reporting and Data System for Prostate Cancer guidelines

Xiang Liu   
Tingting Xie   
Zhaonan Sun   
Ying Guo   
Xiaodong Zhang   
Xiaoying Wang 

## PURPOSE

To evaluate interreader agreement on pelvic multiparametric magnetic resonance imaging (mpMRI) interpretation among radiologists using a structured reporting tool based on the METastasis Reporting and Data System for Prostate Cancer (MET-RADS-P) guidelines.

## METHODS

A structured report for follow-up pelvic mpMRI for advanced prostate cancer (APC) patients was formulated based on MET-RADS-P guidelines. In total, 163 paired pelvic mpMRI examinations were performed from December 2017 to February 2021 on 105 patients with APC. These were retrospectively reviewed by two senior and two junior radiologists for metastatic lesion detection and were categorized by these readers using primary/secondary response assessment categories (RACs), with and without the structured report. Interreader agreement regarding metastasis detection and RAC scores was evaluated with Cohen's kappa and weighted Cohen's kappa statistics ( $K$ ), respectively.

## RESULTS

The two senior radiologists showed higher agreement with the reference standard for metastasis detection using the structured report (S1:  $K = 0.83$ ; S2:  $K = 0.73$ ) compared with the conventional report (S1:  $K = 0.72$ ; S2:  $K = 0.61$ ). Junior radiologists showed similar results (J1: 0.66 vs. 0.59; J2: 0.65 vs. 0.57). The overall agreement between the two senior radiologists was excellent for the primary RAC pattern using the structured reports ( $K = 0.81$ ) and was substantial for secondary RAC categorization ( $K = 0.75$ ). The interreader agreement of the two junior radiologists was substantial for both primary and secondary RAC values ( $K = 0.76, 0.68$ ).

## CONCLUSION

Good interreader agreement was found for the follow-up assessment of APC patients between radiologists, where the pelvic mpMRI was reported using MET-RADS-P guidelines. This improvement applied to both metastatic lesion detection and qualitative RAC assessment.

## KEYWORDS

Advanced prostate cancer, interreader agreement, METastasis Reporting and Data System for Prostate Cancer, mpMRI, response assessment category

From the Department of Radiology (X.L., Z.S., Y.G., X.Z., X.W. wangxiaoying@bjmu.edu.cn), Peking University First Hospital, Beijing, China; Department of Radiology (T.X.), Peking University Shenzhen Hospital, Shenzhen, China.

Received 01 December 2021; revision requested 05 January 2022; last revision received 21 February 2022; accepted 14 March 2022.



Epub: 17.01.2023

Publication date: 31.01.2023

DOI: 10.5152/dir.2022.211232

Imaging to describe the metastatic status of patients is the cornerstone for managing biomarker development and therapeutic clinical tests.<sup>1</sup> The imaging of biomarkers can provide information on disease distribution, likely prognosis, therapy-induced changes, and response duration.<sup>2</sup>

Whole-body magnetic resonance imaging (MRI) is now an imaging tool that enables tumor detection and therapy evaluations in patients with advanced prostate cancer (APC). The METastasis Reporting and Data System for Prostate Cancer (MET-RADS-P) is a recently

published practical guide that provides the minimum standards for whole-body MRI scans for image acquisition, interpretation, and reporting of baseline and follow-up APC patients, and it enables the documentation of response heterogeneity using response assessment categories (RACs) at the regional level.<sup>2,3</sup> More importantly, the MET-RADS-P score has been confirmed to be a prognostic imaging biomarker, as it stratifies the cancer-specific survival of patients with castration-resistant prostate cancer (PCa).<sup>4</sup>

One of the important purposes of the MET-RADS-P guide is to ensure the uniformity of imaging interpretations. To date, limited data are available on the interreader agreement of MRI examination reports when using MET-RADS-P guidelines. Pricolo et al.<sup>5</sup> found excellent interobserver agreement for the RAC assessment of bone between a senior radiologist and resident radiologist when using the MET-RADS-P guidelines, but results were mixed for other body regions that relied on limited paired whole-body MRI examinations. Therefore, further improvement of interreader agreement needs to be addressed. Consistency can often be improved through training, while another solution is to use a structured reporting tool.

Structured reports are popular in clinical radiology workflows and have shown great potential in improving practical workflows by providing professional, well-defined, and consistent report templates. Dimarco et al.<sup>6</sup> confirmed that structured reports improved the interreader agreement of pancreatic ductal adenocarcinoma staging compared with free-text reports. Therefore, this study hypothesized that a structured report could also improve the interreader agreement on the metastatic evaluation of PCa, using MET-RADS-P guidelines.

Given that PCa initially and predominantly metastasizes to pelvic lymph nodes and bone, and that extrapelvic metastases in the absence of pelvic involvement are rare,<sup>7,8</sup> a routine pelvic examination is adequate for

the metastasis detection and response evaluation for PCa patients.<sup>9,10</sup> In this setting, the researchers tailored a structured report for follow-up pelvic multiparametric MRI (mpMRI), taking the MET-RADS-P template for reference. This was used with a cohort of patients with APC at the study site, mimicking a typical clinical workflow. The purpose of this study was to evaluate the interreader agreement of pelvic mpMRI interpretation among radiologists using a structured reporting tool based on MET-RADS-P guidelines.

## Methods

### Study participants

This retrospective study was approved by the Peking University First Hospital Institutional Review Board, and informed consent was obtained from all patients in written form (2021-060).

The inclusion criteria for patients in this study included a histologic diagnosis of PCa, with metastatic lesions presented in previous and ongoing follow-up pelvic mpMRI examinations at the institution. Only patients that had a complete pelvic mpMRI dataset before and after systemic therapy were included. The study excluded patients who had an incomplete pelvic mpMRI protocol ( $n = 7$ ), poor image quality ( $n = 5$ ), and absent clinical information ( $n = 11$ ).

In total, 163 pairs of pelvic mpMRI examinations were gathered for analysis. These were performed on 105 patients with APC who had undergone at least two examinations between December 2017 and February 2021 for follow-up assessment after cancer therapy. All patients underwent baseline scanning before therapy. Among them, 58 patients had one follow-up examination (116 scans total, 58 examination pairs), 36 patients had two follow-up examinations (108 scans total, 72 examination pairs), and 11 patients had three follow-up examinations (44 scans total, 33 examination pairs). Pre-MRI clinical information [age, prostate-specific antigen (PSA) values, and therapy method] was collected for all patients.

### Imaging technique

All pelvic mpMRI images were acquired on two 3.0 T MRI scanners (Discovery, GE Healthcare; Intera, Philips Healthcare) using an acquisition protocol that complies with the MET-RADS-P standard. The imaging protocol consisted of multiplanar T1-/T2-weighted imaging and diffusion-weighted imaging with  $b$  values of 800–1,000  $s/mm^2$  along

with reconstructed apparent diffusion coefficient maps. The T1-weighted imaging was obtained using the Dixon technique with in-phase and out-of-phase and three-dimensional dynamic contrast-enhanced MRI.<sup>3</sup> For patients who had previously undergone prostatic biopsies, mpMRI examinations were performed at least four weeks after the latest biopsy.

### MET-RADS-P system

The MET-RADS-P system assigned the presence of clearly identified disease to 14 predefined regions of the body (the primary disease site, seven skeletal and three nodal regions, and lung, liver, and other soft tissue sites); this was used at baseline and follow-up assessments according to the morphological and signal characteristics on all acquired images. For each anatomic region of metastasis, a qualitative response assessment on a scale of RAC 1 to 5 (1: highly likely to be responding; 2: likely to be responding, 3: stable; 4: likely to be progressing; 5: highly likely to be progressing) was recorded and compared with the baseline study.<sup>3</sup>

### Structured report template

A structured report for follow-up pelvic mpMRI for patients with APC was formulated in line with the MET-RADS-P guidelines by two urinary radiologists (with 4 and 15 years of experience in urinary radiology, respectively) (Figure 1). The structured report template consists of four sections: 1) clinical evaluation: a statement regarding the patient's clinical performance, prior treatment methods, current pathological status, and prior/current PSA level; 2) imaging technique: details of the pelvic mpMRI technique, including the imaging protocol and quality [notably, obvious deviations in techniques and artefacts should be recorded with their causes (e.g., metal implant artefacts, patient movement)]; 3) key radiological findings: the presence of metastasis and the RAC scores for each pelvic region (including primary disease, skeletal pelvis, lymph nodes, seminal vesicles, rectum, and bladder) based on the baseline and follow-up examination; and 4) diagnostic impression: an overall diagnostic impression.

### Image interpretation

All examinations were retrospectively and independently reviewed, interpreted, and scored according to MET-RADS-P guidelines by two senior radiologists (all with six years of experience in urinary radiology) and two junior radiologists (all with three years of

#### Main points

- The structured report improved the accuracy of metastasis detection for readers.
- The agreement of senior readers for primary response assessment category (RAC) scoring was higher than that of the secondary RAC scoring.
- The agreement of senior readers for primary RAC scoring was higher than that of junior readers.

**1. Clinical evaluation**

**1.1 Pathological result**  
 Time  Result

**1.2 Prior and current PSA level**

Time	PSA level
<input type="text"/>	<input type="text"/>
<input type="text"/>	<input type="text"/>
<input type="text"/>	<input type="text"/>
<input type="text"/>	<input type="text"/>

**1.3 Prior and current therapy**

radiotherapy

chemotherapy

endocrine therapy

Other

**1.4 Prior MRI**

Primary disease

Metastatic state

**2. Technique evaluation**

Imaging protocol  T2WI  T1WI  DWI  ADC

Imaging quality  incomplete mpMRI protocol  
 Unqualified scanning parameter  
 Image artifact  Metal artifact  
 Motion artifact

**3. Radiological findings**

Primary disease  Skeletal pelvis

Involved  Yes  No  Involved  Yes  No

RAC-1   RAC-2   RAC-1   RAC-2

Lymph nodes  Seminal vesicles

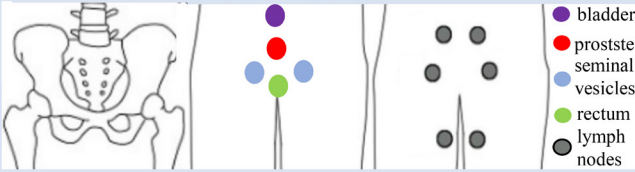
Involved  Yes  No  Involved  Yes  No

RAC-1   RAC-2   RAC-1   RAC-2

Rectum  Bladder

Involved  Yes  No  Involved  Yes  No

RAC-1   RAC-2   RAC-1   RAC-2



**4. Diagnostic impression**

experience in urinary radiology). To reproduce the typical pelvic mpMRI interpretation workflow as much as possible, the four radiologists could obtain access to retrospective MRI examinations on a PACS workstation. For follow-up assessment after therapy, the reports of prior examinations and all clinical information were made available to the radiologists.

Each radiologist read the same pair of MRI examinations twice with and without the structured report template (a structured and conventional report, respectively), with a one-month washout period (each radiologist read the assigned MRI scans without the structured report template for the first time and with the structured report template for the second time after one month). After image interpretation, the presence or absence of metastasis was noted for each anatomic region, and two RAC values between 1–5 (Figures 2, 3) were recorded for the primary and secondary metastatic regions in case of the heterogeneity of responses according to the MET-RADS-P guidelines. The primary RAC value is based on the predominant pattern (more than half of the lesions) of response within the region. The secondary RAC value represents the second most common response pattern within the regions (when assessing a single lesion in a region, the secondary RAC value is exempt). A radiology expert (with more than 15 years of reading experience) reviewed and evaluated all pelvic mpMRI examinations to indicate the reference standard.

### Statistical analysis

After testing, the data was found to be not normally distributed. As such, clinical data (including the age and PSA level of the patient cohort) are represented as medians and interquartile ranges. The interreader agreement between the radiologists for region-based metastatic lesion detection was evaluated by Cohen's kappa statistics (*K*). The primary and secondary RAC scores for each region were evaluated using weighted Cohen's kappa statistics (*K*).<sup>11,12</sup> Interreader agreement was interpreted as none to slight (*K* < 0.20), fair (*K*: 0.21–0.40), moderate (*K*: 0.41–0.60), substantial (*K*: 0.61–0.80), or excellent (*K*: 0.81–1.00). Statistical analysis was carried out with SPSS software (version 23.0, IBM Corp., Armonk, NY, USA). Statistical significance was set at *P* < 0.05.

**Figure 1.** The structured report template of follow-up pelvic multiparametric magnetic resonance imaging based on the METastasis Reporting and Data System for Prostate Cancer guidelines.



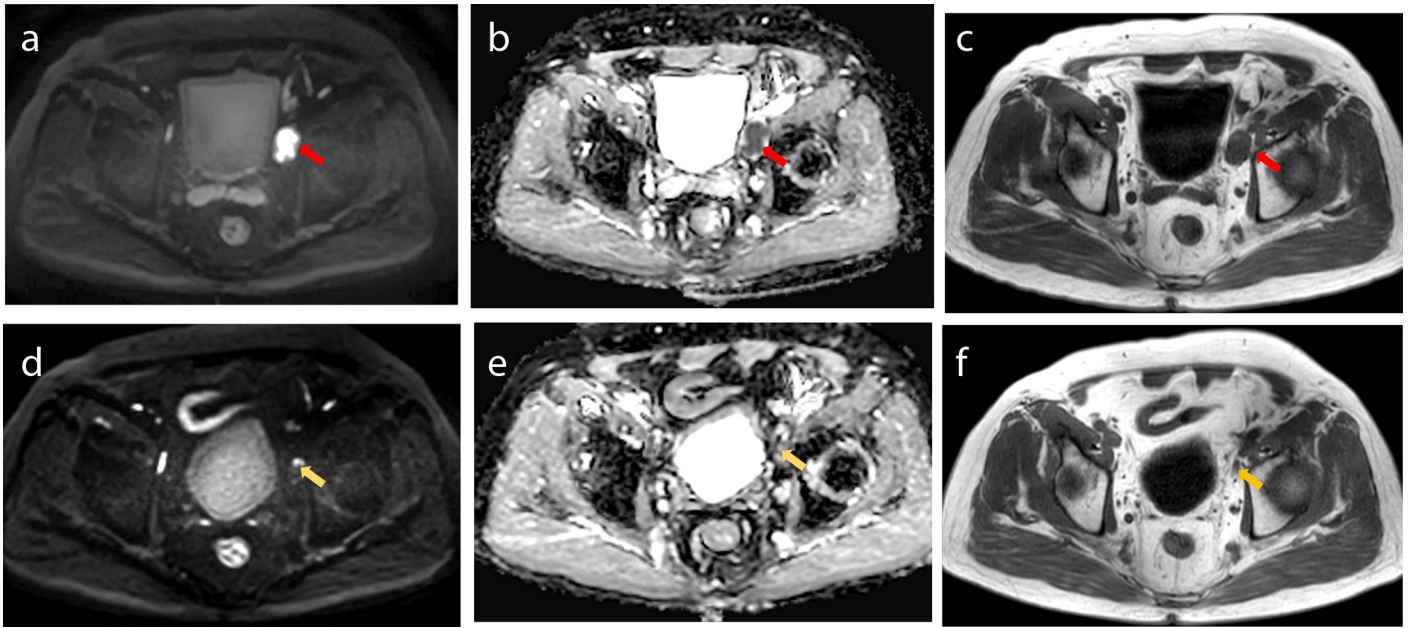


**Figure 2.** Example images of a 72-year-old patient with advanced prostate cancer in response to endocrine therapy, with primary response assessment category 1. (a-c) Axial diffusion-weighted images (DWI) (a), apparent diffusion coefficient (ADC) maps (b), and T1 weighted images (T1WI) (c) before therapy show a metastatic lymph node (red arrow) within the region of the left internal iliac artery. (d-f) The metastatic lymph node (yellow arrow) shrinks on DWI (d), ADC maps (e), and T1WI images (f) after endocrine therapy.

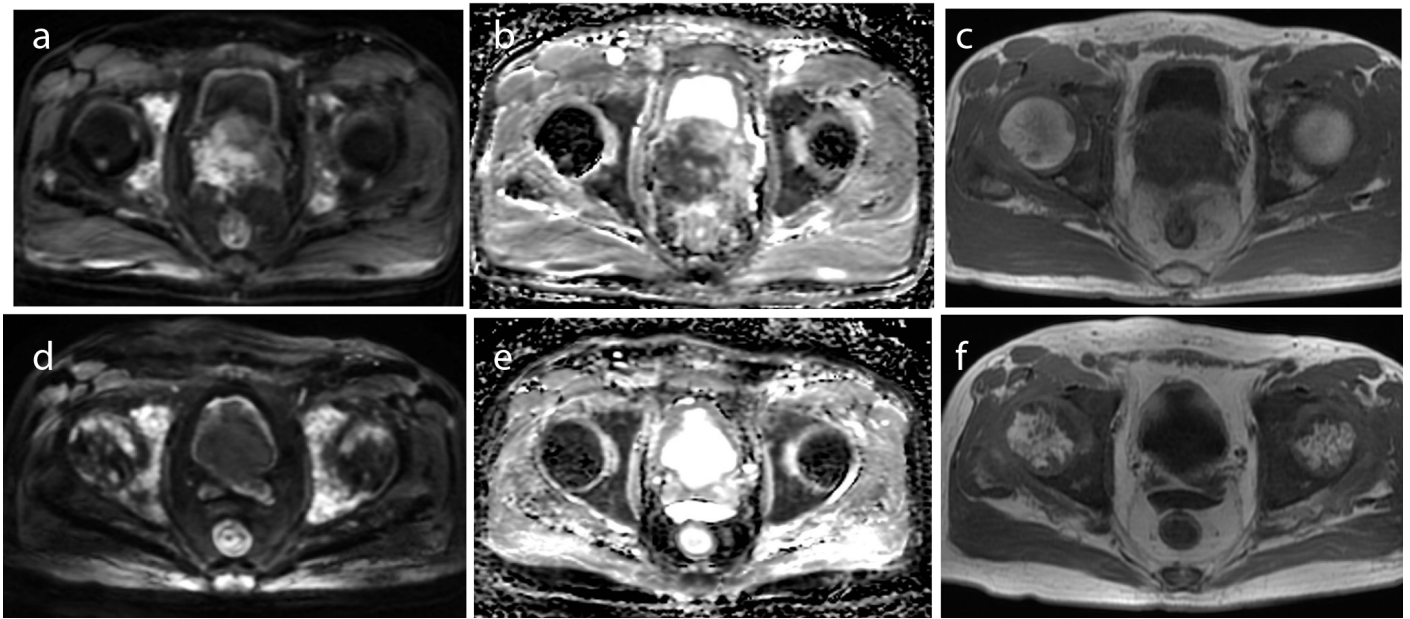


**Figure 3.** Example images of a 78-year-old advanced prostate cancer patient who is progressing, with primary response assessment category 5. (a-c) Axial diffusion-weighted images (DWI) (a), apparent diffusion coefficient (ADC) maps (b), and T1 weighted images (T1WI) (c) at the baseline pelvic show multiparametric magnetic resonance imaging (MRI) the presence of diffuse lesions in pelvic bones. (d-f) The lesions are more extensive in the follow-up MRI of DWI (d), ADC maps (e), and T1WI images (f).

**Table 1.** Baseline characteristics of the study cohort (n = 105)

Parameters	
Age (y)	76 (68, 82)
PSA* level (IQR; ng/mL)	26.33 (3.56, 74.94)
Post-MRI therapy method (no. of patients)	
Radiotherapy	21
Chemotherapy	20
Endocrine therapy	20
Radical prostatectomy	24
Endocrine therapy + radiotherapy	10
Radical prostatectomy + radiotherapy	10
Gleason score <sup>#</sup> (no. of patients)	
4 + 3	13
4 + 4	10
4 + 5	11
Distributed site of pelvic metastases (no. of metastatic lesions)	
Rectum	24
Bladder	31
Lymph nodes	103
Skeletal pelvis	80
Seminal vesicles	37

\*The PSA determinations were performed less than two weeks before baseline pelvic mpMRI scanning. <sup>#</sup>The Gleason score was only available for patients who underwent radical prostatectomy. PSA, prostate specific antigen; IQR, interquartile range; MRI, magnetic resonance imaging; mpMRI, multiparametric magnetic resonance imaging.

## Results

### Patient demographics

The clinical, radiological, and pathological characteristics of the study cohort at the time of inclusion are summarized in Table 1. For 34 of the 105 patients who had undergone radical prostatectomy, a Gleason score (GS) of 4 + 3 was the most common pattern (38%, n = 13), followed by a GS of 4 + 5 (33%, n = 11) and a GS of 4 + 4 (29%, n = 10). The remaining patients were treated with radiotherapy (n = 21), chemotherapy (n = 20), endocrine therapy (n = 20), and endocrine therapy combined with radiotherapy (n = 10).

The number and distribution of metastatic sites at the baseline MRI scanning are shown in Table 1. A total of 275 regions were inspected across the 163 mpMRI examinations, and lymph nodes were the most frequent regions of metastasis (n = 103), followed by bone (n = 80) and seminal vesicles (n = 37). Of the 163 mpMRI examinations, 90 were found to have multiple metastases, and 36 of 90 patients had both lymph node and skeletal pelvis metastases. A more detailed distribution of metastatic sites is shown in the Supplementary Material (Supplementary Table 1).

### Detection of metastatic lesions

As all the patients included in this study had metastatic APC, lesion detection of the primary disease at the prostate site was not analyzed here.

As shown in Table 2, two senior radiologists reported the presence of metastasis in a total of 272 and 278 cases with the conventional report, and 263 and 281 with the structured report, respectively. When using the structured report, the two senior radiologists showed substantial to excellent agreement [K values: S1 vs. reference: 0.83 (0.79–0.88); S2 vs. reference: 0.73 (0.68–0.78)] regarding the reference standard for metastatic lesion detection within the five regions. This value was higher than that of the radiologists using the conventional report [K values: S1 vs. reference: 0.72 (0.67–0.77); S2 vs. reference: 0.61 (0.56–0.67)]. In addition, the interreader agreement between the two senior radiologists improved from substantial [K value of conventional report: 0.77 (0.72–0.81)] to excellent with the structured report [K value: 0.84 (0.79–0.88)].

The two junior radiologists reported the presence of metastasis in a total of 299 and 317 cases with the conventional report, and in 301 and 292 cases with the structured report, respectively. Similar to senior radiologists, structured reports improved

the diagnostic accuracy of metastatic lesions and interreader agreement compared with conventional reports. The two junior radiologists showed substantial agreement [K values: J1 vs. reference: 0.66 (0.60–0.71); J2 vs. reference: 0.65 (0.60–0.71)] regarding the reference standard for metastasis detection using the structured report. This value was higher than that of the radiologists using the conventional report [K values: J1 vs. reference: 0.59 (0.53–0.65); J2 vs. reference: 0.57 (0.51–0.63)]. In addition, the interreader agreement between the two junior radiologists improved from moderate [K value of conventional report: 0.58 (0.52–0.64)] to substantial with the structured report [K value: 0.69 (0.64–0.74)]. A more detailed number and distribution of metastatic regions for the 163 mpMRI examinations are provided in the Supplementary Material (Supplementary Table 2).

### Assessment of primary RAC categorization

Considering that the structured report of pelvic mpMRI based on MET-RADS-P guidelines performed better than the conventional report in lesion detection, the researchers further analyzed its effect on RAC categorization for the two senior radiologists and two junior radiologists.

As shown in Table 3, the two senior radiologists achieved high agreement with

**Table 2.** The diagnostic accuracy and interreader agreement of metastatic lesions

	Rectum	Bladder	Lymph nodes	Skeletal pelvis	Seminal vesicles	Overall
Conventional report (no. of metastatic lesions)						
S1	29	33	101	74	35	272
S2	35	37	93	75	38	278
J1	43	41	95	74	46	299
J2	49	46	98	72	52	317
S1 vs. reference (K, 95% CI)	0.62 (0.45–0.78)	0.57 (0.41–0.73)	0.69 (0.57–0.80)	0.75 (0.65–0.85)	0.68 (0.54–0.82)	0.72 (0.67–0.77)
S2 vs. reference (K, 95% CI)	0.49 (0.32–0.66)	0.43 (0.27–0.60)	0.62 (0.50–0.74)	0.62 (0.50–0.74)	0.57 (0.42–0.72)	0.61 (0.56–0.67)
J1 vs. reference (K, 95% CI)	0.47 (0.31–0.62)	0.43 (0.27–0.60)	0.56 (0.43–0.68)	0.61 (0.49–0.73)	0.57 (0.42–0.71)	0.59 (0.53–0.65)
J2 vs. reference (K, 95% CI)	0.40 (0.25–0.55)	0.45 (0.29–0.61)	0.62 (0.50–0.74)	0.58 (0.46–0.70)	0.47 (0.32–0.62)	0.57 (0.51–0.63)
S1 vs. S2 (K, 95% CI)	0.69 (0.55–0.83)	0.66 (0.52–0.80)	0.77 (0.67–0.87)	0.78 (0.71–0.89)	0.70 (0.57–0.83)	0.77 (0.72–0.81)
J1 vs. J2 (K, 95% CI)	0.52 (0.37–0.67)	0.51 (0.36–0.66)	0.55 (0.42–0.68)	0.63 (0.51–0.75)	0.48 (0.33–0.63)	0.58 (0.52–0.64)
Structured report (no. of metastatic lesions)						
S1	26	30	101	73	33	263
S2	31	36	103	76	35	281
J1	39	46	92	75	49	301
J2	37	39	94	81	41	292
S1 vs. reference (K, 95% CI)	0.67 (0.51–0.83)	0.78 (0.65–0.90)	0.84 (0.76–0.93)	0.87 (0.79–0.94)	0.78 (0.66–0.90)	0.83 (0.79–0.88)
S2 vs. reference (K, 95% CI)	0.63 (0.42–0.75)	0.64 (0.50–0.80)	0.76 (0.66–0.87)	0.71 (0.60–0.81)	0.68 (0.54–0.82)	0.73 (0.68–0.78)
J1 vs. reference (K, 95% CI)	0.48 (0.31–0.64)	0.55 (0.40–0.69)	0.69 (0.46–0.71)	0.82 (0.73–0.90)	0.62 (0.49–0.76)	0.66 (0.60–0.71)
J2 vs. reference (K, 95% CI)	0.48 (0.21–0.55)	0.53 (0.37–0.69)	0.68 (0.57–0.79)	0.72 (0.61–0.83)	0.60 (0.45–0.74)	0.65 (0.60–0.71)
S1 vs. S2 (K, 95% CI)	0.81 (0.69–0.93)	0.77 (0.65–0.89)	0.82 (0.72–0.91)	0.87 (0.72–0.91)	0.81 (0.70–0.93)	0.84 (0.79–0.88)
J1 vs. J2 (K, 95% CI)	0.67 (0.54–0.79)	0.55 (0.40–0.69)	0.70 (0.54–0.77)	0.75 (0.65–0.85)	0.68 (0.56–0.80)	0.69 (0.64–0.74)

S1 and S2 indicate the two senior radiologists; J1 and J2 indicate the two junior radiologists. Values in parenthesis represent a 95% confidence interval (CI).

**Table 3.** The interreader agreement of primary RAC categorization (K, 95% CI)

	Primary disease*	Rectum	Bladder	Lymph nodes	Skeletal pelvis	Seminal vesicles	Overall
S1 vs. reference	0.76 (0.63–0.82)	0.73 (0.70–0.91)	0.86 (0.74–0.95)	0.78 (0.69–0.86)	0.71 (0.62–0.83)	0.82 (0.69–0.95)	0.77 (0.60–0.94)
S2 vs. reference	0.78 (0.63–0.86)	0.82 (0.73–0.92)	0.85 (0.71–0.93)	0.79 (0.65–0.94)	0.74 (0.65–0.79)	0.79 (0.64–0.89)	0.76 (0.62–0.93)
J1 vs. reference	0.68 (0.56–0.76)	0.78 (0.69–0.87)	0.80 (0.74–0.92)	0.72 (0.61–0.84)	0.65 (0.53–0.71)	0.71 (0.57–0.84)	0.67 (0.53–0.85)
J2 vs. reference	0.61 (0.53–0.74)	0.71 (0.65–0.84)	0.73 (0.58–0.82)	0.74 (0.60–0.82)	0.63 (0.52–0.75)	0.74 (0.5–0.84)	0.69 (0.51–0.83)
S1 vs. S2	0.80 (0.63–0.91)	0.87 (0.68–0.96)	0.90 (0.73–1.00)	0.85 (0.62–0.94)	0.72 (0.61–0.83)	0.83 (0.61–0.92)	0.81 (0.70–0.96)
J1 vs. J2	0.71 (0.60–0.81)	0.78 (0.61–0.92)	0.79 (0.64–0.90)	0.81 (0.60–0.95)	0.68 (0.54–0.85)	0.76 (0.62–0.82)	0.76 (0.61–0.85)

\*The response assessment category (RAC) evaluation of the primary disease was only performed for patients who had not undergone radical prostatectomy. S1 and S2 indicate the two senior radiologists; J1 and J2 indicate the two junior radiologists. Values in parenthesis represent a 95% confidence interval (CI).

**Table 4.** The interreader agreement of secondary RAC categorization (*K*, 95% CI)

	Primary disease*	Rectum	Bladder	Lymph nodes	Skeletal pelvis	Seminal vesicles	Overall
S1 vs. reference	0.66 (0.51–0.73)	0.71 (0.58–0.80)	0.78 (0.62–0.94)	0.72 (0.56–0.93)	0.64 (0.54–0.73)	0.76 (0.62–0.85)	0.71 (0.53–0.96)
S2 vs. reference	0.71 (0.60–0.82)	0.74 (0.51–0.93)	0.77 (0.63–0.89)	0.70 (0.57–0.91)	0.66 (0.52–0.78)	0.73 (0.52–0.88)	0.72 (0.54–0.93)
J1 vs. reference	0.53 (0.46–0.74)	0.64 (0.49–0.77)	0.65 (0.54–0.82)	0.69 (0.51–0.80)	0.59 (0.41–0.67)	0.62 (0.45–0.81)	0.58 (0.41–0.72)
J2 vs. reference	0.57 (0.44–0.67)	0.62 (0.50–0.75)	0.63 (0.46–0.81)	0.66 (0.52–0.79)	0.56 (0.45–0.76)	0.61 (0.49–0.75)	0.59 (0.43–0.74)
S1 vs. S2	0.78 (0.65–0.90)	0.75 (0.63–0.89)	0.79 (0.71–0.93)	0.82 (0.61–0.93)	0.73 (0.64–0.91)	0.77 (0.60–0.87)	0.75 (0.61–0.87)
J1 vs. J2	0.67 (0.56–0.82)	0.75 (0.61–0.88)	0.74 (0.59–0.86)	0.72 (0.60–0.83)	0.63 (0.56–0.73)	0.63 (0.47–0.74)	0.68 (0.53–0.86)

\*The response assessment category (RAC) evaluation of the primary disease was only performed for patients who had not undergone a radical prostatectomy. S1 and S2 indicate the two senior radiologists; J1 and J2 indicate the two junior radiologists. Values in parenthesis represent a 95% confidence interval (CI).

the reference standard for the primary RAC values [*K* values: S1 vs. reference: 0.77 (0.60–0.94); S2 vs. reference: 0.76 (0.62–0.93)]. The overall agreement between the two senior radiologists for the primary RAC pattern was excellent [*K* value: 0.81 (0.70–0.96)]. For the two junior radiologists, the agreement using the reference standard was substantial [*K* value: J1 vs. reference: 0.67 (0.53–0.85); J2 vs. reference: 0.69 (0.51–0.83)]. The overall interreader agreement between the two junior radiologists had a *K* value of 0.76 (0.61–0.85).

#### Assessment of secondary RAC categorization

As shown in Table 4, for the four radiologists, the agreement was substantial for S1/S2 and the reference standard [*K* values: S1 vs. reference: 0.71 (0.53–0.96); S2 vs. reference: 0.70 (0.54–0.93)], and moderate for J1/J2 and the reference standard [*K* values: J1 vs. reference: 0.58 (0.41–0.72); J2 vs. reference: 0.59 (0.43–0.74)]. The interreader agreement was substantial for both senior and junior radiologists [S1 vs. S2: 0.75 (0.61–0.87); J1 vs. J2: 0.72 (0.53–0.86)]. The primary and secondary RAC values for each region are summarized in the Supplementary Material (Supplementary Table 3).

## Discussion

In this study, the researchers developed a structured report for pelvic mpMRI using MET-RADS-P guidelines and investigated its reproducibility among multiple radiologists on a large cohort of patients with APC who underwent pelvic mpMRI for follow-up evaluation. The results showed that both the senior and junior radiologists performed better when using the structured report than when using the conventional report for metastasis detection, and high interreader agreement

regarding lesion detection and RAC categorization was found when using the structured report. As expected, the level of interreader agreement was generally higher between senior radiologists than between junior radiologists.

As novel whole-body imaging techniques, whole-body MRI and positron emission tomography/computed tomography (PET/CT) are known for being more accurate for evaluating the treatment responses of patient with APC with bone disease, compared with bone scanning and CT.<sup>13</sup> Whole-body MRI has been noted to provide clear categorization of bone metastasis response and is suggested to be suitable for wide deployment in disease detection settings,<sup>14,15</sup> given its established diagnostic accuracy, wide availability, and multi-organ evaluation capabilities.<sup>13,16</sup> However, in terms of the follow-up treatment evaluation, whole-body MRI is probably not a better technique compared with PET techniques, which are ahead in this specific domain.<sup>17,18</sup> Compared with whole-body MRI, several studies have confirmed the advantages of prostate-specific membrane antigen (PSMA) PET/CT for evaluating disease progression and treatment responses.<sup>19,20</sup> Such research shows that PSMA PET/CT promises to become a powerful alternative to whole-body MRI, assuming the limitations of ionizing radiation exposure and spatial resolution are solved.<sup>21</sup>

The subjective criteria applied for assessing metastatic lesions using whole-body MRI may result in unsatisfactory interreader concordance. The MET-RADS-P guidelines were designed to minimize the inconsistencies caused by various reading criteria.<sup>3</sup> However, for radiologists, especially junior radiologists, the MET-RADS-P guidelines are

too complex to use effectively. The *K* value of the interreader agreement between two radiologists varied from 0.56–1.0 (primary RAC) and 0.44–0.93 (secondary RAC) among different regions when using the MET-RADS-P guidelines.<sup>5</sup> By creating a structured report of follow-up pelvic mpMRI according to the standardization requirements of MET-RADS-P and actual clinical work experience of the unit, the study found improved interreader agreement for both RAC assessments compared with conventional reports. This is crucial for the follow-up evaluation of APC patients, as follow-up pelvic mpMRI examinations are usually reviewed by different medical staff at different periods. In addition, in an analysis of body regions, both senior and junior radiologists showed the highest diagnostic accuracy for metastasis detection in the regions of the skeletal pelvis and lymph node with or without structured reports. This may be attributed to the pelvic lymph node and bone metastases being present in most of the enrolled APC patients and the metastases within the two regions often appearing in the form of multiple metastases.

The RAC value provides a qualitative response assessment category for each anatomic region by comparing the alterations of the metastatic lesions between baseline and follow-up examinations. This study found that the interreader agreement between the two junior radiologists for primary RAC in the skeletal region was slightly lower than that in other regions. The reason for this finding is probably due to the different assessment criteria for bones and soft tissues. For response assessments of soft tissues (prostate, bladder, rectum, lymph nodes, and seminal vesicles), the RAC assessment standard was based on the prescribed and established RECIST guidance.<sup>14,22</sup> For bone disease (skeletal pelvis),

the RAC values were summarized using the newly developed MET-RADS criteria,<sup>3</sup> which were more complicated and mainly relied on subjective morphological features, thus affecting the assessment performance and interobserver agreement for bone metastases. Additionally, the interreader agreement on the secondary RAC pattern was slightly lower than that on the primary RAC pattern for both senior and junior radiologists, which may be because the secondary RAC assessment requires readers to be able to identify the response differences present in a small subgroup of metastases. The comparison of the radiologists and reference standard indicated that the accuracy of RAC categorization for senior radiologists was higher than that of junior radiologists, especially for the secondary RAC evaluation. This suggests that the feasibility and accuracy of the structured report for pelvic mpMRI using MET-RADS-P guidelines can be affected by the reader's experience in clinical practice.

In this research, the overall agreement for both primary and secondary RAC assessment between senior radiologists was slightly higher than that between junior radiologists, which differs from the previous study conducted by Pricolo et al.<sup>5</sup> Their results showed high interreader agreement between two readers with different levels of expertise (a senior radiologist with nine years of experience vs. a resident radiologist after six months of training). This may be attributed to the fact that only two readers were involved in their study and the less experienced resident radiologist was trained by the senior radiologist. Compared with the current study's four independent readers, the results of Pricolo et al.'s<sup>5</sup> study may have been affected by selection bias.

The current study had some limitations. First, it was limited to the follow-up analysis of pelvic mpMRI examination for patients with APC by radiologists, while further analysis of the impact on clinical decision-making processes and patient outcomes is not performed here. Therefore, prospective clinical studies are necessary to further consolidate the results. Second, the soft tissue evaluation of the RAC system in this research is tailored to the pelvic region instead of the whole body, which is currently a speculative and tentative application. In addition, although the readers recruited for the study were four independent radiologists, all readers came from the same institution, which may lead them to adopt similar interpretation schemes to reduce a priori variability in clinical assessments. Multicentre studies may be helpful to

address this limitation. The final limitation was the weak standard of reference used. A pathology reference standard or comparison with other techniques (such as PSMA PET/CT) would be superior to the expertise used here, as this is considered best practice. However, it was difficult to gain access to the necessary histological/PET information.

In conclusion, a good interreader agreement was found for the follow-up assessment of APC patients between radiologists who had different levels of expertise using the structured report for pelvic mpMRI based on MET-RADS-P guidelines. In particular, the agreement was excellent between senior radiologists in metastatic lesion detection and qualitative RAC assessment. The study shows that interreader agreement can be improved using MET-RADS-P guidelines and provides insights into its clinical significance for the clinical management of metastasis in a growing number of APC patients.

#### Conflict of interest disclosure

The authors declare no conflicts of interest.

#### References

- Halabi S, Kelly WK, Ma H, et al. Meta-analysis evaluating the impact of site of metastasis on overall survival in men with castration-resistant prostate cancer. *J Clin Oncol.* 2016;34(14):1652-1659. [Crossref]
- Padhani AR, Lecouvet FE, Tunariu N, et al. METastasis Reporting and Data System for Prostate Cancer: practical guidelines for acquisition, interpretation, and reporting of whole-body magnetic resonance imaging-based evaluations of multiorgan involvement in advanced prostate cancer. *Eur Urol.* 2017;71(1):81-92. [Crossref]
- Padhani AR, Tunariu N. Metastasis Reporting and Data System for Prostate Cancer in Practice. *Magn Reson Imaging Clin N Am.* 2018;26(4):527-542. [Crossref]
- Yoshida S, Takahara T, Ishii C, et al. METastasis Reporting and Data System for prostate cancer as a prognostic imaging marker in castration-resistant prostate cancer. *Clin Genitourin Cancer.* 2020;18(4):e391-e396. [Crossref]
- Pricolo P, Ancona E, Summers P, et al. Whole-body magnetic resonance imaging (WB-MRI) reporting with the METastasis Reporting and Data System for Prostate Cancer (MET-RADS-P): inter-observer agreement between readers of different expertise levels. *Cancer Imaging.* 2020;20(1):77. [Crossref]
- Dimarco M, Cannella R, Pellegrino S, et al. Impact of structured report on the quality of preoperative CT staging of pancreatic ductal adenocarcinoma: assessment of intra- and inter-reader variability. *Abdom Radiol (NY).* 2020;45(2):437-448. [Crossref]

- Ottosson F, Baco E, Lauritzen PM, Rud E. The prevalence and locations of bone metastases using whole-body MRI in treatment-naïve intermediate- and high-risk prostate cancer. *Eur Radiol.* 2021;31(5):2747-2753. [Crossref]
- Woo S, Kim SY, Kim SH, Cho JY. Journal club: identification of bone metastasis with routine prostate MRI: a study of patients with newly diagnosed prostate cancer. *AJR Am J Roentgenol.* 2016;206(6):1156-1163. [Crossref]
- Schmidkonz C, Cordes M, Schmidt D, et al. <sup>68</sup>Ga-PSMA-11 PET/CT-derived metabolic parameters for determination of whole-body tumor burden and treatment response in prostate cancer. *Eur J Nucl Med Mol Imaging.* 2018;45(11):1862-1872. [Crossref]
- Liu X, Han C, Wang H, et al. Fully automated pelvic bone segmentation in multiparametric MRI using a 3D convolutional neural network. *Insights Imaging.* 2021;12(1):93. [Crossref]
- Rengo M, Boru CE, Badia S, et al. Preoperative measurement of the hiatal surface with MDCT: impact on surgical planning. *Radiol Med.* 2021;126(12):1508-1517. [Crossref]
- Miskin N, Gaviola GC, Huang RY, et al. Intra- and intersubspecialty variability in lumbar spine MRI interpretation: a multireader study comparing musculoskeletal radiologists and neuroradiologists. *Curr Probl Diagn Radiol.* 2020;49(3):182-187. [Crossref]
- Padhani AR, Lecouvet FE, Tunariu N, et al. Rationale for modernising imaging in advanced prostate cancer. *Eur Urol Focus.* 2017;3(2-3):223-239. [Crossref]
- Scher HI, Morris MJ, Stadler WM, et al. Trial Design and objectives for castration-resistant prostate cancer: updated recommendations from the prostate cancer clinical trials working group 3. *J Clin Oncol.* 2016;34(12):1402-1418. [Crossref]
- Lecouvet FE. Whole-body MR imaging: musculoskeletal applications. *Radiology.* 2016;279(2):345-365. [Crossref]
- Lecouvet FE, Talbot JN, Messiou C, et al. Monitoring the response of bone metastases to treatment with magnetic resonance imaging and nuclear medicine techniques: a review and position statement by the European Organisation for Research and Treatment of Cancer imaging group. *Eur J Cancer.* 2014;50(15):2519-2531. [Crossref]
- Tschelididis I, Vrachimis A. PSMA PET in imaging prostate cancer. *Front Oncol.* 2022;12:831429. [Crossref]
- Orcajo-Rincon J, Muñoz-Langa J, Sepúlveda-Sánchez JM, et al. Review of imaging techniques for evaluating morphological and functional responses to the treatment of bone metastases in prostate and breast cancer. *Clin Transl Oncol.* 2022;24(7):1290-1310. [Crossref]
- Zhou C, Tang Y, Deng Z, et al. Comparison of <sup>68</sup>Ga-PSMA PET/CT and multiparametric MRI for the detection of low- and intermediate-risk prostate cancer. *EJNMMI Res.* 2022;12(1):10. [Crossref]

20. Dyrberg E, Hendel HW, Huynh THV, et al. <sup>68</sup>Ga-PSMA-PET/CT in comparison with <sup>18</sup>F-fluoride-PET/CT and whole-body MRI for the detection of bone metastases in patients with prostate cancer: a prospective diagnostic accuracy study. *Eur Radiol.* 2019;29(3):1221-1230. [\[Crossref\]](#)
21. Mosavi F, Johansson S, Sandberg DT, Turesson I, Sörensen J, Ahlström H. Whole-body diffusion-weighted MRI compared with (18) F-NaF PET/CT for detection of bone metastases in patients with high-risk prostate carcinoma. *AJR Am J Roentgenol.* 2012;199(5):1114-1120. [\[Crossref\]](#)
22. Eisenhauer EA, Therasse P, Bogaerts J, et al. New response evaluation criteria in solid tumours: revised RECIST guideline (version 1.1). *Eur J Cancer.* 2009;45(2):228-247. [\[Crossref\]](#)

Supplementary Table 1. Detailed distribution of pelvic metastases at the time of inclusion	
Regions	Number of lesions
Single region involvement	
Rectum	6
Bladder	8
Lymph nodes	27
Skeletal pelvis	22
Seminal vesicles	10
Multiple region involvement	
Bladder + rectum	2
Lymph nodes + rectum	6
Lymph nodes + bladder	8
Bladder + skeletal pelvis	3
Rectum + skeletal pelvis	2
Bladder + seminal vesicles	2
Seminal vesicles + rectum	1
Lymph nodes + skeletal pelvis	36
Seminal vesicles + skeletal pelvis	3
Lymph nodes + seminal vesicles	8
Lymph nodes + bladder + rectum	1
Lymph nodes + rectum + skeletal pelvis	1
Lymph nodes + bladder+ skeletal pelvis	4
Lymph nodes + seminal vesicles+ rectum	2
Seminal vesicles + rectum + skeletal pelvis	1
Lymph nodes + bladder + seminal vesicles	2
Lymph nodes + seminal vesicles + skeletal pelvis	6
Lymph nodes + seminal vesicles + rectum + skeletal pelvis	1
Lymph nodes + bladder + seminal vesicles + skeletal pelvis	1

**Supplementary Table 2.** The number and distribution of metastatic regions for the 163 multiparametric magnetic resonance imaging examinations

Distribution	Reference standard	Conventional report				Structured report			
		S1	S2	J1	J2	S1	S2	J1	J2
<b>Single region involvement</b>									
Rectum	6	9	10	7	6	8	9	7	7
Bladder	8	11	11	7	8	11	12	12	9
Lymph nodes	27	31	29	26	24	33	28	14	24
Skeletal pelvis	22	20	21	16	16	18	13	16	16
Seminal vesicles	10	5	8	11	10	11	9	13	10
<b>Multiple region involvement</b>									
Bladder + rectum	2	2	3	1	1	4	4	3	3
Lymph nodes + rectum	6	4	2	8	8	4	4	8	7
Lymph nodes + bladder	8	6	8	8	6	4	4	10	4
Rectum + skeletal pelvis	2	2	2	7	3	1	3	2	2
Seminal vesicles + rectum	1	1	1	1	2	2	1	5	3
Bladder + skeletal pelvis	3	4	4	8	5	2	6	3	4
Bladder + seminal vesicles	2	3	2	3	2	1	2	3	3
Lymph nodes + skeletal pelvis	36	32	25	20	17	38	39	24	29
Seminal vesicles + skeletal pelvis	3	3	3	3	2	4	3	2	8
Lymph nodes + seminal vesicles	8	10	7	7	9	7	5	7	5
Lymph nodes + bladder + rectum	1	2	1	3	4	3	3	2	3
Bladder + rectum + skeletal pelvis	-	-	1	2	2	-	-	2	2
Bladder + seminal vesicles + rectum	-	1	1	1	2	-	-	-	1
Lymph nodes + bladder + skeletal pelvis	4	2	2	-	1	3	2	6	6
Lymph nodes + seminal vesicles + rectum	2	3	2	3	4	3	2	3	2
Seminal vesicles + rectum + skeletal pelvis	1	1	2	2	3	-	2	1	-
Bladder + seminal vesicles + skeletal pelvis	-	1	-	-	3	-	-	1	1
Lymph nodes + bladder + seminal vesicles	2	1	2	3	4	1	2	3	2
Lymph nodes + seminal vesicles + skeletal pelvis	6	5	5	6	6	3	5	9	5
Lymph nodes + seminal vesicles + rectum + skeletal pelvis	1	1	3	2	1	-	3	2	1
Lymph nodes + bladder + seminal vesicles + skeletal pelvis	1	-	1	2	2	1	1	1	-
Lymph nodes + bladder + rectum + skeletal pelvis	-	-	1	3	5	-	-	-	1
Lymph nodes + bladder + seminal vesicles + rectum	-	-	1	1	1	-	1	-	-
Lymph nodes + bladder + seminal vesicles + rectum + skeletal pelvis	-	-	-	-	1	-	-	-	-

S1 and S2 indicate the two senior radiologists; J1 and J2 indicate the two junior radiologists.

**Supplementary Table 3.** The distribution of primary and secondary RAC for each radiologist

Regions	Primary RAC					Secondary RAC				
	Reference standard	S1	S2	J1	J2	Reference standard	S1	S2	J1	J2
<b>Primary disease*</b>										
RAC-1	23	20	21	18	18	18	16	15	14	17
RAC-2	27	29	25	29	31	23	25	22	26	21
RAC-3	15	17	18	18	17	12	15	16	11	13
RAC-4	3	4	2	2	2	1	2	2	3	3
RAC-5	2	2	3	3	2	-	1	-	-	1
<b>Bladder</b>										
RAC-1	9	7	11	14	9	10	9	8	7	9
RAC-2	13	12	15	20	15	5	6	7	6	4
RAC-3	7	7	8	8	10	5	4	3	4	3
RAC-4	1	2	3	3	3	-	1	1	-	-
RAC-5	1	2	-	1	2	1	1	1	1	-
<b>Rectum</b>										
RAC-1	11	12	14	13	11	4	3	4	5	4
RAC-2	6	6	7	13	9	7	9	5	4	4
RAC-3	4	5	6	10	9	4	3	4	6	1
RAC-4	2	2	3	1	4	-	1	-	-	-
RAC-5	1	1	1	2	4	2	3	2	2	2
<b>Lymph nodes</b>										
RAC-1	42	34	39	31	26	32	29	27	22	26
RAC-2	35	34	31	33	28	33	32	30	26	28
RAC-3	15	20	21	15	21	23	23	23	20	21
RAC-4	6	7	6	8	1	3	3	2	2	1
RAC-5	5	6	6	5	2	2	2	3	2	2
<b>Skeletal pelvis</b>										
RAC-1	27	20	22	24	27	22	19	17	19	17
RAC-2	30	26	30	31	27	27	23	24	24	24
RAC-3	16	17	13	14	19	17	18	12	15	17
RAC-4	6	9	9	6	6	4	4	5	3	2
RAC-5	1	1	2	-	1	-	-	1	-	-
<b>Seminal vesicles</b>										
RAC-1	13	10	9	18	10	11	9	7	9	10
RAC-2	14	13	12	18	17	7	9	4	8	5
RAC-3	6	6	8	8	5	6	5	6	5	2
RAC-4	3	3	4	4	6	4	3	3	4	3
RAC-5	1	1	1	2	3	-	-	-	-	-

\*The response assessment category (RAC) evaluation of the primary disease was only performed for the patients who had not undergone radical prostatectomy. S1 and S2 indicate the two senior radiologists; J1 and J2 indicate the two junior radiologists.





# Artificial intelligence in diagnostic ultrasonography

Oğuz Dicle

## ABSTRACT

Artificial intelligence (AI) continues to change paradigms in the field of medicine with new applications that are applicable to daily life. The field of ultrasonography, which has been developing since the 1950s and continues to be one of the most powerful tools in the field of diagnosis, is also the subject of AI studies, despite its unique problems. It is predicted that many operations, such as appropriate diagnostic tool selection, use of the most relevant parameters, improvement of low-quality images, automatic lesion detection and diagnosis from the image, and classification of pathologies, will be performed using AI tools in the near future. Especially with the use of convolutional neural networks, successful results can be obtained for lesion detection, segmentation, and classification from images. In this review, relevant developments are summarized based on the literature, and examples of the tools used in the field are presented.

## KEYWORDS

Artificial intelligence, deep learning, machine learning, radiology, ultrasonography

Ultrasonography has been an effective diagnostic tool since the 1950s. As ultrasonography is a diagnostic tool providing a cross-sectional examination, its real-time evaluation capacity and absence of ionizing radiation are its outstanding strengths. Over the years, higher-quality images have been obtained in ultrasonography, and the use of the method has been expanded with applications such as Power Doppler, harmonic tissue imaging, contrast-enhanced ultrasonography, three-dimensional (3D) and four-dimensional imaging, and elastography, as well as Doppler imaging. Significant gains have been made in the clinical field with applications such as transrectal and intraoperative ultrasonography.

However, there are still various problems in ultrasonography imaging that can make diagnosis challenging. The main problems are the noise and artifacts that occur in imaging.<sup>1</sup> Artifacts usually appear due to the transmission and reflection behaviors of sound waves in tissues and sampling problems.<sup>2</sup> Noise sources are also varied. The main types of noise observed in ultrasound images are salt-and-pepper noise, Poisson noise, Gaussian noise, and speckling. Salt-and-pepper noise, also called random or impulse noise, is the difference in color and density in one pixel compared with the neighboring pixels, depending on sudden signal changes. The noise, called speckling, is caused by the interference of the reflected and rotating sound wave with other waves and causes distortions in the image that can result in diagnostic errors. Gaussian noise is also known as electronic noise and is connected to the device. Poisson noise is also caused by the electronic system. Various filter methods have been developed to eliminate these problems and improve image quality.<sup>3</sup>

In addition to the problems in image quality, as in all radiological examinations, we need to detect, differentiate, and define the lesions and specify which pathology they are associated with. After diagnosis, procedures such as classification and staging are required. However, since the ultrasonography examination is in real time and user dependent, it causes problems specific to this modality. This can lead to major differences in pathology detection, identification, and diagnosis. There are also image quality differences between devices from different

From the Department of Radiology (O.D. ✉ odicle59@gmail.com), Dokuz Eylül University Faculty of Medicine, Izmir, Turkey.

Received 03 January 2022; revision requested 13 February 2022; accepted 28 March 2022.



Epub: 02.01.2023

Publication date: 31.01.2023

DOI: 10.4274/dir.2022.211260

You may cite this article as: Dicle O. Artificial intelligence in diagnostic ultrasonography. *Diagn Interv Radiol.* 2023;29(1):40-45.

manufacturers, and the sensitivity of observing the same pathology may vary in different devices.<sup>4</sup>

With the artificial intelligence (AI) studies that have developed in recent years, a new solution opportunity has emerged in the image quality and diagnostic processes described above. This opportunity arose when deep learning from machine-learning methods, a sub-element of AI, used convolutional neural networks. However, the data obtained are very large scale, and improvements in computing speeds accelerate this process.<sup>5</sup>

Machine learning aims to obtain an output after analyzing the data at hand and making sense of the variables in the data for a situation that needs to be solved using different techniques.<sup>5</sup> In this way, it is possible to easily perform complex, time-consuming, and inadequately sensitive operations for human beings through machines. In recent years, machine learning has started to be replaced by deep learning using the methods developed. Machine learning requires an educational process, similar to that in humans. For this purpose, appropriate training sets are prepared where necessary. Three types of learning methods are used: supervised, unsupervised, and reinforced learning methods. The most common among them is supervised learning. In supervised learning, the preparation of the training set and the labeling of the data content are carried out by an expert. Thus, a gold standard is prepared for the machine, which is called ground truth in the field of machine learning.<sup>5</sup> For an AI study to be used to determine thyroid nodules from ultrasonography images, it is necessary to draw nodule boundaries in a certain number of images and define the content and boundary properties to indicate whether the lesion is benign or malignant. Supervised learning is very useful in operations

such as classifying lesions, characterizing them, and comparing the similarities. As might be expected, these operations require a large amount of time-consuming labeling and may contain serious errors. Therefore, unsupervised learning methods have been developed.<sup>6,7</sup>

In unsupervised learning, attributes, patterns, and clustered information in a data set can be extracted through generated pathways (algorithms) without the need to label them. Attributes are properties that define the organ or lesion to be distinguished. It is the name given to descriptive properties, such as the size, shape, edge properties, internal structure, and echogenicity of the lesion. Reinforced learning is a unified and dynamic form of these two methods, and learning is performed with continuous positive or negative feedback.

There are several pathways used according to the method that is selected during the learning process. For supervised learning, a method, (for example, support vector machines, logistic regression, Naive Bayes, random forest, K-nearest neighbor, or decision tree) is chosen. Clustering methods, self-organizing maps, principal component analyses, and K-means are used in unsupervised learning. Choosing the right method to provide the most appropriate solution is important for success.<sup>8,9</sup>

Deep learning, an important area of machine learning, uses multilayered artificial neural networks. These networks, which imitate natural neural networks, evaluate the input data in terms of compliance with the gold standard obtained from the training set at every port it encounters on the network. If a threshold value can be exceeded in compliance, this information turns into ready-to-use information for other pathways in the network.

Because layers are 3D, a path that moves between nonlinear but hidden layers is used. In multilayered convolutional neural networks, attributes in the input are first collected in a representative pool. Attribute information that comes to the pool from different paths of the network is collected in new pools and reaches a fully connected layer by advancing and gradually purifying the threshold values in the network, as in neurons. After the classification has been made, the output (action) and gain are obtained. This flow in deep learning is schematized in Figure 1. Convolutional networks can be used successfully for purposes such as classification, lesion detection, and segmentation.

Since there are hidden layers in deep-learning paths, and it is not known how feature extraction is achieved, this process has been likened to a black box. This created a credibility problem and led to new studies called “explainable AI” in the field of AI.<sup>10</sup> Most of these studies are ongoing studies and have not yet reached full maturity.

Different elements play a role in a successful AI application. The most important of these are numerous and well-marked data sets. There are various limitations when it comes to ultrasonography. Ultrasonography examinations are obtained in real time, with the image quality preferred by the user and preferred cross-section angle and probe type, apart from the automatically obtained 3D ultrasound breast scans. In daily practice, images remain unarchived, and only selected sample images are stored. This greatly destroys the image standard and prevents the creation of training sets that reflect real life. Devices from different companies also create another obstacle. The spatial resolution of ultrasonography images is low, and artifacts can be very high. Therefore, serious preliminary image improvement work is re-

#### Main points

- Artificial intelligence (AI) can assist with difficult, time-consuming, and accurate processes, such as image quality improvement, lesion detection, segmentation, and classification, in ultrasonography examinations.
- The main challenges of AI studies in ultrasonography are the real-time imaging of the examination, its dependency on the user, and the abundance of noise sources in the image.
- AI studies, as a new field of terminology and knowledge, require multidisciplinary collaborations, and radiologists need to adopt the necessary roles in field-specific data management.

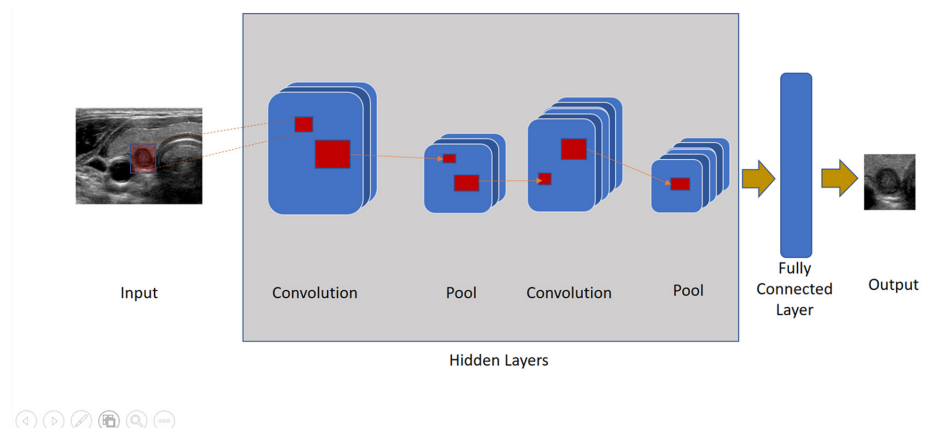


Figure 1. Basic data processing in convolutional networks

quired for healthy feature extraction in AI studies related to ultrasonography.<sup>11</sup>

Various methods to obtain an artifact-free ultrasonography image have been tried. One of the methods developed for this is real-time spatial compound imaging.<sup>12</sup> In this method, special transducers that can take sections from the imaged object from different angles at the same time by scattering sound waves are used. In general, the average of the three to nine sections obtained is taken as the real-time representative image. Speckle, clutter, and other acoustic artifacts are significantly reduced in these images. One method of image enhancement is harmonic imaging. Reverberation and side-lobe artifacts are reduced through this imaging method, which considers harmonics that are basic or multiples of the transmitted frequency from the tissue due to the nonlinear emission of sound waves throughout the body tissues. A clearer appearance of cysts, improvements in the signal-to-noise ratio, and better results are achieved, especially in overweight patients.<sup>13</sup>

General image enhancement tools have also been used to improve the quality of ultrasonography images. In addition to filters and iterative back-projection methods, studies have been conducted in this field using machine or deep-learning methods.<sup>14,15</sup> One focus in studies on ultrasonography has been acoustic shadow determination pathways. Geometric and statistical methods have been tried for this.<sup>16</sup> In these studies, the inability to prepare quality training sets remains the largest obstacle.

Ultrasonography image analysis studies are collected into three groups: classification, determination, and segmentation.<sup>14</sup> Classification studies are used to separate the sections that are the most suitable from the numerous section images taken or to separate the self-qualities extracted in deep-learning studies. The five basic methods used in classification are logistic regression, Naive Bayes, K-nearest neighbors, decision tree, and support vector machines.<sup>5</sup>

Image determination aims to distinguish between anatomical formations or pathological findings. Effective segmentation is required for these studies, and then, classification paths are used. This creates a path to diagnosis. Segmentation has formed the basis of computer-aided diagnosis. The main methods used in image segmentation are summarized in Table 1.<sup>17</sup>

As presented in Table 1, the methods have advantages and weaknesses, and the performance levels are generally increased with the combination or successive use of these methods. Significant gains have been made in this field through the utilization of learning systems.<sup>18</sup> Algorithms used in the segmentation studies performed using convolutional neural networks and their descriptive properties are listed in Table 2.<sup>18-23</sup>

In deep learning, architectural models are developed by different researchers for convolutional neural networks and subsequent classification algorithms. Examples include the residual neural network, visual geometry group (VGG), auxiliary classifier generative

adversarial network (GAN), and neuro-fuzzy system.<sup>24-27</sup>

## Clinical applications

After many years of studies, products that produce solutions based on machine learning and AI have started to enter clinical practice. One of the areas where studies have gained intensity is the diagnosis and classification of thyroid nodules. There are also products related to the breast and bladder. In addition, most US Food and Drug Administration-approved products are in the field of cardiac ultrasounds. Table 3 provides examples of these products.<sup>11</sup>

There are many publications with deep-learning methods based on convolutional networks and applications, with diagnostic sensitivity and specificity that are equivalent to or better than those of radiologists.<sup>28-31</sup> In a study of 589 thyroid nodules, 396 of which were malignant and 193 of which were benign, Ko et al.<sup>30</sup> found the area under the curve (AUC) to diagnose thyroid malignancy to be 0.805–0.860 for radiologists and 0.845, 0.835, and 0.850 for three convolutional neural networks, respectively. According to the results of this study, there was no significant difference in the AUC between radiologists and convolutional neural networks.<sup>30</sup> In a retrospective multi-cohort study conducted by Li et al.<sup>28</sup> using ultrasound images obtained from three different hospitals, models trained with a set of 131,731 ultrasound images with thyroid cancer were compared with the diagnoses of 16 radiologists. When the results of the models

**Table 1.** Main methods used in image segmentation

Approach	Definition	Superiority	Weakness
Region-based	Grouping pixels with similar properties in a region based on seed points	Simple, performs well with noise	In low-quality ultrasound images, the seeding point should be selected manually Different seed points may give different outputs High edge determination does not guarantee success Needs high computational time and memory
Threshold-based	Achieve threshold value based on peaks and valleys on the histogram of images, which corresponds to regions	Simple	Does not work well with images with a color spectrum Noise sensitivity is high
Edge-based	It works based on identifying sharp discontinuities in the image	Easy to perceive by humans Works well when the edge is prominent and image contrast is high	Very sensitive to noise Does not work well on images with low contrast and smooth change Could not be applied to images with multiple edges
Clustering-based	Categorizes objects into specific groups based on their similarities	Easy to implement. It is an unsupervised path	Very sensitive to noise. Requires a long processing time
Artificial neural networks	It uses the neural network consisting of nodes	Uses training data to solve a complex problem and easily detect errors	The training process is time-consuming

**Table 2.** Algorithms used in segmentation with deep learning

Algorithm	Definition
3D-Unet	A path used in 3D data segmentation, which is preferred in precise volume calculations
AIDAN	An algorithm that improves the performance in ultrasound imaging
CSC	Using consecutive time series in ultrasound videos reduces noise artifacts and performs organ division
DeepLap	Using a custom convolution architecture, the decoder and encoder perform successful segments with a pyramidal pathway in pooling
GAN	An algorithm that improves GAN-based edge forecasting with indiscriminate learning
Decoder–encoder architecture	A semi-automatic segmentation algorithm used in 3D ultrasounds for volume measurement
MFCY	It successfully segments cylindrical-shaped organs using consecutive time series in ultrasound videos
U-net	An algorithm that makes successful segments based on convolutional networks with a small number of training sets

AIDAN, attention guided dual path network; CSC, cropping-segmentation-calibration; GAN, generative adversarial network; 3D, three-dimensional; MFCY, multi-frame cylinder.

**Table 3.** Examples of machine learning tools that have received US Food and Drug Administration approval in the field of ultrasonography

Product name	FDA year of approval	Organ	Vendor	Function
ClearView CAD	2016	Breast	ClearView diagnostics	Using machine learning provides automatic classes and location information according to BI-RADs
AmCAD-UT detection 2.2	2018	Thyroid	BioMed corporation	Calculates the probability of the malignancies of thyroid nodules by evaluating an area marked by the user
Koios DS	2019	Breast	Koios Medical	Using machine learning, it provides automatic classes and location information about a lesion marked by the user according to BI-RADs
EchoGo core	2019	Heart	Ultrasonics Ltd.	It calculates automatic ejection fraction, global longitudinal strain, and left ventricular volume through machine learning
Medo aria	2020	Buttock	Medo.ai Inc.	It helps to train the diagnosis of hip dysplasia through machine learning
Auto 3D bladder volume tool	2020	Bladder	Butterfly network	Calculates bladder volume with machine learning
AVA	2020	Carotid	See-mode technologies	Performs calculations, including intima-media thickness measurement, by segmenting the vessel
Medo thyroid	2021	Thyroid	Medo.ai Inc.	It helps to train the diagnosis of thyroid nodules through machine learning

FDA, Food and Drug Administration; BI-RADS, Breast imaging-reporting and data system.

and radiologists were compared with the images from three different centers, the sensitivity was between 84.3% and 93.4% for the models, whereas it was 89.0%–96.9% for the radiologists. These values for specificity ranged from 86.1% to 87.8% versus 57.1% to 68.6%.<sup>28</sup>

Studies that predict the prognosis of a lesion and make an appropriate decision for biopsy are also promising. Ultrasonography devices that provide data to the radiologist before the decision by analyzing a thyroid nodule and scoring it according to the American College of Radiology Thyroid Image Reporting and Data System criteria have started to be produced.<sup>32</sup>

Studies on breast lesions are also of interest to researchers. Benign-malignant differentiation of lesions in the breast can be successfully made with the help of convolutional networks. Fujioka et al.<sup>33</sup> retrospectively gathered 480 images of 96 benign breast masses and 467 images of 144 malignant breast masses for training data. The

deep-learning model was constructed using the convolutional neural network architecture GoogLeNet, and three radiologists interpreted the test data. The convolutional neural network model and radiologists had a sensitivity of 0.958 and 0.583–0.917, specificity of 0.925 and 0.604–0.771, and accuracy of 0.925 and 0.658–0.792, respectively. The convolutional neural network model had an equal or better diagnostic performance compared with the radiologists (AUC: 0.913 and 0.728–0.845,  $P = 0.010$ –0.140).<sup>33</sup>

It is possible to parse attributes obtained with convolutional networks with classification methods, such as VGG and support vector machine, and match them with the breast imaging-reporting and data system criteria. With the models developed, lymph node metastasis can be predicted from images detected through ultrasound.<sup>34</sup> Different researchers used the methods presented in Table 2 to segment breast lesions and achieve certain successes. In one of these studies,

researchers used the Multi-U-Net segmentation pathway to divide suspicious breast masses with high performance in ultrasonography.<sup>35</sup> Another group of researchers was able to achieve more successful results than other segmentation methods by automatically segmenting ultrasound images using GAN architecture.<sup>36</sup>

Similar approaches continue to be conducted to evaluate malignancy in cystic and solid masses of ovaries, detect prostate cancer, evaluate ultrasound images in liver masses, and segment kidney masses.<sup>37–41</sup> Schmauch trained an algorithm on a data set proposed during a data challenge. The data set was composed of 367 two-dimensional ultrasound images from 367 individual livers, captured at various institutions. Their model reached mean receiver operating characteristic curve–AUC scores of 0.935 for focal liver lesion detection and 0.916 for focal liver lesion characterization over three shuffled three-fold cross-validations performed using the training data.<sup>40</sup>

One of the areas of interest to researchers is vascular evaluations through ultrasound. A success rate of up to 90% has been achieved in the evaluation of images of carotid vascular walls and plaques with convolutional networks and the segmentation of fat cap, fibrous valve, and calcified sections in plaques.<sup>42</sup> With the carotid intima-media thickness classification, it will be possible to predict the early diagnosis of atherosclerosis. In the same way, models that predict stroke have been created.<sup>43</sup> There are also studies on the detection and division of lesions in deep vein thrombus.<sup>44</sup>

Segmenting organs or structures through selected areas or the entire image in the field of obstetric ultrasonography can contribute to diagnoses. Therefore, a considerable amount of research has been conducted on this subject. The cropping–segmentation–calibration method provided in Table 2 is one of the most commonly used tools in this field. In moving structures, such as heart valves, this model can produce very successful segmentation.<sup>21</sup> Software has also been developed that allows automatic measurements, such as abdominal circumference, femur length, amniotic fluid volume, and placenta volume in the fetus, to be taken using the same methods.<sup>45–47</sup> With these measurements, many clinical studies, especially predicting pregnancy complications, are possible. As mentioned above, the biggest challenge in these studies is the lack of a standard in the image quality and section level and the potential for errors in the data set to be processed. It is thought that deep-learning networks can help to overcome this problem, and a selection of suitable series is used. The automatic detection of congenital anomalies is one of the most anticipated developments in this field. If there is a large enough data set, there will be significant developments in the near future.

As a result, with the widespread use of AI, gains may be expected to increase diagnostic accuracy, provide reliable support to radiologists in clinical decisions, reduce the workload of radiologists, increase their efficiency, and create an opportunity for patients where access to health is limited. To be part of this process, all parties must be included in multidisciplinary working groups, and highly accurate algorithms must be developed by creating excellent data sets.

## References

- Sassaroli E, Crake C, Scorza A, Kim DS, Park MA. Image quality evaluation of ultrasound imaging systems: advanced B-modes. *J Appl Clin Med Phys*. 2019;20(3):115-124. [\[CrossRef\]](#)
- Feldman MK, Katyal S, Blackwood MS. US artifacts. *Radiographics*. 2009;29(4):1179-1189. [\[CrossRef\]](#)
- Gupta M, Taneja U, Chand L. Performance enhancement and analysis of filters in ultrasound image denoising. *Procedia Comp Science*. 2018;132:643-652. [\[CrossRef\]](#)
- Park SH. Artificial intelligence for ultrasonography: unique opportunities and challenges. *Ultrasonography*. 2021;40(1):3-6. [\[CrossRef\]](#)
- Choy G, Khalilzadeh O, Michalski M, et al. Current applications and future impact of machine learning in radiology. *Radiology*. 2018;288(2):318-328. [\[CrossRef\]](#)
- Erickson BJ, Korfiatis P, Akkus Z, Kline TL. Machine learning for medical imaging. *Radiographics*. 2017;37(2):505-515. [\[CrossRef\]](#)
- Wang S, Summers RM. Machine learning and radiology. *Med Image Anal*. 2012;16(5):933-951. [\[CrossRef\]](#)
- Jordan MI, Mitchell TM. Machine learning: trends, perspectives, and prospects. *Science*. 2015;349(6245):255-260. [\[CrossRef\]](#)
- Kohli M, Prevedello LM, Filice RW, Geis JR. Implementing machine learning in radiology practice and research. *AJR Am J Roentgenol*. 2017;208(4):754-760. [\[CrossRef\]](#)
- Arrita AB, Rodríguez ND, Ser JD, et al. Explainable artificial intelligence (XAI): concepts, taxonomies, opportunities and challenges responsible toward AI. *Information Fusion*. 2020;58:82-115. [\[CrossRef\]](#)
- Komatsu M, Sakai A, Dozen A, et al. Towards clinical application of artificial intelligence in ultrasound imaging. *Biomedicines*. 2021;9(7):720. [\[CrossRef\]](#)
- Entrekin RR, Porter BA, Sillesen HH, Wong AD, Cooperberg PL, Fix CH. Real-time spatial compound imaging: application to breast, vascular, and musculoskeletal ultrasound. *Semin Ultrasound CT MR*. 2001;22(1):50-64. [\[CrossRef\]](#)
- Desser TS, Jeffrey RB Jr, Lane MJ, Ralls PW. Tissue harmonic imaging: utility in abdominal and pelvic sonography. *J Clin Ultrasound*. 1999;27(3):135-142. [\[CrossRef\]](#)
- Ortiz SHC, Chiu T, Fox MD. Ultrasound image enhancement: a review. *Biomedical Signal Processing and Control*. 2012;7(5):419-428. [\[CrossRef\]](#)
- Joel T, Sivakumar R. Despeckling of ultrasound medical images: a survey. *Journal of Image and Graphics*. 2013;1(3):161-165. [\[CrossRef\]](#)
- Yasutomi S, Arakaki T, Matsuoka R, et al. Shadow estimation for ultrasound images using auto-encoding structures and synthetic shadows. *Appl Sci*. 2021;11(3):1127. [\[CrossRef\]](#)
- Liu X, Song L, Liu S, Zhang Y. A review of deep-learning-based medical image segmentation methods. *Sustainability*. 2021;13(3):1224. [\[CrossRef\]](#)
- Litjens G, Kooi T, Bejnordi BE, et al. A survey on deep learning in medical image analysis. *Med Image Anal*. 2017;42:60-88. [\[CrossRef\]](#)
- Ronneberger O, Fischer P, Brox T. U-Net: convolutional networks for biomedical image segmentation. In: Navab N, Hornegger J, Wells W, Frangi A, eds. *Medical Image Computing and Computer-Assisted Intervention – MICCAI 2015*. MICCAI 2015. Lecture Notes in Computer Science, vol 9351. Springer, Cham. [https://doi.org/10.1007/978-3-319-24574-4\\_28](https://doi.org/10.1007/978-3-319-24574-4_28) [\[CrossRef\]](#)
- Chen LC, Papandreou G, Kokkinos I, Murphy K, Yuille AL. Deeplab: Semantic image segmentation with deep convolutional nets, atrous convolution, and fully connected crfs. *IEEE Trans Pattern Anal Mach Intell*. 2018;40(4):834-848. [\[CrossRef\]](#)
- Dozen A, Komatsu M, Sakai A, et al. Image Segmentation of the ventricular septum in fetal cardiac ultrasound videos based on deep learning using time-series information. *Biomolecules*. 2020;10(11):1526. [\[CrossRef\]](#)
- Goodfellow I, Pouget-Abadie J, Mirza M, et al. Generative adversarial networks. *Commun ACM*. 2020;63(11):139-144. [\[CrossRef\]](#)
- Çiçek Ö, Abdulkadir A, Lienkamp SS, Brox T, Ronneberger O. 3D U-Net: learning dense volumetric segmentation from sparse annotation; proceedings of the international conference on medical image computing and computer-assisted intervention; Istanbul, Turkey. 17–21 October 2016; pp. 424-432. [\[CrossRef\]](#)
- Ren H, El-khany M, Lee J. DN-ResNet: efficient deep residual network for image denoising. *Asian Conference on Computer Vision*. 2018:215-230. [\[CrossRef\]](#)
- Mei Y, Jin H, Yu B, Wu E, Yang K. Visual geometry group-UNet: deep learning ultrasonic image reconstruction for curved parts. *J Acoust Soc Am*. 2021;149(5):2997. [\[CrossRef\]](#)
- Shi G, Wang J, Qiang Y, et al. Knowledge-guided synthetic medical image adversarial augmentation for ultrasonography thyroid nodule classification. *Comput Methods Programs Biomed*. 2020;196:105611. [\[CrossRef\]](#)
- Hosseini MS, Zekri M. Review of medical image classification using the adaptive neuro-fuzzy inference system. *J Med Signals Sens*. 2012;2(1):49-60. [\[CrossRef\]](#)
- Li X, Zhang S, Zhang Q, et al. Diagnosis of thyroid cancer using deep convolutional neural network models applied to sonographic images: a retrospective, multicohort, diagnostic study. *Lancet Oncol*. 2019;20(2):193-201. Erratum in: *Lancet Oncol*. 2020;21(10):e462. [\[CrossRef\]](#)

29. Guan Q, Wang Y, Du J, et al. Deep learning-based classification of ultrasound images for thyroid nodules: A large scale of a pilot study. *Ann Transl Med.* 2019;7(7):137. [\[CrossRef\]](#)
30. Ko SY, Lee JH, Yoon JH, et al. Deep convolutional neural network for the diagnosis of thyroid nodules on ultrasound. *Head Neck.* 2019;41(4):885-891. [\[CrossRef\]](#)
31. Moussa O, Khachnaoui H, Guetari R, Khlifa N. Thyroid nodules classification and diagnosis in ultrasound images using fine-tuning deep convolutional neural network. *Int J Imaging Syst Technol.* 2020;30(1):185-195. [\[CrossRef\]](#)
32. Han M, Ha EJ, Park JH. Computer-aided diagnosis system for thyroid nodules on ultrasonography: diagnostic performance based on the thyroid imaging reporting and data system classification and dichotomous outcomes. *AJNR Am J Neuroradiol.* 2021;42(3):559-565. [\[CrossRef\]](#)
33. Fujioka T, Kubota K, Mori M, et al. Distinction between benign and malignant breast masses at breast ultrasound using deep learning method with a convolutional neural network. *Jpn J Radiol.* 2019;37(6):466-472. [\[CrossRef\]](#)
34. Zhou LQ, Wu XL, Huang SY, et al. Lymph node metastasis prediction from primary breast cancer US images using deep learning. *Radiology.* 2020;294(1):19-28. [\[CrossRef\]](#)
35. Kumar V, Webb JM, Gregory A, et al. Automated and real-time segmentation of suspicious breast masses using convolutional neural network. *PLoS One.* 2018;13(5):e0195816. [\[CrossRef\]](#)
36. Singh VK, Abdel-Nasser M, Akram F, et al. Breast tumor segmentation in ultrasound images using contextual-information-aware deep adversarial learning framework. *Expert Syst Appl.* 2020;162:113870. [\[CrossRef\]](#)
37. Christiansen F, Epstein EL, Smedberg E, Åkerlund M, Smith K, Epstein E. Ultrasound image analysis using deep neural networks for discriminating between benign and malignant ovarian tumors: comparison with expert subjective assessment. *Ultrasound Obstet Gynecol.* 2021;57(1):155-163. [\[CrossRef\]](#)
38. Feng Y, Yang F, Zhou X, et al. A deep learning approach for targeted contrast-enhanced ultrasound based prostate cancer detection. *IEEE/ACM Trans Comput Biol Bioinform.* 2019;16(6):1794-1801. [\[CrossRef\]](#)
39. Hassan TM, Elmogy M, Sallam ES. Diagnosis of Focal liver diseases based on deep learning technique for ultrasound images. *Arab J Sci Eng.* 2017;42:3127-3140. [\[CrossRef\]](#)
40. Schmauch B, Herent P, Jehanno P, et al. Diagnosis of focal liver lesions from ultrasound using deep learning. *Diagn Interv Imaging.* 2019;100(4):227-233. [\[CrossRef\]](#)
41. Sudharson S, Kokil P. An ensemble of deep neural networks for kidney ultrasound image classification. *Comput Methods Programs Biomed.* 2020;197:105709. [\[CrossRef\]](#)
42. Lekadir K, Galimzianova A, Betriu A, et al. A convolutional neural network for automatic characterization of plaque composition in carotid ultrasound. *IEEE J Biomed Health Inform.* 2017;21(1):48-55. [\[CrossRef\]](#)
43. Araki T, Jain PK, Suri HS, et al. Stroke risk stratification and its validation using ultrasonic echolucent carotid wall plaque morphology: a machine learning paradigm. *Comput Biol Med.* 2017;80:77-96. [\[CrossRef\]](#)
44. Kainz B, Heinrich MP, Makropoulos, et al. Non-invasive diagnosis of deep vein thrombosis from ultrasound with machine learning. *NPJ Digit Med.* 2021;4(1):137. [\[CrossRef\]](#)
45. Li P, Zhao H, Liu P, Cao F. Automated measurement network for accurate segmentation and parameter modification in fetal head ultrasound images. *Med Biol Eng Comput.* 2020;58(11):2879-2892. [\[CrossRef\]](#)
46. Chen X, He M, Dan T, et al. Automatic measurements of fetal lateral ventricles in 2D ultrasound images using deep learning. *Front Neurol.* 2020;11:526. [\[CrossRef\]](#)
47. Cho HC, Sun S, Min Hyun C, et al. Automated ultrasound assessment of amniotic fluid index using deep learning. *Med Image Anal.* 2021;69:101951. [\[CrossRef\]](#)



# A snapshot of teleradiology practice in Turkey: the results of a survey among radiologists

Oğuz Dicle

Utku Şenol

Mustafa Nasuh Özmen

Üstün Aydıngöz

## PURPOSE

This study featured a survey that offers a snapshot of various teleradiology practices in Turkey, a Group of Twenty country that has undertaken a major transformation of its health care system during the last two decades and is currently the world leader in terms of the combined number of per capita magnetic resonance imaging and computed tomography examinations performed (which represent the bulk of teleradiology services worldwide).

## METHODS

The study data was collected from 4736 Turkish Society of Radiology (TSR) members via an electronic platform in the web environment through a questionnaire consisting of 24 questions. The survey was conducted in a 3-month time window (March–May 2021). Statistical tools were used for the analysis of the quantitative data.

## RESULTS

Responses from 156 members of the TSR comprised the study data, revealing that teleradiology is used for various applications in Turkey. Almost half of the participants (49%) performed teleradiology only in the private sector. Half of the respondents (51%) stated that they reported images at home for multiple centers. Moreover, 38% of the participants had been reporting more than 50 examinations per day, and 74% of the respondents earned less than 0.50 Euro per examination they reported. The overall satisfaction with teleradiology among the teleradiologists was, on average, 4.7 out of 10 points.

## CONCLUSION

The results are both promising for the future (i.e., concerning the propensity for adopting new technology) and alarming for the current state of affairs (i.e., insufficient radiologist reimbursement and lack of licensing and accreditation of teleradiology service providers). Periodic surveys performed in countries with different health care systems concerning financial, technical, and medicolegal aspects might reveal an up-to-date landscape of teleradiology practices worldwide and help guide local and regional decision-makers.

## KEYWORDS

Teleradiology, survey, Turkey

From the Department of Radiology (O.D. ✉ odicle59@gmail.com), Dokuz Eylül University Faculty of Medicine, İzmir, Turkey; Department of Radiology (U.Ş.), Akdeniz University Faculty of Medicine, Antalya, Turkey; Department of Radiology (M.N.Ö., Ü.A.), Hacettepe University Faculty of Medicine, Ankara, Turkey.

Received 14 June 2022; revision requested 11 August 2022; accepted 05 October 2022.



Epub: 05.01.2023

Publication date: 31.01.2023

DOI: 10.4274/dir.2022.221713

**T**eleradiology continues to progress in line with both the technological developments and needs arising in the field of health care. It is now being used extensively in many parts of the world, including Turkey. However, there is a paucity of data on how teleradiology practices actually operate and whether these services are performed in accordance with standards.

As of 2022, Turkey's population of 84.3 million people put this Group of Twenty (G20) country in 17<sup>th</sup> place out of 235 countries, with its population making up 1.1% of the entire world.<sup>1</sup> Although a small part of the population uses extra coverage from private health insurance providers, Turkey's health care system is effectively "state-sponsored universal" –even encompassing the >4 million refugees in the country. The first comprehensive and fully digital

You may cite this article as: Dicle O, Şenol U, Özmen MN, Aydıngöz Ü. A snapshot of teleradiology practice in Turkey: the results of a survey among radiologists. *Diagn Interv Radiol.* 2023;29(1):46-52.

departmental radiology applications in the country started in 2001. Over the last two decades, picture archiving and communication system (PACS) applications have spread to nearly all hospitals, making up most of the local teleradiology practice.

A bilingual (Turkish and English) electronic health information system called e-Nabız (e-Pulse in English), which was developed by the Turkish Ministry of Health in the last decade, has become one of the more advanced systems in the world. It collects all hospital records, including imaging-based services, across the country in a central database and shares them with health care professionals and patients.<sup>2</sup> This is especially striking in light of the fact that, according to data from the Turkish Ministry of Health and the Organization for Economic Cooperation and Development, Turkey ranks first and second in the world in terms of the number of magnetic resonance imaging (MRI) and computed tomography (CT) examinations per 1.000 people, respectively.<sup>3,4</sup> Currently, these two imaging modalities make up the vast majority of teleradiology applications worldwide in terms of the number of images reviewed. As part of this Big Data environment and central health care management, the first nationwide online radiological image distribution project was implemented in 2014. By the end of the first year, the coverage rate of the project in public hospitals had reached 98%.<sup>5</sup>

The first standards on teleradiology were published by the Turkish Society of Radiology (TSR) in 2010.<sup>6</sup> An updated version of the TSR standards was published in June 2021.<sup>7</sup> Of the nearly 5.000 active working radiologists in Turkey, the number engaged in teleradiology is unknown. There is still no licensing and accreditation of teleradiology services, which remain outside of reimbursement coverage through the universal health care system in Turkey.

This study aims to obtain cross-sectional information about the daily functioning of teleradiology in Turkey from the perspective

of one group of its major stakeholders (i.e., the radiologists) and to seek clues that reflect the real picture in this G20 country. The research also sets out to check the radiologists' satisfaction level pertaining to the framework of teleradiology services in Turkey and to gauge how widely the standards of the national professional association of radiologists have been adopted.

## Methods

A questionnaire that consisted of 24 questions was designed by the researchers. The researchers were four senior academic radiologists who were all members of the committee that prepared the TSR teleradiology standards. A free web-based platform was used for the survey templates and data collection.<sup>8</sup> At the start of the survey, it was explicitly stipulated that only "radiologists currently practicing teleradiology" were supposed to participate. This work was supported by the TSR. Ethics committee approval was received for the subject matter and the content of the questionnaire. The study was approved by the Ethics Committee of Dokuz Eylul University (reference no: 2021/11-27: 05.04.2021). All participants were informed of the aim and content of the study before taking part in the questionnaire, and their consent was obtained.

The respondents were asked to answer questions about their age, their mode of service (institutional vs. self-employed), their experience in radiology, the teleradiology infrastructure that was available to them, and their practical experience with teleradiology, including their teleradiology-based income. The participants were also asked to submit their opinions on the advantages and disadvantages of teleradiology. The survey link was sent through the mailing list of the TSR to all member radiologists (n = 4.736). Participants were informed about the purpose of the questionnaire. Data were automatically saved in the survey platform database. The survey was conducted within a three-month time window (March–May 2021). Free questionnaire statistical tools were used for the analysis of the quantitative data.<sup>9</sup> A 10-point Likert scale was used to understand the respondents' satisfaction level, where 10 represented the highest satisfaction level and 1 the lowest. Free text fields were also available to obtain the participants' opinions on their satisfaction with and acceptance of teleradiology. The survey is provided in Appendix 1.

## Statistical analysis

Descriptive statistics for the continuous variables were calculated, and frequencies and percentages were given for the categorical variables. The Shapiro–Wilk test was used to check the normality assumption of the continuous variables. The Wilcoxon rank-sum (Mann–Whitney U) test was performed to compare continuous variables between groups. Pearson's chi-square test was used for the analysis of the categorical variables in groups. A *P*-value of less than 0.05 was considered statistically significant. All statistical analyses were performed IBM SPSS version 25.0 software (Chicago, IL, USA).

## Results

In total, 153 radiologists participated in the online survey. This number corresponded to 3.2% of the 4,736 member radiologists of the TSR.<sup>9</sup> The demographic data are given in Table 1. Nearly half of the respondents (48%) were radiologists with more than 10 years of professional experience. The majority of the participants (76%) were male, with a somewhat overrepresentation of the male radiologists (60%) among the TSR membership.<sup>10</sup> Moreover, 74% of the participants were from non-academic centers. Three-quarters of the respondents (75%) reported that they had not received any teleradiology training, and the majority (76%) were unaware of the TSR Teleradiology Standards. Awareness of the TSR Teleradiology Standards was found to be statistically higher in the group with work experience of 4–9 years.

Almost half of the participants (49%) performed teleradiology only in the private sector ("private sector" denoted here also covered the companies to whom imaging services of public hospitals, or their reporting, were outsourced by the government). Additionally, 28% of the participants were working only in the public sector, while the remaining 23% stated that they work in both sectors.

When asked to reveal their workplace status and coverage of teleradiology services, half of the respondents (51%) stated that they reported images at home for multiple centers. The remainder performed teleradiology on-site for a single center (17%), on-site for multiple centers (14%), or at home for a single center (18%).

Approximately half of the respondents (51%) performed teleradiology services full-time in their routine practice. The majority of the participants (88%) had not given a writ-

### Main points

- Teleradiology has different modes of use due to rapidly changing requirements.
- In Turkey, teleradiology has permeated health care services in diversified forms.
- Non-standard applications and low fees emerged as the most important problems.
- Widespread use of questionnaires might contribute to shaping the future of teleradiology.



ten confirmation that they would perform the teleradiology service according to certain standards. While 38% of the participants had been reporting more than 50 examinations per day, 29% serviced 11–50 examinations daily. In addition, 78% of the practitioners of teleradiology stated that their patients were not informed about their reports being made via teleradiology. A further 58% of the respondents could access their patients' clinical information at the time of reporting.

Half of the respondents (48%) could access their patients' previously archived images. While 65% of the participants stated that the examinations they reported were from other cities, 8% performed international reporting. According to the electronic survey records, the participants were from 23 different cities. The majority were from Istanbul (31.5%), Ankara (18.5%), Izmir (10.2%), and Antalya (5.5%).

Only 18% of respondents stated that they reported examinations with diagnostic monitors; the majority of the radiologists preferred standard personal computer monitors for reporting. Moreover, 35% of participants used a simple or basic electronic signature. In 37% of the reports, only the name of the reporting person was written, without any type of electronic or digital signature. Neither a signature nor a name was included in the reports of 28% of the participants.

Approximately 74% of the respondents stated that they earned less than 0.50 Euro per examination they reported, while 13% of

the respondents received no fee-for-service payment (their service was covered under a fixed salary).

In total, 63% of the respondents' teleradiology service providers stored the radiological images. For the rest of the respondents, the acquisition site was responsible for the storage.

Structured reporting was preferred by most of the teleradiologists. However, a quarter of radiologists provided narrative reports with no differential diagnosis. Finally, 29% of the respondents inserted diagnostic codes (International Classification of Diseases, 10th Revision) in their teleradiology reports. All of the answers given for the "yes or no" survey questions are given in Table 2.

The overall satisfaction with teleradiology among the teleradiologists was, on average, 4.7 out of 10 points. Approximately 60% of the participants gave a score of 5 or higher. The mean values and statistical analyses for the satisfaction levels according to gender and affiliated institution are given in Table 3. Satisfaction levels were found to be higher among the female and academic participants. Among the reasons for the positive view regarding teleradiology, the item "bringing additional income" was the most frequently marked. The response rates for the other options are given in Figure 1. The statistical analysis showed that significantly more female than male radiologists believed that teleradiology facilitated after-hours reporting. These re-

sults are given in Table 4. Concerning the negative views, the opinion that "Teleradiology causes a cheap labor problem" (the most obvious reason for dissatisfaction) was more common among non-academic respondents ( $P = 0.017$ ; Pearson's chi-square).

Among the free-text opinions in favor of teleradiology were the following: "I use teleradiology as an extension of my hospital's PACS. I can also access patients' data which makes my evaluation comfortable"; "Teleradiology provides me a silent medium to be concentrated and focus on images"; "In pandemic conditions, teleradiology made the normal workflow possible"; and "It is the health system that makes teleradiology unproductive, not the teleradiology itself." Among the reasons given for the negative view regarding teleradiology, the item "It exploits labor" was marked the most. The response rates for other options are given in Figure 2. Some of the free-text opinions against teleradiology were as follows: "Teleradiology means low prices, poor quality"; "I feel it will bring the end of radiology"; "Teleradiology for me is too much effort without a rational income"; "Teleradiology with this fee means millions of meaningless reports"; and "Reporting without previous images and clinical data is a kind of Russian roulette."

## Discussion

A G20 country since the conception of this group of the top 20 economies worldwide in 1999, Turkey has experienced controversial paradigm shifts in health care services since 2002, some of which have been heralded as international success stories.<sup>11</sup> An important part of this transformation concerns the procurement of some services, which also significantly encouraged teleradiology applications. For example, the rate of outsourcing of health care services in the public sector, which was nonexistent in 2002, reached 80% in 2012.<sup>12,13</sup> The systematic promotion of easier access to health care services and the resulting uncontrolled competition caused an excessive increase in the number of CT and MRI examinations performed.<sup>3</sup> During this process, teleradiology was quickly adopted and widely implemented, primarily due to its cost-reducing effect. The importance of the current study is underscored by its cross-sectional depiction of teleradiology services from the standpoint of teleradiologists in an environment created by the major policy shift that has occurred over the last two decades.

**Table 1.** Demographic data of the survey respondents

	Number	Percentage
<b>Gender</b>		
Male	111	76.0
Female	35	24.0
<b>Experience in radiology (years)</b>		
1–3	36	24.0
4–9	42	28.0
≥10	72	48.0
<b>Affiliated institution</b>		
Academic	39	26.1
Non-academic	110	73.9
<b>Training in teleradiology</b>		
Yes	37	24.8
No	112	75.2
<b>Employer</b>		
Public	43	28.5
Private sector	74	49.0
Both	34	22.5

As with many other technologies, teleradiology has been found to fit different roles and areas of use from its initially defined functions due to rapidly changing requirements and continuous technological advances. The number of surveys that have been conducted to understand this evolution of the practice of teleradiology in different countries and regions is surprisingly small.<sup>14-17</sup> When conducted with an appropriate sample population, such surveys can help reveal the bigger picture to a large extent. Although the results of these survey studies are not fully comparable due to the different conditions, regulations, and policies among various countries and regions,

their technical infrastructure and usage concepts are comparable with global applications. Several remarkable results were obtained in the current study that were not addressed in other surveys,<sup>14-17</sup> which were not specifically aimed at practicing teleradiologists.

In general, the practice of teleradiology in Turkey has permeated the country's health care services in all of its forms of application (i.e., on-site for a single center, on-site for multiple centers, at home for a single center, and at home for multiple centers). Among the survey participants, the percentage of those who provided teleradiology services was close to half. However, due to the large

number of service procurements, it was difficult to determine these rates exactly considering that radiology reports are given by publicly employed radiologists through teleradiology as part of the service provided by the private sector.

As can be understood from the answers of the participants, a significant amount of patient and clinical data and archived images can be accessed during teleradiology applications. Insufficient integration of clinical history is an important downside of teleradiology in Turkey, identified in a revealing 63% of responses in a 2015 study.<sup>18</sup> However, the current survey revealed that the main complaint here was the low income provided in return for the service rendered. Moreover, although it was not asked as a separate question in the survey, it was known that the fees per review stated by the participants were the same regardless of the type of examination performed. The number of daily reports per radiologist was quite high, and high dissatisfaction regarding the monetary return was evident. Nevertheless, the most important motivation for the radiologists to perform teleradiology was cited as financial income. Low pricing is expected to result in poor reporting quality and dissatisfaction with teleradiology. The latter point was clearly expressed in the feedback received. This dramatic result revealed that teleradiology can turn into an abusive technological tool against the background of health policies that prioritize quantity while ignoring adequate setup and implementation of regulations and controls.

All of the regulatory and supervisory authority pertaining to health in Turkey resides with the Ministry of Health. However, no training and certification program specific to teleradiology exists in the country. Against this background, the TSR has published teleradiology standards to help radiologists employ up-to-date standards,<sup>6</sup> which, unfortunately, remained obscure to a significant portion of the participants. This necessitates increased activity on the part of the national professional association of radiologists to propagate these standards.

As mentioned in a study by Karthiyayini and Karthikeyan,<sup>18</sup> an acceptable and efficient teleradiology service in favor of patients will only be possible with appropriate public regulations. These arrangements should be made with the participation of all parties involved and in a way that prioritizes the benefit of the patient. Continuous con-

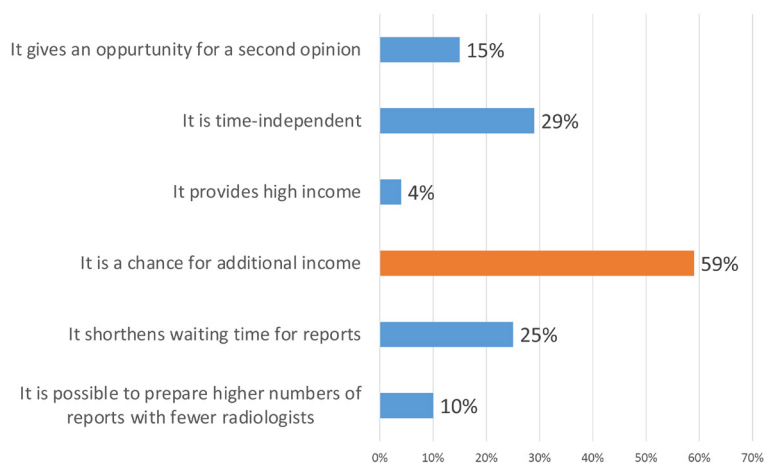


**Figure 1.** Distribution of opinions in favor of teleradiology service. The distribution of the answers given to the question, which was arranged as a sentence-completion activity. The reason(s) teleradiology was viewed positively were selected. More than one answer could be given. Respondents chose the opinion that was complementary to the following sentence: "I'm in favor of teleradiology service because..."

Question	Number of respondents	Answer	
		Yes (%)	No (%)
Do you work in an academic institution?	149	26	74
Did you get any training in teleradiology?	149	25	75
Do you perform teleradiology full time?	150	51	49
Are you aware of the TSR Teleradiology Standards?	143	24	76
Did you give a written confirmation that you will perform the applications according to the standards when starting the business?	150	12	88
Are patients informed that their examinations are reported by teleradiology?	148	28	72
Do you have access to clinical information at the time of reporting?	149	58	42
Do you have access to the patient's previous examinations at the time of reporting?	145	48	52
Are the images stored at the teleradiology site?	140	63	27
Do you use structured reports (that consist of technical data, exam protocol, findings, results, and recommendations) in teleradiology reports?	147	66	24
Do you insert any diagnostic code in teleradiology reports?	146	29	61

TSR, Turkish Society of Radiology.

control and improvement with the use and revision of quality criteria should be essential.

This study has some limitations. First, it only provides a snapshot of the situation at a time point that coincided with the extraordinary circumstances of the coronavirus disease-2019 pandemic. Such a period naturally entailed an accelerated transition to teleradiology in many centers. However, some norms that were being established during the pandemic might well be long term, if not permanent. The hybrid use of teleradiology and on-site reporting for even in-house services might well be one such norm, at least for some centers. Obviously, trends in the practice of teleradiology need to be monitored by the use of surveys as well as other tools. Another limitation of this study is the relatively low number of respondents, who made up approximately 3% of the potential

pool. Nevertheless, unlike in similar studies,<sup>14-17</sup> only radiologists actively performing teleradiology participated in the current study. The country-level participation rates were similar when compared to those of other published surveys.<sup>15,16</sup>

The strengths of this study include the specifically targeted population of practicing teleradiologists (which is unique among published surveys in the literature), the extensive outreach performed through the TSR mailing list (which essentially afforded the randomization of the sample), the diversified content of the questionnaire (which captured various implementations of the teleradiology practice), the balanced distribution of answer options for each question, the web-based data collection (which provided easy access to the survey by the participants), and the high number of filled-out personal feedback areas

in the questionnaires. Another upside of this study is that it was performed in a country with the highest numbers of CT and MRI examinations worldwide (adjusted for population), as these are the foremost subjects of teleradiology.

In conclusion, this study revealed that teleradiology in Turkey has a variety of applications and practices that are already shaping the future of radiology services in this G20 country. It is hoped that this study, which underlines the effects of the radical change in health care policy in Turkey over the last two decades, will be useful for future discussions on this subject. The results are both promising for the future (i.e., concerning the propensity for adopting new technology) and alarming for the current state of affairs (i.e., insufficient radiologist reimbursement and lack of licensing and accreditation of service providers). Periodic surveys performed in countries with different health systems may help illustrate the current landscape of teleradiology practices worldwide, and financial, technical, and medicolegal research also involving non-radiologists could be an effective tool to help guide local and regional decision-makers.

### Acknowledgements

The authors kindly thank the Turkish Society of Radiology Executive Board for their support in disseminating the questionnaire to the society members. They are also grateful to Dr. Deniz Akata for her critical review of the draft manuscript. The authors also express their sincere thanks to Dr. Aslı Karakülah and Dr. Yeşim Şenol for their contributions to statistical analysis and interpretation.

### Conflict of interest disclosure

The authors declared no conflicts of interest.

### References

1. Worldometer. <https://www.worldometers.info/world-population/population-by-country/>. Accessed 17 March 2022. [CrossRef]
2. E-nabiz Personal Health System. <https://enabiz.gov.tr/>. Accessed 17 March 2022. [CrossRef]
3. Turkish Republic Ministry of Health. Annual of Turkey Health statistics. Ministry of Health publication, 2021. Ankara. <https://sbu.saglik.gov.tr/Ekutuphane/kitaplar/health-statistics-yearbook-2019pdf.pdf>. [CrossRef]
4. OECD. Health at a Glance 2021: OECD Indicators, OECD Publishing; Paris. 2021.

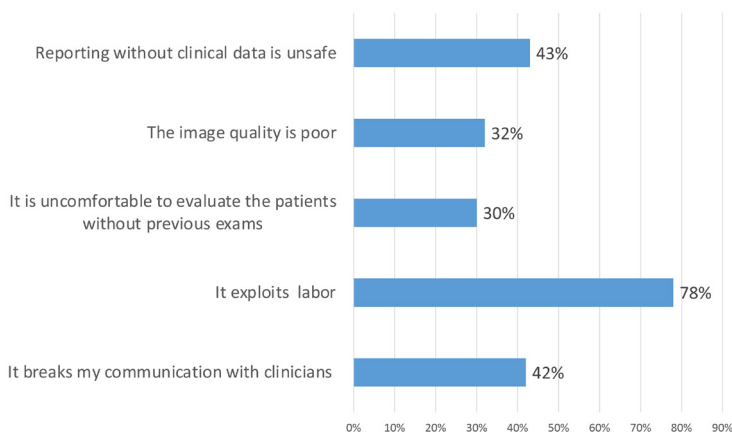


**Figure 2.** Distribution of opinions against teleradiology service. The distribution of the answers given to the question, which was arranged as a sentence-completion activity. The reason(s) teleradiology was viewed negatively were selected. More than one answer could be given. Respondents chose the opinion that was complementary to the following sentence: “I’m not in favor of teleradiology service because...”

**Table 3.** Mean values of satisfaction levels in teleradiology practice

	Mean rank	P*
<b>Gender</b>		
Male	67.05	0.010
Female	87.88	
<b>Affiliated institution</b>		
Academic	91.42	0.020
Non-academic	66.97	

\*Mann-Whitney U test.

**Table 4.** Distribution of the opinion that “Teleradiology facilitates after-hours reporting” (second-ranking reason for satisfaction) by gender

	Male		Female		P*
	n	%	n	%	
Teleradiology facilitates after-hours reporting					
Disagree	92	80.0	23	20.0	0.020
Agree	19	61.3	12	38.7	

\*Pearson’s chi-square

- <https://doi.org/10.1787/ae3016b9-en> [CrossRef]
5. Birinci Ş, Ülgü M. National teleradiology system in Turkey. *Health Management*. 2017; 17(3):248-250. [CrossRef]
  6. Turkish Society of Radiology Board of Qualification and Standards. TSR Standards for the Practice of Teleradiology [Turkish]. Turkish Society of Radiology: Ankara, Turkey. 9 April 2010. [CrossRef]
  7. Özmen MN, Dicle O, Şenol U, Aydınöz Ü. TSR guidelines for the practice of teleradiology: 2021 update. *Diagn Interv Radiol*. 2021;27(4):504-510. [CrossRef]
  8. Online survey platform. <https://freeonlinesurveys.com/>. Accessed 20 March 2022. [CrossRef]
  9. Turkish Society of Radiology. Official data. <http://www.trd.org.tr> Accessed 10 Jan 2022. [CrossRef]
  10. Akdağ R. Lessons from health transformation in Turkey: leadership and challenges. *Health Syst Reform*. 2015;1(1):3-8. [CrossRef]
  11. Akbulut Y, Terekli G, Yıldırım T. Outsourcing in Turkish hospitals: a systematic review. *Ankara Sađ Hiz Derg*. 2012;11(2):25-33. [CrossRef]
  12. Turkish Ministry of Health, Department of Health Services, Audit and Evaluation Center (2012) Health Services Medical Audit Reports I-II-III, Ankara. [CrossRef]
  13. European Society of Radiology (ESR). ESR teleradiology survey: results. *Insights Imaging*. 2016;7(4):463-479.
  14. Lienemann B, Hodler J, Luetolf M, Pfirrmann CW. Swiss teleradiology survey: present situation and future trends. *Eur Radiol*. 2005;15(10):2157-2162. [CrossRef]
  15. Coppola F, Bibbolino C, Grassi R, et al. Results of an Italian survey on teleradiology. *Radiol Med*. 2016;121(8):652-659. [CrossRef]
  16. Rosenkrantz AB, Hanna TN, Steenburg SD, Tarrant MJ, Pyatt RS, Friedberg EB. The Current State of Teleradiology Across the United States: A National Survey of Radiologists' Habits, Attitudes, and Perceptions on Teleradiology Practice. *J Am Coll Radiol*. 2019;16(12):1677-1687. [CrossRef]
  17. Petik B, Sırık M, Çolak D, Duman T. The use of teleradiology in Turkey: current situation and attitudes of radiologists. *Turkiye Klinikleri J Med Sci*. 2015;35(4):225-232. [CrossRef]
  18. Karthiyayini S, Karthikeyan N. A survey of teleradiology: future trends. *J Appl Sci Comput*. 2019;6(5):1059-1065. [CrossRef]

## Appendix 1. Survey questions

1. How many years have you been a radiologist? .....
2. What is your gender?.....
3. Type of institution you work for: academics or non-academics.....
4. Did you get any training in teleradiology?  
 Yes  No
5. Your employer in teleradiology: only state, only private sector, both?.....
6. Type of teleradiology performance: on-site, single center; on-site, multiple centers; at-home, single center; at-home, multiple centers?  
.....
7. What is the share of teleradiology in your routine radiology service: full-time or part-time?.....
8. Are you aware of TSR Teleradiology Standards?  
 Yes  No
9. Did you give a written confirmation that you will perform the applications according to the standards when starting the business?  
 Yes  No
10. How many exams do you report with teleradiology per day?  
 1-5,  6-10,  11-50,  51-100,  100+
11. Are patients informed that their examinations are reported by teleradiology?  
 Yes  No
12. Do you have access to clinical information at the time of reporting?  
 Yes  No
13. Do you have access to the patient's previous examinations at the time of reporting?  
 Yes  No
14. Reporting site: home, office, imaging center, hospital? .....
15. How far is the image acquisition from your reporting site: at the same site, within the same city, another city, another country?  
.....
16. What kind of monitor are you using in teleradiology reporting: standard PC, high-resolution PC, diagnostic?  
.....
17. How do you sign your report: fresh signature, electronic signature, only name, unsigned? .....
18. How much you are paid for each teleradiology exam report:  
 0,1-0,5,  0,6-2,  2-5,  5+ euros ?
19. Are the images stored on the teleradiology site?  
 Yes  No
20. Do you use structured reports (consists of technical data, exam protocol, findings, results, and recommendations) in Teleradiology reports?  
 Yes  No
21. Do you insert any diagnostic code in teleradiology reports?  
 Yes  No
22. What is your satisfaction level with the Teleradiology Service? (10 point scale) .....
23. I'm in favor of Teleradiology Service because it.....:  
  - gives an opportunity for a second opinion
  - is time-independent
  - provides high income
  - is a chance for additional income
  - shortens waiting time for reports
  - is possible to prepare higher numbers of reports with the fewer radiologist
24. I'm not in favor of Teleradiology Service because.....:  
  - reporting without clinical data is unsafe
  - the image quality is poor
  - I'm unable to reach patients' previous exams
  - it exploits the labor
  - I'm unable to communicate with the patients' physicians



# Radiological and clinicopathological findings of breast cancer during the COVID-19 pandemic: a comparative study with the pre-pandemic era

Merve Gürsoy   
Özge Aslan   
Aşenur Oktay Alfatlı   
Osman Zekioğlu   
Berk Göktepe 

## PURPOSE

The diagnosis and surgical treatment delays that occurred during the coronavirus disease-2019 (COVID-19) pandemic may have affected breast cancer presentation. This study aimed to determine whether there was a difference in the clinicopathological characteristics of breast cancers during the pandemic by comparing them with similar cases from the previous year. The study also aimed to determine the radiological findings of breast cancers during the pandemic.

## METHODS

A retrospective review was made of patients who underwent surgery for breast cancer between March 11, 2020, and December 11, 2020 (the pandemic group). These patients were compared with similar patients from the previous year (the pre-pandemic group). The postoperative histopathology results of both groups were compared, and the preoperative radiological findings of the pandemic group were defined.

## RESULTS

There were 71 patients in the pandemic group and 219 patients in the pre-pandemic group. The tumor size was significantly greater, lymph node involvement was more frequent, and waiting time for surgery was longer in the pandemic group ( $P < 0.001$ ,  $P = 0.044$ ,  $P = 0.001$ , respectively). There was no significant difference between the groups in respect of *in situ*/invasive tumor distribution, histological type and histological grade of tumor, the presence of lymphovascular/perineural invasion, multifocal/multicentric focus, and Breast Imaging Reporting and Data System Classification ( $P > 0.15$ ). The radiologic findings of breast cancer during the pandemic typically showed characteristics of malignancy.

## CONCLUSION

Patients diagnosed with breast cancer during the COVID-19 pandemic had larger tumor sizes, more frequent lymph node involvement and longer waiting time for surgical treatment. Screening programs should be continued as soon as possible by taking necessary precautions.

## KEYWORDS

COVID-19, breast cancer, mammography, screening interruption, surgery delay

From the Department of Radiology (M.G. ✉ gursoymerve@yahoo.com), İzmir Katip Çelebi University Faculty of Medicine, İzmir, Turkey; Department of Radiology (Ö.A., A.O.A.), Ege University Faculty of Medicine, İzmir, Turkey; Department of Pathology (O.Z.), Ege University Faculty of Medicine, İzmir, Turkey; Department of General Surgery (B.G.), Ege University Faculty of Medicine, İzmir, Turkey.

Received 13 June 2021; revision requested 20 July 2021; accepted 18 October 2021.



Epub: 02.01.2023

Publication date: 31.01.2023

DOI: 10.5152/dir.2022.21646

Although coronavirus disease-2019 (COVID-19) was first seen in China in the last month of 2019, it quickly spread all over the world due to fast human-to-human transmission. Following the first recorded case in Turkey on March 11, 2020, a re-organization of the healthcare system was implemented that required a series of restrictions, just as in other countries. Within these restrictions was the proviso that while emergency medical interventions would continue, there would be delays in the diagnosis and treatment of oncology cases. The management of breast cancer was affected by these changes, and in accordance with the recommendations of several national and international scientific communities, breast cancer screening programs were temporarily postponed.<sup>1-3</sup>

You may cite this article as: Gürsoy M, Aslan Ö, Oktay Alfatlı A, Zekioğlu O, Göktepe B. Radiological and clinicopathological findings of breast cancer during the COVID-19 pandemic: a comparative study with the pre-pandemic era. *Diagn Interv Radiol.* 2023;29(1):53-58.

These guidelines, which were formed for the diagnosis and treatment of breast cancer during the pandemic, consider the increasing demand for medical resources and aim to balance the risk of delaying treatment against potential exposure to the virus. Breast cancer screening was interrupted in this period, and radiological examinations were restricted to a limited number of symptomatic diagnostic cases. Due to the screening programs that are widely applied throughout the world, breast cancer can be detected at an earlier stage. In a study conducted in Italy, the incidence of late-stage breast cancer (T2–T4) decreased steadily by 30% in a period of fewer than eight years following the introduction of organized mammography screening.<sup>4</sup> Consequently, breast cancer mortality was shown to decrease by up to 40%.<sup>5</sup>

It has been assumed that because of the temporary cessation of screening programs or the delay in surgical treatment for confirmed cancers due to the pandemic, the clinicopathological characteristics of breast cancer could change. Therefore, the aim of this study was to determine whether there was a difference in the clinicopathological characteristics of breast cancers diagnosed during the pandemic by comparing these with cases in the corresponding period before the pandemic. The study also aimed to determine the radiological characteristics of breast cancers diagnosed during the pandemic.

## Methods

This retrospective study was approved by the Institutional Review Board of Ege University (21-3.1T/44). Since the study was retrospective, informed consent by patients and providers was not required.

### Patients

A retrospective review was made of patients diagnosed with breast cancer in a

9-month period starting from March 11, 2020, when the first COVID-19 case was recorded in Turkey, to December 11, 2020. During this period, 158 patients were diagnosed with breast cancer. Of these, 87 were excluded from the study, including 56 who received neoadjuvant chemotherapy, 9 with a history of breast cancer surgery, 5 with radiological examinations performed at another center, and 17 with operations performed at another center. Thus, a total of 71 patients who met the criteria and were operated on were included in the study for evaluation as the pandemic group.

These patients were compared with patients who underwent surgery for breast cancer in the corresponding period of the previous year (March 11, 2019–December 11, 2019). The same exclusion criteria were applied to these patients. In the pre-pandemic period, a total of 352 patients were diagnosed with breast cancer, of which 219 were operated on and were included in the study as the pre-pandemic group. The remaining patients were excluded, as 83 received neoadjuvant chemotherapy, 23 had a history of breast cancer surgery, 8 had radiological examinations performed at another center, and 19 had operations performed at another center.

### Variables

The imaging findings of the patients with breast cancer in the pandemic group were determined by their preoperative radiological examinations [mammography, ultrasonography (US), and breast magnetic resonance imaging (MRI)]. The evaluation of the findings was made in accordance with the Breast Imaging Reporting and Data System (BI-RADS), version 5.

The postoperative histopathology results of the patients in both groups were reviewed. The largest tumor diameter was accepted as the histological size of the tumor and reported in millimeters. In the presence of more than one focus, the largest focal size was accepted as the tumor size. The presence or absence of metastatic axillary lymph nodes was also recorded for each patient, and, if present, the number of lymph nodes involved was recorded. Pathological T and N staging was based on the recommendations of the AJCC (2018) (edition VIII) for classification.<sup>6</sup> The status of the tumor was also recorded as *in situ* or invasive.

The histological type of the tumor was categorized into three groups: invasive ductal carcinoma, invasive lobular carcinoma,

and others (medullary, apocrine, etc.). Tumor grading was evaluated according to the modified Scarff–Bloom–Richardson grading system. The histological grades of the tumor were classified into two groups: low grade and high grade. Grade 1 tumors were accepted as low grade, and grade 2 and 3 tumors were accepted as high grade. Lymphovascular invasion (LVI), perineural invasion (PNI), and multifocal/multicentric focus were also evaluated and categorized as present or absent. Waiting time for surgery was calculated as the number of days between the date of the first radiological examination of the breast cancer and the date of surgery. The BI-RADS classification of the tumor was also evaluated and categorized as BI-RADS 4 and 5.

The two groups (pre-pandemic and pandemic) were compared in terms of age, histological size of the tumor, axillary lymph nodes status, number of metastatic lymph nodes, T and N stages, *in situ*/invasive tumor distribution, histological type of the tumor, histological grade of the tumor, presence of LVI and PNI, presence of multifocal/multicentric focus, waiting time for surgery, and BI-RADS classification of the tumor.

### Statistical analysis

Data analyses were performed using SPSS (SPSS Inc., Chicago, IL, USA) software, version 22.0. Data distributions were evaluated with the Shapiro–Wilk test for normality. All variables without normal distribution were reported as median, min–max values, and interquartile ranges (Q1–Q3, 25<sup>th</sup>–75<sup>th</sup> percentile values). The categorical variables were reported as numbers and percentages. The Mann–Whitney U test was used to compare age distribution, histological size of the tumor, number of metastatic lymph nodes, and waiting time for surgery between the groups. The frequency distributions of axillary lymph node status, histological type, presence of LVI and PNI, presence of multifocal/multicentric focus, and BI-RADS classification of the tumor in the two groups were examined using a Pearson chi-squared analysis. The frequency distributions of histological grade, T/N stages, and *in situ*/invasive tumors in the two groups were examined using Fisher's exact test. Variables with assigned values of  $P < 0.05$  were considered statistically significant.

## Results

Comparisons were made between the pandemic group of 71 patients, who underwent breast cancer surgery between March

### Main points

- The diagnosis and surgical treatment delays due to the coronavirus disease-2019 (COVID-19) pandemic have affected breast cancer presentation.
- Tumor size was larger and lymph node involvement was more frequent in breast cancers diagnosed during the COVID-19 pandemic than in the pre-pandemic era.
- Patients diagnosed during the pandemic period may have had to wait longer for surgical treatment.

11, 2020, and December 11, 2020, and the pre-pandemic group of 219 patients, who underwent breast cancer surgery in the corresponding period of 2019. The median age of the patients was 56 years (Q1–Q3, 46.5–65 years; range: 27–83 years) in the pre-pandemic group and 60 years (Q1–Q3, 46–68.5 years; range: 31–88 years) in the pandemic group. There was no significant difference in the age distribution of the two groups ( $P = 0.22$ ).

### Imaging characteristics of patients in the pandemic group

The interpretation of the radiological examinations of the 71 patients in the pandemic group yielded that mammography tests were present for 69 patients and absent for 2 (aged 32 and 33 years). US examinations were conducted in 56 cases and breast MRI examinations in 34 cases. Breast cancer was detected with mammography and US in 56 patients, with mammography alone in 13 patients, and with US alone in 2 patients. When the mammography, US, and breast MRI results were evaluated according to the BI-RADS classification, 23 patients (23/71, 32.4%) were evaluated as BI-RADS 4, and 48 patients (48/71, 67.6%) were evaluated as BI-RADS 5.

In the interpretation of the mammography characteristics, the presentation in 46 cases was as a mass, in 9 cases as structural distortion, and in 8 cases as asymmetrical density; in 1 case, there was no abnormal finding on mammography. When the presence of microcalcification was examined, pathological microcalcification was the sole finding observed on mammography in 5 cases was, while other findings accompanied microcalcifications in 30 cases.

When the US images of the masses were evaluated, the most common morphology was seen to be an irregular shape, in non-parallel orientation, without a circumscribed margin, in a hypo/heterogenous echo pattern, and providing posterior acoustic shadowing. The findings of the 34 cases evaluated by MRI were a mass in 24 cases and non-mass enhancement in 9. In 1 case, there was diffuse brightness in the skin and parenchyma, suggestive of inflammatory-type breast cancer. The characteristics of all 3 imaging modalities (mammography, US, and MRI) of the patients are shown in detail in Table 1.

### Clinical and histopathological characteristics

The largest tumor diameters in the pre-pandemic group were between 3 and

100 mm, with a median value of 20 mm (Q1–Q3, 15–27 mm), while in the pandemic group they were between 9 and 78 mm, with a median value of 30 mm (Q1–Q3, 19.5–47

**Table 1.** Mammography, ultrasonography, and magnetic resonance imaging characteristics of breast cancer in the pandemic group

Findings	n (%)	
Mammography	Mass	47 (68.1%)
	Architectural distortion	8 (11.6%)
	Focal asymmetry	8 (11.6%)
	Calcification only	5 (7.3%)
	No findings	1 (1.4%)
Mammography shape	Round/oval	6 (12.8%)
	Irregular	41 (87.2%)
Mammography margin	Circumscribed	1 (2.1%)
	Obscured	4 (8.5%)
	Micro-lobulated	5 (10.7%)
	Indistinct	14 (29.8%)
Mammography density	Spiculated	23 (48.9%)
	High density	34 (72.3%)
	Equal density	13 (27.7%)
US	Mass	53
	Calcification only	2
	Diffuse edema	1
US shape	Round/oval	7 (13.2%)
	Irregular	46 (86.8%)
US margin	Circumscribed	1 (1.9%)
	Not circumscribed	52 (98.1%)
US echo pattern	Hypoechoic	53 (100%)
US orientation	Parallel	10 (18.9%)
	Not parallel	43 (81.1%)
US posterior features	No posterior features	28 (52.8%)
	Enhancement	2 (3.8%)
	Shadowing	23 (43.4%)
MRI	Mass	24 (70.6%)
	NME	9 (26.5%)
	Skin thickening, edema, diffuse non-mass-like enhancement	1 (2.9%)
Mass shape	Round/oval	0
	Irregular	24 (100%)
Mass margin	Circumscribed	0
	Not circumscribed	24 (100%)
Internal enhancement characteristics	Heterogeneous	18 (75%)
	Rim enhancement	6 (25%)
NME distribution	Linear	1 (11.1%)
	Segmental	6 (66.7%)
	Multiple regions	1 (11.1%)
	Diffuse	1 (11.1%)
NME internal enhancement patterns	Heterogeneous	5 (55.6%)
	Clumped	4 (44.4%)

n, number of patients; US, ultrasonography; MRI, magnetic resonance imaging; NME, non-mass enhancement.



mm). The median tumor size was significantly greater in the pandemic group ( $P < 0.001$ ) (Table 2). Lymph node involvement was present in 32% of the pre-pandemic group patients and 45.1% of those in the pandemic group. A statistically significantly higher rate of patients in the pandemic group had lymph node involvement ( $P = 0.044$ ). The mean number of lymph nodes involved was 3.9 in the pandemic group and 2.9 in the pre-pandemic group. The median number of lymph nodes involved was 2 in both groups (Q1–Q3, 1–4; range: 1–14 for the pre-pandemic group and Q1–Q3, 1–3.25; range: 1–32 for the pandemic group), with no statistically significant difference ( $P = 0.87$ ). The comparison of the two groups in respect of T and N stages yielded a statistically significant difference between groups in respect of the T stage of the tumor ( $P = 0.002$ ). In the subsequent paired comparisons, T3 stage tumors were seen at a statistically significantly higher rate than Tis, T1, and T2 in the pandemic group ( $P = 0.001$ ,  $P < 0.001$ ,  $P = 0.002$ , respectively). The N stage distribution between the groups did not show a statistically significant difference ( $P = 0.11$ ) (Table 3). While the pre-pandemic group had a surgery waiting time ranging between 11 and 104 days, with a median value of 44 days (Q1–Q3, 32–60.5 days), the waiting time for surgery was between 12 and 210 days, with a median value of 56 days (Q1–Q3, 36.5–80.5 days), in the pandemic group. The time from the first radiological examination to surgery was statistically significantly longer in the pandemic group ( $P = 0.001$ ).

There were no significant differences between the groups in respect of *in situ*/invasive tumor distribution ( $P = 0.22$ ), histological type of tumor ( $P = 0.50$ ), histological grade of tumor ( $P = 0.17$ ), the presence of LVI ( $P = 0.38$ ) and PNI ( $P = 0.97$ ), the presence of multifocal/multicentric focus ( $P = 0.78$ ), and BI-RADS classification of the tumor ( $P = 0.88$ ) (Table 2).

## Discussion

The results of this study showed that the mammography, US, and MRI findings of breast cancer during the pandemic typically showed characteristics of malignancy. On mammography, breast cancers most often presented as a mass of irregular shape, with a spiculated margin, and with high density. When the US images of the masses were evaluated, the most common presentation was seen to be a typical malignant presentation of an irregular shape, in non-parallel orientation, not circumscribed, in a hypo/heterogenous echo pattern, and providing

posterior acoustic shadowing. On MRI, the most common presentation was a mass of irregular shape, with a non-circumscribed margin and heterogenous enhancement.

This study hypothesized that because of the delays in breast cancer screening and surgical treatments due to the pandemic, there could be several changes in the clinicopathological characteristics of breast cancers determined in this period. The results of the study showed that tumors determined during the pandemic were larger compared with those in the pre-pandemic period (20 vs. 30 mm). When T staging distribution was evaluated, with the high incidence of T3, it can be said that the tumors determined during the pandemic were at a more advanced stage. In contrast, in a study by Vanni et al.<sup>7</sup> that examined the effects on breast cancer presentation of the delays in the diagnosis and treatment experienced during the COVID-19 pandemic, no significant difference was determined between lockdown

and pre-lockdown groups in respect of tumor size. The authors attributed this to the brief time between the suspension of breast cancer screening and the study and stated that larger sized and more clinically evident tumors may be observed in the following months. Vanni et al.'s<sup>7</sup> study included patients in a 2.5-month period from the onset of the pandemic, whereas in the current study, this period was 9 months. Therefore, it can be considered that the longer duration of our study affected the determination of a larger tumor size in the pandemic group. When the doubling time of breast cancer is considered, a certain period of time is needed for the emergence of the results of delayed diagnosis and treatment.<sup>8</sup> Despite the pandemic waves that have been experienced throughout the world and the decrease in case numbers from time to time, breast cancer screening programs have not completely returned to normal pre-pandemic levels. The entire world has experienced more than one peak

**Table 2.** Demographic and clinicopathological characteristics of the groups

Characteristics	Groups		P
	Pre-pandemic n	Pandemic n	
Age (years), median (Q1–Q3)	56 (46.5–65)	60 (46–68.5)	0.22
Tumor size (mm), median (Q1–Q3)	20 (15–27)	30 (19.5–47)	<b>&lt;0.001</b>
<b>Axillary lymph nodes status</b>			
Negative	149 (68%)	39 (54.9%)	<b>0.044</b>
Positive	70 (32%)	32 (45.1%)	
Number of metastatic lymph nodes, median (Q1–Q3)	2 (1–4)	2 (1–3.25)	0.87
<b>Invasive/in situ tumor distribution</b>			
<i>In situ</i>			0.22
Invasive	23 (10.5%) 196 (89.5%)	4 (5.6%) 67 (94.4%)	
<b>Histological type</b>			
IDC	132 (67.3%)	40 (59.7%)	0.50
ILC	29 (14.8%)	13 (19.4%)	
Others	35 (17.9%)	14 (20.9%)	
<b>Histological grade</b>			
Low	23 (11.7%)	4 (6%)	0.17
High	173 (88.3%)	63 (94%)	
<b>LVI</b>			
Yes	80 (36.5%)	30 (42.3%)	0.38
No	139 (63.5%)	41 (57.7%)	
<b>PNI</b>			
Yes	25 (11.4%)	8 (11.3%)	0.97
No	194 (88.6%)	63 (88.7%)	
<b>Multifocal/multicentric focus</b>			
Yes	55 (25.1%)	19 (26.8%)	0.78
No	164 (74.9%)	52 (73.2%)	
Waiting time for surgery (days), median (Q1–Q3)	44 (32–60.5)	56 (36.5–80.5)	<b>0.001</b>
<b>BI-RADS</b>			
BI-RADS 4	69 (31.5%)	23 (32.4%)	0.88
BI-RADS 5	150 (68.5%)	48 (67.6%)	

Bold values indicate statistical significance. n, number of patients; IDC, invasive ductal carcinoma; ILC, invasive lobular carcinoma; LVI, lymphovascular invasion; PNI, perineural invasion; BI-RADS, Breast Imaging Reporting and Data System.

**Table 3.** T and N stage distribution between the groups

	Groups		P
	Pre-pandemic n (%)	Pandemic n (%)	
T			<b>0.002</b>
Tis	23 (10.5%)	4 (5.6%)	
T1	97 (44.3%)	23 (32.4%)	
T2	89 (40.6%)	30 (42.3%)	
T3	8 (3.7%)	12 (16.9%)	
T4	2 (0.9%)	2 (2.8%)	
N			0.11
N0	150 (68.5%)	39 (54.9%)	
N1	50 (22.8%)	24 (33.8%)	
N2	15 (6.9%)	5 (7.1%)	
N3	4 (1.8%)	3 (4.2%)	

Bold values indicate statistical significance. n, number of patients; T, tumor; Tis, carcinoma *in situ*, N, lymph nodes.

in COVID-19 case numbers. Therefore, the current study is of value in showing changes in breast cancer presentation over a longer period.

When the involvement of malignant axillary lymph nodes was evaluated, there was reported to be significantly more malignant lymph node involvement in the lockdown group in Vanni et al.'s<sup>7</sup> study. A significantly high N2 incidence in the lockdown group was also determined when N stage distribution was examined. Another study by Toss et al.<sup>9</sup> reported that a 2-month pause in mammography screening during the pandemic caused an 11.2% increase in the incidence of node-positive breast cancer when compared with the corresponding period of the previous year. Similarly, in the current study, axillary lymph node involvement was significantly more frequent in the pandemic group (45.1% vs. 32%). However, no difference was determined between the groups in respect of N stages.

Both tumor size and lymph node involvement are used in breast cancer staging and are prognostic factors.<sup>10</sup> In the current study, both findings (tumor size and lymph node involvement) indicated that more advanced-stage tumors were determined during the pandemic compared with the pre-pandemic period. Similarly, Yılmaz et al.<sup>11</sup> determined early-stage breast cancers at the rate of 52.9% during the pandemic, compared with 81.2% in the pre-pandemic period, and advanced-stage cancers at 47.1% and 18.8%, respectively. Factors due to the pandemic, including the interruption of breast cancer screening programs during the COVID-19 period, the practice of limiting hospital admissions to symptomatic

patients, and the hesitation of symptomatic patients to visit any health institution, may have affected this result. Another factor affecting this result was thought to be the delays experienced in the treatment of patients diagnosed with breast cancer. In a study on pregnant patients with breast cancer, it was reported that delays in treatment of 1, 3, and 6 months increased the risk of axillary lymph node involvement by 0.9%, 2.6%, and 5.1%, respectively.<sup>12</sup> In another study, Smith et al.<sup>13</sup> showed that the treatment delay time has a significant effect on the 5-year survival rate after a breast cancer diagnosis. In that study, women with a delay in treatment of >6 weeks were seen to have shorter survival times than those who underwent surgery in a shorter period after diagnosis (<2 weeks), with 5-year survival rates of 80% and 90%, respectively. In the current study, the waiting time for surgery was significantly longer in the pandemic group than in the pre-pandemic group (44 vs. 56 days). During the COVID-19 pandemic, many non-urgent operations were postponed in an effort to protect hospital resources and limit the spread of the virus. It has been estimated that in the first 12-week peak of the pandemic, approximately 38% of cancer operations were canceled worldwide.<sup>14</sup> Therefore, in the current study, the longer waiting time for surgery in the pandemic group is an expected result. However, the definitions of "waiting time for surgery" in the literature show some differences. In some studies, it is defined as the number of days between the date of histological diagnosis of cancer (not the radiological diagnosis) and the date of surgery.<sup>15,16</sup> In the current study, it was calculated as the total number of days between the first radiological examination (mammography, US, or

MRI) that reported suspected breast cancer (BI-RADS 4/5) and the date of surgery.

The problems experienced in the management of breast cancer during the COVID-19 pandemic were not only delays to operations but were also experienced at several stages, such as the performance of biopsies and evaluations of histopathological results. As it was thought to be more correct to take all these steps into consideration, the date of the first radiological examination that reported suspected malignancy was taken as the basis for the current study.

In Turkey and throughout the world, there was a significant drop in the number of cancer cases during the COVID-19 pandemic. In a study conducted in the USA, the mean weekly number of newly identified patients with breast cancer during the pandemic was determined to have fallen by 51.8% compared with the pre-pandemic period (2208 to 1064 patients).<sup>17</sup> Another study in Italy reported a drop of 26% in the number of patients newly diagnosed with breast cancer during the pandemic compared with the previous year.<sup>18</sup> In the current study, the total number of breast cancer cases diagnosed in our hospital during the COVID-19 pandemic showed a decrease of 55.1% (352 to 158 patients) compared with the corresponding period of the previous year, and the number of patients with breast cancer underwent surgery fell by 67.5% (219 to 71 patients). However, this decrease does not reflect a decrease in the actual number of patients with breast cancer. The main reasons for this decrease in the incidence of breast cancers appear to be the suspension of screening programs and the re-allocation of healthcare system resources for COVID-19. In addition, the fact that a lower number of patients in the pandemic period had a larger tumor size and more frequent lymph node metastasis suggests that patients either delayed presenting at the hospital or experienced delays in receiving treatment.

There were some limitations of this study, primarily because it was retrospective in design and conducted in a single center, so the sample size was relatively small. However, it is an important study, as it is one of the few to have examined the effects of the COVID-19 pandemic on breast cancer presentation. Moreover, it can be considered more sensitive than abovementioned research (Vanni) since it shows the changes in patients with breast cancer over the longer period of 9 months from the onset of the pandemic.

In conclusion, the results of this study demonstrate that breast cancers during the pandemic showed typical malignant radiological findings. This study also demonstrates that the tumor size was larger and lymph node involvement was more frequent in breast cancers diagnosed during the COVID-19 pandemic. Furthermore, patients diagnosed during this period could have to wait longer for surgical treatment. Despite the significant decrease in mortality rates and the increase in survival as consequences of the widespread implementation of breast cancer screening programs and developments in treatments, the suspension of screening programs and delays in treatments because of COVID-19 have had a negative impact on breast cancer management. The effects of these delays on long-time breast cancer outcomes (disease-free survival and overall survival) would require longer follow-ups. As screening programs are a key element of the early diagnosis of breast cancer, and it is not known when the pandemic will end, it can be recommended that screening programs should be continued without interruption, with all the necessary precautions taken to prevent the spread of infection.

#### Conflict of interest disclosure

The authors declared no conflicts of interest.

#### References

1. Curigliano G, Cardoso MJ, Poortmans P, et al. Recommendations for triage, prioritization and treatment of breast cancer patients during the COVID-19 pandemic. *Breast*. 2020;52:8-16. [\[CrossRef\]](#)
2. Pediconi F, Mann RM, Gilbert FJ, et al. European Society of Breast Imaging (EUSOBI) recommendations for breast imaging and cancer diagnosis during and after the COVID-19 pandemic 2020. EUSOBI, 2020. Available at: <https://www.eusobi.org/news/recommendations-breast-covid19/> [\[CrossRef\]](#)
3. Seely J, Barry M. Canadian Society of Breast Imaging and Canadian Association of Radiologists Joint Position Statement on COVID-19. Canadian Society of Breast Imaging, 2020. Available at: <https://car.ca/news/canadian-society-of-breast-imaging-and-canadian-association-of-radiologists-joint-position-statement-on-covid-19/> [\[CrossRef\]](#)
4. Foca F, Mancini S, Bucchi L, et al. Decreasing incidence of late-stage breast cancer after the introduction of organized mammography screening in Italy. *Cancer*. 2013;119(11):2022-2028. [\[CrossRef\]](#)
5. Lauby-Secretan B, Scoccianti C, Loomis D, et al. Breast-cancer screening—viewpoint of the IARC Working Group. *N Engl J Med*. 2015;372(24):2353-2358. [\[CrossRef\]](#)
6. AJCC (American Joint Committee on Cancer) Cancer Staging Manual. In: Amin MB, Edge SB, Greene FL, et al, eds. 8th ed. 3rd printing. Chicago: Springer, 2018. [\[CrossRef\]](#)
7. Vanni G, Tazzioli G, Pellicciaro M, et al. Delay in breast cancer treatments during the first COVID-19 lockdown. A multicentric analysis of 432 patients. *Anticancer Res*. 2020;40(12):7119-7125. [\[CrossRef\]](#)
8. Weedon-Fekjaer H, Lindqvist BH, Vatten LJ, Aalen OO, Tretli S. Breast cancer tumor growth estimated through mammography screening data. *Breast Cancer Res*. 2008;10(3):R41. [\[CrossRef\]](#)
9. Toss A, Isca C, Venturelli M, et al. Two-month stop in mammographic screening significantly impacts on breast cancer stage at diagnosis and upfront treatment in the COVID era. *ESMO Open*. 2021;6(2):100055. [\[CrossRef\]](#)
10. Michaelson JS, Silverstein M, Sgroi D, et al. The effect of tumor size and lymph node status on breast carcinoma lethality. *Cancer*. 2003;98(10):2133-2143. [\[CrossRef\]](#)
11. Yılmaz E, Güldoğan N, Arıbal E. The effect of COVID-19 pandemic on breast imaging: clinical observations. *Diagn Interv Radiol*. 2020;26(6):603. [\[CrossRef\]](#)
12. Nettleton J, Long J, Kuban D, Wu R, Shaeffer J, El-Mahdi A. Breast cancer during pregnancy: Quantifying the risk of treatment delay. *Obstet Gynecol*. 1996;87(3):414-418. [\[CrossRef\]](#)
13. Smith EC, Ziogas A, Anton-Culver H. Delay in surgical treatment and survival after breast cancer diagnosis in young women by race/ethnicity. *JAMA Surg*. 2013;148(6):516-523. [\[CrossRef\]](#)
14. COVIDSurg Collaborative. Elective surgery cancellations due to the COVID-19 pandemic: global predictive modelling to inform surgical recovery plans. *Br J Surg*. 2020;107(11):1440-1449. [\[CrossRef\]](#)
15. Fancellu A, Sanna V, Rubino C, et al. The COVID-19 outbreak may be associated to a reduced level of care for breast cancer. A comparative study with the pre-covid era in an Italian breast unit. *Healthcare (Basel)*. 2020;8(4):474. [\[CrossRef\]](#)
16. Eaglehouse YL, Georg MW, Shriver CD, Zhu K. Time-to-surgery and overall survival after breast cancer diagnosis in a universal health system. *Breast Canc Res Treat*. 2019;178(2):441-450. [\[CrossRef\]](#)
17. Kaufman HW, Chen Z, Niles J, Fesko Y. Changes in the number of US patients with newly identified cancer before and during the coronavirus disease 2019 (COVID-19) pandemic. *JAMA Netw Open*. 2020;3(8):e2017267. [\[CrossRef\]](#)
18. De Vincentiis L, Carr RA, Mariani MP, Ferrara G. Cancer diagnostic rates during the 2020 'lockdown', due to COVID-19 pandemic, compared with the 2018-2019: an audit study from cellular pathology. *J Clin Pathol*. 2021;74(3):187-189. [\[CrossRef\]](#)



# Multimodality imaging and histopathology of metaplastic breast cancer

Hakkı Çelik   
İşıl Başara Akın   
Merih Güray Durak   
Pınar Balcı 

## ABSTRACT

Metaplastic breast cancer (MBC) is a rare subtype of invasive breast cancer characterized by mixed epithelial and mesenchymal differentiation. Commonly seen subtypes include squamous cell carcinoma, spindle cell carcinoma, and metaplastic carcinoma with heterologous mesenchymal differentiation. MBC tends to have a more aggressive clinical presentation, higher metastatic potential, higher rates of local recurrence, and a worse prognosis compared with invasive breast carcinoma of no special type. Most MBCs are triple-negative breast cancers, which explains their resistance to most systemic therapies. Therefore, accurately diagnosing MBC early is crucial for deciding the treatment strategy and predicting the prognosis. In this pictorial essay, the imaging findings of MBC in different modalities and the histopathologic features of its subtypes are reviewed.

## KEYWORDS

Metaplastic breast cancer, mammography, ultrasonography, magnetic resonance imaging, histopathology

**M**etaplastic breast cancer (MBC) is a rare subtype of invasive breast cancer that accounts for less than 1% of all breast cancers.<sup>1</sup> Currently, the diagnosis of MBC is made more frequently as the histologic features are clearly defined, and the pathology methods have improved. Histologically, MBC is characterized by the presence of two or more malignant cell types, commonly a mixture of epithelial and mesenchymal components. According to the most recent World Health Organization classification of breast tumors, the histologic types of MBC are low-grade adenosquamous carcinoma, fibromatosis-like metaplastic carcinoma, spindle cell carcinoma, squamous cell carcinoma, metaplastic carcinoma with heterologous mesenchymal differentiation, and mixed metaplastic carcinoma.<sup>2</sup> In a large international multicenter study of 405 patients with histologic confirmation of MBC, spindle cell (34%) was the most common subtype in the Western series, and squamous cell (34%) was the most common subtype in the Asian series, followed by metaplastic carcinoma with heterologous mesenchymal differentiation in both series (29% and 24%, respectively).<sup>3</sup>

MBC usually presents as a fast-growing large palpable mass in women older than 50 years, with no predilection for the left or right breast,<sup>4</sup> and it tends to metastasize hematogenously rather than through the lymphatic system.<sup>5</sup> This is why axillary lymph node metastasis is rare, while the lungs and bones are the most common sites for MBC to metastasize, which may explain why patients usually present in the advanced stages more frequently than with invasive breast carcinoma of no special type (IBC-NST).

The differential diagnosis between MBC and IBC-NST is important for the clinical management, treatment strategy, and prognosis prediction.<sup>6</sup> MBC tends to have a more aggressive clinical presentation, higher metastatic potential, higher rates of local recurrence, and worse prognosis compared with IBC-NST.<sup>7</sup> The majority of MBC is triple-negative breast cancer, in which estrogen receptor, progesterone receptor, and human epidermal growth factor re-

From the Department of Radiology (H.Ç., ✉ dr.celik90@gmail.com, I.B.A., M.G.D., P.B.), Dokuz Eylül University Faculty of Medicine, İzmir, Turkey.

Received 28 January 2022; revision requested 14 March 2022; last revision received 18 May 2022; accepted 08 June 2022.



Epub: 12.01.2023

Publication date: 31.01.2023

DOI: 10.4274/dir.2022.221363

ceptor-2 are negative. Triple-negative breast cancers are resistant to chemotherapy, hormonal therapy, and targeted molecular therapy, which explains the poor prognosis and the challenging clinical management for patients with MBC.<sup>8,9</sup> Therefore, accurately diagnosing MBC at an early stage is crucial for survival. This article aims to review the imaging findings of MBC in different modalities and describe the histopathologic features of its subtypes.

## Imaging findings

### Mammography (MG) findings

In MG examinations, MBCs tend to present with benign imaging features; these cancers are commonly hyperdense lesions with round (Figure 1) or oval (Figures 2, 3) shapes.<sup>10,11</sup> The margins of these lesions may be circumscribed (Figure 1), obscured (Figures 3, 4), or indistinct (Figures 5, 6).<sup>1,10,11</sup> Partially circumscribed margins are a frequently encountered and possible distinctive imaging feature, reflecting the presence of both the metaplastic and invasive carcinoma components.<sup>1</sup> An irregular shape (Figure 6) and spiculated margins are uncommon imaging features in MBCs.<sup>6,10,12</sup> Additionally, MBCs are generally large tumors with a mean size of 3.9 cm according to the cases reviewed (Figures 1, 2).<sup>13,14</sup> One study reported that 20.4% of MBCs were larger than 5 cm, compared with only 5.2% of invasive ductal carcinomas.<sup>15</sup> Microcalcifications (Figure 6) are less common in MBCs than in IBC-NST.<sup>6</sup> Calcifications are often absent in MBCs and are described in up to 25% of cases, with greater frequency in

matrix-producing subtypes, such as carcinomas with chondroid metaplasia.<sup>16</sup> If present, they can be amorphous, coarse, punctate, or pleomorphic.

Different histologic subtypes of MBC may present with distinctive MG findings. Squamous cell carcinoma usually presents as an irregularly shaped mass (Figure 6) with spiculated margins and high density, while spindle cell carcinoma and matrix-producing carcinoma tend to present as an oval-shaped mass with circumscribed margins and slightly high density (Figure 2).<sup>17</sup> Spindle cell carcinoma usually demonstrates benign imaging features on MG since it is surrounded by a fibrous capsule.<sup>18</sup> Microplastic breast cancer lesions with heterologous mesenchymal differentiation are more likely to be calcified. A circumscribed margin with a spiculated portion is often seen in MBC with a mixture of metaplastic and invasive carcinoma.<sup>1</sup>

### Ultrasonography (US) findings

On US, MBC is frequently encountered as a mass with a complex echo structure containing a cystic component secondary to necrosis (Figures 1, 3), although it can also be detected as a solid mass (Figure 4).<sup>1,6,12</sup> In one study, central necrosis constituting more

than 50% of the tumor was observed in 66% of patients.<sup>4</sup> The shape of the lesions may be round, oval, or irregular. In addition, MBCs can have circumscribed (Figure 1), indistinct (Figure 4), or microlobulated (Figure 7) margins.<sup>1,6,12</sup> Benign US imaging findings are more common in MBC than in IBC-NST,<sup>6</sup> and MBCs often demonstrate posterior acoustic enhancement (Figures 1, 3) rather than posterior acoustic shadowing, making their differentiation from benign lesions even more challenging.<sup>6</sup> Commonly detected US findings of MBC are round or oval-shaped lesions with well-defined margins, complex echogenicity, and posterior acoustic enhancement.<sup>12,16</sup>

There are some US features that help to identify the subtypes of MBCs. Lesions with large cystic areas usually contain a squamous component (Figure 1).<sup>11</sup> Similar to MG, spindle cell carcinoma tends to show benign imaging features on US, such as round or oval-shaped lesions with circumscribed margins (Figure 2). Rapidly growing high-grade MBCs are usually associated with ill-defined margins and less desmoplastic reaction at peritumoral sites.<sup>19</sup>

Routine B-mode ultrasound has long been the first-choice imaging guidance for breast biopsy as it is practical and effective.

#### Main points

- Metaplastic breast cancer (MBC) tends to demonstrate benign imaging features on mammography (MG) and ultrasound.
- A predominantly circumscribed high-density mass without calcifications on MG should raise suspicion of MBC.
- High T2-weighted signal intensity, rim enhancement, and non-enhancing internal components on magnetic resonance imaging help differentiate MBC from other breast malignancies.
- Squamous cell carcinoma tends to reveal an irregularly-shaped cystic mass with spiculated margins, while spindle cell carcinoma is more likely to show benign imaging features, such as an oval shape and circumscribed margins.
- Histopathologic evaluation, including immunohistochemistry analysis, is essential for diagnosing MBC.

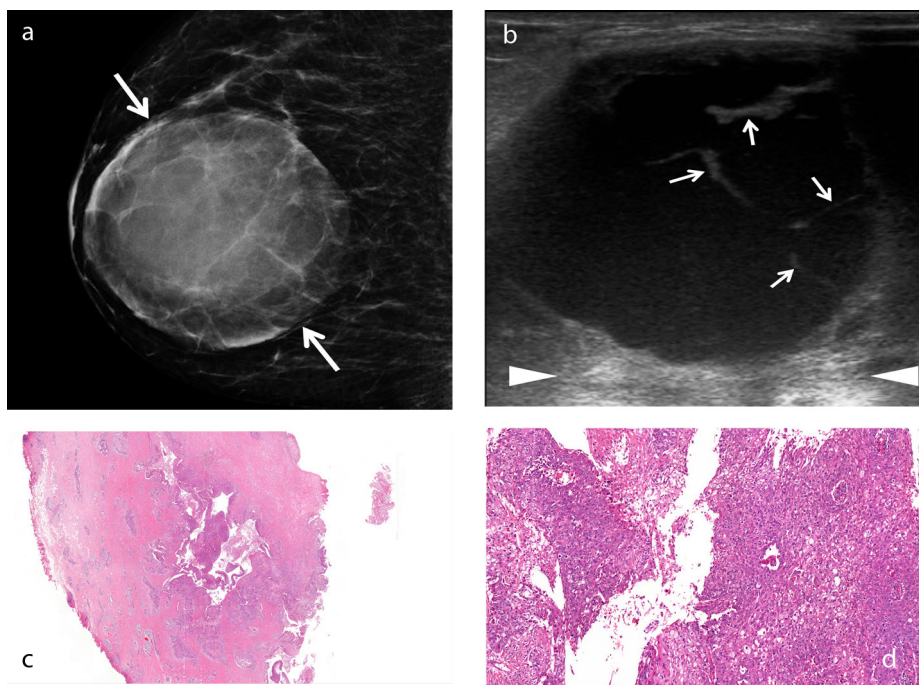


**Figure 1.** An example of squamous cell metaplastic breast carcinoma with extensive central necrosis. A 38-year-old female patient presented with a rapidly growing palpable mass in the right breast. Mammogram (a) reveals a large, well-defined round density mass measuring 8 × 7.5 cm with circumscribed margins (arrows). Gray-scale ultrasound image (b) shows a complex cystic mass with thick septa (b, arrows) and posterior acoustic enhancement (arrowheads). Histopathology of the cystic lesion (c) reveals atypical squamous cells lining the cavity and infiltrating the adjacent stroma [hematoxylin and eosin (H&E), ×2]. Photomicrograph (d) shows that the neoplastic cells lining the irregular spaces are atypical squamous cells with abundant eosinophilic cytoplasm and large, vesicular nuclei (H&E, ×20).

However, in the presence of hemorrhage or necrosis, the probability of misdiagnosis increases due to inadequate sampling or poor sampling site selection.<sup>11</sup> Doppler US reveals the angioarchitecture of the lesions, allowing the differentiation of viable and necrotic portions (Figure 2). Therefore, adding color Doppler to routine B-mode US during the biopsy of these tumors would increase the chance of obtaining sufficient material for histopathologic examination.

### Magnetic resonance imaging (MRI) findings

Breast MRI is a potential problem-solving tool with higher sensitivity and specificity in cases of ambiguous findings with conventional breast imaging modalities.<sup>20</sup> On T1-weighted images, the signal of the MBC lesion is generally isointense or hypointense when compared with the normal fibroglandular tissue (Figure 3), similar to other histologic types of IBC.<sup>7</sup> Heterogeneous high signal intensity on T2-weighted images is

a significant MRI feature of MBC (Figures 2, 3).<sup>4,8</sup> The T2 hyperintensity is related to the necrotic component of the tumor, a frequent finding in MBC. Therefore, the T2 hyperintensity helps distinguish MBC from other histologic types of invasive breast cancer, although differentiating from mucinous carcinoma and, less frequently, necrotic infiltrating ductal carcinoma is needed.<sup>4</sup>

The most common pattern of enhancement is a ring-like enhancement (Figures 2, 3), which can be partially explained by the extensive central necrosis observed in these tumors.<sup>10</sup> Non-enhancing solid portions in the peripheral areas of the tumor might be explained by the presence of metaplastic tissue.<sup>8</sup>

Table 1 shows a comparison of the multimodality imaging features of MBC compared with IBC-NST. Table 2 shows the MG and US imaging characteristics of the major histologic subtypes of MBC.

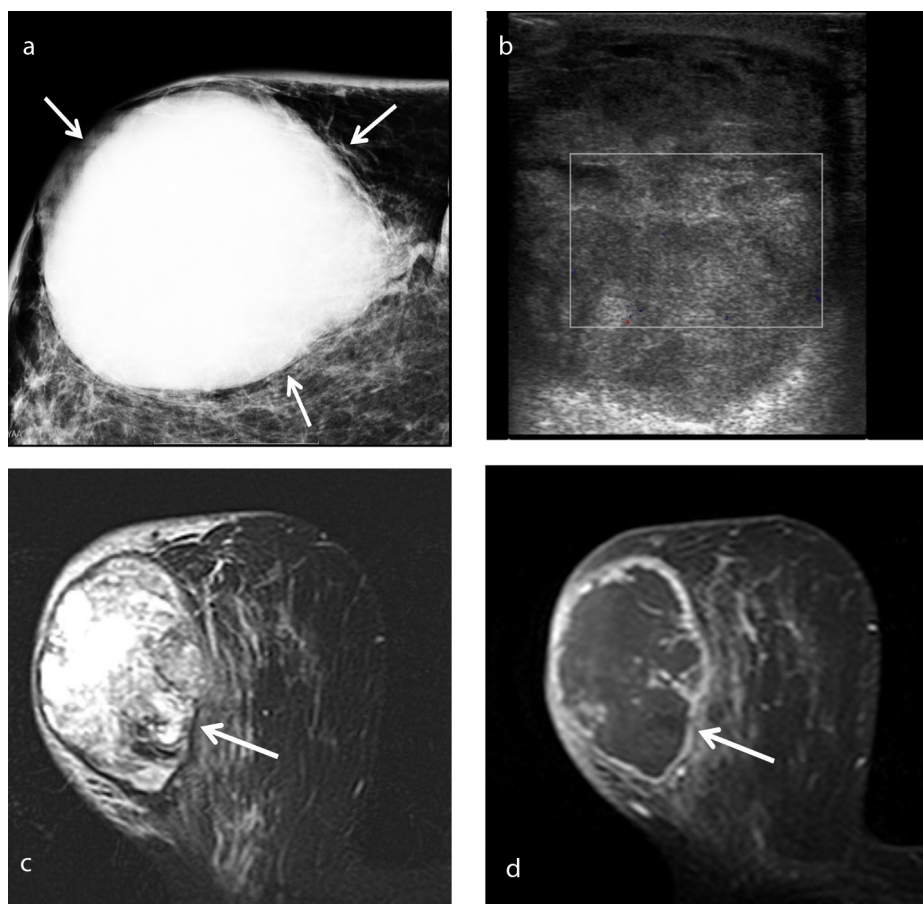


**Figure 2.** An example of spindle cell type metaplastic breast carcinoma in a 70-year-old female patient who presented with a palpable mass in her right breast. Mammogram (a) shows a high-density oval mass measuring 7.5 × 6 cm with obscured margins (arrows). Color Doppler ultrasound (b) shows a lesion adjacent to the skin with a heterogeneous echo pattern and no significant internal vascularity. T2-weighted magnetic resonance imaging (c) reveals a mass with heterogeneous intermediate-to-high signal intensity. Axial subtracted contrast-enhanced T1-weighted image (d) shows a rim-enhancing lesion (arrow) with a large non-enhancing central area consistent with necrosis, corresponding to the avascular area on the Doppler ultrasound image.

## Advanced imaging techniques

Digital breast tomosynthesis (DBT) and contrast-enhanced MG are techniques that have the potential to improve the sensitivity of conventional MG. DBT significantly improves lesion detection by minimizing the effect of overlying breast tissue, and it can reveal architectural distortion better than conventional MG, particularly in dense breast tissue. Detection of architectural distortion on DBT (Figure 5) can be a valuable finding for diagnosing MBC, which tends to demonstrate benign imaging features.<sup>11</sup> Contrast-enhanced MG is a novel technique that visualizes neovascularity using intravenous iodinated contrast material.

Sonoelastography is an imaging technique developed to improve the specificity of B-mode US, which reveals the relative stiffness of the target tissue compared to the surrounding tissue. Stiff breast lesions have a higher risk of being malignant. Based on our experience, MBC tends to reveal increased stiffness in shear wave sonoelastography (Figures 5, 6).

Diffusion-weighted imaging (DWI) and dynamic contrast-enhanced MRI are advanced MRI techniques commonly used in breast imaging. MBCs usually show restricted diffusion on DWI (Figure 3), which can be a valuable finding in differentiating MBCs from benign lesions. In a retrospective study including nineteen patients with MBC, DWI showed diffusion restriction in all cases.<sup>8</sup> Early enhancement and delayed washout in the peripheral rim and non-enhancing internal components would be beneficial in distinguishing MBCs from other types of breast malignancies.<sup>7</sup> The most frequent pharmacokinetic time–signal intensity curves are types two and three (Figure 7), which is not a specific characteristic of MBC.<sup>4</sup>

The high risk of early distant metastases in MBC necessitates systemic staging as part of the initial evaluation. Fluorodeoxyglucose positron emission tomography/computed tomography (FDG PET/CT) can detect metastases (Figure 3) that may not be visible on other imaging modalities. The specificity of FDG PET/CT is low within the breast as inflammatory causes, infections, benign tumors such as fibroadenomas, and even physiological conditions such as lactation may be markedly FDG avid.<sup>21</sup> Other major roles of 18F-FDG PET/CT in breast cancer are monitoring the response to treatment and early detection of recurrence.<sup>22</sup>

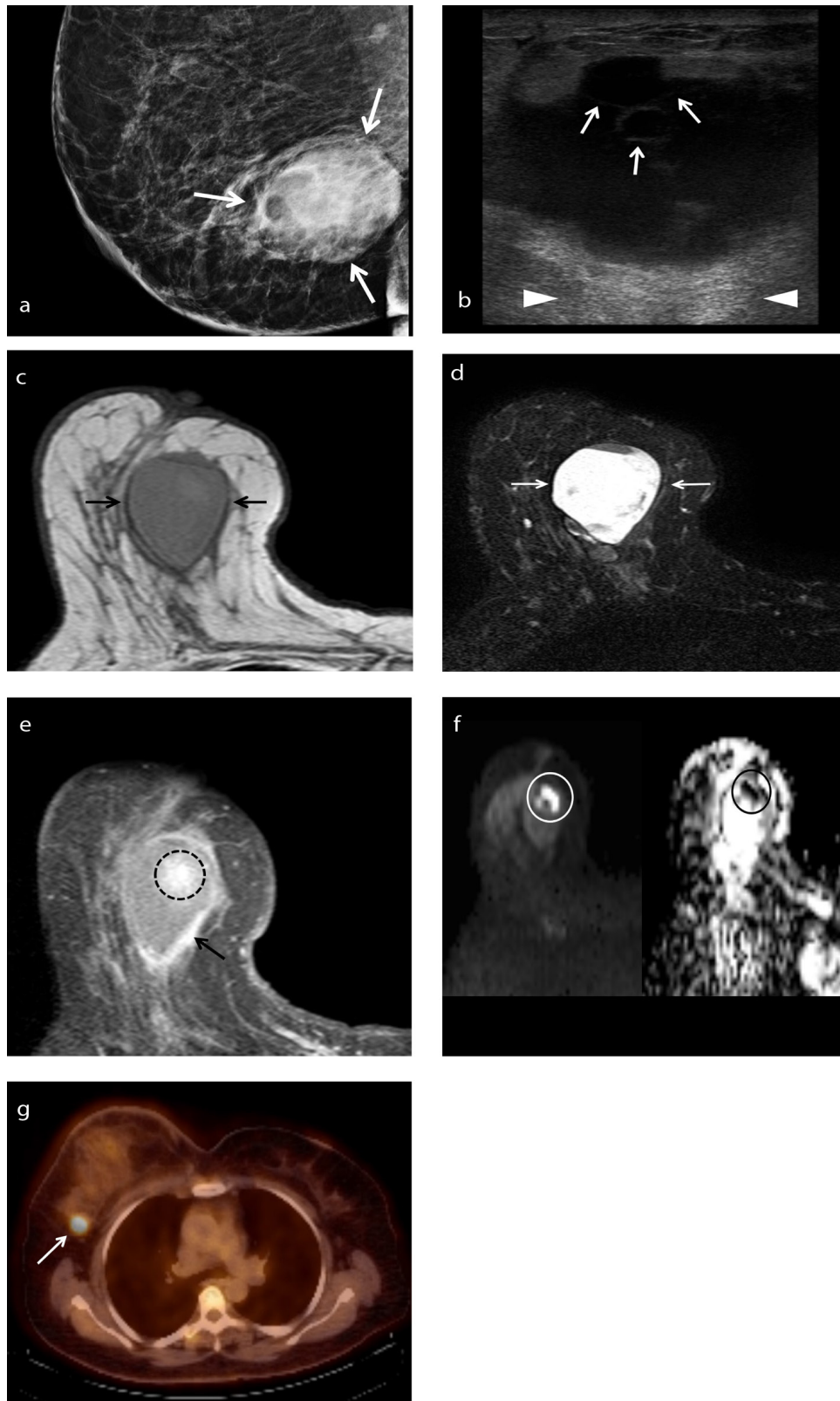


**Figure 3.** An example of squamous cell metaplastic breast carcinoma in a 58-year-old female patient who presented with a palpable mass in her right breast. Mammogram (a) shows a large high-density mass measuring  $4.7 \times 3.8$  cm with obscured margins (arrows). Gray-scale ultrasound image (b) shows a cystic mass with septa (arrows) and posterior acoustic enhancement (arrowheads). T1-weighted magnetic resonance image (c) shows an oval lesion with circumscribed margins and isointense relative to surrounding fibroglandular tissue. Axial fat-suppressed T2-weighted magnetic resonance image (d) shows a heterogeneous high signal intensity mass. T1-weighted fat-suppressed post-contrast image (e) shows an irregular enhancing rim (arrow) at the tumor periphery and a central area of heterogeneous enhancement (dashed circle). Diffusion-weighted imaging (f) reveals that the central contrast-enhancing area restricts diffusion (circles, left: diffusion-weighted image, right: corresponding apparent diffusion coefficient map). Axial fused fluorodeoxyglucose positron emission tomography/computed tomography image (g) shows the right axillary lymph node with intense fluorodeoxyglucose uptake (standardized uptake value max: 5.3, arrow), consistent with metastasis.

**Table 1.** Comparison of multimodality imaging features of MBC compared with IBC-NST

	MBC	IBC-NST
<b>Mammography</b>		
Shape	Round, oval	Irregular
Margin	Circumscribed, obscured	Spiculated
Density	High	High
Architectural distortion	Uncommon	Common
Microcalcifications	Usually, non-calcified	Common
Associated features	Large tumor size	Axillary adenopathy
<b>Ultrasound</b>		
Shape	Round, oval	Irregular
Margins	Circumscribed, indistinct, microlobulated	Spiculated, angular
Echo pattern	Complex echogenicity	Hypoechoic mass
Posterior features	Acoustic enhancement	Acoustic shadowing
Doppler ultrasound	Vascularity in solid portions	Highly vascular
Sonoelastography	Increased stiffness	Increased stiffness
<b>MRI</b>		
T1 signal*	Iso to hypointense	Iso to hypointense
T2 signal*	Hyperintense	Iso to hypointense
Enhancement	Rim enhancement and non-enhancing internal components	Irregular rim enhancement with centripetal progression
Kinetics	Type 2 and 3	Type 2 and 3
DWI	Restricted diffusion	Restricted diffusion
*Signal intensity compared to parenchyma; MBC, metaplastic breast cancer; IBC-NST, invasive breast cancer of no special type; MRI, magnetic resonance imaging; DWI, diffusion-weighted imaging.		

**Table 2.** Mammography and ultrasound imaging features of major histologic subtypes of MBC

Histopathologic subtype	Distinctive imaging features
Squamous cell MBC	Cystic areas on US* Irregular shape on MG and US Spiculated margins on MG and US High density on MG
Spindle cell MBC	Circumscribed margins on MG and US* Oval shape on MG Slightly high density on MG
MBC with heterologous mesenchymal differentiation	Calcification on MG and US* Oval shape on MG and US Slightly high density on MG
*Distinctive imaging feature of the relevant histologic subtype; MBC, metaplastic breast cancer; US, ultrasonography; MG, mammography.	

## Histopathologic features

MBCs are composed of one or more cell populations that have undergone metaplastic differentiation, meaning that the cells have transformed from glandular to non-glandular morphology. According to their behavior and histopathologic features, MBCs can be subclassified as high-grade and low-grade.<sup>13</sup> High-grade MBC includes squamous cell carcinoma, spindle cell carcinoma, and MBC with heterologous mesenchymal differentiation, while low-grade MBC includes

low-grade adenosquamous carcinoma and fibromatosis-like MBC. Mixed MBC is composed of more than one histologic subtype.

The spindle cell subtype is more likely to have an oval shape with circumscribed margins, detected both radiologically and pathologically (Figures 2, 8).<sup>1</sup> Histologically, spindle cell carcinoma reveals atypical spindle cells arranged in various architectural patterns (Figures 8).<sup>13</sup> Squamous cell MBCs are frequently cystic tumors in which a central cavity lined by atypical squamous cells

is encircled by neoplastic cells, with various degrees of squamous differentiation and a reactive stroma (Figures 1).<sup>2,12</sup> Squamous cell carcinoma of the breast also tends to reveal an irregularly-shaped mass (Figures 6, 7) with spiculated margins.<sup>17</sup> MBC with heterologous mesenchymal differentiation is comprised of a mixture of mesenchymal components with carcinomatous areas that can show squamous or glandular differentiation.<sup>2</sup> This subtype is also denominated as matrix-producing MBC. The most frequent mesenchymal (heterologous) elements seen in these



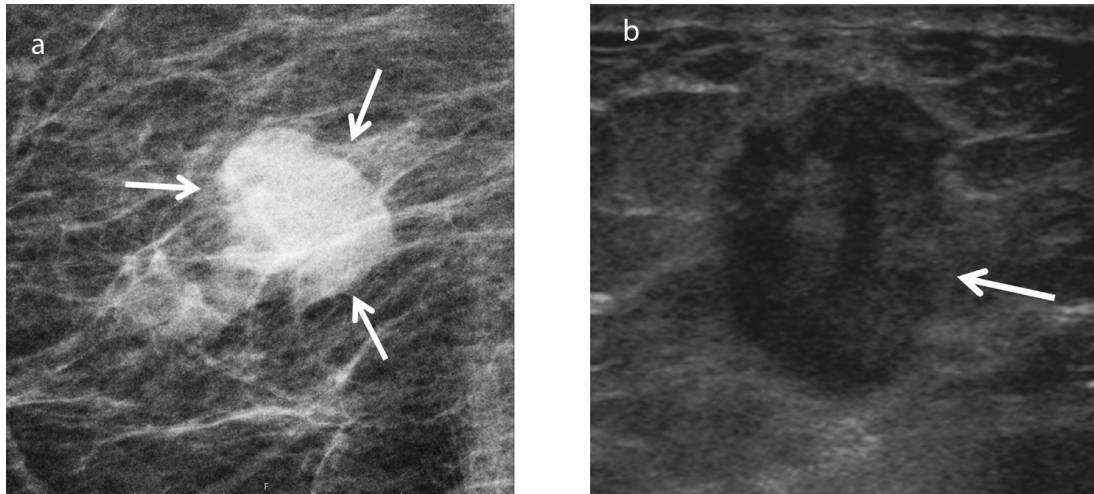


**Figure 4.** An example of chondroid matrix-producing metaplastic breast carcinoma in a 77-year-old female patient who presented with a palpable lump in her right breast. Mammogram (a) shows a density with obscured margins (arrows). Gray-scale ultrasound (b) shows an oval, vertically oriented, hypoechoic lesion measuring 1.3 × 1.8 cm with indistinct borders (arrow) and posterior acoustic enhancement.

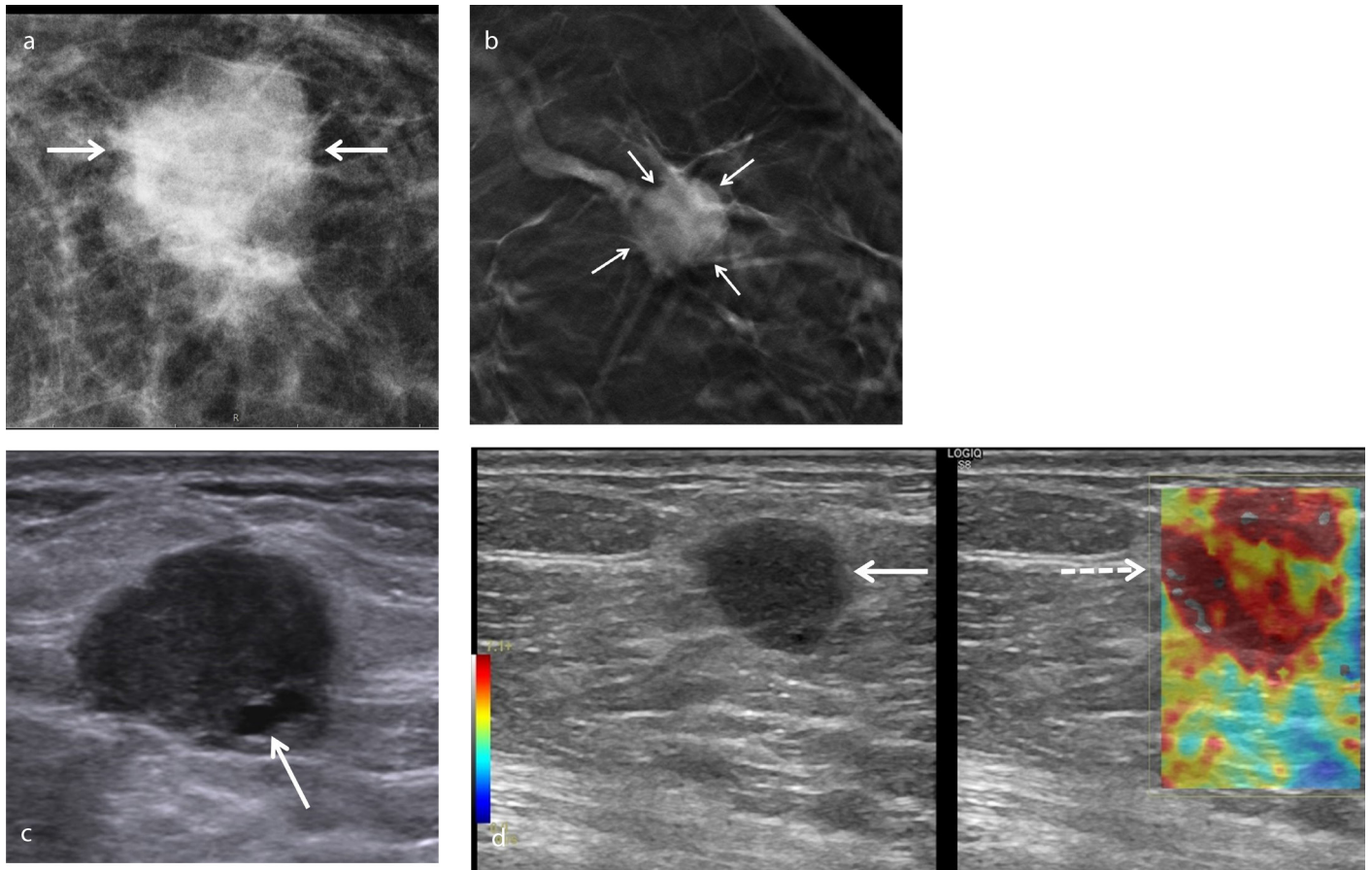


**Figure 5.** An example of squamous cell metaplastic breast carcinoma in a 51-year-old asymptomatic female patient. Mammogram (a) shows a round opacity with indistinct margins. Digital breast tomosynthesis (b) better demonstrates architectural distortion caused by the lesion (arrows). Gray-scale ultrasound (c) shows a round hypoechoic lesion measuring 1.8 × 1.4 cm with microlobulated margins and a small cystic area (arrow). Shear wave elastography image (d) reveals increased stiffness within and around the lesion.

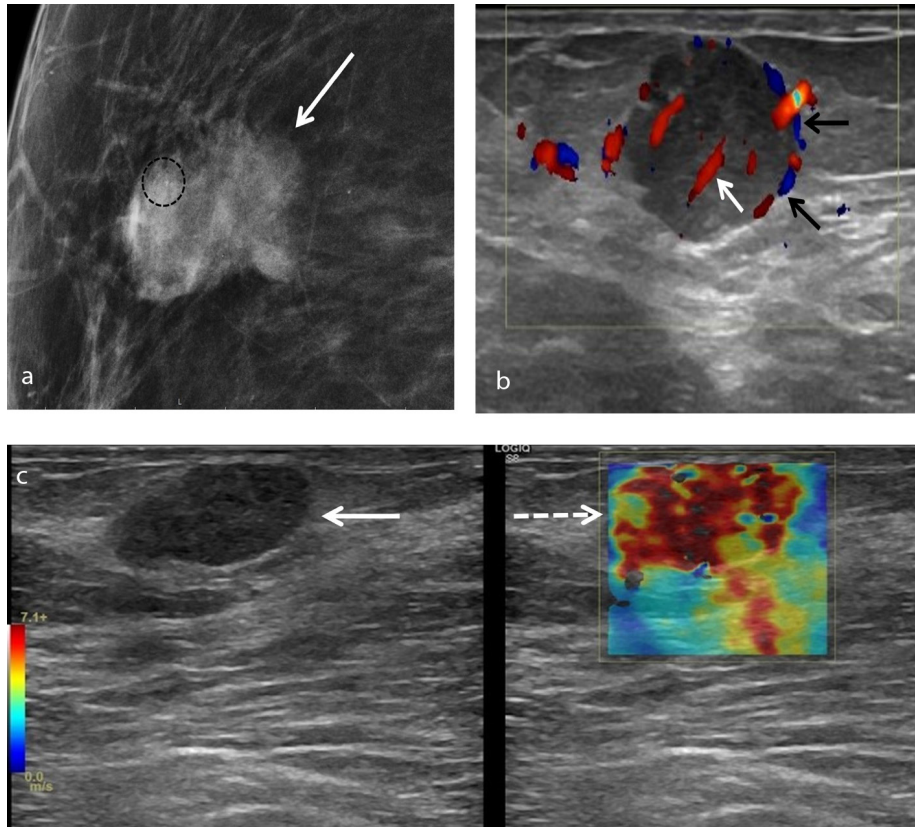


**Figure 6.** An example of squamous cell metaplastic breast carcinoma in a 72-year-old female patient who presented with a palpable superficial right breast mass. Mammogram (a) shows an irregularly shaped density (arrow) with indistinct margins and microcalcifications (circle). Color Doppler ultrasound (b) reveals an oval hypoechoic lesion measuring  $2.3 \times 1.9$  cm with microlobulated margins, showing both peripheral (black arrows) and central (white arrow) vascularity. On shear wave elastography (c), the lesion displays increased stiffness compared to the surrounding fibroglandular tissue.

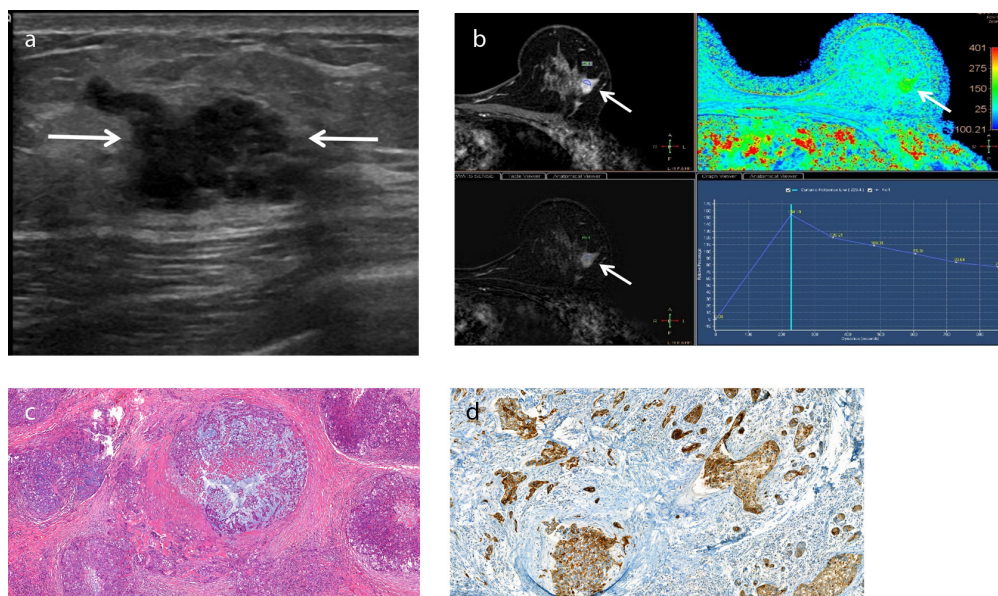


**Figure 7.** An example of metaplastic breast carcinoma with heterologous mesenchymal (chondroid) differentiation in a 43-year-old female patient who presented with a palpable mass in her left breast. Metaplastic breast carcinoma with heterologous mesenchymal (chondroid) differentiation. Gray-scale ultrasound (a) shows an irregularly shaped lesion measuring  $2 \times 1$  cm with microlobulated and partially indistinct margins (arrows). T1-weighted dynamic contrast-enhanced magnetic resonance imaging (DCE-MRI) (b) demonstrates an irregularly shaped mass showing heterogeneous enhancement (arrows). Pharmacokinetic analysis of DCE-MRI (b, bottom-right) reveals a type three time-intensity curve. Photomicrograph (c) shows irregular nests of malignant epithelial cells are admixed with the chondroid component, which shows moderate pleomorphism (Hematoxylin and eosin,  $\times 10$ ). Immunohistochemical staining of high-molecular-weight cytokeratin (d) demonstrates cytoplasmic staining of the malignant epithelial cells (34 $\beta$ E12,  $\times 20$ ).

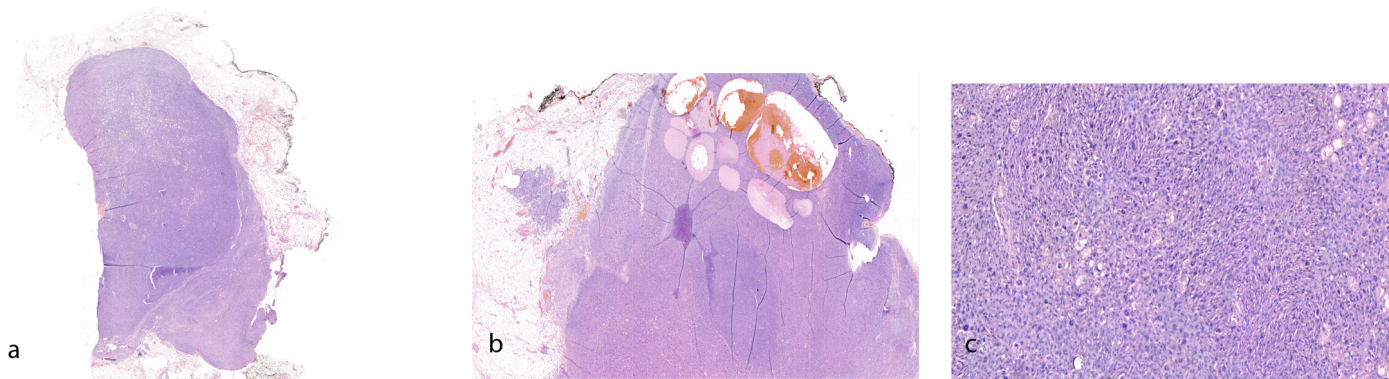


**Figure 8.** An example of spindle cell type metaplastic breast carcinoma in a 70-year-old female patient who presented with a palpable mass in her right breast. Excisional biopsy (a) reveals a tumor with relatively well-circumscribed margins in the majority of the sections [hematoxylin and eosin (H&E),  $\times 1.2$ ]. In some sections (b), the margins are irregular microscopically and show infiltration to the adipose tissue (H&E,  $\times 2.6$ ). Photomicrograph (c) shows the tumor composed of interlacing fascicles of highly atypical spindle cells with numerous mitotic figures. The tumor cells show prominent nuclear pleomorphism, elongated to plump eosinophilic cytoplasm (H&E,  $\times 20$ ).

tumors are cartilage and bone (Figure 7). In cases with a predominant mesenchymal component, extensive tissue sampling may be required to find the associated epithelial elements and, therefore, differentiate these tumors from sarcomas. In some cases, immunohistochemical staining can be helpful. Immunostains for epithelial markers, such as cytokeratins, may provide the proper diagnosis (Figure 7).

## MBC prognosis and treatment

Except for fibromatous-like carcinoma and low-grade adenosquamous carcinoma, all histopathologic subtypes are aggressive, chemoresistant, and have a high tendency to metastasize. Diagnosis below the age of 40 years, skin invasion, and squamous cell component in nodal tumors are associated with a poorer outcome.<sup>5</sup> Rakha et al.<sup>3</sup> reported that lymph node stage, lymphovascular invasion, and histologic subtype were associated with outcome but tumor size and grade were not. Matrix-producing carcinoma is generally associated with a better prognosis compared with spindle cell and squamous cell carcinomas.<sup>3</sup> The biological behavior of squamous cell carcinoma is similar to that of invasive ductal carcinoma with invasive growth, which explains the malignant features seen in squamous cell carcinoma.<sup>9</sup> Tumors with benign imaging features like circumscribed margins might represent higher histologic tumor grades and aggressive malignancies associated with poor prognoses.<sup>6</sup>

Currently, there is no standard therapeutic approach for MBC. MBC tends to be resistant to conventional chemotherapy. Nevertheless, adjuvant chemotherapy remains the

backbone of the treatment protocol as studies show that it improves the prognosis, particularly when administered for early-stage disease. Moreover, because these tumors are generally triple negative, hormone therapy and targeted therapies such as trastuzumab are likely to be ineffective.

## Conclusion

MBC tends to demonstrate benign imaging features, such as an oval shape and circumscribed margins on MG and US. Awareness of these overlapping findings, investigation of the clinical features, and using MRI techniques can assist in differentiating between MBC and benign tumors or other types of breast cancer. T2 high signal intensity, rim enhancement, and non-enhancing internal components on MRI would help differentiate MBC from other breast malignancies. In addition to multimodality imaging, histopathologic evaluation, including immunohistochemistry analysis, is essential for diagnosing MBC.

## Conflict of interest disclosure

The authors declared no conflicts of interest.

## References

- Günhan-Bilgen I, Memiş A, Ustün EE, Zekioglu O, Ozdemir N. Metaplastic carcinoma of the breast: clinical, mammographic, and sonographic findings with histopathologic correlation. *AJR Am J Roentgenol*. 2002;178(6):1421-1425. [CrossRef]
- WHO Classification of Tumours Editorial Board. Breast Tumours. Lyon (France): International Agency for Research on Cancer; 2019. (WHO

classification of tumours series, 5th ed.; vol. 2). <https://publications.iarc.fr/581>. [CrossRef]

- Rakha EA, Tan PH, Varga Z, et al. Prognostic factors in metaplastic carcinoma of the breast: a multi-institutional study. *Br J Cancer*. 2015;112(2):283-289. [CrossRef]
- Velasco M, Santamaría G, Ganau S, et al. MRI of metaplastic carcinoma of the breast. *AJR Am J Roentgenol*. 2005;184(4):1274-1278. [CrossRef]
- McKinnon E, Xiao P. Metaplastic carcinoma of the breast. *Arch Pathol Lab Med*. 2015;139(6):819-822. [CrossRef]
- Yang WT, Hennessy B, Broglio K, et al. Imaging differences in metaplastic and invasive ductal carcinomas of the breast. *AJR Am J Roentgenol*. 2007;189(6):1288-1293. [CrossRef]
- Kim HJ, Kim SY, Huh S. Multimodality imaging findings of metaplastic breast carcinomas: a report of five cases. *Ultrasound Q*. 2018;34(2):88-93. [CrossRef]
- Jia Y, He C, Liu L, et al. A retrospective study of the Imaging and Pathological Features of Metaplastic Breast Carcinoma and Review of the Literature. *Med Sci Monit*. 2019;25:248-258. [CrossRef]
- Song Y, Liu X, Zhang G, et al. Unique clinicopathological features of metaplastic breast carcinoma compared with invasive ductal carcinoma and poor prognostic indicators. *World J Surg Oncol*. 2013;11:129. [CrossRef]
- Choi BB, Shu KS. Metaplastic carcinoma of the breast: multimodality imaging and histopathologic assessment. *Acta Radiol*. 2012;53(1):5-11. [CrossRef]
- Leddy R, Irshad A, Rumboldt T, Cluver A, Campbell A, Ackerman S. Review of metaplastic carcinoma of the breast: imaging findings and pathologic features. *J Clin Imaging Sci*. 2012;2:21. [CrossRef]

12. Park JM, Han BK, Moon WK, Choe YH, Ahn SH, Gong G. Metaplastic carcinoma of the breast: mammographic and sonographic findings. *J Clin Ultrasound*. 2000;28(4):179-186. [\[CrossRef\]](#)
13. González-Martínez S, Pérez-Mies B, Carretero-Barrio I, et al. Molecular Features of Metaplastic Breast Carcinoma: An Infrequent Subtype of Triple Negative Breast Carcinoma. *Cancers (Basel)*. 2020;12(7):1832. [\[CrossRef\]](#)
14. Luini A, Aguilar M, Gatti G, et al. Metaplastic carcinoma of the breast, an unusual disease with worse prognosis: the experience of the European Institute of Oncology and review of the literature. *Breast Cancer Res Treat*. 2007;101(3):349-353. [\[CrossRef\]](#)
15. Pezzi CM, Patel-Parekh L, Cole K, Franko J, Klimberg VS, Bland K. Characteristics and treatment of metaplastic breast cancer: Analysis of 892 cases from the national cancer data base. *Ann Surg Oncol*. 2007;14(1):166-173. [\[CrossRef\]](#)
16. Donato H, Candelária I, Oliveira P, Gonçalo M, Caseiro-Alves F. Imaging findings of metaplastic carcinoma of the breast with pathologic correlation. *J Belg Soc Radiol*. 2018;102(1):46. [\[CrossRef\]](#)
17. Bian T, Lin Q, Wu Z, et al. Metaplastic carcinoma of the breast: imaging and pathological features. *Oncol Lett*. 2016;12(5):3975-3980. [\[CrossRef\]](#)
18. Shin HJ, Kim HH, Kim SM, et al. Imaging features of metaplastic carcinoma with chondroid differentiation of the breast. *AJR Am J Roentgenol*. 2007;188(3):691-696. Erratum in: *AJR Am J Roentgenol*. 2007;188(5):1170. [\[CrossRef\]](#)
19. Langlands F, Cornford E, Rakha E, et al. Imaging overview of metaplastic carcinomas of the breast: a large study of 71 cases. *Br J Radiol*. 2016;89(1064):20140644. [\[CrossRef\]](#)
20. Chang YW, Lee MH, Kwon KH, et al. Magnetic resonance imaging of metaplastic carcinoma of the breast: sonographic and pathologic correlation. *Acta radiol*. 2004;45(1):18-22. [\[CrossRef\]](#)
21. Benveniste AP, Yang W, Benveniste MF, Mawlawi OR, Marom EM. Benign breast lesions detected by positron emission tomography-computed tomography. *Eur J Radiol*. 2014;83(6):919-929. [\[CrossRef\]](#)
22. Sang KY, Cho N, Woo KM. The role of PET/CT for evaluating breast cancer. *Korean J Radiol*. 2007;8(5):429-437. [\[CrossRef\]](#)



# Cross-sectional imaging findings of cardiac outpouchings

Furkan Ufuk   
Tuncay Hazırolan 

## ABSTRACT

A cardiac outpouching (CO) is a protrusion in a heart chamber's internal anatomical lining. Most COs are clinically insignificant, but some are of vital importance, requiring immediate surgery. Cross-sectional imaging findings of COs, such as location, morphology, size, and accompanying wall motion abnormalities, play an essential role in determining the correct diagnosis and appropriate clinical management. Therefore, radiologists should be familiar with them. This article reviews the key cross-sectional imaging findings and differential diagnoses of COs.

## KEYWORDS

Aneurysm, cardiac catheterization, computed topography angiography, congenital heart disease, coronary artery disease, diagnosis, diverticulum, echocardiogram, embolism, magnetic resonance imaging, outpouching, pericardial, pseudoaneurysm, three-dimensional, ventricles

**A** cardiac outpouching (CO) is a protrusion in a heart chamber's internal anatomical lining.<sup>1,2</sup> Although most COs are clinically insignificant, some may be vital, requiring immediate surgery. Moreover, identifying COs, which may be responsible for thromboembolic events, before performing invasive procedures is crucial. Therefore, the recognition and characterization of COs are of great importance.<sup>1</sup> Imaging findings of COs, such as location, morphology, size, and accompanying wall motion abnormalities, should be carefully evaluated along with the patient's clinical history to determine the correct diagnosis and appropriate clinical management.<sup>2</sup> This article reviews the key cross-sectional imaging findings and differential diagnoses of COs (Figure 1). COs that occur as a result of surgery are outside the scope of this article.

## Ventricular outpouchings

### Ventricular true aneurysms (VTAs)

VTAs are usually wide-necked outpouchings, surrounded by dyskinetic and scarred myocardium. The presence of a smooth transition between the healthy myocardium and outpouching walls is a crucial finding for VTAs.<sup>1-3</sup> The walls of VTAs often exhibit late gadolinium elevation (LGE) on magnetic resonance imaging (MRI) caused by scarred myocardium. Moreover, this scarred myocardial tissue may contain fatty metaplasia and calcification.<sup>3</sup> (Supplementary Figure 1). Because VTAs may contain thrombi, the presence of thrombus should be carefully examined when a VTA is detected (Figure 2, Supplementary Video 1). VTAs are often detected on the left ventricle (LV) but can also be seen on the right ventricle (RV). The etio-pathogenesis of VTAs may include myocardial infarction (MI), myocarditis, Chagas disease, and trauma,<sup>1,3,4</sup> their medical management may consist of anticoagulation to prevent thromboembolism and afterload reduction. Surgical treatment may be considered for large VTAs, a VTA with an increased size during follow-up, angina, rupture, or heart failure.

### Ventricular pseudoaneurysms (VPs)

VPs are often outpouchings in the posterior-inferior wall of the LV; they have a narrow neck and are surrounded by the pericardium as the result of a full-thickness myocardial tear

From the Department of Radiology (F.U. ✉ furkan.ufuk@hotmail.com), Pamukkale University Faculty of Medicine, Denizli, Turkey; Department of Radiology (T.H.), Hacettepe University Faculty of Medicine, Ankara, Turkey.

Received 08 February 2022; revision requested 07 March 2022; accepted 28 March 2022.



Epub: 02.01.2023

Publication date: 31.01.2023

DOI: 10.4274/dir.2022.221419

You may cite this article as: Ufuk F, Hazırolan T. Cross-sectional imaging findings of cardiac outpouchings. *Diagn Interv Radiol.* 2023;29(1):68-79.

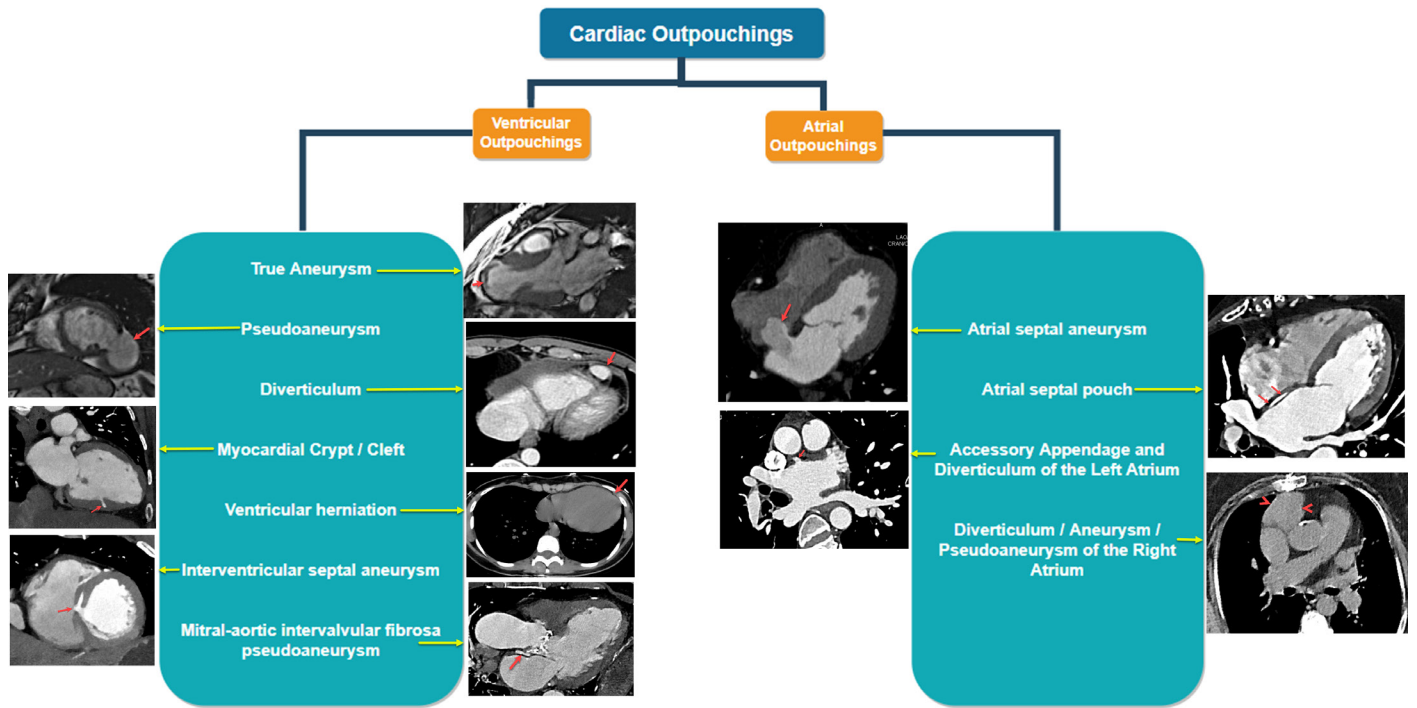


Figure 1. Atrial and ventricular outpouchings.

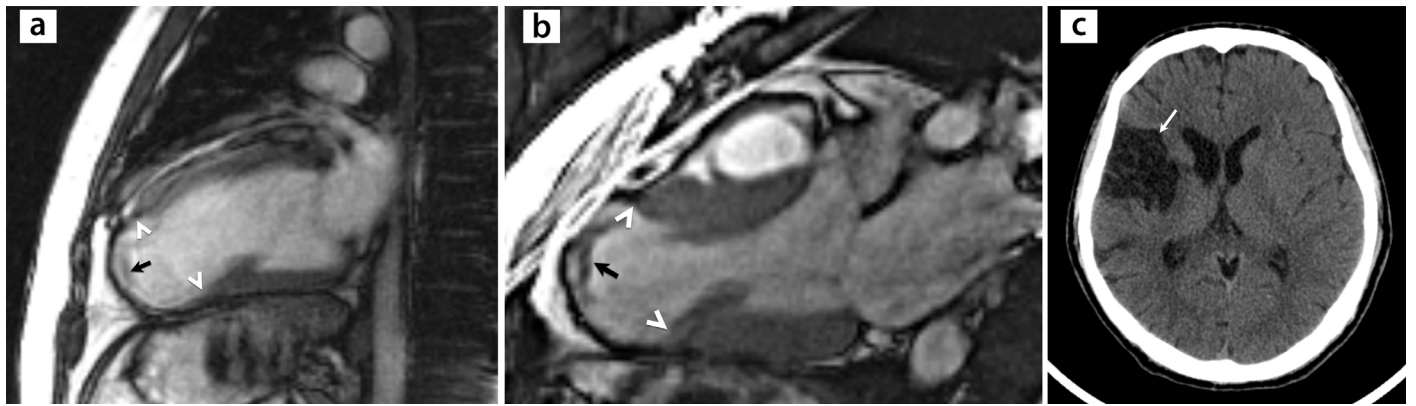


Figure 2. (a-c) A 73-year-old male patient with a history of myocardial infarction and cerebrovascular events underwent cardiac magnetic resonance (MR) imaging with a suspected left ventricular thrombus. Cardiac MR images of a left ventricle apical true aneurysm. Balanced steady-state free precession MR images with (a) a two-chamber view during mid-diastole and (b) a left ventricular outflow tract view during end systole revealing left ventricular apical dilatation with smooth transition between the healthy and thinned myocardium (arrowheads). Note the left ventricular thrombus (arrows). (c) Axial cranial computed tomography image depicting chronic right middle cerebral artery territory infarction (arrow). See also Supplementary Video 1.

or rupture (Figure 3, Supplementary Figure 2, Supplementary Video 2).<sup>3</sup> The presence of an abrupt transition between the healthy myo-

#### Main points

- A cardiac outpouching (CO) is a protrusion in a heart chamber's internal anatomical lining.
- Most CO are clinically insignificant, but some may be vital, requiring immediate surgery.
- The imaging findings of COs should be carefully evaluated along with the patient's clinical history to determine the correct diagnosis and appropriate clinical management.

cardium and outpouching is a crucial imaging finding for VPs, unlike VTAs.<sup>1-3</sup> Moreover, VPs are often accompanied by hemorrhagic pericardial effusion, and focal LGE can be seen in the pericardium surrounding the VP. The etiopathogenesis of VPs may include MI, trauma, infection, and iatrogenic injury (Figure 4).<sup>2,3</sup> Untreated VPs have high mortality, and surgery is the treatment of choice in patients with VP.

#### Ventricular diverticulum (VD)

VD is an outpouching surrounded by healthy myocardial tissue. Therefore, VD exhibits synchronous contractility with

the ventricles, and VD walls do not exhibit LGE on MRI, unlike VTAs and VPs.<sup>1,5</sup> Notably, VDs are often congenital, but they may rarely be acquired (Figure 5, Supplementary Figure 3). Although rare, VDs may be associated with ventricular thrombus, thromboembolism, and ventricular arrhythmias. Follow-up of patients is usually sufficient, and treatment should be based on complications (Supplementary Figure 4). Arrhythmogenic right ventricular cardiomyopathy (ARVC) can mimic VDs and is characterized by functional and wall motion abnormalities (akinesia, dyskinesia) of the RV and ventricular tachyarrhythmias. A

corrugated pattern (accordion-like) can be seen on the RV-free wall caused by multiple outpouchings. Unlike VDs, outpouchings in ARVCs are akinetic or dyskinetic, and RV dysfunction is present (Supplementary Figure 5).<sup>6</sup>

### Myocardial crypts (MCs) or clefts

MCs, also known as myocardial clefts, are narrow outpouchings of the ventricles, usually perpendicular to the interventricular septum. They are generally detected in

the basal inferoseptal region of the LV and have uncertain clinical significance (Figure 6).<sup>1</sup> Patients with MCs are almost entirely asymptomatic and do not require treatment. MCs decrease in size or disappear during ventricular systole and do not cause wall

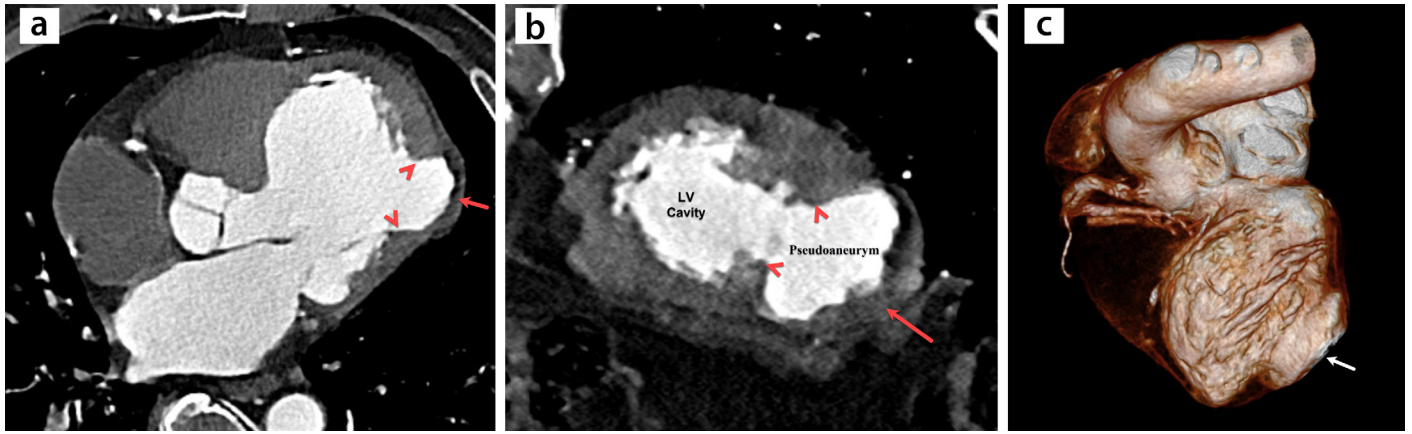


**Figure 3.** (a-c) A 68-year-old male patient presented to the emergency department with acute chest pain and underwent chest computed tomography (CT) angiography with a suspected acute aortic syndrome. The CT angiography images reveal a left ventricular pseudoaneurysm. Multiplanar reformatted CT angiography images with (a) left ventricular outflow tract view and (b) two-chamber view depicting outpouching in the left ventricle (arrows), with an abrupt transition between the healthy and thinned myocardium (arrowheads). The patient underwent surgery, and the pseudoaneurysm was repaired.

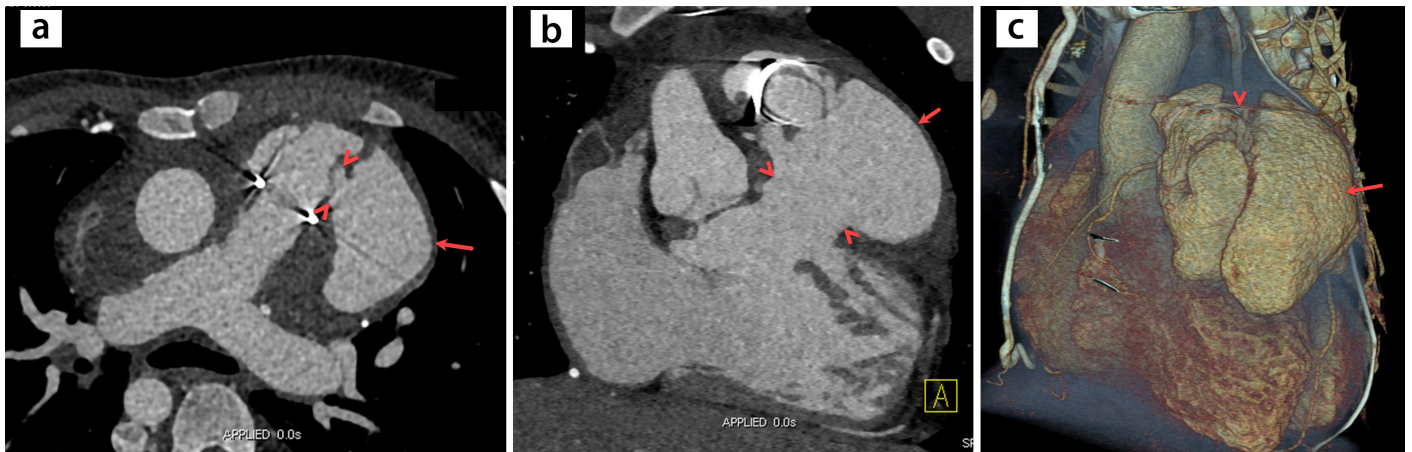


**Figure 4.** (a-c) A 15-year-old boy with a history of pulmonary valve replacement for tetralogy of Fallot underwent cardiac computed tomography (CT) angiography with a suspected right ventricle outflow tract pseudoaneurysm. (a) Axial and (b) coronal CT images revealing a giant multiloculated pseudoaneurysm (arrows) with a narrow neck (arrowheads). (c) Three-dimensional volume rendering CT image demonstrating a right ventricular pseudoaneurysm (arrow) with a narrow neck (arrowhead).

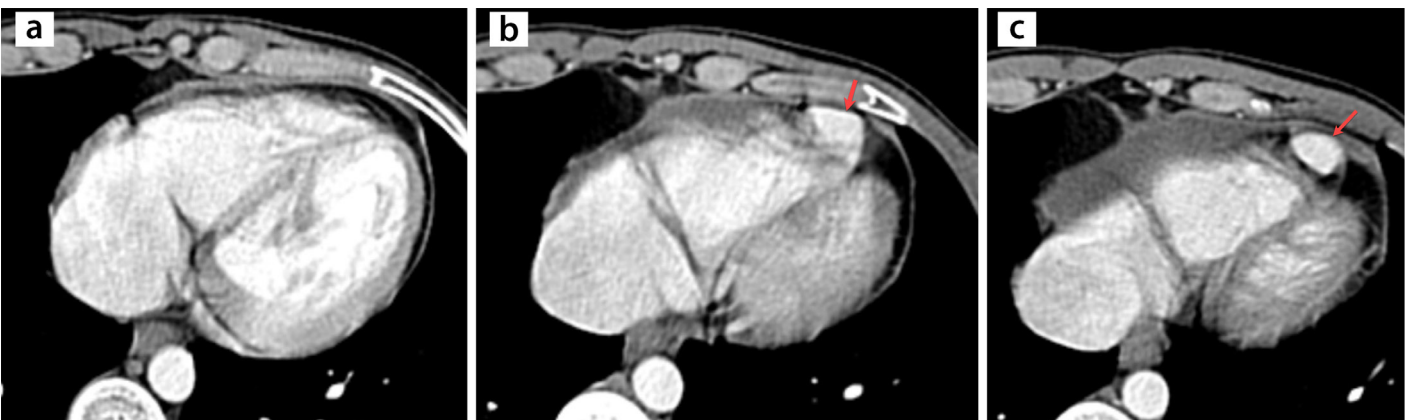


**Figure 5.** (a-c) A 19-year-old male patient with right lower quadrant abdominal pain underwent contrast-enhanced abdominal computed tomography (CT) with a suspected acute appendicitis. (a-c) Consecutive axial CT images at the lung bases revealing right ventricular apical outpouching (arrows). Because of the high risk of thromboembolism, the patient underwent surgery, and the diagnosis of the right ventricular diverticulum was histopathologically confirmed.

motion defects. They are more common in patients with hypertrophic cardiomyopathy (HCM) than in healthy populations. In addition, MCs have been suggested as a predictor of gene carrier status in HCM, and when they are multiple, the patient should be examined for HCM.<sup>7</sup>

### Ventricular herniation

Ventricular herniation may result from the outpouching of healthy ventricles caused by a congenital, traumatic, or iatrogenic pericardial defect (Figure 7, Supplementary Figure 6).<sup>1,2,8</sup> Although patients with ventricular herniation are almost completely asymp-

tomatic, incarceration, cardiac valvular insufficiency, or coronary artery compression may rarely be detected. Surgery is preferred in cases that develop complications or are symptomatic.

### Interventricular septal aneurysm (IVSAs)

IVSAs are characterized by an outpouching of the interventricular septum to either side. They have two forms, membranous or muscular (Figures 8 and 9), and are often seen in the membranous region and are usually congenital. Rarely, IVSAs may occur secondary to trauma, ischemia, surgery, or infection.<sup>9,10</sup> Although IVSAs are often detected incidentally, they carry risks such as rupture, thrombosis, arrhythmias, right ventricular outflow obstruction, paradoxical thromboembolism, and infective endocarditis. Moreover, IVSAs may be associated with congenital cardiac anomalies, such as transposition of the great arteries and ventricular septal defects.<sup>1,5,9,10</sup> Although anticoagulation is recommended in asymptomatic cases of IVSAs, surgical treatment is considered in symptomatic patients and those who develop complications. In the differential diagnosis for muscular IVSA, MCs should be considered. Although muscular IVSA indents toward the right ventricle, MCs terminate in the myocardium and do not indent the RV.<sup>1,5,9</sup>

### Mitral-aortic intervalvular fibrosa pseudoaneurysm (MAIVF)

The fibrous connection between the mitral and aortic valve is known as the MAIVF. Pseudoaneurysm formation may rarely occur in the MAIVF as a result of infective endocarditis, surgery, or trauma (Figure 10). An MAIVF pseudoaneurysm may cause thromboembolism, septic embolism, mitral valve

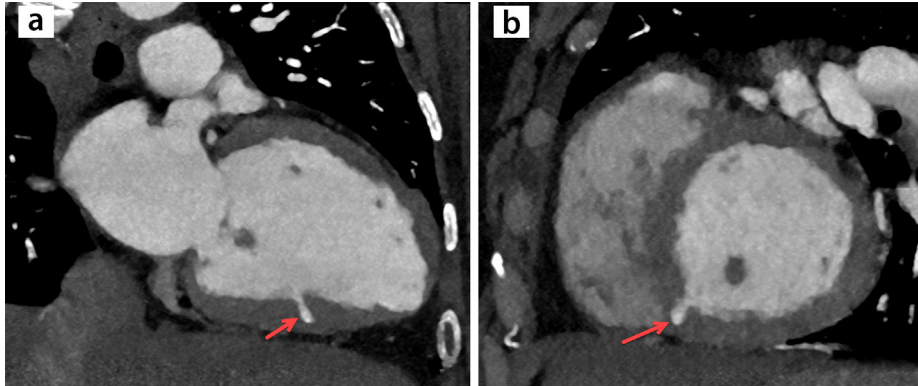


**Figure 6.** (a, b) A 39-year-old male patient with atypical chest pain underwent contrast-enhanced coronary computed tomography (CT) angiography. Multiplanar reformatted (a) two-chamber and (b) short-axis view CT angiography images demonstrating a narrow outpouching of the left ventricle cavity into the inferoseptal myocardium (arrows), consistent with myocardial crypt (cleft). Coronary CT angiography did not detect any coronary artery lesions, and the patient was followed up without treatment.

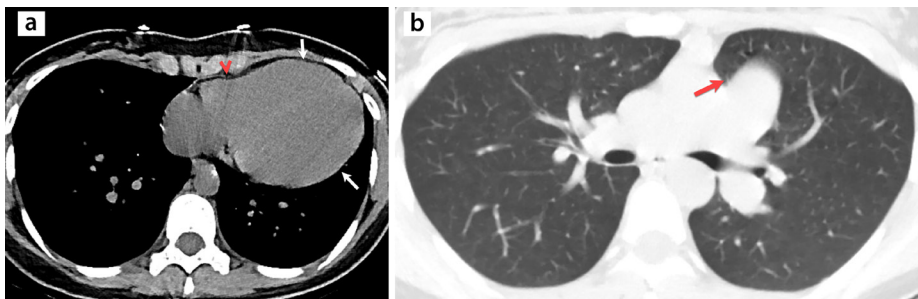


**Figure 7.** (a, b) A 27-year-old male patient underwent unenhanced chest computed tomography (CT) as a result of abnormal findings on chest radiography. (a) Axial CT image with mediastinum window settings revealing the levo-position of the heart and biventricular apical ballooning (arrows). Note an interruption of the pericardium at the level of the right atrioventricular groove (arrowhead). (b) Axial CT image with lung window settings depicting herniation of lung tissue between the aorta and main pulmonary artery (arrow) consistent with partial pericardial agenesis.

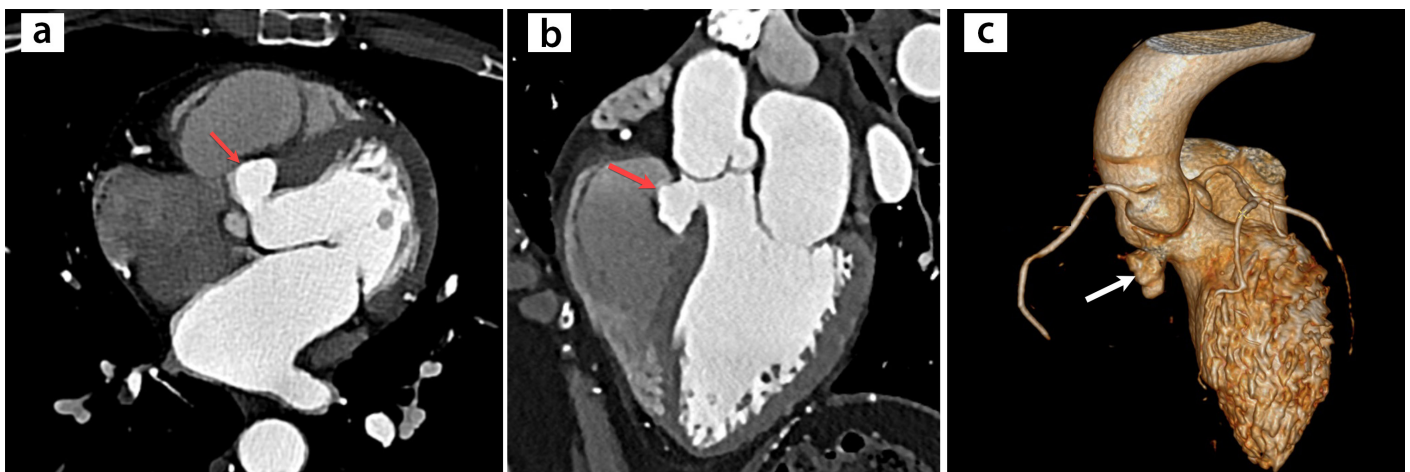


**Figure 8.** (a-c) A 45-year-old female patient with an abnormal finding on echocardiography underwent contrast-enhanced cardiac computed tomography (CT) angiography. (a) Axial, (b) multiplanar reformatted, and (c) three-dimensional volume rendering CT images demonstrating the bowing of the interventricular septum to the right (arrows), consistent with membranous interventricular septal aneurysm. The patient refused surgery and was followed up with anticoagulation.



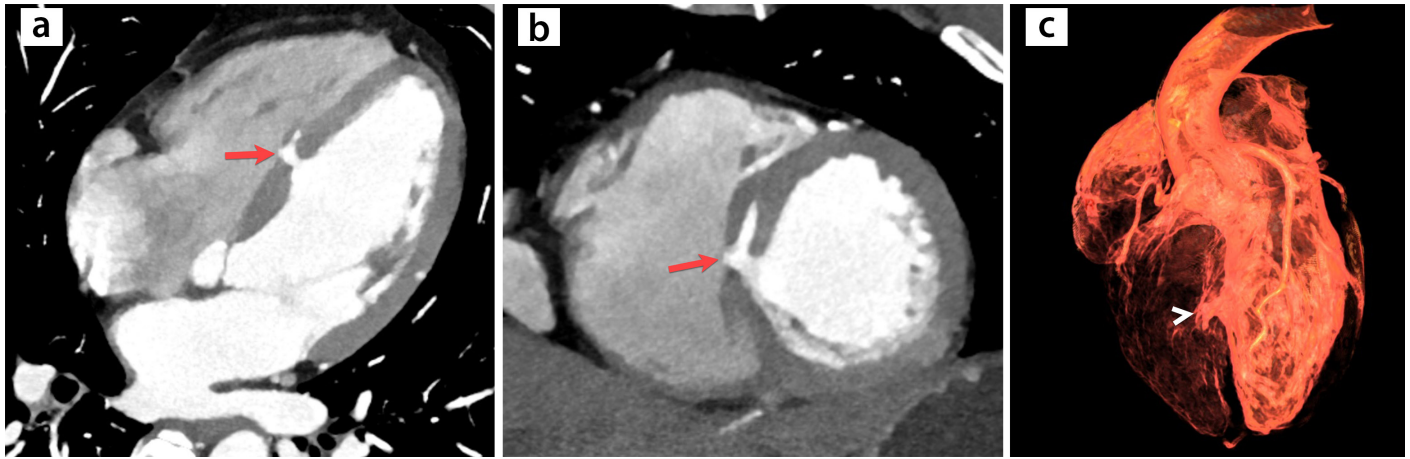


**Figure 9.** (a-c) A 46-year-old female patient with atypical chest pain underwent contrast-enhanced coronary computed tomography (CT) angiography. Multiplanar reformatted (a) four-chamber view and (b) shot axis view CT images revealing the bowing of the muscular interventricular septum and left ventricular outpouching (arrows). (c) Three-dimensional volume rendering CT images demonstrating the outpouching of the left ventricle to the right (arrowhead).

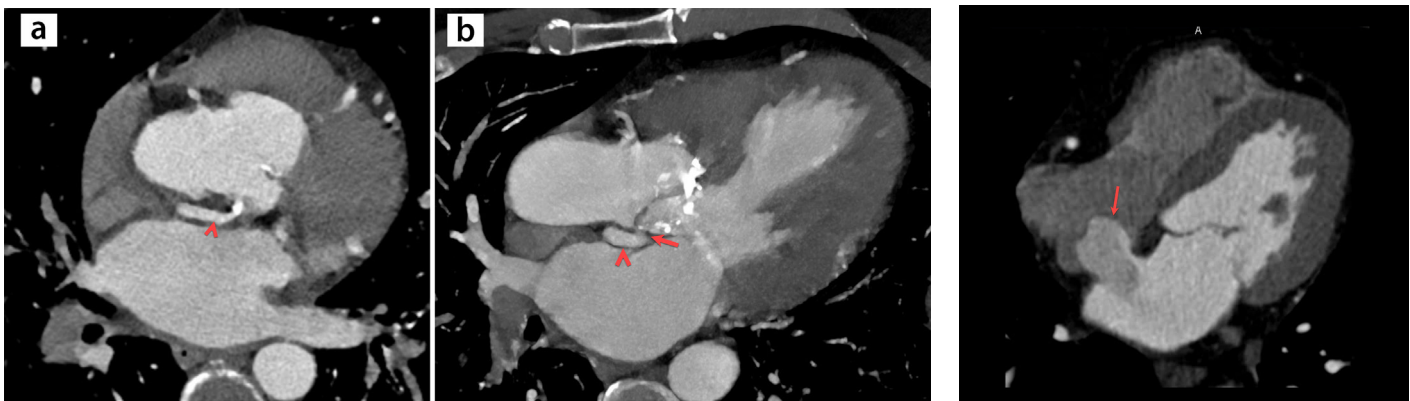


**Figure 10.** (a, b) A 40-year-old male patient with a history of rheumatic heart disease and endocarditis underwent contrast-enhanced coronary computed tomography (CT) angiography. (a) Axial and (b) multiplanar reformatted CT images revealing a pseudoaneurysm between the mitral and aortic valve (arrowheads), with a narrow connection to the left ventricle outflow tract (arrow). The patient underwent surgery, and the pseudoaneurysm was repaired.

dysfunction, and rupture. Rarely, it can cause the compression of adjacent structures, including the coronary arteries.<sup>11</sup> Surgery is the preferred treatment because of the high risk of serious complications.

## Atrial outpouchings

### Atrial septal aneurysm

Atrial or interatrial septal aneurysms (ASAs) are characterized as outpouchings (with a protrusion >11 mm to either side in adults) of the interatrial septum beyond the interatrial septal plane (Figure 11, Supplementary Video 3).<sup>12,13</sup> They are often congenital, and patients with ASAs are usually asymptomatic. Atrial septal aneurysms are divided into different subgroups according to their dynamic protrusion into the right and left atrium (LA) on echocardiography.<sup>12</sup>

They can be associated with patent foramen ovale (PFO), atrial septal defect, stroke, and thromboembolism.<sup>13</sup> Therefore, when ASAs are detected, accompanying findings should be carefully examined. Treatment is not recommended in patients with ASAs unless complications occur.

### Atrial septal pouch (ASP)

ASPs are characterized by a well-defined pouch along the interatrial septum and can occur on either the left side (40.8%), right side (5.1%), or both (3.7%). ASPs can cause thrombus formation, and arrhythmogenic focus can be detected in ASPs (Figure 12).<sup>14</sup> Left-sided ASPs have been associated with thromboembolism, stroke, PFO, and atrial fibrillation. Treatment is not recommended in patients with ASPs unless complications develop.<sup>12,14</sup>

**Figure 11.** A 54-year-old female patient with atypical chest pain underwent contrast-enhanced coronary computed tomography (CT) angiography. Multiplanar reformatted four-chamber view CT image demonstrating the outpouching of the interatrial septum (arrow), consistent with atrial septal aneurysm. See also Supplementary Video 2.

### Accessory appendage (AA) and diverticulum of the left atrium

AAs and diverticula of the LA are common outpouchings of the LA, and both are considered anatomical variants.<sup>1,13</sup> Although AAs are characterized by outpouchings with trabeculated contours and a small base, LA diverticula are characterized by outpouchings with smooth contours and a broad base (Figure 13). Both are usually located in the anterior upper wall of the LA and can be associated with thromboembolism, stroke, and arrhythmia.<sup>1,2,13</sup> The presence of these outpouchings should be examined before invasive procedures (such as radiofrequency ablation) to prevent complications, such as wall penetration and atrioesophageal fistula.<sup>1,3</sup>

### Diverticulum, aneurysm, and pseudoaneurysm of the right atrium (RA)

Diverticula, aneurysms, and pseudoaneurysms of the RA are unusual outpouchings and may present similar clinical and radiological findings. These are characterized by outpouchings that originate from the RA appendage (Figure 14). Distinguishing between diverticula, aneurysms, and pseudoaneurysms definitively without surgery is

often impossible. These RA outpouchings are usually congenital and detected incidentally, but they may present various clinical symptoms.<sup>1,2,13</sup> The subthebesian sinus, also known as subeustachian or Keith sinus, is an outpouching of the RA wall below the coronary sinus ostium. It is an anatomical variant that should not be misdiagnosed as a diverticulum or aneurysm (Figure 15).<sup>15</sup> Right atrial diverticula, aneurysms, and pseudoaneurysms may cause fatal complications, such

as pulmonary thromboembolism, arrhythmias, and sudden cardiac death. Although follow-up and anticoagulation are recommended in patients with RA outpouchings who are asymptomatic, surgery is preferred in patients who are symptomatic.<sup>13,15</sup>

Ventricular and atrial outpouchings and differential diagnoses are summarized in Table 1.

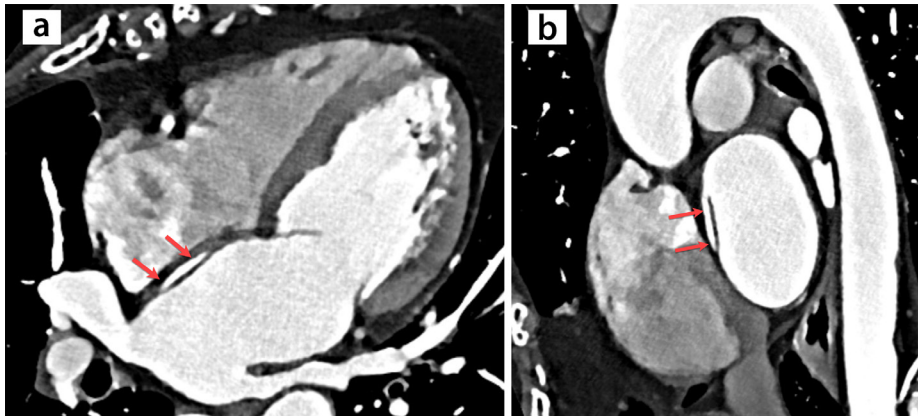


**Figure 12.** (a, b) A 44-year-old female patient with chest pain underwent contrast-enhanced coronary computed tomography (CT) angiography. (a, b) Multiplanar reformatted CT images depicting a well-defined outpouching along the interatrial septum (arrows), consistent with atrial septal pouch.

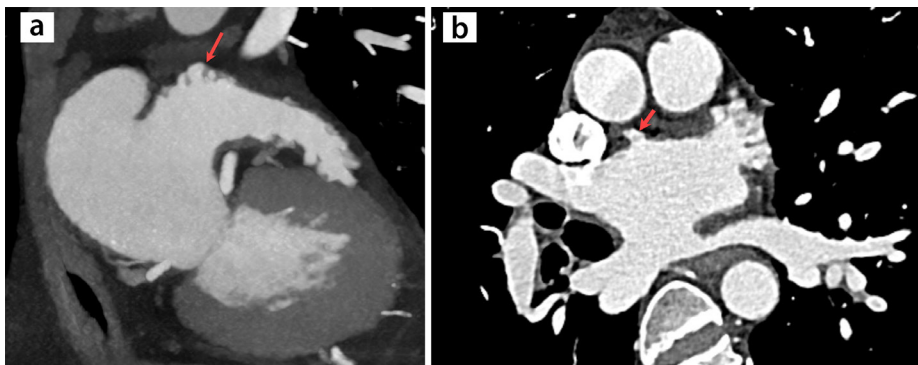


**Figure 13.** (a, b) Left atrial outpouchings in patients on coronary computed tomography (CT) angiography. (a) Multiplanar reformatted CT image depicting multiple outpouchings in the left atrium with trabeculated contours and narrow necks (arrow), consistent with accessory appendage. (b) Multiplanar reformatted CT image revealing an outpouching in the left atrium with smooth contours and a broad neck (arrow), consistent with diverticulum.

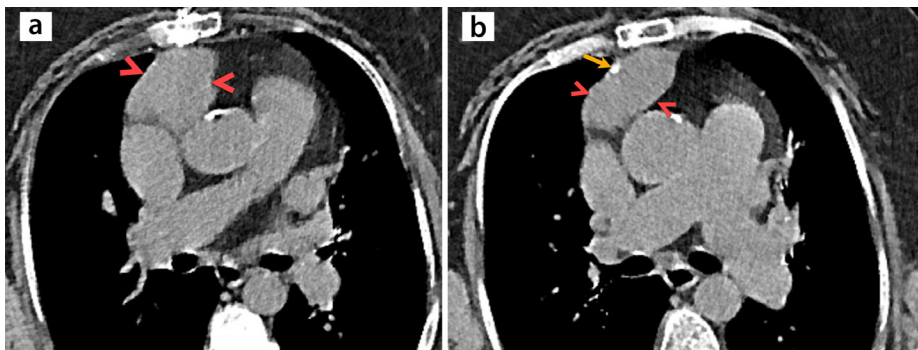


**Figure 14.** (a, b) A 78-year-old female patient with a history of coronary artery bypass grafting, recurrent pulmonary thromboembolism, and chronic kidney disease referred for unenhanced chest computed tomography (CT) because of abnormal findings on echocardiography. (a, b) Consecutive axial CT images demonstrating a right atrial outpouching (arrowheads), including calcification (arrow). The diagnosis of the right atrial pseudoaneurysm was pathologically confirmed, and the calcification was found to be consistent with chronic thrombus.

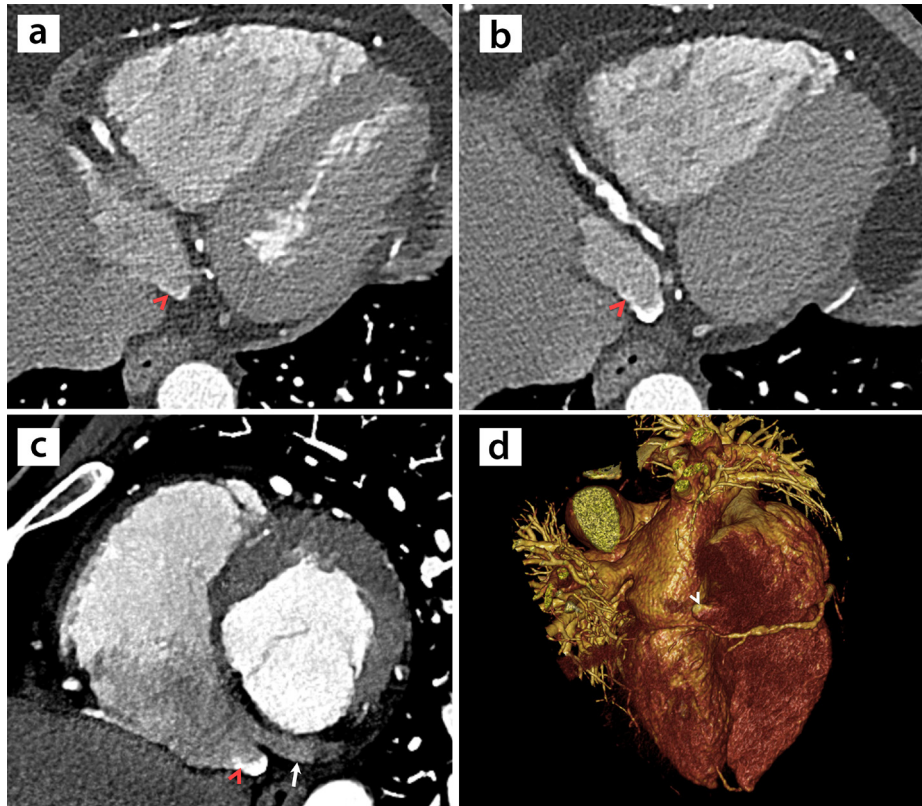


**Figure 15.** (a-c) A 61-year-old male patient with chest pain underwent contrast-enhanced coronary computed tomography (CT) angiography. (a, b) Consecutive axial and (c) multiplanar reformatted CT images demonstrating an outpouching of the right atrial wall (arrowheads) below the coronary sinus ostium (arrow), indicating a subthebesian (subeustachian or Keith) sinus. (d) Three-dimensional volume rendering CT images demonstrating the outpouching of the right atrium (arrowhead).

Table 1. Cardiac outpouchings and differential diagnoses on cross-sectional imaging		
Condition	Common imaging features	Differential diagnosis
Ventricular true aneurysm	Wide-necked outpouchings located on the apical or anterior wall of the LV and surrounded by dyskinetic myocardium; smooth transition between the healthy and thinned (scarred) myocardium; fatty metaplasia and calcification can be seen in the scarred myocardium surrounding the aneurysms	<p><b>Pseudoaneurysm</b> (narrow-necked outpouchings, surrounded by the pericardium, accompanied by hemorrhagic pericardial effusion and abrupt transition between the healthy and scarred myocardium)</p> <p><b>Takotsubo cardiomyopathy</b> (transient regional wall motion abnormalities of the LV caused by a stressful trigger, absence of LGE, and no myocardial thinning on MRI)</p> <p><b>Apical aneurysm associated with midventricular hypertrophic cardiomyopathy</b> (midventricular myocardial hypertrophy is apparent)</p>
Ventricular pseudoaneurysm	Narrow-necked outpouchings surrounded by the pericardium, accompanied by hemorrhagic pericardial effusion and abrupt transition between the healthy and scarred myocardium and located on the basal or posterior wall of the LV	<p><b>True aneurysm</b> (wide-necked outpouchings located on the apical or anterior wall of the LV and surrounded by dyskinetic myocardium; smooth transition between the healthy and scarred myocardium)</p> <p><b>Takotsubo cardiomyopathy</b> (transient regional wall motion abnormalities of the LV caused by a stressful trigger, absence of LGE, and no myocardial thinning on MRI)</p> <p><b>Apical aneurysm associated with midventricular hypertrophic cardiomyopathy</b> (midventricular myocardial hypertrophy is apparent)</p>
Ventricular diverticulum	Includes all myocardial layers and shows synchronous contractility with the associated ventricular myocardium; diverticulum walls do not show LGE on MRI	<p><b>True aneurysm</b> (wide-necked outpouchings surrounded by dyskinetic scarred myocardium; aneurysm walls show LGE on MRI)</p> <p><b>Pseudoaneurysm</b> (surrounded by the pericardium; pericardium shows LGE on MRI, accompanied by hemorrhagic pericardial effusion)</p> <p><b>Apical aneurysm associated with midventricular hypertrophic cardiomyopathy</b> (midventricular myocardial hypertrophy is apparent)</p> <p><b>Arrhythmogenic RV cardiomyopathy</b> (functional and wall motion abnormalities of the RV and ventricular tachyarrhythmias; akinetic or dyskinetic multiple diverticulum-like outpouchings on the RV-free wall)</p> <p><b>Butterfly apex</b> (anatomic variation; both the RV and LV form separate apices) (Supplementary Video 4, Supplementary Figure 7)</p>

Table 1. Continued		
Condition	Common imaging features	Differential diagnosis
Myocardial crypts/clefts	Narrow invaginations usually perpendicular to the LV wall, which decrease in size or disappear during ventricular systole, do not cause wall motion defects, and are usually seen in the basal inferoseptal region	<b>Ventricular septal defect</b> (connection between both ventricles) <b>Interventricular septal aneurysm</b> (muscular interventricular septal aneurysm expands to the depth of the myocardium, and myocardial crypts gradually narrow toward the depth of the myocardium)
Ventricular herniation	Protrusion of the healthy RV or LV from iatrogenic or congenital pericardial defects	<b>True aneurysm</b> (wide-necked outpouchings located on the apical or anterior wall of the LV and surrounded by dyskinetic myocardium; smooth transition between the healthy and scarred myocardium) <b>Pseudoaneurysm</b> (narrow-necked outpouchings surrounded by the pericardium, accompanied by hemorrhagic pericardial effusion and an abrupt transition between the healthy and scarred myocardium)
Interventricular septal aneurysm	Interventricular septum bowed to either side, which may be found in the membranous or muscular interventricular septum	<b>Myocardial crypts/clefts</b> (narrow invaginations usually perpendicular to the LV wall, which decrease in size or disappear during ventricular systole and gradually narrow toward the depth of the myocardium)
Mitral-aortic intervalvular fibrosa pseudoaneurysm	Originates from the fibrous connection between the mitral and aortic valve and is seen as an outpouching between the ascending aorta and LA	<b>Sinus of valsalva aneurysm</b> (abnormal dilatation of one of the aortic sinuses, causing thoracic aortic dilatation)
Atrial septal aneurysm	Abnormal bowing (with a base diameter $\geq 15$ mm and deviation $\geq 10$ mm to either side) of the interatrial septum beyond the interatrial septal plane	<b>Atrial septal pouch</b> (well-defined pouch along the interatrial septum) <b>Accessory left atrial appendage</b> (outpouching of the LA with trabeculated contours and small base) <b>Diverticulum of the LA</b> (outpouching of the LA with smooth contours and broad base)
Atrial septal pouch	Well-defined pouch along the interatrial septum	<b>Atrial septal aneurysm</b> (abnormal bowing of the interatrial septum beyond interatrial septal plane) <b>Accessory atrial appendage</b> (outpouching of the atria with trabeculated contours and small base) <b>Diverticulum of the atrium</b> (outpouching of the atria with smooth contours and broad base)
Accessory appendage of the LA	Outpouching of the LA with trabeculated contours and small base	<b>Atrial septal aneurysm</b> (abnormal bowing of the interatrial septum beyond the interatrial septal plane) <b>Atrial septal pouch</b> (Well-defined pouch along the interatrial septum) <b>Diverticulum of the atrium</b> (outpouching of the atria with smooth contours and broad base)
Diverticulum	Outpouching of the atria with smooth contours and broad base	<b>Atrial septal aneurysm</b> (abnormal bowing of the interatrial septum beyond the interatrial septal plane) <b>Atrial septal pouch</b> (well-defined pouch along the interatrial septum) <b>Accessory appendage</b> (Outpouching of the LA with trabeculated contours and small base)
Aneurysm and pseudoaneurysm of the RA	Outpouching that originates from the RA appendage	<b>Subthebesian sinus</b> (also known as subeustachian sinus or Keith sinus; an outpouching of the right atrial wall below the coronary sinus ostium) <b>Diverticulum of the atrium</b> (Outpouching of the atria with smooth contours and surrounded by musculature)

LV, left ventricle; RV, right ventricle; LGE, late gadolinium enhancement; MRI, magnetic resonance imaging; LA, left atrium; RA, right atrium.

## Conclusion

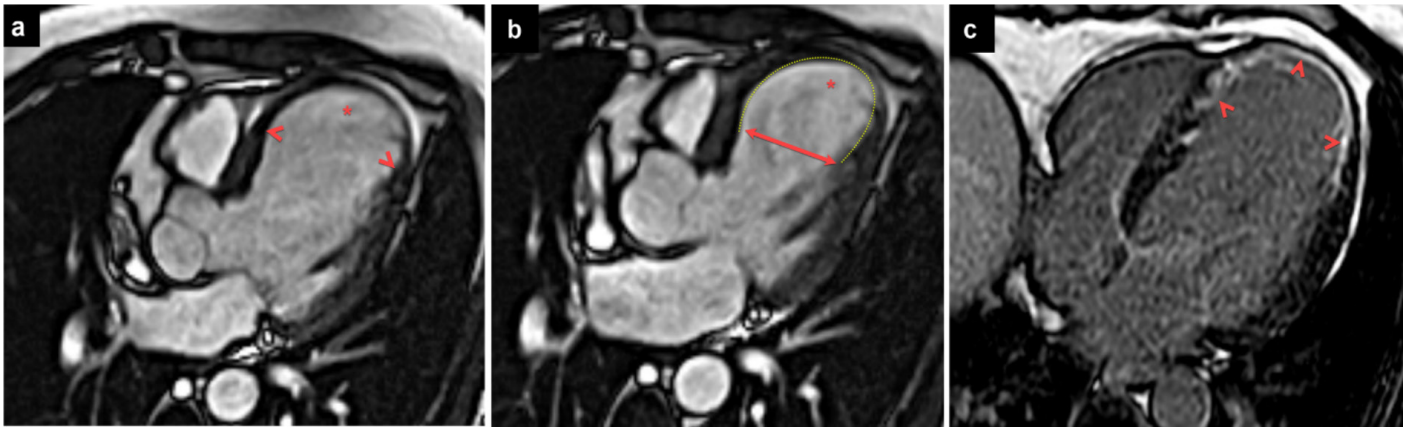
Radiologists should be familiar with COs on cross-sectional imaging, as the timely characterization of COs is essential to ensure optimal clinical management and therapeutic approaches.

## Conflict of interest disclosure

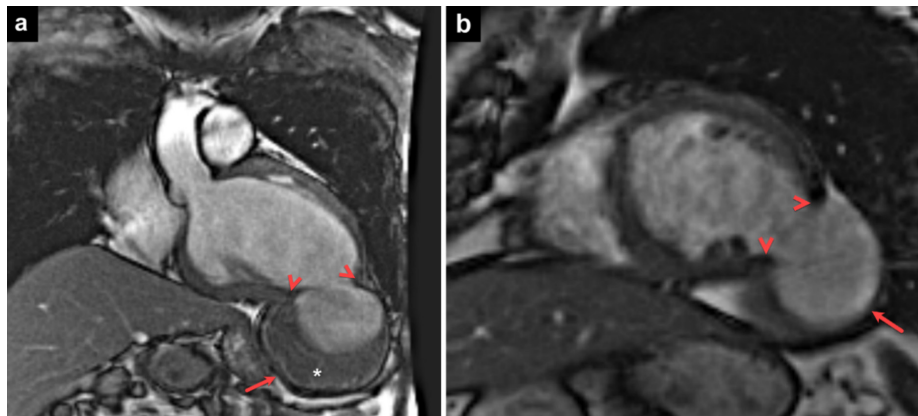
The authors declared no conflicts of interest.

## References

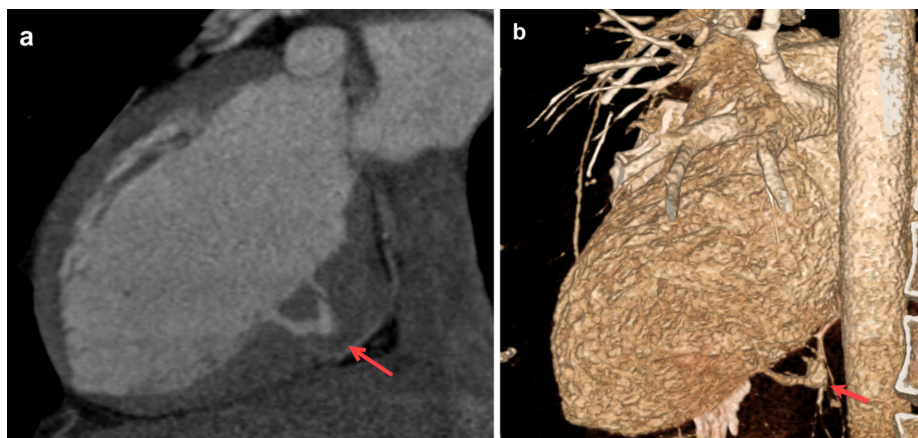
1. Scagliola R, Rosa GM, Seitun S. Cardiac outpouchings: definitions, differential diagnosis, and therapeutic approach. *Cardiol Res Pract.* 2021;2021:6792643. [\[CrossRef\]](#)
2. Malik SB, Chen N, Parker RA 3rd, Hsu JY. Transthoracic echocardiography: pitfalls and limitations as delineated at cardiac CT and MR imaging. *Radiographics.* 2017;37(2):383-406. Erratum in: *Radiographics.* 2017;37(3):1004. [\[CrossRef\]](#)
3. Konen E, Merchant N, Gutierrez C, et al. True versus false left ventricular aneurysm: differentiation with MR imaging--initial experience. *Radiology.* 2005;236(1):65-70. [\[CrossRef\]](#)
4. Priya S, Nagpal P, Aggarwal T, Huynh J, Khandelwal K, Khandelwal A. Review of multi-modality imaging update and diagnostic work up of Takotsubo cardiomyopathy. *Clin Imaging.* 2021;80:334-347. [\[CrossRef\]](#)
5. Tao TY, Yahyavi-Firouz-Abadi N, Singh GK, Bhalla S. Pediatric cardiac tumors: clinical and imaging features. *Radiographics.* 2014;34(4):1031-1046. [\[CrossRef\]](#)
6. Rastegar N, Burt JR, Corona-Villalobos CP, et al. Cardiac MR findings and potential diagnostic pitfalls in patients evaluated for arrhythmogenic right ventricular cardiomyopathy. *Radiographics.* 2014;34(6):1553-1570. [\[CrossRef\]](#)
7. O'Donnell DH, Abbara S, Chaithiraphan V, et al. Cardiac MR imaging of nonischemic cardiomyopathies: imaging protocols and spectra of appearances. *Radiology.* 2015;277(1):308. Erratum for: *Radiology.* 2012;262(2):403-422. [\[CrossRef\]](#)
8. Fadl SA, Nasrullah A, Harris A, Edwards R, Kicska G. Comprehensive review of pericardial diseases using different imaging modalities. *Int J Cardiovasc Imaging.* 2020;36(5):947-969. [\[CrossRef\]](#)
9. Carcano C, Kanne JP, Kirsch J. Interventricular membranous septal aneurysm: CT and MR manifestations. *Insights Imaging.* 2016;7(1):111-117. [\[CrossRef\]](#)
10. Stamm C, Feit LR, Geva T, del Nido PJ. Repair of ventricular septal defect and left ventricular aneurysm following blunt chest trauma. *Eur J Cardiothorac Surg.* 2002;22(1):154-156. [\[CrossRef\]](#)
11. Saremi F, Sánchez-Quintana D, Mori S, et al. Fibrous skeleton of the heart: anatomic overview and evaluation of pathologic conditions with CT and MR imaging. *Radiographics.* 2017;37(5):1330-1351. [\[CrossRef\]](#)
12. Olivares-Reyes A, Chan S, Lazar EJ, Bandlamudi K, Narla V, Ong K. Atrial septal aneurysm: a new classification in two hundred five adults. *J Am Soc Echocardiogr.* 1997;10(6):644-656. [\[CrossRef\]](#)
13. Öztürk E, Kafadar C, Tutar S, Bozlar U, Hagspiel KD. Non-coronary abnormalities of the left heart: CT angiography findings. *Anatol J Cardiol.* 2016;16(9):720-727. [\[CrossRef\]](#)
14. Michałowska I, Dudzińska K, Kowalik I, et al. Left atrial septal pouch-is it really a new risk factor for ischemic stroke?: Subanalysis of the ASSAM study. *J Thorac Imaging.* 2022;37(3):168-172. [\[CrossRef\]](#)
15. Shah SS, Teague SD, Lu JC, Dorfman AL, Kazerooni EA, Agarwal PP. Imaging of the coronary sinus: normal anatomy and congenital abnormalities. *Radiographics.* 2012;32(4):991-1008. [\[CrossRef\]](#)



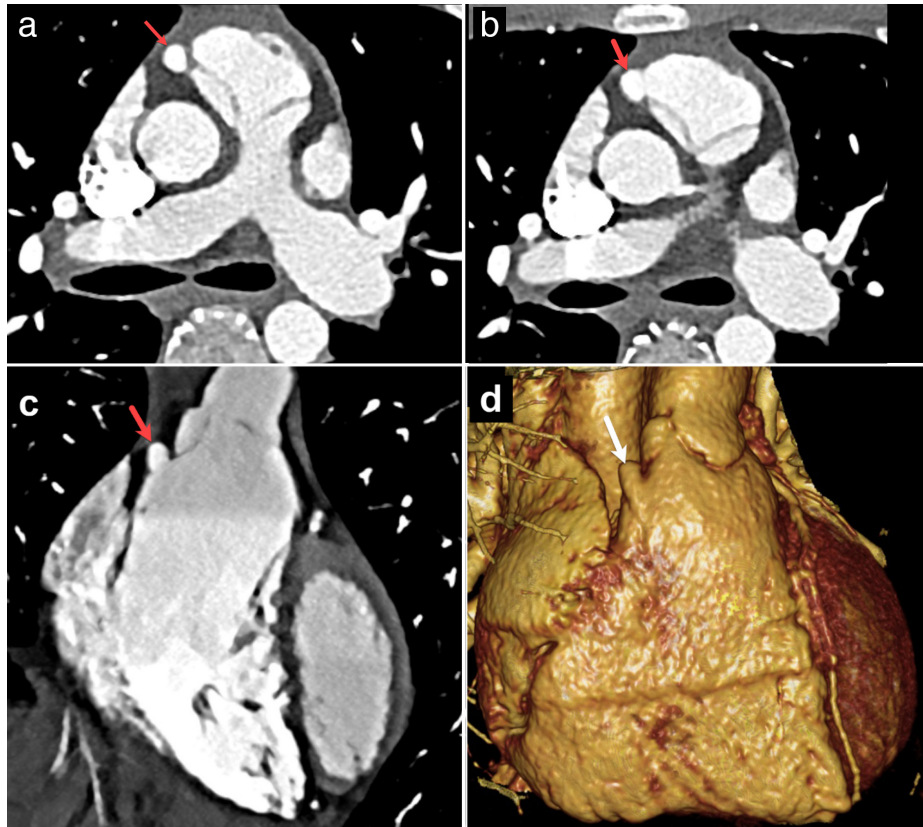
**Supplementary Figure 1.** (a-c) A 71-year-old male patient with a history of myocardial infarction and coronary bypass grafting. Balanced steady-state free precession magnetic resonance (MR) images with a left ventricular outflow tract view during (a) mid-diastole and (b) end systole revealing left ventricle (LV) apical dilatation (\*) with a wide neck (two-way arrow). Note the smooth transition between the healthy and thinned myocardium (arrowheads). (c) Phase-sensitive inversion-recovery MR image depicting LV apical late gadolinium enhancement (arrowheads).



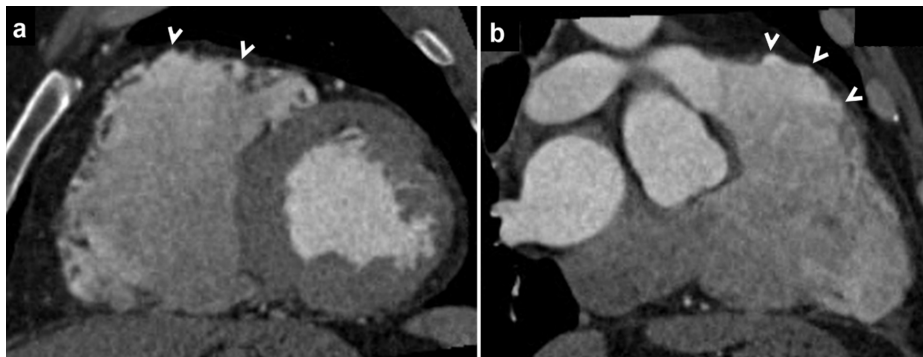
**Supplementary Figure 2.** (a, b) A 65-year-old male patient presented with acute chest pain and underwent cardiac magnetic resonance (MR) imaging with a suspected ventricular aneurysm. Balanced steady-state free precession MR images with (a) left ventricular outflow tract view and (b) short-axis view reveal a large outpouching in the left ventricle lateral wall (arrows) with thrombus (\*). Note the abrupt transition between the healthy and thinned myocardium (arrowheads), consistent with pseudoaneurysm. The patient underwent surgery, and the pseudoaneurysm was repaired.



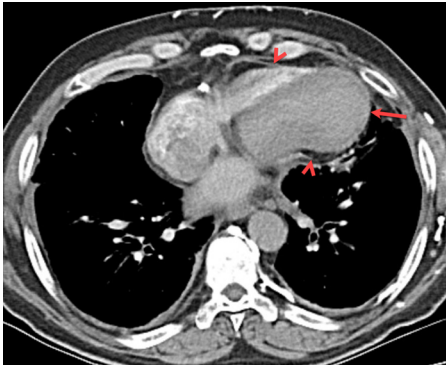
**Supplementary Figure 3.** (a, b) A 37-year-old male patient with atypical chest pain underwent contrast-enhanced coronary computed tomography (CT) angiography. (a) Multiplanar reformatted and (b) three-dimensional volume rendering CT images demonstrating a left ventricle outpouching (arrows), consistent with a submittal left ventricular diverticulum. Because the patient was asymptomatic, follow-up without treatment was recommended.



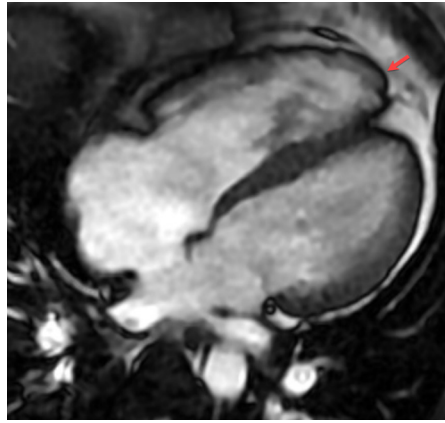
**Supplementary Figure 4.** (a-d) A 45-year-old female patient with ventricular tachycardia (VT) underwent contrast-enhanced cardiac computed tomography (CT) angiography. (a, b) Consecutive axial and (c) coronal reformatted CT images revealing an outpouching in the right ventricle (RV) outflow tract (RVOT, arrows). (d) Three-dimensional volume rendering CT image demonstrating the RV diverticulum (arrows). In the intracardiac electrophysiological study, continuous monomorphic self-terminating VT was induced at the RVOT level. Excision of the RVOT diverticulum and surgical ablation of the arrhythmogenic focus were performed, and the patient's complaints completely disappeared.



**Supplementary Figure 5.** (a, b) Arrhythmogenic right ventricular cardiomyopathy in a 45-year-old male patient. (a, b) Multiplanar reformatted cardiac computed tomography images revealing dilation of the right ventricle (RV) and corrugated (accordion-like) pattern on the RV-free wall caused by multiple outpouchings (diverticulum-like).



**Supplementary Figure 6.** A 66-year-old male patient with a history of partial pericardiectomy 28 years ago caused by constrictive pericarditis. Contrast-enhanced chest computed tomography image revealing ventricular herniation from an iatrogenic pericardial defect and left ventricular apical ballooning (arrow). Note an abrupt interruption of the pericardium at the midventricular level (arrowheads).



**Supplementary Figure 7.** Butterfly apex, an anatomic variation that is not to be confused with pathological conditions. Balanced steady-state free precession magnetic resonance image with a four-chamber view demonstrating both the right (arrow) and left ventricles forming separate apices.

---

**Supplementary Video 1 link:** [https://www.youtube.com/shorts/\\_i8Rb8vV7E](https://www.youtube.com/shorts/_i8Rb8vV7E)

**Supplementary Video 1.** Balanced steady-state free precession cine magnetic resonance imaging revealing left ventricular apical dyskinesia and dilation with a wide neck, compatible with a true ventricular aneurysm.

**Supplementary Video 2 link:** <https://www.youtube.com/shorts/Hq-ur3V5rYk>

**Supplementary Video 2.** Balanced steady-state free precession cine magnetic resonance imaging demonstrating a large outpouching in the basal part of the left ventricle with a narrow neck and abrupt transition between the healthy and thinned myocardium, consistent with a left ventricular pseudoaneurysm.

**Supplementary Video 3 link:** <https://www.youtube.com/watch?v=5K9JkTEPj4>

**Supplementary Video 3.** Cardiac computed tomography images demonstrating the bidirectional abnormal motion and bowing of the interatrial septum during different cardiac phases, consistent with atrial septal aneurysm.

**Supplementary Video 4 link:** <https://www.youtube.com/shorts/n6jV56LQ0mQ>

**Supplementary Video 4.** Cine cardiac magnetic resonance imaging depicting both the right and left ventricles forming separate apices, consistent with a butterfly apex. Butterfly apex is an anatomic variation that is not to be confused with pathological conditions.





# Drug-induced lung disease: a brief update for radiologists

Furkan Ufuk   
Selen Bayraktaroğlu   
Ayşe Rüksan Ütebey 

## ABSTRACT

Pulmonary adverse events and drug-induced lung disease (DILD) can occur when treating many conditions. The incidence of DILDs in clinical practice and the variety of radiological findings have increased, mainly due to the increased use of novel therapeutic agents. It is crucial to determine whether the newly emerging clinical and imaging findings in these patients are due to the progression of the underlying disease, infection, pulmonary edema, or drug use, as this will change the patient management. Although the diagnosis of DILD is usually obtained by excluding other possible causes, radiologists should be aware of the imaging findings of DILD. This article reviews the essential radiological results of DILD and summarizes the critical clinical and imaging findings with an emphasis on novel therapeutic agents.

## KEYWORDS

Computed tomography, immunotherapy, lung, pneumonitis, pulmonary toxicity, therapy

When treating many diseases, pulmonary adverse events (AEs) and drug-induced lung disease (DILD) may occur due to medications. Although most of these AEs are clinically mild, they can be severe and even life threatening.<sup>1,2</sup> Patients with malignancy, systemic inflammatory diseases, and elderly patients are at high risk for DILD.<sup>2</sup> The increasing use of novel therapeutic agents, including immune checkpoint inhibitors (ICIs) and molecular targeting agents, have increased the frequency and spectrum of DILD.<sup>3-5</sup> It is also crucial to determine whether the clinical and imaging findings in these patients are due to an underlying condition, infection, pulmonary edema, hemorrhage, or medication. Computed tomography (CT) plays a crucial role in diagnosis and can reveal the pattern-based distribution and severity of pulmonary abnormalities.<sup>6</sup> This article reviews the essential radiological results of DILD and summarizes the critical clinical and imaging findings, emphasizing novel therapeutic agents.

## Clinical features of DILD

The reported incidence of DILD varies widely, but a recent systematic analysis reported an incidence of DILD in 0.4–1.24/100,000 cases per year.<sup>2</sup> Moreover, approximately 3%–5% of all cases of diffuse interstitial lung disease are due to medication.<sup>2,7,8</sup> The temporal relationship between drug intake and the onset of pulmonary symptoms is essential for the clinical suspicion of DILD, but this timescale can vary widely.<sup>2,4,6</sup> Although the clinical condition of patients with DILD can range from asymptomatic to life-threatening, symptoms are usually mild and depend on the severity of the lung disease. Shortness of breath, coughing, and wheezing are the most frequently reported symptoms of DILD.<sup>1,2,7</sup>

A simple clinical grading system has been defined for drug-induced organ toxicity. It is used as an indicator, both in the management of DILD and for determining the patient's prognosis (Supplementary Table S1).<sup>9</sup>

From the Department of Radiology  
(F.U. ✉ furkan.ufuk@hotmail.com, A.R.Ü.) Pamukkale  
University Faculty of Medicine, Denizli, Turkey;  
Department of Radiology (S.B.) Ege University Faculty of  
Medicine, Izmir, Turkey.

Received 3 June 2021; revision requested 15 July 2021;  
last revision received 30 August 2021; accepted 1  
September 2021.



Epub: 29.11.2022

Publication date: 31.01.2023

DOI: 10.5152/dir.2022.21614

You may cite this article as: Ufuk F, Bayraktaroğlu S, Rüksan Ütebey A. Drug-induced lung disease: a brief update for radiologists.  
*Diagn Interv Radiol.* 2023;29(1):80-90.

## Radiological findings of DILD

Imaging methods, particularly chest CT, play a crucial role in diagnosing DILD in patients receiving medications that potentially cause pulmonary toxicity.<sup>6</sup> Although chest X-ray is usually the first-choice imaging tool and provides helpful information in evaluating patients with mild-to-moderate symptoms for DILD, it has low sensitivity and specificity in assessing the presence of pulmonary infiltration and disease extent.<sup>10</sup> Thin-slice chest CT is a valuable tool for a pattern-based assessment of DILD in the presence of appropriate medical history and clinical findings. Moreover, chest CT can reveal other causes of respiratory symptoms or pulmonary infiltrations, and the severity of pulmonary infiltrations in patients with DILD can be assessed visually or quantitatively using CT (Supplementary Figure S1).<sup>11</sup>

As recently stated in a Fleischner Society position paper, five commonly described radiological patterns and rare drug-induced lung abnormalities [such as sarcoid-like granulomatosis (SLG), radiation recall, and pneumonitis flare] may be encountered in chest CT due to novel therapeutic agents (Figure 1).<sup>6</sup> Pneumonitis flare, SLG, and radiation recall pneumonitis do not have typical radiological findings, and clinical history is of great importance when diagnosing these entities.<sup>5,6,10</sup>

### Radiologic organizing pneumonia (OP) pattern

The OP pattern is a form of acute lung injury and is the most common form of DILD.<sup>5,9,12</sup> Histopathologically, it is characterized by intra-alveolar, intra-bronchial granulation tissue and interstitial inflammation.<sup>3</sup> Bilateral, multifocal, peripheral, and peribronchovascular ground-glass opacities (GGOs) and/or consolidation areas with mid-lower lung zone predominance are common imaging findings.<sup>4-6,12</sup> Areas of GGO with a periph-

eral rim of consolidation (also known as reverse-halo or atoll sign) can be found but are not specific (Figure 2 and Supplementary Figure S2). Airspace opacities can be migratory and change configuration over time.<sup>4-6,12</sup> Although eosinophilic pneumonia (EP) can be present in similar imaging findings with an OP pattern, EP is characterized by peripheral band-like opacities and predominance in the upper lobes (Figure 3).<sup>5,6</sup>

### Radiologic non-specific interstitial pneumonia (NSIP) pattern

The NSIP pattern is the second most common form of DILD and is associated with a median of grade 1 toxic effects.<sup>5,9,12</sup> Histopathologically, it is characterized by the thickening of the pulmonary interstitium due to an inflammatory infiltrate (cellular NSIP) and/or fibrosis (fibrotic NSIP).<sup>3,6</sup> Bilateral, patchy, or diffuse GGOs with or

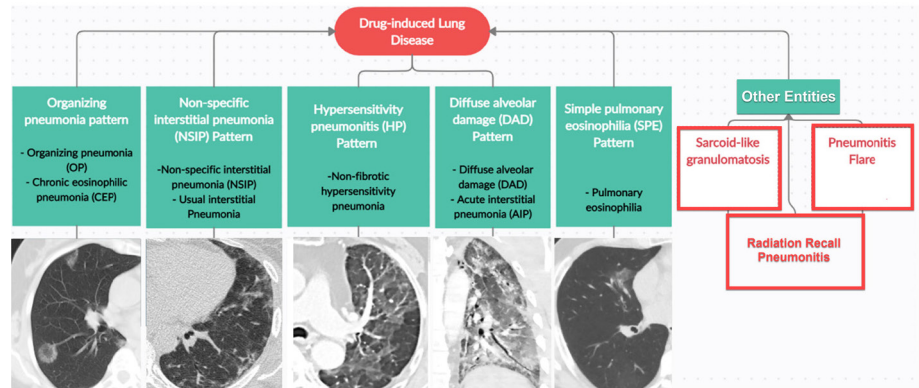


Figure 1. Radiological findings of drug-induced lung disease during chest computed tomography.

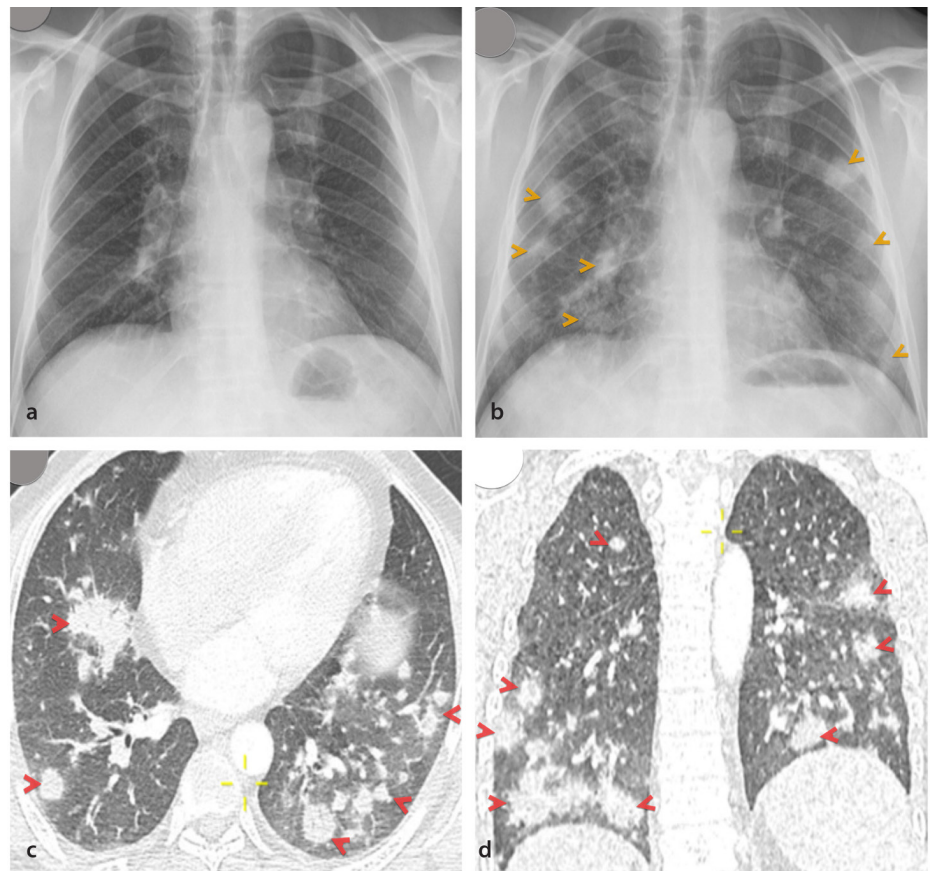
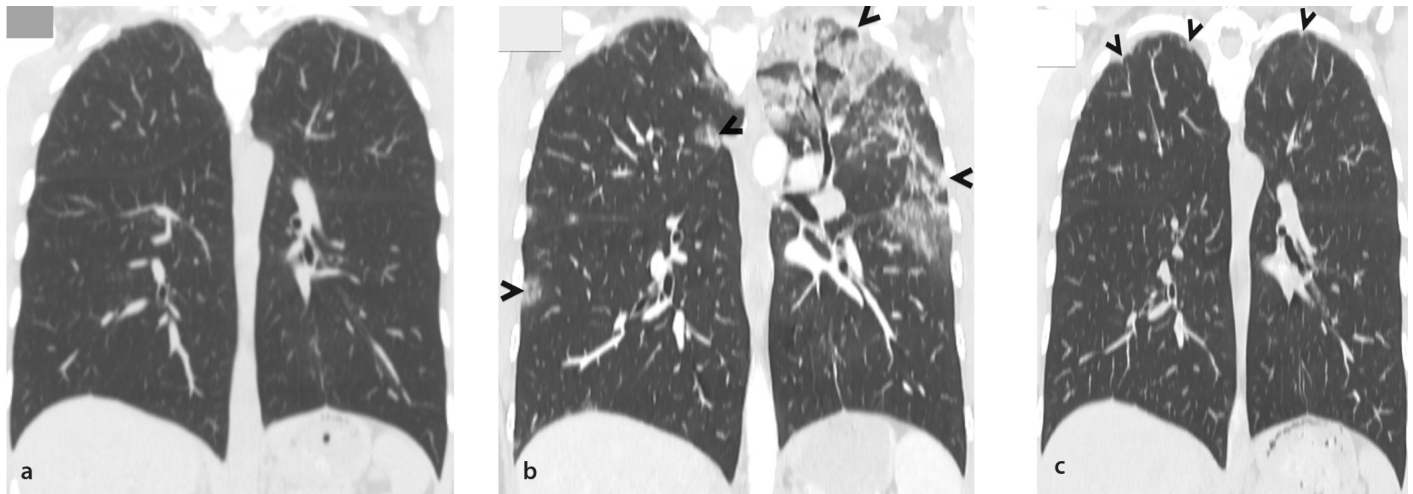


Figure 2. Nivolumab-related organizing pneumonia (OP) pattern in a 49-year-old male with metastatic malignant melanoma. (a) Baseline chest X-ray and (b) 3 weeks after the initiation of pembrolizumab therapy shows newly onset nodular lung opacities (arrowheads). (c) Axial and (d) coronal chest computed tomography images show peripheral and peribronchovascular nodular opacities consistent with the OP pattern. A chest X-ray obtained 8 weeks later, after withholding nivolumab therapy and administering 1 mg/kg/day of prednisolone therapy, demonstrates the complete regression of lung opacities (not shown).

#### Main points

- Pulmonary adverse events and drug-induced lung disease (DILD) can occur in treating many conditions.
- Although DILD is difficult to distinguish clinically from other causes of diffuse pulmonary opacities, radiological findings play a key role.
- Radiologists should be familiar with DILD because the proper management of DILD is vital.



**Figure 3.** Pembrolizumab-related eosinophilic pneumonia in a 43-year-old female with metastatic malignant melanoma. (a) Baseline coronal chest computed tomography (CT) image shows the lungs before therapy and (b) three months after the initiation of pembrolizumab therapy, which demonstrates bilateral, peripheral ground-glass opacities with an upper lobe predominance (arrowheads). The patient had no respiratory symptoms, but laboratory analysis showed an elevated peripheral eosinophil count (857/mcL, normal range: <200/mcL) and bronchoalveolar lavage fluid (BALF) obtained from the left upper lobe bronchus revealed a high cell count ( $1.9 \times 10^5$ /mL) with significantly elevated eosinophils (59.3%). The bacterial/fungal culture was negative for BALF. Pembrolizumab was discontinued, and no treatment was introduced for her eosinophilic pneumonia. (c) The chest CT obtained two months later shows the complete regression of lung opacities with millimetric subpleural atelectasis.

without reticular opacities with peripheral and basilar predominance are the common imaging manifestations of NSIP. Immediate subpleural sparing can also be seen in NSIP cases, and consolidative opacities are unusual. Lung fibrosis shows temporal and spatial homogeneity, and lung abnormalities are usually bilateral and symmetrical (Figures 4, 5).<sup>5,9,12</sup>

#### Radiologic hypersensitivity pneumonitis (HP) pattern

The HP pattern is a rare form of DILD associated with a median of grade 1 toxic effects and mild clinical symptoms.<sup>9,12</sup> Histopathologically, the HP pattern is characterized by cellular bronchiolitis, granulomas, multinucleated giant cells, and interstitial inflammation.<sup>3</sup> Areas of GGO with or without air trapping and centrilobular nodules, which may be diffuse or predominantly distributed in the upper lobes, are common CT findings (Figure 6).<sup>5,6,12</sup> Parenchymal abnormalities, such as traction bronchiectasis, a honeycomb appearance, and upper lobe fibrosis consistent with fibrotic HP, are unusual in DILD.<sup>5,6</sup>

#### Radiologic diffuse alveolar damage (DAD) pattern

The DAD pattern, or acute interstitial pneumonia (AIP), is a rare pattern of DILD often associated with acute clinical symptoms and diffuse pulmonary infiltrations on imaging.<sup>6,9,12</sup> Histopathologically, it is characterized by necrosis of type 2 pneumocytes, alveolar edema, and alveolar endothelial cell

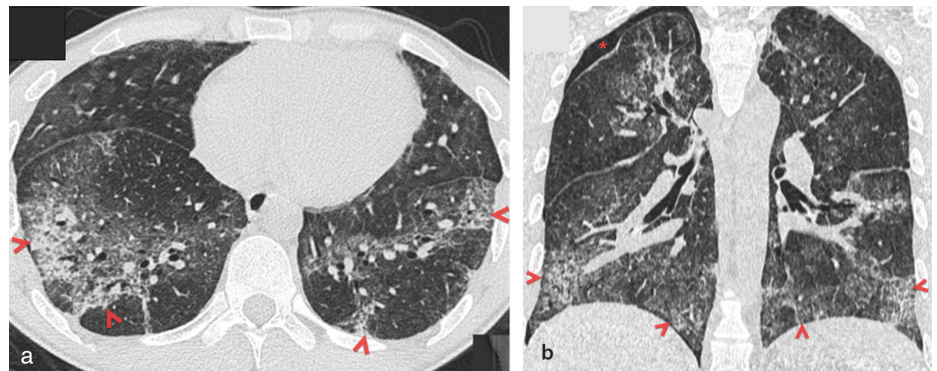


**Figure 4.** Bleomycin-related non-specific interstitial pneumonia pattern in a 29-year-old male with a testicular germ-cell tumor. Baseline chest computed tomography (CT) was unremarkable (not shown). (a) Axial and (b) coronal chest CT images, which were obtained three months after the initiation of chemotherapy, show bilateral, patchy ground-glass opacity areas with a peripheral and basilar predominance (arrowheads). Note the immediate subpleural sparing and right pneumothorax (\*). The bleomycin was discontinued, and the patient was followed up with hospitalization. A control chest CT obtained one year later demonstrates the complete regression of lung opacities (not shown).

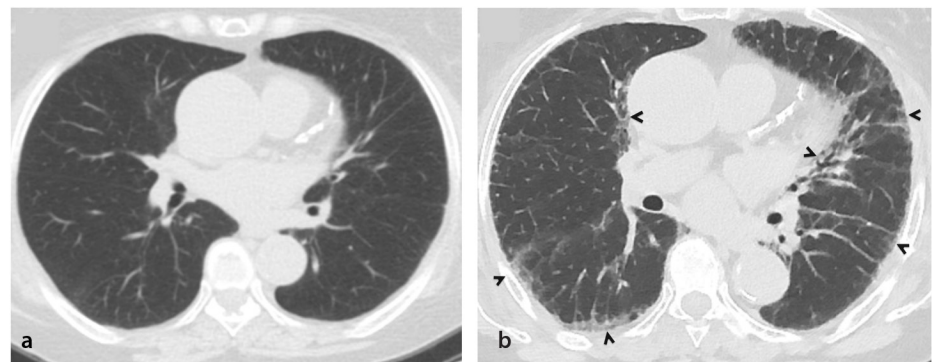


**Figure 5.** Combined ipilimumab and nivolumab therapy-related non-specific interstitial pneumonia (NSIP) pattern in a 65-year-old male with metastatic malignant melanoma. (a) Baseline chest computed tomography (CT) image shows no interstitial abnormalities. (b) Axial chest CT image, which was obtained six months after the initiation of therapy, shows bilateral, patchy ground-glass opacities and subpleural reticulations with peripheral predominance (arrowheads), consistent with an NSIP pattern. Nivolumab and ipilimumab were discontinued, and 0.5 mg/kg/day of prednisone was started for three months. An axial chest CT image obtained six months later demonstrates the partial regression of interstitial lung opacities (not shown).

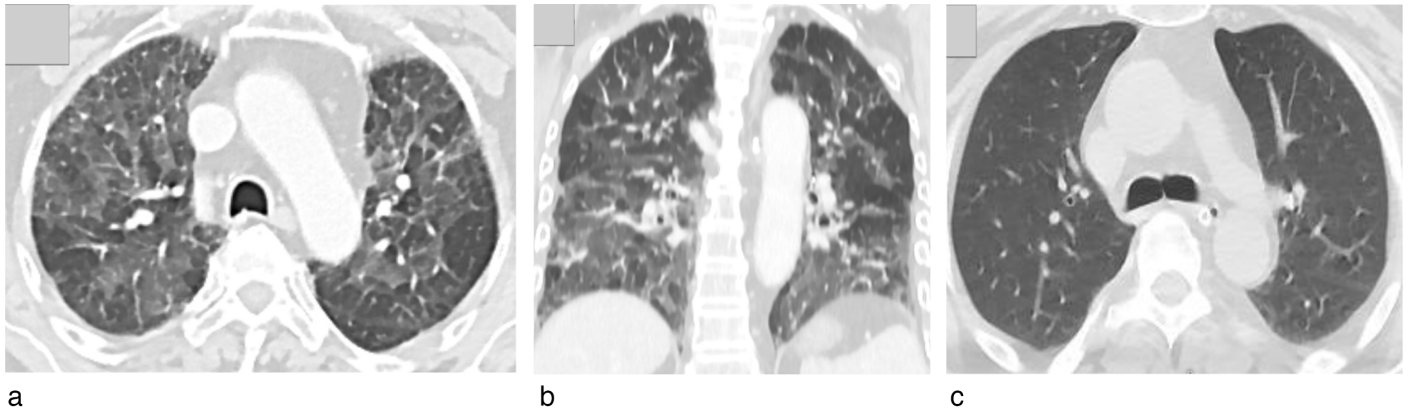


**Figure 6.** Nivolumab-related hypersensitivity pneumonitis pattern in a 59-year-old male with metastatic renal cell carcinoma. Baseline chest computed tomography (CT) was unremarkable (not shown). (a) Axial and (b) coronal chest CT images, which were obtained 3 months after the initiation of nivolumab, show patchy ground-glass opacity areas with air trapping, resulting in mosaic attenuation consistent with non-fibrotic hypersensitivity pneumonitis. Nivolumab was discontinued, and additional treatment was not given, because the patient’s symptoms were mild. (c) Axial chest CT image obtained 3 months later demonstrates the regression of lung opacities.

necrosis.<sup>3,6</sup> The DAD pattern is characterized by GGOs or dependent consolidation areas on imaging that usually affect the majority

of, and sometimes, the entirety of the lung area (Figure 7). The “crazy paving” pattern characterized by interlobular septal thicken-

ing and intralobular lines can often be seen in the DAD pattern. In addition, other patterns, such as OP, can progress to DAD if not treated early (Figures 8, 9, and Supplementary Figure S3).<sup>5,6,12,13</sup>

DAD–AIP findings can also be seen in extra-pulmonary causes, such as acute respiratory distress syndrome, sepsis, and transfusion-related acute lung injury (Supplementary Figure S4).<sup>5,14</sup> Furthermore, diffuse alveolar opacities can be observed on CT in patients with acute promyelocytic leukemia due to differentiation syndrome, which is a rare condition that occurs during all-trans retinoic acid therapy (Supplementary Figure S5).<sup>5</sup>

#### Radiologic simple pulmonary eosinophilia (SPEo) pattern

Although SPEo is generally reported in therapies with ICIs (especially with osimertinib), its etiopathogenesis is not fully understood.<sup>6</sup> Patients with an SPEo pattern are usually clinically asymptomatic and indicate a median of grade 1 toxic effects.<sup>6</sup> SPEo is radiologically characterized by unilateral or bilateral non-segmental, patchy GGOs or areas of consolidation. These lung abnormalities are typically transient and spontaneously resolve within a few weeks (Figure 10).<sup>6,13</sup>

#### Sarcoid-like granulomatosis

Sarcoid-like granulomatosis is an atypical presentation of DILD and is usually associated with ICI therapy. It has been reported in 5%–7% of patients with malignant melanoma treated with ipilimumab.<sup>12</sup> The condition is characterized by histopathological and imaging features identical to sarcoidosis and includes enlarged hilar, mediastinal, and

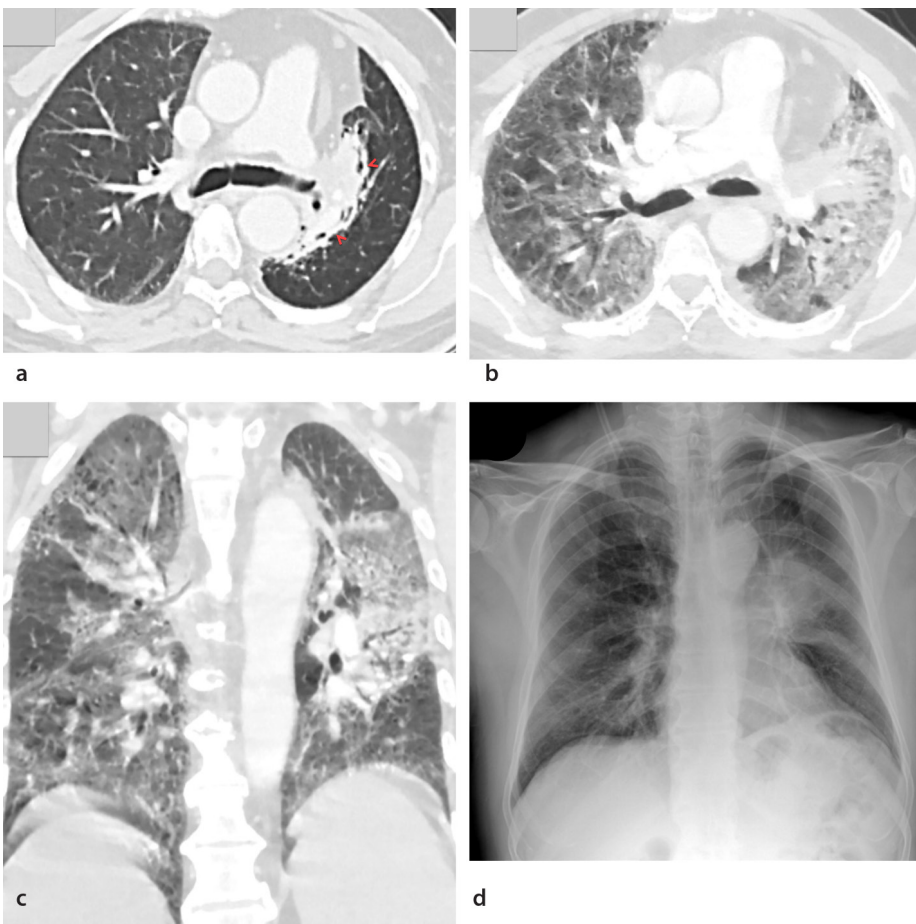


**Figure 7.** Pembrolizumab-related diffuse alveolar damage (DAD) pattern in a 52-year-old male with metastatic non-small cell lung carcinoma. (a) Baseline axial chest computed tomography (CT) image shows a left hilar mass with perilesional fibrosis due to radiotherapy (arrowheads). (b) Axial and (c) coronal chest CT images, which were obtained two weeks after the initiation of pembrolizumab, show diffuse ground-glass opacity areas that affect most lung areas consistent with a DAD pattern. The pembrolizumab was discontinued, the patient was hospitalized, and 1 mg/kg/day of prednisone therapy was started. (d) Two months later, a chest X-ray shows the regression of lung opacities.

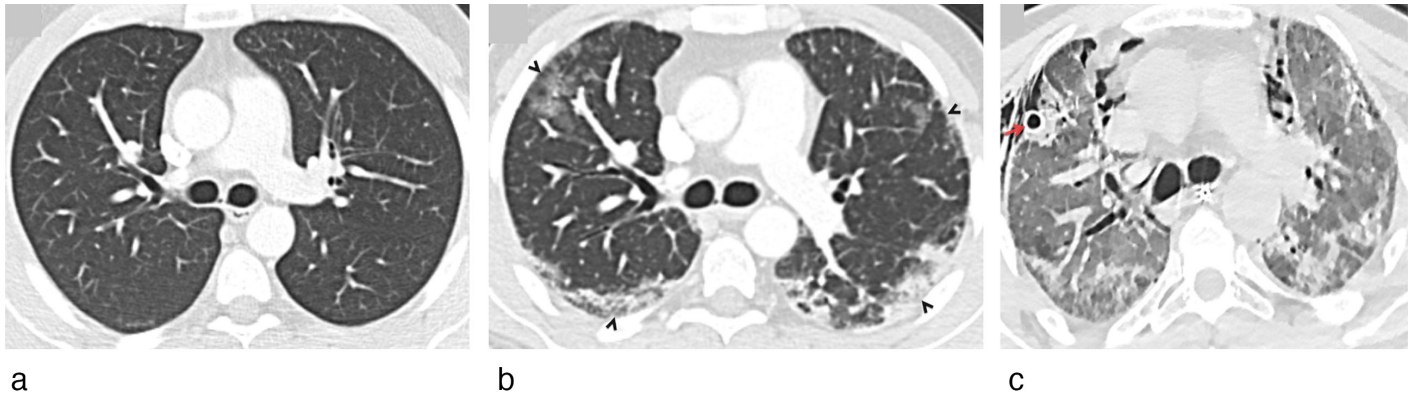


**Figure 8.** Erlotinib-related diffuse alveolar damage (DAD) pattern in a 42-year-old male with metastatic non-small cell lung cancer. (a) Baseline axial chest computed tomography (CT) image at the left main pulmonary artery level shows no parenchymal abnormality. (b) Axial chest CT image, which was obtained three weeks after the initiation of erlotinib therapy, shows bilateral, patchy consolidation and ground-glass opacity areas with peripheral predominance (arrowheads) consistent with an organizing pneumonia pattern. Bronchoalveolar lavage fluid (BALF) was obtained, but the BALF results were unremarkable, and the bacterial/fungal culture was negative. Erlotinib was discontinued, but the patient's general condition worsened, and he was intubated five days after CT. During the second day of intubation, pneumothorax and pneumomediastinum were detected, and chest tube replacement was performed. (c) Axial chest CT image obtained three days after intubation demonstrates diffuse ground-glass opacity areas that affect the entirety of the lung areas, consistent with a DAD pattern. Note the chest tube on the right side (arrow). The patient died on the eighth day of intubation.

abdominal lymph nodes and perilymphatic (along with interlobular septae and bronchovascular bundles) lung nodules (Figure 11).<sup>4-6,10,12</sup> In positron emission tomography CT, lymph nodes and lung nodules can mimic metastatic disease by showing intense <sup>18</sup>F-fluoro-2-deoxy-d-glucose uptake in patients with SLG. Therefore, it is important to be aware of this rare but important drug-induced disorder and consider this diagnosis appropriately to avoid false-positive interpretations of metastatic disease.<sup>12</sup>

### Pneumonitis flare

A pneumonitis flare is a rare entity and is defined in patients on ICI therapy. Pneumonitis flares were reported in only 1 case out of 20 patients with ICI-related pneumonitis.<sup>10</sup> The flaring of ICI pneumonitis is characterized as a flare-up (exacerbation) of pneumonitis when tapering, or during, the cessation of corticosteroid intake without the re-treatment of ICIs (Figure 12).<sup>5,10,12</sup>

### Radiation recall

Radiation recall is an acute inflammatory condition that occurs in a previously irradiated field after exposure to a provocative agent and is observed in many organs or systems, including the lungs.<sup>5,12</sup> In the past, reports of radiation recall pneumonitis were common in treatments with taxane-based chemotherapy agents and gemcitabine, although radiation recall pneumonitis due to ICI therapy has been reported recently with increasing frequency. Shibaki et al.<sup>15</sup> recently reported that the average time between radiotherapy and radiation recall pneumonitis

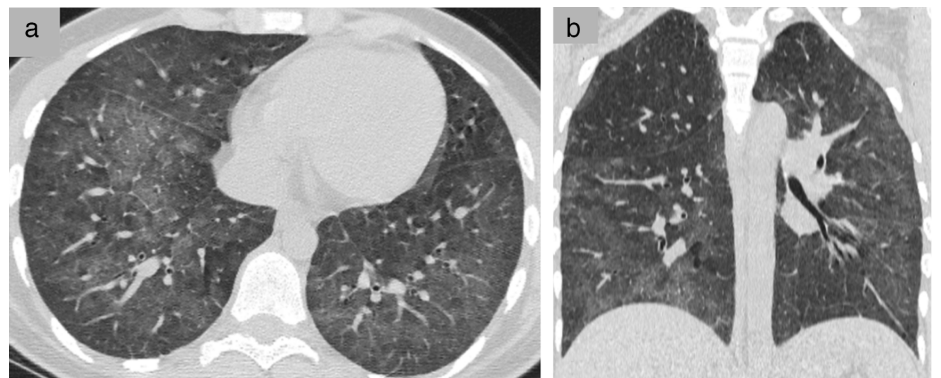


**Figure 9.** Bleomycin-related diffuse alveolar damage pattern in a 20-year-old female patient with Hodgkin's lymphoma. The baseline chest computed tomography (CT) was unremarkable (not shown). (a) Axial and (b) coronal chest CT scans obtained 3.5 months after the initiation of bleomycin therapy show bilateral, diffuse ground-glass opacities and centrilobular ground-glass nodules. The patient had no clinical or laboratory findings consistent with infectious pneumonia. The viral panel was negative, including for *Cytomegalovirus*, and a bronchoalveolar lavage fluid culture was negative for *Pneumocystis jirovecii*. Bleomycin was discontinued, 0.5 mg/kg/day of prednisone was started, and the patient's clinical and imaging findings were resolved.

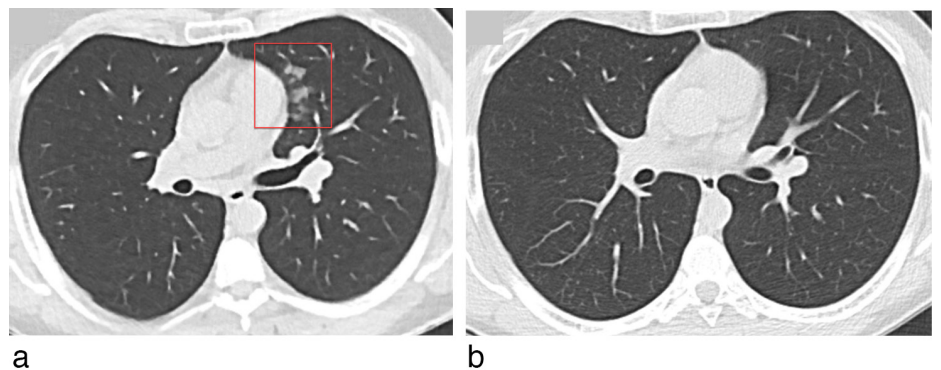


**Figure 10.** Osimertinib-related simple pulmonary eosinophilia pattern in a 40-year-old male with lung adenocarcinoma. (a) Axial chest computed tomography (CT) image at the level of the proximal left upper lobe bronchi shows multifocal ground-glass nodules (red rectangle) during osimertinib therapy. The patient was completely asymptomatic, and laboratory findings were within normal limits. Osimertinib therapy was continued. (b) Axial chest CT image, which was obtained 10 weeks later, shows that pulmonary opacities had disappeared entirely without any additional therapy.

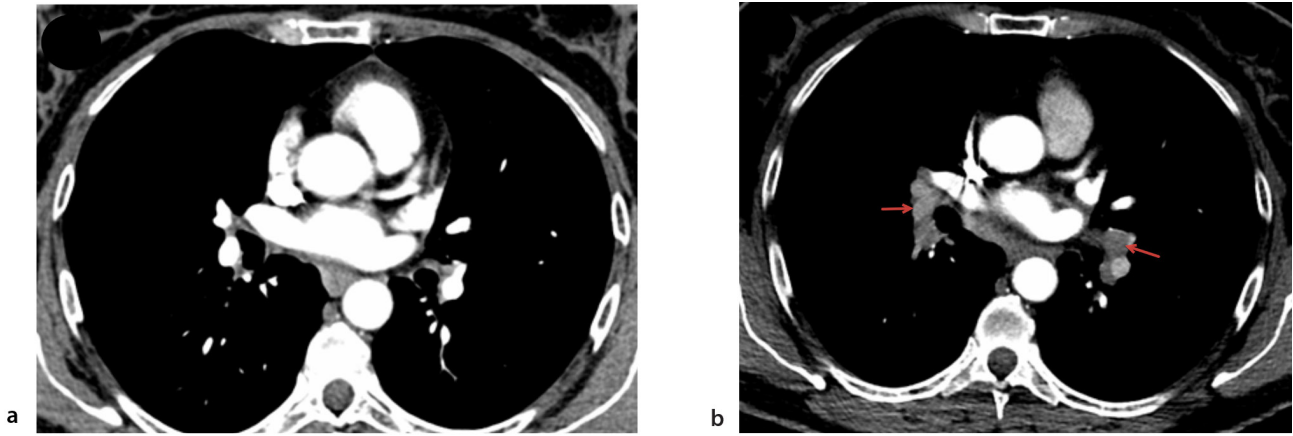


**Figure 11.** Ipilimumab-related sarcoid-like granulomatosis in an asymptomatic 41-year-old female patient with metastatic malignant melanoma. (a) The baseline contrast-enhanced axial chest computed tomography (CT) image at the left atrium levels shows no lymphadenopathies. (b) Contrast-enhanced axial chest CT scan obtained six months after the initiation of ipilimumab therapy shows new bilateral symmetric hilar (arrows) lymphadenopathies resembling sarcoidosis. A lymph node biopsy was performed for suspicion of metastasis, and a non-caseating granulomatous reaction was found histopathologically.

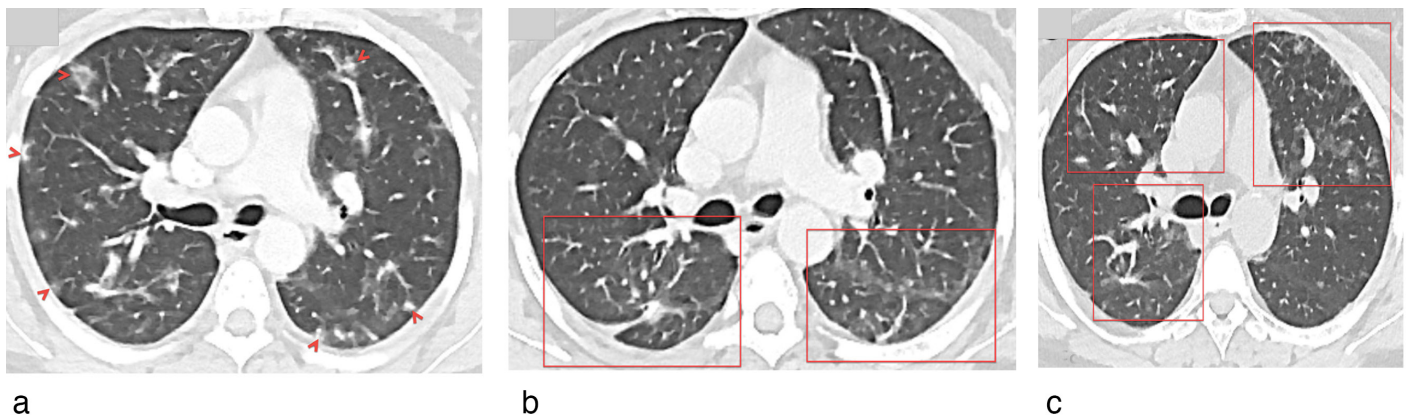


**Figure 12.** Nivolumab-related pneumonitis flare in a 44-year-old symptomatic female patient with metastatic urothelial carcinoma. Baseline chest computed tomography (CT) was unremarkable (not shown). (a) Axial chest CT scan obtained 2 months after the initiation of nivolumab therapy shows the bilateral, multifocal, peripheral, and peribronchovascular distribution of ground-glass opacity nodules compatible with an organizing pneumonia pattern (arrowheads). The patient had no clinical or laboratory findings consistent with infection. Nivolumab was discontinued, 1 mg/kg/day of oral prednisone was started, and the patient's clinical findings were resolved. (b) Axial chest CT scan obtained 3 months later shows mild residual ground-glass opacity areas (red rectangles) and pulmonary opacities that had regressed almost completely. Corticosteroid treatment was discontinued. (c) Chest CT obtained 1 month after the discontinuation of corticosteroid therapy shows newly emerged patchy ground-glass opacities and nodules in both lungs (red rectangles). The patient was treated with anti-TNF- $\alpha$  (infliximab) and 1 mg/kg/day of oral prednisone, and the patient's clinical and imaging findings were resolved.

diagnosis due to ICI therapy was approximately two years. The frequency of radiation recall pneumonitis was reported as 4.4% in patients who had previously received radiotherapy and were treated with tyrosine kinase inhibitors.<sup>16</sup> Although its etiopathogenesis is unclear, an awareness of this condition is essential to avoid the misdiagnosis of underlying disease progression.<sup>12</sup>

#### Diagnosis and management of DILD

Early diagnosis and prompt clinical management are essential for DILD. Although DILD is difficult to distinguish clinically from other causes of diffuse pulmonary opacities,

radiological findings play a key role (Table 1).<sup>5,6</sup> Additionally, laboratory findings, along with clinical and medication history, are complementary in the diagnosis of DILD. Bronchoscopy and biopsy may rarely be preferred for diagnosis depending on the clinical situation and benefit–risk analysis. Recently, the Fleischner Society recommended the following diagnostic criteria for DILD: (a) newly identified pulmonary opacities, (b) temporal relationship of presentation with the initiation of medication, and (c) exclusion of other possible causes.<sup>6</sup>

Multidisciplinary discussion is recommended when determining the diagnosis and management of patients with suspected DILD.<sup>5,6,17</sup> The clinical grading and man-

agement of drug-induced organ toxicity are shown in Supplementary Table S1, and the drugs that are most likely to cause pulmonary toxicity are shown in Supplementary Table S2.

#### Conclusion

Radiologists should be familiar with DILD, as the condition requires a prompt diagnosis to initiate the appropriate treatment and prevent further morbidity and mortality.

**Table 1. Drug-induced pneumonitis patterns and differential diagnoses**

Radiological findings	Imaging features	Differential diagnosis	Median grade of toxicity <sup>9</sup>
Organizing pneumonia (OP)	Peripheral or peribronchovascular, multifocal GGO or consolidation areas. Mid-lower lung predominance. Air bronchogram and reverse-halo sign (atoll sign). Opacities can be migratory and change configuration over time.	<b>Progression of malignancy</b> (concurrent worsening of disease in other body areas). <b>Infectious pneumonia, especially COVID-19 pneumonia</b> (clinical and laboratory findings compatible with infection). <b>Chronic eosinophilic pneumonia</b> (eosinophilia, peripheral, band-like opacities, upper lobe predominance). <b>E-cigarette or Vaping Product Use-Associated Lung Injury (EVALI)</b> (history of e-cigarette or vaping product use). <b>OP unrelated to medication</b> (no temporal relationship with drug, long-term process).	Grade 2
Non-specific interstitial pneumonia (NSIP)	Bilateral, symmetric, patchy, or diffuse GGO areas, with or without reticular opacities. Peripheral and basilar predominance. Immediate subpleural sparing can be seen. Lung fibrosis is temporarily homogeneous.	<b>Infectious pneumonia</b> (clinical and laboratory findings compatible with infection, response to appropriate treatment). <b>Usual interstitial pneumonia</b> (subpleural sparing is not seen, lung fibrosis is temporarily heterogeneous). <b>NSIP associated with connective tissue disease</b> (appropriate medical history and disease-specific laboratory markers, no temporal relationship with drug).	Grade 1
Hypersensitivity pneumonitis (HP)	Diffuse or upper lobe predominant GGO areas with or without centrilobular lung nodules. Air trapping.	<b>Atypical infection</b> (clinical and laboratory findings compatible with infection, response to appropriate treatment). <b>Respiratory bronchiolitis</b> (history of smoking, presence of emphysema, and bronchial wall thickening on CT). <b>Follicular bronchiolitis</b> (history of underlying connective tissue disease or acquired immunodeficiency syndrome, lung cysts with a peribronchial distribution on CT). <b>EVALI</b> (history of e-cigarette or vaping product use). <b>Exposure-related HP</b> (appropriate exposure and occupational history, no temporal relationship with drug).	Grade 1
Diffuse alveolar damage (DAD)	GGO or consolidation areas that affect the majority, and sometimes, the entirety of the lung. Predominantly affect dependent lung areas. "Crazy paving" pattern.	<b>Infectious pneumonia</b> (clinical and laboratory findings compatible with infection, response to appropriate treatment). <b>Pulmonary edema</b> (cardiomegaly, pleural effusion, pulmonary vascular redistribution, peribronchial cuffing, Kerley lines). <b>Alveolar hemorrhage</b> (underlying coagulopathy or capillaritis, hemoptysis, anemia).	Grade 3
Simple pulmonary eosinophilia	Unilateral or bilateral, non-segmental, patchy GGO or consolidation areas. Opacities are migratory and spontaneously resolved within a few weeks.	<b>Infectious pneumonia</b> (clinical and laboratory findings compatible with infection, response to appropriate treatment). <b>Alveolar hemorrhage</b> (underlying coagulopathy or capillaritis, hemoptysis, anemia).	Grade 1
Sarcoid-like granulomatosis	Enlarged hilar and mediastinal lymph nodes. Perilymphatic lung nodules.	<b>Progression of malignancy</b> (concurrent worsening of disease in other body areas). <b>Infection</b> (clinical and laboratory findings compatible with infection, response to appropriate treatment). <b>Sarcoidosis</b> (no temporal relationship with drug, long-term process).	N/A
Pneumonitis flare	Flare-up of pneumonitis.	<b>Infectious pneumonia</b> (clinical and laboratory findings compatible with infection, response to appropriate treatment). <b>OP unrelated to medication</b> (no temporal relationship with drug, long-term process).	N/A
Radiation recall	GGO or consolidation in a previously irradiated field.	<b>Infection</b> (clinical and laboratory findings compatible with infection, response to appropriate treatment). <b>Progression of malignancy</b> (concurrent worsening of disease in other body areas).	N/A

GGO, ground-glass opacity; CT, computed tomography; HP, Hypersensitivity pneumonitis; COVID-19, coronavirus disease-2019

## Conflict of interest disclosure

The authors declared no conflicts of interest.

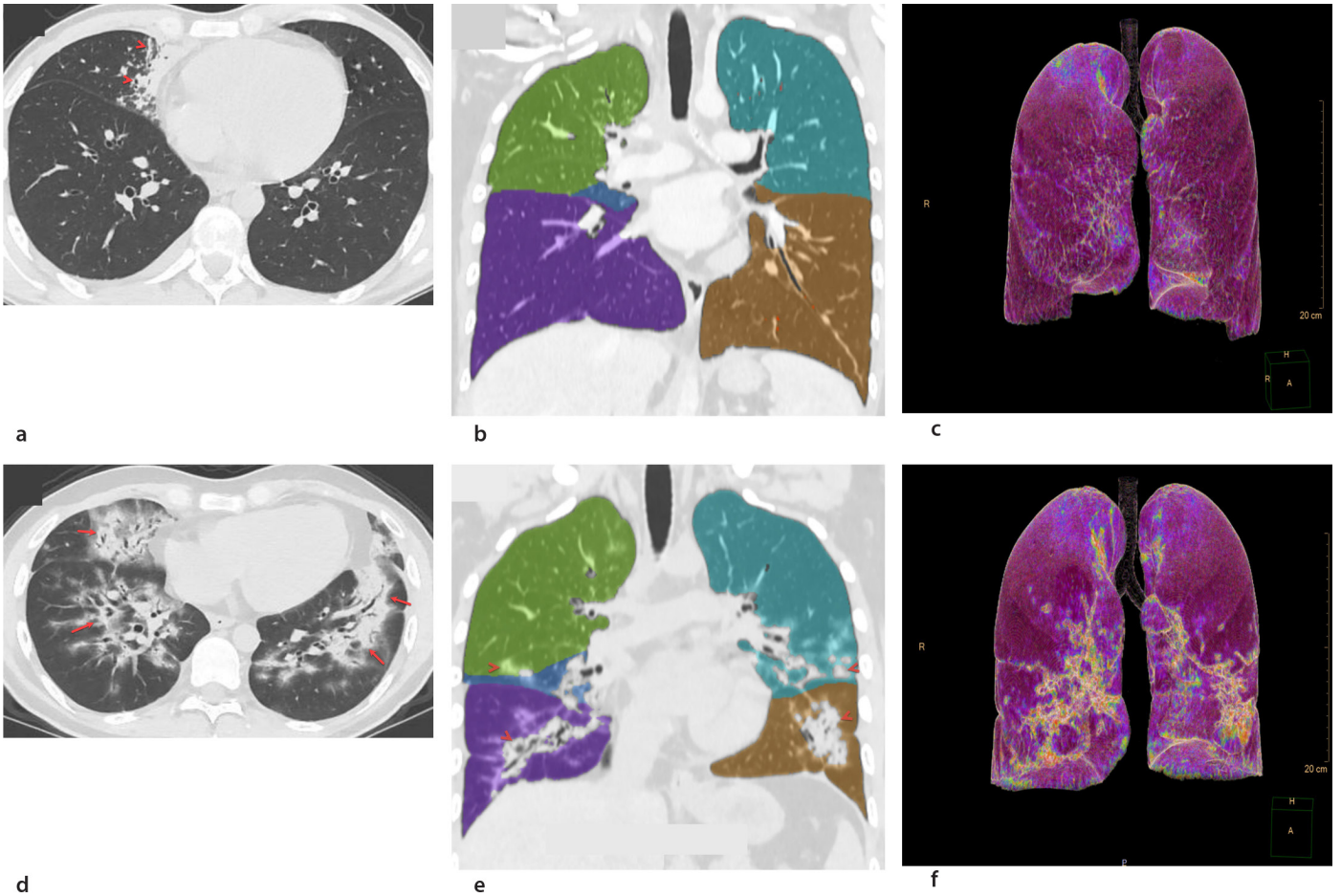
## References

1. Jessurun NT, Drent M, van Puijenbroek EP, Bekers O, Wijnen PA, Bast A. Drug-induced interstitial lung disease: role of pharmacogenetics in predicting cytotoxic mechanisms and risks of side effects. *Curr Opin Pulm Med*. 2019;25(5):468-477. [\[CrossRef\]](#)
2. Skeoch S, Weatherley N, Swift AJ, et al. Drug-induced interstitial lung disease: a systematic review. *J Clin Med*. 2018;7(10):356. [\[CrossRef\]](#)
3. Roden AC, Camus P. Iatrogenic pulmonary lesions. *Semin Diagn Pathol*. 2018;35(4):260-271. [\[CrossRef\]](#)
4. Nishino M, Hatabu H, Hodi FS. Imaging of cancer immunotherapy: current approaches and future directions. *Radiology*. 2019;290(1):9-22. [\[CrossRef\]](#)
5. Wang GX, Kurra V, Gainor JF, et al. Immune checkpoint inhibitor cancer therapy: spectrum of imaging findings. *Radiographics*. 2017;37(7):2132-2144. [\[CrossRef\]](#)
6. Johkoh T, Lee KS, Nishino M, et al. Chest CT diagnosis and clinical management of drug-related pneumonitis in patients receiving molecular targeting agents and immune checkpoint inhibitors: a position paper from the Fleischner Society. *Radiology*. 2021;298(3):550-566. [\[CrossRef\]](#)
7. Duchemann B, Annesi-Maesano I, Jacobe de Naurois C, et al. Prevalence and incidence of interstitial lung diseases in a multi-ethnic county of Greater Paris. *Eur Respir J*. 2017;50(2):1602419. [\[CrossRef\]](#)
8. Thomeer MJ, Costabe U, Rizzato G, Poletti V, Demedts M. Comparison of registries of interstitial lung diseases in three European countries. *Eur Respir J Suppl*. 2001;32:114s-118s. [\[CrossRef\]](#)
9. U.S. Department of Health and Human Services. Cancer Therapy Evaluation Program. Common Terminology Criteria for Adverse Events. Version 5.0. [https://ctep.cancer.gov/protocoldevelopment/electronic\\_applications/docs/ctcae\\_v5\\_quick\\_reference\\_5x7.pdf](https://ctep.cancer.gov/protocoldevelopment/electronic_applications/docs/ctcae_v5_quick_reference_5x7.pdf) Published November 27, 2017. Accessed May 17, 2021.
10. Nishino M, Ramaiya NH, Awad MM, et al. PD-1 inhibitor-related pneumonitis in advanced cancer patients: radiographic patterns and clinical course. *Clin Cancer Res*. 2016;22(24):6051-6060. [\[CrossRef\]](#)
11. Taylor CR. Diagnostic imaging techniques in the evaluation of drug-induced pulmonary disease. *Clin Chest Med*. 1990;11(1):87-94. [\[CrossRef\]](#)
12. Nishino M, Hatabu H, Sholl LM, Ramaiya NH. Thoracic complications of precision cancer therapies: a practical guide for radiologists in the new era of cancer care. *Radiographics*. 2017;37(5):1371-1387. [\[CrossRef\]](#)
13. Min JH, Lee HY, Lim H, et al. Drug-induced interstitial lung disease in tyrosine kinase inhibitor therapy for non-small cell lung cancer: a review on current insight. *Cancer Chemother Pharmacol*. 2011;68(5):1099-1109. [\[CrossRef\]](#)
14. Carcano C, Okafor N, Martinez F, Ramirez J, Kanne J, Kirsch J. Radiographic manifestations of transfusion-related acute lung injury. *Clin Imaging*. 2013;37(6):1020-1023. [\[CrossRef\]](#)
15. Shibaki R, Akamatsu H, Fujimoto M, Koh Y, Yamamoto N. Nivolumab induced radiation recall pneumonitis after two years of radiotherapy. *Ann Oncol*. 2017;28(6):1404-1405. [\[CrossRef\]](#)
16. Chiang CL, Chen YW, Wu MH, Huang HC, Tsai CM, Chiu CH. Radiation recall pneumonitis induced by epidermal growth factor receptor-tyrosine kinase inhibitor in patients with advanced nonsmall-cell lung cancer. *J Chin Med Assoc*. 2016;79(5):248-255. [\[CrossRef\]](#)
17. Brahmer JR, Lacchetti C, Thompson JA. Management of immune-related adverse events in patients treated with immune checkpoint inhibitor therapy: American Society of Clinical Oncology Clinical Practice Guideline Summary. *J Oncol Pract*. 2018;14(4):247-249. [\[CrossRef\]](#)

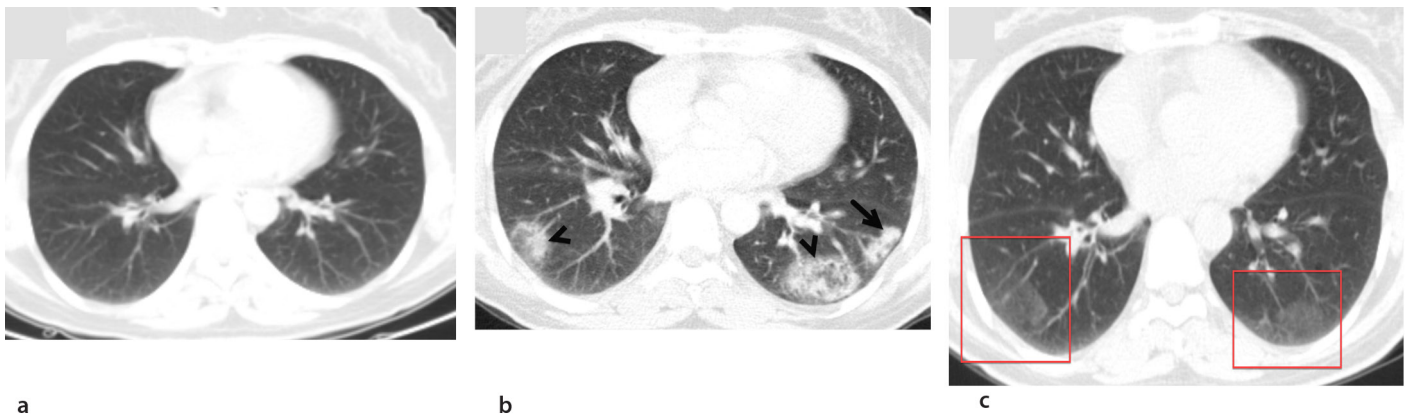


Supplementary Table S1. Clinical grading system of drug-induced lung disease <sup>9</sup>		
Pneumonitis grade	Clinical findings	Management
1	Asymptomatic	Clinical observations only, intervention not recommended
2	Symptomatic (limitation of instrumental daily living activities)	Medical intervention indicated
3	Severe symptoms (limitation of self-care living activities)	Oxygen indicated
4	Life-threatening respiratory compromise	Urgent medical intervention indicated (e.g., intubation, mechanical ventilation)
5	Death	-

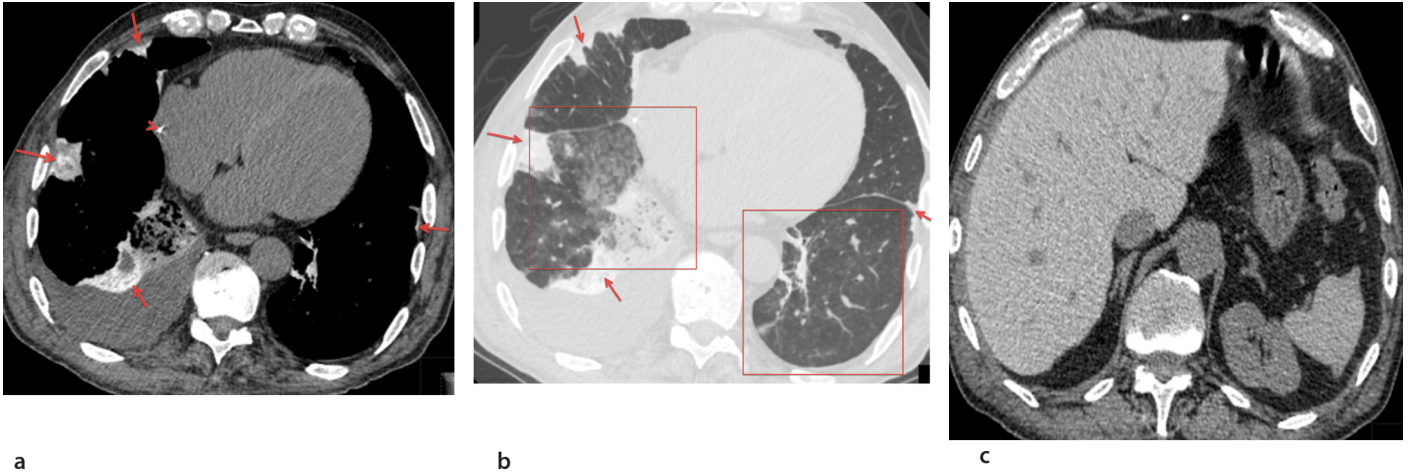
Supplementary Table S2. Drug-related radiological findings and the drugs most likely to cause them	
Radiological findings	Most likely causative drugs
Organizing pneumonia	Adalimumab, amiodarone, amphotericin B, azathioprine, bleomycin, busulfan, cocaine, crizotinib, cyclophosphamide, dasatinib, doxorubicin, erlotinib, etanercept, FOLFOX chemotherapy regimen, imatinib, infliximab, ipilimumab, methotrexate, nitrofurantoin, nivolumab, pembrolizumab, penicillamine, rituximab, sirolimus, sulfasalazine
Non-specific interstitial pneumonia	Adalimumab, alemtuzumab, amiodarone, azathioprine, bleomycin, busulfan, crizotinib, cyclophosphamide, docetaxel, etanercept, gemcitabine, imatinib, infliximab, methotrexate, nitrofurantoin, osimertinib, pembrolizumab, vincristine
Hypersensitivity pneumonitis	Atezolizumab, cytarabine, durvalumab, erlotinib, gefitinib, osimertinib, methotrexate, nitrofurantoin, non-steroidal anti-inflammatory drugs, penicillin, rituximab, sirolimus
Diffuse alveolar damage	Amiodarone, bleomycin, busulfan, carmustine, cyclophosphamide, cytosine arabinoside, erlotinib, fluorouracil, gefitinib, gemcitabine, methotrexate, paclitaxel, pembrolizumab, rituximab, vinblastine
Simple pulmonary eosinophilia	Adalimumab, osimertinib, nivolumab, non-steroidal anti-inflammatory drugs, pembrolizumab, sulfasalazine
Sarcoid-like granulomatosis	Adalimumab, alemtuzumab, anakinra, atezolizumab, capecitabine, etanercept, FOLFOX chemotherapy regimen, infliximab, interferon, ipilimumab, methotrexate, nivolumab, pembrolizumab, rituximab
Pneumonitis flare	Ipilimumab, nivolumab, pembrolizumab
Radiation recall	Cabazitaxel, carmustine, erlotinib, gemcitabine, nivolumab, paclitaxel, pembrolizumab



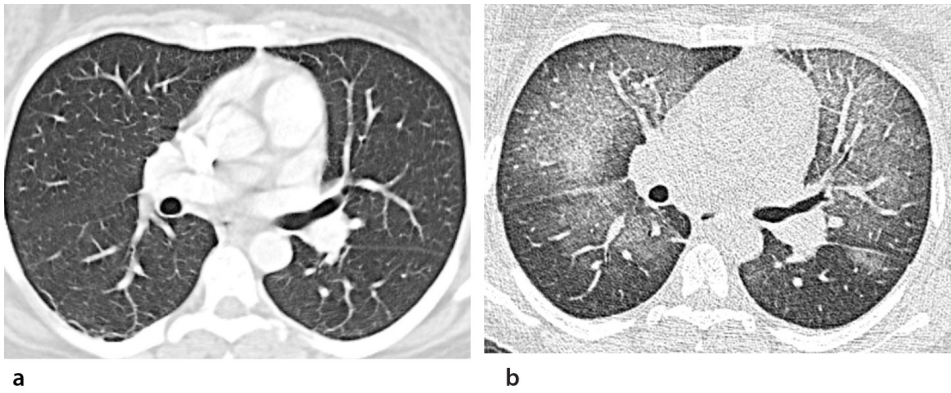
**Supplementary Figure S1.** Nivolumab-related organizing pneumonia (OP) pattern in a 24-year-old male with Hodgkin's lymphoma. (a) Baseline axial chest computed tomography (CT) image at the middle lobe level shows centrilobular nodules and consolidation area (arrowheads) in the middle lobe compatible with radiation pneumonitis. (b) Automatic lung segmentation map of the baseline CT image. (c) Three-dimensional reconstruction CT image with rainbow colors according to CT attenuation values. In the baseline CT, healthy lung volume (HLV), attenuation values between  $-950$  and  $-800$  HU were calculated as  $4.384$  cc, and the mean lung attenuation as  $-878$  HU. (d) In the axial chest CT image obtained 1 week after the initiation of nivolumab treatment, ground-glass opacities and consolidation areas (arrows) were observed in both lungs and were consistent with an OP pattern. (e) The automatic lung segmentation map of the control CT image shows lung opacities (arrowheads) and interval lung volume loss compatible with OP. (f) Three-dimensional reconstruction CT image with rainbow colors according to CT attenuation values. In the control CT, the HLV was calculated as  $3.975$  cc, and the mean lung attenuation was  $-856$  HU.



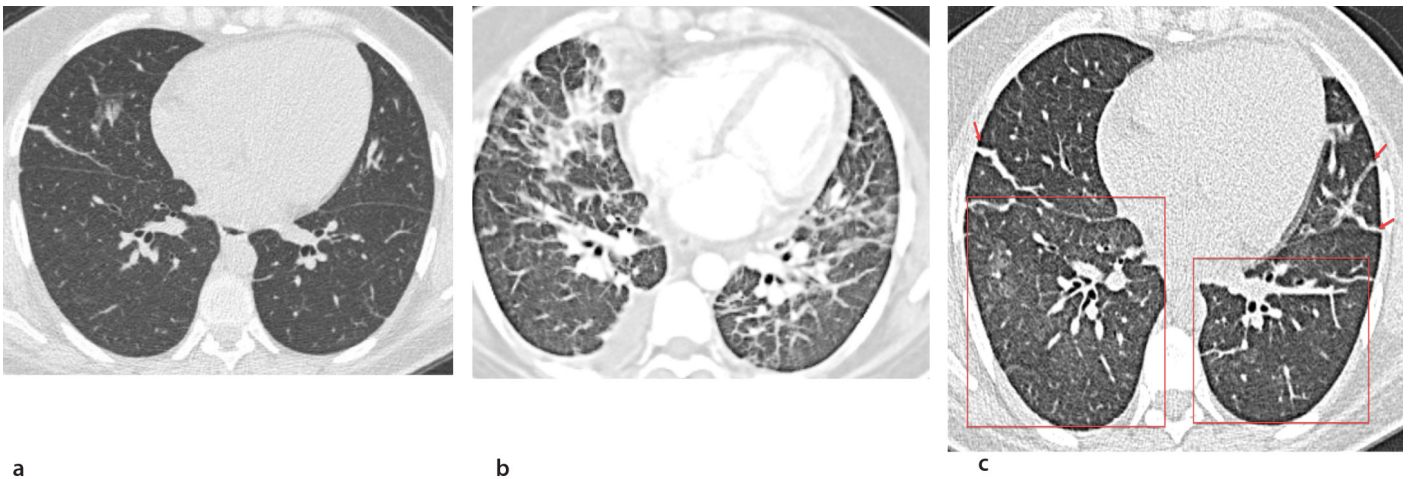
**Supplementary Figure S2.** Organizing pneumonia (OP) pattern in a 51-year-old female during FOLFIRINOX (5-fluorouracil/leucovorin, irinotecan, oxaliplatin) therapy for metastatic pancreas adenocarcinoma. (a) Baseline axial chest computed tomography (CT) image at the inferior pulmonary vein level shows the lungs before chemotherapy was initiated. (b) Axial chest CT image obtained three months later, after FOLFIRINOX therapy, shows peripheral consolidation (arrow) and airspace opacities with reverse halo sign (arrowheads) consistent with an OP pattern of pneumonitis. (c) Axial chest CT image obtained four weeks later, after withholding FOLFIRINOX therapy and administering  $0.5$  mg/kg/day of prednisolone therapy, demonstrates that the residual ground-glass opacities and lung opacities had significantly improved (red rectangles).



**Supplementary Figure S3.** Amiodarone-related alveolar pattern in a 64-year-old male patient with arrhythmia and heart failure. (a) Axial unenhanced chest computed tomography (CT) image shows right pleural effusion, peripheral consolidation areas with high attenuation (arrows), and a pacemaker catheter (arrowhead). (b) Axial CT image with lung window settings shows peripheral consolidation areas with high attenuation (arrows) and centrilobular ground-glass nodules in both lower lobes (red rectangles). (c) Axial unenhanced CT images at the adrenal gland levels show the increased attenuation of the liver with 108 HU. Bronchoalveolar lavage fluid was obtained, and lipid-laden macrophages were detected. Additionally, amiodarone-induced corneal toxicity was found, and amiodarone was discontinued.










**Supplementary Figure S4.** Transfusion-related acute lung injury in a 31-year-old female with known acute myeloid leukemia who developed dyspnea shortly after transfusion. (a) Pretransfusion axial chest computed tomography (CT) image shows clear lungs. (b) Post-transfusion axial chest CT image obtained approximately six hours after transfusion shows developing alveolar opacities with perihilar predominance in the bilateral lung zones.



**Supplementary Figure S5.** All-trans retinoic acid (ATRA)-related alveolar pattern in a 24-year-old male with acute promyelocytic leukemia. (a) Pre-treatment axial unenhanced chest computed tomography (CT) image shows clear lungs except for linear atelectasis and a small area of ground-glass opacity in the right middle lobe. (b) The patient developed respiratory distress 12 hours after the initiation of therapy, and an axial CT image shows bilateral patchy ground-glass opacities, interstitial thickening, and bilateral mild pleural effusion. The ATRA was discontinued, and intravenous systemic corticosteroid therapy (dexamethasone 8 mg/m<sup>2</sup>) was initiated. The patient's clinical condition improved rapidly. (c) Axial chest CT image obtained one month later shows mild residual ground-glass opacities (red rectangles) and linear atelectasis (red arrows).



# Chest computed tomography radiomics to predict the outcome for patients with COVID-19 at an early stage

Shan Wu   
 Ranying Zhang   
 Xinjian Wan   
 Ting Yao   
 Qingwei Zhang   
 Xiaohua Chen   
 Xiaohong Fan 

Shan Wu and Ranying Zhang contributed equally to this work.

From the Department of Endoscopy, (S.W., X.W.) Shanghai Sixth People's Hospital Affiliated to Shanghai Jiao Tong University School of Medicine, Shanghai, China; Department of Radiology (R.Z.), Zhongshan Hospital, Fudan University, and Shanghai Institute of Medical Imaging, Shanghai, China; Department of Infectious Disease (T.Y., X.C. ✉chenxiaohua2000@163.com), Shanghai Sixth People's Hospital Affiliated to Shanghai Jiao Tong University School of Medicine, Shanghai, China; Division of Gastroenterology and Hepatology (Q.Z. ✉zhangqingweif@hotmail.com), Key Laboratory of Gastroenterology and Hepatology, Ministry of Health, Renji Hospital, School of Medicine, Shanghai Jiao Tong University, Shanghai Institute of Digestive Disease, Shanghai, China; Department of Respiratory Medicine, Shanghai Sixth People's Hospital Affiliated to Shanghai Jiao Tong University School of Medicine; Department of Respiratory and Critical Care (X.F. ✉fanxiaohong@shphc.org.cn), Shanghai Public Health Clinical Center, Fudan University, Shanghai, China.

Received 18 June 2021; revision requested 05 July 2021; last revision received 01 December 2021; accepted 27 December 2021.



Epub: 18.01.2023

Publication date: 31.01.2023

DOI: 10.5152/dir.2022.21576

## PURPOSE

Early monitoring and intervention for patients with novel coronavirus disease-2019 (COVID-19) will benefit both patients and the medical system. Chest computed tomography (CT) radiomics provide more information regarding the prognosis of COVID-19.

## METHODS

A total of 833 quantitative features of 157 COVID-19 patients in the hospital were extracted. By filtering unstable features using the least absolute shrinkage and selection operator algorithm, a radiomic signature was built to predict the prognosis of COVID-19 pneumonia. The main outcomes were the area under the curve (AUC) of the prediction models for death, clinical stage, and complications. Internal validation was performed using the bootstrapping validation technique.

## RESULTS

The AUC of each model demonstrated good predictive accuracy [death, 0.846; stage, 0.918; complication, 0.919; acute respiratory distress syndrome (ARDS), 0.852]. After finding the optimal cut-off for each outcome, the respective accuracy, sensitivity, and specificity were 0.854, 0.700, and 0.864 for the prediction of the death of COVID-19 patients; 0.814, 0.949, and 0.732 for the prediction of a higher stage of COVID-19; 0.846, 0.920, and 0.832 for the prediction of complications of COVID-19 patients; and 0.814, 0.818, and 0.814 for ARDS of COVID-19 patients. The AUCs after bootstrapping were 0.846 [95% confidence interval (CI): 0.844–0.848] for the death prediction model, 0.919 (95% CI: 0.917–0.922) for the stage prediction model, 0.919 (95% CI: 0.916–0.921) for the complication prediction model, and 0.853 (95% CI: 0.852–0.855) for the ARDS prediction model in the internal validation. Based on the decision curve analysis, the radiomics nomogram was clinically significant and useful.

## CONCLUSION

The radiomic signature from the chest CT was significantly associated with the prognosis of COVID-19. A radiomic signature model achieved maximum accuracy in the prognosis prediction. Although our results provide vital insights into the prognosis of COVID-19, they need to be verified by large samples in multiple centers.

## KEYWORDS

Radiomic signature, prognosis, COVID-19, prediction

The novel coronavirus disease-2019 (COVID-19) has caused a global pandemic, which presents a threat to human health. The COVID-19 infection causes a fever, cough, and diarrhea, among other symptoms. It can affect several tissues, lead to rapid organ failure, and has a poor prognosis and high mortality rate. Once patients progress to a severe stage of pneumonia, over 60% of them die.<sup>1</sup> To date, there is no effective treatment for COVID-19. However, early diagnosis, immediate patient isolation, and extensive vaccination could effectively prevent the transmission of the SARS-CoV-2 virus.<sup>2</sup> Accurate predictive models are needed to identify the risk of patients experiencing a poor clinical outcome and plan early intervention to improve outcomes.<sup>3-5</sup>

A chest computed tomography (CT) scan combined with a positive molecular polymerase chain reaction (PCR) test is the most important diagnostic method for COVID-19. Compared with the test conducted in standard laboratories, the CT scan procedure has a faster turnaround time and can provide more detailed information about the prognostic significance of the severity of lung damage. Several studies on quantitative CT radiomics or deep-learning techniques have shown the efficiency of a rapid diagnosis of COVID-19.<sup>6,7</sup> It is unknown whether quantitative CT radiomics could provide more information for patients. The quantitative image provides data on clinical decisions and prediction prognoses in many fields,<sup>8,9</sup> and radiomics provide more detailed information on the severity of the lung damage and prognosis of patients with COVID-19.

In this paper, we have developed a radiomics prediction model, a novel tool that extracts hundreds of quantitative features based on the shape, intensity, size, or volume of the target lesions, to predict the outcomes of COVID-19.

## Methods

### Patients

We retrospectively analyzed 157 patients with confirmed positive results of COVID-19 from a viral nucleic acid reverse transcription-PCR test of respiratory secretions via a nasopharyngeal or oropharyngeal swab in Wuhan Leishenshan Hospital. The Ethics Committee of Shanghai Sixth's People's Hos-

pital approved this retrospective study, and written informed consent was waived (approval no.: 2020-KY-013).

All patients' first CT scans after hospitalization were included (Incisive CT, Philips Healthcare and Revolution Maxima, GE Healthcare). The scanning range was from the apex to the lung base. The main scanning parameters were as follows: tube voltage = 120 kVp, tube current = 360 mAs/287 mAs, matrix = 512 × 512, slice thickness = 5 mm, spacing between slices = 5 mm, field of view = 350 mm × 350 mm, window level = 600 Hounsfield units (HU), and window width = 1.200 HU.

### Clinical variables and the primary outcome

Clinical data were collected, including the clinical signs and symptoms (fever, headache, cough, expectoration, fatigue, dyspnea, nausea and vomiting, diarrhea, arthralgia, and myalgia), imaging results, demographic variables (age, sex, smoking status, and time between onset of symptoms to admission), and medical history (comorbidities, respiratory diseases, diabetes, hypertension, coronary artery disease, cerebrovascular disease, cancer, and chronic renal disease).

The primary endpoint in the study was efficacy in the predictions of death, clinical stage, and complications. Complications, including stroke, acute kidney injury, acute respiratory distress syndrome (ARDS), and heart failure, which appeared secondary to pneumonia, were defined as positive if the patient had one or more of these complications.

### Image segmentation and blinding

All non-contrasted CT images were performed using ITK-SNAP software (version 2.2.0; www.itksnap.org) for manual segmentation of the regions of interest (ROIs). Since the presence of lesions interfered with the automatic identification of the chest, we manually delineated along the edge of the pulmonary parenchyma, slice by slice, for each patient. A three-dimensional ROI of the whole lung was then automatically generated by the software. The hilus pulmonis and the trachea were also included in the ROI (Figure 1). All the images were evaluated by two experienced radiologists who were blinded to the patients' clinical information (Ran-ying Zhang, Reader 1, with seven years of radiologist experience; Ting Yao, Reader 2, with four years of experience).

### Radiomic signature building

Figure 1 demonstrates our workflow. The radiomic features were extracted from each ROI using PyRadiomics on Python (version 3.7).<sup>10</sup> Before extraction, all the chest CT images were subjected to image normalization (the intensity of the image was scaled to 0–500). During the normalization process, the binwidth was set to 25, and the intensity of the image of from 1 to 25 bin, 26 to 50, 51 to 75 and so on was regarded as the same intensity in avoid of diversity due to the different parameter setting of CT machine and personal difference. Then, the normalized image was resampled to the same resolution (1 mm × 1 mm × 1 mm) using the interpolation method of sitkBSpline to avoid any

**Main points**

- Early monitoring and intervention for patients with coronavirus disease-2019 (COVID-19) will benefit both patients and the medical system.
- Chest computed tomography (CT) radiomics provide more information for the prognosis of COVID-19 pneumonia.
- The area under the curve of each model demonstrated good predictive accuracy [death: 0.846; stage: 0.918; complication: 0.919; acute respiratory distress syndrome (ARDS): 0.852]. After finding the optimal cut-off for each outcome, the respective accuracy, sensitivity, and specificity were 0.854, 0.700, and 0.864 for the prediction of death of COVID-19 patients; 0.814, 0.949, and 0.732 for the prediction of higher-stage COVID-19; 0.846, 0.920, and 0.832 for the prediction of complications of COVID-19; and 0.814, 0.818, and 0.814 for ARDS in COVID-19 patients.

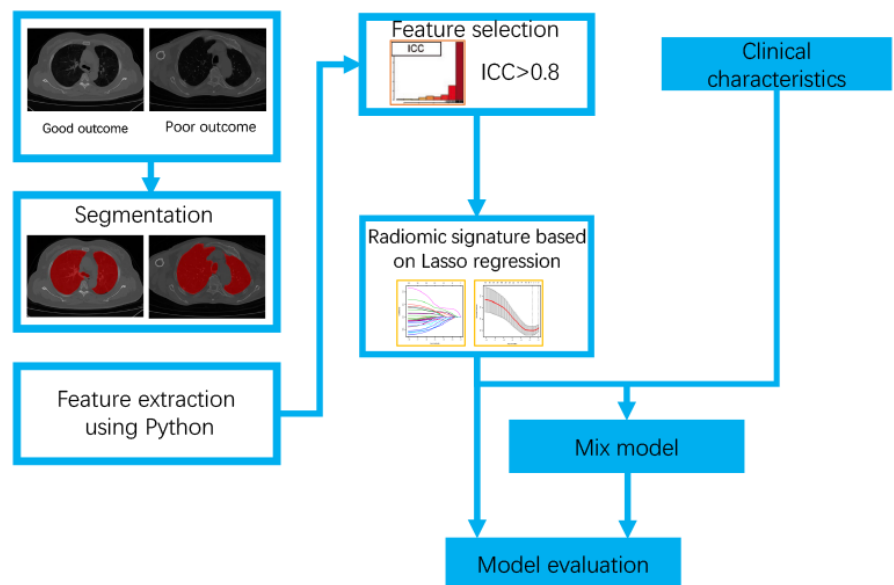


Figure 1. Schematic diagram of the proposed workflow. ICC, inter-class correlation coefficient.

possible data heterogeneity. This procedure was followed by a filtering process to implement image smoothing. After filtering, the radiomic features were extracted from the ROI of the original image and its corresponding filtered results, which included features of first-order statistics, shape, grey-level co-occurrence matrix, grey-level run-length matrix, grey-level size-zone matrix, gray-level dependence matrix, and wavelet features.

The radiomic features of all patients were standardized using the z-score method. Intra-/inter-class correlation coefficients (ICCs) were calculated for each extracted radiomic feature, and those with ICCs of >0.8 were selected. In addition, we calculated the *P* value of the paired t-test for radiomic features with ICCs of >0.8. We chose the least absolute shrinkage and selection operator (LASSO) algorithm to complete the radiomic signature building and form radiomic models with features of non-zero regression coefficients. Each endpoint (stage, death, complication, respiratory failure) had a corresponding model. In total, four radiomic models were constructed to predict the occurrence of the endpoints.

To build a predictive radiomics model for each outcome, we followed several steps. First, the method of normalization to z distribution [(value – mean value)/standard deviation] was applied for each extracted feature. Second, the ICCs were calculated for each extracted radiomic feature, and those with ICCs of >0.8 were selected. Third, the LASSO algorithm was applied for further feature reduction. The most significant features with the smallest deviance were then selected using the LASSO algorithm for the final features. The LASSO algorithm is a penalized regression method that has been successfully applied to oncologic research. The LASSO algorithm can estimate the regression coefficients by maximizing the log-likelihood function (or the sum of squared residuals) with the constraint, reduce the coefficients of indistinctive covariates to zero, and enable the non-zero features to be combined into a radiomics model.<sup>11,12</sup> With this model, the risk score for each patient was calculated using the following formula weighted by regression coefficients for each outcome: risk score = constant + coefficients × features.

### Statistical analysis

The predictive accuracy of the radiomic signature was evaluated using a receiver operating characteristic curve analysis. To determine the optimal cut-off value to pre-

dict each outcome, the Youden index was calculated for all possible cut-off values ( $c$ ) [(Youden index = maxc (sensitivity + specificity – 1)],<sup>13</sup> and the value of  $c$  that achieves the maximized index was considered optimal. For each model, the accuracy, sensitivity, and specificity were also measured using the defined optimal cut-off values. For internal validation, the corrected area under the curve (AUC) was calculated using bootstrapping validation (1,000 bootstrap resamples).<sup>14</sup> In addition, a decision curve analysis (DCA) was performed to evaluate the clinical usefulness of the radiomic signature by quantifying the net benefit at different threshold probabilities.<sup>15</sup>

To explore the clinical utility of the addition of a radiomics signature for each outcome to the models with only clinical data included, we first constructed the clinical model using stepwise backward regression. We initially included the demographics of patients, their symptoms, and their past medical history by calculating the AUC for each outcome. Then, the AUC was calculated for the mixed models by including the clinical models and radiomics signature. Meanwhile, the net reclassification index (NRI), an alternative to AUC to assess the improvement in risk prediction and measure the usefulness of a new model,<sup>16</sup> was calculated to evaluate the clinical benefits and utility of the mixed models compared with the clinical models. A statistical analysis was performed using R software (version 3.5.0, packages: irr, caret, glmnet, caTools, OptimalCutpoints, rms, rmda), and  $P < 0.05$  was considered statistically significant.<sup>17</sup>

## Results

### Patient characteristics

We collected data from 157 patients in Wuhan Leishenshan Hospital between February 19, 2020, and April 10, 2020. The mean (standard deviation) age of these patients was 63.13 (14.14), and 86 of them were women (55.13%). At hospital admission, 59 patients were severe, and 25 patients had severe complications. The overall mortality was 6.3% (Table 1).

### Feature selection and radiomic signature building

For each ROI, a total of 833 quantitative features were extracted. Using an ICC of 0.80 as a cut-off for determining good reproducibility, a total of 257 radiomic features were selected for the next assessment. As shown

in Supplementary Table 1, almost all the *P* values of the paired t-test for radiomic features for all 257 radiomic features were larger than 0.05. After applying the LASSO logistic algorithm, 60 radiomic features were used to develop all the radiomic models.

As shown in Table 2, the AUC of each model demonstrated good predictive accuracy (death model, 0.846; stage model, 0.918; complications model, 0.919; ARDS model, 0.852). After finding the optimal cut-off for each outcome, the respective accuracy, sensitivity, and specificity were 0.854, 0.700, and 0.864 for the prediction of death of COVID-19 patients; 0.814, 0.949, and 0.732 for the prediction of higher-stage COVID-19; 0.846, 0.920, and 0.832 for the prediction of complications of COVID-19 patients; and 0.814, 0.818, and 0.814 for ARDS of COVID-19 patients. The AUCs after bootstrapping were 0.846 for the death prediction model, 0.919 for the stage prediction model, 0.919 for the complications prediction model, and 0.853 for the ARDS prediction model in the internal validation, which indicates that the models were stable. The DCA for the four radiomic models with different endpoints is presented in Figure 2 and shows good performance in terms of clinical application.

We next explored the clinical utility of the addition of the radiomics signature for each outcome to the models with only clinical data included. As shown in Table 3, the AUCs of the clinical models were 0.728, 0.952, 0.726, and 0.861 for the higher stage, death, complications, and ARDS prediction models, respectively. After combining the radiomics signatures and clinical parameters, the AUCs of the mixed models were 0.925, 0.990, 0.929, and 0.903 for the higher stage, death, complications, and ARDS prediction models, respectively. The AUCs of the mixed models were higher than the clinical models. In addition, a significantly increased NRI (stage:  $P < 0.001$ ; death:  $P = 0.013$ ; complications:  $P < 0.001$ ; ARDS:  $P < 0.001$ ) was found for the mixed models compared with the clinical models.

## Discussion

In this study, we described a prediction model for COVID-19 based on radiomic signatures. Based on the first CT scan after hospitalization, we can predict the prognosis of these patients early with high accuracy and intervene where necessary.

COVID-19 can influence several tissues and lead to organ failure rapidly. It has a poor prognosis and a high mortality rate. A

chest CT combined with a positive molecular PCR test is the most important diagnostic method for COVID-19. Compared with tests conducted in standard laboratories, the CT scan procedure has a faster turnaround time and can provide more detailed information regarding lung damage severity and acute respiratory failure.<sup>18,19</sup> Features of CT images

can present with ground-glass opacities, linear opacities, consolidation, bronchial wall thickening, lymph node enlargement, pericardial effusion, or pleural effusion. However, the CT characteristics in some stages are somewhat similar, such as in severe and critical cases. Therefore, a single qualitative radiological diagnosis cannot fully meet our ne-

eds to predict the prognosis of the disease. Radiomics features can quantitatively reflect the invisible details of the lesions. First-order features (e.g., entropy, skewness, and kurtosis) describe the distribution of the values of individual voxels without concern for spatial relationships. Second-order (texture) features describe the statistical interrelationships

**Table 1.** Clinical characteristics

Characteristics	Overall	Survival cases	Death cases
<b>Sex, n (%)</b>			
Female	86 (55.13)	81 (55.1)	5 (55.56)
Male	70 (44.87)	66 (44.9)	4 (44.44)
<b>Age, mean (SD)</b>	63.13 (14.14)	62.44 (14.14)	74.56 (8.35)
<b>Smoking</b>			
No	145 (94.16)	138 (93.88)	7 (100)
Yes	9 (5.84)	9 (6.12)	0 (0)
<b>Clinical symptoms</b>			
Fever, n (%)	96 (62.34)	92 (62.59)	4 (57.14)
Cough, n (%)	98 (63.64)	93 (63.27)	5 (71.43)
Chest pain, n (%)	40 (25.97)	37 (25.17)	3 (42.86)
Hypodynamia (%)	75 (48.7)	73 (49.66)	2 (28.57)
Diarrhea, n (%)	15 (9.74)	15 (10.2)	0 (0)
<b>Comorbidities</b>			
Diabetes, n (%)	35 (22.73)	34 (23.13)	1 (14.29)
HTN, n (%)	76 (49.35)	72 (48.98)	4 (57.14)
Respiratory diseases, n (%)	14 (9.09)	13 (8.84)	1 (14.29)
Heart diseases, n (%)	28 (18.3)	28 (19.18)	0 (0)
Tumors, n (%)	6 (3.9)	5 (3.4)	1 (14.29)
<b>Stage, n (%)</b>			
Mild	97 (62.18)	97 (65.99)	0 (0)
Severe	59 (37.82)	50 (34.01)	9 (100)
<b>Complication, n (%)</b>			
No	131 (83.97)	130 (88.44)	1 (11.11)
Yes	25 (16.03)	17 (11.56)	8 (88.89)
Respiratory failure, n (%)	19 (12.18)	13 (8.84)	6 (66.67)
ARDS, n (%)	11 (7.05)	5 (3.4)	6 (66.67)
Heart failure, n (%)	7 (4.49)	5 (3.4)	2 (22.22)
<b>AKI, n (%)</b>			
0	143 (91.67)	139 (94.56)	4 (44.44)
1	7 (4.49)	3 (2.04)	4 (44.44)
2	2 (1.28)	2 (1.36)	0 (0)
3	4 (2.56)	3 (2.04)	1 (11.11)
WBC, median (Q1, Q3)	5.92 (4.71, 7.29)	5.91 (4.7, 7.17)	6.48 (5.08, 10.36)
CRP, median (Q1, Q3)	2.91 (0.5, 19.66)	2.37 (0.5, 15.18)	40 (22.22, 108.8)
Lymphocyte, median (Q1, Q3)	1.33 (0.84, 1.75)	1.37 (0.88, 1.75)	0.54 (0.19, 0.72)
Time between onset of symptoms to admission, median (Q1, Q3)	22 (15, 30)	22 (15.5, 30.5)	20 (13, 23.75)

AKI, acute kidney injury; SD, standard deviation; WBC, white blood cells; CRP, C-reactive protein; ARDS, acute respiratory distress syndrome; HTN, hypertension.

between voxels with similar (or dissimilar) contrast values. Higher-order statistical methods impose filter grids on the image to extract repetitive or non-repetitive patterns. For instance, among the final selected features, firstorder\_10Percentile indicated the 10<sup>th</sup> percentile of intensity in the ROI, which may reflect the relationship between the density of lesions and the disease grade.

Several studies on CT radiomics and the deep-learning technique have shown the efficiency of a rapid diagnosis of COVID-19. In a large cohort of 3,777 patients, the artificial intelligence diagnostic model can differentiate NCP from other common pneumonia with 92.49% accuracy, 94.93% sensitivity, 91.13% specificity, and an area under the ROC curve of 0.9797.<sup>6</sup> Another deep-learning artificial intelligence-enabled rapid diagnosis system also showed a clinical benefit. However, studies focusing on prognosis prediction using quantitative image features are rare. Our research was the first study to investigate the role of CT radiomics in predicting the prognosis of patients with COVID-19. The AUCs of each model demonstrated good predictive accuracy (0.85–0.92). The DCA also indicated

a good performance in terms of clinical application.

Several retrospective cohort studies have described the multi-organ damage caused by COVID-19, including respiratory, cardiovascular, digestive, urinary, endocrine, and nervous system damage.<sup>20,21</sup> Accurate predictive models are needed to identify the risk of patients experiencing a poor clinical outcome and plan early intervention to improve outcomes. Previous studies have found several variables that are risk factors for a severe prognosis related to COVID-19 and have built effective prediction models for patient management.<sup>22,23</sup> The following factors contain comprehensive clinical data: chest radiography abnormality, age, interleukin-6, dyspnea, number of comorbidities, cancer history, lower lymphocyte count, higher lactate dehydrogenase neutrophil-to-lymphocyte ratio, lactate dehydrogenase, creatinine, and direct bilirubin. However, these data rely on large data collection samples and patient follow ups for the entire study, which might lead to economic issues. In our preliminary study, the first CT image on arrival at the medical center could bring us more infor-

mation than chest lesions. An important advancement in the use of imaging is assisting clinical management in identifying high-risk groups and intervening early to reduce mortality. However, the lack of widely used CT scanning equipment and experienced radiologists might affect the clinical application of these prediction models. Similar to previous research, the data models used in the present research relied on accurate labeling by professional radiologists. Moreover, the clinical characteristics and outcomes were estimated by the expert radiologists for the description of the state of the patient but did not consider the real severity.<sup>5</sup> One limitation of this study is the small sample size for validation and the use of patients in the same country, which could cause bias. This retrospective study could also contain missing data. Additional prospective global multi-center validation studies of COVID-19 are recommended.

In conclusion, the radiomic signature provided vital information for predicting the prognosis of COVID-19. We built a model consisting of a radiomic signature that had maximum accuracy in the prediction of the

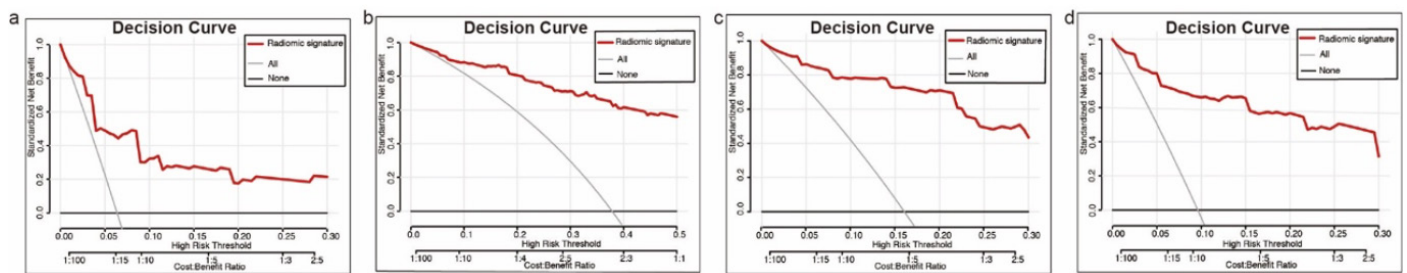


**Figure 2.** Predictive accuracy of the radiomic signature, as evaluated by the Harrell's C-index. (a) Predictive value for death; (b) predictive value for stage; (c) predictive value for complications; (d) predictive value for acute respiratory distress syndrome.

**Table 2.** AUC and NRI with the corresponding *P* value of the clinical models and mixed models for predicting the outcome and NRI value to compare COVID-19 patients

	AUC for the clinical model (SE, 95% CI)	AUC for the mixed models (SE, 95% CI)	NRI	<i>P</i> value <sup>1</sup>
Stage	0.728 (0.042, 0.646-0.809)	0.925 (0.020, 0.885-0.966)	1.34	<0.001
Death	0.952 (0.018, 0.917-0.986)	0.990 (0.019, 0.953-1.000)	0.280	0.013
Complications	0.726 (0.056, 0.616-0.836)	0.929 (0.043, 0.844-0.969)	1.064	<0.001
ARDS	0.861 (0.058, 0.748-0.975)	0.903 (0.060, 0.786-1.000)	0.787	<0.001

<sup>1</sup>*P* < 0.05 indicated the calculated NRI was statistically significant. AUC, area under curve; SE, standard error; CI, confidence interval; NRI, net reclassification index; ARDS, acute respiratory distress syndrome; COVID-19, coronavirus disease-2019.

**Table 3.** Efficacy of the radiomic signature in the prediction of the outcome

Outcome	Harrell's C-index	C-index after bootstrap (95% CI)	Accuracy	Sensitivity	Specificity
Stage	0.918	0.919 (0.917–0.922)	0.814	0.949	0.732
Death	0.846	0.846 (0.844–0.848)	0.854	0.700	0.864
Complications	0.919	0.919 (0.916–0.921)	0.846	0.920	0.832
ARDS	0.852	0.853 (0.852–0.855)	0.814	0.818	0.814

CI, confidence interval; ARDS, acute respiratory distress syndrome.



prognosis. Our study provided vital insight into important preoperative clinical decisions and is expected to be applied in multiple medical centers to optimize future diagnoses and treatments.

### Conflict of interest disclosure

The authors declared no conflicts of interest.

### Funding

This study was supported by Shanghai Science and Technology Commission Clinical Research Project (grant number: 19411951500); Shanghai Sailing Program (grant no. 20YF1436300).

### References

1. Guan WJ, Ni ZY, Hu Y, et al. Clinical characteristics of coronavirus disease 2019 in China. *N Engl J Med*. 2020;382(18):1708-1720. [\[CrossRef\]](#)
2. Majumder J, Minko T. Recent developments on therapeutic and diagnostic approaches for COVID-19. *AAPS J*. 2021;23(1):14. [\[CrossRef\]](#)
3. Wei W, Hu XW, Cheng Q, Zhao YM, Ge YQ. Identification of common and severe COVID-19: the value of CT texture analysis and correlation with clinical characteristics. *Eur Radiol*. 2020;30(12):6788-6796. [\[CrossRef\]](#)
4. Fang X, Kruger U, Homayounieh F, et al. Association of AI quantified COVID-19 chest CT and patient outcome. *Int J Comput Assist Radiol Surg*. 2021;16(3):435-445. [\[CrossRef\]](#)
5. Biondi R, Curti N, Coppola F, et al. Classification performance for COVID patient prognosis from automatic AI segmentation--a single-center study. *Appl Sci*. 2021; 11(12):5438. [\[CrossRef\]](#)
6. Zhang K, Liu X, Shen J, et al. Clinically applicable AI System for Accurate Diagnosis, Quantitative Measurements, and Prognosis of COVID-19 pneumonia using computed tomography. *Cell*. 2020;181(6):1423-1433. [\[CrossRef\]](#)
7. Huang P, Liu T, Huang L, et al. Use of chest CT in combination with negative RT-PCR assay for the 2019 novel coronavirus but high clinical suspicion. *Radiology*. 2020;295(1):22-23. [\[CrossRef\]](#)
8. Sun R, Limkin EJ, Vakalopoulou M, et al. A radiomics approach to assess tumour-infiltrating CD8 cells and response to anti-PD-1 or anti-PD-L1 immunotherapy: an imaging biomarker, retrospective multicohort study. *Lancet Oncol*. 2018;19(9):1180-1191. [\[CrossRef\]](#)
9. Lambin P, Leijenaar RTH, Deist TM, et al. Radiomics: the bridge between medical imaging and personalized medicine. *Nat Rev Clin Oncol*. 2017;14(12):749-762. [\[CrossRef\]](#)
10. van Griethuysen JJM, Fedorov A, Parmar C, et al. Computational radiomics system to decode the radiographic phenotype. *Cancer Res*. 2017;77(21):104-107. [\[CrossRef\]](#)
11. Zhang QW, Gao YJ, Zhang RY, et al. Personalized CT-based radiomics nomogram preoperative predicting Ki-67 expression in gastrointestinal stromal tumors: a multicenter development and validation cohort. *Clin Transl Med*. 2020;9(1):12. [\[CrossRef\]](#)
12. Zhang QW, Zhou XX, Zhang RY, et al. Comparison of malignancy-prediction efficiency between contrast and non-contrast CT-based radiomics features in gastrointestinal stromal tumors: a multicenter study. *Clin Transl Med*. 2020;10(3):e291. [\[CrossRef\]](#)
13. Fluss R, Faraggi D, Reiser B. Estimation of the Youden index and its associated cutoff point. *Biom J*. 2005;47(4):458-472. [\[CrossRef\]](#)
14. Smith PJ, Hoaglin DC, Battaglia MP, Barker L, et al. Implementation and applications of bootstrap methods for the National Immunization Survey. *Stat Med*. 2003;22(15): 2487-2502. [\[CrossRef\]](#)
15. Vickers AJ, Van Calster B, Steyerberg EW. Net benefit approaches to the evaluation of prediction models, molecular markers, and diagnostic tests. *BMJ*. 2016;352:i6. [\[CrossRef\]](#)
16. Uno H, Tian L, Cai T, Kohane IS, Wei LJ. A unified inference procedure for a class of measures to assess improvement in risk prediction systems with survival data. *Stat Med*. 2013;32(14):2430-2442. [\[CrossRef\]](#)
17. De Jay N, Papillon-Cavanagh S, Olsen C, El-Hachem N, Bontempi G, Haibe-Kains B. mRMRe: an R package for parallelized mRMR ensemble feature selection. *Bioinformatics*. 2013;29(18):2365-2368. [\[CrossRef\]](#)
18. Shi H, Han X, Jiang N, et al. Radiological findings from 81 patients with COVID-19 pneumonia in Wuhan, China: a descriptive study. *Lancet Infect Dis*. 2020;20(4):425-434. [\[CrossRef\]](#)
19. Yang X, Yu Y, Xu J, et al. Clinical course and outcomes of critically ill patients with SARS-CoV-2 pneumonia in Wuhan, China: a single-centered, retrospective, observational study. *Lancet Respir Med*. 2020;8(5):475-481. [\[CrossRef\]](#)
20. Wu C, Chen X, Cai Y et al. Risk factors associated with acute respiratory distress syndrome and death in patients with coronavirus disease 2019 pneumonia in Wuhan, China. *JAMA Intern Med*. 2020;180(7):934-943. [\[CrossRef\]](#)
21. Wu Z, McGoogan JM. Characteristics of and important lessons from the coronavirus disease 2019 (COVID-19) outbreak in China: summary of a report of 72 314 cases from the Chinese Center for Disease Control and Prevention. *JAMA*. 2020;323(13):1239-1242. [\[CrossRef\]](#)
22. Liang W, Liang H, Ou L, et al. Development and validation of a clinical risk score to predict the occurrence of critical illness in hospitalized patients with COVID-19. *JAMA Intern Med*. 2020;180(8):1081-1089. [\[CrossRef\]](#)
23. Zhou F, Yu T, Du R, et al. Clinical course and risk factors for mortality of adult inpatients with COVID-19 in Wuhan, China: a retrospective cohort study. *Lancet*. 2020;395(10229):1054-1062. [\[CrossRef\]](#)

**Supplementary Table 1.** Results of paired samples t-test and interclass or intraclass correlation coefficient calculations for radiomics paramaters

Paramater	Inter-class correlation coefficients		Paired samples t-test	
	Same researcher at different time	Different researcher at same time	Same researcher at different time	Different researcher at same time
original_firstorder_10Percentile	0.999997	0.998569	0.340784	0.89771
original_firstorder_90Percentile	0.931262	0.912729	0.077749	0.29402
original_firstorder_Energy	0.981199	0.951514	0.104202	0.77724
original_firstorder_Entropy	0.976015	0.86105	0.081715	0.773565
original_firstorder_InterquartileRange	0.970405	0.894157	0.211248	0.899302
original_firstorder_Kurtosis	0.804423	0.816997	0.027186	0.150026
original_firstorder_Mean	0.998257	0.996387	0.09966	0.616588
original_firstorder_MeanAbsoluteDeviation	0.956756	0.854623	0.071953	0.490757
original_firstorder_Median	0.999905	0.998343	0.33764	0.579896
original_firstorder_Minimum	0.999795	0.970584	0.305204	0.994862
original_firstorder_Range	0.985947	0.881659	0.259128	0.710139
original_firstorder_RobustMeanAbsoluteDeviation	0.947647	0.876259	0.126852	0.726577
original_firstorder_RootMeanSquared	0.997488	0.993777	0.091024	0.565349
original_firstorder_Skewness	0.902097	0.93577	0.040829	0.369576
original_firstorder_TotalEnergy	0.981199	0.951514	0.104202	0.77724
original_firstorder_Uniformity	0.989356	0.818425	0.067482	0.994303
original_firstorder_Variance	0.981203	0.847101	0.09128	0.458786
original_glcm_Autocorrelation	0.986151	0.892283	0.2128	0.902616
original_glcm_ClusterProminence	0.989671	0.893246	0.29526	0.433852
original_glcm_ClusterShade	0.988522	0.890284	0.208842	0.379651
original_glcm_ClusterTendency	0.981285	0.869552	0.094478	0.477418
original_glcm_Contrast	0.99549	0.803835	0.10815	0.531676
original_glcm_DifferenceVariance	0.994748	0.807939	0.09233	0.53265
original_glcm_JointAverage	0.993272	0.825104	0.121628	0.937817
original_glcm_SumEntropy	0.978179	0.89127	0.077978	0.793367
original_glcm_SumSquares	0.983116	0.864382	0.094545	0.479741
original_gldm_DependenceEntropy	0.976726	0.853071	0.073941	0.817061
original_gldm_GrayLevelNonUniformity	0.998773	0.872752	0.049065	0.957319
original_gldm_GrayLevelVariance	0.981222	0.847155	0.091383	0.458466
original_gldm_HighGrayLevelEmphasis	0.985763	0.887965	0.200588	0.850271
original_gldm_SmallDependenceHighGrayLevelEmphasis	0.990101	0.899873	0.247325	0.48425
original_glrIm_GrayLevelNonUniformityNormalized	0.919503	0.939251	0.064681	0.603984
original_glrIm_GrayLevelVariance	0.980288	0.868816	0.071361	0.478433
original_glrIm_HighGrayLevelRunEmphasis	0.983907	0.90651	0.149272	0.851096
original_glrIm_LongRunHighGrayLevelEmphasis	0.973192	0.899739	0.316009	0.928954
original_glrIm_ShortRunHighGrayLevelEmphasis	0.983982	0.905354	0.144339	0.790248
original_glszm_GrayLevelNonUniformity	0.997252	0.828012	0.138214	0.565119
original_glszm_GrayLevelVariance	0.993678	0.816953	0.076984	0.464003
original_glszm_HighGrayLevelZoneEmphasis	0.987263	0.926078	0.107404	0.683375
original_glszm_SizeZoneNonUniformity	0.997713	0.887896	0.052518	0.378143
original_glszm_SizeZoneNonUniformityNormalized	0.995576	0.968844	0.954024	0.794447
original_glszm_SmallAreaEmphasis	0.994757	0.960487	0.825246	0.867285
original_glszm_SmallAreaHighGrayLevelEmphasis	0.990794	0.93481	0.132973	0.643441
original_glszm_ZonePercentage	0.996098	0.822963	0.090173	0.608169
original_ngtdm_Complexity	0.996361	0.872722	0.377178	0.592898

**Supplementary Table 1. Continues**

Parameter	Inter-class correlation coefficients		Paired samples t-test	
	Same researcher at different time	Different researcher at same time	Same researcher at different time	Different researcher at same time
original_shape_Flatness	0.990597	0.82496	0.250526	0.609563
original_shape_LeastAxisLength	0.99722	0.943945	0.314855	0.662473
original_shape_MajorAxisLength	0.999914	0.995239	0.04126	0.453035
original_shape_Maximum2DDiameterColumn	0.997574	0.979956	0.121475	0.595147
original_shape_Maximum2DDiameterSlice	0.999441	0.997251	0.221079	0.093845
original_shape_Maximum3DDiameter	0.990835	0.933314	0.523592	0.572199
original_shape_MeshVolume	0.992537	0.979207	0.094729	0.745679
original_shape_MinorAxisLength	0.993714	0.987656	0.183195	0.787999
original_shape_Sphericity	0.993593	0.963324	0.863871	0.437983
original_shape_SurfaceArea	0.991339	0.967048	0.102698	0.902472
original_shape_SurfaceVolumeRatio	0.99673	0.97189	0.207659	0.89069
original_shape_VoxelVolume	0.992549	0.97913	0.095193	0.747323
wavelet.HHH_firstorder_Energy	0.992533	0.978802	0.091866	0.74983
wavelet.HHH_firstorder_Entropy	0.9976	0.853074	0.339822	0.570975
wavelet.HHH_firstorder_Kurtosis	0.987216	0.943184	0.108393	0.801723
wavelet.HHH_firstorder_Mean	0.956551	0.870222	0.07011	0.988223
wavelet.HHH_firstorder_RootMeanSquared	0.983791	0.881095	0.070903	0.634193
wavelet.HHH_firstorder_TotalEnergy	0.992533	0.978802	0.091866	0.74983
wavelet.HHH_firstorder_Uniformity	0.996915	0.867726	0.340438	0.575115
wavelet.HHH_glcm_SumSquares	0.996365	0.873037	0.333482	0.578942
wavelet.HHH_gldm_DependenceNonUniformity	0.993546	0.903916	0.093858	0.592758
wavelet.HHH_gldm_GrayLevelNonUniformity	0.992541	0.979206	0.095415	0.750379
wavelet.HHH_gldm_GrayLevelVariance	0.997083	0.872956	0.340921	0.589302
wavelet.HHH_glrIm_GrayLevelNonUniformity	0.992771	0.952948	0.09509	0.663165
wavelet.HHH_glrIm_GrayLevelNonUniformityNormalized	0.997063	0.868934	0.28946	0.565452
wavelet.HHH_glrIm_GrayLevelVariance	0.997263	0.875035	0.327481	0.584239
wavelet.HHH_glrIm_RunLengthNonUniformity	0.993162	0.909943	0.09408	0.606215
wavelet.HHH_glszm_GrayLevelNonUniformity	0.997211	0.924464	0.1783	0.501813
wavelet.HHH_glszm_SizeZoneNonUniformity	0.994287	0.898315	0.614822	0.517346
wavelet.HHH_glszm_ZonePercentage	0.994332	0.890479	0.582649	0.498157
wavelet.HHH_ngtdm_Coarseness	0.995103	0.922732	0.295053	0.577228
wavelet.HHL_firstorder_Energy	0.992573	0.97842	0.095536	0.752877
wavelet.HHL_firstorder_Kurtosis	0.995111	0.934285	0.128894	0.58736
wavelet.HHL_firstorder_Mean	0.958346	0.983521	0.061073	0.284902
wavelet.HHL_firstorder_TotalEnergy	0.992573	0.97842	0.095536	0.752877
wavelet.HHL_glcm_ClusterProminence	0.995852	0.826601	0.386051	0.81669
wavelet.HHL_gldm_SmallDependenceHighGrayLevelEmphasis	0.999973	0.869799	0.37208	0.478685
wavelet.HHL_ngtdm_Coarseness	0.997978	0.818081	0.373987	0.668612
wavelet.HHL_ngtdm_Complexity	0.999973	0.836216	0.90023	0.613464
wavelet.HLH_firstorder_Energy	0.992497	0.978972	0.09724	0.760804
wavelet.HLH_firstorder_Mean	0.812382	0.841375	0.254883	0.913161
wavelet.HLH_firstorder_TotalEnergy	0.992497	0.978972	0.09724	0.760804
wavelet.HLH_firstorder_Variance	0.999676	0.800837	0.309301	0.523766
wavelet.HLH_glcm_ClusterProminence	0.997213	0.964836	0.25719	0.19153
wavelet.HLH_glcm_DifferenceVariance	0.998513	0.808758	0.731429	0.454816

**Supplementary Table 1. Continues**

Parameter	Inter-class correlation coefficients		Paired samples t-test	
	Same researcher at different time	Different researcher at same time	Same researcher at different time	Different researcher at same time
wavelet.HLH_gldm_GrayLevelNonUniformity	0.992458	0.980414	0.096699	0.831004
wavelet.HLH_gldm_GrayLevelVariance	0.998752	0.851739	0.347758	0.344964
wavelet.HLH_gldm_LargeDependenceHighGrayLevelEmphasis	0.999988	0.809386	0.543159	0.65892
wavelet.HLH_gldm_SmallDependenceHighGrayLevelEmphasis	0.999972	0.825346	0.581967	0.565302
wavelet.HLH_glrlm_GrayLevelNonUniformity	0.994352	0.85521	0.095236	0.699494
wavelet.HLH_glrlm_GrayLevelVariance	0.998828	0.860282	0.385184	0.343714
wavelet.HLH_glszm_SizeZoneNonUniformity	0.998773	0.827246	0.048067	0.326173
wavelet.HLH_glszm_SmallAreaHighGrayLevelEmphasis	0.984661	0.803754	0.267622	0.857598
wavelet.HLH_glszm_ZonePercentage	0.996543	0.810394	0.135219	0.334475
wavelet.HLH_ngtdm_Coarseness	0.995668	0.836895	0.215283	0.564965
wavelet.HLH_ngtdm_Complexity	0.999999	0.815922	0.710351	0.649103
wavelet.HLH_ngtdm_Strength	0.999796	0.918313	0.395136	0.77281
wavelet.HLL_firstorder_Energy	0.992859	0.978	0.091609	0.727026
wavelet.HLL_firstorder_Mean	0.970284	0.962328	0.091242	0.299141
wavelet.HLL_firstorder_Median	0.988699	0.949159	0.294879	0.531518
wavelet.HLL_firstorder_RootMeanSquared	0.997913	0.896491	0.076846	0.689229
wavelet.HLL_firstorder_TotalEnergy	0.992859	0.978	0.091609	0.727026
wavelet.HLL_glcm_Idn	0.999305	0.895923	0.41531	0.670298
wavelet.HLL_glrlm_GrayLevelNonUniformity	0.997355	0.830152	0.114151	0.692293
wavelet.HLL_glszm_LargeAreaHighGrayLevelEmphasis	0.959884	0.801546	0.146286	0.490789
wavelet.HLL_ngtdm_Coarseness	0.998071	0.920443	0.450353	0.670578
wavelet.LHH_firstorder_Energy	0.992543	0.978972	0.10106	0.760804
wavelet.LHH_firstorder_Entropy	0.999483	0.858038	0.397848	0.461672
wavelet.LHH_firstorder_Kurtosis	0.986817	0.936929	0.068087	0.951105
wavelet.LHH_firstorder_Mean	0.983004	0.963404	0.965327	0.384285
wavelet.LHH_firstorder_Median	0.837757	0.883881	0.883249	0.7669
wavelet.LHH_firstorder_RootMeanSquared	0.969978	0.840774	0.990503	0.404368
wavelet.LHH_firstorder_TotalEnergy	0.992543	0.978972	0.10106	0.760804
wavelet.LHH_firstorder_Uniformity	0.99912	0.871824	0.258251	0.448879
wavelet.LHH_firstorder_Variance	0.999802	0.816434	0.245848	0.586159
wavelet.LHH_glcm_ClusterProminence	0.998194	0.848527	0.221417	0.523894
wavelet.LHH_glcm_DifferenceEntropy	0.99955	0.838622	0.935167	0.642927
wavelet.LHH_glcm_DifferenceVariance	0.999334	0.879789	0.960564	0.655147
wavelet.LHH_glcm_JointEntropy	0.999484	0.854578	0.663912	0.515146
wavelet.LHH_glcm_SumSquares	0.999241	0.889891	0.399138	0.42814
wavelet.LHH_gldm_DependenceNonUniformity	0.993966	0.900768	0.102525	0.710826
wavelet.LHH_gldm_GrayLevelNonUniformity	0.992463	0.979784	0.09628	0.788401
wavelet.LHH_gldm_GrayLevelVariance	0.999191	0.884752	0.349828	0.435273
wavelet.LHH_gldm_LargeDependenceHighGrayLevelEmphasis	0.98298	0.83397	0.338624	0.63401
wavelet.LHH_glrlm_GrayLevelNonUniformity	0.994184	0.840796	0.099308	0.662251
wavelet.LHH_glrlm_GrayLevelNonUniformityNormalized	0.999397	0.878896	0.371097	0.426207
wavelet.LHH_glrlm_GrayLevelVariance	0.999255	0.887979	0.392979	0.429678
wavelet.LHH_glrlm_LongRunHighGrayLevelEmphasis	0.980785	0.813507	0.338373	0.630056

**Supplementary Table 1. Continues**

Parameter	Inter-class correlation coefficients		Paired samples t-test	
	Same researcher at different time	Different researcher at same time	Same researcher at different time	Different researcher at same time
wavelet.LHH_glszm_ZonePercentage	0.999538	0.88587	0.805809	0.328586
wavelet.LHH_ngtdm_Coarseness	0.994722	0.827216	0.254063	0.579548
wavelet.LHH_ngtdm_Complexity	0.998412	0.862594	0.344281	0.54478
wavelet.LHH_ngtdm_Strength	0.999182	0.950617	0.518519	0.698336
wavelet.LHL_firstorder_Energy	0.992982	0.977993	0.09054	0.737466
wavelet.LHL_firstorder_Kurtosis	0.985251	0.960151	0.21718	0.576139
wavelet.LHL_firstorder_Mean	0.989189	0.975507	0.206571	0.432871
wavelet.LHL_firstorder_Median	0.993039	0.960395	0.381912	0.757776
wavelet.LHL_firstorder_RootMeanSquared	0.998785	0.900936	0.269623	0.919027
wavelet.LHL_firstorder_TotalEnergy	0.992982	0.977993	0.09054	0.737466
wavelet.LHL_glcm_ClusterProminence	0.999094	0.821714	0.481395	0.962621
wavelet.LHL_glcm_Idn	0.988052	0.829679	0.243423	0.301559
wavelet.LHL_glcm_Imc2	0.921777	0.884274	0.075303	0.464799
wavelet.LHL_gldm_SmallDependenceHighGrayLevelEmphasis	0.999981	0.922039	0.10615	0.917856
wavelet.LHL_glrIm_LongRunHighGrayLevelEmphasis	0.994766	0.829221	0.123789	0.630026
wavelet.LHL_glrIm_RunEntropy	0.992932	0.814147	0.077034	0.935768
wavelet.LHL_glszm_SmallAreaHighGrayLevelEmphasis	0.99991	0.819829	0.10075	0.814189
wavelet.LHL_ngtdm_Coarseness	0.997763	0.907867	0.34602	0.687538
wavelet.LHL_ngtdm_Complexity	0.999964	0.847661	0.353431	0.842677
wavelet.LLH_firstorder_10Percentile	0.978338	0.861756	0.2552	0.586535
wavelet.LLH_firstorder_90Percentile	0.999921	0.972858	0.911368	0.826339
wavelet.LLH_firstorder_Energy	0.992656	0.979233	0.092076	0.736285
wavelet.LLH_firstorder_Entropy	0.999675	0.971114	0.1583	0.572401
wavelet.LLH_firstorder_InterquartileRange	0.998833	0.951668	0.278588	0.684967
wavelet.LLH_firstorder_Kurtosis	0.955345	0.956023	0.115104	0.195984
wavelet.LLH_firstorder_Maximum	0.999904	0.952952	0.167866	0.55534
wavelet.LLH_firstorder_Mean	0.957527	0.906466	0.352751	0.642735
wavelet.LLH_firstorder_MeanAbsoluteDeviation	0.999102	0.954881	0.228338	0.698042
wavelet.LLH_firstorder_Median	0.965658	0.885736	0.730984	0.925662
wavelet.LLH_firstorder_Minimum	0.999988	0.806223	0.343436	0.397651
wavelet.LLH_firstorder_Range	0.999979	0.912403	0.085281	0.639698
wavelet.LLH_firstorder_RobustMeanAbsoluteDeviation	0.99889	0.95315	0.286438	0.677357
wavelet.LLH_firstorder_RootMeanSquared	0.964063	0.922758	0.354273	0.655446
wavelet.LLH_firstorder_TotalEnergy	0.992656	0.979233	0.092076	0.736285
wavelet.LLH_firstorder_Uniformity	0.998027	0.963139	0.227154	0.554834
wavelet.LLH_firstorder_Variance	0.999634	0.96951	0.221421	0.474875
wavelet.LLH_glcm_ClusterProminence	0.999958	0.979225	0.339388	0.321153
wavelet.LLH_glcm_ClusterShade	0.992615	0.979219	0.901948	0.909563
wavelet.LLH_glcm_ClusterTendency	0.999786	0.986402	0.282204	0.274228
wavelet.LLH_glcm_DifferenceVariance	0.999782	0.803254	0.249572	0.697979
wavelet.LLH_glcm_Idmn	0.999972	0.800171	0.330608	0.226989
wavelet.LLH_glcm_Idn	0.999875	0.949396	0.299252	0.042735
wavelet.LLH_glcm_JointEnergy	0.999321	0.803753	0.252054	0.908083
wavelet.LLH_glcm_JointEntropy	0.999815	0.929506	0.172814	0.723083
wavelet.LLH_glcm_SumEntropy	0.999791	0.95771	0.186376	0.744586

**Supplementary Table 1. Continues**




Parameter	Inter-class correlation coefficients		Paired samples t-test	
	Same researcher at different time	Different researcher at same time	Same researcher at different time	Different researcher at same time
wavelet.LLH_gldm_DependenceNonUniformity	0.989604	0.823667	0.121778	0.686674
wavelet.LLH_gldm_DependenceVariance	0.990269	0.963407	0.354859	0.165496
wavelet.LLH_gldm_GrayLevelNonUniformity	0.992945	0.984785	0.103752	0.779552
wavelet.LLH_gldm_GrayLevelVariance	0.999734	0.973184	0.199483	0.380729
wavelet.LLH_gldm_SmallDependenceEmphasis	0.995889	0.835482	0.263067	0.779956
wavelet.LLH_gIrlm_GrayLevelNonUniformityNormalized	0.999866	0.978885	0.213947	0.60723
wavelet.LLH_gIrlm_GrayLevelVariance	0.999868	0.979676	0.302364	0.418486
wavelet.LLH_glszm_GrayLevelNonUniformity	0.945718	0.850553	0.034748	0.978811
wavelet.LLH_glszm_GrayLevelVariance	0.970813	0.839983	0.113992	0.664453
wavelet.LLH_glszm_SizeZoneNonUniformity	0.984696	0.855923	0.091929	0.844812
wavelet.LLH_glszm_ZonePercentage	0.992001	0.912203	0.202902	0.849231
wavelet.LLH_ngtdm_Complexity	1	0.833586	0.359565	0.608493
wavelet.LLH_ngtdm_Strength	0.999846	0.810294	0.347613	0.332152
wavelet.LLL_firstorder_10Percentile	0.999997	0.999439	0.301835	0.710013
wavelet.LLL_firstorder_90Percentile	0.934659	0.923225	0.078896	0.281365
wavelet.LLL_firstorder_Energy	0.972452	0.950174	0.106066	0.819672
wavelet.LLL_firstorder_Entropy	0.974177	0.918957	0.083673	0.798059
wavelet.LLL_firstorder_InterquartileRange	0.968017	0.912124	0.202452	0.847176
wavelet.LLL_firstorder_Maximum	0.956997	0.815744	0.160508	0.566333
wavelet.LLL_firstorder_Mean	0.998299	0.996389	0.099534	0.618757
wavelet.LLL_firstorder_MeanAbsoluteDeviation	0.954272	0.872252	0.072324	0.453276
wavelet.LLL_firstorder_Median	0.999906	0.998387	0.332724	0.550646
wavelet.LLL_firstorder_Minimum	1	0.987012	1	0.879349
wavelet.LLL_firstorder_Range	0.984956	0.927874	0.160508	0.659921
wavelet.LLL_firstorder_RobustMeanAbsoluteDeviation	0.943418	0.896723	0.123869	0.697487
wavelet.LLL_firstorder_RootMeanSquared	0.994469	0.985452	0.084579	0.524268
wavelet.LLL_firstorder_Skewness	0.89596	0.952381	0.042098	0.292629
wavelet.LLL_firstorder_TotalEnergy	0.972452	0.950174	0.106066	0.819672
wavelet.LLL_firstorder_Uniformity	0.989123	0.896448	0.066958	0.736956
wavelet.LLL_firstorder_Variance	0.979827	0.857975	0.091453	0.448699
wavelet.LLL_glcm_Autocorrelation	0.99588	0.901572	0.113141	0.914279
wavelet.LLL_glcm_ClusterProminence	0.988996	0.897991	0.295485	0.442857
wavelet.LLL_glcm_ClusterShade	0.988002	0.892853	0.209302	0.383499
wavelet.LLL_glcm_ClusterTendency	0.980493	0.875003	0.093982	0.470409
wavelet.LLL_glcm_Contrast	0.993183	0.863679	0.100833	0.49317
wavelet.LLL_glcm_DifferenceAverage	0.987753	0.818154	0.101494	0.668156
wavelet.LLL_glcm_DifferenceVariance	0.993249	0.861779	0.087696	0.483506
wavelet.LLL_glcm_InverseVariance	0.97276	0.811101	0.132027	0.502651
wavelet.LLL_glcm_JointAverage	0.996637	0.88368	0.096733	0.894735
wavelet.LLL_glcm_JointEntropy	0.983888	0.829103	0.090435	0.860867
wavelet.LLL_glcm_SumEntropy	0.975198	0.941017	0.08001	0.772539
wavelet.LLL_glcm_SumSquares	0.981578	0.874546	0.093701	0.470034
wavelet.LLL_gldm_DependenceEntropy	0.95646	0.973771	0.072763	0.671473
wavelet.LLL_gldm_DependenceNonUniformity	0.991417	0.837811	0.120744	0.520914
wavelet.LLL_gldm_DependenceNonUniformityNormalized	0.996895	0.807106	0.240026	0.695228

**Supplementary Table 1. Continues**

Parameter	Inter-class correlation coefficients		Paired samples t-test	
	Same researcher at different time	Different researcher at same time	Same researcher at different time	Different researcher at same time
wavelet.LLL_gldm_HighGrayLevelEmphasis	0.994784	0.896677	0.115249	0.853046
wavelet.LLL_gldm_LargeDependenceHighGrayLevelEmphasis	0.993485	0.807918	0.61861	0.180537
wavelet.LLL_gldm_SmallDependenceEmphasis	0.97975	0.816085	0.122701	0.700424
wavelet.LLL_gldm_SmallDependenceHighGrayLevelEmphasis	0.99369	0.903136	0.14232	0.508733
wavelet.LLL_gldm_SmallDependenceLowGrayLevelEmphasis	0.999841	0.847811	0.492586	0.315844
wavelet.LLL_glrIm_GrayLevelNonUniformity	0.996362	0.998659	0.047327	0.478971
wavelet.LLL_glrIm_GrayLevelNonUniformityNormalized	0.972085	0.945134	0.063713	0.951928
wavelet.LLL_glrIm_GrayLevelVariance	0.979409	0.864066	0.081358	0.442235
wavelet.LLL_glrIm_HighGrayLevelRunEmphasis	0.993533	0.905425	0.100201	0.810979
wavelet.LLL_glrIm_LongRunHighGrayLevelEmphasis	0.994926	0.885049	0.11525	0.760629
wavelet.LLL_glrIm_RunEntropy	0.910947	0.982523	0.076571	0.296386
wavelet.LLL_glrIm_ShortRunHighGrayLevelEmphasis	0.993121	0.906709	0.101465	0.756248
wavelet.LLL_glszm_GrayLevelNonUniformity	0.994386	0.859811	0.384187	0.822736
wavelet.LLL_glszm_GrayLevelVariance	0.99037	0.868936	0.094182	0.45735
wavelet.LLL_glszm_HighGrayLevelZoneEmphasis	0.991484	0.921692	0.082135	0.635025
wavelet.LLL_glszm_LargeAreaHighGrayLevelEmphasis	0.968182	0.89771	0.043252	0.058174
wavelet.LLL_glszm_SizeZoneNonUniformity	0.985194	0.91284	0.066956	0.382645
wavelet.LLL_glszm_SizeZoneNonUniformityNormalized	0.981661	0.964778	0.077366	0.291391
wavelet.LLL_glszm_SmallAreaEmphasis	0.979067	0.96374	0.086227	0.322612
wavelet.LLL_glszm_SmallAreaHighGrayLevelEmphasis	0.99303	0.926193	0.080552	0.571575
wavelet.LLL_glszm_ZonePercentage	0.975948	0.805756	0.132691	0.739583
wavelet.LLL_ngtdm_Coarseness	0.999928	0.810494	0.318255	0.507877
wavelet.LLL_ngtdm_Complexity	0.997228	0.910728	0.414899	0.626529
wavelet.LLL_ngtdm_Strength	0.979982	0.94111	0.509235	0.962508



# Long-term lung perfusion changes related to COVID-19: a dual energy computed tomography study

Sonay Aydın   
Erdal Karavaş   
Edhem Ünver   
Düzgün Can Şenbil   
Mecit Kantarcı 

## PURPOSE

Although the findings of acute new coronavirus disease (COVID-19) infection on dual-energy computed tomography (DECT) have recently been defined, the long-term changes in lung perfusion associated with COVID-19 pneumonia have not yet been clarified. We aimed to examine the long-term course of lung perfusion in COVID-19 pneumonia cases using DECT and to compare changes in lung perfusion to clinical and laboratory findings.

## METHODS

On initial and follow-up DECT scans, the presence and extent of perfusion deficit (PD) and parenchymal changes were assessed. The associations between PD presence and laboratory parameters, initial DECT severity score, and symptoms were evaluated.

## RESULTS

The study population included 18 females and 26 males with an average age of  $61.32 \pm 11.3$  years. Follow-up DECT examinations were performed after the mean of  $83.12 \pm 7.1$  (80–94 days) days. PDs were detected on the follow-up DECT scans of 16 (36.3%) patients. These 16 patients also had ground-glass parenchymal lesions on the follow-up DECT scans. Patients with persistent lung PDs had significantly higher mean initial D-dimer, fibrinogen, and C-reactive protein values than patients without PDs. Patients with persistent PDs also had significantly higher rates of persistent symptoms.

## CONCLUSION

Ground-glass opacities and lung PDs associated with COVID-19 pneumonia can persist for up to 80–90 days. Dual-energy computed tomography can be used to reveal long-term parenchymal and perfusion changes. Persistent PDs are commonly seen together with persistent COVID-19 symptoms.

## KEYWORDS

DECT, COVID-19, follow-up, perfusion deficit, lung

From the Department of Radiology (S.A., E.K., D.C.Ş. [senbilcan@gmail.com](mailto:senbilcan@gmail.com), M.K.), Erzincan University Faculty of Medicine, Erzincan, Turkey; Department of Chest Disease (E.Ü.), Erzincan University Faculty of Medicine, Erzincan, Turkey; Department of Radiology (M.K.), Atatürk University Faculty of Medicine, Erzurum, Turkey.

Received 14 October 2021; revision requested 15 November 2021; last revision received 15 February 2022; accepted 16 March 2022.



Epub: 23.01.2023

Publication date: 31.01.2023

DOI: 10.5152/dir.2022.211090

The novel coronavirus disease (COVID-19) is caused by coronavirus 2 that results in severe acute respiratory syndrome. In March 2020, the World Health Organization declared it a pandemic. Since the first cases were reported in Wuhan, China, COVID-19 has infected millions of people and killed thousands.<sup>1</sup>

A diagnosis of COVID-19 has been associated with both systemic coagulation abnormalities and microangiopathy. In COVID-19 patients, D-dimer and fibrinogen degradation product levels can be elevated, and these elevated levels have been associated with poor prognoses. Vasculopathy is more prevalent in the vessels of the lungs.<sup>2</sup> In COVID-19, the rate of pulmonary embolism (PE) is increased (20.6%–40%), and the presence of PE is associated with a severe disease course.<sup>3,4</sup> In comparison to standard computed tomography (CT) pulmonary angiography, dual-energy computed tomography (DECT) can provide sufficient diagnostic



information about the presence of PE and lung perfusion in a single session without increasing the radiation dose. A sufficient consistency between perfusion on DECT and scintigraphy has also been shown.<sup>5,6</sup> Additionally, DECT has recently proven to be effective in detecting changes in lung perfusion in patients with COVID-19 pneumonia who do not have PE.<sup>7-9</sup>

Endotheliitis-induced pulmonary microvascular damage and occlusion/vasoconstriction has previously been defined as the primary cause of perfusion deficit (PD) in COVID-19 pneumonia, particularly parenchyma, which is commonly observed.<sup>7,10</sup> PD can also occur in opacified-lung parenchyma due to a degraded ventilation-perfusion (V/Q) ratio. Previously, severe V/Q mismatches were defined in COVID-19 pneumonia cases.<sup>11,12</sup>

Although the DECT findings of acute COVID-19 infection have recently been defined,<sup>7,9,13,14</sup> the long-term changes in lung perfusion associated with COVID-19 pneumonia have yet to be clarified. The current study sought to investigate the long-term course of lung perfusion in COVID-19 pneumonia cases using DECT, as well as to correlate changes in lung perfusion with clinical and laboratory findings.

## Methods

The Institutional Review Board of Erzinçan Binali Yıldırım University approved this retrospective study (protocol number: KAEEKBYU-2020/03/11). Due to the retrospective nature of this study, informed consent was waived.

Between July 2020 and January 2021, patients with a positive reverse transcription polymerase chain reaction (RT-PCR) result for COVID-19 were examined. Patients with two DECT scans with a minimum interval of three weeks were included in the study. Patients

with non-contrast enhanced CT scans, mono-energy CT scans, low-quality DECT scans, insufficient clinical/laboratory data, or pulmonary comorbidities were excluded (five patients). In addition, patients diagnosed with pneumonia in the second DECT examination were also excluded (two patients). Subsequently, a total of 44 patients were enrolled in the study.

Data on age and gender were gathered. At the time of the first and second DECT scans, D-dimer, white blood cell, platelet, lymphocyte, neutrophil, fibrinogen, and C-reactive protein (CRP) levels were measured. ( $\pm$  2 days before/after DECT scans). At the time of the first and second DECT scans, the patients' symptoms were also recorded.

The CT severity scores of the patients were calculated and recorded at the time of COVID-19 diagnosis using the Pan et al.<sup>15</sup> method (Table 1).

The DECT examinations were performed with a third-generation device (Somatom Force, Siemens Healthineers, Erlangen, Germany). Intravenous administration of 50–60 mL iohexol (rate = 4.0 mL/s) through the antecubital vein was followed by a 40-mL saline bolus. Following the acquisition of scouts, imaging was performed in the supine position, scanning in the cranio-caudal direction with the following parameters: 80/140 Sn kVp, 60 mAs, rotation time 0.33 s. Slice thickness was 1.5 mm. Image reconstruction was performed in the axial, coronal, and sagittal planes.

On a workstation, the DECT images were evaluated (Syngo.via, Siemens Healthineers, Erlangen, Germany). Two radiologists evaluated the images and clinical data blind. A third radiologist's opinion was sought in cases where the two radiologists disagreed, and consensus was reached. Images of perfusion blood volume (PBV) were used to detect PD.

Along with PBV images, iodine maps were generated. The ground-glass opacities' (GGO) and consolidations' iodine uptake values

were determined by placing region-of-interest (ROI) circles on the iodine maps. Three ROI circles were placed on the lesions, and the final value was calculated as the mean of the three measurements.

## Statistical analysis

The Statistical Package for Social Sciences (SPSS) for Windows 20 software was used to analyze the data (IBM SPSS Inc., Chicago, IL, USA). The Kolmogorov-Smirnov test was used to determine whether the data conformed to a normal distribution. Numerical variables with a normal distribution were represented as mean  $\pm$  standard deviation values, and categorical variables as numbers (n) and percentage values (%). The Student's t-test was used to compare patients with and without persistent lung perfusion. To define cutoff values for the prediction of future PDs, receiver-operating-characteristic (ROC) analysis was used. The chi-square test was used to compare two groups of categorical variables. Interobserver agreement was assessed using categorical correlation analysis (Cohen kappa values).

Statistical significance was defined as a two-tailed value of  $P < 0.050$ .

## Results

The study population included 18 females (40.9%) and 26 males (59%) with an average age of  $61.32 \pm 11.3$  years (range, 22–87 years).

On the initial DECT examinations performed within one week of a positive RT-PCR result for COVID-19, all of the patients had PDs. All of the PDs were found near parenchymal pneumonia lesions.

Follow-up DECT examinations were performed at mean of  $83.12 \pm 7.1$  days (range: 80–94 days) after the initial DECT scan. No PDs were detected on the follow-up DECT examination of 28 (63.6%) patients (Figures 1-4). Of these 28 patients, ground-glass parenchymal lesions (regressed in comparison with the initial CT scans) were determined in 4 patients

### Main points

- The presence of ground-glass opacities and lung perfusion deficits (PDs) of coronavirus disease-2019 (COVID-19) pneumonia can continue for as long as 80–90 days.
- Dual-energy computed tomography can be used to reveal both long-term parenchymal and perfusion changes.
- Computed tomography severity values, D-dimer, and C-reactive protein levels can be useful in predicting future persistent PD presence.
- Persistent PDs are commonly observed along with persistent COVID-19 symptoms.

**Table 1.** CT severity scoring

CT severity score	The extent of lesions in each lung lobe
0	0%
1	<5%
2	5%–25%
3	26%–50%
4	51%–75%
5	>75%

Each lobe was assigned a score, and the sum of the lobe scores equals the total lung score. Scale of total points: 0–25. CT, computed tomography.

on the follow-up DECT scans, and the other 24 patients had normal lung parenchyma.

PDs were determined on the follow-up DECT scans of 16 (36.3%) patients (Figures 5-8). All 16 patients also had ground-glass parenchymal lesions on the follow-up DECT scans. Of these 16 patients, the ground-glass parenchymal lesions and PDs were seen to be regressed in comparison with the initial CT scans in 15 cases. Only one patient (an 87-year-old female, finally diagnosed as non-specific interstitial pneumonia after COVID-19 infection) was seen to have progression of the ground-glass parenchymal lesions and PDs. In all patients, parenchymal abnormalities involved the same lung regions where PDs were detected.

Interobserver agreement for PD presence and change was strong ( $\kappa$  values of 0.86 and 0.84, respectively).

The laboratory data and symptoms of the patients were compared based on the presence of persistent PDs. Patients with persistent lung PDs had a significantly higher mean age than patients without PDs ( $72.13 \pm 8.9$  years vs.  $60.8 \pm 10.3$  years,  $P < 0.001$ ). There was no gender difference in the presence of persistent lung PDs ( $P = 0.105$ ). Patients with persistent lung PDs had sig-

nificantly higher initial mean D-dimer, fibrinogen, and CRP values than patients without PDs. Patients with persistent lung PDs had significantly higher mean CT severity scores at the time of COVID-19 diagnosis (Table 2). According to the ROC analysis, D-dimer and CRP levels were the best predictors of a future persistent PD. Measures of D-dimer, CRP, CT severity scoring, and fibrinogen had area-under-the-curve values with 95% confidence intervals (CIs) of 0.725 (0.67–0.78, 95% CI), 0.693 (0.635–0.751, 95% CI), 0.587 (0.526–0.648, 95% CI), and 0.522 (0.457–0.587, 95% CI), respectively (Figure 9, Table 3).

A D-dimer value  $>1,315$  was determined to predict persistent PD presence with a sensitivity of 87.5% and specificity of 100%. A CRP value  $>92$  was seen to predict persistent PD presence with sensitivity of 75% and specificity of 100%.

Patients with persistent lung PDs had significantly higher mean CRP and D-dimer values at PF.

Dyspnea, coughing, and fatigue were observed as persistent symptoms in the interval between the two DECT examinations. Patients with persistent PDs had significantly higher rates of persistent symptoms (Table 4). Dyspnea was not found in any of the

patients who did not have persistent PDs. Coughing was present in only two patients without PDs, and both of these two patients were determined to have GGOs that had regressed but still persisted in the second DECT examination.

Consolidations derived from iodine uptake maps had a higher mean Hounsfield Unit value than GGOs ( $-91.11 \pm -8.61$  vs.  $-573.9 \pm -100.7$ , respectively).

All patients were given 6,000 anti-Xa IU/0.6 mL enoxaparin in accordance with the Turkish Ministry of Health's treatment guidelines after initial diagnosis. None of the patients had a history of being admitted to the intensive care unit due to COVID-19.

## Discussion

The findings of this study show that lung perfusion abnormalities caused by COVID-19 pneumonia can last for up to two to three months. Persistent PDs are associated with laboratory markers and persistent symptoms.

As the number of patients with COVID-19 infections has grown, and research has focused on the disease's progression, the symptoms that persist after infection have now been identified. It has been found that 10% of COVID-19 patients experience a variety of symptoms that can last for up to three months following the initial diagnosis.<sup>16,17</sup>

Research has shown DECT to be effective at detecting small PEs that are missed by conventional CT angiography, as well as parenchymal PDs.<sup>18</sup> Although a number of recent studies have defined the changes in lung perfusion associated with COVID-19 pneumonia,<sup>8,9</sup> to our knowledge, no study in English literature has examined long-term lung perfusion changes in COVID-19 cases treated with DECT during follow-up.

The absorption stage of GGOs of COVID-19 pneumonia can last for as long as one month after the initial diagnosis,<sup>19</sup> and although at a smaller prevalence, GGOs may be detected up to 100 days after the initial diagnosis.<sup>20</sup> Similar to findings in the literature, GGOs were determined after a mean of 83 days in the current study. These persistent GGOs were mostly accompanied by persistent PDs. GGOs and PDs had generally regressed by the time of the follow-up examinations with the exception of one patient who was eventually diagnosed with interstitial lung disease. Regression of lung manifestations of COVID-19 is a known and expected enti-



**Figure 1.** Thirty-two-year-old male. Initial dual-energy computed tomography image. Consolidations (arrows) are present.

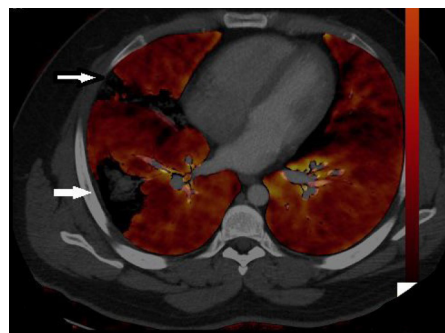


**Figure 2.** The same patient as in Figure 1. Initial dual-energy computed tomography images. Consolidation-related perfusion deficits are observed (arrows).



**Figure 3, 4.** Follow-up (after 87 days) dual-energy computed tomography (DECT) images of the same patient as in Figures 1 and 2. Follow-up DECT scan reveals no parenchymal (Figure 3) or perfusion (Figure 4) abnormality.



**Figure 5.** Fifty-year-old male. Initial dual-energy computed tomography images. Ground-glass opacities (arrows) are marked.

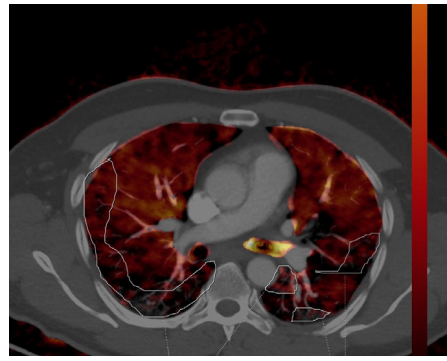
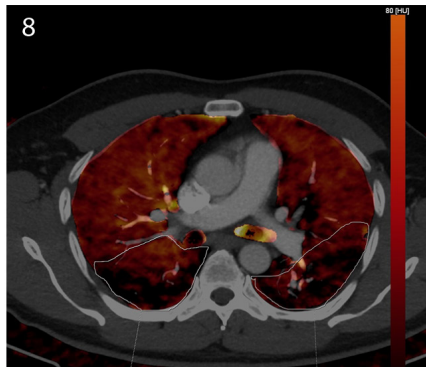
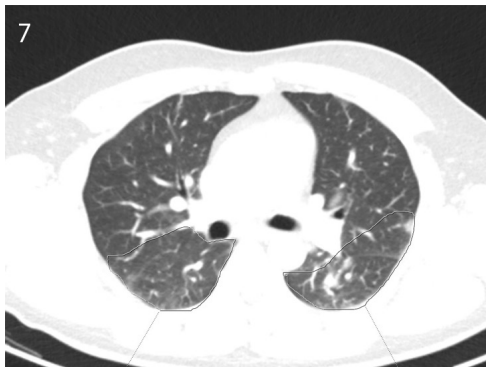


**Figure 6.** The same patient as in **Figure 5**. Initial dual-energy computed tomography images. Consolidation-related perfusion deficits are marked.



**Figures 7, 8.** Follow-up (after 81 days) dual-energy computed tomography images of the same patient as in **Figures 5 and 6**. The regressed parenchymal opacities (**Figure 7**) and their corresponding regressed perfusion deficit (**Figure 8**) are indicated.

**Table 2.** Mean values of the parameters at the time of the initial DECT scan based on the presence of persistent PD

Parameters	Patients without persistent PD	Patients with persistent PD	<i>P</i> value
CT severity score	5.3 ± 2.34	9.75 ± 3.29	0.004
D-dimer (μg/L)	571.23 ± 21.87	1.225.23 ± 112	0.001
Fibrinogen (mg/dL)	365.23 ± 54.01	423.12 ± 64.43	0.003
CRP (mg/dL)	37.17 ± 8.3	83.72 ± 5.3	0.001
Platelet (×10 <sup>9</sup> /L)	214.21 ± 63.14	243.15 ± 25.16	0.072
Neutrophil count (×10 <sup>9</sup> /L)	4.45 ± 1.48	5.83 ± 2.01	0.120
White blood cell (×10 <sup>9</sup> /L)	5.45 ± 0.3	6.25 ± 0.3	0.090

Bold indicates statistical significance. DECT, dual-energy computed tomography; CT, computed tomography; CRP, C-reactive protein; PD, perfusion deficit.

ty,<sup>19</sup> although, as in the above-mentioned case, irreversible pulmonary fibrosis has also been previously reported.<sup>21</sup> No data could be found in the literature pertaining to the persistence of lung PD, so the information presented in this study can be considered of value as it may alter the perceptions of the content and extent of COVID-19 sequelae.

COVID-19 has a greater impact on older patients, and persistent COVID-19 symptoms are associated with age.<sup>22,23</sup> Furthermore, CT severity values, CRP, and D-dimer levels have been discovered to be good predictors of disease course, severity, and persistence symp-

toms of COVID-19.<sup>24,25</sup> The data of the current study demonstrated that in addition to their ability to predict severe disease, these parameters are also associated with long-term PD presence. D-dimer is an important indicator of the microangiopathic nature of COVID-19. The association between D-dimer and long-term PD also confirms the microangiopathic damage of COVID-19 pneumonia and reveals its extent. Fibrinogen levels are another indicator of the microangiopathic nature of COVID-19-related pneumonia. Levels of CRP have been defined as a significant indicator of a severe disease course due to

their role as a major marker of inflammation. Additionally, it was discovered that CT severity values were correlated with both CRP levels and clinical disease severity. The CRP and D-dimer values were also found to be positively correlated, implying that increased inflammation is associated with more severe angiopathy.<sup>25,26</sup> It was also previously emphasized that severe disease course was associated with more frequent post-COVID-19 symptoms.<sup>25,27</sup> As previously stated, the presence and severity of a PD is consistent with a severe inflammatory/microangiopathic process. Similarly, we believe that the persistence of PDs and their association with post-COVID-19 symptoms, D-dimer, CRP, fibrinogen, and CT severity values can be explained by an inflammatory/microangiopathic etiology. The current study results also revealed that the presence of persistent PDs was more common in older patients, which is consistent with previously known data that the presence of post-COVID-19 symptoms increases with age.<sup>28</sup>

Defining the presence of long-term PD raises the question of its clinical importance. Although a relatively small population was included in this current study, all the patients with persistent PDs also had persistent COVID-19 symptoms. Dyspnea, in particular, was found to be strongly associated with PD presence, and can thus be accepted as a finding that confirms the importance of PDs as a secondary sign for the hypoxemia associated with PDs.

There was a significant difference in iodine density values between the consolidations and GGOs. Similar findings have been reported in other studies.<sup>7,14</sup>

Despite the fact that all of the patients were provided with enoxaparin, a significant number of them had long-term PDs. It has been proposed that thrombosis prevention should include not only anticoagulant therapy but also antiplatelet agents.<sup>7,29</sup> The use of aspirin has recently been linked to improved outcomes.<sup>30</sup> When the presence of long-term PDs in patients taking enoxaparin treatment are considered, the presented data can point to the need for an additional antiplatelet agent. In addition, a reconsideration of the dosage of enoxaparin might be needed. None of the patients included in the study had a history of intensive care admission due to COVID-19. Nonetheless, we discovered persistent PDs in some of these patients. Similarly, clinical severity was previously associated with long COVID-19 symptoms; however, young patients with no comorbidities were found to have persistent COVID-19 symptoms as well.<sup>25,31</sup>

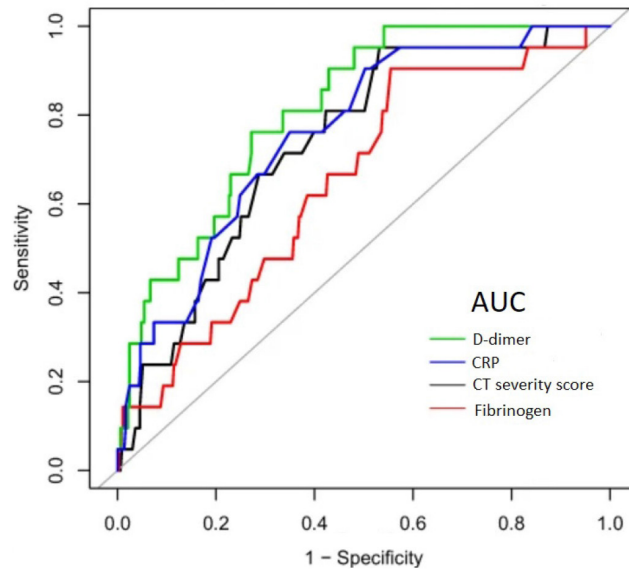


**Figure 9.** Receiver-operating-characteristic curve of the D-dimer, C-reactive protein, computed tomography severity index, and fibrinogen levels to predict future perfusion deficits. AUC; area under the curve; CT; computed tomography; CRP, C-reactive protein.

**Table 3.** Mean values of the parameters at the time of the second DECT scan based on the presence of persistent PD

Parameters	Patients without persistent PD	Patients with persistent PD	P value
D-dimer ( $\mu\text{g/L}$ )	<b>236.17 <math>\pm</math> 78.52</b>	<b>613.18 <math>\pm</math> 76.39</b>	<b>0.005</b>
Fibrinogen (mg/dL)	215.73 $\pm$ 22.91	288.43 $\pm$ 51.39	0.320
CRP (mg/dL)	<b>9.23 <math>\pm</math> 1.46</b>	<b>33.64 <math>\pm</math> 11.4</b>	<b>0.001</b>
Platelet ( $\times 10^9/\text{L}$ )	197.15 $\pm$ 66.18	211.23 $\pm$ 27.28	0.061
Neutrophil count ( $\times 10^9/\text{L}$ )	4.27 $\pm$ 0.97	4.83 $\pm$ 1.34	0.590
White blood cell ( $\times 10^9/\text{L}$ )	5.26 $\pm$ 1.8	6.15 $\pm$ 2	0.700

Bold indicates statistical significance. DECT, dual-energy computed tomography; CRP, C-reactive protein; PD, perfusion deficit.

**Table 4.** Distribution of the frequency of persisting symptoms according to persistent perfusion deficit presence

Symptom	Frequency n (%)		P value
	Patients without persistent PD	Patients with persistent PD	
Dyspnea	0 (0%)	16 (16/16, 100%)	$P < 0.001$
Cough	4 (4/28, 14.2%)	10 (10/16, 62.5%)	$P = 0.003$
Fatigue	8 (8/28, 28.5%)	12 (12/16, 75%)	$P = 0.010$

PD, perfusion deficit.

This study had some limitations, the most notable of which was the relatively small number of patients due to it being a retrospective, single-center study. Further studies using a greater number of patients would be better able to reveal the extent and duration of the sequelae of GGOs and PDs. This study looked at the long-term presence of PDs and their connection to clinical and laboratory data, but it did not investigate the extent and severity of PDs or their connection with other conditions or symptoms. There were insufficient data about the non-pulmonary comorbidities of the patients; as a result, the presence of comorbidities could not be correlated with PDs.

In conclusion, these preliminary results have demonstrated that the presence of GGOs and lung PDs related to COVID-19

pneumonia can last for as long as 80–90 days. In addition, DECT can be used to reveal both long-term parenchymal and perfusion changes. CT severity values, D-dimer, and CRP levels can be useful for the prediction of future persistent PDs. Persistent PDs are commonly seen together with persistent COVID-19 symptoms.

#### Conflict of interest disclosure

The authors declared no conflicts of interest.


#### References

- Zhou F, Yu T, Du R, et al. Clinical course and risk factors for mortality of adult inpatients with COVID-19 in Wuhan, China: a retrospective cohort study. *Lancet*. 2020;395(10229):1054-1062. [\[CrossRef\]](#)
- Ciceri F, Beretta L, Scandroglio AM, et al. Microvascular COVID-19 lung vessels obstructive thromboinflammatory syndrome (MicroCLOTS): an atypical acute respiratory distress syndrome working hypothesis. *Crit Care Resusc*. 2020;22(2):95-97. [\[CrossRef\]](#)
- Middeldorp S, Coppens M, van Haaps TF, et al. Incidence of venous thromboembolism in hospitalized patients with COVID-19. *J Thromb Haemost*. 2020;18(8):1995-2002. [\[CrossRef\]](#)
- Léonard-Lorant I, Delabranche X, Séverac F, et al. Acute pulmonary embolism in patients with COVID-19 at CT angiography and relationship to d-Dimer levels. *Radiology*. 2020.296(3):189-191. [\[CrossRef\]](#)
- Fuld MK, Halaweish AF, Haynes SE, Divekar AA, Guo J, Hoffman EA. Pulmonary perfused blood volume with dual-energy CT as surrogate for

- pulmonary perfusion assessed with dynamic multidetector CT. *Radiology*. 2013;267(3):747-756. [\[CrossRef\]](#)
6. Masy M, Giordano J, Petyt G, et al. Dual-energy CT (DECT) lung perfusion in pulmonary hypertension: concordance rate with V/Q scintigraphy in diagnosing chronic thromboembolic pulmonary hypertension (CTEPH). *Eur Radiol*. 2018;28(12):5100-5110. [\[CrossRef\]](#)
  7. Aydin S, Kantarci M, Karavas E, Unver E, Yalcin S, Aydin F. Lung perfusion changes in COVID-19 pneumonia: a dual energy computerized tomography study. *Br J Radiol*. 2021;94(1125):20201380. [\[CrossRef\]](#)
  8. Lang M, Som A, Mendoza DP, et al. Hypoxaemia related to COVID-19: vascular and perfusion abnormalities on dual-energy CT. *Lancet Infect Dis*. 2020;20(12):1365-1366. [\[CrossRef\]](#)
  9. Ridge CA, Desai SR, Jeyin N, et al. Dual-energy CT pulmonary angiography (DECTPA) quantifies vasculopathy in severe COVID-19 pneumonia. *Radiol Cardiothorac Imaging*. 2020;2(5):e200428. [\[CrossRef\]](#)
  10. Ackermann M, Verleden SE, Kuehnel M, et al. Pulmonary vascular endothelialitis, thrombosis, and angiogenesis in Covid-19. *N Engl J Med*. 2020;383(2):120-128. [\[CrossRef\]](#)
  11. Herrmann J, Mori V, Bates JHT, Suki B. Modeling lung perfusion abnormalities to explain early COVID-19 hypoxemia. *Nat Commun*. 2020;11(1):4883. [\[CrossRef\]](#)
  12. Santamarina MG, Boisier D, Contreras R, Baque M, Volpacchio M, Beddings I. COVID-19: a hypothesis regarding the ventilation-perfusion mismatch. *Crit Care*. 2020;24(1):395. [\[CrossRef\]](#)
  13. Grillet F, Busse-Coté A, Calame P, Behr J, Delabrousse E, Aubry S. COVID-19 pneumonia: microvascular disease revealed on pulmonary dual-energy computed tomography angiography. *Quant Imaging Med Surg*. 2020;10(9):1852-1862. [\[CrossRef\]](#)
  14. Idilman IS, Dizman GT, Duzgun SA, et al. Lung and kidney perfusion deficits diagnosed by dual-energy computed tomography in patients with COVID-19-related systemic microangiopathy. *Eur Radiol*. 2021;31(2):1090-1099. [\[CrossRef\]](#)
  15. Pan F, Ye T, Sun P, et al. Time course of lung changes at chest CT during recovery from coronavirus disease 2019 (COVID-19). *Radiology*. 2020;295(3):715-721. [\[CrossRef\]](#)
  16. Greenhalgh T, Knight M, A'Court C, Buxton M, Husain L. Management of post-acute covid-19 in primary care. *BMJ*. 2020;370:m3026. [\[CrossRef\]](#)
  17. Sudre CH, Murray B, Varsavsky T, et al. Attributes and predictors of Long-COVID: analysis of COVID cases and their symptoms collected by the Covid Symptoms Study App. *medRxiv*. 2020. [\[CrossRef\]](#)
  18. Weidman EK, Plodkowski AJ, Halpenny DF, et al. Dual-energy CT angiography for detection of pulmonary emboli: incremental benefit of iodine maps. *Radiology*. 2018;289(2):546-553. [\[CrossRef\]](#)
  19. Salehi S, Reddy S, Gholamrezanezhad A. Long-term pulmonary consequences of coronavirus disease 2019 (COVID-19): what we know and what to expect. *J Thorac Imaging*. 2020;35(4):87-89. [\[CrossRef\]](#)
  20. Sonnweber T, Sahanic S, Pizzini A, et al. Cardiopulmonary recovery after COVID-19: an observational prospective multicenter trial. *Eur Respir J*. 2020;57(4):2003481. [\[CrossRef\]](#)
  21. Rai DK, Sharma P, Kumar R. Post covid 19 pulmonary fibrosis. Is it real threat? *Indian J Tuberc*. 2020;68(3):330-333. [\[CrossRef\]](#)
  22. Carvalho-Schneider C, Laurent E, Lemaigen A, et al. Follow-up of adults with noncritical COVID-19 two months after symptom onset. *Clin Microbiol Infect*. 2021;27(2):258-263. [\[CrossRef\]](#)
  23. Wang L, He W, Yu X, et al. Coronavirus disease 2019 in elderly patients: characteristics and prognostic factors based on 4-week follow-up. *J Infect*. 2020;80(6):639-645. [\[CrossRef\]](#)
  24. Francone M, Iafrate F, Masci GM, et al. Chest CT score in COVID-19 patients: correlation with disease severity and short-term prognosis. *Eur Radiol*. 2020;30(12):6808-6817. [\[CrossRef\]](#)
  25. Aydin S, Unver E, Karavas E, Yalcin S, Kantarci M. Computed tomography at every step: long coronavirus disease. *Respir Investig*. 2021;59(5):622-627. [\[CrossRef\]](#)
  26. Zhao W, Zhong Z, Xie X, Yu Q, Liu J. Relation between chest CT findings and clinical conditions of coronavirus disease (COVID-19) pneumonia: a multicenter study. *AJR Am J Roentgenol*. 2020;214(5):1072-1077. [\[CrossRef\]](#)
  27. Garrigues E, Janvier P, Kherabi Y, et al. Post-discharge persistent symptoms and health-related quality of life after hospitalization for COVID-19. *J Infect*. 2020;81(6):4-6. [\[CrossRef\]](#)
  28. Carvalho-Schneider C, Laurent E, Lemaigen, et al. Follow-up of adults with noncritical COVID-19 two months after symptom onset. *Clin Microbiol Infect*. 2021;27(2):258-263. [\[CrossRef\]](#)
  29. Thachil J, Srivastava A. SARS-2 coronavirus-associated hemostatic lung abnormality in COVID-19: is it pulmonary thrombosis or pulmonary embolism? *Semin Thromb Hemost*. 2020;46(7):777-780. [\[CrossRef\]](#)
  30. Chow JH, Khanna AK, Kethireddy S, et al. Aspirin use is associated with decreased mechanical ventilation, intensive care unit admission, and in-hospital mortality in hospitalized patients with coronavirus disease 2019. *Anesth Analg*. 2021;132(4):930-941. [\[CrossRef\]](#)
  31. Tenforde MW, Kim SS, Lindsell CJ, et al. Symptom duration and risk factors for delayed return to usual health among outpatients with COVID-19 in a multistate health care systems network - United States, March-June 2020. *MMWR Morb Mortal Wkly Rep*. 2020;69(30):993-998. [\[CrossRef\]](#)



# Peritumoral imaging features of thymic epithelial tumors for the prediction of transcapsular invasion: beyond intratumoral analysis

Jongmin Park\*   
 Byunggeon Park\*   
 Jihoon Hong   
 Jung Guen Cha   
 Kyung Min Shin   
 Jaehee Lee   
 An Na Seo   
 Young Woo Do   
 Won Kee Lee   
 Jae-Kwang Lim 

\*These authors contributed equally to this work.

From the Department of Radiology (J.P., J.H., J.G.C., J-K.L. [✉ limjk@knu.ac.kr](mailto:limjk@knu.ac.kr)), School of Medicine, Kyungpook National University, Daegu, South Korea; Department of Radiology (B.P., K.M.S.), School of Medicine, Kyungpook National University, Kyungpook National University Chilgok Hospital, Daegu, South Korea; Department of Internal Medicine (J.L.), School of Medicine, Kyungpook National University, Daegu, South Korea; Department of Pathology (A.N.S.), School of Medicine, Kyungpook National University, Kyungpook National University Chilgok Hospital, Daegu, South Korea; Department of Thoracic and Cardiovascular Surgery (Y.W.D.), School of Medicine, Kyungpook National University, Daegu, South Korea; Medical Research Collaboration Center in Kyungpook National University Hospital (W.K.L.), School of Medicine, Kyungpook National University, Daegu, South Korea.

Received 25 August 2021; revision requested 13 September 2021; last revision received 18 March 2022; accepted 25 April 2022.



Epub: 03.01.2023

Publication date: 31.01.2023

DOI: 10.4274/dir.2022.21803

## PURPOSE

The purpose of this study was to differentiate cases without transcapsular invasion (Masaoka–Koga stage I) from cases with transcapsular invasion (Masaoka–Koga stage II or higher) in patients with thymic epithelial tumors (TETs) using tumoral and peritumoral computed tomography (CT) features.

## METHODS

This retrospective study included 116 patients with pathological diagnoses of TETs. Two radiologists evaluated clinical variables and CT features, including size, shape, capsule integrity, presence of calcification, internal necrosis, heterogeneous enhancement, pleural effusion, pericardial effusion, and vascularity grade. Vascularity grade was defined as the extent of peritumoral vascular structures in the anterior mediastinum. The factors associated with transcapsular invasion were analyzed using multivariable logistic regression. In addition, the interobserver agreement for CT features was assessed using Cohen's or weighted kappa coefficients. The difference between the transcapsular invasion group and that without transcapsular invasion was evaluated statistically using the Student's *t*-test, Mann–Whitney U test, chi-square test, and Fisher's exact test.

## RESULTS

Based on pathology reports, 37 TET cases without and 79 with transcapsular invasion were identified. Lobular or irregular shape [odds ratio (OR): 4.19; 95% confidence interval (CI): 1.53–12.09;  $P = 0.006$ ], partial complete capsule integrity (OR: 5.03; 95% CI: 1.85–15.13;  $P = 0.002$ ), and vascularity grade 2 (OR: 10.09; 95% CI: 2.59–45.48;  $P = 0.001$ ) were significantly associated with transcapsular invasion. The interobserver agreement for shape classification, capsule integrity, and vascularity grade was 0.840, 0.526, and 0.752, respectively ( $P < 0.001$  for all).

## CONCLUSION

Shape, capsule integrity, and vascularity grade were independently associated with transcapsular invasion of TETs. Furthermore, three CT TET features demonstrated good reproducibility and help differentiate between TET cases with and without transcapsular invasion.

## KEYWORDS

Cancer, computed tomography, thymic epithelial tumor, thymoma, tumor

Thymic epithelial tumors (TETs), originating in thymic epithelial cells, are rare tumors of the anterior (prevascular) mediastinum, with a reported annual incidence ranging from 1.3 to 3.2 per million globally.<sup>1,2</sup> Histologically, various staging systems have been proposed for TETs, including the tumor, nodes, and metastases (TNM) classification of malignant tumors and non-TNM based staging systems.<sup>3</sup> The Masaoka–Koga staging system has been extensively used to classify and stage TETs, including thymomas and thymic carcinomas, based on the extent of tumor invasion.<sup>4,5</sup> In the Masaoka–Koga staging system, the distinction

between stages I and II is based on whether the tumor exhibits transcapsular invasion.<sup>6</sup> Transcapsular invasion is a key factor associated with disease recurrence and patient survival.<sup>7,8</sup> In Masaoka–Koga stages I and II, the 10-year survival rates are 90% and 70% and the average recurrence rates 3% and 11%, respectively.<sup>7</sup> Additionally, prognostic difference can influence the treatment plan for patients with TET.

Enhanced chest computed tomography (CT) is currently the preferred imaging examination for the initial assessment of patients with TET. Although several studies have suggested an association between the Masaoka–Koga staging system and TET CT features, such as tumor size, shape, and internal characteristics, distinguishing between Masaoka–Koga stages I and II remains challenging when using a preoperative chest CT.<sup>9–13</sup> Although pleural effusion, enlarged lymph nodes, and pleural or pulmonary nodules have been assessed in patients with TETs, CT analysis has limited value in the prediction of the Masaoka–Koga stage.<sup>10–14</sup> However, to our knowledge, no studies have analyzed the association between the peritumoral CT features of TETs and the Masaoka–Koga staging system.

Distinguishing between Masaoka–Koga stages I and II preoperatively is crucial for determining an appropriate surgical plan of either complete thymectomy or thymomec-tomy.<sup>15–17</sup> The aim of this study was to retro-spectively investigate the potential factors relating to tumoral and peritumoral CT fea-tures that influence transcapsular invasion using preoperative chest CT.

## Methods

The institutional review board of the participating hospitals approved this retrospec-tive study, and the requirement for patient consent was waived (KNUH 2021-03-004).

### Main points

- The peritumoral computed tomography (CT) features of thymic epithelial tumors (TET) provide additional information for predicting transcapsular invasion.
- The intratumoral and peritumoral CT features of TETs exhibit good reproducibility.
- In patients with TETs, the CT features of shape, capsule integrity, and peritumoral vascularity help differentiate between those with transcapsular invasion and those with-out.

## Study population and computed tomogra-phy acquisition

We retrospectively reviewed 132 pre-operative chest CT scans of patients diag-nosed with TETs between January 2012 and December 2020 from Kyungpook National University Hospital and Kyungpook Nation-al University Chilgok Hospital, Daegu, South Korea. Patients who only underwent chest CT at other hospitals were analyzed using the CT images acquired from these hospitals. All patients underwent chest CT scans within 2 weeks prior to surgery. In total, 16 patients were excluded from our study for the follow-ing reasons: radiation therapy before surgery (3/16, 18.8%), inappropriate pathology re-sults (1/16, 6.3%), definite signs of seeding or the invasion of adjacent structures such as large vessels (4/16, 25%), surgical biopsy without total tumor resection (2/16, 12.5%), non-enhanced CT scans (4/16, 25%), and poor CT imaging quality (2/16, 12.5%). In total, 116 chest CT images from 116 pa-tients were included in this study, some of which originated from our hospital (n = 57) and the remainder from other hospitals (n = 59). According to the Masaoka–Koga stage, there were 37 (31.9%) patients at stage I, 37 (31.9%) at stage IIa, 27 (23.3%) at stage IIb, 13 (11.2%) at stage III, and 2 (1.7%) at stage IV. All CT scans were performed using multiple multidetector CT scanners, including 16-, 64-, 128-, 192-, and 320-slice scanners. The CT scans were obtained in the supine posi-tion at full inspiration using contrast media. Axial and coronal images were reconstruct-ed with a sharp or standard reconstruction kernel. In all patients, the CT examination used slice thicknesses of 1.0–5.0 mm, a slice gap of 1.0–5.0 mm, kVp values in the range of 90–140, CT dose index–volume values in the range of 2.251–62.24, and dose-length product values in the range of 148.1–914. An automatic tube current was used for all patients.

## Clinical variables and computed tomography image analysis

The following clinical data of each pa-tient at admission were collected from the medical records: age, sex, and presence of myasthenia gravis. Two radiologists (J.P. and B.P., with 8- and 5-years' experience in tho-racic radiology, respectively) independently performed a retrospective assessment of TET chest CT features based on enhanced images, including tumor size, shape, capsule integrity, internal necrosis, presence of calci-fication, pleural effusion, pericardial effusion, and vascularity grade, without knowledge of

the clinical and pathological results. We also evaluated non-contrast CT images to evalu-ate the presence of calcification and the het-erogeneous enhancement of TETs.

In case of disagreement, final decisions on the TET features on chest CTs were reached by consensus. Tumor size was defined as the longest diameter among the axial and cor-onal images of the chest CT. Shape was clas-sified as round, oval, lobulated, or irregular, with or without capsule integrity. Capsule integrity was defined as almost complete (smooth or shallow lobulation) and partial complete (deep lobulation or spiculate pro-tuberance).<sup>18,19</sup> Vascularity grade was de-fined as the extent of peritumoral vascular structures in the anterior mediastinum and was evaluated at the largest distribution of the vascular structure among the axial and coronal images in the mediastinal setting [width, 440 Hounsfield units (HU); level, 45 HU] of the enhanced chest CT based on the use of CT images at magnifications in the range of  $\times 3$ – $\times 4$ . It was evaluated subjectively using a 3-point grading scale according to the following criteria: 0, no visible peritu-moral vascular structure; 1, non-measurable slit-like peritumoral vascular structure; 2, measurable peritumoral hypertrophied vas-cular structure, with a size  $> 1$  mm (Figure 1). Representative cases of TETs are presented in Figure 2.

## Pathological analysis

All pathological specimens were formalin fixed, paraffin embedded, and stained with hematoxylin and eosin. All histopathological specimens were classified by two patholo-gists with more than 10-years' experience in line with the fourth edition of the World Health Organization (WHO) classification and Masaoka–Koga staging system.

## Statistical Analysis

Categorical variables were expressed as frequency and percentages (%) and were compared between the two groups using the chi-square or Fisher's exact tests. Con-tinuous variables were tested for normal-ity using the Shapiro–Wilk test. Normally distributed data were presented as mean  $\pm$  standard deviation and analyzed using the Student's t-test; however, non-normally distributed data were expressed as median and interquartile range (IQR) and analyzed using the Mann–Whitney U test. The odds ratio (OR) and confidence interval (CI) from the multivariable logistic analysis were used to identify factors that were independently

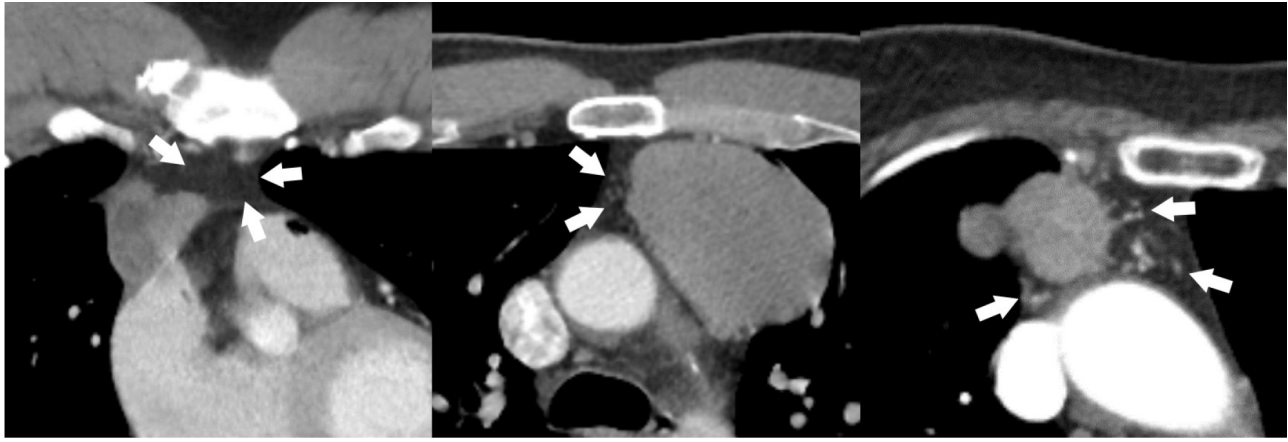


**Figure 1.** Vascularity grade on representative thymic epithelial tumors (TETs). Vascularity grade was assessed as the extent of peritumoral vascular structures in the anterior mediastinum. Vascularity grade 0 signified no visible vascular structure around the TET in the anterior mediastinum (left image). Vascularity grade 1 was defined as the presence of non-measurable, slit-like vascular structures (arrows) around the TET in the anterior mediastinum (middle image). Vascularity grade 2 was defined as the presence of measurable vascular structures with a size  $\geq 1$  mm around the TET in the anterior mediastinum (right image).

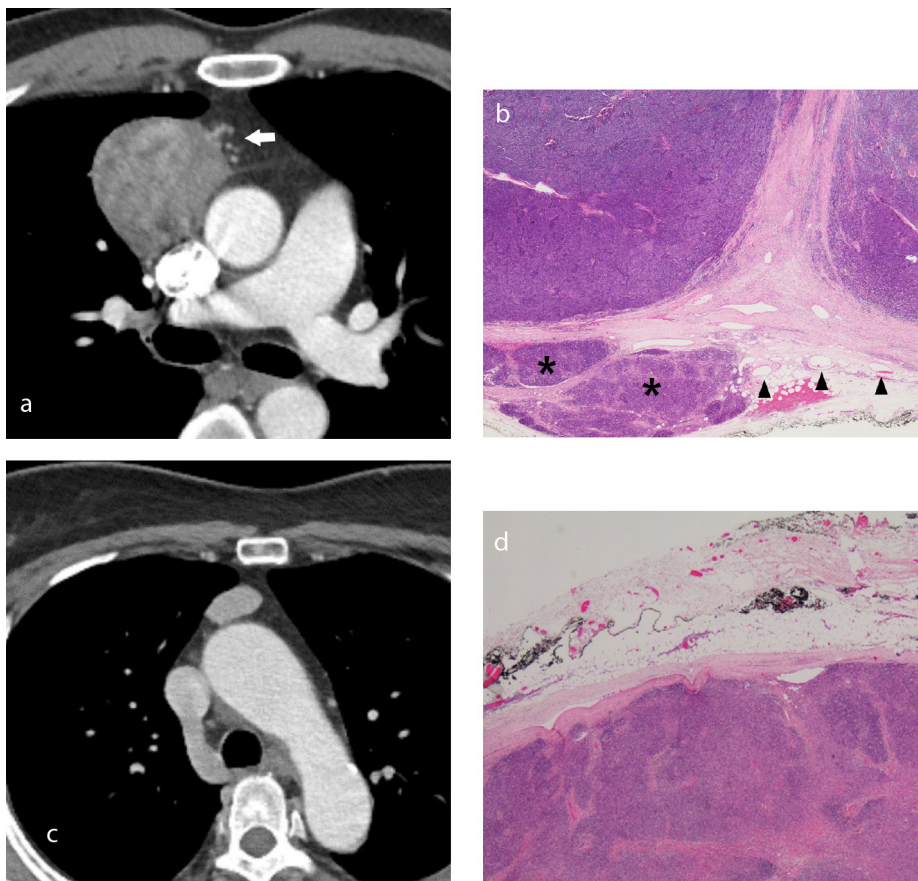


**Figure 2.** Representative cases of thymic epithelial tumors (TETs).

(a) Axial enhanced computed tomography (CT) image of a tumor measuring 7.1 cm, with a round shape, almost complete capsule integrity, and heterogeneous enhancement in the anterior mediastinum in a 48-year-old male patient. The tumor has measurable vascular structures around it (arrow), suggesting vascularity grade 2. (b) Example of a World Health Organization (WHO) type B1 and Masaoka–Koga stage II B TET. Thymoma with pericapsular invasion (asterisks), containing vessels in the pericapsular fat tissue (hematoxylin–eosin, original magnification  $\times 20$ ). (c) Axial enhanced CT image reveals a 2.6-cm oval-shaped mass with almost complete capsule integrity and homogeneous enhancement in the anterior mediastinum in a 58-year-old female patient. The tumor has no visible vascular structure around the TET, suggesting vascularity grade 0. (d) Example of a WHO type AB and Masaoka–Koga stage I TET. The TET is well encapsulated, without transcapsular or pericapsular invasion, and has no visible vessel in the pericapsular fat tissue (hematoxylin–eosin, original magnification  $\times 20$ ).

associated with transcapsular invasion in patients with TETs. Variables with  $P < 0.20$  in the univariable analysis were included as input variables for the multivariable logistic regression analysis using the backward stepwise method. Goodness of fit for the logistic regression model was assessed using the Hosmer–Lemeshow and Omnibus tests. We also constructed a nomogram to predict the transcapsular invasion probability of a TET. Interobserver agreements for TETs on chest CT were assessed using Cohen's or weighted kappa coefficients. For all statistical analyses, the level of significance was set as  $P < 0.05$ . All statistical analyses were performed using SPSS statistical software (IBM, Armonk, NY, USA) and the R software package (version 4.0.3, The R Foundation for Statistical Computing).

## Results

### Clinical variables

The demographics of patients with TETs are listed in Table 1. A total of 116 patients, 52 (44.8%) men and 64 (55.2%) women and a mean age of  $54.4 \pm 12.3$  years, were enrolled in the study. The patients were divided into a group without transcapsular invasion ( $n = 37$ ) and a group with transcapsular invasion ( $n = 79$ ) based on their pathology results. According to the WHO pathological classification, there were 5 (13.5%) patients with type A, 8 (21.6%) with type AB, 10 (27.0%) with type B1, 11 (29.7%) with type B2, 1 (2.7%) with type B3, and 2 (5.4%) with thymic carcinoma in the group without transcapsular invasion. There were 5 (6.3%) patients with type A, 9 (11.4%) with type AB, 19 (24.1%) with type B1, 19 (24.1%) with type B2, 9 (11.4%) with type B3, and 18 (22.8%)



**Table 1.** Clinical demographics and computed tomography image features of patients with thymic epithelial tumors

Characteristic or findings	Total cohort	Masaoka–Koga stage		P value
	(n = 116)	Group without transcapsular invasion (n = 37)	Group with transcapsular invasion (n = 79)	
Age <sup>†</sup>	54.4 ± 12.3	53.0 ± 12.7	55.0 ± 12.2	0.415
Sex				0.151
Male	52 (44.8%)	13 (35.1%)	39 (49.4%)	
Female	64 (55.2%)	24 (64.9%)	40 (50.6%)	
Myasthenia gravis				0.418
No	98 (84.5%)	33 (89.2%)	65 (82.3%)	
Yes	18 (15.5%)	4 (10.8%)	14 (17.7%)	
Size (cm)*	4.8 (2.8, 1.6–12.2)	4.3 (2.8, 1.9–9.5)	4.8 (2.6, 1.6–12.2)	0.438
Shape classification				<0.001
Round, oval	33 (28.4%)	19 (51.4%)	14 (17.7%)	
Lobular, irregular	83 (71.6%)	18 (48.6%)	65 (82.3%)	
Capsule integrity				<0.001
Almost complete	54 (46.6%)	27 (73.0%)	27 (34.2%)	
Partial complete	62 (53.4%)	10 (27.0%)	52 (65.8%)	
Calcification				0.467
No	96 (82.8%)	32 (86.5%)	64 (81.0%)	
Yes	20 (17.2%)	5 (13.5%)	15 (19.0%)	
Internal necrosis				0.380
No	95 (81.9%)	32 (86.5%)	63 (79.7%)	
Yes	21 (18.1%)	5 (13.5%)	16 (20.3%)	
Heterogenous enhancement				0.055
No	57 (49.1%)	23 (62.2%)	34 (43.0%)	
Yes	59 (50.9%)	14 (37.8%)	45 (57.0%)	
Pleural effusion				1.000
No	113 (97.4%)	36 (97.3%)	77 (97.5%)	
Yes	3 (2.6%)	1 (2.7%)	2 (2.5%)	
Pericardial effusion				1.000
No	111 (95.7%)	36 (97.3%)	75 (94.9%)	
Yes	5 (4.3%)	1 (2.7%)	4 (5.1%)	
Vascularity grade				<0.001
0	16 (13.8%)	11 (29.7%)	5 (6.3%)	
1	27 (23.3%)	14 (37.8%)	13 (16.5%)	
2	73 (62.9%)	12 (32.4%)	61 (77.2%)	
WHO				0.066
A	10 (8.6%)	5 (13.5%)	5 (6.3%)	
AB	17 (14.7%)	8 (21.6%)	9 (11.4%)	
B1	29 (25.0%)	10 (27.0%)	19 (24.1%)	
B2	30 (25.9%)	11 (29.7%)	19 (24.1%)	
B3	10 (8.6%)	1 (2.7%)	9 (11.4%)	
Carcinoma	20 (17.2%)	2 (5.4%)	18 (22.8%)	

<sup>†</sup> Variable is shown as mean ± standard deviation. \*Variable is expressed with median, interquartile range, and range in parenthesis. Categorical variables are expressed as frequencies and percentage in parenthesis. WHO, World Health Organization.

with thymic carcinoma in the group with transcapsular invasion. There were no statistically significant differences in age, sex, or the presence of myasthenia gravis between the two groups ( $P > 0.05$  for all).

### Computed tomography image features

The TETs in the group with transcapsular invasion were more likely to have lobular or irregular shapes (65/79, 82.3%) than those in the group without (18/37, 48.6%) ( $P < 0.001$ ). A significant difference was observed for capsule integrity ( $P < 0.001$ ). The percentage of TETs with almost complete capsule integrity was higher in the group without transcapsular invasion (27/37, 73%) than in the group with transcapsular invasion (27/79, 34.2%). A significant difference was also observed for vascularity grade ( $P < 0.001$ ). The percentage of TETs with vascularity grade 2 was higher in the group with transcapsular invasion (61/79, 77.2%) than in the group without (12/37, 32.4%). The median size of TETs was 4.3 (IQR = 2.8; range, 1.9–9.5) in the group without transcapsular invasion and 4.8 (IQR = 2.6; range, 1.6–12.2) in the group with transcapsular invasion ( $P = 0.438$ ). Other CT image features, such as internal necrosis, heterogeneous enhancement, presence of calcification in the TET, pleural effusion, and pericardial effusion, were not significantly different between the two groups ( $P > 0.05$  for all).

### Interobserver agreement

Table 2 presents the interobserver agreement for the TET CT image evaluation of both observers. The shape classification yielded almost perfect agreement, with a Cohen's kappa value of 0.840 (95% CI: 0.761–0.893;  $P < 0.001$ ). Capsule integrity yielded moderate agreement, with a Cohen's kappa value of 0.526 (95% CI: 0.292–0.682;  $P < 0.001$ ). The vascularity grade indicated substantial agreement, with a weighted kappa value of 0.752 (95% CI: 0.662–0.841;  $P < 0.001$ ). Other

variables (calcification, internal necrosis, and heterogeneous enhancement) also yielded almost perfect agreement (Cohen's kappa value  $> 0.9$  for all;  $P < 0.001$ ).

### Univariable and multivariable analyses for transcapsular invasion

Table 3 lists the results of the univariable and multivariable analyses used to assess the association between transcapsular invasion and the clinical and radiological features on the preoperative chest CT in patients with TETs. The result of the Hosmer–Lemeshow test was  $P = 0.681$  and that of the Omnibus test was  $P < 0.001$ , indicating that the logistic regression model had a good fit. In the univariable analysis, lobular or irregular shape (OR = 4.90; 95% CI: 2.09–11.90;  $P < 0.001$ ), partial complete capsule integrity (OR = 5.20; 95% CI: 2.26–12.79;  $P < 0.001$ ), and vascularity grade 2 (OR = 11.18; 95% CI: 3.44–41.35;  $P < 0.001$ ) were significantly associated with transcapsular invasion. The variables of sex, shape, capsule integrity, heterogeneous enhancement, and vascularity grade were included in the multivariable analysis using backward stepwise selection.

The multivariable analyses indicated that shape, capsule integrity, and vascularity grade were consistently associated with transcapsular invasion. A lobular or irregular shape had a 4.19 times higher risk (95% CI: 1.53–12.09;  $P = 0.006$ ) than a round or oval shape of transcapsular invasion. In addition, partial complete capsule integrity had a 5.03 times higher risk (95% CI: 1.85–15.13;  $P = 0.002$ ) than almost complete capsule integrity. Vascularity grade 2 had a 10.09 times higher risk (95% CI: 2.59–45.48;  $P = 0.001$ ) than vascularity grade 0. Based on the multivariable logistic regression analysis, a graphical representation of a nomogram was constructed to predict transcapsular invasion in patients with TETs (Figure 3).

## Discussion

The main results of our study revealed that shape classification, capsule integrity, and vascularity grade were independently associated with transcapsular invasion in patients with TETs. The interobserver agreements for shape classification, capsule integrity, and vascularity grade suggest that TET CT features have good reproducibility and help predict transcapsular invasion.

Based on the results, we assumed that vascularity grade reflects the degree of vascular proliferation in the anterior mediastinum. The vascular structures around the TETs were also confirmed in the pathological findings. Angiogenesis is indispensable for a tumor's growth.<sup>20</sup> Tomita et al.<sup>21</sup> demonstrated a significant correlation between tumor angiogenesis and invasiveness in patients with TETs. However, there are no studies on the growth of blood vessels around the TETs. The clinical implications of peritumoral vascularity on malignant tumors have been reported. In breast cancer, adjacent vessel signs, defined as the presence of peritumoral vessels that lead to a tumor, were significantly associated with the malignancy of a breast lesion and tumoral neovascularization; this finding was suggested as a possible explanation of the phenomenon. Additionally, adjacent vessel signs were significantly associated with malignancy and were observed more frequently in invasive cancers than in preinvasive cancers.<sup>22,23</sup> Zhang et al.<sup>24</sup> demonstrated that peritumoral vascularity was significantly associated with more aggressive subtypes of renal cell carcinoma. Therefore, the authors believe that peritumoral vascularity can represent the neovascularization of the tumor and may be associated with the invasiveness of TETs.

A few studies have reported interobserver agreements for shape, calcification, cystic or necrotic changes, enhancement

**Table 2.** Interobserver agreement for computed tomography features of thymic epithelial tumors

Variable	Agreement	Assessment
Shape classification	0.840 (0.761–0.893, $P < 0.001$ ) <sup>a</sup>	Almost perfect
Capsule integrity	0.526 (0.292–0.682, $P < 0.001$ ) <sup>a</sup>	Moderate
Calcification	0.984 (0.976–0.989, $P < 0.001$ ) <sup>a</sup>	Almost perfect
Internal necrosis	0.904 (0.856–0.935, $P < 0.001$ ) <sup>a</sup>	Almost perfect
Heterogeneous enhancement	0.913 (0.870–0.941, $P < 0.001$ ) <sup>a</sup>	Almost perfect
Vascularity grade	0.752 (0.662–0.841, $P < 0.001$ ) <sup>b</sup>	Substantial

<sup>a</sup>Cohen's Kappa value (95% confidence interval), <sup>b</sup>weighted Kappa value (95% confidence interval).

**Table 3.** Univariable and multivariable logistic regression analyses to assess the association between transcapsular invasion and clinical and radiological features on preoperative chest computed tomography in patients with thymic epithelial tumors

Characteristic or findings	Univariable logistic regression analysis			Multivariable logistic regression analysis		
	OR	95% CI	P value	OR	95% CI	P value
Age	1.01	0.98, 1.05	0.412			
Sex*			0.153	Stepwise eliminated		
Male		Reference				
Female	1.80	0.81, 4.11				
Myasthenia gravis			0.343			
No		Reference				
Yes	1.78	0.58, 6.65				
Size, cm	1.07	0.9, 1.3	0.457			
Shape classification*			<0.001			
Round, oval		Reference			Reference	
Lobular, irregular	4.90	2.09, 11.9		4.19	1.53, 12.09	0.006
Capsule integrity*			<0.001			
Almost complete		Reference			Reference	
Partial complete	5.20	2.26, 12.79		5.03	1.85, 15.13	0.002
Calcification			0.469			
No		Reference				
Yes	1.50	0.53, 4.94				
Internal necrosis			0.383			
No		Reference				
Yes	1.63	0.58, 5.33				
Heterogenous enhancement			0.057	Stepwise eliminated		
No		Reference				
Yes	2.17	0.99, 4.93				
Pleural effusion			0.957			
No		Reference				
Yes	0.94	0.09, 20.51				
Pericardial effusion			0.566			
No		Reference				
Yes	1.92	0.27, 38.29				
Vascularity grade*						
0		Reference			Reference	
1	2.04	0.57, 7.99	0.281	1.41	0.31, 6.67	0.657
2	11.18	3.44, 41.35	<0.001	10.09	2.59, 45.48	0.001

OR, odds ratio; CI, confidence interval; \*variables with P value <0.20 in the univariable analysis were included in the multivariable analysis.

patterns, enhancement degree, and the margin in TETs.<sup>25,26</sup> These findings are consistent with the results of the present study with the exception of shape classification. Although Yamazaki et al.<sup>26</sup> found that the interobserver agreement for shape classification demonstrated moderate agreement with a kappa value of 0.55, our interobserver agreement for shape classification yielded an almost perfect agreement, with a kappa value of 0.840. These differences are related to whether lobulated and irregular TET shapes

were categorized in the same group when shape groups were classified. In the present study, classifying lobulated and irregular TET shapes in the same group was also associated with transcapsular invasion and yielded improved reproducibility.

Although additional validation is needed, the constructed nomogram can help predict transcapsular invasion in patients with TETs using preoperative chest CT. Complete thymectomy, which includes the complete removal of the thymus and surrounding me-

diastinal fat, is a standard method for treating TETs,<sup>15,17</sup> especially in patients at stage II or higher and those with concomitant myasthenia gravis. Thymomectomy, defined as the resection of the thymoma without perithymic tissue, is performed routinely on patients with TETs at Masaoka-Koga stage I. Thymomectomy is a less invasive procedure and is associated with a shorter operative time and hospitalization period.<sup>27,28</sup> Therefore, it is crucial to distinguish Masaoka-Koga stage I (no transcapsular invasion) from

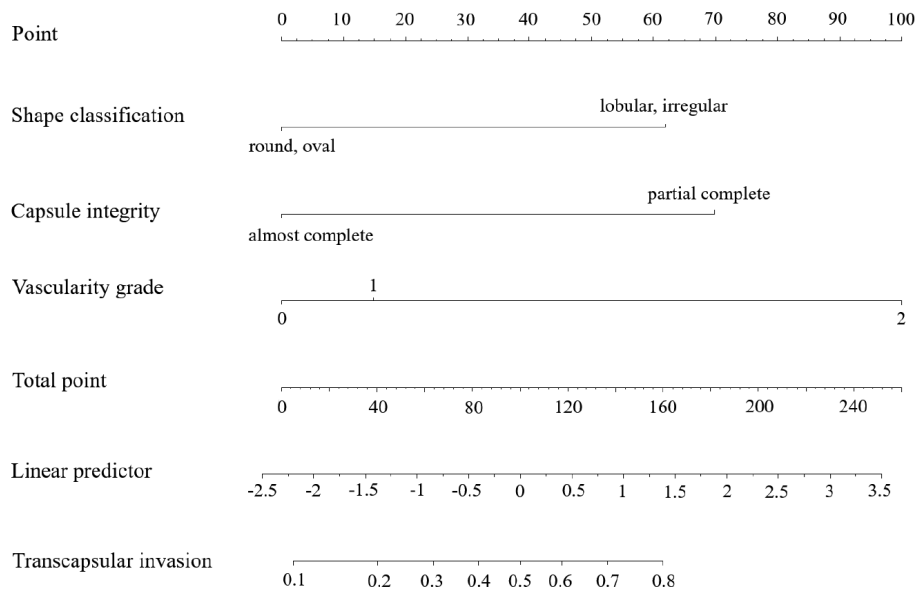


**Figure 3.** Nomogram to predict the likelihood of transcapsular invasion in patients with thymic epithelial tumors. The first row (point) is the point assignment for each computed tomography feature. Rows 2–4 represent the variables included in the model. The assigned points for three variables have been summed, and the total is shown in row 5 (total point). Once the total point is located, a vertical line is drawn between the fifth and final row (predicted probability of transcapsular invasion).

Masaoka–Koga stage II (or higher) in patients with TETs before surgery.

Our study has several limitations. First, this study was a retrospective analysis using clinical data from two institutions. Consequently, there may be an unintended selection bias. Second, we applied vascularity grade, which is a subjective, not quantitative, variable, in the prediction of the transcapsular invasion of TETs. We believe that the impact was minimal because the vascularity grades identified by the two experienced thoracic radiologists were in agreement. Third, we analyzed the CT features of TETs produced using various CT scanners with different CT protocols and contrast medium techniques, which could affect the CT features. However, we considered that the impact was minimal because the patients with poor CT image quality were excluded. We also assumed that the visual analysis of the TET CT images was minimally affected by the chest CT protocol, but additional research is needed on the qualitative analyses of TETs using CT images performed with standardized protocols. Finally, although vascularity grade reflects the extent of the peritumoral vascular structure, there is a lack of evidence to explain the association between peritumoral vascularity and tumor invasiveness. Therefore, an additional study is needed to clarify this association.

In conclusion, lobular or irregular shapes with partial complete capsule integrity and

vascularity grade 2 exhibited good reproducibility outcomes and were independent predictors of transcapsular invasion on chest CT in patients with TETs. Therefore, the TET CT features of shape classification, capsule integrity, and vascularity grade can help identify transcapsular invasion in patients with TETs.

#### Conflict of interest disclosure

The authors declared no conflicts of interest.

#### References

1. Carter BW, Tomiyama N, Bhora FY, et al. A modern definition of mediastinal compartments. *J Thorac Oncol.* 2014;9(9 Suppl 2):97-101. [\[CrossRef\]](#)
2. de Jong WK, Blaauwgeers JL, Schaapveld M, Timens W, Klinkenberg TJ, Groen HJ. Thymic epithelial tumours: a population-based study of the incidence, diagnostic procedures and therapy. *Eur J Cancer.* 2008;44(1):123-130. [\[CrossRef\]](#)
3. Filosso PL, Ruffini E, Lausi PO, Lucchi M, Oliaro A, Detterbeck F. Historical perspectives: the evolution of the thymic epithelial tumors staging system. *Lung Cancer.* 2014;83(2):126-132. [\[CrossRef\]](#)
4. Masaoka A, Monden Y, Nakahara K, Tanioka T. Follow-up study of thymomas with special reference to their clinical stages. *Cancer.* 1981;48(11):2485-2492. [\[CrossRef\]](#)

5. Koga K, Matsuno Y, Noguchi M, et al. A review of 79 thymomas: modification of staging system and reappraisal of conventional division into invasive and non-invasive thymoma. *Pathol Int.* 1994;44(5):359-367. [\[CrossRef\]](#)
6. Jackson MW, Palma DA, Camidge DR, et al. The impact of postoperative radiotherapy for thymoma and thymic carcinoma. *J Thorac Oncol.* 2017;12(4):734-744. [\[CrossRef\]](#)
7. Detterbeck FC. Evaluation and treatment of stage I and II thymoma. *J Thorac Oncol.* 2010;5(10 Suppl 4):318-322. [\[CrossRef\]](#)
8. Roden AC, Yi ES, Jenkins SM, et al. Modified Masaoka stage and size are independent prognostic predictors in thymoma and modified Masaoka stage is superior to histopathologic classifications. *J Thorac Oncol.* 2015;10(4):691-700. [\[CrossRef\]](#)
9. Zhao Y, Chen H, Shi J, Fan L, Hu D, Zhao H. The correlation of morphological features of chest computed tomographic scans with clinical characteristics of thymoma. *Eur J Cardiothorac Surg.* 2015;48(5):698-704. [\[CrossRef\]](#)
10. Qu YJ, Liu GB, Shi HS, Liao MY, Yang GF, Tian ZX. Preoperative CT findings of thymoma are correlated with postoperative Masaoka clinical stage. *Acad Radiol.* 2013;20(1):66-72. [\[CrossRef\]](#)
11. Priola AM, Priola SM, Di Franco M, Cataldi A, Durando S, Fava C. Computed tomography and thymoma: distinctive findings in invasive and noninvasive thymoma and predictive features of recurrence. *Radiol Med.* 2010;115(1):1-21. [\[CrossRef\]](#)
12. Tomiyama N, Müller NL, Ellis SJ, et al. Invasive and noninvasive thymoma: distinctive CT features. *J Comput Assist Tomogr.* 2001;25(3):388-393. [\[CrossRef\]](#)
13. Marom EM, Milito MA, Moran CA, et al. Computed tomography findings predicting invasiveness of thymoma. *J Thorac Oncol.* 2011;6(7):1274-1281. [\[CrossRef\]](#)
14. Shen Y, Gu Z, Ye J, Mao T, Fang W, Chen W. CT staging and preoperative assessment of resectability for thymic epithelial tumors. *J Thorac Dis.* 2016;8(4):646-655. [\[CrossRef\]](#)
15. Gu Z, Fu J, Shen Y, et al. Thymectomy versus tumor resection for early-stage thymic malignancies: a Chinese Alliance for Research in Thymomas retrospective database analysis. *J Thorac Dis.* 2016;8(4):680-686. [\[CrossRef\]](#)
16. Onuki T, Ishikawa S, Iguchi K, et al. Limited thymectomy for stage I or II thymomas. *Lung Cancer.* 2010;68(3):460-465. [\[CrossRef\]](#)
17. Miller SJ. The National Comprehensive Cancer Network (NCCN) guidelines of care for nonmelanoma skin cancers. *Dermatol Surg.* 2000;26(3):289-292. [\[CrossRef\]](#)
18. Sadohara J, Fujimoto K, Müller NL, et al. Thymic epithelial tumors: comparison of CT and MR imaging findings of low-risk thymomas, high-risk thymomas, and thymic carcinomas. *Eur J Radiol.* 2006;60(1):70-79. [\[CrossRef\]](#)

19. Hu YC, Wu L, Yan LF, et al. Predicting subtypes of thymic epithelial tumors using CT: new perspective based on a comprehensive analysis of 216 patients. *Sci Rep.* 2014;4(1):6984. [\[CrossRef\]](#)
20. Viallard C, Larrivé B. Tumor angiogenesis and vascular normalization: alternative therapeutic targets. *Angiogenesis.* 2017;20(4):409-426. [\[CrossRef\]](#)
21. Tomita M, Matsuzaki Y, Edagawa M, et al. Correlation between tumor angiogenesis and invasiveness in thymic epithelial tumors. *J Thorac Cardiovasc Surg.* 2002;124(3):493-498. [\[CrossRef\]](#)
22. Dietzel M, Baltzer PA, Vag T, et al. The adjacent vessel sign on breast MRI: new data and a subgroup analysis for 1,084 histologically verified cases. *Korean J Radiol.* 2010;11(2):178-186. [\[CrossRef\]](#)
23. Fischer DR, Malich A, Wurdinger S, Boettcher J, Dietzel M, Kaiser WA. The adjacent vessel on dynamic contrast-enhanced breast MRI. *AJR Am J Roentgenol.* 2006;187(2):147-151. [\[CrossRef\]](#)
24. Zhang J, Lefkowitz RA, Wang L, et al. Significance of peritumoral vascularity on CT in evaluation of renal cortical tumor. *J Computer Assis Tomogr.* 2007;31(5):717-723. [\[CrossRef\]](#)
25. Chen X, Feng B, Li C, et al. A radiomics model to predict the invasiveness of thymic epithelial tumors based on contrast-enhanced computed tomography. *Oncol Rep.* 2020;43(4):1256-1266. [\[CrossRef\]](#)
26. Yamazaki M, Oyanagi K, Umezu H, et al. Quantitative 3D shape analysis of CT images of thymoma: a comparison with histological types. *AJR Am J Roentgenol.* 2020;214(2):341-347. [\[CrossRef\]](#)
27. Tseng YC, Hsieh CC, Huang HY S, et al. Is thymectomy necessary in nonmyasthenic patients with early thymoma? *J Thorac Oncol.* 2013;8(7):952-958. [\[CrossRef\]](#)
28. Nakagawa K, Yokoi K, Nakajima J, et al. Is thymectomy alone appropriate for stage I (T1N0M0) thymoma? Results of a propensity-score analysis. *Ann Thorac Surg.* 2016;101(2):520-526. [\[CrossRef\]](#)



# The spectrum of computed tomography findings in blunt trauma of the subclavian/axillary artery: a pictorial essay

Emanuele Barabino

Diego Ivaldi

Giulia Pittaluga

Arianna Nivolli

Matteo Arnò

Paolo Gazzo

## ABSTRACT

Traumatic injuries of the subclavian and axillary arteries are uncommon but have high morbidity and mortality. In contrast to penetrating injuries, which are often lethal, blunt injuries present a wide and heterogeneous spectrum of imaging findings. If a vessel tear or transection is a life-threatening circumstance, minor injuries might be overlooked in an emergency setting but could cause or aggravate the functional loss of a limb. The aim of this pictorial essay is to acquaint radiologists with the spectrum of imaging findings that could be encountered during the radiological evaluation of the subclavian/axillary artery (SAA) in trauma patients and offer tips and tricks to improve the diagnostic workup of patients with suspected blunt SAA injuries.

## KEYWORDS

Subclavian artery, axillary artery, trauma, computed tomography, emergency radiology

Injuries to the subclavian/axillary artery (SAA) are relatively uncommon, accounting for 5% of traumatic arterial injuries.<sup>1</sup> The SAA can be injured by penetrating objects that disrupt the integrity of the skin from the outside or by blunt trauma. Penetrating traumas are mostly described in series from the United States and are relatively uncommon in European or Asian papers.<sup>2</sup> Penetrating injuries of the SAA are mostly caused by gunshot or stab wounds and are often lethal. They will not be discussed in this paper.<sup>1,3</sup>

Blunt SAA injuries (BSAAs) are uncommon, representing 0.4–5%<sup>4,5</sup> of traumatic vascular injuries, and they are mostly determined by high-energy traumas,<sup>6</sup> commonly high-speed road traffic accidents.<sup>2,4</sup> The specific mortality rate for BSAAs remains difficult to establish, as most of the published data do not report the type of injury nor distinguish blunt from penetrating trauma. Papers that have reported detailed mortality for penetrating and blunt injuries agree that BSAAs present a lower mortality rate (blunt 0–24%, penetrating 20–38%).<sup>7–9</sup> However, BSAAs are heterogeneous, and most patients with severe injuries sustained high-energy trauma and presented in shock with multiple associated lesions. Therefore, the specific mortality rate for BSAAs is challenging to determine.

BSAAs can present with a wide imaging spectrum. In some cases, the clinical and radiological presentation is very subtle. Therefore, it could easily remain unnoticed, particularly in a polytrauma setting, resulting in a higher morbidity rate when compared with penetrating injuries.<sup>5</sup> Morbidity after trauma to the thoracic outlet or upper limb depends on multiple factors, including an associated brachial plexus injury. Maintaining an adequate arterial supply to nerve roots is critical for the healing process and outcomes of surgical management.<sup>10</sup> The imaging modality of choice in trauma patients and the diagnostic workup of traumatic injuries of the SAA is computed tomography (CT). In a systematic review, Jens et al.<sup>11</sup> reported a pooled sensitivity and specificity of 96.2% and 99.2%, respectively, in the diagnosis of traumatic arterial injury of the upper and lower limb. Digital subtraction angiography is mainly used for therapeutic purposes but, in some cases, could be used to investigate unclear CT

From the Department of Interventional Angiography (E.B. ✉ emanuele.barabino@gmail.com, D.I., G.P., A.N., M.A., P.G.), Ospedale Santa Corona, Pietra Ligure, Italia.

Received 21 December 2021; revision requested 24 January 2022; last revision received 21 February 2022; accepted 16 March 2022.



Epub: 02.01.2023

Publication date: 31.01.2023

DOI: 10.5152/dir.2022.211271

findings. Depending on the type of injury, BSAAs can be treated either using an endovascular (stent or stent grafts) or a surgical approach.<sup>9</sup>

The aim of this pictorial review is to illustrate the spectrum of CT findings in SAA blunt trauma and show tips and tricks to simplify the diagnostic workup of patients with suspected BSAAs.

## Anatomical considerations

The subclavian and axillary arteries are the major blood supply of the upper limbs and posterior cerebral fossa. In left-sided aortic arches, the right subclavian artery originates from the brachiocephalic trunk (innominate artery), while the left subclavian artery emerges from the aorta (see Figure 1a). This pattern is appreciable in 70–80% of patients.<sup>12</sup> Anatomical variants are uncommon but should be described to optimize treatment: in 0.16–4.4% of cases, the right subclavian artery originates from the distal part of the aortic arch<sup>13–15</sup> and typically presents a retro-esophageal course (see Figure 1b). Less frequent variants (incidence <1%) include a common carotid trunk (see Figure 1c), in which both the subclavian arteries arise directly from the aortic arch, and the right aortic arch (see Figure 1d), in which the pattern of emergence of the vessels from the aorta is mirrored.<sup>16</sup> The branching pattern of the subclavian artery from the aortic arch is essential in planning an endovascular approach (i.e., the choice of catheter and the anterograde/retrograde/rendezvous approach). Both subclavian arteries emerge through the thoracic outlet, where they come in contact with the clavicle, the first rib, and the scalene muscles. They then pass behind the clavicle until the outer margin of the first rib, where they become the axillary artery. The axillary artery is the continuation of the subclavian artery beyond the outer border of the first rib until the inferior border of the teres major,<sup>17</sup> where

it becomes the brachial artery. The anatomy of the axillary artery is quite consistent, and anatomical variants are rare; in 2% of cases, the ulnar or radial artery might originate from the axillary artery.<sup>18</sup> A high origin of the radial or ulnar artery should be included in the radiological report, as it could influence the choice for endovascular arterial access (radial or brachial). A high origin of the radial artery might preclude its use and influence the choice of treatment, as the involvement of the origin of the radial/ulnar, depending on the branching pattern in the forearm, may preclude the employment of stent grafts and make a surgical approach mandatory.

## Mechanisms of injury

Bony (clavicle and ribs), muscular (scalene and subclavian muscles), and fascial (deep cervical fascia) structures that surround the subclavian artery protect it from trauma. The axillary artery is protected by the humerus laterally. Direct, blunt injuries to the SAA are usually determined by high-energy forces that disrupt the integrity of the thoracic outlet, such as falls from heights, road traffic accidents, and motorcycle collisions.<sup>19,20</sup> Bone fractures should be carefully evaluated because these can indirectly indicate the forces applied to subclavian or axillary arteries (see Figures 2, 3a, and 4b). Moreover, the subclavian artery is fixed at the thoracic outlet but highly mobile at its distal end and could be damaged by relatively low-energy impacts that produce extreme shear forces (i.e., a fall on an outstretched arm) that create an excessive strain load on the vessel.<sup>4,21</sup> Injury to the subclavian artery commonly involves the distal segment of the vessel.<sup>19</sup>

## Clinical features

Clinical evaluation is essential in assessing BSAAs because the recognition of the injured arm will permit the tailoring of imaging. The clinical appearance of BSAAs depends on the type of injury. Clinical signs of arterial injury of the extremities have been divided into hard signs (absent distal pulse, distal ischemia, active hemorrhage, large hematoma, bruit, or thrill) and soft signs (history of hemorrhage, small hematoma, hypotension, or deficit of the associated peripheral nerve). However, only 50% of patients present with hard signs of traumatic injury of the SAA.<sup>22</sup> The presence of an arterial pulse cannot rule out a BSAAI, as the collateral circulation could efficiently compensate for the occlusion of the main trunk.<sup>1</sup> The clinical presentation of BSAAs often overlaps with

brachial plexus injury, making clinical evaluation more arduous. Vascular injuries should always be excluded in the presence of an injury to the brachial plexus (pain, numbness, loss of feeling, or paralysis of the arm).<sup>10</sup>

## CT technique

Managing the CT evaluation of BSAAs could be challenging, as these lesions commonly present in polytrauma settings. Integrating an appropriate evaluation of the upper limbs in a polytrauma protocol could be difficult, particularly if the BSAAI is not clinically suspected (i.e., minor lesions such as intimal tears or a non-occluding dissection) or in the case of unconscious patients. Moreover, polytrauma CT protocols are not completely standardized and could vary on a regional basis (i.e., employment of enhanced and venous phases or split bolus). Therefore this section will focus on methods to customize the exam in case of suspected BSAAI.

## Venous access

During trauma diagnostic workups, a contrast medium is typically injected into a vein of the arm or through a central venous catheter in the jugular or subclavian vein. As CT angiography necessitates elevated flow rates (3.5–5 mL/s), the bolus of the contrast medium is usually very dense and could generate beam-hardening artifacts in the neck, reducing the quality and diagnostic potential of the exam (see Figure 5a). In the case of clinically suspected injury to the SAA, the venous access for the contrast medium injection should be in the contralateral arm or a lower extremity.<sup>20</sup>

## CT acquisition

The subclavian artery is included in the CT acquisition of the thorax, but the axillary artery may not be, depending on the position of the arm. Moreover, the evaluation of the entire limb is critical in the management of BSAAs to estimate distal vascularization (distal ischemia and the presence of a viable brachial artery for an endovascular approach), and the entire arm should always be included, if possible, in the acquisition. According to the guidelines of the European Society of Emergency Radiology for polytrauma patients,<sup>23</sup> arms could be positioned down to optimize time (Time/Precision Protocol) or up to reduce radiation exposure (Dose Protocol), and the extremities should not be included in whole-body CT protocols. However, if there is a

### Main points

- Blunt subclavian/axillary artery injuries (BSAAs) are uncommon lesions with high morbidity and mortality rates.
- The spectrum of imaging findings of BSAAs is very wide and heterogeneous, but even minor lesions, when overlooked, might have detrimental effects on the functioning and healing of a limb.
- Prompt and correct identification and description of BSAAs reduce time-to-treatment and limb-threatening complications.

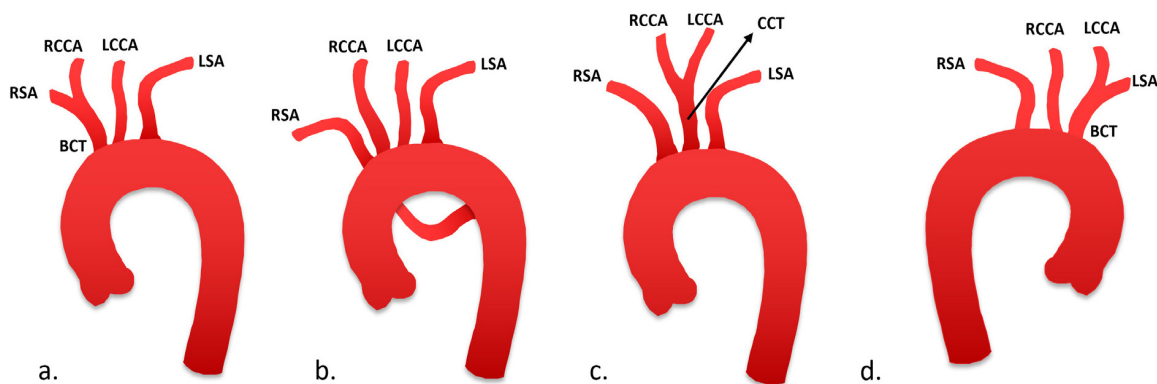


**Figure 1.** Branching patterns of the subclavian artery from the aortic arch. (a) The most typical pattern in which the aorta is left-sided, and the BCT (or innominate artery), the LCCA, and the LSA emerge from the aortic arch. (b) Aberrant RSA or “arteria lusoria”. The RSA emerges from the distal part of the aortic arch and presents a retroesophageal course (c) CCT. In this case, the common carotid arteries emerge from a small carotid trunk, and the subclavian artery originates from the aortic arch on both sides. (d) Right-sided aortic arch. The LSA originates from the left BCT, and the RSA emerges from the distal part of the aortic arch but does not present a retroesophageal course. BCT, brachiocephalic trunk; RSA, right subclavian artery; RCCA, right common carotid artery; LCCA, left common carotid artery; LSA, left subclavian artery; CCT, common carotid trunk.

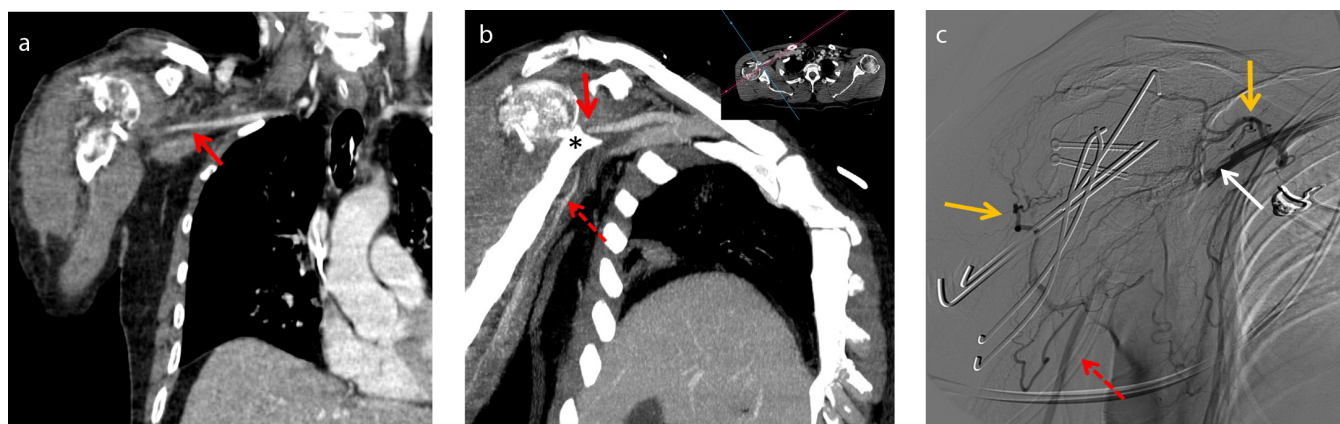


**Figure 2.** Dissection and occlusion. A 54-year-old male patient who sustained a fracture of the humeral head after a road traffic accident. (a) Coronal-reconstructed computed tomography (CT) angiography demonstrated a faint axillary artery but no contrast medium extravasation. (b) A coronal-reformatted maximum intensity projection reconstruction of the venous phase demonstrated an entrapment of the axillary artery (red arrow) within the bony fragments of the humerus (\*) and the brachial artery (red dotted arrow) refilled by collateral vessels. This injury was overlooked on the admission CT. The patient underwent surgery to reduce the fracture of the humeral head the day after the accident. After 15 days, the patient was dismissed from the intensive care unit and described functional limitation of the right upper limb. (c) Angiography confirmed the CT findings and demonstrated complete occlusion of the axillary artery (red arrow), probably due to dissection: part of the dissection flap and floating thrombotic material are appreciable at the proximal end of the occlusion (white arrow). In this image, the large and efficient collateral circulation of the upper limb is appreciable and more evident around the glenohumeral joint (yellow arrows).

high suspicion of a BSAAI, the limb should be positioned alongside the body, or an arm can be placed on the patient’s abdomen to redistribute possible streaking artifacts.<sup>23</sup> Some authors suggest positioning the arm of the patient with a suspected arterial injury of the upper limb over the head in prone decubitus (“superman position”).<sup>24</sup> The shoulders of the patient should not touch the gantry to avoid possible artifacts (see Figure 5b).

CT angiography is fundamental to evaluating the SAA: excellent vascular opacification can be obtained with a compacted and high-density bolus that necessitates vascular accesses with a high rate of infusion.<sup>6</sup> An enhanced phase may be performed if active

bleeding is suspected to distinguish bony fragments or calcification from active extravasation. Dual-energy CT acquisition during the arterial phase permits the production of virtual, non-enhanced reconstructions and can be employed to avoid unnecessary radiation exposure. In our opinion, a venous phase should always be performed in case of suspected BSAAI: dissection and occlusion could cause a low run-off in the vessels, both upstream and downstream of the injury, which could give the impression of reduced vascularization of the limb or generate false radiological signs of occlusion (pseudo-thrombus).<sup>24,25</sup> Even in cases of rupture or transection, we suggest a venous phase because the hematoma could determine a

mass effect on the vessel (see Figure 6) that slows down the blood flow. Moreover, in the case of reduced flow, a venous phase is fundamental in determining the distal vascularization of the limb and estimating bleeding activity.<sup>23</sup>

### CT post-processing

The axial plane offers a poor depiction of the subclavian artery due to its horizontal and slightly curved course. The course of the axillary artery depends on the position of the arm during CT acquisition. A proper evaluation of the subclavian and axillary arteries should include coronal and sagittal reformatting, as well as non-orthogonal planes. Maximum intensity projection reconstructions



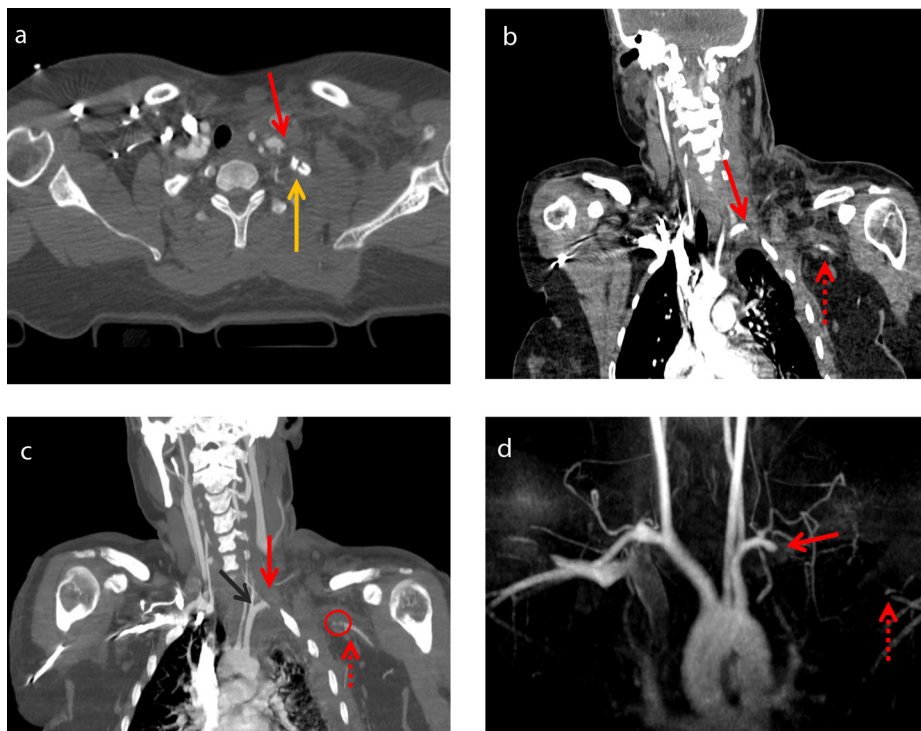


**Figure 3.** Dissection and occlusion. A 26-year-old female patient who was involved in a motor vehicle accident and sustained an impact to the left shoulder. The patient presented with complete palsy of the left upper limb. (a, b) Computed tomography angiography with maximum intensity projection reconstructions. (c) Occlusion of the left subclavian artery (red arrow) was demonstrated; slight, retrograde perfusion of the axillary artery is appreciable (red dotted arrow). Small defects are visible in the distal portion of the subclavian artery (red circle). In this case, the mechanism of injury was possibly a dissection downstream of the origin of the vertebral artery (black arrow) and determined massive thrombosis in the lumen of the vessel with consequent occlusion. The injury passed unnoticed during the diagnostic workup, and physicians focused on the brachial plexus injury. (d) Magnetic resonance angiography performed after one month during the evaluation of the brachial plexus revealed the complete occlusion of the subclavian artery (red arrow) and an axillary artery perfused by collateral vessels (red dotted arrow).

are a valuable tool in evaluating endoluminal defects, creating images that resemble an angiographic view, which can be useful in planning endovascular approaches (see Figures 2b, 3c). Volume rendering reconstructions are very helpful in demonstrating the three-dimensional relationship of the vessel with bony structures (see Figure 7d). Vessel reconstructions on a curved multiplanar plane help to evaluate the lumen's caliber and delineate endovascular signs, such as intimal tears and flaps (see Figure 7).

## Radiological findings

### Vasospasm

Vasospasm is determined by the contraction of the smooth muscle fibers within the arterial wall and represents the mildest response of the vessel to an injury.<sup>26</sup> Vasospasm appears as one or multiple segmental contractions of the arterial wall and, when focal (see Figure 8), could be indistinguishable from an intimal tear (see Figure 9). Unlike an intimal tear, vasospasm is transient and tends to reduce or disappear over time.<sup>26</sup> Mild vasospasm could be unnoticed on contrast-enhanced CT, but it is usually well appreciable at DSA.

### Intimal tear

An intimal tear is a small rupture of the innermost layer of the vessel that separates the intimal layer from the medial layer and creates a small flap.<sup>26</sup> Intimal tears are primarily seen in blunt aortic traumas. On CT and an-

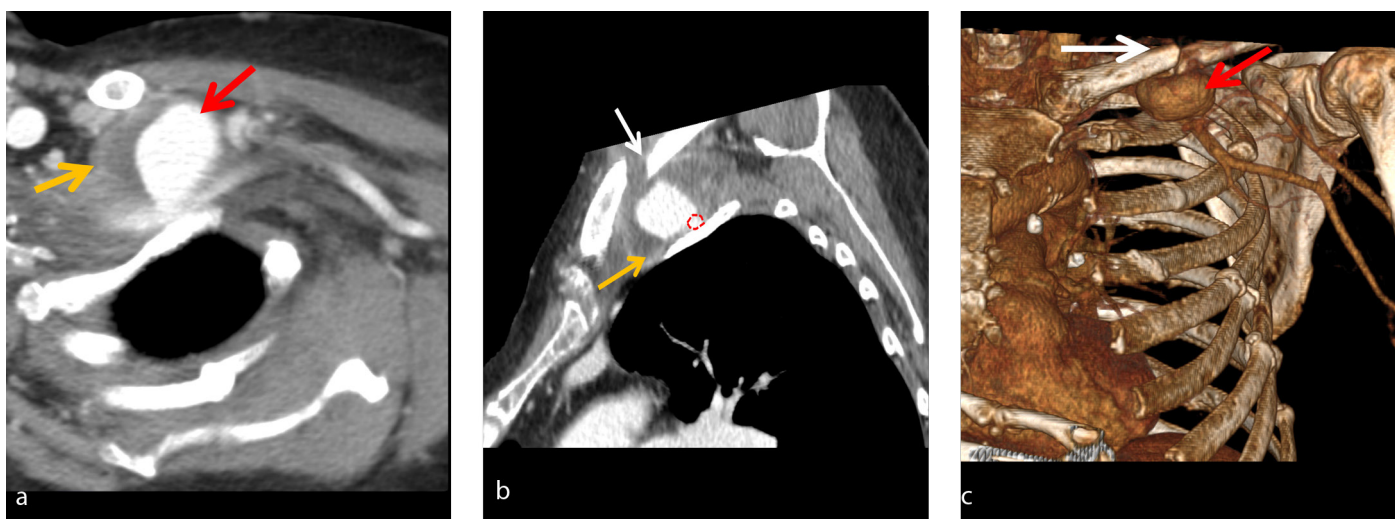


**Figure 4.** Pseudoaneurysm. A 64-year-old patient who sustained a fracture of the clavicle after trauma to the left shoulder due to a car accident. (a) Computed tomography (CT) angiography revealed a large pseudoaneurysm of the subclavian artery. The patent lumen (red arrow) and the wall (yellow arrow) are visible on the axial plane. (b) CT angiography reformatted on the sagittal plane demonstrated the lumen of the subclavian artery (red dashed circle), the wall of the pseudoaneurysm (yellow arrow) with parietal thrombus, and a fracture of the clavicle (white arrow). This image offers a good clue about the mechanism of injury that created the pseudoaneurysm: the distal stump of the fractured clavicle probably pierced the subclavian artery against the first rib, damaging the arterial wall. (c) Three-dimensional volume rendering offers an optimal depiction of the relationship of the pseudoaneurysm with bony structures.

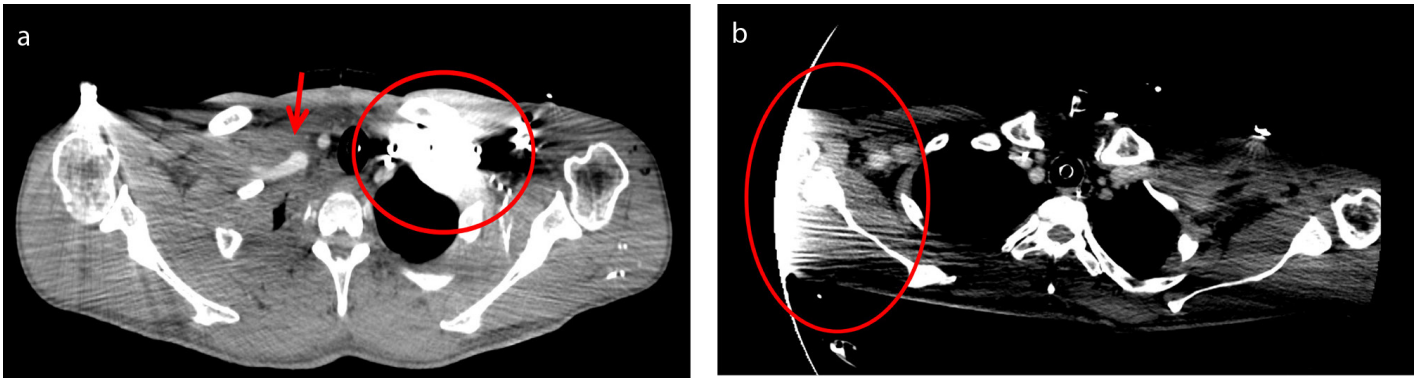


**Figure 5.** Artifacts. (a) A 56-year-old patient sustained a thoracic trauma. Contrast-enhanced computed tomography (CT) was performed, and a contrast medium was injected (flow rate 4 mL/s; 110 mL) into an antecubital vein of the left arm. The compacted bolus of the contrast medium created a streaking artifact (red circle) in the subclavian vein that deleted the signal from nearby anatomical structures. The right subclavian artery is appreciable on the contralateral side (red arrow). (b) Streaking artifact by the collision of the shoulder of the patient with the CT gantry.

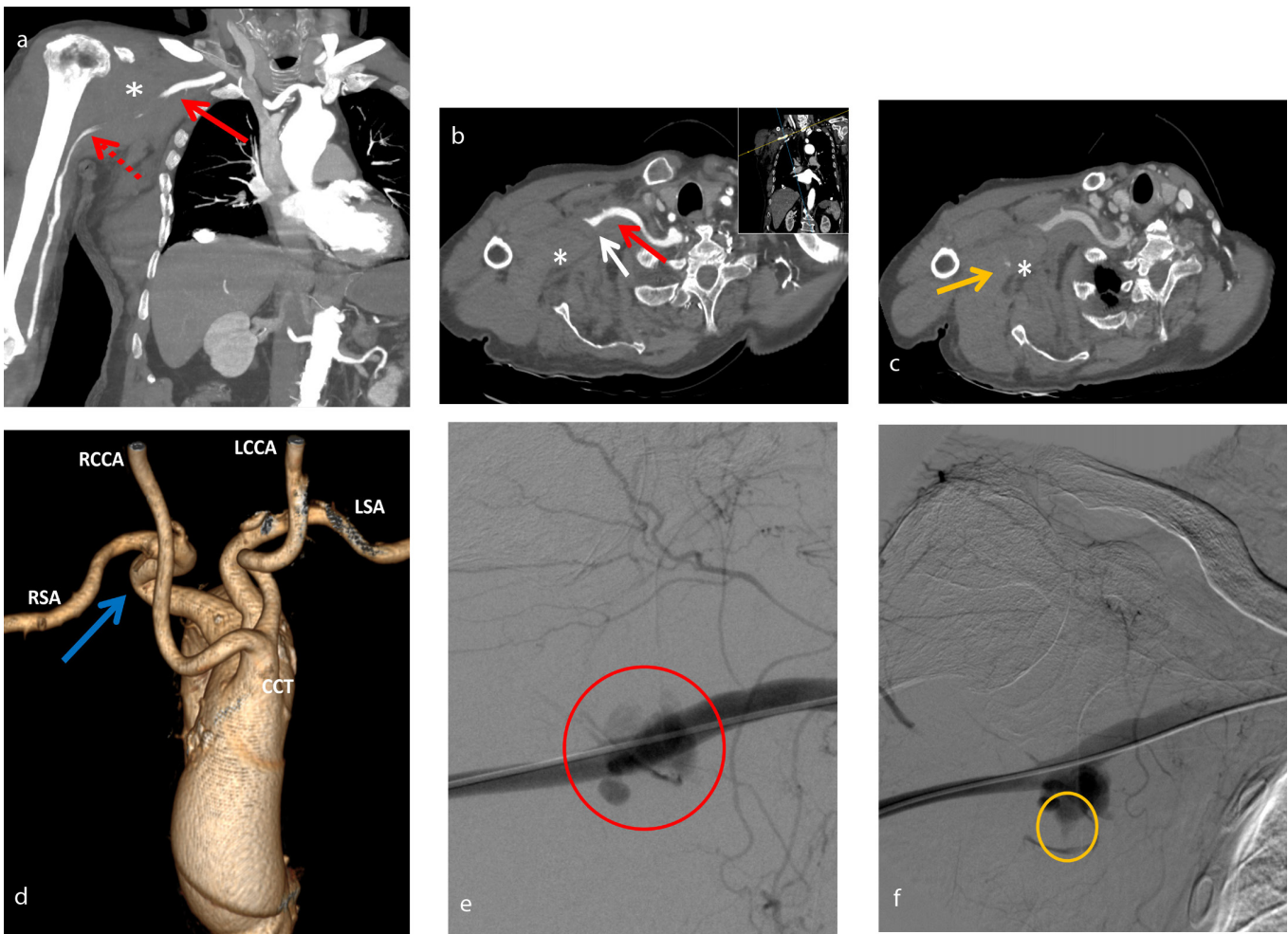


**Figure 6.** Ruptured pseudoaneurysm. An 84-year-old patient who fell from a bike and landed on an outstretched arm. (a) Computed tomography (CT) angiography coronal-reformatted maximum intensity projection demonstrated the course of the subclavian (red arrow) and axillary (red dotted arrow) arteries compressed by a hematoma (\*). (b) CT angiography demonstrated a hematoma of the right shoulder (\*) that dislocated the subclavian and axillary arteries. The subclavian artery presented a narrowing in its distal third (white arrow) that involved the axillary artery (red dotted arrow). The acute margin at the proximal part of the subclavian artery (white arrow) might suggest the presence of a dissection flap with occlusion of the vascular lumen. (c) However, the venous phase demonstrated the presence of active contrast medium extravasation within the hematoma (yellow arrow). (d) Volume rendering demonstrated the presence of a common carotid trunk and a right aberrant subclavian artery with a retroesophageal course and a tight kinking in its middle part (blue arrow). (e, f) A selective angiogram of the subclavian artery was performed using a retrograde approach from the brachial artery. The exam revealed the presence of a pseudoaneurysm (red circle) and active contrast medium extravasation (yellow circle). No endoluminal defect or dissection was appreciable on the angiogram. The complete angiographic sequence is available in Supplementary Video 1. In this case, the mass effect of the hematoma nearly occluded the vessel and created an ambiguous radiological scenario. This represents a good example of the hemodynamic alteration created by hematomas.

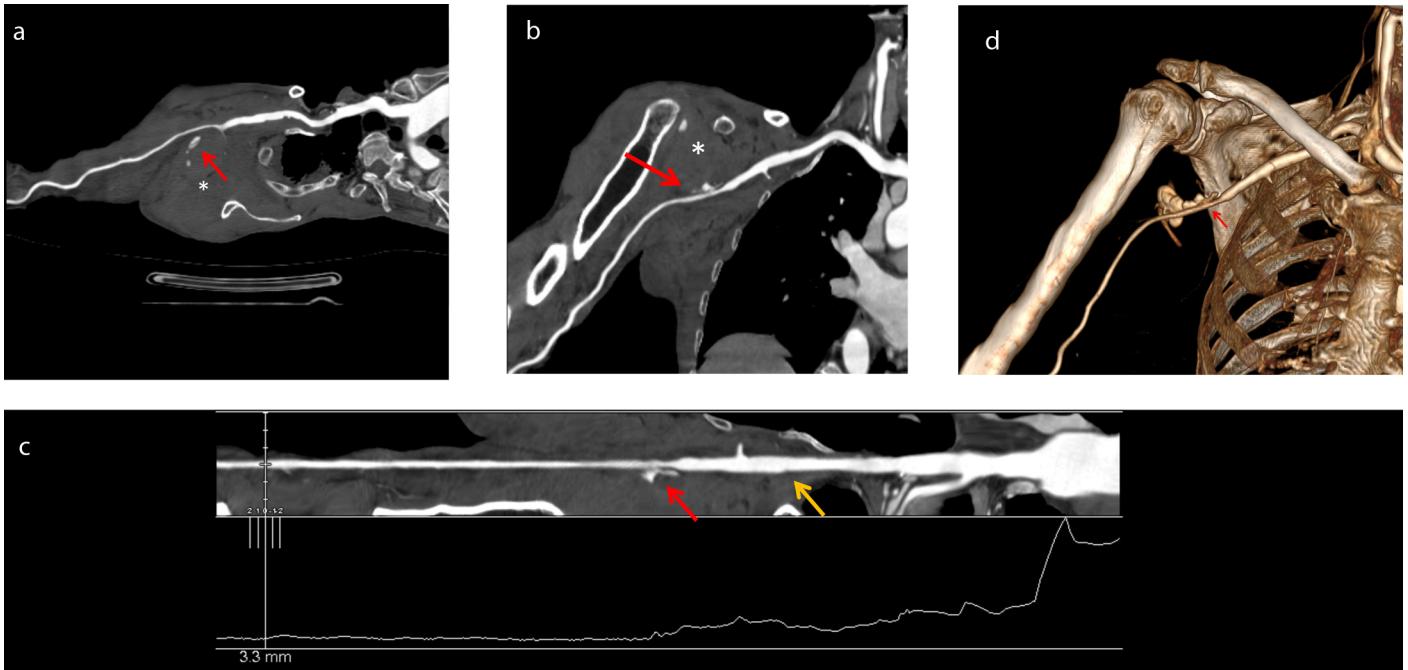


**Figure 7.** Computed tomography post-processing. A 76-year-old patient who fell from a bike and sustained a partial tear (red arrow) of the right axillary artery. Curved reformatting reconstruction along the lumen of the vessel on the (a) axial, (b) coronal, and (c) orthogonal planes of the lumen with caliber calculation. (d) Three-dimensional volume rendering demonstrating the subclavian-axillary artery. A partial tear is appreciable in the first third of the axillary artery (yellow arrow).

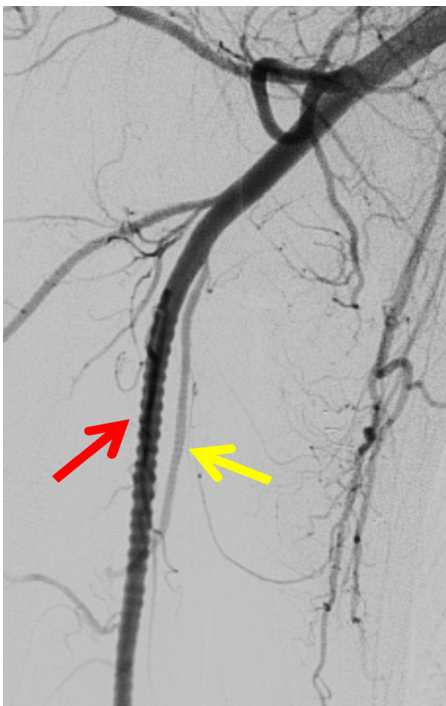


**Figure 8.** Vasospasm. A 37-year-old male patient who sustained major injuries to the upper limbs during a traffic accident. The patient was ejected from his motorcycle after a collision with a car. At admission, the left arm was pulseless, and the right arm presented a faint pulse. Computed tomography revealed a dissection with occlusion of the left axillary artery and a regular right subclavian/axillary artery. The right arm was evaluated during angiography to rule out possible damage. The selective angiogram demonstrated the presence of marked vasospasm of the axillary artery (red arrow) that involved the collateral branches (yellow arrow).

giography, it appears as a small intraluminal defect floating in the vessels (see Figure 10). Intimal tears can be a source of thromboembolic material or evolve into large dissection flaps, but most heal spontaneously (see Figure 9).<sup>26</sup>

### Arteriovenous fistula (AVF)

An AVF is generated by injuries that involve both the SAA and vein (i.e., a bone fragment that penetrates both vessels). The pressure difference creates a passage of blood from the artery to the vein. AVFs are more commonly seen in penetrating traumas<sup>26</sup> and are exceedingly rare in blunt injury. During contrast-enhanced CT and DSA, early and asymmetrical opacification of a vein near an arterial vessel might be consistent with AVF (see Figure 10), even if the breach in the vessel is not appreciable.<sup>6,24</sup>

### Dissection and occlusion

A dissection is an intimal tear that creates a large intimal flap. Depending on the flap shape and characteristics, it can float within the lumen or adhere to the vessel's wall, causing stenosis of the lumen (see Figure 11) or creating a false lumen in which blood collects. If the dissection creates a false lumen, blood flow could propagate the dissection along the vessel. Dissection can ultimately result in stenosis or occlusion if the false lumen obstructs the true lumen and

blood coagulates within it (see Figures 3, 4, and 12). In such cases, on contrast-enhanced CT, the stenosis typically presents smooth margins that could create an acute interface (see Figures 3 and 12). The presence of flaps in the lumen proximal to the occlusion is suggestive of a dissection that causes an occlusion (see Figure 2c). If the vessel is occluded, the diagnostic differential between dissection and occlusion could be challenging. If the tear in the vessel reaches the sub-adventitial medial layer, the dissection could generate a pseudoaneurysm.<sup>26</sup> At DSA, the dissection flap is well appreciable within the lumen, and it usually appears as a linear defect that fluctuates with blood flow or is pushed against the wall of the vessel (see Figure 11b-d).

### Pseudoaneurysm

A pseudoaneurysm is determined by a tear in the arterial wall involving the intimal and medial layers. The blood collects into the breach and creates a lumen outside the vessels delimited only by the adventitial layer. A pseudoaneurysm could occur or become clinically noticeable days after the initial trauma.<sup>6</sup> On CT, pseudoaneurysms show round and smooth margins. The lumen of the pseudoaneurysm presents early opacification in the arterial phase that persists in the venous phase due to internal turbulence (see Figures 4 and 13). The wall of the pseudoaneurysm could exhibit variable parietal

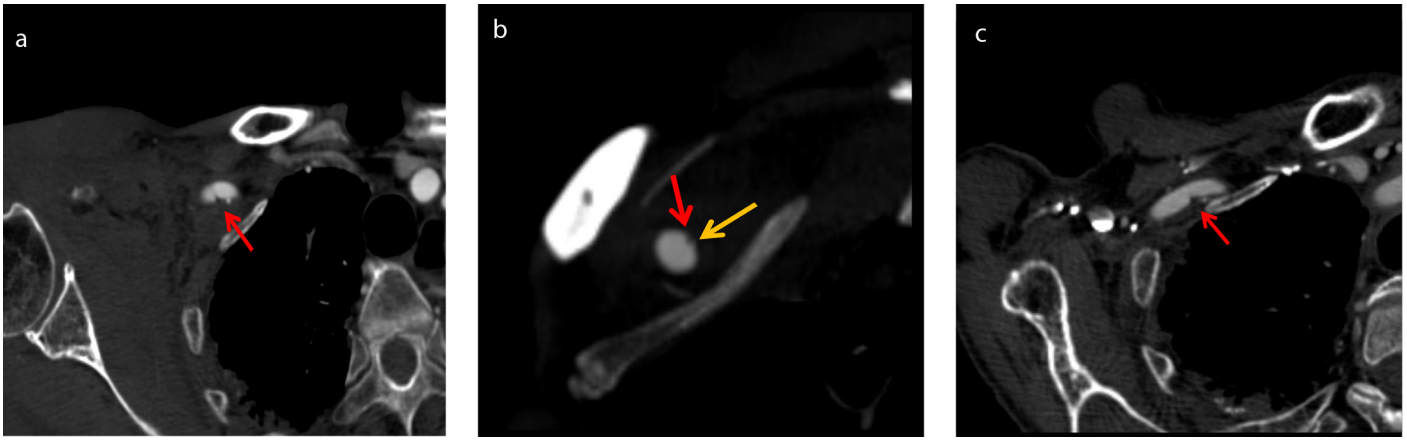


**Figure 9.** Intimal tear. A 76-year-old patient who fell from a bike and sustained a partial tear of the right axillary artery. (a) The axillary artery presented a small intimal tear and a non-occluding luminal defect with a sharp margin (red arrow), referable to a small intimal flap. (b) Computed tomography (CT) angiography sagittal-reformatted reconstruction demonstrated the presence of a very small intimal tear (red arrow) and a defect in the wall (yellow arrow). These findings could also be consistent with focal vasospasm. (c) A CT after 18 months demonstrated the persistence of the intimal flap and mild lumen stenosis.

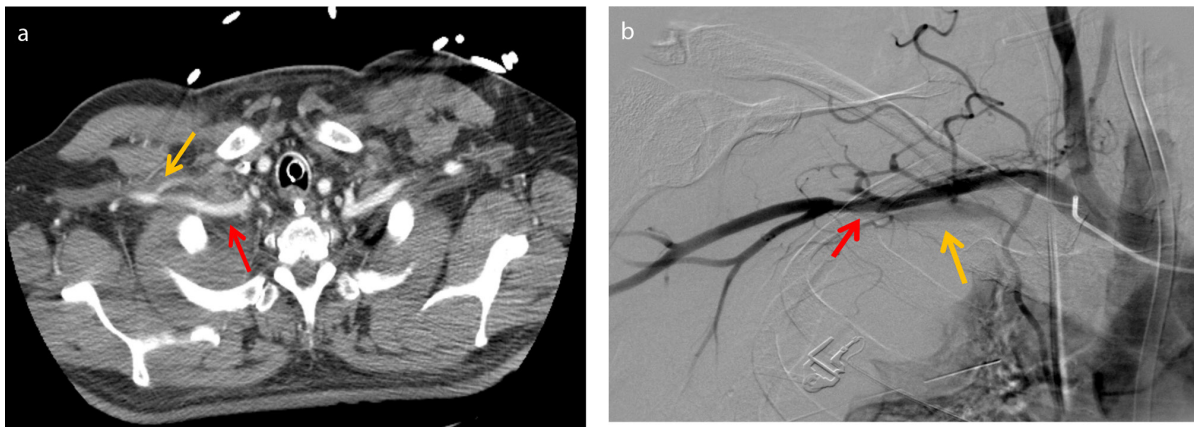


**Figure 10.** Arteriovenous fistula. A 61-year-old male patient who sustained a fall from a three-meter wall. (a) Computed tomography angiography of the upper thorax demonstrated an intact right subclavian artery (red arrow) but early, linear enhancement of the right subclavian vein (yellow arrow). (b) The selective angiogram of the right subclavian artery confirmed the presence of an arteriovenous fistula between the subclavian artery (red arrow) and vein (yellow arrow) at its distal end.

thrombotic apposition, and in such cases, the lumen will demonstrate partial filling with contrast media.<sup>6</sup> In contrast to a partial tear, if the wall of the pseudoaneurysm remains intact, there is no hematoma, but there could be appreciable stranding in the nearby tissue due to small breaches in the wall. If the adventitial layer ultimately disrupts, blood passes into surrounding tissues and creates a hematoma (see Figure 13). Angiography could better delineate the size of the pseudoaneurysm and demonstrate the ruptured wall.

### Partial tear

A partial tear is a breach in the arterial wall that involves all the layers but does not involve the entire circumference of the vessel. In case of a partial tear, the continuity of the vessel is preserved, and the patient can

be treated using an endovascular approach. The breach produces a direct communication between the lumen and the perivascular tissues, resulting in a hematoma (see Figures 14 and 15). The margins of a hematoma are irregular. The hematoma could be hyperdense in unenhanced acquisition due to internal clotting processes. In contrast to penetrating injuries, the blood collects in the space around the vessel, limiting the bleeding to varying degrees. The hematoma could even determine a mass effect on the injured vessel, producing ambiguous radiological signs that could be mistaken for dissection or occlusion.

### Vessel transection

Vessel transection is the complete rupture of the vessel. It is a life-threatening situation with a poor prognosis. A massive

hematoma with active contrast medium extravasation is typically appreciable on contrast-enhanced CT. Transection is the result of extreme shear forces applied to the vessel, and arterial stumps could be projected away from one another due to elastic recoiling (see Figure 16). Digital subtraction angiography might demonstrate active contrast medium extravasation or a truncated vessel.

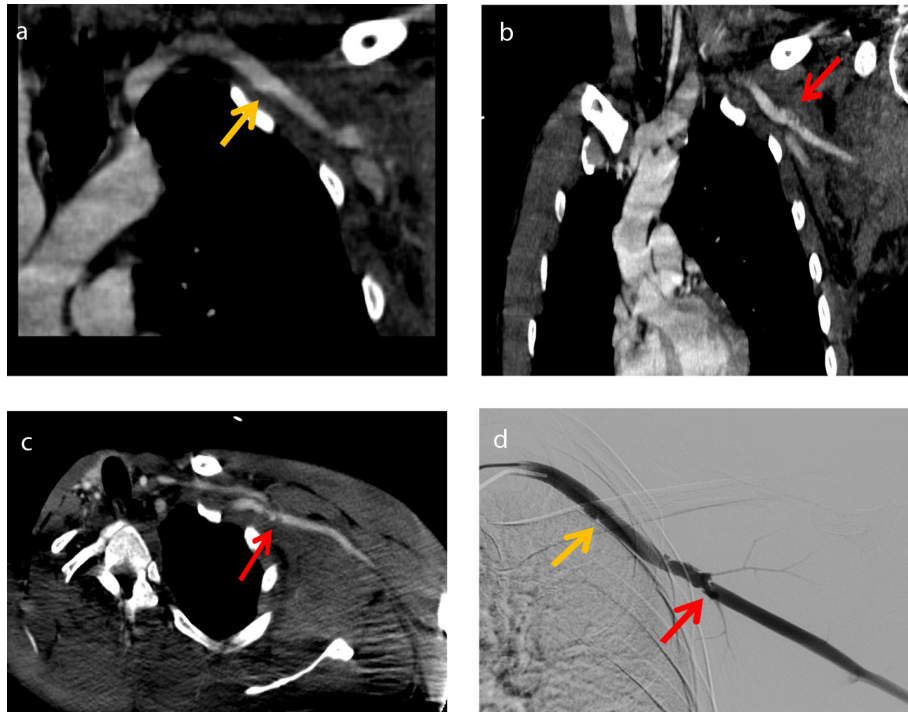


**Figure 11.** Dissection. A 33-year-old male patient who sustained a distraction injury after falling from a motorcycle. (a) Coronal reformatted computed tomography angiography demonstrated the presence of a small intimal tear (yellow arrow) in the left subclavian artery and an irregular endoluminal defect (red arrow) in the proximal portion of the axillary artery (b). These findings are consistent with a dissection without thrombosis. (c) The venous phase confirmed the presence of an endoluminal defect in the axillary artery, referable to a dissection flap adherent to the arterial wall (red arrow). (d) The selective angiogram of the left subclavian artery confirmed the presence of an intimal tear (yellow arrow) and an irregular wall in the proximal axillary artery consistent with a dissection flap.

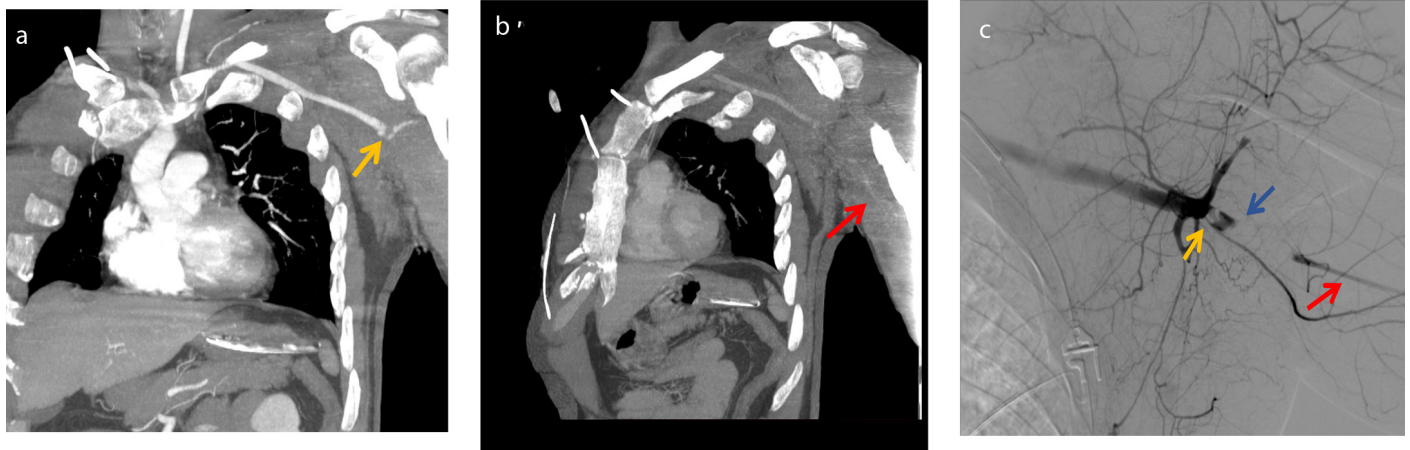


**Figure 12.** Dissection and occlusion. A 47-year-old male patient who underwent a traffic accident. The left arm was pulseless on arrival at the emergency department, but no swelling was appreciable at the first examination. (a) Computed tomography angiography reconstructed along the plane of the subclavian/axillary artery demonstrated an intact subclavian artery but a small defect in the lumen of the axillary artery (yellow arrow) and scarce distal vascularization. No hematoma was appreciable. (b) The venous phase demonstrated the presence of the brachial artery revascularized by collateral vessels (red arrow). (c) Digital subtraction angiography confirmed the presence of a thrombus within the lumen of the axillary artery (yellow arrow) and revascularization of the brachial artery (red arrow). The sharp margin of occlusion (blue arrow) is probably a dissection flap that occludes the axillary artery. The complete angiographic sequence is available in Supplementary Video 2.

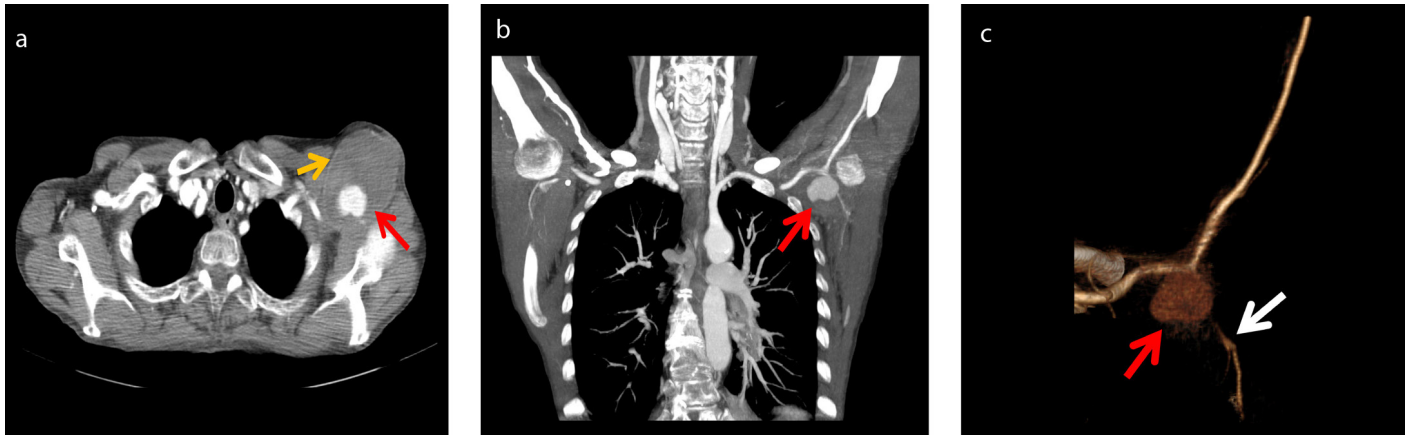


**Figure 13.** Pseudoaneurysm. A 56-year-old female patient who suffered a minor trauma to the left shoulder, which determined the emergence of a large, palpable, and pulsatile swelling above the humerus. (a) Computed tomography angiography demonstrated the presence of a massive pseudoaneurysm of the axillary artery with a definite wall (yellow arrow), partial parietal thrombosis, and a patent central lumen (red arrow). No signs of parietal fissures or extraluminal hematoma were appreciable. Coronal reformatted maximum intensity projection reconstruction (b) and three-dimensional volume rendering (c) demonstrated the relationship of the pseudoaneurysm with the axillary artery and a small neck near the origin of the lateral thoracic artery, which was partially compressed (white arrow).

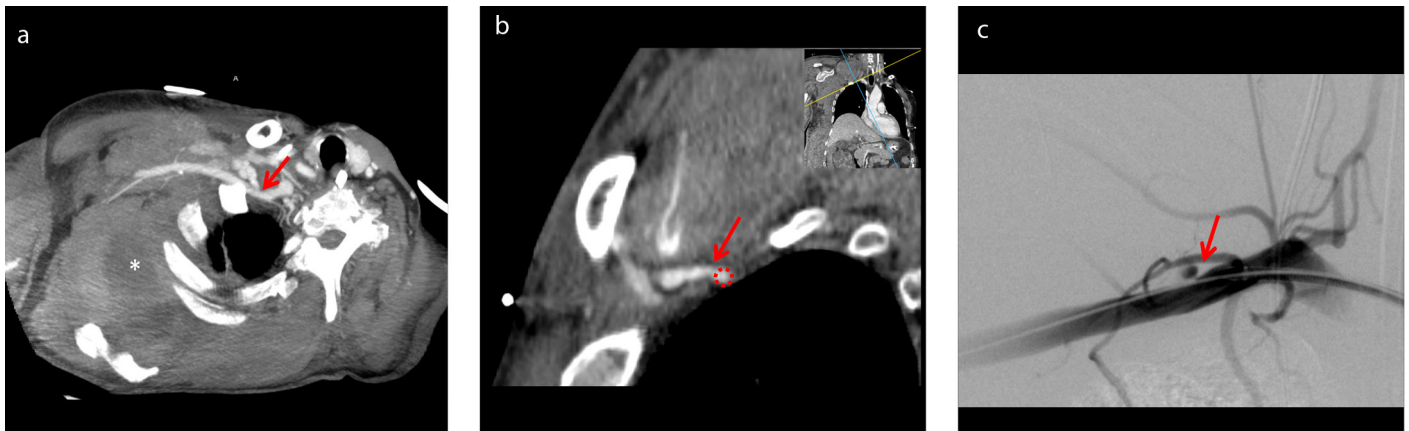


**Figure 14.** Partial tear. A 70-year-old man who fell from a two-meter wall. The patient was on antiplatelet therapy and presented with massive swelling of the supraclavicular fossa and axilla. (a) Maximum intensity projection computed tomography angiography revealed a partial tear of the subclavian (red arrow). (b) Sagittal reformatted demonstrated the lumen of the subclavian artery (red dotted circle) and a tear in the anterosuperior part of the arterial wall (red arrow). (c) The selective angiogram of the right subclavian artery confirmed the tear in the subclavian artery (red arrow).

## Relevant ancillary findings

Ancillary findings may improve the detection of an arterial lesion and the diagnostic and therapeutic workup. Bone fractures are a direct or indirect sign of the forces applied to the body during trauma, and looking at the artery near bone fractures could unveil scarcely visible signs of BSAAs (see Figures 2, 3a, and 4b).

The vascular anatomy of the aortic arch and the branching pattern of the SAA should always be described, as it could determine the type and timing of treatment (endovascular or open surgery and the type of arterial access). Aberrant origins from the aortic arch could necessitate different endovascular approaches. The vertebral artery is one of the most important branches of the

subclavian artery. A BSAAI that involves the vertebral artery constitutes a life-threatening condition because of the possible impact on cerebral perfusion. Moreover, the origin of the vertebral artery and its distance from the injury should always be included in the radiologic report to improve treatment planning (i.e., the employment of a stent graft could be hazardous if the BSAAI is near the origin of the vertebral artery). The internal thoracic artery could be employed in coronary bypass surgery, and dissection or occlusion that involves the ostium of the internal thoracic artery could result in myocardial infarction.

Finally, the distal revascularization (i.e., viable brachial or radial artery) of the arm should be described in the radiologic report because it depicts the ischemic injury and

time of devascularization. If the patient is suitable for endovascular or hybrid management, the interventional radiologist/vascular surgeon might make use of brachial or radial arterial access.

In conclusion, BSAAs have a wide and heterogeneous spectrum of CT findings. Hematomas could slow the arrival time of contrast media and generate ambiguous radiological scenarios. BSAAs presenting with active extravasation should be properly evaluated and could require adjunctive acquisition (venous and delayed phases). The role of the radiologist in the setting of a BSAAI is to perform high-quality diagnostic imaging and provide essential information to optimize treatment.

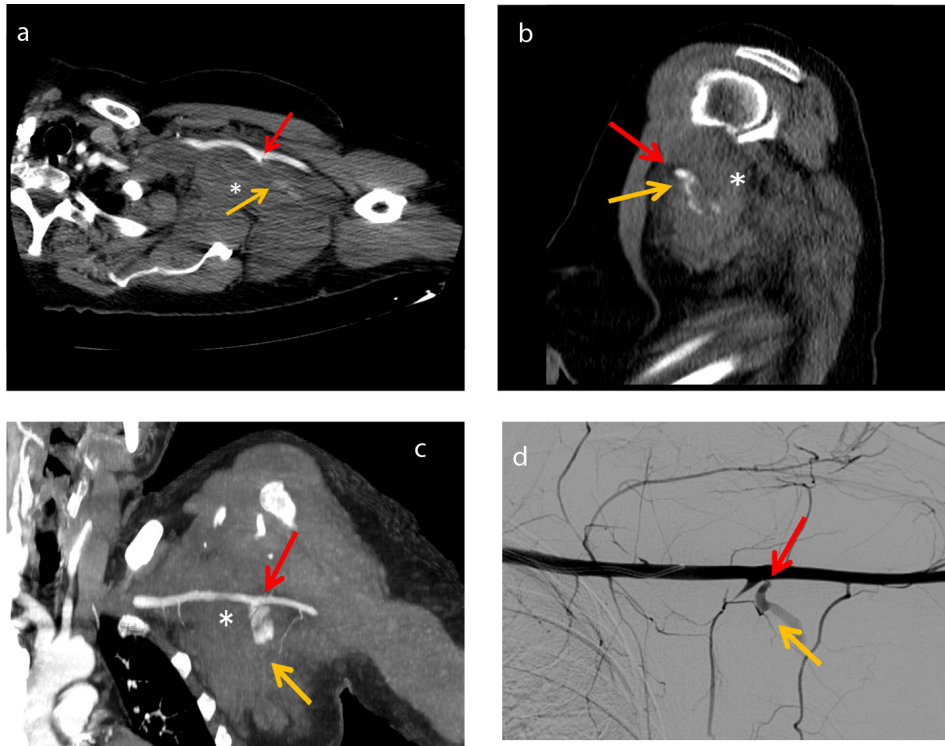


**Figure 15.** Partial tear. A 63-year-old female patient who was involved in a road traffic accident. (a) Axial and (b) sagittal computed tomography angiography demonstrated a partial tear in the axillary artery (red arrow), a hematoma (\*), and (c) active contrast medium extravasation within it (yellow arrow). (d) Maximum intensity projection reconstruction created an image resembling a selective angiogram.

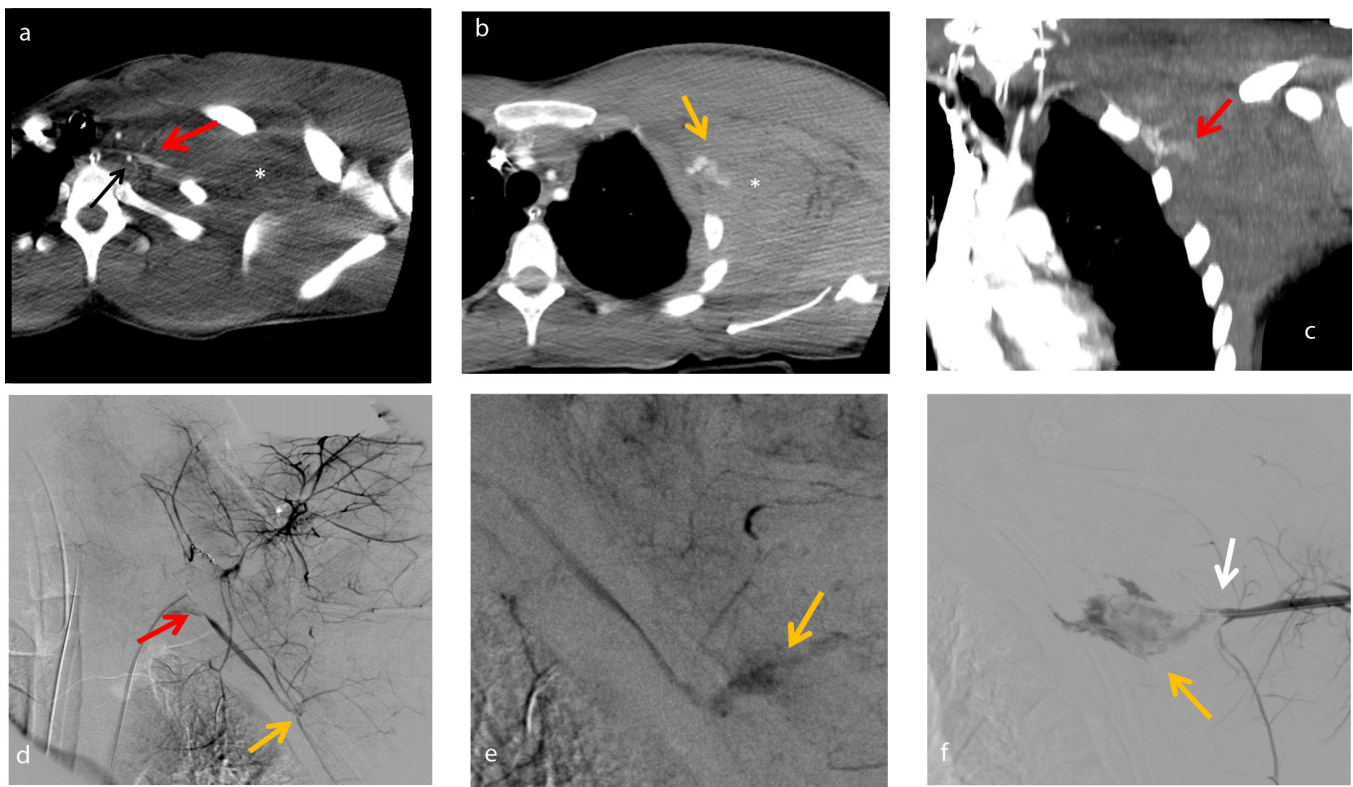


**Figure 16.** Transection. A 19-year-old male patient who was involved in a motorcycle accident during a competition. (a) Computed tomography angiography shows the subclavian artery, which seems occluded a few centimeters distal to the origin of the vertebral artery (black arrow). (b) A massive hematoma is appreciable in the lateral thoracic wall (\*); signs of active bleeding are noticeable within it (yellow arrow). (c) Coronal reformatting revealed the subclavian artery, which is compressed against the ribs, and active extravasation from the proximal arterial stumps (red arrow). (d) The selective angiogram of the subclavian artery confirmed that the subclavian artery was compressed against the thoracic wall (red arrow), with signs of contrast medium extravasation (yellow arrow). In this case, blood flow was slowed by the compression of the hematoma, and active bleeding was seen better in the delayed phase (e). (f) The selective angiogram performed using a retrograde approach from the radial artery revealed the location of the distal arterial stump (white arrow) several centimeters from the proximal one.

## References

1. Smith AA, Gupta N. Subclavian Artery Trauma. 2022. In: StatPearls [Internet]. Treasure Island (FL): StatPearls Publishing; 2022. [CrossRef]
2. Kou HW, Liao CH, Huang JF, et al. Eighteen years' experience of traumatic subclavian vascular injury in a tertiary referral trauma center. *Eur J Trauma Emerg Surg.* 2019;45(6):973-978. [CrossRef]
3. McKinley AG, Carrim AT, Robbs JV. Management of proximal axillary and subclavian artery injuries. *Br J Surg.* 2000;87(1):79-85. [CrossRef]
4. Assenza M, Centonze L, Valesini L, Campana G, Corona M, Modini C. Traumatic subclavian arterial rupture: a case report and review of literature. *World J Emerg Surg.* 2012;7(1):18. [CrossRef]
5. Aksoy M, Tunca F, Yanar H, Guloglu R, Ertekin C, Kurtoglu M. Traumatic injuries to the subclavian and axillary arteries: a 13-year review. *Surg Today.* 2005;35(7):561-565. [CrossRef]
6. Fritz J, Efron DT, Fishman EK. Multidetector CT and three-dimensional CT angiography of upper extremity arterial injury. *Emerg Radiol.* 2015;22(3):269-282. [CrossRef]
7. Cox CS Jr, Allen GS, Fischer RP, et al. Blunt versus penetrating subclavian artery injury: presentation, injury pattern, and outcome. *J Trauma.* 1999;46(3):445-449. [CrossRef]
8. Hoff SJ, Reilly MK, Merrill WH, Stewart J, Frist WH, Morris JA Jr. Analysis of blunt and penetrating injury of the innominate and subclavian arteries. *Am Surg.* 1994;60(2):151-154. [CrossRef]
9. Kou HW, Liao CH, Huang JF, et al. Eighteen years' experience of traumatic subclavian vascular injury in a tertiary referral trauma center. *Eur J Trauma Emerg Surg.* 2019;45(6):973-978. [CrossRef]
10. Gao AB, Lv YC, Wang AP, et al. The zonal pattern of arterial supply to the brachial plexus and its clinical significance. *Surg Radiol Anat.* 2018;40(7):815-822. [CrossRef]
11. Jens S, Kerstens MK, Legemate DA, Reekers JA, Bipat S, Koelemay MJ. Diagnostic performance of computed tomography angiography in peripheral arterial injury due to trauma: a systematic review and meta-analysis. *Eur J Vasc Endovasc Surg.* 2013;46(3):329-337. [CrossRef]
12. Hanneman K, Newman B, Chan F. Congenital variants and anomalies of the aortic arch. *Radiographics.* 2017;37(1):32-51. [CrossRef]
13. Türkvtan A, Büyükbayraktar FG, Olçer T, Cumhuri T. Congenital anomalies of the aortic arch: evaluation with the use of multidetector computed tomography. *Korean J Radiol.* 2009;10(2):176-184. [CrossRef]
14. Buffoli B, Verzeletti V, Hirtler L, Rezzani R, Rodella LF. Retroesophageal right subclavian artery associated with a bicarotid trunk and an ectopic origin of vertebral arteries. *Surg Radiol Anat.* 2021;43(9):1491-1495. [CrossRef]
15. Natsis K, Didagelos M, Gkiouliava A, Lazaridis N, Vyzas V, Piagkou M. The aberrant right subclavian artery: cadaveric study and literature review. *Surg Radiol Anat.* 2017;39(5):559-565. [CrossRef]
16. Popieluszko P, Henry BM, Sanna B, et al. A systematic review and meta-analysis of variations in branching patterns of the adult aortic arch. *J Vasc Surg.* 2018;68(1):298-306. e10. [CrossRef]
17. Gray's Anatomy: The Anatomical basis of Clinical Practice, 41th edition, Elsevier; 2015. [CrossRef]
18. Uglietta JP, Kadir S. Arteriographic study of variant arterial anatomy of the upper extremities. *Cardiovasc Intervent Radiol.* 1989;12(3):145-148. [CrossRef]
19. Connor JV, Byrne C, Scalea TM, Griffith BP, Neschis DG. Vascular injuries after blunt chest trauma: diagnosis and management. *Scand J Trauma Resusc Emerg Med.* 2009;17:42. [CrossRef]
20. Elkbuli A, Shaikh S, McKenney M, Boneva D. Subclavian artery avulsion following blunt trauma: a case report and literature review. *Int J Surg Case Rep.* 2019;61:157-160. [CrossRef]
21. Shaw AD, Milne AA, Christie J, Jenkins AM, Murie JA, Ruckley CV. Vascular trauma of the upper limb and associated nerve injuries. *Injury.* 1995;26(8):515-518. [CrossRef]
22. Romagnoli AN, DuBose J, Dua A, et al. Hard signs gone soft: a critical evaluation of presenting signs of extremity vascular injury. *J Trauma Acute Care Surg.* 2021;90(1):1-10. [CrossRef]
23. Wirth S, Hebebrand J, Basilico R, et al. European Society of Emergency Radiology: guideline on radiological polytrauma imaging and service (full version). *Insights Imaging.* 2020;11(1):135. [CrossRef]
24. Walkoff L, Nagpal P, Khandelwal A. Imaging primer for CT angiography in peripheral vascular trauma. *Emerg Radiol.* 2021;28(1):143-152. [CrossRef]
25. Fishman EK, Horton KM, Johnson PT. Multidetector CT and three-dimensional CT angiography for suspected vascular trauma of the extremities. *Radiographics.* 2008;28(3):653-665; discussion 665-666. [CrossRef]
26. Jean-François H. Geschwind and Michael D. Dake, Abram's Angiography : Interventional Radiology 3<sup>rd</sup> edition, Lippincott Williams; 2013. [CrossRef]

---

Video 1: [https://www.youtube.com/shorts/q\\_X0IVnXBVY](https://www.youtube.com/shorts/q_X0IVnXBVY)

Video 2: <https://www.youtube.com/shorts/lae87vyy83Q>





# Optimized visualization of focal liver lesions and vascular structures in real-time T1-weighted gradient echo sequences for magnetic resonance-guided liver procedures

Vanessa Franziska Schmidt

Olaf Dietrich

Philipp Maximilian Kazmierczak

Max Seidensticker

Jens Ricke

Marco Armbruster

## PURPOSE

This study aimed to determine the optimal sequence parameters of a real-time T1-weighted (T1w) gradient echo (GRE) sequence for magnetic resonance (MR)-guided liver interventions.

## METHODS

We included 94 patients who underwent diagnostic liver MR imaging (MRI) and acquired additional real-time T1w GRE sequences with a closed 1.5-T MRI scanner 20 min after a liver-specific contrast agent was injected. In four measurement series, one of the following four sequence parameters was changed, and repeated scans with different values for this parameter were acquired: flip angle (FA) (10–90°), repetition time (TR) (5.47–8.58 ms), bandwidth (BW) (300–700 Hz/pixel), and matrix (96 × 96–256 × 256). Two readers rated the visualizations of the target and risk structures (7-point Likert scale) and the extent of artifacts (6-point Likert scale); they also quantified the lesion–liver contrast ratio, the lesion–liver contrast-to-noise ratio (CNR), and the liver signal-to-noise ratio (SNR). Substratification analyses were performed for differences in overall visual and quantitative assessments depending on the lesion size, type, and the presence of cirrhosis.

## RESULTS

For the utilized FAs and matrix sizes, significant differences were found in the visual assessments of the conspicuity of target lesions, risk structures, and the extent of artifacts as well as in the quantitative assessments of lesion–liver contrast ratios and liver SNRs (all  $P < 0.001$ ). No differences were observed for modified TR and BW. Significantly increased conspicuity of the target and vascular structures was observed for both higher FAs and matrix sizes, while the ghosting artifacts increased and decreased, respectively. For primary liver tumors compared with metastatic lesions, and for cirrhotic livers compared with normal liver parenchyma, significantly decreased conspicuity of the target lesions ( $P = 0.005$ ,  $P = 0.005$ ), lesion–liver CNRs ( $P = 0.005$ ,  $P = 0.032$ ), and lesion–liver contrast ratios ( $P = 0.015$ ,  $P = 0.032$ ) were found. All results showed no significant correlation with lesion size.

## CONCLUSION

We recommend an FA of 30°–45° and a matrix size of 128 × 128–192 × 192 for MR-guided liver interventions with real-time T1w sequences to provide a balance between good visualizations of target and risk structures, high signal intensities, and low ghosting artifacts. The visualization of the target lesion may vary due to clinical conditions, such as lesion type or associated chronic liver disease.

## KEYWORDS

Interventional, lesion-liver CNR, liver SNR, MRI, real-time sequence, sequence parameter, signal intensity, visualization

From the Department of Radiology (V.F.S. ✉ vanessa.schmidt@med.uni-muenchen.de, O.D., P.M.K., M.S., J.R., M.A.), University Hospital, LMU Munich, München, Germany.

Received 18 March 2021; revision requested 19 April 2021; last revision received 13 August 2021; accepted 13 September 2021.



Epub: 05.12.2022

Publication date: 31.01.2023

DOI: 10.5152/dir.2022.21212

Currently, most radiologic interventions are performed using computed tomography, X-ray fluoroscopy, or ultrasound. However, magnetic resonance imaging (MRI) guidance of percutaneous interventions offers numerous advantages for certain procedures, particularly in soft tissue organs like the breast, liver, or prostate.<sup>1-4</sup> This is primarily because the

You may cite this article as: Schmidt VF, Dietrich O, Kazmierczak PM, Seidensticker M, Ricke J, Armbruster M. Optimized visualization of focal liver lesions and vascular structures in real-time T1-weighted gradient echo sequences for magnetic resonance-guided liver procedures.

*Diagn Interv Radiol.* 2023;29(1):128-137.

superior soft tissue contrasts in MRIs result in excellent visualizations of target lesions and adjacent structures.<sup>5-7</sup> Therefore, precise needle positioning is supported, and damage to surrounding risk structures that might not have been visualized with other imaging modalities is prevented.<sup>6,8,9</sup> The ability to intra-procedurally monitor thermally induced tissue damage with MR thermometry represents a further benefit of using MR guidance for interventions, particularly for radiofrequency ablation or microwave ablation, and it enables the real-time monitoring of therapy success. Additionally, the real-time multi-planar imaging abilities of fluoroscopic MRI sequences allow the visualization of target lesions and the tracking of instruments in any orientation and in three dimensions; this can be considered an advantage over computerized tomography (CT) guidance, in which pushing the needle outside of the axial planes and working off-plane may be challenging.<sup>10</sup> The lack of ionizing radiation is another key advantage, especially for pediatric patients, women of childbearing age, and repeated or long procedures, and it constitutes a major benefit for treated patients as well as for the medical staff who perform these procedures frequently.<sup>10-12</sup>

Despite these advantages, interventional MRIs are still in the early stages, and CT and ultrasound remain the methods of choice for most percutaneous procedures. However,

### Main points

- The results of this study highlight the possibility of optimizing real-time T1-weighted magnetic resonance imaging sequences to achieve appropriate conditions for interventional liver procedures.
- Varied flip angles (FAs) and matrix sizes might affect the conspicuity of target and risk structures, the extent of ghosting artifacts, and signal intensities [lesion–liver contrast-to-noise ratios (CNRs), liver signal-to-noise ratios (SNRs)], while repetition time and bandwidth might be unaffected.
- All results in the visual and quantitative assessments showed no significant correlation with lesion size, while the visualization of the target lesion, lesion–liver CNR, and lesion–liver contrast ratio varied due to clinical conditions, including lesion type and associated chronic liver disease.
- We recommend an FA of 30°–45° and a matrix size of 128 × 128–192 × 192 to provide the optimal balance between a low artifact extent and a good visualization of target lesions and vascular structures in combination with high lesion–liver CNRs and liver SNRs.

the introduction of wide-bore MRI systems and real-time high-resolution imaging sequences have significantly improved the acceptance and clinical importance of this technique.<sup>13</sup> Some MR-guided procedures are well established in clinical routines for several indications, e.g., biopsies of breast and prostate lesions,<sup>14,15</sup> while other formats, such as MR-guided procedures in the liver, are continually expanding. In addition to short acquisition times, optimized visualizations of target and risk structures are key to the successful implementation of these procedures.<sup>16-19</sup>

The objective of this prospective monocentric trial was to determine the optimal sequence parameters of a real-time T1-weighted (T1w) gradient echo (GRE) sequence suitable for MR-guided liver interventions with respect to the *in vivo* visualization of focal liver lesions (FLLs), hepatic vascular structures, the extent of ghosting artifacts, and quantitative signal intensities.

## Methods

### Study design and eligibility criteria

The study was approved by the Local Ethics Committee (application no: 19-976), and informed consent was obtained from each participant. All procedures were performed in accordance with relevant guidelines and regulations according to the Helsinki Declaration of 2013. We included 94 patients with clinical indications who underwent diagnostic MRI examinations of the upper abdomen with weight-based doses of 1.0 mL/10 kg of a liver-specific contrast agent (Gd-EOB-DTPA) (Primovist, Bayer Vital, Leverkusen, Germany). Clinical indications were suspected or known FLL, cirrhosis, or vascular anomalies. Previously treated patients (ablative therapy, liver resection, and/or chemotherapy) and therapy-naïve patients were included. During these diagnostic MRIs, additional real-time T1w GRE sequences were acquired within a scan pause immediately prior to the routine measurement of the hepatobiliary phase (20 min after the injection of Gd-EOB-DTPA). Therefore, the overall scan times were not affected by the additionally acquired sequences. The duration of these additional sequences totaled approximately 60 seconds. The exclusion criteria for this study were contraindications against MRI examination or Gd-EOB-DTPA.

The primary endpoint of this study was the visualization of liver lesions and vascular structures in real-time T1w GRE sequenc-

es. Secondary endpoints were the extent of visible artifacts as well as the quantitative assessments of lesion–liver contrast ratios, lesion–liver contrast-to-noise ratios (CNRs), and signal-to-noise ratios (SNRs) of the liver parenchyma. In addition, the influence of lesion size in relation to the visual and quantitative assessments was evaluated.

### Real-time, T1w MRI sequences at 1.5 T

We performed real-time T1w MRI using a closed whole-body 1.5-T scanner (Magnetom Aera, Siemens Healthineers, Erlangen, Germany) with a short open-bore design (cover-to-cover system length: 145 cm, bore diameter: 70 cm). The gradient system had a maximum gradient strength of 33 mT/m and a slew rate of 125 T/m/s. We acquired four different measurement series, each in axial as well as coronal and sagittal single slices, at the mid hepatic level of the portal vein, via breath-hold acquisitions without acceleration techniques. The slice thicknesses were 10 mm, the fields of view were 360 × 360 mm<sup>2</sup>, and the acquisition times were 613–900 ms. In each series, one of the following parameters was systematically and sequentially modified: flip angle (FA), repetition time (TR), bandwidth (BW), and matrix. Each parameter was evaluated in a subgroup of 20 to 30 patients. For each patient, the real-time T1w MRI sequence was repeated with different values per parameter (e.g., FA: 15°, 30°, 45°, 60°), while the other three parameters were held constant. Measurement series 1 was split into two subgroups, with increasing and decreasing values for the varied parameter FAs to evaluate exemplarily the influence of confounding variables, such as the decreasing ability of patients to hold their breath towards the end of the acquisition series. For details on the study design, see Table 1.

### Qualitative and quantitative sequence analyses

Image evaluation was performed using Syngo Studio VB36E (Siemens Healthineers, Erlangen, Germany). Two readers with 8 and 2 years' experience in diagnostic liver MRIs independently evaluated the delineations of liver lesions using a Likert-rated scale, as follows: –1= no target lesion within the acquired field of view, 0= lesion not visible, 1= very poor, 2= poor, 3= sufficient, 4= good, and 5= excellent (sharply delineated). The visibility of the vascular structures was graded accordingly from 0 to 5. We employed a rating scale for the visual assessments of the extent of ghosting artifacts, as follows: 0= no

artifacts, 1= very low extent of artifacts, 2= low extent of artifacts, 3= moderate extent of artifacts, 4= strong extent of artifacts, and 5= very strong extent of artifacts.

For the quantitative assessments of the lesion–liver contrast ratios, the lesion–liver CNRs and SNRs of the liver parenchyma in the regions of interest (ROI) of at least 20 mm<sup>2</sup> were used. The ROIs inside the lesions were placed, avoiding areas with hemorrhage or necrosis to prevent susceptibility artifacts. The ROIs within the adjacent liver parenchyma were defined at identical anatomical depths as the lesions to avoid influences of surface coil sensitivity profiles. The sizes and shapes of the ROIs were kept nearly identical for all measurements. Since the intensity of the background noise could not be reliably measured outside the body due to influences of image filters (e.g., intensity normalization and large field-of-view filters),<sup>20,21</sup> we used the standard deviation (SD) of the foreground signal within each ROI to substitute for the noise SD. Then, the SNRs were calculated as the ratios of the foreground signals (the mean value within the ROI) and signal variations (the standard variation within the ROI). The lesion–liver CNRs were determined using the following formula: lesion–liver CNR= (signal intensity<sub>liver</sub> – signal intensity<sub>lesion</sub>) / sqrt [(SD<sub>liver</sub><sup>2</sup> + SD<sub>lesion</sub><sup>2</sup>) / 2]. The lesion–liver contrast ratios were defined using the following formula: lesion–liver contrast ratio= signal intensity<sub>lesion</sub> / signal intensity<sub>liver</sub>.

### Statistical analysis

The statistical analysis was performed using SPSS software, version 26 (SPSS Inc., Chicago, Illinois, USA). The visual and quantitative ratings of the two readers were averaged, yielding the primary and secondary efficacy variables for the study. For the descriptive statistics, the numerical values are presented as means plus SD. The Kolmogorov–Smirnov test was used for the assessment of normality. For the k= 24 differences in the conspicuity of the target lesions and vascular structures, artifact behavior, and the quantitative assessments of signal intensities between the modified variables, confirmatory testing was conducted using Friedman’s test based on an adjusted significance level of  $\alpha = \alpha/k = 0.05/24 = 0.00208333$ , with a Bonferroni correction. All other study testing was performed based on an exploratory significance level of  $\alpha = 0.05$ . In the Mann–Whitney U test, substratification analyses were performed for differences in total visual and quantitative assessments (of all measurement series) depending on the presence of cirrhosis and the type of lesion. In addition, the relations between lesion sizes and both assessments were tested using Spearman’s rank correlation coefficient.

## Results

### Patient characteristics

Between January 2020 and May 2020, 94 patients (49 female), with a mean age of 59

years (range: 24–88 years), were included in this study. Liver MRIs were conducted on 91 patients to evaluate known FLLs; thereof, 61/91 patients (67.0%) showed metastatic lesions of various origins (predominantly neuroendocrine and gastrointestinal), 21/91 (23.1%) showed primary liver tumors (hepatocellular carcinoma and cholangiocellular carcinoma), and 5/91 (5.5%) showed benign lesions (liver adenoma/vascular anomaly/liver cyst). In addition, 4/91 (4.4%) patients presented with cirrhosis without any FLL, and 3/91 patients (3.3%) underwent MRIs of the upper abdomen for reasons other than liver pathologies. The FLLs were within the scan range of the fluoroscopic single-slice MRI sequences in 47/91 cases (51.6%), while 44 patients (48.4%) had FLLs outside the acquired scan range. Since we chose a standardized acquisition using a single-slice technique at the level of the hepatic portal vein to achieve the best possible comparability, not all FLLs were included in the datasets. Only one target lesion was chosen randomly for patients with more than one lesion in the image data. These FLLs were primarily metastatic lesions (33/47, 70.2%), followed by hepatocellular carcinomas (6/47, 12.8%), cholangiocellular carcinomas (3/47, 6.4%), liver adenomas (2/47, 4.3%), vascular anomalies (2/47, 4.3%), and liver cysts (1/47, 2.1%). All 94 patients were assessed for the analysis of the visualization of vascular structures and the evaluations of artifact behaviors. In total, 61/91 patients (67.0%) had been treated with previous therapies, of which 35/91 (38.5%) received chemotherapy, 23/91 (25.3%) had liver resections, and 31/91 (38.5%) had local ablative liver procedures. Table 2 lists the additional demographic and clinical characteristics of the patients.

### Results of measurement series

Sample images of all the modified measurement series are shown in Figures 1–4. Detailed results of the visual and quantitative assessments and the results of Friedman’s test are presented in Tables 3 and 4.

### Flip angle

There were significant differences for all qualitative and quantitative variables assessed at different FAs (15°–60°) (see Figure 1). Regarding the visualization of the target lesions, the conspicuity of the lesions was significantly different between the selected FAs ( $P = 0.001$ ). Assessed by the Likert scale, the conspicuity of the lesions showed a mean  $\pm$  SD score of  $1.7 \pm 0.3$  at FA= 15°, 3.1

**Table 1.** Flowchart of study profile. Systematical modification of sequence parameters of real-time T1-weighted gradient-recalled echo sequences of the liver

	Series 1a	Series 1b	Series 2	Series 3	Series 4
	FA (degree)	FA (degree)	TR (ms)	BW (Hz/pixel)	Matrix size
Varied	15	60	5.47	300	96 × 96
	30	45	6.25	400	128 × 128
	45	30	7.03	500	192 × 192
	60	15	7.81	600	256 × 256
			8.58	700	
Fixed					
FA (°)	Varied	Varied	60	60	60
TR (ms)	4.79	7.03	Varied	7.03	9.4–3.5
BW (Hz/pixel)	795	530	500	Varied	530
Matrix	128 × 128	128 × 128	128 × 128	128 × 128	varied
TE (ms)	2.21	2.5	2.5	3.2	2.5–2.8
FOV	360 × 360	360 × 360	360 × 360	360 × 360	360 × 360
Acquisition time (ms)	613	900	700–1.100	900	900
Slice orientation	cor, ax, sag	cor, ax, sag	cor, ax, sag	cor, ax, sag	cor, ax, sag
Slice thickness (mm)	10	10	10	10	10

FA, flip angle; TR, repetition time; TE, echo time; BW, bandwidth; ms, milliseconds; Hz, Hertz; cor, coronal; ax, axial; sag, sagittal.

$\pm 0.4$  at FA= 30°,  $3.2 \pm 0.7$  at FA= 45°, and  $3.6 \pm 0.8$  at FA= 60°. Regarding the visualization of the vascular structures, there were significant differences ( $P < 0.001$ ) in the measurement series, with a Likert-scaled mean  $\pm$  SD score of  $2.0 \pm 0.4$  at FA= 15°,  $3.2 \pm 0.6$  at FA= 30°,  $3.4 \pm 0.5$  at FA= 45°, and  $3.8 \pm 0.5$  at FA= 60°. Significant differences occurred in the extent of ghosting artifacts between the individual FAs, with more severe artifacts occurring for higher FAs, with a mean  $\pm$  SD score of  $1.0 \pm 0.4$  at FA= 15°,  $1.8 \pm 0.5$  at FA= 30°,  $2.9 \pm 0.6$  at FA= 45°, and  $3.2 \pm 0.8$  at FA= 60°.

Similar results were found for the quantitative assessments of signal intensities; the lesion–liver contrast ratios and the liver SNRs presented with significant differences

between the selected FAs ( $P < 0.001$ ,  $P < 0.001$ ). The lowest value of the lesion–liver contrast ratio corresponding to the highest difference of signal intensities between lesion and liver parenchyma was found with a mean  $\pm$  SD score of  $0.4 \pm 0.2$  for medium and high FAs of 30°, 45°, and 60°, respectively. Conversely, high lesion–liver CNRs were shown for the FAs of 15°, 45°, and 60°, with a mean  $\pm$  SD score of  $8.4 \pm 4.6$ ,  $8.8 \pm 3.2$ , and  $8.9 \pm 3.9$ , respectively. The highest liver SNR with a mean  $\pm$  SD score of  $16.9 \pm 6.8$  was revealed for FA= 15°.

### Repetition time

There were no significant differences in the assessed qualitative and quantitative variables for different TRs (5.47–8.58 ms); the

conspicuity of the target lesions ( $P = 0.14$ ), the vascular structures ( $P = 0.51$ ), the artifact extents ( $P = 0.53$ ), the lesion–liver contrast ratios ( $P = 0.42$ ), the lesion–liver CNRs ( $P = 0.22$ ), and the liver SNRs ( $P = 0.31$ ) were not dependent on the different selected TRs (see Figure 2).

### Bandwidth

There were no significant differences for the assessed qualitative and quantitative variables for different BWs (300–700 Hz/pixel); the conspicuity of the target lesions ( $P = 0.85$ ), the vascular structures ( $P = 0.87$ ), the artifact extents ( $P = 0.80$ ), the lesion–liver contrast ratios ( $P = 0.11$ ), the lesion–liver CNRs ( $P = 0.44$ ), and the liver SNRs ( $P = 0.26$ ) were not dependent on different selected BWs (see Figure 3).

### Matrix

There were significant differences for all qualitative and quantitative variables assessed at different matrix sizes ( $96 \times 96$ – $256 \times 256$ ) (see Figure 4). Regarding the visualizations of target lesions, there was better conspicuity of the lesions for larger matrix sizes ( $P < 0.001$ ). The conspicuity of the target lesions showed a mean  $\pm$  SD score of  $1.8 \pm 0.6$  at  $96 \times 96$ ,  $2.7 \pm 0.5$  at  $128 \times 128$ ,  $3.5 \pm 0.5$  at  $192 \times 192$ , and  $3.8 \pm 0.6$  at  $256 \times 256$ . In the visual assessments of the vascular structures, there was a better delimitation of structures with larger matrices ( $P < 0.001$ ). Rated by a Likert scale, the series of the vascular structure yielded a mean  $\pm$  SD score of  $2.0 \pm 0.2$  at  $96 \times 96$ ,  $3.0 \pm 0.3$  at  $128 \times 128$ ,  $3.7 \pm 0.5$  at  $192 \times 192$ , and  $4.2 \pm 0.6$  at  $256 \times 256$ . There was a significantly different extent of ghosting artifacts depending on the chosen matrix size ( $P < 0.001$ ), with fewer artifacts for larger matrices, with a mean  $\pm$  SD score of  $3.5 \pm 0.5$  at  $96 \times 96$ ,  $2.4 \pm 0.5$  at  $128 \times 128$ ,  $1.4 \pm 0.5$  at  $192 \times 192$ , and  $0.7 \pm 0.8$  at  $256 \times 256$  (see Figure 5).

The following results were found for the quantitative assessments of signal intensities: the liver SNR presented with significant differences between the selected matrix sizes ( $P < 0.001$ ), but the highest value of the lesion–liver contrast ratio corresponding to the lowest difference of signal intensities between lesions and the liver parenchyma was found with a mean  $\pm$  SD score of  $0.5 \pm 0.3$  for low matrix sizes of  $96 \times 96$ . The highest lesion–liver CNR, with a mean  $\pm$  SD score of  $9.7 \pm 6.1$ , and liver SNR, with a mean  $\pm$  SD score of  $15.9 \pm 6.2$ , were shown at  $96 \times 96$  (see Figure 6).

**Table 2.** Patient and clinical characteristics of the study cohort (n = 94)

Characteristics	n (%)
Sex	
Male	45 (47.9%)
Female	49 (52.1%)
Age (years), mean $\pm$ SD	59 $\pm$ 17
Liver disease	91 (96.8%)
CCA	6 (6.4%)
HCC	15 (16.0%)
Metastasis	61 (64.9%)
BC	4 (4.3%)
CRC	10 (10.6%)
GCT	1 (1.1%)
LMS	2 (2.1%)
MM	4 (4.3%)
NET	33 (35.1%)
NSCLC	1 (1.1%)
PC	1 (1.1%)
STS	1 (1.1%)
TC	2 (2.1%)
UC	2 (2.1%)
Liver adenoma	2 (2.1%)
Liver cyst	1 (1.1%)
Vascular anomaly	2 (2.1%)
Cirrhosis	4 (4.3%)
No liver disease	3 (3.2%)
Previous therapies	61 (64.9%)
Chemotherapy	35 (37.2%)
Liver resection	23 (24.5%)
Ablative therapy	31 (33.0%)
FLL size (mm), mean $\pm$ SD	38.8 $\pm$ 20.0

BC, breast cancer; CCA, cholangiocarcinoma; HCC, hepatocellular carcinoma; CRC, colorectal cancer; GCT, germ-cell tumor; LMS, leiomyosarcoma; MM, malignant melanoma; NSCLC, non-small cell lung carcinoma; PC, pancreatic cancer; STS, soft tissue sarcoma; TC, thyroid cancer; UC, urothelial cancer; FLL, focal liver lesion; SD, standard deviation.

## Impact of type of lesion, liver cirrhosis, and lesion size

Regarding the total visual and quantitative assessments, compared with patients with primary liver tumors ( $n = 10$ ), the group with metastatic lesions ( $n = 33$ ) presented with significantly higher mean conspicuity of

the target lesions ( $P = 0.005$ ) as well as significantly increased mean lesion–liver CNRs ( $P = 0.005$ ) and lesion–liver contrast ratios ( $P = 0.015$ ). No significant differences were seen in the conspicuity of the vascular structures ( $P = 0.96$ ), the artifact extents ( $P = 0.28$ ), or the liver SNRs ( $P = 0.98$ ). Compared with the group with normal liver parenchyma ( $n = 41$ ),

the patients with cirrhotic liver disease ( $n = 6$ ) revealed significantly decreased mean conspicuity of the target lesions ( $P = 0.005$ ) as well as significantly decreased mean lesion–liver CNRs ( $P = 0.032$ ) and lesion–liver contrast ratios ( $P = 0.032$ ). No significant differences were observed in the conspicuity of vascular structures ( $P = 0.45$ ), artifact extents ( $P = 0.16$ ), or liver SNRs ( $P = 0.74$ ). The detailed results are presented in Tables 5 and 6. The mean ( $\pm$  SD) size of the evaluated FLLs was 38.8 mm ( $\pm$  20.0 mm). The results of the visual and quantitative assessments showed no significant correlations with lesion size (all  $P > 0.84$ ).

## Discussion

Concerning MR-guided liver interventions, the purpose of this study was to determine the optimal sequence parameters of a real-time T1w GRE sequence, which was acquired 20 min after the injection of a liver-specific contrast agent. In the literature, various real-time sequences have been evaluated for image-guided procedures of the liver, exemplarily by Rempp et al.<sup>17</sup> They assessed the conspicuity of FLL with a non-contrast T1w spoiled GRE sequence as well as a predominantly T2w balanced steady-state free precession sequence, revealing that 20% of hepatic lesions could not be detected through the use of these sequences. Consequently, the use of liver-specific contrast agents may be beneficial in interventional settings, comparable to diagnostic MRIs, in which contrast-enhanced T1w sequences constitute the current reference standard to detect and characterize FLLs.<sup>22</sup>

In this systematic evaluation of sequence parameters, significant differences were found for the visual assessments of the target and risk structures and the extent of artifacts as well as for the quantitative assessment of signal intensities depending on the used FA and matrix size. No differences were found for TR and BW.

Regarding the FA, better conspicuity of the lesions and vascular structures was observed for higher FAs, with better results for 30° compared with 15°, while there were only minor differences between 30° and 60°. This is in contrast to contrast-enhanced MRI using the T1w GRE sequence for diagnostic purposes, in which the FA usually ranges from 10° to 15°.<sup>23</sup>

Another aspect to consider is the decrease in SNR with increasing FA above the Ernst angle ( $\alpha_E$ ) in fluoroscopic GRE sequences. It is known that the MR signal is maximized at  $\alpha_E$ .

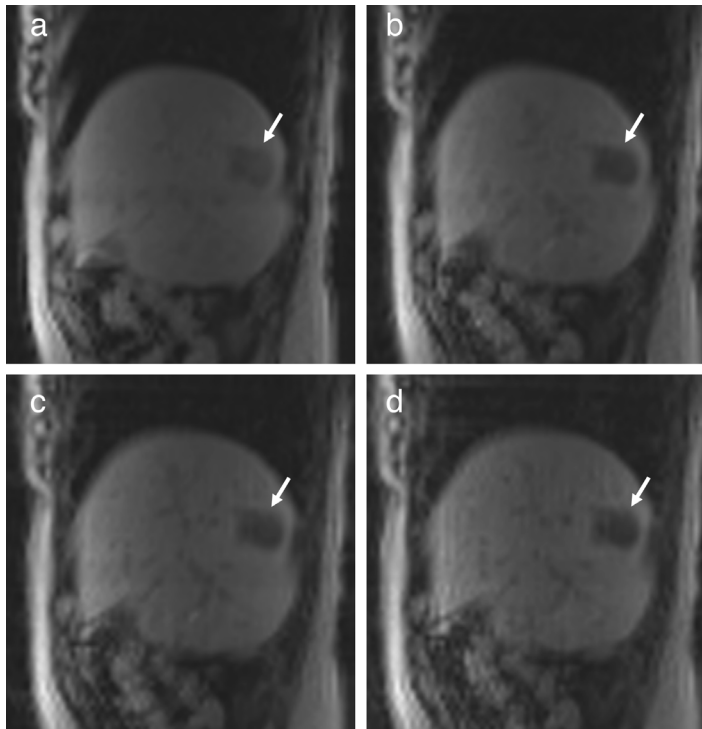


**Figure 1.** Measurement series (a, b). Real-time T1-weighted gradient-recalled echo sequences showing sagittal planes with different flip angles performed in increasing order (measurement series 1a), 15°, 30°, 45°, and 60° (a-d). Note the different conspicuity of the hypointense target lesion (arrows) and vascular structures and the different extent of artifacts. Measurement series 1b in decreasing order (60°, 45°, 30°, and 15°) showed similar results.

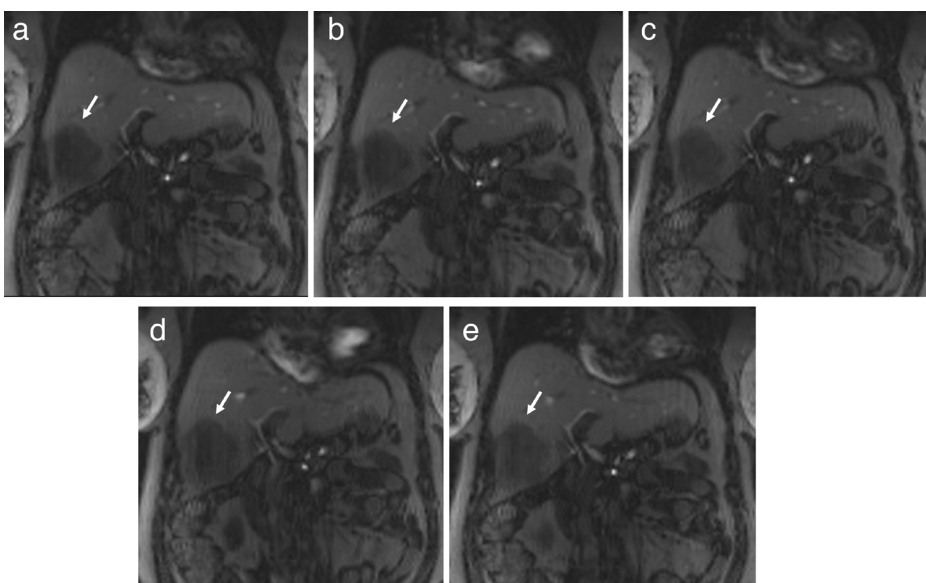


**Figure 2.** Measurement series 2. Real-time T1-weighted gradient-recalled echo sequences showing coronal planes with different repetition times of 5.47, 6.25, 7.03, 7.81, and 8.59 ms (a-e). Note the absence of difference in the conspicuity of hypointense target lesion (arrows) and vascular structures and the similar extent of artifacts.

which can be calculated from the equation  $\alpha_E = \arccos[\exp(-TR/T1)]^{24}$ . As exemplarily presented in previous work by Nagle et al.<sup>25</sup>, this equation leads to the highest liver SNR at 20°–35° in diagnostic hepatocyte phase imaging. In our study, the  $\alpha_E$  was lower in combination with a short TR (4.79–7.03 ms) in the fluoroscopic GRE sequences, so high and medium FAs did not lead to optimal liver SNRs. However, for MR interventions, and with respect to target conspicuity, the lesion–liver CNR, which was maximized at 30° and 45° in our assessment, can be considered more im-

portant than the SNR of the liver parenchyma in the setting of MR interventions. Increasing the FA in the hepatocyte phase reduces the SNR of non-hepatocyte-containing tissues, e.g., of FLL, without an effective transport mechanism, resulting in an improved lesion–liver CNR with the highest values at 30°–45°. Due to higher  $SD_{liver}$  and  $SD_{lesion}$  at 60°, the CNR is lower again at these FAs, while the lesion–liver contrast ratio is similarly high at 60°, compared with that at 30° and 40°. These contrast ratios are the consequence of increasing T1 weighting, causing greater

differences in contrast agent loads and thus optimizing the image contrasts between the FLL and the surrounding liver parenchyma.<sup>23</sup> However, a theoretical calculation is difficult and might not be feasible due to the unknown T1 values of the different FLLs, which are necessary for the calculation. In measurement series 1 of this study, more severe artifacts occurred for higher FAs (see Figure 1) in both increasing and decreasing measurement orders, indicating that this was a true effect; it was not confounded by the acquisition of higher FA measurements later during the scan and might have been affected by strong breathing artifacts. More precisely, we evaluated large differences in artifact extent between 15° and 30° and between 30° and 45°, while there were only slight differences between 45° and 60°. This is in line with the results of previous work. Exemplarily, Epstein et al.<sup>26</sup> evaluated RF-spoiled GRE sequences in a phantom study and compared FAs from 10° to 40°, resulting in more severe artifacts with an increased FA of 40°.

Regarding the matrix, there was better conspicuity of the target lesions and vascular structures as the matrix was increased. The greatest difference in the visual and quantitative assessments of the target lesions and vascular structures was found between 128 × 128 and 192 × 192. However, this difference in the conspicuity of the FLLs and vascular structures between the two matrix sizes is less than the difference between FAs of 15° and 30°. The chosen matrix size determines the voxel size, and thus, the spatial resolution; therefore, it is a quality feature of the acquired image data.<sup>27</sup> Thus, it is reasonable that a lower matrix size leads to worse conspicuity of target lesions and vascular structures due to an increased blurring of the images. On the other hand, the quantitative assessments of signal intensities showed significantly higher liver SNRs with decreasing matrix sizes. Thereby, the lesion–liver CNR also demonstrated increases; however, in comparison with the FA measurement series, these differences were not significant, as potentially may be expected with a larger sample size. Previous work has already revealed the effect of matrix and voxel size on signal intensities, concurring with our findings.<sup>28</sup> Our results suggest that for the visualization of target and risk structures in fluoroscopy images, spatial resolution and image quality have more impact than the corresponding differences in signal intensities.

Regarding the extent of ghosting artifacts, fewer artifacts occurred as the matrix sizes increased. More precisely, we evaluated

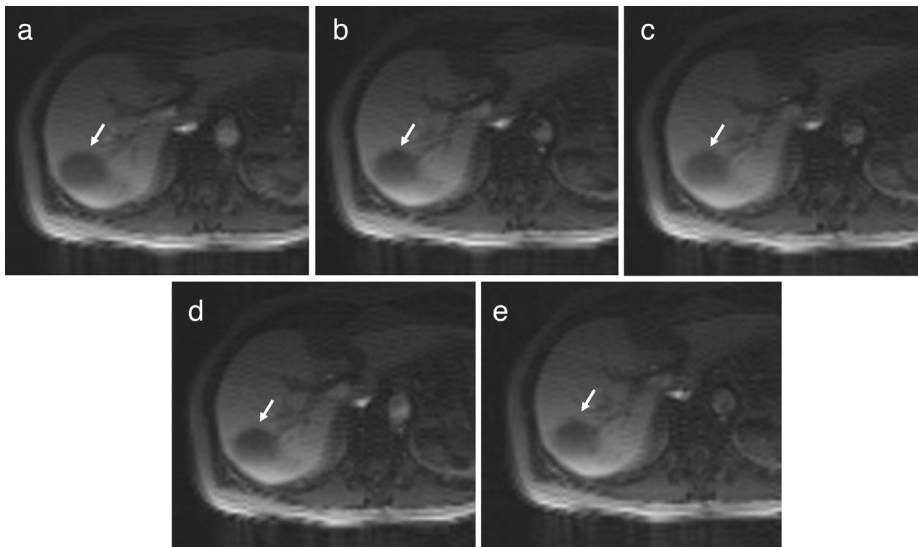


**Figure 3.** Measurement series 3. Real-time T1-weighted gradient-recalled echo sequences showing axial planes with different bandwidths of 300, 400, 500, 600, and 700 Hz/pixel (a–e). Note the absent difference in conspicuity of hypointense target lesion and vascular structures and the similar extent of artifacts.

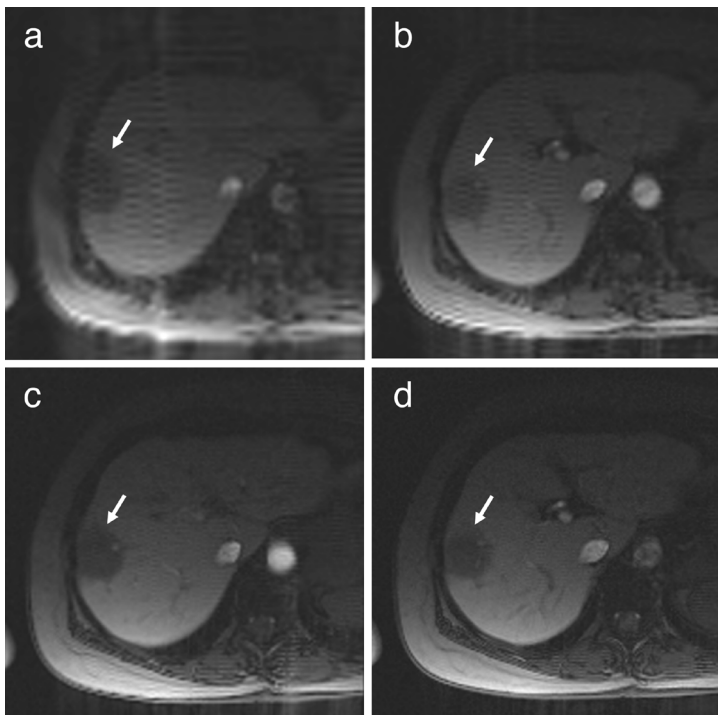


**Figure 4.** Measurement series 4. Real-time T1-weighted gradient-recalled echo sequences showing axial planes with different matrix sizes: 96 × 96, 128 × 128, 192 × 192, and 256 × 256 (a–d). Note the difference in the conspicuity of hypointense target lesion (arrows) and vascular structures and the different extent of artifacts.

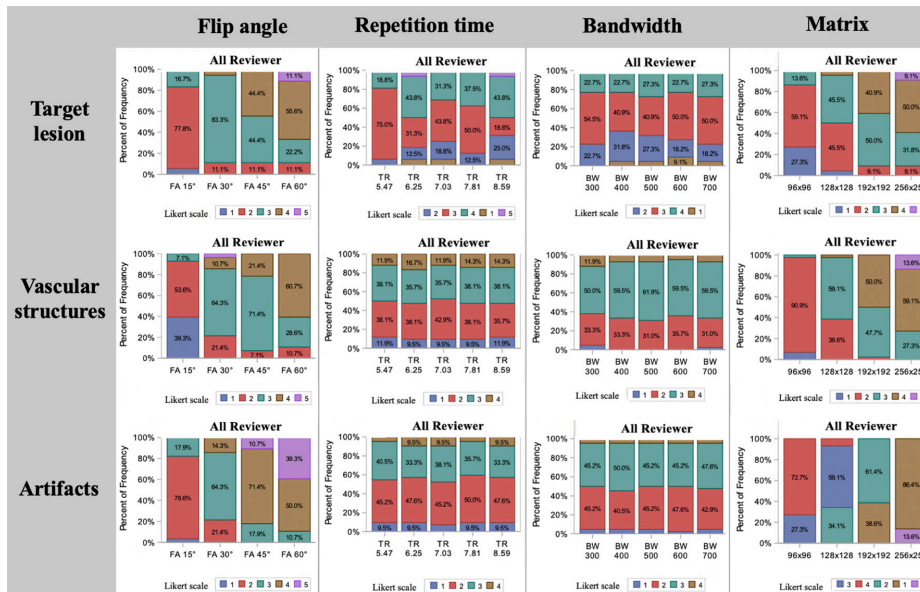


**Figure 5.** Results of visual assessment. Stacked column chart of measurement results of both readers (first row, conspicuity of target lesion; second row, conspicuity of vascular structures; third row, extent of artifacts) relative to the varied sequence parameters flip angle (first column, 15°–60°), repetition time (second column, 5.47–8.59 ms), bandwidth (third column, 300–700 Hz/pixel), and matrix size (fourth column, 96 × 96–256 × 256).

**Table 3.** Visual assessment for modified sequence parameters of T1-weighted gradient-recalled echo fluoroscopy images by two independent readers. Qualitative data assessment in the use of a Likert scale for the visualization of the target lesion and vascular structures (–1 to 5), artifact behavior (0 to 5), and corresponding Friedman’s test results. Values of both readers were averaged and are presented as means ± standard deviation

	Target lesion <i>P</i> value	Vascular structures <i>P</i> value	Artifacts <i>P</i> value
FA (n = 30)	<i>P</i> = 0.001*	<i>P</i> < 0.001*	<i>P</i> < 0.001*
15	1.7 ± 0.3	2.0 ± 0.4	1.1 ± 0.6
30	3.1 ± 0.4	3.2 ± 0.6	1.9 ± 0.5
40	3.2 ± 0.7	3.4 ± 0.5	3.0 ± 0.6
60	3.6 ± 0.8	3.8 ± 0.5	3.5 ± 0.7
TR (n = 21)	<i>P</i> = 0.14	<i>P</i> = 0.51	<i>P</i> = 0.53
5.46	3.1 ± 0.4	2.6 ± 0.9	2.6 ± 0.9
6.25	2.5 ± 1.2	2.7 ± 0.8	2.6 ± 0.9
7.03	2.9 ± 1.1	2.6 ± 0.8	2.6 ± 0.9
7.81	3.4 ± 0.7	2.8 ± 0.9	2.4 ± 0.9
8.58	3.4 ± 1.3	2.7 ± 0.9	2.6 ± 0.9
BW (n = 21)	<i>P</i> = 0.85	<i>P</i> = 0.87	<i>P</i> = 0.80
300	3.1 ± 0.5	2.6 ± 0.5	2.3 ± 0.7
400	2.9 ± 0.7	2.7 ± 0.5	2.4 ± 0.7
500	3.1 ± 0.7	2.7 ± 0.5	2.3 ± 0.7
600	3.0 ± 0.9	2.6 ± 0.5	2.4 ± 0.6
700	3.1 ± 0.9	2.7 ± 0.5	2.4 ± 0.7
Matrix (n = 22)	<i>P</i> < 0.001*	<i>P</i> < 0.001*	<i>P</i> < 0.001*
96 × 96	1.8 ± 0.6	2.0 ± 0.2	3.5 ± 0.5
128 × 128	2.7 ± 0.5	3.0 ± 0.3	2.4 ± 0.5
192 × 192	3.5 ± 0.5	3.7 ± 0.5	1.4 ± 0.5
256 × 256	3.8 ± 0.6	4.2 ± 0.6	0.7 ± 0.5

\*Statistical significance was considered at *P* < 0.0021 using a Bonferroni correction. FA, flip angle (degree); TR, repetition time (ms); BW, bandwidth (Hz/pixel); SD, standard deviation.

differences in artifact extent proportional to the matrix size (see Figure 4). The advantages of a higher matrix size are offset—besides by decreasing the SNR and CNR—by a longer acquisition time, resulting in a worse temporal resolution, which is crucial for guidance control and safety during interventions. Consequently, as a compromise, a medium matrix size proves to be optimal.

Regarding the chosen BW, our findings showed no differences in the visual assessments of the target and risk structures and the extent of artifacts or in the quantitative assessments of signal intensities. Contingently, the evaluated range was too small, although it was selected to clinical standards. It is well known that a higher BW enables faster data acquisition and minimizes chemical shift artifacts, but it also reduces SNR, as more noise is included. In addition, the chosen BW alters the extent of susceptibility artifacts, which are particularly important for needle interventions.<sup>27</sup> In summary, our study also suggests high BW values that are preferable to reduce metal artifacts while not significantly decreasing image quality. Regarding the TR, no significant differences in visual and quantitative assessments were found, which is of interest, as lower TRs result in shorter acquisition times, with consequently shorter image refresh rates during MR fluoroscopy.

Furthermore, our evaluation of the total visual and quantitative assessments revealed increased target visualizations and higher lesion–liver CNRs and contrast ratios of metastatic lesions in comparison with primary liver tumors. This is in line with the results of previous studies. Okada et al.<sup>29</sup> reported decreased visual conspicuity and signal intensities for hepatocellular carcinomas, compared with metastatic lesions, during FA modification using a contrast-enhanced T1w MRI protocol. In addition, when comparing cirrhotic with normal liver parenchyma, we found decreased target visualizations and decreased lesion–liver CNRs and contrast ratios in the event of chronic liver disease. This may be due to the circumstance of decreased contrast agent uptake of hepatocytes in cirrhotic liver parenchyma. Consequently, cirrhotic liver parenchyma may show reduced enhancement in the hepatobiliary phase, resulting in decreased lesion–liver contrast.<sup>30,31</sup> All the results of the visual and quantitative assessments showed no significant correlations to lesion size, similar to the findings of Rempp et al.<sup>17</sup> Accordingly, the individual clinical conditions of patients may have more impact on

the conspicuity of FLLs during MR-guided procedures than lesion sizes.

The present study has certain limitations. Some of the included patients had no FLLs, and additionally, not all FLLs were

included in the datasets of the acquired scan range because of the standardized acquisition by the single-slice technique at the level of the hepatic portal vein. Furthermore, a part of the cohort had re-

ceived previous therapy (partial liver resection and/or local ablation), which may have led to anatomical distortion and impacted the visualization of target and risk structures compared with the situation in therapy-naive patients. However, this heterogeneous cohort with both pre-treated and therapy-naive patients may illustrate a realistic view of MR-guided liver procedures, which are performed mainly in patients suffering from oncologic diseases, where there is a need for multimodal therapy concepts. Imaging was performed with just one MR scanner with 1.5-T field strength, and the influence of different magnetic field strengths was not considered. In addition, the measurement series was performed during routine imaging in diagnostic settings and not under interventional conditions. Consequently, there may be additional factors that influence the visualization of target and risk structures during interventional procedures that may hamper the direct extrapolation of our results. Finally, MR-guided interventions do not require only sequences adapted for the optimal visualization of target and vascular structures; the sequences also must be adapted to interventional instruments to minimize the extent of susceptibility artifacts. Thus, the analysis of susceptibility artifacts for different interventional needles using the optimized and specified sequences should be the subject of future studies.

Concerning the clinical practice and further developments of interventional MRIs of the liver, e.g., for biopsies, microwave ablations, percutaneous transhepatic cholangiodrainage, radiofrequency ablations, or brachytherapy, the results of this study highlight the possibility of optimizing real-time T1w MRI sequences to achieve appropriate conditions for interventional procedures.

In conclusion, we recommend an FA of 30°–45° and a matrix size of 128 × 128–192 × 192 to provide the optimal balance between a low extent of artifacts and a good visualization of target lesions and vascular structures in combination with high lesion–liver CNRs and liver SNRs. The visualization of the target lesion may vary due to clinical conditions, such as lesion type or associated chronic liver disease.

#### Conflict of interest disclosure

The authors declared no conflicts of interest.

**Table 4.** Quantitative assessment of lesion–liver contrast ratio (0 to 1), lesion–liver contrast-to-noise ratio, and liver signal-to-noise ratio for modified sequence parameters of T1-weighted gradient-recalled echo fluoroscopy images and the corresponding Friedman's test results. Values of both readers were averaged and are represented as means ± standard deviation

Mean lesion size (mm)	Mean lesion–liver CNR <i>P</i> value	Mean SNR liver <i>P</i> value	Mean lesion–liver contrast ratio <i>P</i> value
FA (n = 30)	40.4 ± 18.2	<i>P</i> = 0.004	<i>P</i> < 0.001*
15	8.4 ± 4.6	16.9 ± 6.8	0.6 ± 0.2
30	8.8 ± 3.2	13.5 ± 4.5	0.4 ± 0.2
45	8.9 ± 3.9	12.2 ± 4.4	0.4 ± 0.2
60	7.0 ± 3.1	10.1 ± 3.9	0.4 ± 0.2
TR (n = 21)	32.5 ± 22.4	<i>P</i> = 0.22	<i>P</i> = 0.31
5.46	8.5 ± 4.9	13.9 ± 5.0	0.5 ± 0.3
6.25	7.8 ± 4.2	12.7 ± 4.3	0.5 ± 0.3
7.03	9.2 ± 4.8	13.5 ± 5.1	0.5 ± 0.2
7.81	8.8 ± 4.5	13.8 ± 6.1	0.5 ± 0.3
8.58	8.5 ± 4.7	13.9 ± 6.3	0.5 ± 0.2
BW (n = 21)	38.3 ± 18.0	<i>P</i> = 0.44	<i>P</i> = 0.26
300	8.5 ± 3.6	13.6 ± 4.3	0.4 ± 0.1
400	9.1 ± 4.2	14.5 ± 7.1	0.4 ± 0.2
500	8.2 ± 4.4	13.2 ± 5.3	0.4 ± 0.1
600	9.2 ± 4.4	15.0 ± 6.3	0.4 ± 0.1
700	9.1 ± 4.7	13.8 ± 5.7	0.4 ± 0.2
Matrix (n = 20)	42.6 ± 23.1	<i>P</i> = 0.037	<i>P</i> < 0.001*
96 × 96	9.7 ± 6.1	15.9 ± 6.2	0.5 ± 0.3
128 × 128	9.4 ± 5.1	13.4 ± 3.5	0.4 ± 0.2
192 × 192	8.3 ± 4.5	11.6 ± 2.5	0.4 ± 0.2
256 × 256	7.5 ± 4.0	10.2 ± 2.7	0.4 ± 0.2

\*Statistical significance was considered at *P* < 0.0021 using a Bonferroni correction. FA, flip angle (degree); TR, repetition time (ms); BW, bandwidth (Hz/pixel); CNR, contrast-to-noise ratio; SNR, signal-to-noise ratio.

**Table 5.** Substratification analyses. The results of a Mann–Whitney U test between the group with metastatic lesions (n = 33) and patients with primary liver tumors (n = 10) present significant differences in the visual assessment of the target lesion and in the lesion–liver contrast-to-noise ratios and lesion–liver region-of-interest ratios. Values are presented as medians (interquartile range)

Total assessment	Primary liver tumor (n = 10)	Metastatic lesion (n = 33)	<i>P</i> value
Target lesions	3.0 (2.0–3.0)	3.0 (3.0–4.0)	<i>P</i> = 0.005*
Vascular structures	3.0 (2.0–3.0)	3.0 (2.0–3.0)	<i>P</i> = 0.96
Artifacts	3.0 (2.0–3.0)	2.0 (2.0–3.0)	<i>P</i> = 0.28
Lesion–liver ROI ratio	0.4 (0.3–0.6)	0.3 (0.2–0.5)	<i>P</i> = 0.015*
Liver SNR	13.0 (9.5–16.2)	13.1 (10.2–19.6)	<i>P</i> = 0.98
Lesion–liver CNR	7.7 (5.6–10.8)	10.0 (7.2–13.5)	<i>P</i> = 0.005*

\*Statistical significance was considered at *P* < 0.05. ROI, region of interest; SNR, signal-to-noise ratio; CNR, contrast-to-noise ratio.



**Table 6.** Substratification analyses. The results of a Mann–Whitney U test between the group with cirrhotic liver parenchyma (n = 6) and patients with normal liver parenchyma (n = 41) present significant differences in the visual assessment of the target lesion and in the lesion–liver contrast-to-noise ratio and lesion–liver region-of-interest ratio. Values are presented as medians (interquartile range)

Total assessment	Liver cirrhosis (n = 6)	Normal liver parenchyma (n = 41)	P value
Target lesion	2.0 (2.0–3.0)	3.0 (3.0–4.0)	P = 0.005*
Vascular structures	3.0 (2.0–3.0)	3.0 (2.0–3.0)	P = 0.45
Artifacts	3.0 (2.0–3.0)	2.0 (2.0–3.0)	P = 0.16
Lesion–liver ROI ratio	0.4 (0.3–0.6)	0.3 (0.2–0.5)	P = 0.032*
Liver SNR	12.1 (9.0–16.3)	13.0 (9.5–15.9)	P = 0.74
Lesion–liver CNR	7.6 (5.0–11.0)	9.7 (6.8–13.3)	P = 0.032*

\*Statistical significance was considered at P < 0.05. ROI, region of interest; SNR, signal-to-noise ratio; CNR, contrast-to-noise ratio.

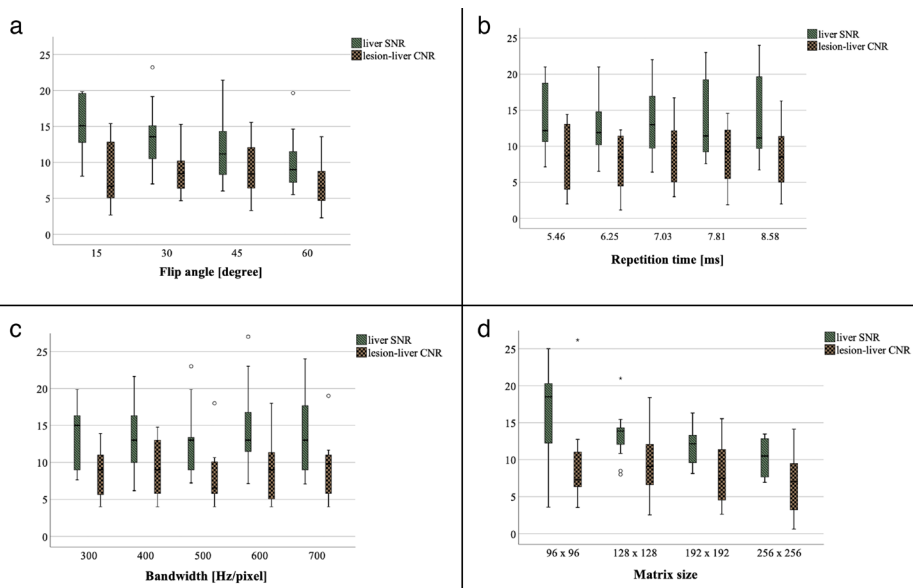


**Figure 6.** Results of qualitative assessment. Box and whisker plots of the lesion–liver contrast-to-noise ratio (CNR) and the liver signal-to-noise ratio (SNR) for the modified sequence parameters of T1-weighted gradient-recalled echo fluoroscopy images (a–d). The upper and lower ends of the vertical lines show the upper and lower extremes, respectively. The upper and lower margins of the boxes show the upper and lower quartiles, respectively. The horizontal lines in the boxes show the medians. Note the dependence of signal on the flip angle, with significantly higher liver SNR at 15° and lesion–liver CNR at 30°–60° (a). The SNR of the liver parenchyma and the lesion–liver CNR significantly decreases with higher matrix sizes (d).

## References

- Winkelmann MT, Gohla G, Kubler J, et al. MR-guided high-power microwave ablation in hepatic malignancies: initial results in clinical routine. *Cardiovasc Intervent Radiol.* 2020;43(11):1631–1638. [CrossRef]
- Elfatairy KK, Filson CP, Sanda MG, Osunkoya AO, Nour SG. In-Bore MRI-guided prostate biopsies in patients with prior positive transrectal US-guided biopsy results: pathologic outcomes and predictors of missed cancers. *Radiol Imaging Cancer.* 2020;2(5):e190078. [CrossRef]
- Winkelmann MT, Archid R, Gohla G, et al. MRI-guided percutaneous thermoablation in combination with hepatic resection as parenchyma-sparing approach in patients

- with primary and secondary hepatic malignancies: single center long-term experience. *Cancer Imaging.* 2020;20(1):37. [CrossRef]
- Weiss J, Hoffmann R, Rempp H, et al. Feasibility, efficacy, and safety of percutaneous MR-guided ablation of small (<=12 mm) hepatic malignancies. *J Magn Reson Imaging.* 2019;49(2):374–381. [CrossRef]
- Fischbach F, Thormann M, Seidensticker M, Kropf S, Pech M, Ricke J. Assessment of fast dynamic imaging and the use of Gd-EOB-DTPA for MR-guided liver interventions. *J Magn Reson Imaging.* 2011;34(4):874–879. [CrossRef]
- Fischbach F, Bunke J, Thormann M, et al. MR-guided freehand biopsy of liver lesions

- with fast continuous imaging using a 1.0-T open MRI scanner: experience in 50 patients. *Cardiovasc Intervent Radiol.* 2011;34(1):188–192. [CrossRef]
- Donato H, França M, Candelária I, Caseiro-Alves F. Liver MRI: from basic protocol to advanced techniques. *Eur J Radiol.* 2017;93:30–39. [CrossRef]
- Bock M, Umathum R, Zuehlsdorff S, et al. Interventional magnetic resonance imaging: an alternative to image guidance with ionising radiation. *Radiat Prot Dosimetry.* 2005;117(1–3):74–78. [CrossRef]
- Weiss J, Hoffmann R, Clasen S. MR-guided liver interventions. *Top Magn Reson Imaging.* 2018;27(3):163–170. [CrossRef]
- Barkhausen J, Kahn T, Krombach GA, et al. White paper: interventional MRI: current status and potential for development considering economic perspectives, part 1: general application. *Rofo.* 2017;189(7):611–623. [CrossRef]
- Ricke J, Thormann M, Ludewig M, et al. MR-guided liver tumor ablation employing open high-field 1.0T MRI for image-guided brachytherapy. *Eur Radiol.* 2010;20(8):1985–1993. [CrossRef]
- Fischbach F, Fischbach K, Ricke J. Percutaneous interventions in an open MR system: technical background and clinical indications. *Radiologe.* 2013;53(11):993–1000. [CrossRef]
- Fischbach F, Porsch M, Krenzien F, et al. MR imaging guided percutaneous nephrostomy using a 1.0 Tesla open MR scanner. *Cardiovasc Intervent Radiol.* 2011;34(4):857–863. [CrossRef]
- Fischbach F, Wien L, Krueger S, et al. Feasibility study of MR-guided transluteal targeted in-bore biopsy for suspicious lesions of the prostate at 3 Tesla using a freehand approach. *Eur Radiol.* 2018;28(6):2690–2699. [CrossRef]
- Gossmann A, Bangard C, Warm M, Schmutzler RK, Mallmann P, Lackner KJ. Real-time MR-guided wire localization of breast lesions by using an open 1.0-T imager: initial experience. *Radiology.* 2008;247:535–542. [CrossRef]
- Neri E, Bali MA, Ba-Ssalamah A, et al. ESGAR consensus statement on liver MR imaging and clinical use of liver-specific contrast agents. *Eur Radiol.* 2016;26(4):921–931. [CrossRef]
- Rempp H, Loh H, Hoffmann R, et al. Liver lesion conspicuity during real-time MR-guided radiofrequency applicator placement using spoiled gradient echo and balanced steady-state free precession imaging. *J Magn Reson Imaging.* 2014;40(2):432–439. [CrossRef]
- Yutzy SR, Duerk JL. Pulse sequences and system interfaces for interventional and real-time MRI. *J Magn Reson Imaging.* 2008;27:267–275. [CrossRef]
- Richard HM, McMillan A, Staats PN, d’Othee BJ. Real-time MR imaging guidance for percutaneous core biopsy of US- and

- CT-negative lesion. *J Vasc Interv Radiol*. 2012;23(11):1539-1542. [\[CrossRef\]](#)
20. Dietrich O, Raya JG, Reeder SB, Reiser MF, Schoenberg SO. Measurement of signal-to-noise ratios in MR images: influence of multichannel coils, parallel imaging, and reconstruction filters. *J Magn Reson Imaging*. 2007;26(2):375-385. [\[CrossRef\]](#)
  21. Dietrich O, Raya JG, Reeder SB, Ingris M, Reiser MF, Schoenberg SO. Influence of multichannel combination, parallel imaging and other reconstruction techniques on MRI noise characteristics. *Magn Reson Imaging*. 2008;26(6):754-762.
  22. Zech CJ, Herrmann KA, Reiser MF, Schoenberg SO. MR imaging in patients with suspected liver metastases: value of liver-specific contrast agent Gd-EOB-DTPA. *Magn Reson Med Sci*. 2007;6(1):43-52. [\[CrossRef\]](#)
  23. Bashir MR, Merkle EM. Improved liver lesion conspicuity by increasing the flip angle during hepatocyte phase MR imaging. *Eur Radiol*. 2011;21(2):291-294. [\[CrossRef\]](#)
  24. Ernst RR, Anderson WA. Application of fourier transform spectroscopy to magnetic resonance. *Review of Scientific Instruments*. 1966;37:93. [\[CrossRef\]](#)
  25. Nagle SK, Busse RF, Brau AC, et al. High resolution navigated three-dimensional T<sub>1</sub>-weighted hepatobiliary MRI using gadoxetic acid optimized for 1.5 Tesla. *J Magn Reson Imaging*. 2012;36(4):890-899. [\[CrossRef\]](#)
  26. Epstein FH, Mugler JP, Brookeman JR. Spoiling of transverse magnetization in gradient-echo (GRE) imaging during the approach to steady state. *Magn Reson Med*. 1996;35(2):237-245. [\[CrossRef\]](#)
  27. Frahm C, Gehl HB, Melchert UH, Weiss HD. Visualization of magnetic resonance-compatible needles at 1.5 and 0.2 Tesla. *Cardiovasc Intervent Radiol*. 1996;19(5):335-340. [\[CrossRef\]](#)
  28. Ogura A, Maeda F, Miyai A, Kikumoto R. Effects of slice thickness and matrix size on MRI for signal detection. *Nihon Hoshasen Gijutsu Gakkai Zasshi*. 2005;61:1140-1143. [\[CrossRef\]](#)
  29. Okada M, Wakayama T, Yada N, et al. Optimal flip angle of Gd-EOB-DTPA-enhanced MRI in patients with hepatocellular carcinoma and liver metastasis. *Abdom Imaging*. 2014;39(4):694-701. [\[CrossRef\]](#)
  30. Kim HY, Choi JY, Park CH, et al. Clinical factors predictive of insufficient liver enhancement on the hepatocyte-phase of Gd-EOB-DTPA-enhanced magnetic resonance imaging in patients with liver cirrhosis. *J Gastroenterol*. 2013;48(10):1180-1187. [\[CrossRef\]](#)
  31. Xiao YD, Ma C, Liu J, Li HB, Zhang ZS, Zhou SK. Evaluation of hypointense liver lesions during hepatobiliary phase MR imaging in normal and cirrhotic livers: is increasing flip angle reliable? *Sci Rep*. 2016;6:18942. [\[CrossRef\]](#)



# Catheters in vascular interventional radiology: an illustrated review

Vineeta Ojha   
Sreenivasa Narayana Raju   
Amit Deshpande   
Kartik P. Ganga   
Sanjeev Kumar 

## ABSTRACT

The past five decades have seen significant developments in the knowledge and practice of interventional radiology. Advancements in angiographic equipment have made interventional radiology a safe, minimally invasive preferred option in the treatment of a variety of diseases. Today, a range of catheters are available in the armamentarium of the interventional radiologist to suit different needs when conducting diagnostic angiograms or performing interventions in various vascular territories. The hardware required for interventions includes needles, wires, catheters, balloons, and stents. Catheters, in particular, are an invaluable tool for interventionists. The purpose of this review is to describe the identification characteristics, properties, and uses of the common angiographic catheters used in interventional radiology, with a special focus on peripheral vascular interventions (excluding neurointerventions).

## KEYWORDS

Angiocardiography, catheter, catheter angiography, interventional, vascular

The catheter is an invaluable tool for interventional radiologists. In 1929, Dr. Werner Forssmann demonstrated the catheterization of the pulmonary artery with a simple rubber catheter by performing an angiogram through the ante-cubital vein.<sup>1</sup> Today, a variety of catheters are available in the armamentarium of the interventional radiologist to suit different needs. However, the literature lacks a comprehensive compilation of the properties, types, and uses of catheters. In this review, we aim to describe the characteristics, properties, and uses of the common angiographic catheters used in vascular interventions.

## Properties of catheters

A catheter is a flexible hollow tube that can be inserted into a duct, body cavity, or vessel. It consists of a hub at the rear end and a distal tubular shaft. The shaft can be straight or molded into different curved shapes (primary, secondary, or tertiary curves) and can have a tapered or non-tapered tip (Figure 1). Catheterization is the process of inserting a catheter. Angiographic catheters are the most important tool in any vascular intervention. They are introduced through a sheath placed at the vascular access site. Wires introduced via these catheters are navigated to enter the target vessels. Once the catheters are inside the vessel, they can be used to conduct diagnostic angiography of the intended vascular territory and as a conduit for the delivery of balloons and stents for endovascular intervention at the intended location.

An ideal catheter should have strength, good torque control, radiopacity, flexibility, an atraumatic tip, and low surface friction for good trackability over a guidewire.<sup>2</sup>

## Construction

i) Surface coating: surface coatings can modify the catheter's friction coefficient, thrombogenicity, or antimicrobial properties. ii) Outer layer: angiographic catheters can be made of polyethylene, polyurethane, nylon, polytetrafluoroethylene, silicone, polyvinyl chloride, or a combination of these materials. Their respective properties, advantages, and disadvantages are discussed in Table 1.<sup>3,4</sup> The coefficient of friction on the luminal side is important for easy passage of the wire and achieving high flow rates of contrast during angiography. Conversely, a low coefficient of friction on the catheter's outer surface helps its trackability,

From the Department of Cardiovascular Radiology and Endovascular Interventions (V.O., S.N.R., A.D., K.P.G., S.K. [✉ sanjeevradio@gmail.com](mailto:sanjeevradio@gmail.com)) All India Institute of Medical Sciences, New Delhi, India.

Received 5 August 2021; revision requested 15 June 2021; last revision received 9 September 2021; accepted 13 September 2021.



Epub: 28.12.2022

Publication date: 31.01.2023

DOI: 10.5152/dir.2022.21233

You may cite this article as: Ojha V, Raju SN, Deshpande A, Ganga KP, Kumar S. Catheters in vascular interventional radiology: an illustrated review. *Diagn Interv Radiol.* 2023;29(1):138-145.

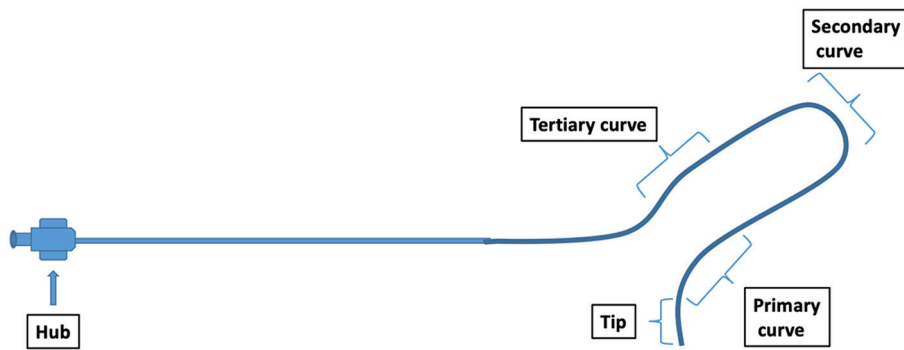


**Figure 1.** Basic construction of a catheter. Catheter consists of a hub at the rear end and a distal tubular shaft. The shaft can be straight and molded into different curves (primary, secondary or tertiary) and can have a tapered or non-tapered tip.

although this is at the expense of positional stability during injection.<sup>5</sup> The rigidity of the material allows the catheter to withstand the pressure sure exerted by the blood over an extended length of time. Selective catheters made of polyethylene are frequently braided with stiffer materials, such as nylon or stainless steel, to help maintain their torsional strength as well as increase torque control. The pushability of the catheter is also dependent on the bending stiffness of the material and the coefficient of friction at the external surface of the catheter. Catheters made with materials with less stiffness, like polyethylene, are more likely to negotiate the tortuosity of vessels, but they are more prone to bending or buckling. Buckling may also occur if the friction between the external surface of the catheter and the vessel wall is increased. Additionally, it can occur when the catheter is wedged on the wall of the vessel without perforating it.<sup>6</sup> iii) Tip: a rounded tip is less traumatic than square or bevel-ended tubing and is easier to insert. iv) Reinforcement: single or double wire braiding is utilized for extra torquability.<sup>3</sup>

### Measurement

The size of the catheter is represented by its outer diameter, measured in French (Fr) units (1 Fr= 0.333 mm/0.013 in). A 3-F catheter

means the outer diameter of the catheter is 1 mm. Mostly, a catheter is narrower at the advancing end and wider at the hub. For example, a Progreat™ (Terumo Interventional Systems) catheter specified as 2.4/3 F means the outer diameter of its tip is 2.4 Fr, and it measures 3 Fr at the hub end.<sup>7</sup> A disadvantage of this scale is that it does not specify the inner diameter of the catheter or tub-

ing. The catheter diameter specified by the manufacturer corresponds to its outer diameter and to the inner diameter of a vascular sheath. Thus, a 4-F catheter can pass through a 4-F vascular sheath.

Most angiographies are performed with 4 or 5-F catheters over 0.035 or 0.038-in guidewires. The diameter of the catheter to be used is determined by the age of the patient, size of the vessel, rate of blood flow, and whether a selective or super-selective study is desired.

The inner diameter of a catheter is measured in inches (in). Knowledge of the inner diameter is necessary for introducing compatible guidewires inside the catheter. For example, the Progreat catheter (2.4/3 F) has an inner diameter of 0.022 in. Hence, it can admit guidewires with a diameter of less than 0.022 in. This information is usually stated on the packaging of the catheter.<sup>8</sup>

A guiding catheter is represented by its outer diameter in Fr.<sup>9</sup> The inner diameter of a guide catheter is larger than the correspond-

**Table 1.** Properties of materials used for constructing catheters

Material	Coefficient of friction	Stiffness	Torsional strength	Advantages	Disadvantages	Used in
PTFE	Low	High	Low	Kink resistant, easier to track through scarred or obese groin tissue	Reduced flexibility, difficult negotiation across tortuous vessels	Sheaths and dilators Inner layer of guiding catheter
Polyethylene	Moderate	Low	Moderate	Good shape memory Pliable	Tends to become soft with repeated use with resultant loss of shape and torsional rigidity Often reinforced with braiding (nylon or stainless steel) to prevent loss of shape	Selective catheters
Nylon	High	High	High	Resists softening with repeated use Can withstand high pressure during flush injections	Reduced flexibility Difficult negotiation across tortuous vessels	Flush catheters Mechanical braiding of selective catheters and guide catheters
Polyurethane	High	Low	Moderate to high	Soft and pliable	Difficult passage over wire	Outer surface of guide catheters

PTFE, polytetrafluoroethylene.

### Main points

- The catheter is an invaluable tool for interventionalists.
- The purpose of this review is to describe the identification characteristics, properties, and uses of common angiographic catheters used in interventional radiology, with a special focus on peripheral vascular interventions.
- The appropriate selection of catheters in various scenarios and vessels is of the utmost importance and is discussed.

ing diagnostic catheter with the same outer diameter. For example, the inner diameters of a 6-F Radifocus™ Optitorque™ (Terumo Corporation, Tokyo, Japan) angiographic catheter and a 6-F Heartrail™ III (Terumo Corporation, Tokyo, Japan) guiding catheter are 1.3 and 1.8 mm, respectively, with a 2-mm outer diameter (Figure 2).<sup>10,11</sup>

The length of the catheter used is determined by the access site and the desired application. Ideally, it should be of sufficient length to reach the target site and still have enough of its entire length remaining outside the patient. For example, to perform a cerebral angiogram from the femoral approach, a 100-cm catheter is used; however, a 65-cm catheter will suffice for a renal arteriogram (Table 2). Resistance is directly proportional to length, so excessive length should be avoided.

### Torsional strength

This refers to the ability to steer the curve at the distal tip in a certain direction by rotating the proximal end of the catheter. This is considered a function of catheter diameter and is proportional to the difference between the fourth powers of the outer and inner diameters (Figure 3). The approximate torsional strength also varies according to the material of the catheter; for instance, the ratio of the torsional strength of Teflon–polyethylene–nylon is approximately 1:2:4. Wire reinforcement increases rotational stability by a factor of 3.<sup>12</sup>

### The flow rate of contrast

The flow rate of contrast is specified by the manufacturer. It follows Poiseuille's law and depends upon the viscosity of the contrast, the pressure gradient across the tubing, and the diameter and length of the catheter (Table 3). Doubling the inner diameter increases the flow rate by 16 times, in concordance with Poiseuille's law.<sup>13</sup> Doubling the length of the catheter decreases the contrast flow rate by half, which is inversely proportional to the viscosity of the contrast (Figure 4). Increasing the pressure maximizes the flow. Because of this, the pressure-bearing capacity of the catheter wall is an important consideration.

### Technical properties

*Trackability* is the ability of a catheter to follow a guidewire. *Pushability* is defined as the forward movement of the tip of the catheter due to the force applied by the operator at the hub of the catheter. *Crossability* is defined as the ability of a catheter to navigate across a tortuous or diseased arterial segment. *Steerability/torquability* refers to the rotational strength; i.e., the steering responsiveness of the catheter tip to handling maneuvers performed at the hub.<sup>14</sup>

### Catheter shapes

Catheter shapes are derived from the presence or absence of curves, such as the primary curve, secondary curve, and occasionally, the tertiary curve. The various types are i) straight catheter (no curve), ii) pigtailed

catheter (for flush aortograms), iii) simple curve or single curve catheters [(e.g., the multipurpose Head Hunter (H1) catheter)], and iv) complex curve catheters, which are usually a primary, secondary, and occasionally, a tertiary curve; these are subdivided into double curve [e.g., Cobra catheter, renal double-curve (RDC) catheter] and reverse-curve catheters (i.e., sidewinder catheters, e.g., Simmons and SOS Omni catheters). Both pigtailed and straight catheters have multiple side holes, which help in injecting a large volume of contrast at a high rate (velocity). They are also called *flush* catheters.<sup>15</sup>

### Side holes

Catheters can also be classified depending on the number and type of side holes: i) single hole, ii) end hole with side holes (flush catheters for high-pressure and high-volume contrast injections), and iii) blocked end with side holes only. Side holes have multiple advantages, such as reducing resistance, reducing recoiling, allowing the effective distribution of contrast in large vessel lumens, and improving the opacification of proximal arterial side branches. However, at high injection pressures close to the catheter tolerance level, high-flow jets of contrast may escape from the side holes, which can cause the subintimal extravasation of contrast and vessel wall injury. This is known as the *jet effect*, which is a relatively uncommon but well-known complication of angiography.<sup>16</sup>

### Types of catheters used in an interventional radiology suite

Vascular catheters can be broadly classified on the basis of the abovementioned properties:

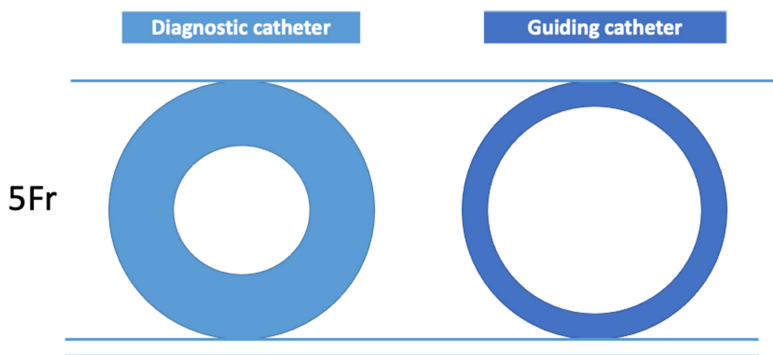


**Figure 2.** Diameter of the guiding catheter lumen is larger than the diagnostic catheter for similar French sizes.

Length (cm)	Purpose (from transfemoral approach)
15–20	Dilator
65	Abdominal aortography with lower extremity runoff, contralateral iliac artery injections
65–80	Selective renal and visceral catheterizations
90	Arch aortography, thoracic aortography
100	Selective cerebral catheters

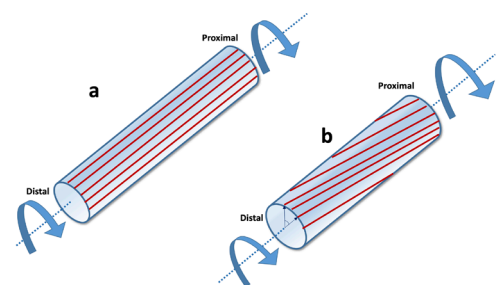


**Figure 3.** Schematic diagram showing the concept of torsion, i.e., the measure of the ability of a material to withstand a twisting load. Torsion is a moment that twists/deforms a member about its longitudinal axis. (a) Stiff catheter (e.g., nylon) with no deformation of longitudinal lines on applying torsion. (b) Non-stiff catheter (e.g., polytetrafluoroethylene) with deformation of longitudinal lines on applying torsion.

**Table 3.** Contrast-media flow rates<sup>20</sup>

Type of catheter	Caliber (in French)	Length (in cm)	Maximum flow rate (in mL/second) for 65- and 100-cm catheters, respectively (max pressure: 1.200 psi)
Flush (multiple side holes)	4	65, 100	19, 15
	5	65, 100	32, 27
Selective (end hole only)	5	65, 100	15, 11

Data from Cook Medical.

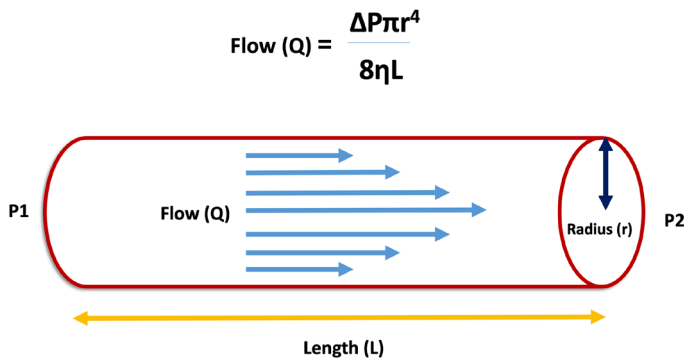


**Figure 4.** Schematic diagram showing Poiseuille's law. It states that the flow (Q) of fluid is related to a number of factors: the viscosity ( $\eta$ ) of the fluid, the pressure gradient across the tubing (P), and the length (L) and radius (r) of the tubing.

- A. Selective catheters,
- B. Hemodynamic catheters,
- C. Guide catheters,
- D. Special catheters (e.g., microcatheters, flush catheters, drainage catheters, central venous catheters, sizing catheters, exchange catheters, and balloon catheters).

#### A) Selective catheters

Selective diagnostic catheter sizes range from 4 to 6 F, with lengths from 50 to 125 cm, respectively. Most of these catheters are braided and have soft tips. The following are examples of common selective catheters. The principles behind the selection of diagnostic catheters are described in a later section.

##### a) Catheters for arch vessel cannulation:

- **Cerebral catheters (for arch vessel cannulation):** Simple curve, Head Hunter (H1), Bentson Hanafee Wilson (JB1), Bernstein, multipurpose (MPA, MPB), vertebral, Picard, and internal mammary catheters.
- **Complex curve catheters:** Head Hunter (H2, H3), Bentson Hanafee Wilson (JB2, JB3), Simmons (SIM1, 2), Newton (HN3, HN4), Mani, and Judkin's right coronary catheters.

##### b) Catheters for visceral artery cannulation:

- **End-hole catheters:** Cobra (C1, C2, C3), Rosch Celiac (RC1, RC2, RC3), shepherd's

hook, Mikaelsson, SOS Omni, sidewinder (SIM1, 2, 3), and RDC catheters.

- **Superselective end-hole catheters:** Rosch left gastric, Rosch hepatic, and Rosch dorsal pancreatic

The features of some common visceral catheters are described below:

- **Cobra catheter:** This type has a primary and secondary curve (double-curve catheter). The C1 and C2 types are progressively more curved (Figure 5). The Cobra catheter is relatively easy to direct, and its shape helps in the cannulation of visceral arteries, such as renal, bronchial, or celiac arteries. It is used extensively in renal arterial procedures, bronchial artery embolization, and aortopulmonary collateral embolization in patients with congenital heart disease.
- **Renal double-curve catheter:** This is a double-curve catheter with the tip pointing downwards. It is designed specifically to catheterize the acutely originating renal artery.
- **Sidewinder/Simmons' catheter:** This was first described in 1972. It is a reverse-curve catheter that is used for cannulating the arch vessels in tortuous anatomy, as it advances with a withdrawal motion. It has three curves, and the secondary curve is also known as the *knee*. The tertiary curve helps in the anchorage at the aorta. Sim-

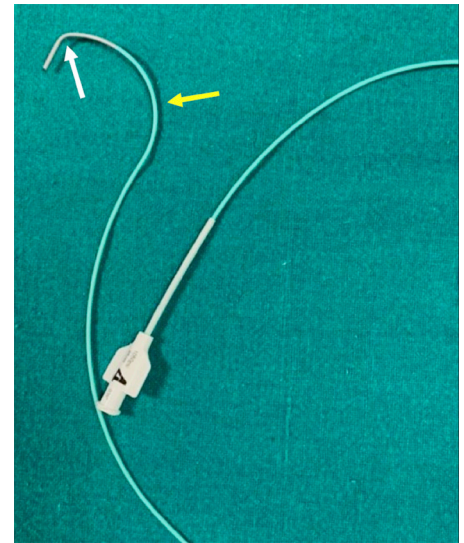


**Figure 5.** Cobra catheter with primary curve (white arrow) and secondary curve (yellow arrow).

mon's catheter can be used in open or closed-loop configurations. There are various methods described for its formation, such as the left subclavian method, renal method, aortic bifurcation, or ascending aorta method. The left subclavian method of formation is considered the best and safest. Simmons' catheter is prone to becoming knotted, so care is required when it is being operated. A Beacon<sup>®</sup>-tipped Simmons' catheter can break; hence, it should be checked for length after use.<sup>17</sup>

- **Rosch celiac catheter:** The simple "C"-shaped curve of this catheter is the most appropriate for the celiac and superior mesenteric artery. If using the contralateral femoral approach, the common iliac artery is catheterized easily with an RC1. The RC3 is also known as the Rosch inferior mesenteric artery catheter and is used specifically for the catheterization of the inferior mesenteric artery.
- **Multipurpose catheter:** This is made of polyurethane. The MPA1 has a single-end hole, and the MPA2 has a single-end hole and two side holes (Figure 6). This type comes in 65, 80, 100, and 125-cm lengths and diameters of 4 to 7 F. Multipurpose catheters have a gentle 120° primary curve. They are the most commonly used catheter for selective angiograms. There is another MPA variant known as the Gensini MPA catheter. It comes in diameters of 4 to 7 F, with one end hole and six side

holes, and it is used for flush aortograms. The MPB catheter differs from the MPA in that it has a gentle 90° primary curve. Similar to MPA, MPB1 is an end-hole catheter, and MPB2 has an end hole and two side holes.

- **Robert's uterine artery catheter:** Anne Christine Roberts, an American interventional radiologist, designed this unique catheter. It has a long, sharp curve that facilitates access to both uterine arteries. This catheter tapers from 5-F (proximal end) to 4 F (distal end), and it has a soft radiopaque tip.<sup>18</sup>

### B) Hemodynamic catheters

The Swan-Ganz, Berman, and reverse Berman catheters are commonly used for pulmonary catheterization and hemodynamic assessment. They are used primarily for the assessment of portal and pulmonary hypertension. Usually, a balloon is attached to the catheter tip, and it can be inflated for measuring, for example, the hepatic and pulmonary capillary wedge pressures. A transducer is placed in the catheter, with which the

pressure waveform can be seen on a monitor during catheterization.

- **Swan-Ganz catheter:** This comes in sizes ranging from 60 to 110 cm in length and in calibers of 4 to 8 F. A balloon is proximal to the end hole. It is available with two to five lumens; each lumen has a different function, with the end hole utilized for pressure monitoring.
- **Berman and reverse Berman catheters:** These are available in sizes 4–8 F and in lengths from 50–110 cm. They do not have end holes but have multiple side holes. Since there is no end hole, wedge pressure cannot be measured. In the standard Berman catheter, the balloon is at the distal end and the side holes are proximal, so it can be used for balloon occlusion angiography of the proximal chamber or for measuring wedge pressure. In the reverse Berman catheter, the balloon is proximal (as in the Swan-Ganz catheter), and there are multiple side holes distal to the balloon.

### C) Guide catheters

These are special types of catheters that do not taper towards the tip and have a reinforced construction. Table 4 summarizes the basic uses and differences of guide catheters vs. diagnostic catheters. Guide catheters are generally 6 to 8 F in diameter and range from 65 to 100 cm in length. The properties of a guide catheter are determined by its diameter. A narrower guide catheter (e.g., 6 F) requires a smaller puncture and can be engaged deep into the artery; however, it provides less support and torquability compared to a guide catheter with larger diameter. It also limits the size of the device/stent that can be used. A larger guide catheter (7 to 8 F) provides more support, torque, and visualization, and it also allows the use of larger devices. However, this type of catheter also results in an increased use of contrast. The selection of the guide catheter to be used is based on the size of the aorta and the location and ostium of the vessel to be hooked, e.g., renal, right coronary, and MP guide catheters (Figure 7).<sup>15</sup>

### D) Special catheters

#### a) Microcatheters

These are 3 F or smaller in size and are designed for the catheterization of distal vessels. They are placed over a 0.010 to 0.025-in guidewire and are helpful in peripheral intervention for super selectively catheterizing smaller vessels for embolization. The 2.5-F Cantata microcatheter (Cook Medical, Bloomington, IN, USA) has a 0.021-in inner diameter and can deliver particles up to 500 µm in size. A 2.8-F Cantata microcatheter (Cook Medical, Bloomington, IN, USA) has an inner diameter of 0.025 in and can deliver particles up to 700 µm. They can be coaxially used only with catheters with an inner diameter of more than 0.035 in. They have

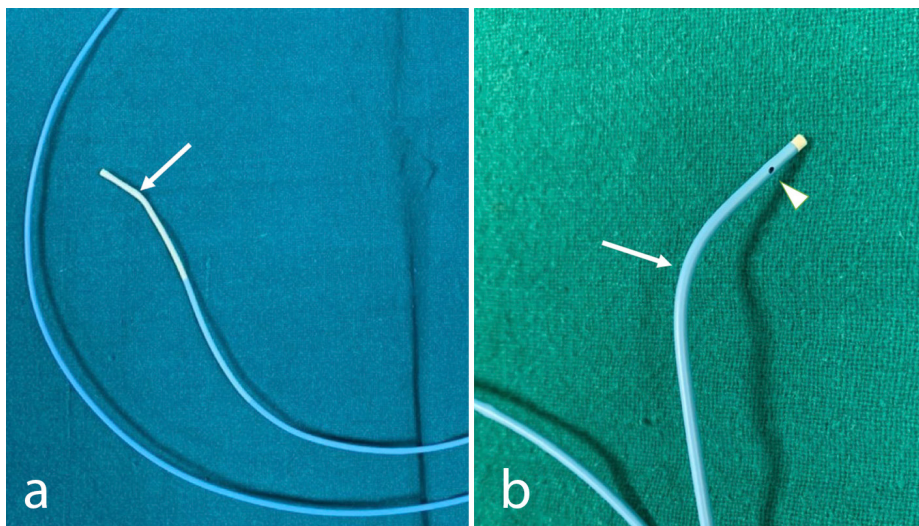


**Figure 6.** Multipurpose catheter (MPA 1) (a) with simple primary curve (arrow) and no side holes. Multipurpose catheter (MPA 2) (b) with simple primary curve (arrow) and side hole.

Table 4. Differences between diagnostic catheters and guide catheters	
Diagnostic catheter	Guide catheter
Engage arteries	Conduit for device/balloon and wire
Inner diameter small	Larger inner diameter allows for better contrast opacification, better guide support, and enables pressure monitoring
Pressure assessment less accurate than guide catheter	Better pressure monitoring
Only angiographic assessment	Both angiography and supporting diagnostic catheters/balloons/stents
More flexible shaft	Stiffer shaft
Tapered ends (usually), which can cause trauma	Non-tapered ends: atraumatic

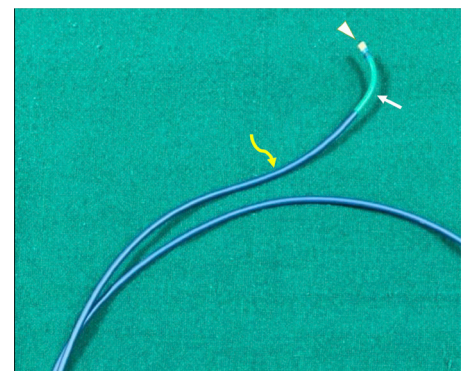


**Figure 7.** Renal double-curve guiding catheter with non-tapering tip (arrowhead) with primary (white arrow) and secondary curves (yellow curved arrow).

a braided construction for superior control, kink resistance, and trackability, with a radiopaque band for improved visibility. They are lipiodol/dimethyl sulfoxide compatible and have a hydrophilic coating for facilitating the introduction and reducing trauma.<sup>19</sup>

### b) Flush catheters

These catheters have one end hole and multiple side holes, which help in minimizing a jet effect that might destabilize arterial plaque or thrombus. They are used for high-pressure injections (up to 1,200 psi), such as those used in aortography and some peripheral arteriography. The shape of the catheter head may be altered dramatically using a guidewire. The main purpose of flush catheters is to achieve an optimum contrast opacification in high-flow large vessels (aorta, IVC) with a minimum amount of contrast.<sup>20</sup>

A pigtail catheter is an example of a flush catheter which is made of polyurethane or polyethylene and has 4–12 non-laterally opposite side holes in the last 5 cm. It is available in sizes 5 to 8 F and in lengths of 65 to 110 cm (Figure 8). The major advantages of this type are that there is no catheter recoiling, it avoids subintimal injection of contrast, it reduces the risk of small-branch vessel catheterization, and its multiple side holes contribute to effective contrast distribution. The loop of the pigtail catheter is designed to prevent the end hole coming in direct contact with the endocardium. Pigtail catheters are atraumatic, with reduced recoil and risk of perforation. Various modified pigtail catheters are available, including Positrol, Nycone, Ducor high flow, Merit, Quanticor, Grollman, and Van Tassel.

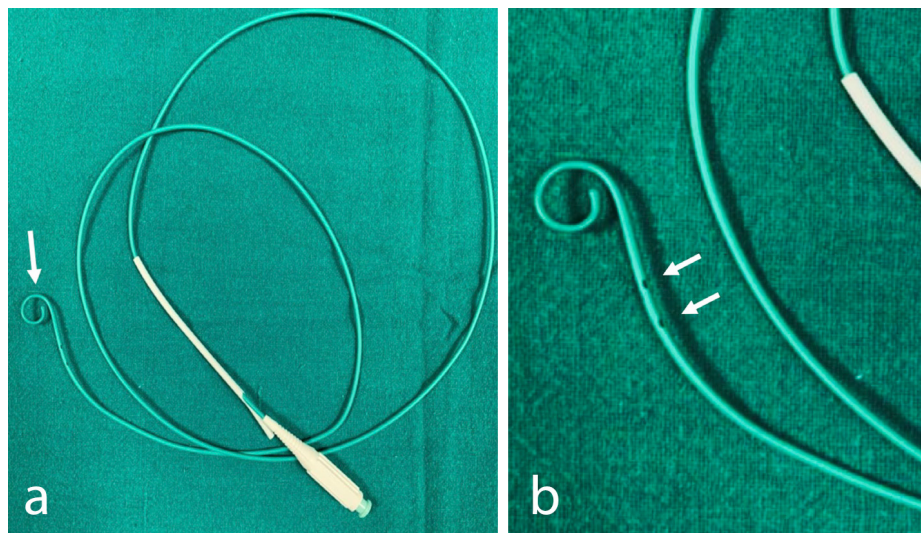


**Figure 8.** Pigtail catheter (a) with a pigtail loop (arrow). Sides are proximal to the pigtail loop (b) in the straight segment of the catheter (arrows).

### c) Balloon (angioplasty) catheters

These are either soft and pliable for use as occlusion balloons or Fogarty balloons (to retract thrombus) or they can be rigid for use in dilatation (angioplasty). Balloons for dilatation can be divided into two main categories: the monorail type (Figure 9), which has a single lumen, with the wire extending proximally, and the over-the-wire type (Figure 10), which has a different lumen for balloon inflation and the wire. There are two properties of these catheters: the rated burst pressure, which is up to and including the pressure at which balloons will not burst upon single inflation, and nominal pressure, which refers to the pressure at which the balloon reaches its labelled diameter.

### d) Sizing catheters

These are used to measure the lengths of vascular segments accurately, and they have metal markings on their body at regular intervals. For example, a marker pigtail catheter is used before the deployment of aortic stent grafts (Figure 11).

### e) Infusion catheters

These are special catheters used for the infusion of therapeutic drugs during catheter-directed thrombolysis (CDT). These catheters usually have two radiopaque bands at the distal end, with multiple side holes in between for the infusion of drugs. The length is called the infusion length of the catheter. The Cragg-McNamar™ catheter (Medtronic, USA) is widely used for CDT. It is available in 4 and 5-F diameters, with an infusion length varying from 5 to 50 cm. Finally, the MicroMewi infusion catheter (Medtronic, USA) is a micro-infu-

sion catheter available in a diameter of 2.9 F, with an infusion length of 5 or 10 cm.

### Principles of selecting a suitable catheter

The principles of selecting a particular catheter depend upon the angle of origin of the target artery and the access site (femoral or brachial/radial). The presence of ostial narrowing precludes the use of high-pressure injection in the diseased part, as it can lead to distal embolization of the clot. A catheter is selected according to the desired direction of travel.

**Tip length:** Increased length gives more stability in the target vessel at the cost of maneuverability in the parent vessel.

**Primary curve:** Chosen by assessing the angle of the target vessel from its parent artery.

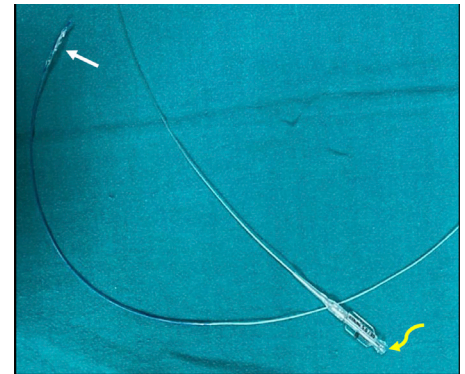


**Figure 9.** Monorail balloon catheter with the hub having only one inline lumen (curved yellow arrow) for the balloon inflation device with side port for the wire absent. The white arrow shows the tip of the catheter with a deflated balloon.

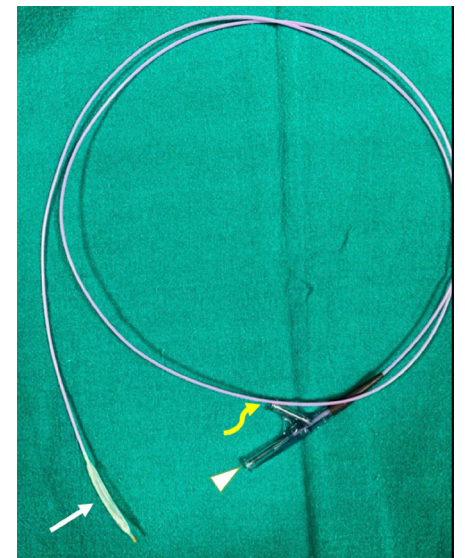


**Figure 10.** Over-the-wire balloon catheter with the hub having two lumens, the side port (yellow arrow) for the balloon inflation device, and the inline port (arrowhead) for the wire. The white arrow shows the tip of the catheter with a deflated balloon.



**Secondary curve:** Chosen by assessing the width of the parent vessel.

**Tertiary curve:** Chosen by assessing the normal curvature of the parent vessel.

**Catheter length:** As described earlier (Table 1).

**Arch vessel cannulation:** The simple curve catheters are preferred in the type 1 aortic arch; however, a complex curve catheter will be required in type 2, type 3, or bovine aortic arches to cannulate a particular branch vessel. A simple curve catheter, such as the Picard catheter (90° primary curve) (Figure 12), or complex double catheters, such as Judkin's right coronary catheter or internal mammary catheter, can be used to cannulate the internal mammary artery depending upon the angle of origin.

The simple curve catheters may not suffice in the brachial/radial approach, and complex curve catheters will be required in most cases.

**Visceral vessel cannulation:** Chuang<sup>21</sup> proposed the 110 rule for selective visceral artery cannulation; it states that the length of the catheter tip distal to the primary curve and the curve width should be 110% of the native artery at the level of the target branch

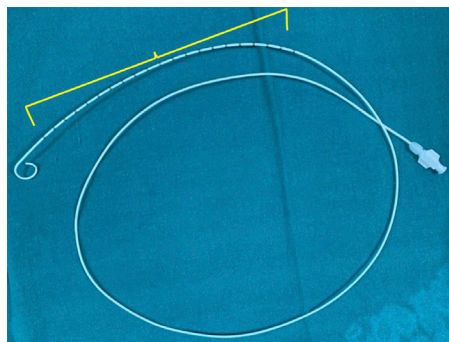


**Figure 11.** Marker pigtail catheter with platinum markers along the straight segment (bracket).

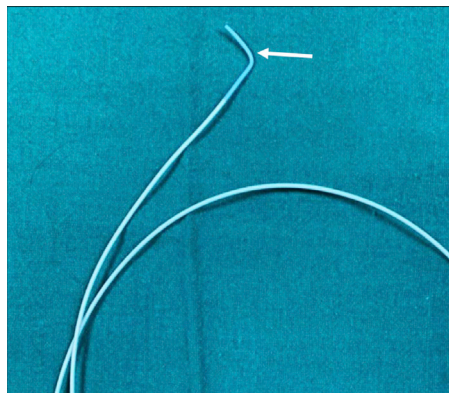


**Figure 12.** Picard catheter with 90° primary curve (arrow).

vessel (Figure 13). The use of specific catheters according to the angle of the origin of the renal artery is discussed in Figure 14. The celiac, superior, and inferior mesenteric arteries usually have <90° angle of origin with the aorta. These can be selectively cannulated with a Cobra or specialized catheter, such as the RC artery catheter.

### Handling catheters

The catheter is prepared by flushing and wiping with a heparinized saline solution.<sup>22</sup> It is strongly advised that nothing is to be injected until there is an appropriate blood return. Contrast should be injected to verify the placement of the catheter and ensure that the catheter tip is in a safe position be-

fore high-pressure injection is performed. The catheter should be twirled using fluoroscopy to ensure its free movement. Contrast is injected to confirm that it rapidly enters the flow stream rather than staining the wall of the vessel or remaining stagnant. The catheter is removed over a guidewire to straighten its head. Initial catheter placement is performed using bony landmarks or other anatomical signs. After the catheter is in place, it is aspirated for the backflow of blood, flushed with heparin-saline, and connected to the injector (if indicated), meniscus to meniscus. The catheter shape may be changed by heating it with steam, bending it to the required shape, and quickly quenching it in a cold sterile saline solution.

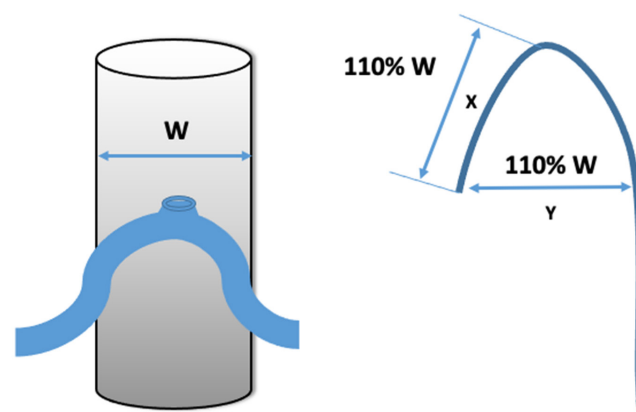


**Figure 13.** Length of the catheter tip distal to the primary curve (X) and the curve width (Y) should be 110% of the native artery width (W) at the level of the target branch vessel.

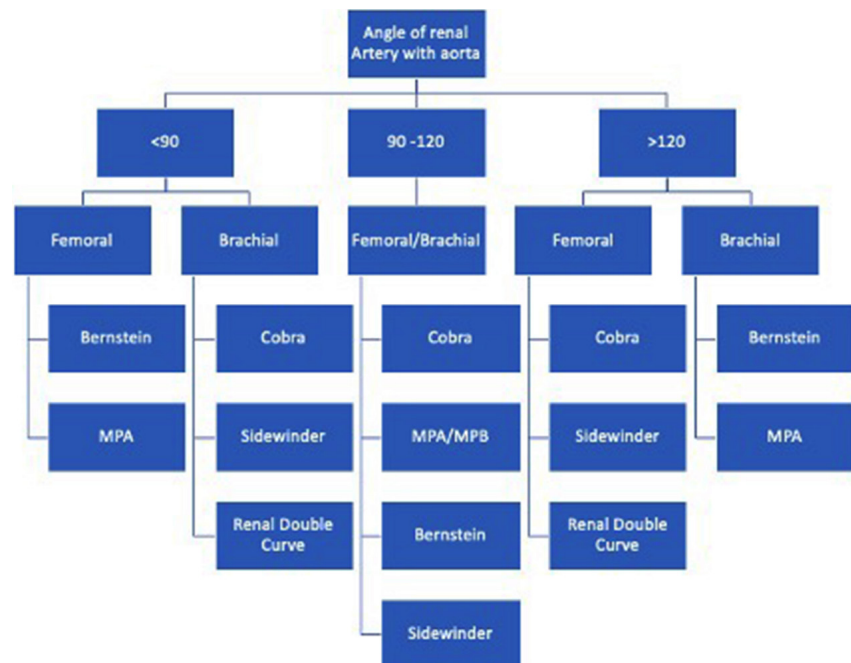


**Figure 14.** Algorithmic approach for renal artery cannulation.

The method of cleaning and sterilizing catheters is via liquid sterilant or gaseous/plasma sterilization (or both) to ensure the complete and efficient decontamination of the catheter. The outer surfaces of the catheter and the guidewire lumen of the catheter are cleaned, decontaminated, and sterilized with the liquid sterilant. The filling and draining of the sterilant are conducted until the interior of the catheter's lumen is sterilized.

### Conflict of interest disclosure

The authors declared no conflicts of interest.

## References

- Meyer JA, Werner Forssmann and catheterization of the heart, 1929. *Ann Thorac Surg.* 1990;49(3):497-499. [\[CrossRef\]](#)
- Mauro MA, Murphy K, Thomson K, Venbrux A, Morgan RA. Image-Guided Interventions. 2nd ed. Elsevier Inc. Chapter 4: Diagnostic Catheters and Guidewires; 2013. [\[CrossRef\]](#)
- Endovascular Skills Guidewire and Catheter Skills for Endovascular Surgery. 4<sup>th</sup> ed. New York: Taylor & Francis Group; Chapter 6: Handling Catheters; 2018. [\[CrossRef\]](#)
- Image-Guided Interventions. 2nd ed. Elsevier Health Sciences; Chapter 4: Diagnostic Catheters and Guidewires; 2013. [\[CrossRef\]](#)
- Nakagawa N, Yashiro N, Nakajima Y, Barnhart WH, Wakabayashi M. Hydrogel-coated glide catheter: experimental studies and initial clinical experience. *AJR Am J Roentgenol.* 1994;163(5):1227-1229. [\[CrossRef\]](#)
- Carey J, Emery D, McCracken P. Buckling test as a new approach to testing flexural rigidities of angiographic catheters. *J Biomed Mater Res B Appl Biomater.* 2006;76(1):211-218. [\[CrossRef\]](#)
- PROGREAT<sup>™</sup> Microcatheters [Internet]. [cited 2020 Oct 7]. Available from: <https://www.terumo.com/products/catheters/progreat.html> [\[CrossRef\]](#)
- CatheterS [Instructions for Use]. Somerset, NJ: Terumo Medical Corporation; 2016. [\[CrossRef\]](#)
- Endovascular Skills Guidewire and Catheter Skills for Endovascular Surgery. 4<sup>th</sup> ed. New York: Taylor & Francis Group; Chapter 14: Access for endovascular therapy; 2018. [\[CrossRef\]](#)
- Radifocus<sup>®</sup> Optitorque<sup>™</sup> Angiographic catheter [Internet]. [cited 2020 Oct 7]. [\[CrossRef\]](#)
- HEARTRAIL<sup>®</sup> III Guiding Catheter [Internet]. [cited 2020 Oct 7]. Available from: <https://www.terumo.com/products/catheters/heartrail.html> [\[CrossRef\]](#)
- Schroeder J. Peripheral Vascular Interventions: An Illustrated Manual [Internet]. Stuttgart: Georg Thieme Verlag; 2013 [cited 2020 Oct 7]. Available from: <http://www.thieme-connect.de/products/ebooks/book/10.1055/b-002-66249> [\[CrossRef\]](#)
- Archer LO. Trauma: emergency resuscitation, perioperative anesthesia, surgical management, volume I. *Prehospital Emergency Care.* 2011;15(3):454-455. [\[CrossRef\]](#)
- Schneider PA. Endovascular Skills: Guidewire and Catheter Skills for Endovascular Surgery. 4<sup>th</sup> ed. New York: Taylor & Francis Group; Chapter 6: Handling Catheters; 2018. [\[CrossRef\]](#)
- Freed RA, Darflinger R, Urdaneta A, Vatakencherry GG. Abstract no. 301: angiographic catheters: a comprehensive review for the interventionalist in-training. *J Vasc Interv Radiol.* 2012;23(Suppl 3):122-123. [\[CrossRef\]](#)
- Daniel TB, Akins EW, Hawkins IF Jr. A solution to the problem of high-flow jets from miniature angiographic catheters. *AJR Am J Roentgenol.* 1990;154(5):1091-1095. [\[CrossRef\]](#)
- Jander HP, Kogutt MS. Sidewinder angiographic catheter: easy formation aortic bifurcation. *AJR Am J Roentgenol.* 1979;133(6):1194-1195. [\[CrossRef\]](#)
- Chouhan R, Sahu B, Verma P, Chouhan S. Uterine fibroids embolization in a tertiary hospital: our initial experience. *Int J Reprod Contracept Obstet Gynecol.* 2015;4(3):824-827. [\[CrossRef\]](#)
- Patel PJ, Kelly QS. A practical approach to embolotherapy access and techniques. *Endovascular Today.* 2014. [\[CrossRef\]](#)
- Northcutt BG, Shah AA, Sheu YR, Carmi L. Wires, catheters, and more: a primer for residents and fellows entering interventional radiology: resident and fellow education feature. *Radiographics.* 2015;35(5):1621-1622. [\[CrossRef\]](#)
- Chuang VP. Basic rule in catheter selection for visceral angiography. *AJR Am J Roentgenol.* 1981;136(2):432-433. [\[CrossRef\]](#)
- Raininko R, Söder H. Clot formation in angiographic catheters--an in vitro comparative study. Effects of heparin and protein coating of the catheter. *Acta Radiol.* 1993;34(1):78-82. [\[CrossRef\]](#)



# A comprehensive review of transvenous obliteration techniques in the management of gastric varices

Irfan Masood   
 Amin Moshksar   
 Brian Wong   
 Hasan Khan   
 Arsalan Saleem 

## ABSTRACT

Bleeding gastric varices (GVs) is a life-threatening complication of portal hypertension, with higher morbidity and mortality rates compared with bleeding esophageal varices (EVs). The endovascular techniques for the management of GVVs are mainly transjugular intrahepatic portosystemic shunt (TIPS) and transvenous obliteration of the GVVs. Transvenous obliteration techniques can be an alternative or an adjunct to TIPS for treatment of GVVs, depending on the clinical scenario, and are less invasive than TIPS. However, these procedures are associated with increased portal pressure and related complications, mainly worsening of the EVs. In this article, the different techniques of transvenous obliteration of GVVs, their indications, contraindications, and outcomes are discussed.

## KEYWORDS

Cirrhosis, gastric varices, TIPS, transvenous obliteration, upper GI bleeding

Upper gastrointestinal bleeding due to gastric varices (GV) in patients with portal hypertension resulting from cirrhosis occurs less frequently than esophageal varices (EVs) but is associated with higher morbidity and mortality rates. This is due to severe blood loss, which results from higher rates of rebleeding and bleeding onset at lower pressures than EV, which are often more difficult to control using traditional endoscopic techniques.<sup>1,2</sup> As per the American Association for the Study of Liver Disease (AASLD), the initial management of choice remains endoscopic management, with endovascular treatment reserved for refractory cases.<sup>3</sup> The endovascular treatment options for GVVs are mainly transjugular intrahepatic portosystemic shunt (TIPS) and transcatheter obliteration of the GVVs.

The TIPS method helps decrease portal pressures by directing blood away from the liver, which decompresses and controls variceal bleeding. However, diverting blood away from the liver (hepatofugal flow) can result in worsening of hepatic encephalopathy (HE) and liver failure, particularly in patients with low hepatic reserve [model for end-stage liver disease (MELD) score >17-20].<sup>4,5</sup> Moreover, GV bleeding occurs at lower pressures than EV, and as Tripathi et al.<sup>6</sup> demonstrated, in patients with pre-TIPS portal pressure gradients of  $\leq 12$  mmHg, further reduction in pressure gradients after performing TIPS does not alter the risk of rebleeding from GVVs.

Transcatheter techniques for the obliteration of GVVs present endovascular alternatives/adjuncts to TIPS. When transvenous obliteration is carried out via the systemic veins, it is known as *retrograde* transvenous obliteration (RTO). The term RTO is a collective term that incorporates balloon-occluded retrograde transvenous obliteration (BRTO), plug-assisted retrograde transvenous obliteration (PARTO), and coil-assisted retrograde transvenous obliteration (CAR-TO). When transvenous obliteration is carried out via the portal vein, it is known as *antegrade* transvenous obliteration (ATO). If antegrade obliteration is performed via balloon-occlusion, vascular plug, or coils, then it is known as balloon-occluded antegrade transvenous obliteration (BATO, PATO, or CATO), respectively. The two most common subtypes of ATO procedures

From the Department of Interventional Radiology (I.M. ✉ irmasood@utmb.edu, A.M., B.W., H.K., A.S.), University of Texas Medical Branch, Texas, USA.

Received Received 19 March 2021; revision requested 12 April 2021; last revision received 12 September 2021; accepted 13 October 2021.



Epub: 11.01.2023

Publication date: 31.01.2023

DOI: 10.5152/dir.2022.21193

You may cite this article as: Masood I, Moshksar A, Wong B, Khan H, Saleem A. A comprehensive review of transvenous obliteration techniques in the management of gastric varices. *Diagn Interv Radiol.* 2023;29(1):146-154.

include percutaneous transhepatic obliteration (PTO) and trans-TIPS obliteration (Table 1). In this review, the focus is on different transvenous obliteration techniques for the management of GVs, the controversies over which technique is superior, and the geographic preferences of one technique over the other.

## Relevant anatomy

Generally, GVs are classified using Sarin's classification,<sup>2</sup> an endoscopic classification taking into account the location of the GVs and their relationship to EVs. Gastroesophageal varices type 1 (GOV1) are EVs that extend below the cardia into the lesser curvature. These are the most common type, accounting for 75% of cases. GOV2 are EVs that extend into the fundus and are associated with the second highest risk of bleeding after type 1 isolated gastric varices (IGV1), which are present in the fundus only and are associated with the highest risk of bleeding. IGV2s are present in the remaining portions of the stomach (body, antrum, pylorus) and are the least common type of varices in patients with cirrhosis. The risk of bleeding is higher in the presence of a large size, red spots on endoscopy, high-risk locations (as described above), and severe liver dysfunction (higher Child–Pugh grade).<sup>7</sup> Overall, IGV1 and GOV2 are the main types of GVs that are amenable to RTO procedures.

The afferent veins of GVs are most commonly the left gastric vein (LGV) and the posterior gastric vein (PGV), and, less commonly, the short gastric vein and gastroepiploic veins. The varices drain through two dominant pathways, which allow hepatofugal flow by redirecting blood away from the portal circulation. The most common pathway is drainage via a gastrosplenic shunt (GRS) (80%–85%) formed by the inferior phrenic vein joining the left renal vein at the same draining point of the left adrenal vein. The second

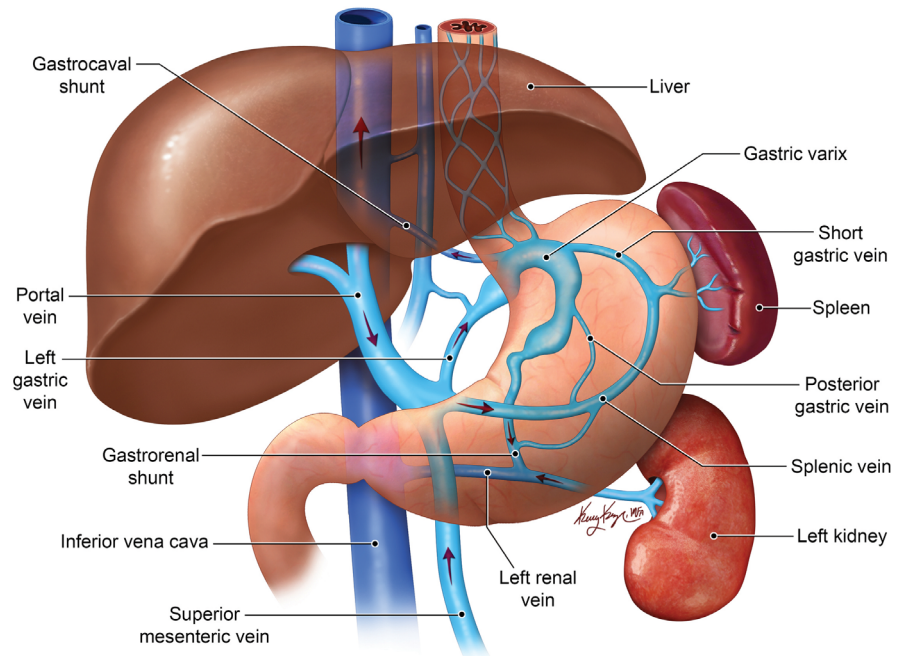


**Figure 1.** Anatomy of gastric variceal complex. Graphic showing that the afferent veins of GVal complex are mainly formed by the left gastric vein, posterior gastric vein, and short gastric vein. The efferent system is formed by the gastrosplenic shunt into the left renal vein and less commonly via gastrocaval shunt.

pathway is via a direct gastrocaval shunt, in which the GVs drain directly into the inferior vena cava (IVC) via the inferior phrenic vein or pericardiophrenic vein (Figure 1).<sup>8</sup>

To guide endovascular interventions, Kiyosue et al.<sup>9</sup> classify GVs based on the anatomy of their afferent (inflow) and efferent (outflow/draining) veins (Table 2). An understanding of this anatomy is of critical importance, as technical success in the obliteration of GVs is related to the anatomy of the varix. Based on afferent veins, the GVs are divided into three types (Figure 2). **Type I** has a single afferent (inflow) vein, either LGV or PGV, and is the easiest type to treat via RTO if the efferent (outflow) veins are occluded, with its high success rate due to high pressure from the portal system allowing the sclerosant to fill the whole variceal complex. **Type II** has two afferent gastric veins, namely, the LGV and the PGV. During the RTO procedure, it is important to know that once the efferent veins are occluded, one of these afferent veins (LGV or PGV) will act as a draining “efferent” vein, resulting in the efflux of sclerosant into the portal system. Type III has single or multiple afferent veins; however, an additional gastric vein drains into the shunt without communication to the varix. Failure to recognize this type can result in reflux of sclerosant into the portal system rather than the GVs. Based on the efferent veins, the GVs are divided into four types (Figure 3), as described in Table 2.<sup>9</sup>

## Preprocedure

### Indications

The main indications for transvenous obliteration of GVs are bleeding GVs refractory to endoscopic management, prevention of rebleeding after successful endoscopic management, refractory HE due to portosystemic shunts, and non-tolerance to TIPS.<sup>3,10,11</sup> The AASLD management recommendations for GVs are summarized in Table 3.<sup>3</sup>

### Contraindications

The contraindications to transvenous obliteration of GVs are severe coagulopathy, refractory ascites, severe liver dysfunction, and high-risk EVs. In patients with high-risk EVs, the EVs should be treated endoscopically prior to treatment with transvenous obliteration of GV. This GV obliteration increases the portal venous pressure following shunt occlusion, which can worsen both ascites and EVs.<sup>10,12,13</sup>

### Imaging

Preprocedural planning is conducted by performing computed tomography angiography, while magnetic resonance angiography can be considered if the patient is allergic to iodinated contrast. The role of preprocedural imaging is to define the anatomy of the shunt and varices, assess the diameter of the GRS, and allow for planning of the ap-

### Main points

- Upper gastrointestinal bleeding due to gastric varices (GVs) is less common than esophageal varices but is associated with higher morbidity and mortality.
- Transvenous obliteration techniques are an important tool in the management of bleeding GVs with ever-evolving modifications.
- Understanding the complex anatomy of a variceal complex is of paramount importance to achieving both high technical and clinical success in treating GVs.

**Table 1.** Endovascular techniques for gastric varices

TIPS
<b>Retrograde transvenous obliteration (via the systemic veins):</b>
• Balloon-occluded retrograde transvenous obliteration
• Plug-assisted retrograde transvenous obliteration
• Coil-assisted retrograde transvenous obliteration
<b>Antegrade transvenous obliteration (via the portal vein):</b>
• This includes balloon-occluded antegrade transvenous obliteration, plug-assisted antegrade transvenous, and coil-assisted antegrade transvenous obliteration with the following subtypes:
1. Percutaneous transhepatic obliteration
2. Transjugular intrahepatic portosystemic shunt obliteration

**Table 2.** Classification of gastric varix based on afferent veins<sup>9</sup>

<b>Type I</b>	It is supplied by a single afferent (inflow) gastric vein—either LGV or PGV
<b>Type II</b>	It is supplied by two afferent gastric veins, namely the LGV and PGV
<b>Type III</b>	It is supplied by a single or multiple afferent veins; however, a separate gastric vein drains into the shunt without communication to the gastric varices
<b>Classification of gastric varix based on efferent veins</b>	
<b>Type A</b>	It has a single draining shunt—splenorenal or gastrocaval shunt
<b>Type B</b>	It has a single draining shunt with single or multiple collaterals
<b>Type C</b>	It has both gastrosplenic and gastrocaval shunts
<b>Type D</b>	It does not have a shunt and drains via small collaterals

LGV, left gastric vein; PGV, posterior gastric vein.

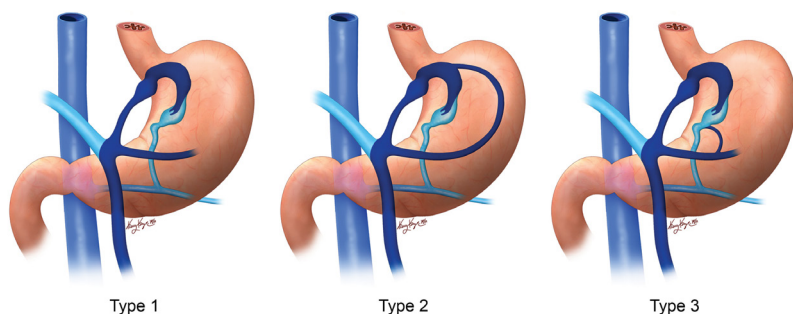


**Figure 2.** Classification of gastric varices on the basis of afferent veins. Type I has a single afferent vein, the left gastric vein in the graphic. Type II is supplied by two afferent veins: the left gastric vein and posterior gastric vein. Type III has a separate vein draining into the gastrorenal shunt without communication with the remaining afferents.

proach to cannulating the shunt, while it also helps identify portal and splenic vein thrombosis, as well as the presence of ascites.

### Sclerosants

The choice of sclerosant varies among interventionalists, with diverse safety profiles of each agent. Sodium tetradecyl sulfate (STS) is a commonly used agent in the US, originally introduced as an alternative to ethanolamine oleate (EO) for BRTO in 2006. It is an inexpensive agent that acts as a chemical irritant causing permanent endothelial damage. The STS foam is made by mixing lipiodol, 3% STS, and gas (air/carbon dioxide) in a ratio of 1:2:3 mL. Several studies have demonstrat-

ed that the result of BRTO with STS is similar to that with EO, with lower rates of complication, reporting a technical success rate of 79%–100% and a rebleeding rate of less than 5%.<sup>14–16</sup> Pulmonary edema and portal vein thrombosis are rarely reported side effects of STS.<sup>17,18</sup>

Polidocanol is another sclerosant that has been used in BRTO. Itou et al.<sup>15</sup> demonstrated that the technical success in achieving obliteration of varices using polidocanol foam is comparable to that of EO with a lower complication rate. In addition, polidocanol was initially used as a local anesthetic, and is therefore associated with significant reduction in pain compared with EO.<sup>15</sup>

In fact, EO was the initial sclerosant of choice, particularly in Asia; however, this agent is associated with hemolysis and release of free hemoglobin, causing renal tubular injury and renal failure, while it is also associated with the following reported side effects: pulmonary edema, cardiogenic shock, and disseminated intravascular coagulation.<sup>16,19–21</sup> Haptoglobin (4,000 U), which binds free hemoglobin, has been used to reduce the renal toxicity of the EO, but this is not approved by the Food and Drug Administration for use in the US. The sclerosant mixture is made by mixing 5%–10% EO with contrast in a ratio of 1:1.

The other agents used are N-butyl-2-cyanoacrylate glue and Gelfoam. Cyanoacrylate glue is expensive but an option for embolizing the collaterals, while Gelfoam is cheap, readily available, and a more familiar agent among interventional radiologists.<sup>21</sup> Jogo et al.<sup>22</sup> demonstrated that the use of GERTO (i.e., gelatin and 5% EO iopamidol mixture in RTO) for the treatment of GV is associated with fewer sclerosants and a shorter operative time compared with conventional BRTO.

## Procedures

### Balloon-occluded retrograde transvenous obliteration

This is one of the subtypes of RTO, in which the left renal vein is cannulated in retrograde via the jugular or femoral vein, followed by occlusion of the shunt by a balloon and infusion of sclerosant to occlude the splenorenal shunt and fundal varices (Figure 4).<sup>23–25</sup> Once the shunt is occluded by the balloon, a digitally subtracted venography is performed to assess the type of varix, as well as its venous drainage.<sup>10</sup> The presence of collateral veins identified via venography may prevent the complete filling of the shunt; therefore, these veins are embolized with coils, Gelfoam, plugs, or glue, as per the size and characteristics of the collaterals.<sup>10,13,26</sup> Following embolization of the collateral veins, sclerosant with a contrast agent is injected into the varix until it is fully opacified with the balloon inflated. Several researchers advocate the use of a coaxial microcatheter system for more selective obliteration of the GVs while keeping the GRS patent.<sup>27</sup> However, a patent GRS may result in technical failure with recurrence of GVs, meaning obliteration of both GRS and GVs is crucial.<sup>28</sup>

The end point of embolization is when minimal filling of the afferent portal branches is noted during balloon occlusion venog-

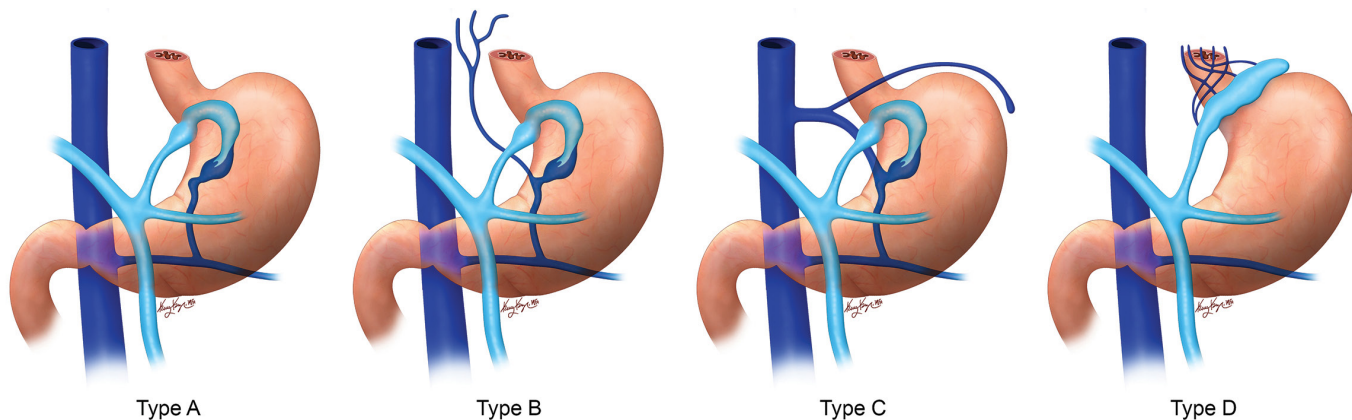


**Figure 3.** Classification of gastric varices on the basis of efferent veins. Type A has a single draining shunt. Type B has a single draining shunt with single or multiple collaterals. Type C has both gastroduodenal shunt and gastrocaval shunt. Type D does not have a shunt and drains via small collaterals.

**Table 3.** AASLD recommendations

**Primary prophylaxis for gastric varices**

- The recommendations for primary prophylaxis for GOV1 are similar to those for esophageal varices, which include either NSBBs or EVL
- In patients with IGV1, NSBBs can be considered for primary prophylaxis; however, the evidence is not as strong
- Neither TIPS nor transvenous obliteration (BRTO and its variations) are recommended for primary prophylaxis of IGV1

**Acute gastric variceal hemorrhage**

- The initial management of choice for bleeding GOV1 is endoscopy with either EVL or cyanoacrylate injection
- TIPS is the management of choice for bleeding cardiofundal varices (GOV2 and IGV1)
- TIPS or BRTO are first-line treatments in the prevention of rebleeding in patients who have recovered from GOV2 and IGV1 bleeding

AASLD, American Association for the Study of Liver Disease; GOV1, gastroesophageal varices type 1; NSBBs, non-selective beta-blockers; EVL, endoscopic variceal ligation; IGV1, type 1 isolated gastric varices; TIPS, transjugular intrahepatic portosystemic shunt; GOV2, gastroesophageal varices type 2; BRTO, balloon-occluded retrograde transvenous obliteration.

raphy. Treatment failure can occur if the sclerosant volume is insufficient to fill the entire variceal complex. Here, the balloon remains inflated while the patient is transferred to the intensive care unit. The duration of balloon inflation time is highly variable and ranges from 4 to 24 hours before the patient is returned to the interventional radiology suite for the deflation of the balloon.<sup>10,13,26</sup> Given the high level of care required for patients undergoing BRTO post-balloon inflation, this procedure has fallen out of favor in the US. Waguri et al.<sup>29,30</sup> demonstrated that BRTO combined with partial splenic embolization may help diminish the increase in portal pressures after BRTO, thereby reducing the exacerbation of EVs.

**Plug-assisted retrograde transvenous obliteration**

This subtype of RTO involves deployment of a permanent vascular plug in the efferent limb of the GRS (Figure 5) and was first described by Gwon et al.<sup>17</sup> Much like BRTO, the procedure involves retrograde cannulation of the left renal vein by the internal jugular or femoral vein following placement of an 8–10 Fr sheath. The GRS is then selected using an angled catheter (Simmons, Cobra), and venography is performed to assess the anatomy of the variceal complex and evaluate the narrowest part of the shunt. This is followed by placement of access sheath into the GRS and advancing a 0.035" guidewire through the sheath into the varix. A vascular plug that is 15%–30% larger than the narrowest portion of the shunt is then deployed (not released) into the narrowest portion of the shunt.<sup>21,31</sup> A 4 Fr catheter is then advanced over guidewire into the GV, and slow retrograde venography is performed after waiting 5–10 min for occlusion of the shunt. If additional collaterals are identified via venography, these are

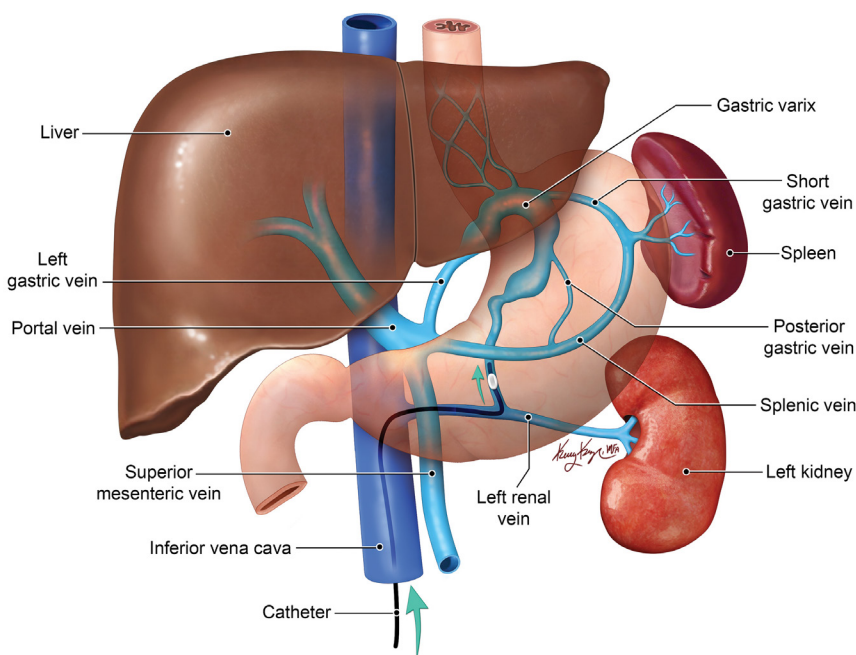
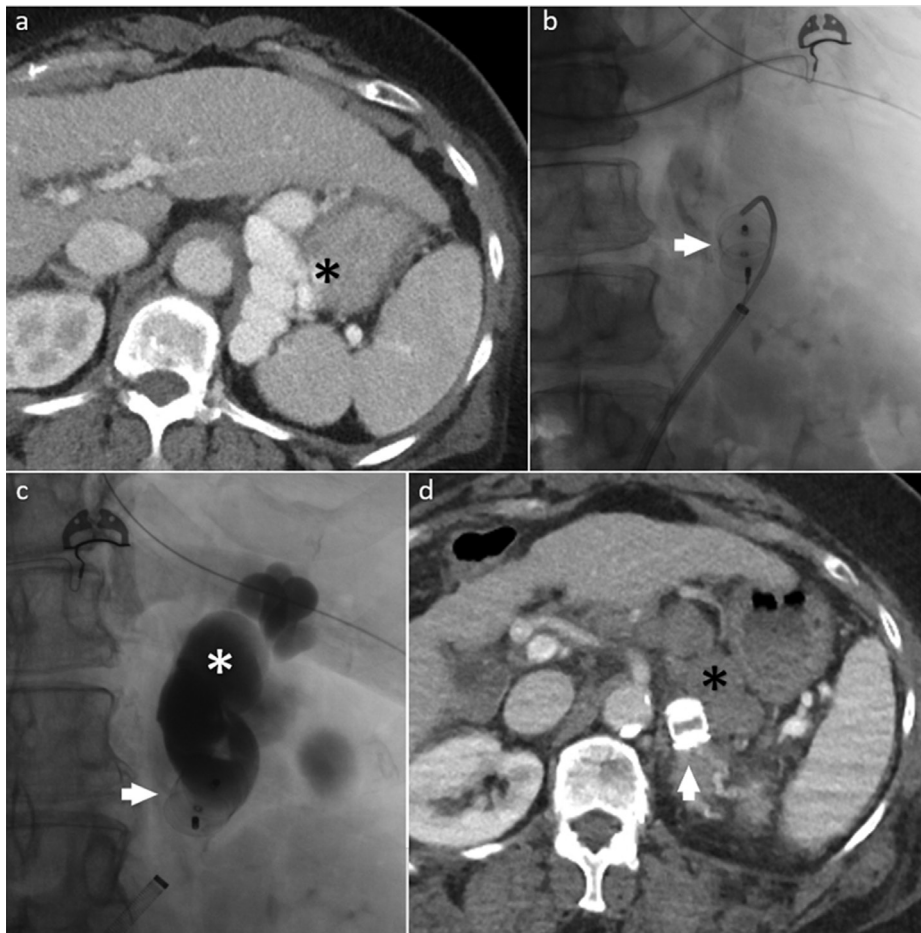


**Figure 4.** Balloon-occluded retrograde transvenous obliteration (BRTO). Graphic shows a BRTO procedure for gastric varices that drain via the gastroduodenal shunt. A balloon catheter is inserted into the outlet of the gastroduodenal shunt (in this drawing) or gastrocaval shunt via femoral venous access. Following balloon-occluded venography, sclerosant is then infused through the balloon catheter to fill the entire variceal complex.



embolized with either Gelfoam or coils via a 4 Fr or coaxial microcatheter. A Gelfoam slurry is then infused through the 4 Fr catheter into the variceal complex. Once the Gelfoam slurry is delivered, the catheter is removed and the vascular plug is detached (released). The Gelfoam slurry is made by mixing a hand-cut Gelfoam sheet with contrast media, while a mixture of Gelfoam with a sclerosant (STS) has also been used.<sup>32</sup>

#### Coil-assisted retrograde transvenous obliteration

This subtype of RTO involves placement of coils and Gelfoam slurry instead of using balloons or plugs. It was first described by Lee et al.<sup>33</sup> and is a useful alternative in patients where the size of the shunt, angle of the shunt, and tortuosity of the vessel are not favorable to either BRTO or PARTO. There are two subtypes of CARTO procedure. The **CARTO-I** procedure involves placement of an access sheath in the efferent limb of the GRS (no balloon catheter). Here, two microcatheter systems are used, with one microcatheter placed proximally at the narrowest part of the GRS, and the second advanced upstream into the GV. Using the microcatheter placed in the GRS, multiple coils are deployed to completely occlude the shunt. Following embolization of the GRS, Gelfoam slurry or STS is injected through the microcatheter into the varix. **CARTO-II** follows the same steps as BRTO with placement of a balloon catheter into the efferent limb of GRS. This is followed by infusion of sclerosant into the variceal complex, followed by deploy-

**Figure 5.** Vascular plug-assisted retrograde transvenous obliteration. A 68-year-old female with cirrhosis presented with upper gastrointestinal bleed and type 1 isolated gastric varices on endoscopy. A contrast-enhanced axial CT image (a) prior to the procedure showing fundal gastric varices (black\*). Fluoroscopic images (b, c) showing vascular plug placement in the left adrenal vein (white arrow) via the right femoral vein access site with embolization of the gastroduodenal shunt and fundal varices (white\*) using a thick slurry of Gelfoam mixed with saline and contrast. Contrast-enhanced axial CT image (d) after the procedure showing complete obliteration of the fundal varices. CT, computed tomography.

**Table 4.** Comparison of RTO and ATO techniques

<b>BRTO</b>	<ul style="list-style-type: none"> <li>• High technical and clinical success rates</li> <li>• Long procedure times (40–360 min in BRTO with EO and 90–163 min in BRTO with STS)<sup>17</sup></li> <li>• Requires indwelling balloon occlusion (4–24 hours)</li> <li>• Requires higher level (ICU) monitoring before bringing patient back for balloon deflation</li> <li>• Balloon can rupture with potential systemic dissemination of sclerosing agent</li> <li>• Potential toxicity of sclerosing agents (pulmonary embolism, hemoglobinuria, renal failure, pulmonary edema, DIC)</li> </ul>
<b>PARTO</b>	<ul style="list-style-type: none"> <li>• High technical and clinical success rates</li> <li>• Shorter procedure times (20–68 min)<sup>32</sup></li> <li>• Does not require balloon occlusion or higher level monitoring</li> <li>• Coil embolization of small collateral veins is not required in all cases</li> <li>• Recurrence of gastric varices may be higher compared with BRTO<sup>17</sup></li> <li>• Limited by GR shunt angle</li> <li>• Limited by GR shunt size (shunts of &gt;18 mm are not routinely occluded)<sup>22</sup></li> </ul>
<b>CARTO</b>	<ul style="list-style-type: none"> <li>• High technical and clinical success rates</li> <li>• Intermediate procedure time 132–168 min compared with 20–68 mins in PARTO<sup>32,34</sup></li> <li>• Does not require balloon occlusion or higher level monitoring</li> <li>• It is not limited by GR shunt angle or size (can be used in shunts up to 25–30 mm)<sup>29</sup></li> </ul>
<b>ATO</b>	<ul style="list-style-type: none"> <li>• It is useful in patients with no GR shunt</li> <li>• It is useful in patients with TIPS</li> <li>• It can be performed via TIPS or via percutaneous transhepatic access</li> </ul>

RTO, retrograde transvenous obliteration; ATO, antegrade transvenous obliteration; BRTO, balloon-occluded retrograde transvenous obliteration; EO, ethanolamine oleate; STS, sodium tetradecyl sulfate; ICU, intensive care unit; DIC, disseminated intravascular coagulation; PARTO, plug-assisted antegrade transvenous obliteration; GR, gastroduodenal; CARTO, coil-assisted retrograde transvenous obliteration; TIPS, transjugular intrahepatic portosystemic shunt.

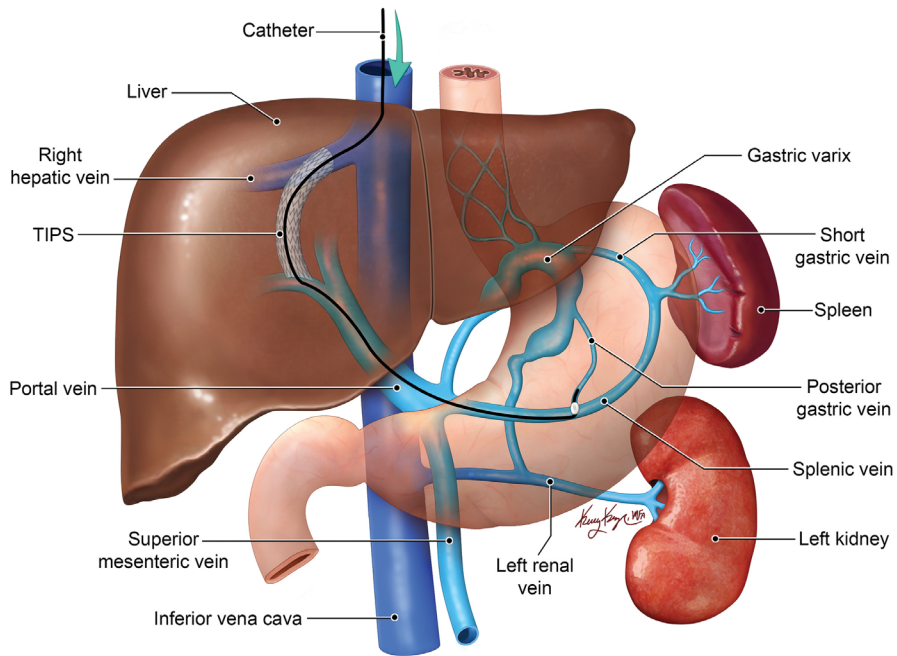


**Figure 6.** Balloon-occluded antegrade transvenous obliteration (BATO). Subtype: trans-transjugular intrahepatic portosystemic shunt (TIPS) BATO: BATO involves embolization of the varices from the portal venous side. The graphic shows a subclassification of the BATO procedure known as trans-TIPS obliteration, in which the portal vein, and subsequently the portal venous side of varices, is accessed via indwelling TIPS.

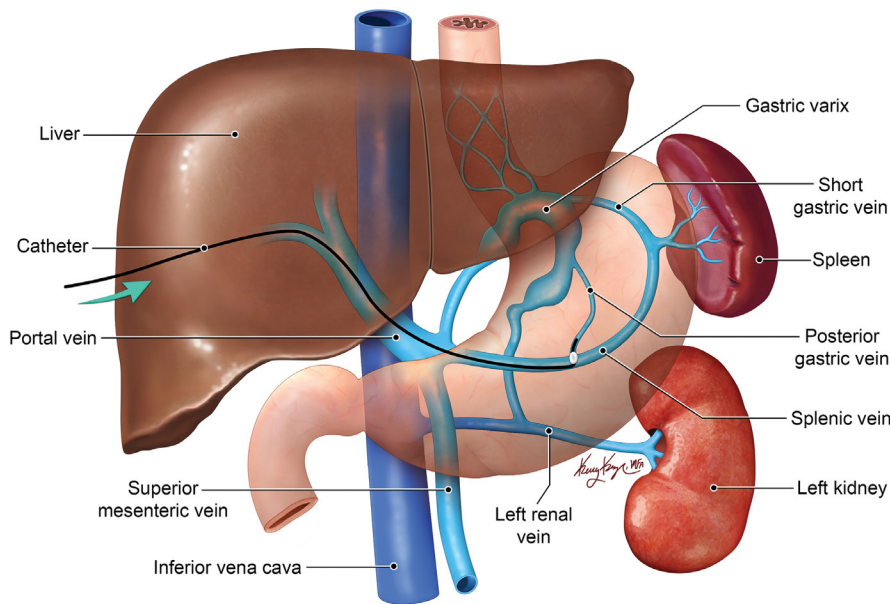


**Figure 7.** Balloon-occluded antegrade transvenous obliteration (BATO). Subtype: percutaneous transhepatic obliteration. BATO involves embolization of the varices from the portal venous side. The graphic shows a subclassification of the BATO procedure known as percutaneous transhepatic obliteration, in which the portal vein, and subsequently the portal venous side of varices, is accessed percutaneously.

ment of multiple metallic coils into the GRS via a balloon catheter. The balloon catheter is then removed approximately 30 min after injection of the sclerosant.<sup>34</sup>

### Antegrade transvenous obliteration

This procedure involves transvenous obliteration of GVs via portal venous access (antegrade) rather than the systemic venous access (retrograde) used in RTO procedures. This can be achieved by using balloon-occlusion (BATO), coils (CATO), or plugs (PATO). The

procedure can be used as an adjunct to RTO procedures or as an alternative procedure in treating GVs without a GRS.<sup>35</sup> The two most common subtypes of the ATO procedure are PTO and trans-TIPS obliteration (Figures 6, 7), with the former involving accessing the portal vein using a micropuncture technique under real-time ultrasound guidance. Once access is achieved, the needle is exchanged for a sheath of adequate size (5–7 Fr) to accommodate most occlusion balloons, coils, or plugs. A venogram is performed to delineate the anatomy. In BATO, if multiple afferent veins are present, the largest vein is left for balloon occlusion, while the small afferent veins are occluded using coils or vascular plugs. Once the small veins are embolized, the largest vein is then occluded by a balloon catheter, with subsequent steps of sclerosant injection into the varix similar to that of a standard BRTO procedure. In the **trans-TIPS** approach, the varices are accessed using the pre-existing TIPS, with the remaining steps similar to those of PTO. The advantage of this approach is that it involves no new access, which minimizes the risk of vascular and biliary injury, while the disadvantages include being an invasive route, being time consuming, and involving long and indirect access to the GVs.<sup>32,35</sup>

## Post-procedure

### Immediate complications

Minor periprocedural complications include access site bleeding and hematoma, access site infection, and pain. Additional transient complications include low-grade fever, hypertension, nausea and vomiting, abdominal and back pain.<sup>36</sup> Major complications include renal failure, pulmonary embolism, and venous thrombosis involving the portal vein, splenic vein, IVC, renal and iliac veins. A major complication specific to BRTO is related to balloon rupture and subsequent systemic dissemination of the embolic agent, which can cause hemoglobinuria, renal failure, and pulmonary embolism. Balloon rupture with embolization of the sclerosing material to the pulmonary arteries is a potentially fatal complication. Balloon rupture occurs in 2.3%–8.7% of BRTO procedures.<sup>37,38</sup> Complications specific to the type of sclerosing agent used are mentioned in the “sclerosant” section above.

### Delayed complications

The RTO procedures redirect blood flow to the liver (increased hepatopetal flow), which increases portal pressure and its re-



lated complications, such as EVs, ascites, and portal gastropathy. In terms of BRTO, EV exacerbation at one, two, and three years has been reported to be 27%–35%, 45%–66%, and 45%–91%, respectively.<sup>39</sup> Choi et al.<sup>40</sup> reported that in BRTO, bleeding from EVs was statistically significant at five and seven years, with *P* values of 0.02 and <0.01, respectively, and no significant bleeding risk at one and three years. In terms of the PARTO procedure, new or exacerbated EVs have been reported at between 22% and 33% at three to nine months.<sup>17,21,31,41</sup> The incidence of EV exacerbation is similar in patients post-CARTO at 23%.<sup>33</sup> Therefore, patients who have undergone a RTO procedure will require long-term endoscopic surveillance for EVs with the initial endoscopy at one to three months after intervention. Independent risk factors for the exacerbation of EVs include total bilirubin of >1.6 mg/dL and a hepatic venous pressure gradient of >13 mmHg.<sup>42</sup> Researchers have described the concomitant use of splenic embolization along with transvenous obliteration to prevent the exacerbation of EVs.<sup>29,30</sup> New or worsening ascites or hepatic hydrothorax is another major complication following BRTO, PARTO, and CARTO, with an incidence rate of 0%–44%, 11%–58%, and 25%, respectively.<sup>19,21,31,33,37,41</sup> Worsening portal gastropathy is reported in 5%–13% of patients following BRTO and 20% after CARTO.<sup>33,37</sup>

## Outcomes

The technical success of the procedure mainly relates to the successful cannulation of the portosystemic shunt, including the GRS, accurate placement of the occlusion device, and filling of the whole shunt with the sclerosant. Clinical success relates to resolution of the GI bleeding without recurrent bleeding, and/or complete obliteration of the shunt on follow-up imaging/endoscopy.

In terms of BRTO, the technical success rates range from 79% to 100%, with clinical success rates of 91%–100%. The technical success rate of BRTO is increased to 98%–100% when combined with BATO.<sup>26</sup> The rates of rebleeding in technically successful procedures range from 0% to 20%, but are typically below 10%. The survival rates at one year, three years, and five years range from 8% to 100%, 75%–100%, and 39%–85%, respectively.<sup>9,10</sup> Improvement in HE is reported in the range of 80%–100% at two to three years post-procedure.<sup>19,37,43,44</sup> This improvement in HE is due to improved hepatopetal flow. Post-BRTO, there is evidence of improved hepatic

synthetic function for six to nine months, after which the hepatic reserve returns to baseline.<sup>37,45</sup> This short-term improvement is due to improved hepatopetal flow and may prove beneficial in patients with a high likelihood of requiring a liver transplant. Given that there is a high incidence of ascites post-BRTO, the MELD score appears to be more sensitive for the assessment of hepatic function compared with the Child–Pugh score in patients who have undergone transvenous obliteration of GVs.<sup>46</sup>

In a recent meta-analysis, Wang et al.<sup>47</sup> compared the effects of TIPS versus BRTO on bleeding GVs, with the results indicating that BRTO was superior to TIPS, with higher overall survival rates and lower rates of rebleeding. These results were similar to those obtained in the meta-analysis conducted by Paleti et al.<sup>48</sup> and the retrospective study conducted by Gimm et al.<sup>49</sup> Increasingly, TIPS and transvenous obliteration are considered to be complementary procedures in treating patients with portal hypertension, reducing the risk of variceal bleeding. Transvenous obliteration procedures control bleeding from GVs by obliterating the spontaneous portosystemic shunt, which, in turn, increases portal pressure and the related complications of EV, ascites, and hepatic hydrothorax. By combining transvenous obliteration with TIPS, the increased portal pressure associated with transvenous obliteration is countered by the creation of the TIPS procedure. There is growing evidence that combining transvenous obliteration procedures with TIPS is more effective in managing GVs than either procedure alone.<sup>50–52</sup>

In terms of PARTO, the technical success rates range from 94.7% to 100%, with clinical success rates of 90.6%–100%. Post-PARTO improvement in the hepatic synthetic function has been reported in up to 67% of patients.<sup>16,17,21,31,41</sup> This improvement in liver function is significant during the first six months compared with the baseline.<sup>53</sup> Patients with a Child–Pugh class of B or C exhibit greater improvement in hepatic function compared with those in Child–Pugh A class.<sup>54</sup> The rebleeding rate is similar to that of BRTO and is reported to be 11% at one year.<sup>16</sup> In a recent retrospective study, Park et al.<sup>53</sup> reported a worsening of EVs in 53% of patients who underwent PARTO, and in this study, 16 out of the 26 patients with worsening of post-PARTO EVs underwent endoscopic variceal ligation.

In terms of CARTO, the technical and clinical success rates are up to 100%, as reported by Lee et al.<sup>33</sup>, with no variceal rebleeding noted during a mean follow-up of around 12 ± 5 months. Similar high technical (100%) and clinical (97.2%) success rates were reported in a retrospective study of 36 patients conducted by Yamamoto et al.<sup>34</sup> Compared with PARTO, the procedure time for CARTO is longer, as it requires deployment of multiple coils during the procedure, in contrast to a single vascular plug in PARTO.

## Conclusion

Generally, GVs are seen in around 20% of patients with cirrhosis and are associated with higher morbidity and mortality rates compared with EVs. Many researchers consider transvenous obliteration techniques to be as effective as placement of TIPS in controlling a GV hemorrhage. Increasingly, TIPS and transvenous obliteration are being considered as complementary procedures in treating patients with portal hypertension, reducing the risk of variceal bleeding. Knowledge of the complex anatomy of GVs, as well as familiarity with various procedural techniques, is essential for favorable clinical outcomes in these patient populations. Newer techniques and advances continue to make these procedures safer, shorter, and more effective in treating these complications and improving the quality of life and survival of the patients.

## Acknowledgment

The illustrations were drawn by Mrs. Kelly Kage, for which we thank her.

## Conflict of interest disclosure

The authors declared no conflicts of interest.

## References








1. de Franchis R, Primignani M. Natural history of portal hypertension in patients with cirrhosis. *Clin Liver Dis*. 2001;5(3):645-663. [\[CrossRef\]](#)
2. Sarin SK, Lahoti D, Saxena SP, Murthy NS, Makwana UK. Prevalence, classification and natural history of gastric varices: a long-term follow-up study in 568 portal hypertension patients. *Hepatology*. 1992;16(6):1343-1349. [\[CrossRef\]](#)
3. Garcia-Tsao G, Abraldes JG, Berzigotti A, Bosch J. Portal hypertensive bleeding in cirrhosis: risk stratification, diagnosis, and management: 2016 practice guidance by the American Association for the study of liver diseases. *Hepatology*. 2017;65(1):310-335. [\[CrossRef\]](#)

4. Ferral H, Gamboa P, Postoak DW, et al. Survival after elective transjugular intrahepatic portosystemic shunt creation: prediction with model for end-stage liver disease score. *Radiology*. 2004;231(1):231-236. [\[CrossRef\]](#)
5. Montgomery A, Ferral H, Vasan R, Postoak DW. MELD score as a predictor of early death in patients undergoing elective transjugular intrahepatic portosystemic shunt (TIPS) procedures. *Cardiovasc Intervent Radiol*. 2005;28(3):307-312. [\[CrossRef\]](#)
6. Tripathi D, Therapondos G, Jackson E, Redhead DN, Hayes PC. The role of the transjugular intrahepatic portosystemic stent shunt (TIPSS) in the management of bleeding gastric varices: clinical and haemodynamic correlations. *Gut*. 2002;51(2):270-274. [\[CrossRef\]](#)
7. Kim T, Shijo H, Kokawa H, et al. Risk factors for hemorrhage from gastric fundal varices. *Hepatology*. 1997;25(2):307-312. [\[CrossRef\]](#)
8. Sabri SS, Saad WE. Anatomy and classification of gastroduodenal and gastrocaval shunts. *Semin Intervent Radiol*. 2011;28(3):296-302. [\[CrossRef\]](#)
9. Kiyosue H, Mori H, Matsumoto S, Yamada Y, Hori Y, Okino Y. Transcatheter obliteration of gastric varices. Part 1. Anatomic classification. *Radiographics*. 2003;23(4):911-920. [\[CrossRef\]](#)
10. Saad WE. Balloon-occluded retrograde transvenous obliteration of gastric varices: concept, basic techniques, and outcomes. *Semin Intervent Radiol*. 2012;29(2):118-128. [\[CrossRef\]](#)
11. Ishikawa T, Sasaki R, Nishimura T, et al. Comparison of patients with hepatic encephalopathy and those with gastric varices before and after balloon-occluded retrograde transvenous obliteration. *Hepatol Res*. 2018;48(12):1020-1030. [\[CrossRef\]](#)
12. Chikamori F, Kuniyoshi N, Shibuya S, Takase Y. Eight years of experience with transjugular retrograde obliteration for gastric varices with gastroduodenal shunts. *Surgery*. 2001;129(4):414-420. [\[CrossRef\]](#)
13. Saad WE, Kitanosono T, Koizumi J, Hirota S. The conventional balloon-occluded retrograde transvenous obliteration procedure: indications, contraindications, and technical applications. *Tech Vasc Interv Radiol*. 2013;16(2):101-151. [\[CrossRef\]](#)
14. Chu HH, Kim M, Kim HC, Lee JH, Jae HJ, Chung JW. Long-term outcomes of balloon-occluded retrograde transvenous obliteration for the treatment of gastric varices: a comparison of ethanolamine oleate and sodium tetradecyl sulfate. *Cardiovasc Intervent Radiol*. 2018;41(4):578-586. [\[CrossRef\]](#)
15. Itou C, Koizumi J, Hashimoto T, et al. Balloon-occluded retrograde transvenous obliteration for the treatment of gastric varices: polidocanol foam versus liquid ethanolamine oleate. *AJR Am J Roentgenol*. 2015;205(3):659-666. [\[CrossRef\]](#)
16. Kim YH, Kim YH, Kim CS, Kang UR, Kim SH, Kim JH. Comparison of balloon-occluded retrograde transvenous obliteration (BRTO) using ethanolamine oleate (EO), BRTO using sodium tetradecyl sulfate (STS) foam and vascular plug-assisted retrograde transvenous obliteration (PARTO). *Cardiovasc Intervent Radiol*. 2016;39(6):840-846. [\[CrossRef\]](#)
17. Gwon DI, Ko GY, Yoon HK, et al. Gastric varices and hepatic encephalopathy: treatment with vascular plug and gelatin sponge-assisted retrograde transvenous obliteration—a primary report. *Radiology*. 2013;268(1):281-287. [\[CrossRef\]](#)
18. Choi SY, Won JY, Kim KA, Lee DY, Lee KH. Foam sclerotherapy using polidocanol for balloon-occluded retrograde transvenous obliteration (BRTO). *Eur Radiol*. 2011;21(1):122-129. [\[CrossRef\]](#)
19. Park JK, Saab S, Kee ST, et al. Balloon-occluded retrograde transvenous obliteration (BRTO) for treatment of gastric varices: review and meta-analysis. *Dig Dis Sci*. 2015;60(6):1543-1553. [\[CrossRef\]](#)
20. Sabri SS, Saad WE. Balloon-occluded retrograde transvenous obliteration (BRTO): technique and intraprocedural imaging. *Semin Intervent Radiol*. 2011;28(3):303-313. [\[CrossRef\]](#)
21. Chang MY, Kim MD, Kim T, et al. Plug-assisted retrograde transvenous obliteration for the treatment of gastric variceal hemorrhage. *Korean J Radiol*. 2016;17(2):230-238. [\[CrossRef\]](#)
22. Jogo A, Yamamoto A, Kaminoh T, et al. Utility of low-dose gelatin sponge particles and 5% ethanolamine oleate iopamidol mixture in retrograde transvenous obliteration (GERTO) for gastric varices. *Br J Radiol*. 2020;93(1108):20190751. [\[CrossRef\]](#)
23. Fukuda T, Hirota S, Sugimura K. Long-term results of balloon-occluded retrograde transvenous obliteration for the treatment of gastric varices and hepatic encephalopathy. *J Vasc Interv Radiol*. 2001;12(3):327-336. [\[CrossRef\]](#)
24. Saad WE. Endovascular management of gastric varices. *Clin Liver Dis*. 2014;18(4):829-851. [\[CrossRef\]](#)
25. Koito K, Namieno T, Nagakawa T, Morita K. Balloon-occluded retrograde transvenous obliteration for gastric varices with gastroduodenal or gastrocaval collaterals. *AJR Am J Roentgenol*. 1996;167(5):1317-1320. [\[CrossRef\]](#)
26. Saad WE, Kitanosono T, Koizumi J. Balloon-occluded antegrade transvenous obliteration with or without balloon-occluded retrograde transvenous obliteration for the management of gastric varices: concept and technical applications. *Tech Vasc Interv Radiol*. 2012;15(3):203-225. [\[CrossRef\]](#)
27. Takahashi K, Yamada T, Hyodoh H, et al. Selective balloon-occluded retrograde sclerosis of gastric varices using a coaxial microcatheter system. *Am J Roentgenol*. 2001;177:1091-1093. [\[CrossRef\]](#)
28. Katoh K, Sone M, Hirose A, Inoue Y, Fujino Y, Onodera M. Balloon-occluded retrograde transvenous obliteration for gastric varices: the relationship between the clinical outcome and gastroduodenal shunt occlusion. *BMC Med Imaging*. 2010;10:2. [\[CrossRef\]](#)
29. Waguri N, Hayashi M, Yokoo T, et al. Simultaneous combined balloon-occluded retrograde transvenous obliteration and partial splenic embolization for portosystemic shunts. *J Vasc Interv Radiol*. 2012;23(5):650-657. [\[CrossRef\]](#)
30. Waguri N, Osaki A, Ikarashi S, et al. Simultaneous combined balloon-occluded retrograde transvenous obliteration and partial splenic embolization for gastric fundal varices. *United European Gastroenterol J*. 2016;4(1):62-69. [\[CrossRef\]](#)
31. Kim T, Yang H, Lee CK, Kim GB. Vascular plug assisted retrograde transvenous obliteration (PARTO) for gastric varix bleeding patients in the emergent clinical setting. *Yonsei Med J*. 2016;57(4):973-979. [\[CrossRef\]](#)
32. Kim DJ, Darcy MD, Mani NB, et al. Modified balloon-occluded retrograde transvenous obliteration (BRTO) techniques for the treatment of gastric varices: vascular plug-assisted retrograde transvenous obliteration (PARTO)/coil-assisted retrograde transvenous obliteration (CARTO)/balloon-occluded antegrade transvenous obliteration (BATO). *Cardiovasc Intervent Radiol*. 2018;41(6):835-847. [\[CrossRef\]](#)
33. Lee EW, Saab S, Gomes AS, et al. Coil-assisted retrograde transvenous obliteration (CARTO) for the treatment of portal hypertensive variceal bleeding: preliminary results. *Clin Transl Gastroenterol*. 2014;5:e61. [\[CrossRef\]](#)
34. Yamamoto A, Jogo A, Kageyama K, et al. Utility of coil-assisted retrograde transvenous obliteration II (CARTO-II) for the treatment of gastric varices. *Cardiovasc Intervent Radiol*. 2020;43(4):565-571. [\[CrossRef\]](#)
35. Saad WE, Sze DY. Variations of balloon-occluded retrograde transvenous obliteration (BRTO): balloon-occluded antegrade transvenous obliteration (BATO) and alternative/adjunctive routes for BRTO. *Semin Intervent Radiol*. 2011;28(3):314-324. [\[CrossRef\]](#)
36. Sauer BG, Sabri SS, Shami VM, Al-Osaimi AM. Balloon-occluded retrograde transvenous obliteration (BRTO): follow-up and postprocedural imaging. *Semin Intervent Radiol*. 2011;28(3):325-332. [\[CrossRef\]](#)
37. Saad WE, Sabri SS. Balloon-occluded Retrograde Transvenous Obliteration (BRTO): technical results and Outcomes. *Semin Intervent Radiol*. 2011;28(3):333-338. [\[CrossRef\]](#)
38. Park SJ, Chung JW, Kim HC, Jae HJ, Park JH. The prevalence, risk factors, and clinical outcome

- of balloon rupture in balloon-occluded retrograde transvenous obliteration of gastric varices. *J Vasc Interv Radiol.* 2010;21(4):503-507. [\[CrossRef\]](#)
39. Saad WE, Darcy MD. Transjugular Intrahepatic Portosystemic Shunt (TIPS) versus balloon-occluded retrograde transvenous obliteration (BRTO) for the management of gastric varices. *Semin Intervent Radiol.* 2011;28(3):339-349. [\[CrossRef\]](#)
  40. Choi YS, Lee JH, Sinn DH, et al. Effect of balloon-occluded retrograde transvenous obliteration on the natural history of coexisting esophageal varices. *J Clin Gastroenterol.* 2008;42(9):974-979. [\[CrossRef\]](#)
  41. Gwon DI, Kim YH, Ko GY, et al. Vascular plug-assisted retrograde transvenous obliteration for the treatment of gastric varices and hepatic encephalopathy: a prospective multicenter study. *J Vasc Interv Radiol.* 2015;26:1589-1595. [\[CrossRef\]](#)
  42. Jogo A, Nishida N, Yamamoto A, et al. Factors associated with aggravation of esophageal varices after B-RTO for gastric varices. *Cardiovasc Intervent Radiol.* 2014;37(5):1243-1250. [\[CrossRef\]](#)
  43. Mukund A, Rajesh S, Arora A, Patidar Y, Jain D, Sarin SK. Efficacy of balloon-occluded retrograde transvenous obliteration of large spontaneous lienorenal shunt in patients with severe recurrent hepatic encephalopathy with foam sclerotherapy: initial experience. *J Vasc Interv Radiol.* 2012;23(9):1200-1206. [\[CrossRef\]](#)
  44. Inoue H, Emori K, Toyonaga A, et al. Long term results of balloon-occluded retrograde transvenous obliteration for portosystemic shunt encephalopathy in patients with liver cirrhosis and portal hypertension. *Kurume Med J.* 2014;61(1-2):1-8. [\[CrossRef\]](#)
  45. Takuma Y, Nouse K, Makino Y, Saito S, Shiratori Y. Prophylactic balloon-occluded retrograde transvenous obliteration for gastric varices in compensated cirrhosis. *Clin Gastroenterol Hepatol.* 2005;3(12):1245-1252. [\[CrossRef\]](#)
  46. Saad WE, Wagner CC, Al-Osaimi A, et al. The effect of balloon-occluded transvenous obliteration of gastric varices and gastrosplenic shunts on the hepatic synthetic function: a comparison between Child-Pugh and model for end-stage liver disease scores. *Vasc Endovascular Surg.* 2013;47(4):281-287. [\[CrossRef\]](#)
  47. Wang ZW, Liu JC, Zhao F, et al. Comparison of the effects of TIPS versus BRTO on bleeding gastric varices: a meta-analysis. *Can J Gastroenterol Hepatol.* 2020;2020:5143013. [\[CrossRef\]](#)
  48. Paleti S, Nutalapati V, Fathallah J, Jeepalyam S, Rustagi T. Balloon-occluded retrograde transvenous obliteration (BRTO) versus transjugular intrahepatic portosystemic shunt (TIPS) for treatment of gastric varices because of portal hypertension: a systematic review and meta-analysis. *J Clin Gastroenterol.* 2020;54(7):655-660. [\[CrossRef\]](#)
  49. Gimm G, Chang Y, Kim HC, et al. Balloon-occluded retrograde transvenous obliteration versus transjugular intrahepatic portosystemic shunt for the management of gastric variceal bleeding. *Gut Liver.* 2018;12(6):704-713. [\[CrossRef\]](#)
  50. Saad WE. Combining transjugular intrahepatic portosystemic shunt with balloon-occluded retrograde transvenous obliteration or augmenting TIPS with variceal embolization for the management of gastric varices: an evolving middle ground? *Semin Intervent Radiol.* 2014;31(3):266-268. [\[CrossRef\]](#)
  51. Sabri SS, Abi-Jaoudeh N, Swee W, et al. Short-term rebleeding rates for isolated gastric varices managed by transjugular intrahepatic portosystemic shunt versus balloon-occluded retrograde transvenous obliteration. *J Vasc Interv Radiol.* 2014;25(3):355-361. [\[CrossRef\]](#)
  52. Saad WE, Wagner CC, Lippert A, et al. Protective value of TIPS against the development of hydrothorax/ascites and upper gastrointestinal bleeding after balloon-occluded retrograde transvenous obliteration (BRTO). *Am J Gastroenterol.* 2013;108(10):1612-1619. [\[CrossRef\]](#)
  53. Park JW, Yoo JJ, Kim SG, et al. Change in portal pressure and clinical outcome in cirrhotic patients with gastric varices after plug-assisted retrograde transvenous obliteration. *Gut Liver.* 2020;14(6):783-791. [\[CrossRef\]](#)
  54. Uehara H, Akahoshi T, Tomikawa M, et al. Prediction of improved liver function after balloon-occluded retrograde transvenous obliteration: relation to hepatic vein pressure gradient. *J Gastroenterol Hepatol.* 2012;27(1):137-141. [\[CrossRef\]](#)



# CT-guided microcoil localization for scapula-blocked pulmonary nodules using penetrating lung puncture before video-assisted thoracic surgery

Ye Tian   
 Jianli An   
 Zibo Zou   
 Yanchao Dong   
 Jingpeng Wu   
 Zhuo Chen   
 Hongtao Niu 

## PURPOSE

To retrospectively analyze the effectiveness and safety of computed tomography (CT)-guided microcoil localization for scapula-blocked pulmonary nodules using penetrating lung puncture prior to video-assisted thoracic surgery (VATS).

## METHODS

One hundred thirty-eight patients with 138 pulmonary nodules were included in this single-center retrospective study. Among them, 110 patients who underwent CT-guided microcoil localization using the routine puncture technique formed the routine group; the other 28 patients who underwent the CT-guided microcoil localization using the penetrating lung puncture technique formed the penetrating lung group. The main outcomes were the success rate and complication rate of the two groups.

## RESULTS

The localization success rate was 95.5% (105/110) in the routine group and 89.3% (25/28) in the penetrating lung group ( $P = 0.205$ ). There was no statistical difference in any of the complications (pneumothorax, intrapulmonary hemorrhage, or moderate and severe chest pain) in both groups ( $P = 0.178$ ,  $P = 0.204$ ,  $P = 0.709$ , respectively). Localization procedure time was significantly increased in the penetrating lung group compared with the routine group ( $31.0 \pm 3.0$  min vs.  $21.2 \pm 2.8$  min,  $P < 0.001$ ).

## CONCLUSION

CT-guided microcoil localization for scapula-blocked pulmonary nodules using penetrating lung puncture prior to VATS resection is effective and safe. However, the deployment of the microcoil using penetrating lung puncture required more time than the routine puncture method.

## KEYWORDS

Computed tomography, hemorrhage, localization, pneumothorax, pulmonary

From the Department of Interventional Treatment (Y.T., J.A., Z.Z., Y.D., J.W., Z.C., H.N. ✉ niuht2004@126.com), First Hospital of Qinhuangdao, Qinhuangdao, China.

Received 1 August 2021; revision requested 16 September 2021; last revision received 4 October 2021; accepted 13 October 2021.



Epub: 28.12.2022

Publication date: 31.01.2023

DOI: 10.5152/dir.2022.21712

With the widespread use of low-dose chest computed tomography (CT) screening, the detection rate of pulmonary nodules has gradually increased, allowing lung cancer to be discovered at an earlier, or possibly more curable, stage.<sup>1</sup> Complete resection by video-assisted thoracoscopic surgery (VATS) is the standard treatment for potentially malignant lung nodules, and VATS in pulmonary wedge resection is a highly effective, minimally invasive procedure under which nodules can be safely removed without a thoracotomy.<sup>2</sup> However, some pulmonary nodules become invisible or inaccessible during the operation because of their small diameter or soft texture, which makes it difficult to successfully remove the nodules. With the development of lung nodule localization technology, surgeons have gradually avoided “blindness” in VATS procedures, thus avoiding the application of thoracotomy.

The method of CT-guided microcoil localization is a reliable and simple marker that effectively assists the surgeon in finding and resecting pulmonary nodules during VATS. The routine puncture technique is used to select an appropriate location and adopt the shortest needle insertion path, leaving one end of the microcoil on the pleural surface, which will provide a direct indication of the location of the VATS resected nodule.<sup>3</sup> Many studies have endeavored to confirm the feasibility and safety of microcoil localization for pulmonary nodules, and continuous improvement of this technique with better coordination of resection procedures has been made.<sup>4-7</sup> However, there are still technical challenges in the accurate localization of some pulmonary nodules in special anatomical positions, such as a scapula-blocked area. Xian et al.<sup>8</sup> proposed a trans-scapular approach to the pulmonary nodules underneath the scapula. Unfortunately, this method greatly increases the operational difficulty. In addition, the distance from the distal end of the coil to the pleura in the path should be as short as possible to preserve the lung parenchyma and protect the lung function during VATS. Sometimes, a viable puncture path without passing through the scapula requires a large angle to the left or right of the axial position, resulting in a significant increase in the distance from the lesion to the pleura.<sup>9</sup>

The authors attempted to locate the scapula-blocked pulmonary nodules using a penetrating lung puncture under CT guidance, retrospectively analyzed the localization parameters and complications of this technique, and compared the results with routine localization methods.

## Methods

### Patient population

This study was approved by the Institutional Review Ethics Committee of Qinhuan-

dao First Hospital on June 2, 2021 (protocol no: 202106B003), and written informed consent was obtained from all participants. Data were obtained from a single medical center. A total of 161 patients were recruited between June 2020 and June 2021 into the routine group, and 28 patients were recruited between January 2019 and June 2021 into the penetrating lung group. At least 12 months of follow-up with CT or positron emission tomography/CT or suspicion of malignant nodules by radiologists with more than 10 years of experience had been employed to initially obviate the possibility of a benign nodule. The necessity and feasibility of preoperative localization of each pulmonary nodule were confirmed in an interdisciplinary meeting involving thoracic surgeons and interventional radiologists before the localization procedure. The primary reason for inclusion in the penetrating lung group was that the pulmonary nodules were shadowed by the scapula, and the nodules could not be coil-localized through the most direct needle path. Demographic, imaging, and surgical data were collected from these patients. Due to multiple pulmonary nodules, 51 patients were excluded from the study. Finally, 138 patients with 138 pulmonary nodules were

included in this single-center retrospective study. Among them, 110 patients who underwent the CT-guided microcoil localization using the routine puncture technique formed the routine group; the other 28 patients who underwent the CT-guided microcoil localization using the penetrating lung puncture technique formed the penetrating lung group (Figure 1). Reviewing the preoperative images, the distribution of nodules was different between the two groups. In the routine group, the pulmonary nodules might appear in any lobe, and the suitable shortest path could be determined. In the penetrating lung group, the nodules were only located in the upper or lower lobe of the area shadowed by the scapula.

### Localization procedure

Two interventional radiologists with at least 10 years of experience performed all the CT scans and localization procedures with the use of a 16-slice multidetector CT (GE Healthcare, Milwaukee, WI, USA). The main parameter settings for CT included the following: scanning method, helical acquisition mode; tube current, 100 mA; tube voltage, 120 kV; rotation speed, 0.8 seconds;

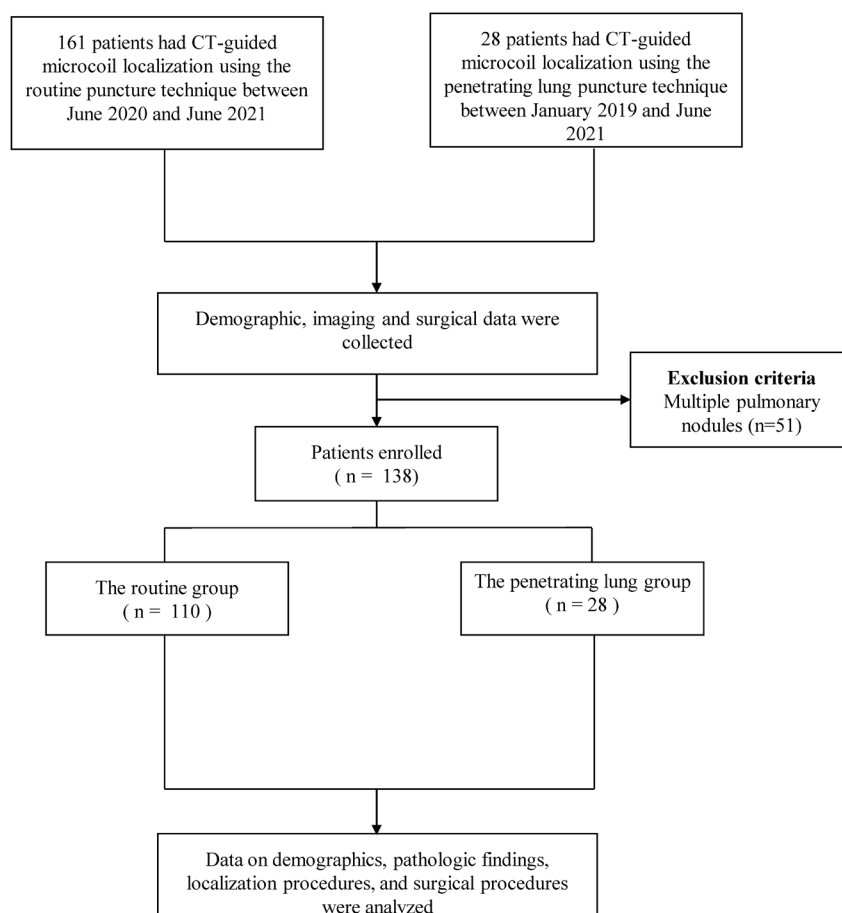


Figure 1. Flow chart showing the inclusion and exclusion criteria for the study.

### Main points

- The accurate localization of some pulmonary nodules in special anatomical positions, such as scapula-blocked areas, is still challenging.
- Computed tomography-guided microcoil localization for scapula-blocked pulmonary nodules using penetrating lung puncture prior to video-assisted thoracic surgery resection is effective and safe.
- The deployment of the microcoil using penetrating lung puncture required more time than the routine puncture method.

slice thickness, 1.25 mm; and reconstruction interval, 1.25 mm. The procedure used a 0.018-inch-diameter, 40-to-70-mm-long (chosen according to the distance from the pulmonary nodule to the pleura) platinum microcoil (Cook Medical, Bloomington, IN, USA), which was originally designed for blood vessel embolization, as well as a 15-cm, 21-G Chiba puncture needle with a coaxial core (Cook Medical, Bloomington, IN, USA). Each patient was placed on the CT scanning bed in a suitable position (prone, supine, or lateral decubitus) according to the location of the targeted lesions. Microcoil localization within the routine group was a modified method based on the procedure reported by Powell et al.<sup>10</sup> First, the location of the lesion and the most direct needle path to the lesion were determined according to the preoperative CT data. After routine disinfection, surgical dressings were placed, and 2% lidocaine was applied for local anesthesia. The patient was instructed to hold their breath after drawing in approximately 50% of the maximum inspiration during needle insertion in order to reduce the effects of respiratory movements and the risk of air embolism. Percutaneous access to the lung followed the planned path with a Chiba needle, advancing the needle tip into the normal lung parenchyma to within 10 mm of the lesions using CT guidance

(Figure 2b). The distance from the needle tip to the pleura was measured using the electronic caliper function available on the CT scanner console. With the loading sleeve tightly connected to the puncture needle, the microcoil was pushed into the needle cavity, and the loading sleeve was removed from the needle. The coaxial needle core was used to release the microcoil into the lung tissue adjacent to the nodule. The puncture needle was slowly withdrawn, with the coaxial needle core remaining stationary until the tail of the microcoil remained outside the pleura (Figure 2c). The needle was removed, and then CT scanning was performed to confirm a satisfactory position of the microcoil and to observe for complications (Figure 2d).

The CT scan parameters and the interventional equipment in the penetrating lung group were the same as those in the routine group. The specific steps for penetrating the lung group were as follows: (1) the intersection point between the reverse extension line of the shortest path from the nodule to the pleura and the chest wall was used as a puncture point. (2) A Chiba needle was percutaneously inserted across long-distance lung tissue along the planned path under the guidance of CT, advancing the needle tip into normal lung parenchyma to within

10 mm of the lesion (Figure 3b) and continuing to penetrate the lung tissue to advance the needle tip into the pleural space. A CT scan was performed to determine that the needle tip reached the appropriate position. (3) With the microcoil loading sleeve tightly connected to the puncture needle, the distal end of the coil was first released to the pleural surface using a coaxial needle core. The puncture needle was slowly withdrawn, with the coaxial needle core remaining stationary until the tail of the microcoil remained near the nodule (Figure 3c). (4) The needle was removed, and a CT scan was also performed to confirm the coil position and any complications.

### VATS procedure

The VATS procedure was performed under single-lung ventilation with a double-lumen endotracheal tube and general anesthesia. The location of the pulmonary nodule was determined using preoperative microcoil localization and thoracoscopic guidance. If the tail of the microcoil was not exposed outside the pleura, its position was ascertained by palpation of the coil or by finding the puncture point. Once the nodule location was determined, wedge resection was performed under microcoil guidance. The complete microcoil and nodules were carefully excised

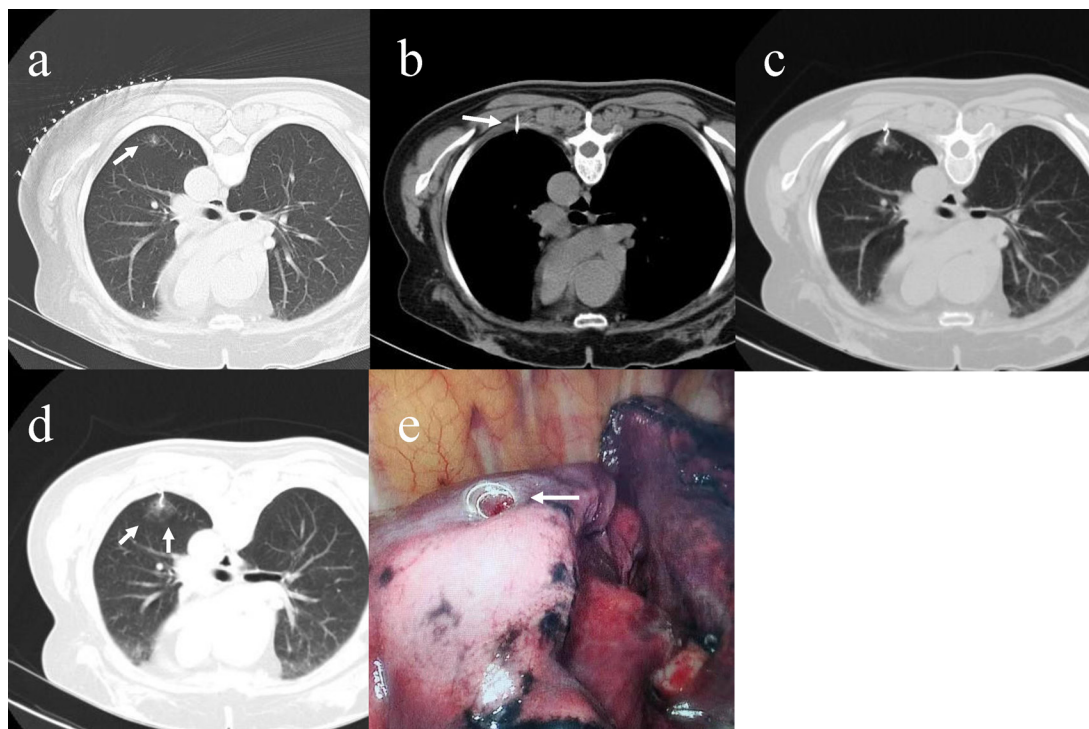


**Figure 2.** A 62-year-old male with a pulmonary nodule in the left lower lobe. (a) Axial CT image showing lesion (arrowhead) in the left lower lobe. (b) Needle tip (arrowhead) was advanced into the normal lung parenchyma to within 10 mm of the lesions. (c) The microcoil was released with the superficial end of the microcoil beyond the visceral pleura and the distal end coiled in the lung parenchyma adjacent to the nodule. (d) A repeat CT scan indicated a satisfactory localization, with new shadows (arrowhead) around the lesion suggestive of intrapulmonary hemorrhage. (e) The superficial end of the microcoil (arrowhead) was visualized using a thoracoscope to guide wedge resection. CT, computed tomography.

by the thoracic surgeons, and the specimen was sent immediately for frozen section. The frozen sections were used to assess whether the lesion had been completely removed or whether extended resection was necessary. There was no difference in the VATS procedure between the two groups.

### Data collection

The following information was extracted from the medical records and radiology information systems: gender, age, nodule position, nodule maximal diameter, nodule to pleural distance, nodule density, patient position, complications of the localization procedure, localization procedure time, surgical operation time, localization success rate, and postoperative pathological diagnosis. Pneumothorax and intrapulmonary hemorrhage complications were confirmed using a CT scan after localization was completed and based on the common terminology criteria for adverse events (CTCAE).<sup>11</sup> A numerical rating scale was used to evaluate chest pain grade.<sup>12</sup>

### Statistical analysis

Continuous variables were summarized using mean  $\pm$  standard deviation, and categorical variables using frequency and percentage. Student's t-test was used for normally distributed continuous variables, and Pearson's chi-square test or Fisher's exact test was used for categorical variables. The software SPSS version 25.0 for Windows (IBM, Armonk, NY, USA) was used for all statistical analyses, and a *P* value of  $<0.05$  was considered statistically significant.

### Results

A total of 138 patients with 138 pulmonary nodules were enrolled in the study, including 110 patients in the routine group and 28 patients in the penetrating lung group. Age, gender, nodule to pleural distance, maximal diameter, nodule density, and nodule position did not differ significantly between the two groups ( $P = 0.547$ ,  $P = 0.791$ ,  $P = 0.116$ ,  $P = 0.173$ ,  $P = 0.756$ , and  $P = 0.223$ , respectively). However, the penetrating lung group had more supine positioning than the routine group (89.9% vs. 41.0%,  $P < 0.001$ ). The

baseline characteristics of the patients and nodules are summarized in Table 1.

Localization procedure time was significantly increased in the penetrating lung group compared with the routine group ( $31.0 \pm 3.0$  min vs.  $21.2 \pm 2.8$  min,  $P < 0.001$ ) (Table 2). A CTCAE grade of 3 or above for adverse events did not occur during the localization procedure of the two groups, and no additional intervention was required in all cases. There was no statistical difference in any of the complications (pneumothorax, intrapulmonary hemorrhage, or moderate and severe chest pain) in both groups ( $P = 0.178$ ,  $P = 0.204$ ,  $P = 0.709$ , respectively).

In all cases, VATS was performed with a success rate of 100%. No statistical difference was observed in surgical operation time between the two groups ( $P = 0.414$ ). The localization success rate was 95.5% (105/110) in the routine group and 89.3% (25/28) in the penetrating lung group ( $P = 0.205$ ). In two of the five failed nodules in the routine group, the microcoil was attached to the thoracic wall muscle, with the distal end of the microcoil pulled out of the lung. Under these circumstances, the surgeons needed to carefully examine the needle track on the lung surface to locate the nodule, and VATS was successfully performed. The superficial end of the microcoil was not exposed in the pleural surface in three of the five failed cases in the routine group, and palpation of the microcoil finally located the nodules. Three nodule localization failures were found in the penetrating lung group. In these cases, the superficial end of the coil did not appear in the pleural cavity. All three patients developed pneumothorax on their last CT scan after localization, and localized pulmonary nodules were finally palpated.

There were 71 patients with benign lesions and 39 patients with malignant lesions in the routine group. Among the 28 patients in the penetrating lung group, 17 were benign, and 11 were malignant lesions. The postoperative pathological diagnoses of the nodules are listed in Table 3.

### Discussion

This study retrospectively describes the effectiveness of CT-guided microcoil localization for scapula-blocked pulmonary nodules using penetrating lung puncture. When performing CT-guided pulmonary interventional procedures, bony structures such as the scapula have the potential to obstruct the needle path, thereby increasing the difficulty

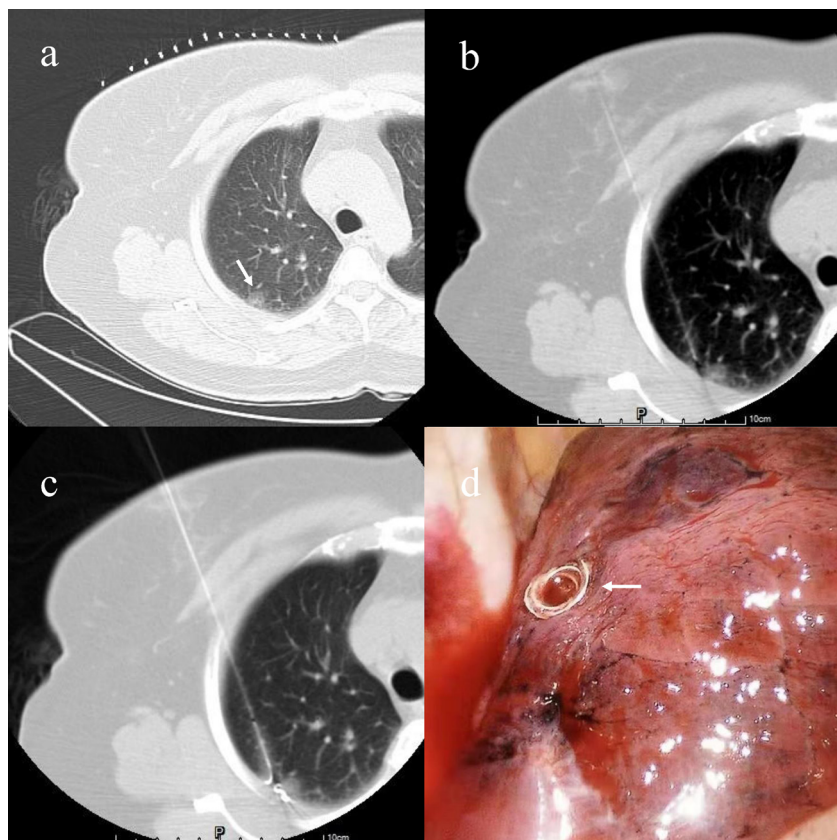


**Figure 3.** A 49-year-old female with a pulmonary nodule in the right upper lobe. (a) Axial CT image showing lesion (arrowhead) in the right upper lobe. (b) Needle tip was advanced into the normal lung parenchyma adjacent to the lesion and continued to advance to the pleural cavity. (c) The distal end of the coil was first released to the pleural surface, and the tail of the microcoil remained near the nodule. (d) The superficial end of the microcoil (arrowhead) was visualized using a thoracoscope to guide wedge resection. CT, computed tomography.

of manipulation.<sup>13,14</sup> Zhang et al.<sup>15</sup> attempted to apply a trans-scapular approach for preoperative CT-guided coil localization of scapula-blocked pulmonary nodules, achieving a technical success rate of 100% and pneumothorax in 9.1% of patients. In fact, avoiding bony structures is considered to be the optimal approach. In the present study, although there were a few unsuccessful localizations in both groups, VATS was successfully performed in all cases without breaking the scapula.

Although the localization success rate was lower in the penetrating lung group (89.3%) than in the routine group (95.5%), this difference was not significant. Consequently, CT-guided microcoil localization using the penetrating lung puncture technique is fea-

sible. Xu et al.<sup>3</sup> considered that the presence of pleural indentation during the procedure was a significant risk factor contributing to microcoil pleura marking failure, which was positively correlated with the existence of pneumothorax. The removal of predisposing factors for pneumothorax (e.g., a reduction in the number of punctures) may contribute to an increased success rate. In the penetrating lung puncture group, localization failed in three cases because the distal end of the coil did not appear on the pleural surface, and all of these patients developed pneumothorax. In this case, the CT image provided misleading information to radiologists that the procedures had been successfully completed. In fact, as the lung tissue re-inflated during the positioning and VATS intervals, the ends of the microcoil retracted from the

pleural surface, and eventually, the microcoil could not appear on the pleural surface. Fortunately, these nodules were all successfully localized under palpation by the surgeons and subsequently resected.

There was no statistical difference in the incidence of any complication between the penetrating lung group and the routine group, with complications of grade 1 or 2, demonstrating that CT-guided microcoil localization for pulmonary nodules using penetrating lung puncture is safe. Penetrating lung puncture inevitably led to a longer puncture path. Although it has been reported that a longer puncture path was linked with the incidence of pneumothorax and intrapulmonary hemorrhage during CT-guided lung biopsy,<sup>16</sup> no similar findings were seen in this study. This may be due to the use of a 21-G needle for the localization of pulmonary nodules, which is thinner than a biopsy needle. Al-Damegh<sup>17</sup> reported that the small needle size in their study was associated with the significant absence of post-procedural complications. The incidence of moderate and severe chest pain was comparable in both groups and not directly related to the penetrating lung puncture. Hu et al.<sup>18</sup> concluded that smaller diameter nodules contributed to the increased incidence of moderate or severe chest pain.

The location of the marking should be the shortest distance from the pleura to the nodule.<sup>19</sup> Considering the shadow effect of the scapula, more patients used the supine position in the penetrating lung group, which was determined by the shortest path from the pleura to the nodules, while no patients used the prone position. In the routine group, the most suitable body position should be determined according to the location of the nodules. This is used to explain why there is a significant difference in body position between the two groups.

The microcoil localization procedure time in the penetrating lung group was 31.0 ± 3.0 minutes, which was much longer than the time in the routine group. The possible reasons that contributed to the long procedure time are as follows: 1) the primary motivation for the penetrating lung puncture was scapular occlusion, which required a more complex path strategy during localization; and 2) a longer puncture path required the radiologist to adjust the insertion route and angle more frequently. In addition, the penetrating lung group first released the distal end of the microcoil on the pleural surface, and more precise adjustment of the posi-

**Table 1.** Clinical characteristics in the routine group and the penetrating lung group

	Routine group	Penetrating lung group	P value
Number, n	110	28	
Age (year), mean ± SD	58.5 ± 9.9	57.1 ± 11.7	0.547
Gender, n (%)			0.791
Male	48 (43.6%)	13 (46.4%)	
Female	62 (56.4%)	15 (53.6%)	
Nodule to pleural distance (mm), mean ± SD	25.8 ± 13.5	21.6 ± 7.8	0.116
Maximal diameter (mm), mean ± SD	11.9 ± 5.5	13.9 ± 7.2	0.173
Nodule density, n (%)			0.756
Solid	28 (25.5%)	8 (28.6%)	
Part-solid	15 (13.6%)	5 (17.9%)	
Non-solid	67 (60.9%)	15 (53.6%)	
Patient position, n (%)			<0.001
Supine	45 (40.9%)	25 (89.3%)	
Prone	36 (32.7%)	0	
Lateral	29 (26.4%)	3 (10.7%)	
Nodule position, n (%)			0.223
Right lung	69 (62.7%)	21 (75.0%)	
Left lung	41 (37.3%)	7 (25.0%)	

SD, standard deviation.

**Table 2.** Comparison of complications, localization, and surgical procedure-related data between the groups

	Routine group	Penetrating lung group	P value
Number, n	110	28	
Pneumothorax, n (%)	19 (17.3%)	8 (28.6%)	0.178
Intrapulmonary hemorrhage, n (%)	12 (10.9%)	6 (21.4%)	0.204
Moderate and severe chest pain, n (%)	9 (8.2%)	3 (10.7%)	0.709
Localization procedure time (minutes), mean ± SD	21.2 ± 2.8	31.0 ± 3.0	<0.001
Surgical operation time (minutes), mean ± SD	118.4 ± 14.3	121.0 ± 16.4	0.414
Success rate, n (%)	105 (95.5%)	25 (89.3%)	0.205

SD, standard deviation.



Table 3. Postoperative pathology of the nodules in the two groups		
Pathology	Routine group (n = 110)	Penetrating lung group (n = 28)
<b>Malignant, n (%)</b>		
invasive adenocarcinoma	41 (37.3%)	7 (25.0%)
Minimally invasive adenocarcinoma	22 (20.0%)	3 (10.7%)
Adenocarcinoma <i>in situ</i>	6 (5.5%)	5 (17.9%)
Squamous cell carcinoma	2 (1.8%)	1 (3.6%)
Metastatic carcinoma	0	1 (3.6%)
<b>Benign, n (%)</b>		
Atypical adenomatous hyperplasia	13 (11.8%)	4 (14.3%)
Tuberculosis	8 (7.3%)	2 (7.1%)
Lymphoid hyperplasia	5 (4.5%)	0
Localized pneumonitis	5 (4.5%)	1 (3.6%)
Fibrous tissue hyperplasia	3 (2.7%)	2 (7.1%)
Intrapulmonary lymph node	2 (1.8%)	0
Pulmonary hamartoma	2 (1.8%)	2 (7.1%)
Sclerosing hemangioma	1 (0.9%)	0

tion of the needle tip was required to reduce damage to the chest wall tissue caused by unnecessary puncture as compared with the routine group. The proximal end of the microcoil in the routine group could be placed within 10 mm of the extrapleural chest wall tissue since the needle had already passed through the chest wall tissue at that site. There was no significant difference in surgical time between the two groups, proving that different puncture methods of microcoil localization had no effect on VATS procedure time.

However, this study had some limitations. First, the sample size was relatively small, so future studies with larger sample sizes are required. Second, this was a single-center evaluation, and a future multicenter study may further confirm the findings. Moreover, it was not possible to evaluate unusual adverse events due to the fact that no such complications occurred in this study.

In conclusion, CT-guided microcoil localization for scapula-blocked pulmonary nodules using penetrating lung puncture prior to VATS resection is effective and safe. However, the deployment of the microcoil using penetrating lung puncture required more time than the routine puncture method.

### Conflict of interest disclosure

The authors declared no conflicts of interest.

## References

- Henschke C, McCauley D, Yankelevitz D, et al. Early Lung Cancer Action Project: overall design and findings from baseline screening. *Lancet*. 1999;354(9173):99-105. [\[CrossRef\]](#)
- Yang F, Zhao H, Sui X, et al. Comparative study on preoperative localization techniques using microcoil and hookwire by propensity score matching. *Thoracic Cancer*. 2020;11(6):1386-1395. [\[CrossRef\]](#)
- Xu Y, Ma L, Sun H, et al. CT-guided microcoil localization for pulmonary nodules before VATS: a retrospective evaluation of risk factors for pleural marking failure. *Eur Radiol*. 2020;30(10):5674-5683. [\[CrossRef\]](#)
- Lee MO, Jin SY, Lee SK, Hwang S, Kim TG, Song YG. Video-assisted thoracoscopic surgical wedge resection using multiplanar computed tomography reconstruction-fluoroscopy after CT guided microcoil localization. *Thorac Cancer*. 2021;12(11):1721-1725. [\[CrossRef\]](#)
- Huang ZG, Wang CL, Sun HL, et al. CT-Guided Microcoil Localization of Small Peripheral Pulmonary Nodules to Direct Video-Assisted Thoracoscopic Resection without the Aid of Intraoperative Fluoroscopy. *Korean J Radiol*. 2021;22(7):1124-1131. [\[CrossRef\]](#)
- Hu L, Gao J, Hong N, et al. Simultaneous preoperative computed tomography-guided microcoil localizations of multiple pulmonary nodules. *Eur Radiol*. 2021;31:6539-6546. [\[CrossRef\]](#)
- Refai M, Andolfi M, Barbisan F, et al. Computed tomography-guided microcoil placement for localizing small pulmonary nodules before uniportal video-assisted thoracoscopic

resection. *Radiol Med*. 2020;125(1):24-30.

[\[CrossRef\]](#)

- Xian YT, Wu AL, Lin J, Teng F, Wang ZS, Xu XJ. Computed tomography-guided coil localization for scapular-blocked lung nodules. *Minim Invasive Ther Allied Technol*. 2022;31(3):468-472. [\[CrossRef\]](#)
- Chuan-Dong L, Hong-Liang S, Zhen-Guo H, et al. CT-guided microcoil implantation for localizing pulmonary ground-glass nodules: feasibility and accuracy of oblique approach for lesions difficult to access on axial images. *Br J Radiol*. 2020;93(1109):20190571. [\[CrossRef\]](#)
- Powell TI, Jangra D, Clifton JC, et al. Peripheral lung nodules: fluoroscopically guided video-assisted thoracoscopic resection after computed tomography-guided localization using platinum microcoils. *Ann Surg*. 2004;240(3):481-488; discussion 488-489. [\[CrossRef\]](#)
- Common Terminology Criteria for Adverse Events (CTCAE) v4.0. 2009. [\[CrossRef\]](#)
- Caraceni A, Cherny N, Fainsinger R, et al. Pain measurement tools and methods in clinical research in palliative care: recommendations of an Expert Working Group of the European Association of Palliative Care. *J Pain Symptom Manage*. 2002;23(3):239-255. [\[CrossRef\]](#)
- Rossi UG, Seitun S, Ferro C. MDCT-guided transthoracic needle aspiration biopsy of the lung using the transscapular approach. *Cardiovasc Intervent Radiol*. 2011;34(1):184-187. [\[CrossRef\]](#)
- Iguchi T, Hiraki T, Ishii H, et al. Transosseous Route for CT Fluoroscopy-Guided Radiofrequency Ablation of Lung Tumors. *J Vascular Interv Radiol*. 2015;26(11):1694-1698. [\[CrossRef\]](#)
- Zhang JH, Zhou SQ, Xia FF, Wang T. Computed tomography-guided trans-scapular coil localization for pulmonary nodules. *Thorac Cardiovasc Surg*. 2021;69(7):679-682. [\[CrossRef\]](#)
- Khan MF, Straub R, Moghaddam SR, et al. Variables affecting the risk of pneumothorax and intrapulmonary hemorrhage in CT-guided transthoracic biopsy. *Eur Radiol*. 2008;18(7):1356-1363. [\[CrossRef\]](#)
- Al-Damegh S. Fine needle aspiration of solitary pulmonary lesions. *Eur J Radiol*. 2001;37(3):200-203. [\[CrossRef\]](#)
- Hu L, Gao J, Chen C, Zhi X, Liu H, Hong N. Comparison between the application of microcoil and hookwire for localizing pulmonary nodules. *Eur Radiol*. 2019;29(8):4036-4043. [\[CrossRef\]](#)
- Fogolin RE, Boscardim PCB, Souza JM. Preoperative computed tomography-guided localization of lung nodules with needle placement: a series of cases. *Rev Col Bras Cir*. 2021;48:e20202890. [\[CrossRef\]](#)



# Prediction of common hepatic artery catheter insertion based on celiac trunk morphology

Atsushi Saiga   
 Hajime Yokota   
 Akira Akutsu   
 Yoshihiko Ooka   
 Yoshihiro Kubota   
 Takeshi Wada   
 Jun Koizumi   
 Takashi Uno 

## PURPOSE

This study aimed to predict the ability to insert a 4–5 French (Fr) catheter insertion with a guidewire into the common hepatic artery (CHA) based on celiac trunk morphology.

## METHODS

This retrospective study included 64 patients who underwent balloon-occluded transcatheter arterial chemoembolization (n = 56), transcatheter arterial chemotherapy (n = 2), or were fitted with an implantable port system (n = 6) between June 2019 and December 2019 in our institution. The morphology of the celiac trunk was classified into three types (upward, horizontal, and downward) based on celiac angiography. The aortic–celiac trunk angle was measured on sagittal images of preprocedural contrast-enhanced computed tomography (CT). We reviewed whether a 4–5-Fr shepherd's hook catheter could advance beyond the CHA using a 0.035-inch guidewire (Radifocus® Guidewire M; Terumo). Three patients were diagnosed with median arcuate ligament syndrome (MALS) based on the characteristic hook shape of the celiac artery on sagittal images of contrast-enhanced CT. The predictive ability of celiac angiography and preprocedural CT for CHA insertion success was evaluated. In unsuccessful cases, the balloon anchor technique (BAT) was attempted as follows: (1) a 2.7/2.8-Fr microballoon catheter (Attendant Delta; Terumo) was placed beyond the proper hepatic artery, and (2) the balloon was inflated as an anchor for parent catheter advancement.

## RESULTS

Upward, horizontal, and downward celiac trunk types were noted in 42, 9, and 13 patients, respectively. The median CT angle was 122.83° (first quartile–third quartile, 102.88°–136.55°). Insertion in the CHA using the guidewire was successful in 56 of 64 patients (87.50%), and the success rate in the downward type was significantly lower than that in the upward type [42/42 (100%) vs. 7/13 (53.85%),  $P < 0.001$ ]. The CT angle was significantly larger downward in the unsuccessful group than in the successful group (121.03° vs. 140.70°,  $P = 0.043$ ). Celiac angiography had a significantly higher area under the curve (AUC) than preprocedural CT (AUC = 0.91 vs. AUC = 0.72,  $P = 0.040$ ). All three cases of MALS showed unsuccessful CHA insertion. In all eight patients with unsuccessful insertion, the catheter could be advanced using the BAT [8/8 (100%)].

## CONCLUSION

Celiac angiography and preprocedural CT could predict CHA catheter insertion using a guidewire, and celiac angiography had high predictability. CT could detect MALS, a risk factor for unsuccessful CHA insertion.

## KEYWORDS

Balloon anchor technique, balloon-occluded transcatheter arterial chemoembolization, celiac trunk morphology, common hepatic artery insertion, the aortic-celiac trunk angle

From the Department of Radiology (A.S. ✉ agiasaiga@gmail.com, A.A., Y.K., T.W., J.K.), Department of Diagnostic Radiology and Radiation Oncology (H.Y., T.U.), Department of Gastroenterology (Y.O.), Chiba University Hospital, Chiba, Japan.

Received 18 January 2021; revision requested 1 February 2021; last revision received 26 October 2021; accepted 3 November 2021.



Epub: 05.12.2022

Publication date: 31.01.2023

DOI: 10.5152/dir.2022.21010

You may cite this article as: Saiga A, Yokota H, Akutsu A, et al. Prediction of common hepatic artery catheter insertion based on celiac trunk morphology. *Diagn Interv Radiol.* 2023;29(1):161-166.

A stable backup of the parent catheter is required when performing ultraselective transcatheter arterial chemoembolization (TACE) for hepatocellular carcinoma (HCC). However, common hepatic artery (CHA) insertion using a 0.035-inch guidewire is difficult or impossible in some cases because of the vessel's tortuous anatomy and severe stenosis of the celiac artery due to arteriosclerosis and median arcuate ligament syndrome (MALS). There are no studies on predictors of the success rate of CHA insertion.

We focused on the association between the success rate of CHA insertion and celiac trunk morphology. The morphology of the celiac trunk can be assessed by celiac angiography and computed tomography (CT). The former is similar to the technique used when performing CHA insertion, while the latter is useful in preprocedural planning and MALS assessment.

A few stabilized catheterization techniques, such as the balloon anchor technique (BAT),<sup>1</sup> the wire anchoring technique,<sup>2</sup> and the AMPLATZ™ Vascular Plug anchoring technique,<sup>3</sup> have been described previously. Among these techniques, Shibuya et al.<sup>1</sup> reported that the BAT is most effective in cases wherein CHA insertion using a guidewire is difficult during TACE. A microballoon catheter is placed beyond the proper hepatic artery, and the balloon is inflated as an anchor for parent catheter advancement. The parent catheter can be inserted along the fixed microballoon catheter.

This study aimed to evaluate the ability to predict the advancement of a 4–5 French (Fr) catheter to the CHA based on celiac trunk morphology. The morphological characteristics of the celiac artery were compared between successful and unsuccessful cases of CHA insertion with a guidewire.

#### Main points

- Common hepatic artery (CHA) insertion tends to be difficult in the downward type on celiac angiography.
- The predictive power of preprocedural computed tomography (CT) was inadequate compared with that of celiac angiography with respect to CHA insertion success.
- Median arcuate ligament syndrome was a risk factor for CHA insertion using a guidewire and was detectable on preprocedural CT.

## Methods

This study was approved by the institutional review board of our hospital (ethics approval number: 3,972) and was not supported by any funding. Written informed consent was obtained from all patients.

### Patients

This study retrospectively included 90 consecutive procedures in 90 patients who underwent contrast-enhanced CT and at least one of three treatments for HCC between June 2019 and December 2019: balloon-occluded TACE (B-TACE), transcatheter arterial chemotherapy, and an implantable port system. As described in a previous study from our institution,<sup>4</sup> the decision to treat patients with Barcelona Clinic Liver Cancer (BCLC) stage-B HCC<sup>5</sup> was based on the following steps. We initially considered whether the most common curative treatment, such as surgical resection and local ablation, could be performed. All remaining patients were considered for TACE, the first-line non-curative treatment for BCLC stage-B HCC. We routinely performed B-TACE to accumulate more dense iodized oil emulsion in HCC than conventional TACE. Because the pressure gradient between the occluded artery and the portal vein was decreased by balloon occlusion, the iodized oil emulsion was limited to the liver parenchyma, and accumulation in the HCC nodules was relatively increased.<sup>6</sup> Balloon occlusion enables the injection of iodized oil emulsion under higher pressure without a backflow of iodized oil.<sup>7</sup>

A total of 26 patients were excluded due to the following reasons: absence of branching of CHA from the celiac artery ( $n = 18$ ), brachial artery approach ( $n = 5$ ), coaxial implantable port system ( $n = 2$ ), and celiac artery dissection ( $n = 1$ ). A total of 64 consecutive patients (50 men and 14 women; median age, 73.00 years; first quartile–third quartile, 67.00–77.00 years) were included in the analyses.

### Classification of celiac trunk morphology on angiography

Celiac trunk morphology was classified into three types (upward, horizontal, and downward) according to celiac angiography (Figure 1a-c) by a radiologist with 13 years' experience in interventional radiology. Celiac angiography was performed from an anteroposterior view at end expiration. The upward type was defined when the celiac artery had an upward course from the level of the catheter tip in the celiac trunk.

The downward type was defined in the opposite way. The horizontal type was defined when the catheter tip and celiac trunk overlapped.

### Measurement of the celiac arterial branching angle on CT

Five-phase (non-contrast, early arterial, late arterial, portal venous, and delayed phases) dynamic CT (Aquilion ONE ViSION or Aquilion PRIME; Canon Medical Systems) for liver assessment was performed at end inspiration with a dose of 2 mL/kg of iodinated contrast medium (iopaque, 300-mg iodine/mL; Fuji Pharma Co., Ltd. or iopromide, 300-mg iodine/mL; Fujifilm Toyama Chemical Co.). The contrast medium was injected at a rate of 2.5–3.5 mL/s via mechanical injection (Dual Shot GX7; Nemoto Kyorindo Co., Ltd.). The anterior side of the abdominal aorta was defined as the baseline, and we measured the celiac arterial branching angle from the cranial side to the baseline using reconstructed sagittal images of the early arterial phase on preprocedural contrast-enhanced CT (Figure 2). Two radiologists (with 13 and 6 years' experience in abdominal radiology) individually assessed the angle, and the average angles were calculated. Additionally, the radiologists diagnosed MALS by consensus from a characteristic hook shape of the celiac artery on sagittal images of contrast-enhanced CT.

### CHA insertion strategy

Right or left femoral artery catheterization was performed under local anesthesia using the Seldinger technique. A 4–5-Fr shepherd's hook diagnostic catheter (4-Fr catheter in B-TACE and transcatheter arterial chemotherapy, and 5-Fr catheter in the implantable port system) was placed in the celiac trunk, and angiography was performed (three images/s, 25 mL, with 5 mL/s). Initially, we advanced the parent catheter beyond the CHA using a 0.035-inch guidewire (Radifocus® Guidewire M; Terumo; 150 cm) to achieve high-quality images of CT during hepatic arteriography and stable backup by the parent catheter in selective B-TACE.

In unsuccessful cases of CHA insertion, the coaxial system was inserted through the parent catheter using a 2.7-Fr microballoon catheter (130 cm) (Attendant Delta; Terumo), and the BAT was attempted as follows (Figure 3a-c, and Video 1): 1) The microballoon catheter was placed beyond the proper hepatic artery with a 0.016-in. micro guidewire (ASA-HI Meister; Asahi Intecc), 2) the balloon was



**Figure 1.** Celiac angiography was classified into three types: (a) upward, (b) horizontal, and (c) downward.



**Figure 2.** An aortic–celiac trunk angle (curved arrow) between the anterior side of the abdominal aorta (dotted yellow line) and the anterior side of the celiac trunk (dotted blue line) was measured on sagittal contrast-enhanced computed tomography.

inflated as an anchor at a non-tumor feeding artery, and 3) the parent catheter was advanced while pulling the balloon catheter in the negative direction.

### Statistical analysis

Continuous variables are presented as median and first quantile–third quantile range and were compared using the Mann–Whitney U test. Categorical variables are shown as frequencies and percentages and were compared using Fisher’s exact test. The success rate of CHA insertion using a guidewire during angiography was compared among the three celiac trunk morphology groups using Fisher’s exact test. When further comparisons were performed to find which pairs in the three groups had significant differences, the *P* value was adjusted to triple according to the Bonferroni method. Fisher’s exact test was also used

to compare the success rate of CHA insertion between 4-Fr and 5-Fr catheters using a guidewire. The celiac arterial branching angles on CT between the groups with successful and unsuccessful CHA insertion with a guidewire were compared using the Mann–Whitney U test. Spearman’s rank correlation coefficient was calculated between the classification of the angiography morphology and CT angles. The intraclass correlation coefficient (ICC) for CT angle measurements was calculated to evaluate the intra-rater reliability of the two radiologists. Receiver operating characteristic (ROC) curves were created for the predictability of CHA insertion with a guidewire, and the area under the curve (AUC) values were computed using the angiography morphology and CT angles. The numbers corresponding to the types of angiography morphology (0= upward, 1= horizontal, and 2= downward type) and CT angles were

input to the ROC analysis. The difference between the two ROC curves was evaluated using DeLong’s test. A two-sided value of *P* < 0.050 was considered significant. All statistical analyses were performed using R software v. 3.5.1 (R Foundation for Statistical Computing; Vienna, Austria). The ICC was calculated using the psych package (<https://cran.r-project.org/web/packages/psych/>), and a ROC analysis was performed using the pROC package (<https://cran.r-project.org/web/packages/pROC/>). The R Base Package was used for all other analyses.

## Results

The technical success rate of CHA insertion using a guidewire was 56/64 (87.50%). No technique-related complications were observed. A balloon derived from the defective product did not deflate in one case. We retrieved the catheter after the intended rupture of the balloon.

The relationship between the morphology type of angiography and CT angles is presented in Table 1. There was a significant correlation between the morphology of the celiac trunk on angiography and the branching angle of the celiac trunk on CT ( $r_s = 0.40$ ,  $P = 0.001$ ) (Figure 4). The ICC for CT angle measurement by the two radiologists was 0.94 (95% confidence interval: 0.91–0.96;  $P < 0.001$ ). The morphological assessment of the celiac angiography showed that the success rates of CHA insertion using a guidewire were 42/42 (100%), 7/9 (77.78%), and 7/13 (53.85%) in the upward, horizontal, and downward types, respectively. A significant difference was observed among the three groups ( $P < 0.001$ ). The success rate in the downward type was significantly lower than that in the upward type [7/13 (53.85%) vs. 42/42 (100%),  $P < 0.001$ ]. However, no significant difference was noted in the success rates between the upward vs. horizontal and the horizontal vs. downward types [42/42 (100%) vs. 7/9 (77.78%),  $P = 0.085$ ; 7/9 (77.78%) vs.

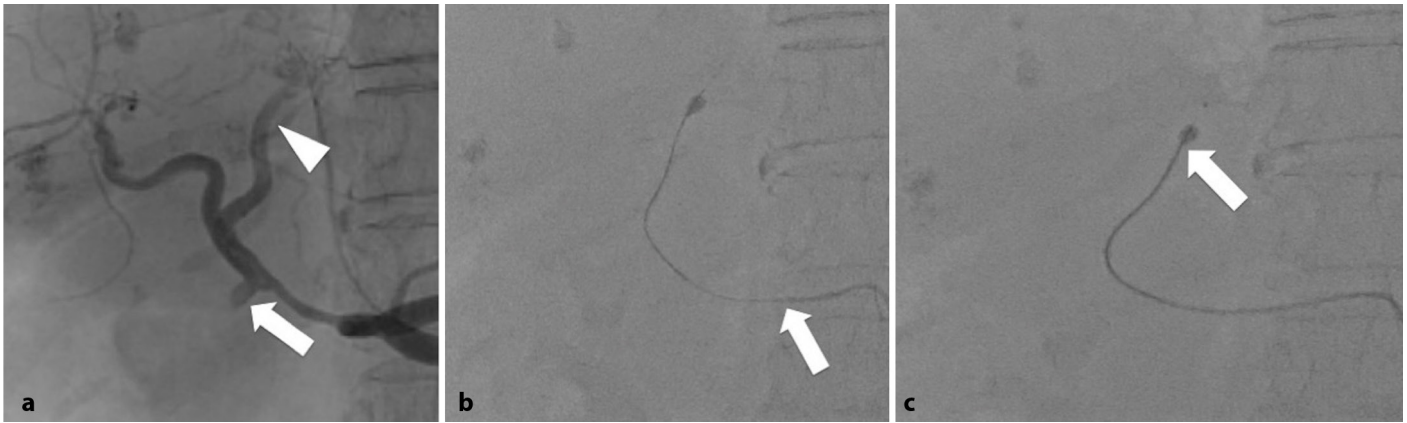


**Figure 3.** The balloon anchor technique was used in a 70-year-old woman with median arcuate ligament syndrome. (a) Although the common hepatic artery was visualized anterogradely, the gastroduodenal artery (arrow) showed stagnant flow due to the flow from the superior mesenteric artery. (b) The balloon was inflated as an anchor in the left hepatic artery [cf. arrowhead on (a)]. The arrow indicates the tip of the parent catheter. (c) The parent catheter was advanced into the left hepatic artery along the fixed microballoon catheter. The arrow indicates the tip of the parent catheter.

**Table 1.** Imaging characteristics of the celiac trunk

Morphology type on celiac angiography	Upward	Horizontal	Downward
	42 (65.63%)	9 (14.06%)	13 (20.31%)
CT angles for each morphology type on angiography*	Median 117.6° (95.5–113.5)	Median 124.3° (104.8–136.7)	Median 138.2° (134.7–146.0)

\* , median (first quantile–third quantile); CT, computed tomography.

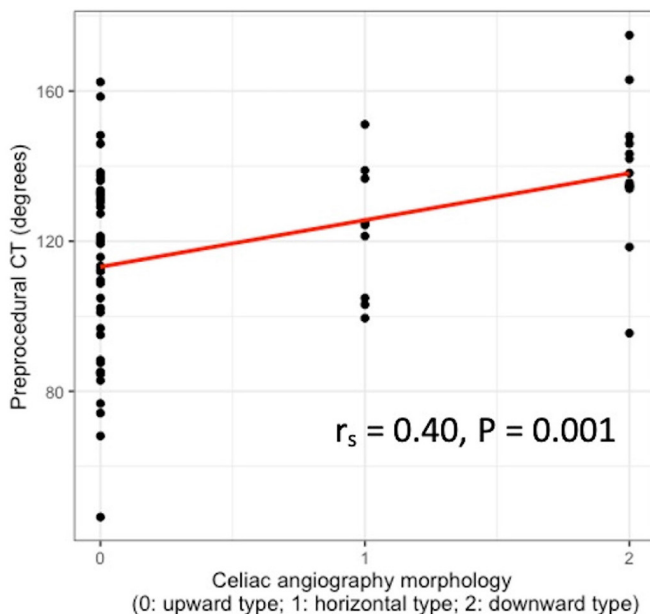


**Figure 4.** The correlation between celiac angiography morphology and preprocedural computed tomography. The  $r_s$  is 0.40 ( $P = 0.001$ ). Celiac angiography morphology is classified into three types: upward, horizontal, and downward. Zero, 1, and 2 on the X-axis indicate the upward, horizontal, and downward types, respectively. CT, computed tomography.

7/13 (53.85%),  $P = 1.000$ ].

Additionally, the success rate of CHA insertion using a guidewire was not significantly different between the 4-Fr (50/58) and 5-Fr (6/6) catheters (86.21% vs. 100%;  $P = 1.000$ ). The CT angle was significantly larger downward in the unsuccessful group than

in the successful group for CHA insertion using a guidewire [median 140.70° (122.84–146.49) vs. median 121.03° (100.66–134.91),  $P = 0.043$ ].

On celiac angiography, six and two cases of the downward and horizontal types, respectively, were included in the unsuccessful

group. All three MALS cases were also included in the unsuccessful group. The cases of MALS were classified into one horizontal and two downward types on the angiography morphology. The ROC curves are shown in Figure 5. Celiac angiography showed a significantly higher AUC than preprocedural CT (AUC = 0.91 vs. AUC = 0.72,  $P = 0.040$ ). The sensitivity and specificity of angiography were 1.00 and 0.75, respectively, at the cut-off point between the downward–horizontal types and the upward type.

In all eight patients with unsuccessful insertion, the catheter could be advanced using the BAT without balloon inflation-related complications.

## Discussion

This study demonstrated that the success rate of CHA insertion using a guidewire in the downward type was significantly lower than that in the upward type on angiography. The morphology of CHA on angiography was a good predictor of CHA insertion. The celiac arterial branching angle on preprocedural CT also predicted CHA insertion success with a guidewire, although its predictive power was lower than that of celiac angiography. MALS was a risk factor in CHA insertion using a guidewire, and it was detectable on preprocedural CT. In patients unsuccessfully inserted with CHA using a guidewire, the BAT may have played a complementary role. However, its effectiveness requires further investigation in the future.

The morphology of the celiac artery was evaluated using angiography and CT. Tokue et al.<sup>8</sup> reported that the branching angle of the celiac trunk on CT was 135° ±

23° (range, 51°–174°), and 1,027 of 1,104 (93.03%) cases had an angle between 91° and 180°. In our study, the branching angle was  $123^\circ \pm 25^\circ$  (range, 47°–175°), and 54 of 64 (84.38%) cases had an angle of between 91° and 180°. The result of our study was consistent with the results of Tokue et al.<sup>8</sup> study. We also demonstrated the discrepancy in celiac trunk morphology between celiac angiography and CT. We speculated the two major causes of this discrepancy were the difference in measurement points (from the tip of the catheter on celiac angiography vs. from the orifice of the celiac trunk on CT) and the difference in breathing (celiac angiography at the expiration phase vs. preprocedural CT at the inspiration phase). Suh et al.<sup>9</sup> reported branch angles of the celiac artery at the inspiration and expiration phases in contrast-enhanced magnetic resonance angiography. The angles were  $126.4^\circ \pm 17.8^\circ$  (mean  $\pm$  standard deviation) and  $125.0^\circ \pm 19.9^\circ$  at the inspiration and expiration phases, respectively. They concluded that the celiac artery showed lower branch angle changes. The discrepancy between celiac angiography and CT may have been affected by the difference in measurement point rather than breathing. The CT angle was significantly larger downward in the unsuccessful group than in the successful group.

In all cases where CHA insertion by a guidewire was unsuccessful, the BAT was

successful. The BAT might have played a complementary role in CHA insertion, although further study with a larger number of participants is needed to evaluate complication rates and clinical significance. Shibuya et al.<sup>1</sup> applied BAT to TACE for hepatic tumors. They used a 1.8-Fr microballoon catheter (Logos; Piolax) and applied this technique in three cases of unsuccessful CHA insertion with a guidewire. They demonstrated that the vessel's tortuous anatomy and severe stenosis of the celiac trunk due to arteriosclerosis and MALS caused unsuccessful insertion. In our experience, CHA insertion was possible in the case of the vessel's tortuous anatomy beyond the proper hepatic artery because a guidewire could be advanced to the gastroduodenal artery and a parent catheter could be followed into the CHA. In contrast, in the case of celiac artery stenosis due to the downward type and MALS, CHA insertion was difficult due to insufficient backup of the parent catheter at the celiac artery.

The balloon size in Shibuya et al.'s<sup>1</sup> study and our research was similar (3–5 mm vs. 4 mm, respectively). However, the tip of the microballoon catheter (1.8-Fr vs. 2.7-Fr) and the size and shape of the parent catheter (5-Fr vs. 4- or 5-Fr; cobra and modified spiral shaped vs. shepherd's hook shaped) were different. Although it is unclear which combination of the microballoon catheter and parent catheter was suitable for the BAT, our choice (a smaller parent catheter and a larger

microballoon catheter) may be effective for the technique due to the smaller gap between the two catheters.

The BAT has been reported previously in other fields. Sharashidze et al.<sup>10</sup> reported it for thrombectomy in large-vessel occlusion acute ischemic strokes. Moreover, Kawaguchi et al.<sup>11</sup> used this technique on endoscopic retrograde cholangiopancreatography with a large balloon catheter. In the field of abdominal surgery, we reported the BAT as a "balloon anchoring and squeezing technique" (Saiga et al.<sup>12</sup>, p. 403) in a case of renal artery aneurysm exclusion using a stent graft. This technique is extremely effective in preventing the risk of vessel injury and facilitating distal advancement of the guiding sheath.<sup>12</sup>

Miyayama et al.<sup>13</sup> reported that ultraselective TACE was effective in controlling local recurrence, especially when accumulating dense iodized oil emulsion in HCC with a greater grade of portal vein visualization. As we routinely tried to advance the microballoon catheter as much as possible to the distal portion of the feeding artery (e.g., the distal subsegmental and distal sub-subsegmental tumor feeding branches), we performed CHA insertion in all patients. Thus, CHA insertion in B-TACE may partially help improve the treatment effect. However, further studies should be conducted in the future.

This study has some limitations: it was retrospective in nature, and the sample size was small. Thus, technique-related complications, such as vascular injuries associated with balloon overinflation, were not fully evaluated. Although no severe complication was observed in this study, the risk should be considered. Moreover, we used only the shepherd's hook catheter as a parent catheter. In clinical practice, the shape of the parent catheter is commonly selected according to the morphology of the celiac trunk. For example, the Rosch hepatic catheter is commonly available on celiac angiography, especially the downward type.

In conclusion, this study demonstrated that CHA insertion tended to be difficult in the downward type on celiac angiography. With regard to CHA insertion success, the predictive power of preprocedural CT was inadequate compared with that of celiac angiography. However, CT could detect MALS, a risk factor for difficult CHA insertion using a guidewire.

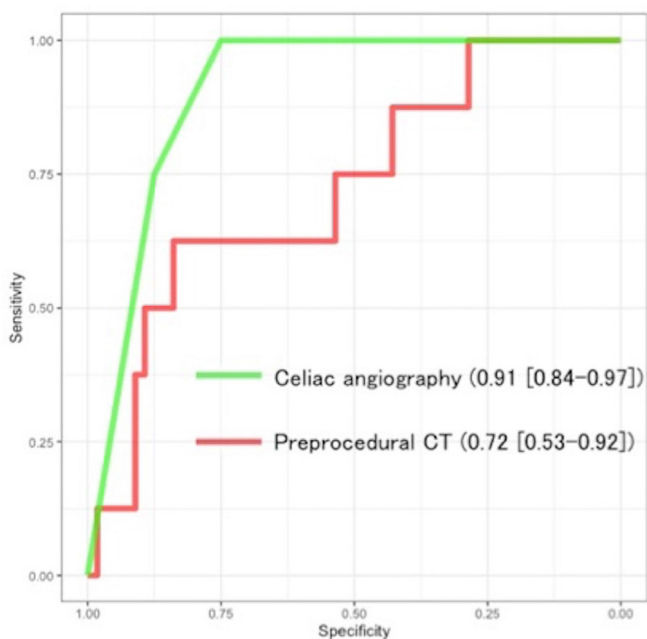


**Figure 5.** Receiver operating characteristic curve of common hepatic artery insertion. The area under the curve of celiac angiography morphology (green line) surpassed that of the preprocedural computed tomography angle (red line) (0.91 vs. 0.72,  $P = 0.040$ ). CT, computed tomography.

## Conflict of interest disclosure

The authors declared no conflicts of interest.

## References

1. Shibuya K, Tahara H, Takeuchi S, Koyama Y, Tsushima Y. New method of parent catheter advancement in the balloon anchor technique during balloon-occluded transarterial chemoembolization for hepatic tumors. *Case Rep Radiol.* 2016;2016:1957129. [CrossRef]
2. Moslemi I, Derbel H, Chiaradia M, et al. Parallel guidewire for catheter stabilization in interventional radiology: the anchoring wire technique. *J Belg Soc Radiol.* 2020;104(1):2. [CrossRef]
3. Onozawa S, Murata S, Mine T, Sugihara F, Yasui D, Kumita SI. Amplatzer vascular plug anchoring technique to stabilize the delivery system for microcoil embolization. *Cardiovasc Intervent Radiol.* 2016;39(5):756-760. [CrossRef]
4. Koroki K, Ogasawara S, Ooka Y, et al. Analyses of intermediate-stage hepatocellular carcinoma patients receiving transarterial chemoembolization prior to designing clinical trials. *Liver Cancer.* 2020;9(5):596-612. [CrossRef]
5. Llovet JM, Fuster J, Bruix J; Barcelona-Clinic Liver Cancer Group. The Barcelona approach: diagnosis, staging, and treatment of hepatocellular carcinoma. *Liver Transpl.* 2004;10(Suppl 2):115-120. [CrossRef]
6. Irie T, Kuramochi M, Takahashi N. Dense accumulation of lipiodol emulsion in hepatocellular carcinoma nodule during selective balloon-occluded transarterial chemoembolization: measurement of balloon-occluded arterial stump pressure. *Cardiovasc Intervent Radiol.* 2013;36(3):706-713. [CrossRef]
7. Hatanaka T, Arai H, Kakizaki S. Balloon-occluded transcatheter arterial chemoembolization for hepatocellular carcinoma. *World J Hepatol.* 2018;10(7):485-495. [CrossRef]
8. Tokue H, Tokue A, Tsushima Y. Multidetector-row computed tomography for evaluating the branching angle of the celiac artery: a descriptive study. *BMC Med Imaging.* 2012;12:36. [CrossRef]
9. Suh GY, Choi G, Herfkens RJ, Dalman RL, Cheng CP. Three-dimensional modeling analysis of visceral arteries and kidneys during respiration. *Ann Vasc Surg.* 2016;34:250260. [CrossRef]
10. Sharashidze V, Nogueira RG, Al-Bayati AR, Grossberg JA, Haussen DC. Balloon anchoring technique for thrombectomy in hostile craniocervical arterial anatomy. *J Neurointerv Surg.* 2020;12(8):763-767. [CrossRef]
11. Kawaguchi S, Ohtsu T, Itai R, Terada S, Endo S, Shirane N. Large balloon anchor technique for endoscopic retrograde cholangiopancreatography required for esophagogastroduodenal deformities. *Intern Med.* 2021;60(14):2175-2180. [CrossRef]
12. Saiga A, Yamamoto M, Kondo H, et al. Bowstring phenomenon in renal artery aneurysm exclusion using a Viabahn stent graft. *Vasc Endovascular Surg.* 2021;55(4):402-404. [CrossRef]
13. Miyayama S, Matsui O, Yamashiro M, et al. Ultrasensitive transcatheter arterial chemoembolization with a 2-f tip microcatheter for small hepatocellular carcinomas: relationship between local tumor recurrence and visualization of the portal vein with iodized oil. *J Vasc Interv Radiol.* 2007;18(3):365-376. [CrossRef]

---

**Video 1 link:** [https://youtube.com/shorts/KIHqx5ou\\_ag](https://youtube.com/shorts/KIHqx5ou_ag)

**Video 1.** The balloon anchor technique was used in a 70-year-old woman with median arcuate ligament syndrome. A 2.7-Fr microballoon catheter (130 cm) (Attendant Delta; Terumo) was inflated as an anchor in the left hepatic artery. Subsequently, a 4-Fr shepherd's hook diagnostic catheter was advanced into the left hepatic artery along the fixed microballoon catheter while the balloon catheter was pulled in the negative direction. FR, French.



# Percutaneous cryoablation of follicular thyroid carcinoma metastasis to the pancreas

Saim Yılmaz

Hatice Ariöz Habibi

## ABSTRACT

The following is a technical report of the successful cryoablation of pancreatic metastasis originating from follicular thyroid carcinoma. The patient was a 72-year-old female who underwent total thyroidectomy and radioiodine ablation for follicular carcinoma. One year after surgery, a positron emission tomography-computed tomography (PET-CT) examination, performed to demonstrate the source of the increased thyroglobulin, showed a fluorodeoxyglucose (FDG) avid mass located in the body of the pancreas. A percutaneous tru-cut biopsy was performed that revealed follicular thyroid carcinoma metastasis to the pancreas. Because of the patient's comorbidities, the patient underwent percutaneous cryoablation and made a successful recovery over the following 13 months. At the most recent follow-up, the thyroglobulin level was undetectable, and a PET-CT scan showed no FDG avid mass in the pancreas. To our knowledge, follicular carcinoma metastasis of the pancreas is extremely rare, and this is the first report of successful cryoablation of a metastatic tumor in the pancreas.

## KEYWORDS

Ablation, cryoablation, metastasis, pancreas, thyroid

Metastases of differentiated thyroid cancers (papillary or follicular) to the pancreas are exceedingly rare. To date, only nine cases have been reported.<sup>1</sup> The majority of these cancers are papillary carcinomas, and follicular carcinoma metastasis to the pancreas has been reported in only two patients.<sup>1,2</sup> The surgical approach varies according to lesion location; however, a pancreaticoduodenectomy is the traditional treatment approach for differentiated thyroid cancers.<sup>3</sup> Some patients may be unfit for surgery due to comorbid conditions or may prefer to forego an operation, considering the relatively indolent course of differentiated thyroid cancers. Herein, we present a case of isolated follicular carcinoma metastasis to the pancreas that was successfully treated with percutaneous cryoablation. To our knowledge, percutaneous ablation of a metastatic pancreatic tumor has not been reported thus far in the literature.

## Technique

A 72-year-old female patient was referred to us to evaluate options for nonsurgical treatment of a pancreatic mass. The patient had undergone a total thyroidectomy and radioiodine ablation for a follicular carcinoma two years earlier. During initial follow-ups, her thyroglobulin levels were normal, but over the last 11 months, a gradual increase in thyroglobulin had been observed, which reached 498 ng/mL at the latest control. A whole-body positron emission tomography-computed tomography (PET-CT) scan was performed to determine the source of the increased thyroglobulin. The scan revealed a 32 x 26 x 28 mm fluorodeoxyglucose (FDG) avid mass ( $SUV_{max}$ : 30) located in the pancreatic body and abutting the inferior surface of the liver (Figure 1). A percutaneous, ultrasound-guided tru-cut biopsy of the mass revealed follicular carcinoma metastasis to the pancreas. A pancreaticoduodenectomy was recommended by the referring surgeon; however, because of the patient's advanced age and comorbidities,

From the Department of Radiology (S.Y., H.A.H. ✉ arioz.hatice@gmail.com), Private Varisyon Radiology Center, Antalya, Turkey.

Received 18 August 2021; revision requested 19 September 2021; last revision received 4 October 2021; accepted 13 November 2021.



Epub: 21.12.2022

Publication date: 31.01.2023

DOI: 10.5152/dir.2022.21708



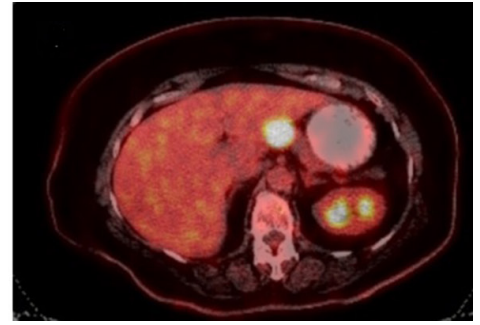
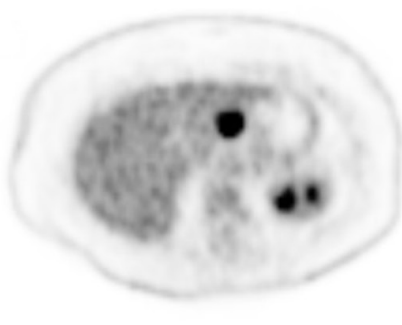
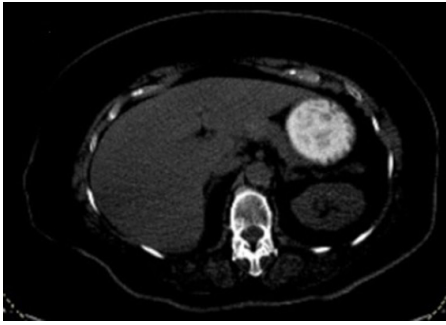


**Figure 1.** PET-CT scan; CT shows a mild hyperdense area in the pancreatic body barely distinguishable from the intact pancreas; a PET-CT image and fusion image show a 32 x 26 x 28 mm FDG avid mass ( $SUV_{max}$ : 30) localized in the pancreatic body and abutting the inferior surface of the liver. PET-CT, positron emission tomography-computed tomography; FDG, fluorodeoxyglucose.

ties, which included diabetes and congestive heart failure, an operation was considered high risk, and the patient was reluctant to undergo the procedure. Percutaneous ablation was considered feasible because the lesion was readily visible on ultrasound (US) and CT, located in a region of the pancreatic corpus that provided relatively easy access, and of a size that was within ablation limits. Based on the favorable results our team had had with cryoablation, we opted for cryoablation over other methods of thermal and non-thermal ablation.

The patient was informed about the possible risks and benefits of the cryoablation procedure, and dedicated informed consent was obtained. All the procedures performed on the patient were in accordance with the ethical standards and principles of the National Research Committee and the Helsinki Declaration of 1964. Percutaneous cryoablation was performed under local anesthesia and conscious sedation. A Siemens Acuson NX3 US device was placed in the CT room. The US examination was performed with a CH5-2 Convex US probe.

After a suitable access route was found on the US, the skin was numbed with a 1% lidocaine solution. After the skin punctured, 40 mL of 0.25% lidocaine solution was injected between the skin and the pancreatic mass for local anesthesia and also provide safe access

to the mass. Next, a 14-gauge cryoablation probe (IceFORCE, Boston Scientific) was inserted through the skin and advanced slowly into the pancreatic mass. Because the size of the lesion was relatively large compared to the expected lethal ablation area of the cryoprobe, we performed two overlapping ablations by placing a single probe eccentrically (first, slightly caudally, then cranially) in the mass (Figure 2). Cryoablation was performed by using the 10 min freeze, 10 min thaw, and 10 min freeze protocol. After the procedure, the patient was observed overnight and discharged without incident.

Two months after the procedure, the patient developed abdominal discomfort and pain. Although thyroglobulin levels were normal, a PET-CT scan was requested by her surgeon to rule out any residual or recurrent tumor. A non-suspicious FDG avid lesion was observed on the scan; however, there was a 9 x 8 x 9 cm cystic lesion in the mid abdomen consistent with a pancreatic pseudocyst (Figure 3). An ultrasound-guided aspiration was performed, but the cyst recurred one month later at the same dimensions. An 8F

multipurpose drainage catheter was placed into the cyst under US guidance and left on free drainage for three weeks, after which it was removed. The cyst did not subsequently recur. A follow-up PET-CT scan performed 13 months after the cryoablation showed almost complete disappearance of the pancreatic mass with no suspicious FDG uptake (Figure 4). Additionally, thyroglobulin levels were in the normal range, and the patient was asymptomatic.

## Discussion

Cryoablation is a well-established treatment option for kidney and prostate cancers.<sup>4</sup> Recently, it has also been used successfully in lung, breast, and pancreatic tumors.<sup>4,5</sup>

The mechanism of cryoablation involves tissue destruction by cycles of freezing (at  $-40$  to  $-160$  °C) and thawing. Compared to other thermal ablation techniques, such as radiofrequency (RF) and microwave (MW) ablation, cryoablation has several advantages. Firstly, since freezing causes much less pain than heating, cryoablation may be performed with local anesthesia and mild sedation, which may be of significant use in old or unfit patients. Secondly, since the ice ball formed is readily visible with US and CT, the operator can see the exact boundaries of the ablation zone and can thus easily avoid or protect critical surrounding structures, such as the bowels or stomach. And thirdly, since cryoablation is a less aggressive ablation method than RF and MW ablation, it better preserves collagen tissue, which may be significant for sensitive organs, such as the pancreas.<sup>4,6</sup>

Because of these considerations, our team favored cryoablation over other methods of ablation for our patient. Although irreversible electroporation, with its non-thermal aspect, may be another reasonable option, it is more expensive and requires general



**Figure 2.** CT-guided cryoablation was performed by inserting a 14-gauge cryoablation probe into the pancreatic mass. The ice ball was monitored clearly on an axial plane. CT, computed tomography.

### Main points

- This is the first report showing the successful treatment by percutaneous cryoablation of a follicular thyroid carcinoma metastasis to the pancreas.
- Surgery is required in the case of metastasis to the pancreas.
- Cryoablation is a safe, effective, and less invasive alternative to surgery and thus preferable for patients with certain comorbidities and other special considerations.

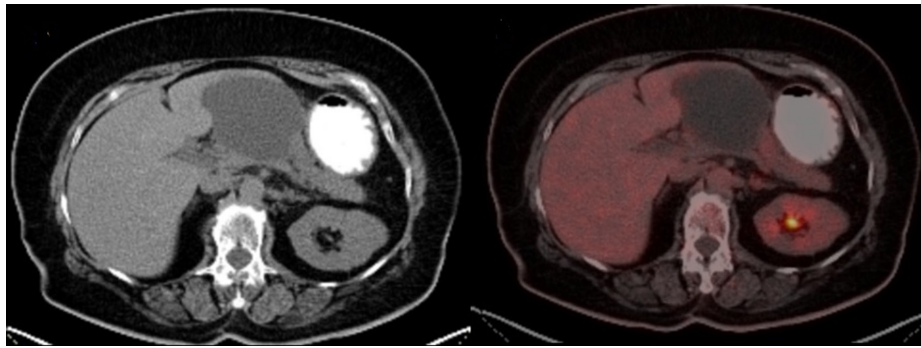


**Figure 3.** PET-CT; no suspicious FDG avid lesion observed; 9 x 8 cm cystic lesion consistent with a pancreatic pseudocyst observed in the mid abdomen. PET-CT, positron emission tomography-computed tomography; FDG, fluorodeoxyglucose.

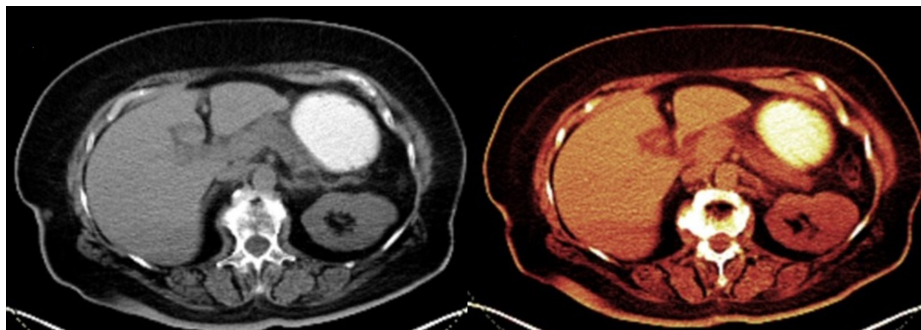


**Figure 4.** Thirteen months post-cryoablation, a follow-up PET-CT scan showed almost complete disappearance of the pancreatic mass with no suspicious FDG uptake. PET-CT, positron emission tomography-computed tomography; FDG, fluorodeoxyglucose.

anesthesia, and concerns remain around the safety and efficacy of its use in pancreatic tumors.<sup>7,8</sup>

Another advantage of cryoablation is its ability to ablate larger tumors by applying the use of multiple cryoprobes.<sup>6</sup> In the case of a 32 x 26 x 28 mm malignant tumor, such as the one in this report, the usual approach would entail using two or three cryoprobes simultaneously to produce a large ice ball and achieve complete ablation. However, the use of multiple probes simultaneously can produce more intensive ablation, which could theoretically increase the risk of com-

plications, including fistulas and pseudocysts.<sup>9</sup> For this reason, we elected to treat the lesion with two overlapping ablations using a single cryoprobe. Despite this approach, the patient developed a pseudocyst, but this was treated successfully by simple catheter drainage.

In conclusion, the present case report may represent an exemplar of percutaneous ablation of pancreatic metastasis. If supported by further reports, percutaneous ablation may become an attractive alternative method in selected patients with metastatic tumors to the pancreas.

## Conflict of interest disclosure







The authors declared no conflicts of interest.

## References

1. Tunio MA, Alasiri M, Riaz K, Alshakweer W. Pancreas as delayed site of metastasis from papillary thyroid carcinoma. *Case Rep Gastrointest Med.* 2013;2013:386263. [\[CrossRef\]](#)
2. Farina E, Monari F, Tallini G, et al. Unusual Thyroid Carcinoma Metastases: a Case Series and Literature Review. *Endocr Pathol.* 2016;27(1):55-64. [\[CrossRef\]](#)
3. Crippa S, Angelini C, Mussi C, et al. Surgical treatment of metastatic tumors to the pancreas: a single center experience and review of the literature *World J Surg.* 2006;30(8):1536-1542. [\[CrossRef\]](#)
4. Yilmaz S, Özdoğan M, Cevener M, et al. Use of cryoablation beyond the prostate. *Insights Imaging.* 2016;7(2):223-232. [\[CrossRef\]](#)
5. Niu L, He L, Zhou L, et al. Percutaneous ultrasonography and computed tomography guided pancreatic cryoablation: feasibility and safety assessment. *Cryobiology.* 2012;65(3):301-307. [\[CrossRef\]](#)
6. Luo XM, Niu LZ, Chen JB, Xu KC. Advances in cryoablation for pancreatic cancer. *World J Gastroenterol.* 2016;14(2):790-800. [\[CrossRef\]](#)
7. Lafranceschina S, Brunetti O, Delvecchio A, et al. Systematic Review of Irreversible Electroporation Role in Management of Locally Advanced Pancreatic Cancer. *Cancers (Basel).* 2019;11(11):1718. [\[CrossRef\]](#)
8. D'Onofrio M, Ciaravino V, De Robertis R, et al. Percutaneous ablation of pancreatic cancer. *World J Gastroenterol.* 2016;22(44):9661-9673. [\[CrossRef\]](#)
9. Erinjeri JP, Clark TW. Cryoablation: mechanism of action and devices. *J Vasc Interv Radiol.* 2010;21(8 Suppl):187-191. [\[CrossRef\]](#)



# Selective arterial embolization of renal angiomyolipoma: comparing ethanol–lipiodol emulsion and polyvinyl alcohol particles as embolic agents

Long Jin   
Ho Jong Chun   
Jung Suk Oh   
Byung Gil Choi   
Hae Gyu Lee   
Il Jung Kim 

## PURPOSE

To examine the effectiveness and safety of two embolic agents, an ethanol–lipiodol emulsion and polyvinyl alcohol (PVA) particles, for selective arterial embolization (SAE) of renal angiomyolipoma (AML).

## METHODS

Retrospectively, we reviewed the medical records and imaging data of renal AML patients who received SAE in our hospitals between July 2007 and January 2018. Among those eligible for analysis were patients with complete medical information, preoperative and postoperative contrast-enhanced computed tomography scans, and follow-up data. An ethanol–lipiodol emulsion was used to embolize 15 AMLs, and PVA particles were used to embolize 16 AMLs. We compared the tumor responses and adverse events between the two embolization-agent groups.

## RESULTS

After embolization, no significant differences were observed in the shrinkage rates:  $34.2\% \pm 3.4\%$  for the ethanol–lipiodol emulsion group and  $26.3\% \pm 3.0\%$  for the PVA particles group ( $P = 0.090$ ). Minor post-embolization complications were also similar between the groups, and there were no severe adverse events. The length of hospital stay after SAE was  $2.5 \pm 0.5$  days for the ethanol–lipiodol emulsion group and  $1.9 \pm 0.5$  days for the PVA particles group and was not significantly different ( $P = 0.425$ ).

## CONCLUSION

The results showed that SAE with ethanol–lipiodol emulsion or PVA particles was safe and efficient in decreasing tumor size and controlling renal AML hemorrhage.

## KEYWORDS

Angiomyolipoma, embolization, ethanol, kidney, polyvinyl alcohol

From the Department of Radiology (L.J., H.J.C.)  
✉ hojongchun@gmail.com, J.S.O., B.G.C., H.G.L.), Seoul St. Mary's Hospital, College of Medicine, The Catholic University of Korea; Department of Medicine Radiology (L.J.), Graduate School of Medical Science, The Catholic University of Korea, Seoul, Republic of Korea; Department of Radiology (I.J.K.), Bucheon St. Mary's Hospital, College of Medicine, The Catholic University of Korea, Bucheon, Gyeonggi-do, Republic of Korea.

Received 30 June 2021; Revision Requested 7 September 2021; Last Revision Received 5 October 2021; Accepted 18 November 2021.



Epub: 07.12.2022

Publication date: 31.01.2023

DOI: 10.5152/dir.2022.21625

**R**enal angiomyolipoma (AML) is a benign renal neoplasm consisting of abnormal vasculature, smooth muscles, and adipose tissue that accounts for 2%–6% of all kidney tumors.<sup>1</sup> Pathologically, AML can be more accurately characterized as a perivascular epithelioid cell neoplasm.<sup>2</sup> Most AMLs occur sporadically, but some are related to a tuberous sclerosis complex.<sup>3</sup> The overall incidence of sporadic AMLs is 0.44% (0.60% in females and 0.28% in males).<sup>4</sup> The abnormal blood vessels in AMLs are fragile and vulnerable to rupture because fibrous tissue replaces smooth muscles, and they lack an internal elastic lamina.<sup>5</sup>

Selective arterial embolization (SAE) has proven to be a potent therapy for reducing tumor size and preventing AML bleeding.<sup>6</sup> Due to its minimal invasiveness and lower risk of serious complications compared to surgery, it has recently been increasingly applied as pre-

ventive therapy for AML.<sup>7</sup> Embolization of AMLs has been conducted with various materials, such as polyvinyl alcohol (PVA) particles, microcoils, gelatin sponge, ethanol, and ethiodized oil (lipiodol). These are widely used to attain total embolization of the distal AML vascular bed. Ethanol is a liquid embolic agent that achieves permanent occlusion of the distal vascular bed and tumor tissue necrosis. The most dangerous complication associated with ethanol application is unspecified embolization caused by ethanol reflux from tumor-feeding vessels, which can lead to devastating consequences.<sup>8,9</sup> As one of the representative particulate embolic agents, PVA particles can also provide permanent occlusion, and there is extensive expertise in their use. Few previous studies have compared the efficacy or complications of different embolic materials used for renal AML embolization. This study aims to compare the efficacies, safety, and outcomes of two types of embolic agents utilized for SAE of renal AMLs: an ethanol–lipiodol emulsion and PVA particles.

## Methods

### Patient population

We retrospectively analyzed the medical information and imaging data of renal AML patients who received SAE at our hospitals between July 2007 and January 2018. Among the patients eligible for this study were those with complete medical information, preoperative and postoperative contrast-enhanced computed tomography (CT) scans, and follow-up data. Demographic information, clinical manifestations, tumor size and location, shrinkage rate, technical success, complications, hospital day after SAE, serum white blood cell count, and creatinine changes were recorded. The indications of SAE were acute hemorrhage, flank pain, and

tumors greater than 4 cm in maximum axial diameter. Our work received ethical approval from the Institutional Review Board of the The Catholic University of Korea's Catholic Medical Center (approval number: 2021-0071-0001).

### Angiography and embolization methods

An angiography was performed on the common femoral artery with the patient under local anesthesia. Abdominal aortography was conducted to identify the renal arteries and determine the presence of alternative feeding vessels. Selective renal artery catheterization and arteriography were performed via 5Fr angiographic catheters. When the target AML's feeding vessels were identified, a coaxial microcatheter was used to perform super-selective catheterization. Based on the size and quantity of the tumor-feeding vessels, a suitable amount of embolic material was carefully injected under continuous fluoroscopic guidance. Ethanol–lipiodol (Lipiodol® Ultra Fluid, Guerbet, France) emulsion and PVA particles (Contour®, Boston Scientific, USA) were chosen as embolic agents and used at the physician's discretion to occlude the AML vessels. Additionally, microcoils (Concerto®, Medtronic, USA; Tornado®, Cook Medical, USA) were used to treat aneurysms or to embolize AMLs' proximal feeding arteries when larger than 2 mm after distal embolic occlusion to avoid the possibility of incomplete occlusion of the feeding artery or recanalization. Tumor devascularization was confirmed by post-embolization arteriography.

### Assessment methods

We examined both the medical information and associated images, along with the clinical success rate, technical success rate, and complications. Clinical success was defined as decreased target tumor size without severe complications attributable to SAE. Technical success was defined as complete tumor devascularization and lack of tumor staining in the target vessels. Tumor size was determined by measuring the maximum diameter on CT axial images. Moreover, the shrinkage rate was computed via a comparison of the maximum lesion diameter on the follow-up CT image with that on the initial CT image. Post-embolization syndrome (PES) was described as pain and fever after embolization treatment.

### Statistical analysis

Continuous variables with normal distribution are expressed as means  $\pm$  standard

deviations (SD). Nominal variables are presented as counts and percentages. Student's t-test was employed for the comparison of continuous variables, and Fisher's exact test was used for the comparison of nominal variables. All data were analyzed using GraphPad Prism 6.01 software (GraphPad Software, San Diego, CA). A two-sided *P* value of  $<0.05$  was set as the significance threshold.

## Results

The demographic information is summarized in Table 1, and follow-up information is presented in Table 2, which includes a comparison of the different embolic agents used on the two groups. This study included 28 patients: 16 females (57.1%) and 12 males (42.9%) with complete medical records in the 11-year study period. The patients underwent 28 embolization procedures for 31 AMLs. The mean patient age at diagnosis was  $49.3 \pm 3.2$  years. Six patients (21.4%) received SAE for hemorrhagic or symptomatic AMLs, whereas SAE was performed as a prophylactic therapy in 22 patients (78.6%). Regarding the location of the AMLs, 15 lesions (48.4%) were located in the right kidney and 16 (51.6%) were in the left kidney. There were multiple lesions in three patients (10.7%). Ethanol–lipiodol emulsion was used to embolize 15 AMLs, and PVA particles were used to embolize 16 AMLs. The mean follow-up duration was  $11.5 \pm 2.1$  months for the ethanol–lipiodol emulsion group and  $7.4 \pm 1.4$  months for the PVA particles group; however, the difference between them was not significant (*P* = 0.098).

The pre-embolization tumor size was  $7.7 \pm 0.7$  cm in the SAE with ethanol–lipiodol emulsion group and  $7.9 \pm 0.6$  cm in the PVA particles group (*P* = 0.809). The size decreases were comparable after SAE, as shown by the ethanol–lipiodol emulsion group's  $34.2\% \pm 3.4\%$  shrinkage rate (Figure 1) and the PVA particles group's  $26.3\% \pm 3.0\%$  shrinkage rate (Figure 2) (*P* = 0.090). With SAE, we achieved technical success in devascularizing the tumor-feeding arteries found on the angiographies of all patients. No patient in either group suffered serious complications after embolization. Furthermore, no patient experienced hemorrhagic complications from AMLs during the follow-up period. Therefore, all patients achieved clinical success. Seventeen patients (60.7%) experienced mild PES, which was resolved with conservative treatment only. Minor post-embolization complications were similar in both groups. The serum white blood cell counts of all patients before

#### Main points

- Selective arterial embolization (SAE) is a highly efficient therapy for reducing tumor size and preventing hemorrhages in renal angiomyolipoma (AML).
- Conducting SAE with the ethanol–lipiodol emulsion or polyvinyl alcohol (PVA) particles was a safe and efficient management option for reducing tumor size and controlling renal AML hemorrhages.
- The use of PVA particles as an embolic agent in SAE for renal AMLs can drastically reduce the tumor size and preserve renal function without imparting the high-risk and potentially devastating consequences associated with ethanol use.

and after SAE were  $6.9 \pm 0.5$  ( $10^9/L$ ) and  $7.6 \pm 0.5$  ( $10^9/L$ ), respectively. However, there was no significant difference ( $P = 0.172$ ). In addition, the serum creatinine levels before and after SAE were all within the normal range. The length of hospital stay after SAE was  $2.5 \pm 0.5$  days for the ethanol–lipiodol emulsion group and  $1.9 \pm 0.5$  days for the PVA parti-

cles group, respectively, with no significant difference ( $P = 0.425$ ).

## Discussion

Hemorrhaging caused by renal AMLs can be life-threatening, so it is common practice to treat patients who display symptoms or have tumors greater than 4 cm.<sup>10</sup> A previous

study found that SAE of renal AMLs greater than 4 cm may reduce the risk of hemorrhaging.<sup>11</sup> The process of SAE has become a favorable management option for renal AMLs in both prophylactic and emergency cases for decades due to the recent technological advances in microcatheters and diagnostic imaging equipment. The current study demonstrates that the size of a renal AML decreases significantly after SAE, but renal function displays no obvious change. The present finding of a  $30.1\% \pm 2.3\%$  reduction in axial dimension is in accordance with previous reports,<sup>12,13</sup> which illustrates SAE's effectiveness in shrinking renal AMLs. Moreover, the present study's major finding concurs with the interpretation of a systematic review that reported a 93.3% average technical success rate with no procedure-related deaths and included 31 reports on 524 renal AML cases treated with SAE.<sup>6</sup> Nevertheless, these reports showed that among 263 AML patients with an average follow-up period of 39 months, there was an average 38.3% shrinkage rate after SAE, which is higher than that of the present study (mean  $\pm$  standard deviation:  $30.1\% \pm 2.3\%$ ). This discrepancy could be attributable to different radiological follow-up periods. The average follow-up duration of our study was only 9.1 months.

The ethanol–lipiodol emulsion and PVA particles in this study were successfully used as primary embolic agents for SAE. Ethanol is a liquid embolizing agent that permanently occludes arteries and capillaries at the distal level of collateral inflow and accelerates necrosis of tumor tissue. The primary risk of employing ethanol is unspecified embolization owing to reflux from tumor-feeding blood vessels, which can lead to devastating consequences.<sup>8,9</sup> Since ethanol is very destructive, SAE performed with ethanol sometimes presents serious problems in the embolization area. An ethanol injection into the proximal part of a tumor results in occlusion of the tumor's proximal blood vessels; however, viable tissue can remain in the distal tumor areas. Therefore, the decrease in tumor size may be inadequate and accompanied by an elevated risk of tumor recurrence.<sup>14</sup> Balloon-assisted SAE with ethanol for renal AML has been suggested<sup>15</sup> to avoid ethanol reflux and occlusion of both proximal arteries. However, the use of a balloon catheter may increase the aneurysmal rupture risk, which results from rising pressure during treatment and makes super-selective catheterization more difficult.<sup>16</sup>

Pulmonary complication is another risk of SAE performed using ethanol for renal AML

**Table 1.** The demographic data

Variable	All patients (n = 28)	Ethanol–lipiodol emulsion (n = 12)	Polyvinyl alcohol particle (n = 16)	Statistical significance (P value)
Age (years)	49.3 $\pm$ 3.2	51.1 $\pm$ 4.5	47.9 $\pm$ 4.6	0.638
Gender				0.459
Male	12	4	8	
Female	16	8	8	
Masses				0.067
Single	25	9	16	
Multiple	3	3	0	
Location of tumor				1.000
Left	13	5	8	
Right	14	6	8	
Bilateral	1	1	0	
Aneurysm				1.000
Yes	2	1	1	
No	26	11	15	
Rupture				0.600
Yes	4	1	3	
No	24	11	13	

**Table 2.** Follow-up data and the comparison between the two groups of different embolic agents

Variable	All patients (n = 28)	Ethanol–lipiodol emulsion (n = 12)	Polyvinyl alcohol particle (n = 16)	Statistical significance (P value)
Follow-up periods (months)	9.1 $\pm$ 1.2	11.5 $\pm$ 2.1	7.4 $\pm$ 1.4	0.098
Tumor size (cm)				
Pre-embolization	7.8 $\pm$ 0.4	7.7 $\pm$ 0.7	7.9 $\pm$ 0.6	0.809
Post-embolization	5.5 $\pm$ 0.4	5.2 $\pm$ 0.6	5.8 $\pm$ 0.5	0.418
Decrease in size (cm)	2.3 $\pm$ 0.2	2.5 $\pm$ 0.2	2.1 $\pm$ 0.3	0.319
Shrinkage rate (%)	30.1 $\pm$ 2.3	34.2 $\pm$ 3.4	26.3 $\pm$ 3.0	0.090
Serum white blood cell counts ( $10^9/L$ )				
Pre-embolization	6.9 $\pm$ 0.5	7.0 $\pm$ 0.8	6.8 $\pm$ 0.6	0.822
Post-embolization	7.6 $\pm$ 0.5	7.0 $\pm$ 0.6	8.1 $\pm$ 0.8	0.310
Serum creatinine (mg/dL)				
Pre-embolization	0.7 $\pm$ 0.03	0.7 $\pm$ 0.03	0.8 $\pm$ 0.05	0.086
Post-embolization	0.8 $\pm$ 0.04	0.7 $\pm$ 0.04	0.8 $\pm$ 0.06	0.156
Post-embolization syndrome				0.253
Yes	17	9	8	
No	11	3	8	
Hospital days	2.0 $\pm$ 0.4	2.5 $\pm$ 0.5	1.9 $\pm$ 0.5	0.425

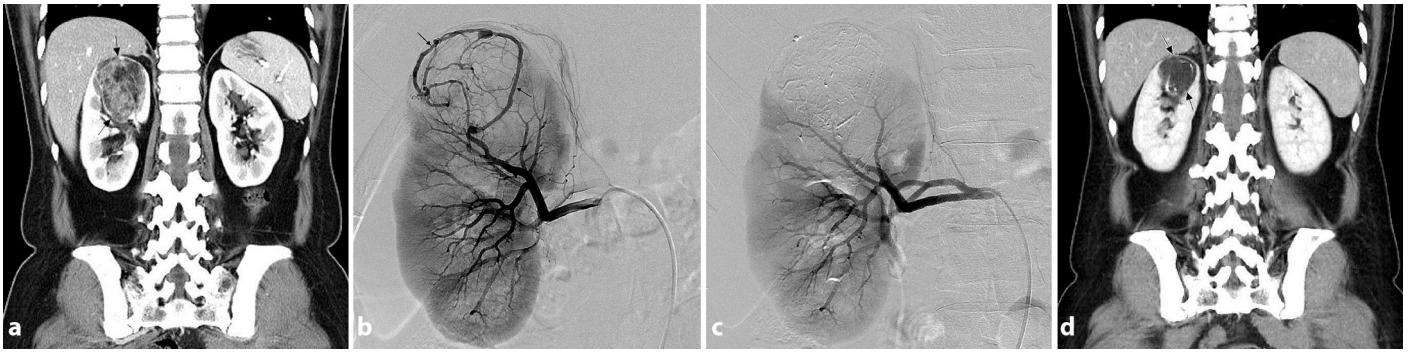


**Figure 1.** A 49-year-old woman presented with angiomyolipoma of the right kidney and underwent SAE with ethanol-lipiodol emulsion. (a) Pre-treatment CT showing a large tumor at the upper pole of the right kidney (arrows) composed of muscular, vascular, and fatty tissue. (b) Selective arteriography displaying a large hypervascular tumor with tortuous and disordered vessels (arrows). (c) Post-embolization arteriography showing complete occlusion of the vessels and no residual tumor staining. (d) A CT 13 months after embolization revealing significant shrinkage of the tumor (arrows). CT, computed tomography; SAE, selective arterial embolization.

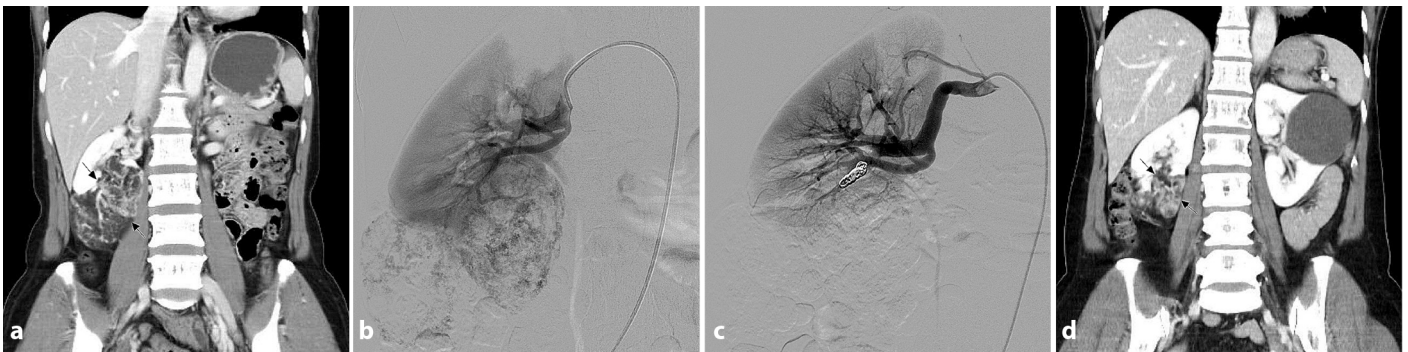


**Figure 2.** A 42-year-old woman presented with angiomyolipoma of the right kidney and underwent selective transarterial embolization with polyvinyl alcohol particles and microcoils. (a) A CT showing a large tumor with fatty content protruding from the right kidney (arrows). (b) Selective arteriography of the right renal artery displaying feeding branches and tumor staining. (c) Post-embolization arteriography showing the tumor staining's complete disappearance. (d) A CT seven months after embolization revealing a significant reduction in the size of the tumor (arrows). CT, computed tomography.

treatment. Pulmonary arterial pressure can accumulate during vascular malformation treatment when using ethanol.<sup>17</sup> Hiraki et al.<sup>18</sup> documented a patient with renal AMLs and lymphangioliomyomatosis afflicted with pulmonary edema following transarterial embolization with ethanol. This patient's pulmonary edema led to the development of dyspnea and hemoptysis. In the latest study, although a micro-balloon catheter was employed to prevent ethanol reflux from injuring normal renal parenchyma, 42% of patients experienced renal parenchyma infarctions.<sup>19</sup> Therefore, ethanol must be employed with caution to prevent pulmonary and renal complications.

Particulate agents, such as PVA particles, are the most common type of embolic materials used for the treatment of renal AMLs and have been classified as permanent embolic agents.<sup>20</sup> With a size of 355–500  $\mu\text{m}$ , PVA particles facilitate distal vascular occlusion of a tumor.<sup>21</sup> Particulate agents cannot be readily eliminated from target lesions following embolization, which leads to a prolonged delay in the recanalization of tumor-feeding

vessels. Commonly, particulate embolization is done with a combination of 355–500  $\mu\text{m}$  PVA particles, which block the target lesions' distal vascular bed. Then, coils are used to occlude the arterial inflow and halt retrograde filling of the aneurysm and reforming of abnormal tumor vessels.<sup>22</sup> The use of coils alone should be avoided because they only provide proximal blood vessel occlusion, which may cause collaterals around or at the distal level of the blockage and make embolization more difficult or impossible.<sup>23,24</sup> In the present study, nine patients underwent SAE with a combination of 150–350  $\mu\text{m}$  PVA particles, six patients underwent SAE with a combination of 355–500  $\mu\text{m}$  PVA particles, and one patient's SAE used 150–350  $\mu\text{m}$  and 560–710  $\mu\text{m}$  PVA particles. This study resulted in no obvious difference between the tumor shrinkage rates of the ethanol–lipiodol emulsion group and the PVA particles group and showed drastic reductions in tumor size post-SAE in both groups.

This study had two limitations: the retrospective design and the small sample population, which was due to AML being an un-

common benign tumor and a rare disease in our country. Studying a large sample may take a very long time. Another reason for the study's small sample size is that several patients with incomplete radiological follow-up data were excluded. Additionally, because of the low level of patient compliance during follow-up, the follow-up duration varied from 1–29 months with a mean of 9.1 months.

In summary, the study demonstrated that SAE with an ethanol–lipiodol emulsion or PVA particles was a safe and efficient management option for controlling hemorrhages and preventing renal AML progression. Using PVA particles as an embolic agent in SAE for renal AMLs can drastically reduce the tumor size and preserve renal function without imparting the high-risk and potentially devastating consequences associated with ethanol use. Prospective investigations of a substantial scale and with prolonged follow-up periods would be useful for identifying improved embolic agents for SAE of renal AMLs.

## Conflict of interest disclosure









The authors declared no conflicts of interest.

## References

1. Skolarus TA, Serrano MF, Berger DA, et al. The distribution of histological subtypes of renal tumors by decade of life using the 2004 WHO classification. *J Urol.* 2008;179(2):439-444. [\[CrossRef\]](#)
2. Zhao Y, Bui MM, Spiess PE, Dhillon J. Sclerosing PEComa of the kidney: clinicopathologic analysis of 2 cases and review of the literature. *Clin Genitourin Cancer.* 2014;12(5):229-232. [\[CrossRef\]](#)
3. Konosu-Fukaya S, Nakamura Y, Fujishima F, et al. Bilateral papillary renal cell carcinoma and angiomyolipoma in the patients with autosomal dominant polycystic kidney disease: case report of two cases and literature review. *Pol J Pathol.* 2013;64(4):303-307. [\[CrossRef\]](#)
4. Fittschen A, Wendlik I, Oeztuerk S, et al. Prevalence of sporadic renal angiomyolipoma: a retrospective analysis of 61,389 in- and out-patients. *Abdom Imaging.* 2014;39(5):1009-1013. [\[CrossRef\]](#)
5. Radhakrishnan R, Verma S. Clinically relevant imaging in tuberous sclerosis. *J Clin Imaging Sci.* 2011;1:39. [\[CrossRef\]](#)
6. Murray TE, Doyle F, Lee M. Transarterial Embolization of Angiomyolipoma: A Systematic Review. *J Urol.* 2015;194(3):635-639. [\[CrossRef\]](#)
7. Sun P, Liu J, Charles H, Hulbert J, Bissler J. Outcomes of angioembolization and nephrectomy for renal angiomyolipoma associated with tuberous sclerosis complex: a real-world US national study. *Curr Med Res Opin.* 2017;33(5):821-827. [\[CrossRef\]](#)
8. Kothary N, Soulen MC, Clark TW, et al. Renal angiomyolipoma: long-term results after arterial embolization. *J Vasc Interv Radiol.* 2005;16(1):45-50. [\[CrossRef\]](#)
9. Loffroy R, Rao P, Kwak BK, et al. Transcatheter arterial embolization in patients with kidney diseases: an overview of the technical aspects and clinical indications. *Korean J Radiol.* 2010;11(3):257-268. [\[CrossRef\]](#)
10. Luo Y, Hou G, Lu M, Chen M, Hu C, Di J. Unclamped nephron-sparing surgery with preoperative selective arterial embolization for the management of bilateral giant renal angiomyolipomas. *Clin Genitourin Cancer.* 2014;12(3):111-114. [\[CrossRef\]](#)
11. Kiefer RM, Stavropoulos SW. The Role of Interventional Radiology Techniques in the Management of Renal Angiomyolipomas. *Curr Urol Rep.* 2017;18(5):36. [\[CrossRef\]](#)
12. Wang C, Yang M, Tong X, et al. Transarterial embolization for renal angiomyolipomas: A single centre experience in 79 patients. *J Int Med Res.* 2017;45:706-713. [\[CrossRef\]](#)
13. Bardin F, Chevallerier O, Bertaut A, et al. Selective arterial embolization of symptomatic and asymptomatic renal angiomyolipomas: a retrospective study of safety, outcomes and tumor size reduction. *Quant Imaging Med Surg.* 2017;7(1):8-23. [\[CrossRef\]](#)
14. Bishay VL, Crino PB, Wein AJ, et al. Embolization of giant renal angiomyolipomas: technique and results. *J Vasc Interv Radiol.* 2010;21(1):67-72. [\[CrossRef\]](#)
15. Takebayashi S, Horikawa A, Arai M, Iso S, Noguchi K. Transarterial ethanol ablation for sporadic and non-hemorrhaging angiomyolipoma in the kidney. *Eur J Radiol.* 2009;72(1):139-145. [\[CrossRef\]](#)
16. Lee W, Kim TS, Chung JW, Han JK, Kim SH, Park JH. Renal angiomyolipoma: embolotherapy with a mixture of alcohol and iodized oil. *J Vasc Interv Radiol.* 1998;9(2):255-261. [\[CrossRef\]](#)
17. Mitchell SE, Shah AM, Schwengel D. Pulmonary artery pressure changes during ethanol embolization procedures to treat vascular malformations: can cardiovascular collapse be predicted? *J Vasc Interv Radiol.* 2006;17(2 Pt 1):253-262. [\[CrossRef\]](#)
18. Hiraki T, Mimura H, Gobara H, et al. Pulmonary Edema as a Complication of Transcatheter Embolization of Renal Angiomyolipoma in a Patient with Pulmonary Lymphangiioleiomyomatosis Due to Tuberous Sclerosis Complex. *J Vasc Interv Radiol.* 2009;20(6):819-823. [\[CrossRef\]](#)
19. Sawada Y, Shimohira M, Hashizume T, et al. Transcatheter Arterial Embolization for Renal Angiomyolipoma Using a Micro-balloon Catheter and a Mixture of Ethanol and Lipiodol. *Cardiovasc Intervent Radiol.* 2017;40(12):1933-1939. [\[CrossRef\]](#)
20. Leyon JJ, Littlehales T, Rangarajan B, Hoey ET, Ganeshan A. Endovascular embolization: review of currently available embolization agents. *Curr Probl Diagn Radiol.* 2014;43(1):35-53. [\[CrossRef\]](#)
21. Gupta P, Gamanagatti S. Preoperative transarterial Embolisation in bone tumors. *World J Radiol.* 2012;4(5):186-192. [\[CrossRef\]](#)
22. Patatas K, Robinson GJ, Ettles DF, Lakshminarayan R. Patterns of renal angiomyolipoma regression post embolisation on medium- to long-term follow-up. *Br J Radiol.* 2013;86(1024):20120633. [\[CrossRef\]](#)
23. Ramon J, Rimon U, Garniek A, et al. Renal angiomyolipoma: long-term results following selective arterial embolization. *Eur Urol.* 2009;55(5):1155-1161. [\[CrossRef\]](#)
24. Urciuoli P, D'Orazi V, Livadoti G, et al. Treatment of renal angiomyolipoma: surgery versus angioembolization. *G Chir.* 2013;34(11-12):326-331. [\[CrossRef\]](#)



# Advanced virtual monoenergetic imaging algorithm for lower extremity computed tomography angiography: effects on image quality, artifacts, and peripheral arterial disease evaluation

Jung Han Hwang   
 Jin Mo Kang   
 Suyoung Park   
 So Hyun Park   
 Jeong Ho Kim   
 Ki Hyun Lee   
 Ji Hoon Shin   
 Seong Yong Pak 

Jung Han Hwang and Jin Mo Kang contributed equally to this study and share the first authorship.

## PURPOSE

To investigate the image quality of lower extremity computed tomography angiography (LE-CTA) using a reconstruction algorithm for monoenergetic images (MEIs) to evaluate peripheral arterial disease (PAD) at different kiloelectron volt (keV) levels.

## METHODS

A total of 146 consecutive patients who underwent LE-CTA on a dual-energy scanner to obtain MEIs at 40, 50, 60, 70, and 80 keV were included. The overall image quality, segmental image quality of the arteries and PAD segments, venous contamination, and metal artifacts from prostheses, which may compromise quality, were analyzed.

## RESULTS

The mean overall image quality of each MEI was  $2.9 \pm 0.7$ ,  $3.6 \pm 0.6$ ,  $3.9 \pm 0.3$ ,  $4.0 \pm 0.2$ , and  $4.0 \pm 0.2$  from 40 to 80 keV, respectively. The segmental image quality gradually increased from 40 to 70–80 keV until reaching its highest value. Among 295 PAD segments in 68 patients, 40 (13.6%) were scored at 1–2 at 40 keV and 13 (4.4%) were scored at 2 at 50 keV, indicating unsatisfactory image quality due to the indistinguishability between high-contrast areas and arterial calcifications. The segments exhibiting metal artifacts and venous contamination were reduced at 70–80 keV ( $2.6 \pm 1.2$ ,  $2.7 \pm 0.5$ ) compared with at 40 keV ( $2.4 \pm 1.1$ ,  $2.5 \pm 0.7$ ).

## CONCLUSION

The LE-CTA method using a reconstruction algorithm for MEIs at 70–80 keV can enhance the image quality for PAD evaluation and improve mitigate venous contamination and metal artifacts.

## KEYWORDS

Artifact, atherosclerosis, computed tomography angiography, peripheral arterial disease, radiation dosage

From the Department of Radiology (J.H.H., S.P. ✉ spgir@naver.com, S.H.P., J.H.K.), Gachon University College of Medicine, Gil Medical Center, Incheon, South Korea; Department of Surgery (J.M.K.), Gachon University College of Medicine, Incheon, South Korea; Department of Radiology and Research Institute of Radiology (J.H.S.), University of Ulsan College of Medicine, Asan Medical Center, Seoul, South Korea; Department of Biomedical Engineering (S.Y.P.), University of Ulsan College of Medicine, Asan Medical Institute of Convergence Science and Technology, Asan Medical Center, Seoul, South Korea.

Received 21 May 2021; revision requested 21 June 2021; last revision received 1 November 2021; accepted 1 December 2021.



Epub: 21.12.2022

Publication date: 31.01.2023

DOI: 10.5152/dir.2022.21551

Peripheral arterial disease (PAD) affects older patients with atherosclerosis and is a common reason for recurrent hospital visits.<sup>1</sup> Lower extremity computed tomography angiography (LE-CTA) can be used to detect PAD, assess anatomic variations, determine suspected limb ischemia, carry out treatment planning, and evaluate stent placement.<sup>2</sup> Likewise, current guidelines recommend LE-CTA examinations to evaluate PAD, the severity of atherosclerosis, and treatment planning.<sup>1,3,4</sup>

Dual-energy CT can enhance both the tissue contrast in monoenergetic images (MEIs) by using reconstruction algorithms<sup>5</sup> and the visualization of vascular anatomy by using bone removal algorithms.<sup>6,7</sup> An MEI enables optimization of the kiloelectron volt (keV) level to evaluate the objective and subjective image quality of tumors, large vessels, metal artifacts, and ancillary features.<sup>8–15</sup> While low keV (40–50 keV) imaging provides a higher contrast than high keV (70–90 keV) imaging, the former presents more severe noise than the latter. Recently,



a noise-reduced virtual MEI reconstruction algorithm (synonym MEI plus) was developed to mitigate image noise at low energy levels.<sup>16</sup> In fact, this algorithm can reduce the image noise at a low keV and improve the image contrast at a high keV, even achieving the highest image contrast, effectively removing image noise at a low keV and enhancing the signal-to-noise ratio and contrast-to-noise ratio in vascular imaging.<sup>17,18</sup> However, to the best of our knowledge, MEI plus has not been used to optimize the keV level in LE-CTA to evaluate PAD, venous contamination, and metal artifacts. In this study, the objective and subjective image quality of MEIs obtained from LE-CTA at different keV levels after applying MEI plus are compared.

## Methods

### Patients

This study was approved by the Basic Science Research Program through the National Research Foundation of Korea and was funded by the Ministry of Science ICT and Future Planning (study number: GBIRB2020-435). Written informed consent was waived due to the retrospective nature of this study. Patients who underwent LE-CTA on a dual-energy scanner for either the evaluation or follow-up of PAD between July 2018 and December 2018 were included. The Picture Archiving and Communication Systems database was searched to collect the data of patients who met the criteria, and 157 consecutive patients were identified. The exclusion criteria included a change in examination protocol and the loss of dose reports. Following screening, 146 patients (91 men and 55 women; mean age =  $64.7 \pm 13.9$  years; age range = 26–92 years) were enrolled in this study (Figure 1). The characteristics of the patients and radiation dose parameters are summarized in Table 1.

### Main points

- Low kiloelectron volt (keV) levels provide a higher contrast but more severe noise than high keV levels.
- Both the objective and the subjective image quality of monoenergetic images (MEIs) obtained from lower extremity computed tomography angiography at different keV levels after applying a noise-reduced virtual MEI reconstruction algorithm were compared.
- The MEIs at 70 and 80 keV levels can both enhance the image quality and mitigate image noise.

### Computed tomography examination protocol

The patients underwent LE-CTA from the T12 vertebra to the lower end of the feet following intravenous injection of 30 mL at 4 mL/s followed by 80 mL at 3 mL/s of iohexol 350 mgI/mL (Bonorex 350; Central Medical Service, Seoul, Republic of Korea). Bolus tracking was used for the imaging. A region of interest (ROI) was positioned at the aortic bifurcation with a trigger threshold of 150 Hounsfield units (HU) before CT scans were acquired using a 128-slice CT scanner (Somatom Definition Flash; Siemens Healthcare, Erlangen, Germany) in the dual-source mode at a tube voltage of 80 kVp (tube detector A; reference, 250 mAs) and 140 kVp with a tin filter (tube detector B; reference, 106 mAs)

using tube current modulation of the dose (CARE Dose 4D; Siemens Healthcare). The images were reconstructed by applying a blending factor of 0.4 ( $M_{0.4}$ ; 40% of 80 kVp and 60% of 140 kVp with a tin filter spectrum). The MEIs with a (axial) slice thickness of 5 mm acquired at 40, 50, 60, 70, and 80 keV were reconstructed on a multimodality workstation (Syngo.via VB20; Siemens Healthcare).

### Qualitative analysis

The MEIs were independently reviewed with blinded patient information in consensus by two interventional radiologists (S.P. and J.H.H.), who had nine and 12 years of experience, respectively, at the time of the study. Any discrepancies were resolved by

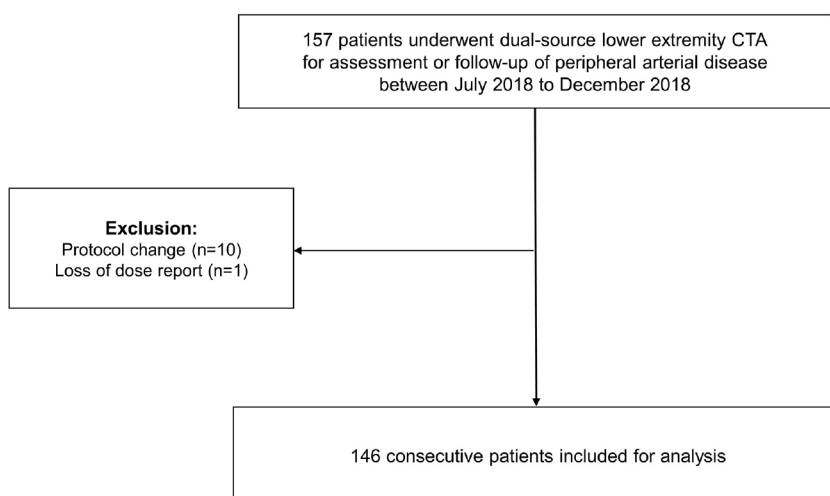


Figure 1. Study flowchart.

Table 1. Patient characteristics and radiation dose parameters

Parameter	All patients (n = 146)
Demographics	
Male <sup>a</sup>	91 (62.3)
Female <sup>a</sup>	55 (37.7)
Age (years) <sup>b</sup>	64.7 ± 13.9 (26–92)
Height (cm) <sup>b</sup>	162.6 ± 9.9 (140–183)
Weight (kg) <sup>b</sup>	61.5 ± 12.2 (36.7–96)
BMI (kg/m <sup>2</sup> ) <sup>b</sup>	23.2 ± 4.8 (13.6–40.7)
Medical history of patients	
Diabetes <sup>a</sup>	53 (36.3)
Hypertension <sup>a</sup>	66 (45.2)
Cardiovascular disease <sup>a</sup>	31 (21.2)
Chronic kidney disease <sup>a</sup>	20 (13.7)
CT angiography parameters	
CTDI <sub>vol</sub> (mGy) <sup>b</sup>	7.6 ± 0.5 (6.9–9.7)
Dose-length product (mGy-cm) <sup>b</sup>	970.3 ± 112.9 (711–1357)

<sup>a</sup>Data are number of patients (percentages); <sup>b</sup>data are means ± standard deviations (ranges). BMI, body mass index; CT, computed tomography; CTDI, CT volume dose index.

consensus. The overall image quality of the CT scans and the segmental image quality of infrarenal abdominal aorta, common iliac arteries (CIAs), external iliac arteries (EIAs), common femoral arteries (CFAs), superficial femoral arteries (SFAs), popliteal arteries (PAs), anterior tibial arteries (ATAs), posterior tibial arteries (PTAs), peroneal arteries, and tibioperoneal trunk (TPT) were scored using a four-point scale,<sup>5,11</sup> where scores of 0 and 1 were considered as unacceptable for vessel assessment. Venous contamination was scored using a three-point scale. The presence of stenosis and/or occlusion of LE arteries was evaluated, and the degree of stenosis was graded in terms of mild, moderate, and severe.<sup>12</sup> Then, the diagnostic value in terms of prosthesis artifacts was scored using a four-point scale (Table 2).

### Quantitative analysis

For comparative analysis, one blinded radiologist established a circular ROI with a size of 1–3 cm<sup>2</sup> at specific levels of axial images from the five image sets at different keV levels. The levels were the infrarenal abdominal aorta and the midportion of the bilateral CIAs. The mean attenuation and standard deviation (i.e. noise) of HU in the ROI were calculated.

### Radiation dose

The CT volume dose index [CTDI<sub>vol</sub> in milligrays (mGy)] and dose-length product (DLP in mGy·cm) were used to estimate the radiation dose from the dose report of the CT scan.

### Statistical analysis

The quantitative image analysis was compared among the five image sets using the analysis of variance method and adjustment with Bonferroni correction for multiple comparisons, with a *P* value of <0.01 regarded as significant. Interobserver agreement regarding the overall image quality on LE-CTA was determined using kappa statistics with the following scales: 0.01–0.20, slight agreement; 0.21–0.40, fair; 0.41–0.60, moderate; 0.61–0.80, substantial; and 0.81–1.00, excellent. All statistical analyses were performed using SPSS statistical software (version 25.0; IBM, Armonk, NY, USA).

## Results

Among the 146 patients, 68 (46.6%) presented PAD in 295 image segment of arteries in the LE-CTA examinations. The arteries with PAD included 12 CIAs, two CFAs, five

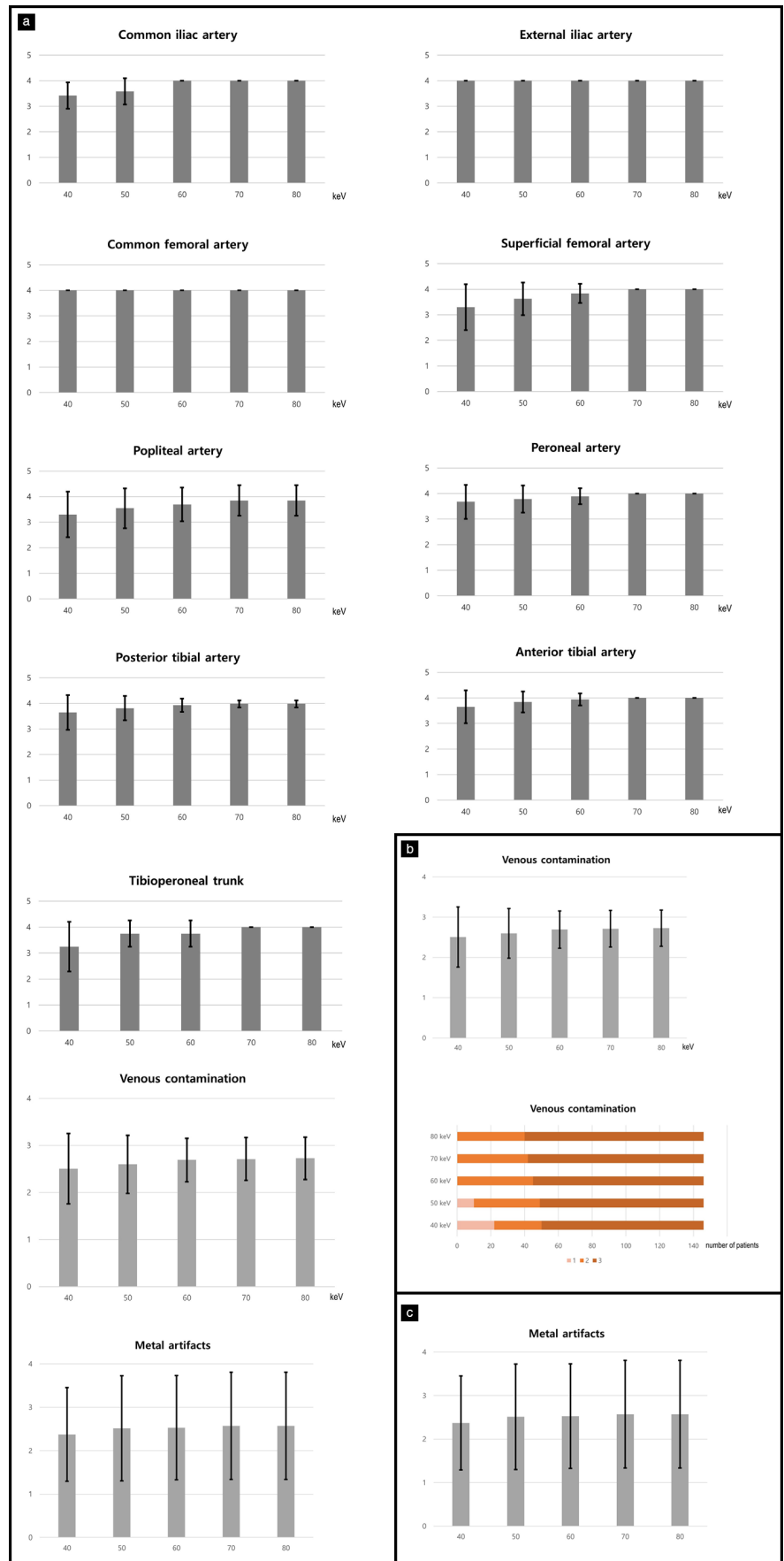


**Figure 2.** (a–c) Mean (bar graphs) and standard deviation (error bar) of the subjective image quality scores from segmental arteries, venous contamination, and metal artifacts at different keV levels. keV, kiloelectron volt.

EIAs, 61 SFAs, 68 ATAs, 54 PTAs, 37 peroneal arteries, 46 PAs, and 10 TPT branches. The LE-CTA examinations of 14 patients revealed 15 segments with stent placement (eight patient stents and seven in-stent restenosis). In addition, 33 patients presented 77 segments (three right CIAs, three left CIAs, one right EIA, one left EIA, four right CFAs, one left CFA, six right SFAs, 10 left SFAs, 16 right PAs, 17 left PAs, five right ATAs, five left ATAs, one right peroneal artery, one left peroneal artery, one right PTA, and two left PTAs) containing metal artifacts of prostheses [14 right total knee replacements (TKRs), 13 left TKRs, seven right leg internal fixations (IFs), 11 left leg IFs, two pelvic bone IFs, two posterior lumbar IFs, three right total hip replacements (THR), one left THR, and one left leg external fixation], all of which may compromise the LE-CTA image quality of the arteries.

The overall quality of the 40, 50, 60, 70, and 80 keV MEIs was  $2.9 \pm 0.7$  (range: 2–4),  $3.6 \pm 0.6$  (range: 2–4),  $3.9 \pm 0.3$  (range: 3–4),  $4.0 \pm 0.2$  (range: 3–4), and  $4.0 \pm 0.2$  (range: 3–4), respectively. All pairwise comparisons, except the 60 vs. 70 vs. 80 keV MEIs, were sig-

nificantly different ( $P < 0.001$ ). Interobserver agreement was excellent for the overall image quality ( $\kappa$ : 0.89).

The subjective segmental image quality significantly increased in the CIA, SFA, PA, peroneal artery, ATA, PTA, and TPT MEIs at 70 and 80 keV compared with lower keV levels (Figure 2). The segmental image quality gradually increased from 40 to 70–80 keV, reaching its highest value at 70 and 80 keV. Among the 295 PAD segments, 40 (13.6%) were scored at 1–2 at 40 keV (score 1, 2 segments; score 2, 38 segments) and 13 (4.4%) were scored at 2 at 50 keV, indicating unsatisfactory image quality due to the indistinguishability between high-contrast areas and arterial calcifications (Figure 3). Meanwhile, 199 (67.5%) of the 295 PAD segments were scored at 4 at 40–80 keV.

Among the 75 segments exhibiting occlusion, 68 (90.7%) were equally scored from 40 to 80 keV. The attenuation and noise of the objective segmental image quality gradually decreased from 40 to 80 keV (Table 3). All pairwise comparisons for attenuation indicated a significant difference ( $P < 0.01$ ). The pairwise comparison for noise, 70 vs. 80 ( $P$

$= 1.000$ ) keV MEI on right CIA, 60 vs. 70 ( $P = 0.565$ ), 60 vs. 80 ( $P = 0.014$ ), and 70 vs. 80 ( $P = 1.000$ ) keV MEI on the left CIA, indicated a difference without significance, while further pairwise comparisons of noise for infrarenal abdominal aorta and bilateral CIAs indicated a significant difference ( $P < 0.01$ ) (Table 4).

The score of segments exhibiting metal artifacts slightly increased from 40 ( $2.4 \pm 1.1$ ) to 70–80 keV ( $2.6 \pm 1.2$ ). Among the 77 segments exhibiting metal artifacts, 63 (81.8%) were identically scored from 40 to 80 keV (score 1: 21 segments; score 2: 12 segments; score 3: 16 segments; score 4: 14 segments). In addition, 22 segments were scored at 1 (non-diagnostic image quality) at 40–50 keV, and 21 segments were scored at 1 at 60–80 keV (Figure 4). Most score differences (10/14 segments) were scored at 3 (slight artifacts) or 4 (excellent image quality) at 40–50 keV compared with the imaging at 60–80 keV.

The score of segments exhibiting venous contamination slightly increased from 40 ( $2.5 \pm 0.7$ ) to 70–80 keV ( $2.7 \pm 0.5$ ). The pairwise comparison, 40 vs. 80 ( $P = 0.008$ ) keV MEI, indicated a significant difference in terms of noise for venous contamination, while further corresponding pairwise comparisons, at 40 vs. 60 ( $P = 0.048$ ), 40 vs. 70 ( $P = 0.017$ ), 50 vs. 80 ( $P = 0.467$ ) keV MEI, indicated a difference without significance. Among the 146 patients, 22 (15.1%) exhibited segments with a score of 1 (visible and compromises diagnostic interpretation) in venous contamination at 40 keV, and 10 (6.8%) exhibited segments with a score of 1 at 50 keV in the LE-CTA examinations, while no imaging results were scored 1 at 60–80 keV.

## Discussion

In this study, the image quality of MEIs acquired at five keV levels in terms of PAD, venous contamination, and metal artifacts were compared to determine the MEI acquisition with the highest image quality. The subjective image quality in segments exhibiting PAD at 70–80 keV was higher than that at 40–60 keV. The venous contamination and metal artifacts were more decreased in the MEIs at 70–80 keV than those at 40–60 keV. In addition, the diagnostic interpretation of 22 and 10 patients was compromised due to venous contamination in the MEIs at 40 and 50 keV, respectively, while venous contamination did not affect the diagnostic interpretation of the MEIs at 60–80 keV. Therefore, MEIs with a low keV level may lead to degraded subjective image quality for PAD evaluation, despite the high contrast.

**Table 2.** Subjective image analysis and evaluation of PAD

### 1. Subjective image analysis

#### a) Overall CT image quality

#### b) Segmented image quality of infrarenal aorta, CIA, EIA, CFA, SFA, PA, ATA, PTA, peroneal artery, and TPT

- 1: If examination did not provide information for diagnosis
- 2: If examination maintained acceptable information but unsatisfactory image quality
- 3: If examination was satisfactory to provide information with adequate image quality
- 4: If examination provided optimal information with excellent image quality

#### c) Venous contamination

- 1: Visible and compromises diagnostic interpretation
- 2: Visible, not affect diagnostic interpretation
- 3: Not visible

### 2. Peripheral arterial disease and artifact evaluation

#### a) Peripheral arterial disease

- Stenosis, 1: mild, decreased luminal diameter below 1/3
- Stenosis, 2: moderate, decreased luminal diameter 1/3–2/3
- Stenosis, 3: severe, decreased luminal diameter above 2/3
- Occlusion

#### b) Diagnostic value in artifact of prosthesis

- 1: Non-diagnostic image quality, strong streak artifacts, insufficient quality for diagnostic purposes
- 2: Severe artifacts causing uncertainty
- 3: Slight artifacts with adequate diagnostic image evaluation
- 4: Excellent image quality, no artifacts

PAD, peripheral arterial disease; CT, computed tomography; CIA, common iliac artery; EIA, external iliac arteries; CFA, common femoral arteries; SFA, superficial femoral artery; PA, popliteal artery; ATA, anterior tibial artery; PTA, posterior tibial arteries; TPT, tibioperoneal trunk.

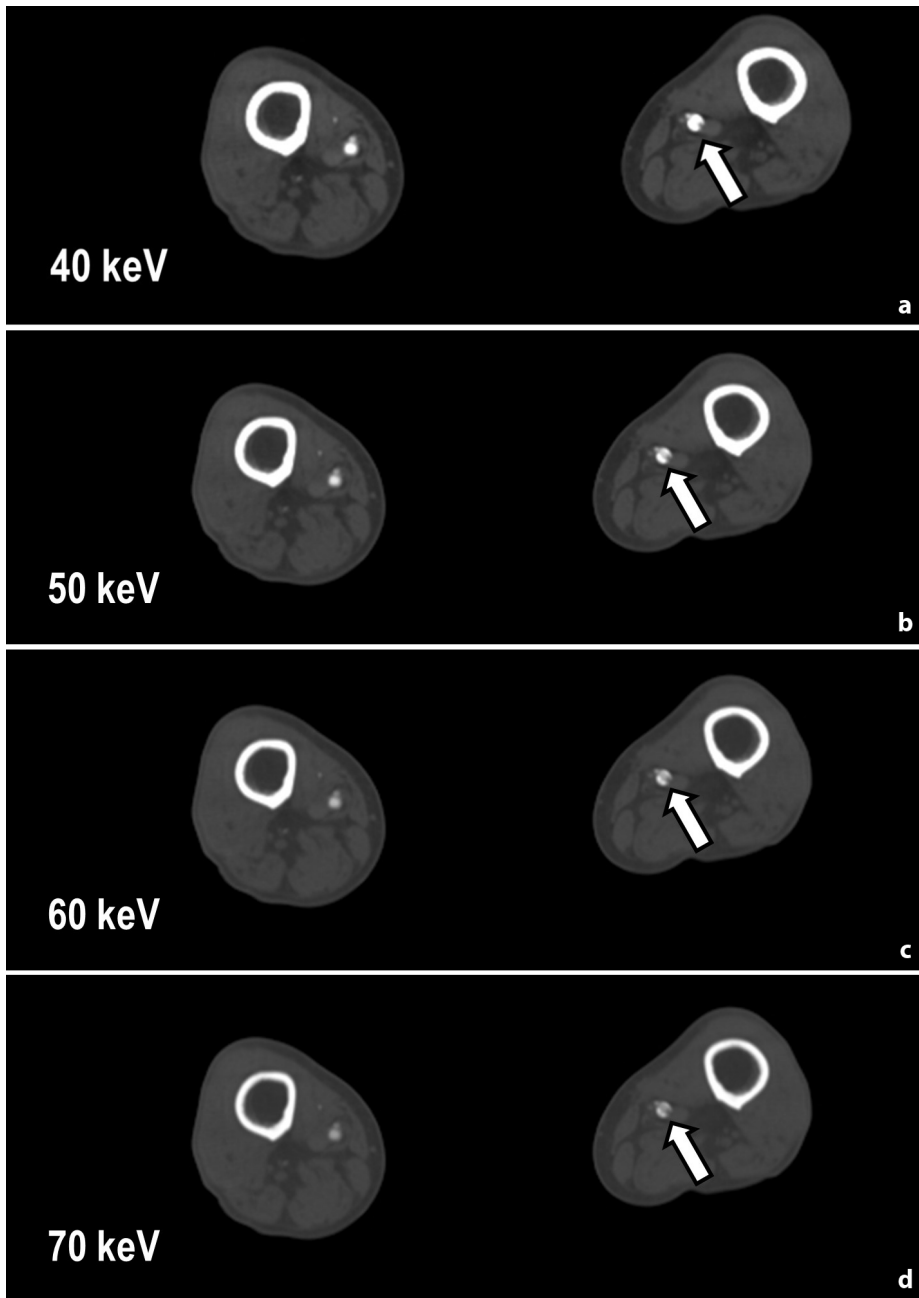


**Figure 3.** (a-d) The LE-CTA using MEI plus in a 71-year-old man with PAD (body mass index: 21.9 kg/m<sup>2</sup>; CTDIvol: 7.1 mGy; DLP: 936 mGy-cm). The patient presented grade 3 stenosis from left SFA (arrowhead) to PA. The 40–50 and 60 keV MEIs were scored 2 and 3, respectively, in terms of diagnostic value in segmental image quality in the left PA. Unsatisfactory image quality was observed for vascular calcification at 40–50 keV, but optimal image quality was achieved at 70–80 keV (score 4). LE-CTA, lower extremity computed tomography angiography; MEIs, monoenergetic images; PAD, peripheral arterial disease; CTDI, CT volume dose index; DLP, dose-length product; SFA, superficial femoral artery; PA, popliteal arteries; keV, kiloelectron volt.

Several studies have reported that the image quality of high-keV (70–100 keV) MEIs is superior for calcific or noncalcified plaque in arterial disease<sup>8,19</sup> and for metal artifacts<sup>9,20,21</sup> compared with low-keV (40–50 keV) MEIs, regardless of the use of noise optimizing methods (e.g., MEI plus algorithm). These findings are consistent with the highest subjective image quality achieved at 70–80 keV for the evaluation of PAD and metal artifacts

in our study. Symons et al.<sup>8</sup> reported low-keV images yielding significantly higher arterial plaque volumes than conventional 90/Sn150-kVp images. Likewise, unsatisfactory image quality was observed in 13.6% PAD segments at 40 keV and 4.4% PAD segments at 50 keV in our study. While small high-contrast structures with blooming artifacts can be mitigated by optimizing the window length/window width,<sup>22,23</sup> low-keV images

with a high contrast can lead to misinterpretation or overestimation of PAD calcification. Therefore, it may not be appropriate to perform PAD evaluation using low-keV MEIs, even if using reconstruction algorithms such as MEI plus.

Beeres et al.<sup>24</sup> reported that MEI plus at a low keV (40–50 keV) provides low image noise in aortic segments, which is not consistent with our results. This difference may be attributed to their evaluation of the aorta (the largest vessel) and their neglect of small vessels, PAD, and metal artifacts. Moreover, their results indicated lower noise at a low keV using MEI plus compared with MEI alone. Our study focused on the image quality of peripheral vessels at low and high keV levels using MEI plus in both cases. Here, low keV levels provided higher objective image noise and lower subjective image quality for PAD, venous contamination, and metal artifacts than high keV levels. We expect our results to be more consistent with clinical practice when evaluating PAD using LE-CTA.

Severe venous contamination was observed in the MEIs from 15.1% of the patients at 40 keV and from 6.8% of the patients at 50 keV, while no compromise in diagnostic interpretation due to venous contamination was determined at 60–80 keV, suggesting another disadvantage of low-keV MEIs. Furthermore, while low-keV MEIs provide a high contrast, this can lead to the overestimation of small venous contamination. While venous contamination at a low keV can be reduced by the optimization of the window settings, venous contamination may also adversely affect LE-CTA at low keV levels.

This study involves certain limitations. First, the images from a small number of patients exhibited stent placement on the evaluated artery segments. Given that stents may also cause artifacts and might reduce the image quality, optimizing the keV level for evaluation of stent patency and in-stent restenosis should be conducted by including more patients with arterial stents. Second, the CT image sets were acquired from a single scanner, and the results may be neither generalizable nor directly comparable with those obtained from other scanners. Third, since the results were not compared to those of catheter angiography, which is the reference standard, the diagnostic accuracy of CTA was not sufficiently evaluated. Fourth, interobserver agreement was not evaluated, except in terms of the overall image quality since the analyses were conducted using the consensus reading method. Finally, the

**Table 3.** Quantitative analysis of MEI attenuation and noise in five image sets

Parameter (keV)	40	50	60	70	80
Quantitative analysis (Hounsfield unit)					
Attenuation					
Infrarenal aorta	1547.2 ± 348.9	1031.2 ± 233.3	725.8 ± 162.8	526.1 ± 115.6	427.6 ± 290.2
Right CIA	1513.9 ± 349.5	1021.0 ± 235.6	753.8 ± 162.0	541.9 ± 119.9	421.4 ± 91.5
Left CIA	1522.4 ± 341.0	1027.2 ± 228.8	724.6 ± 160.5	540.4 ± 119.4	416.9 ± 91.0
Noise					
Infrarenal aorta	46.5 ± 14.6	31.0 ± 9.9	21.6 ± 6.9	16.3 ± 7.8	12.3 ± 3.7
Right CIA	47.2 ± 34.3	32.3 ± 24.4	22.9 ± 18.2	17.4 ± 14.4	14.3 ± 11.9
Left CIA	46.8 ± 29.1	34.8 ± 38.3	23.8 ± 18.8	18.2 ± 15.0	14.5 ± 12.3

Data shown are mean ± standard deviation. MEIs, monoenergetic images; keV, kiloelectron volt; CIA, common iliac artery.

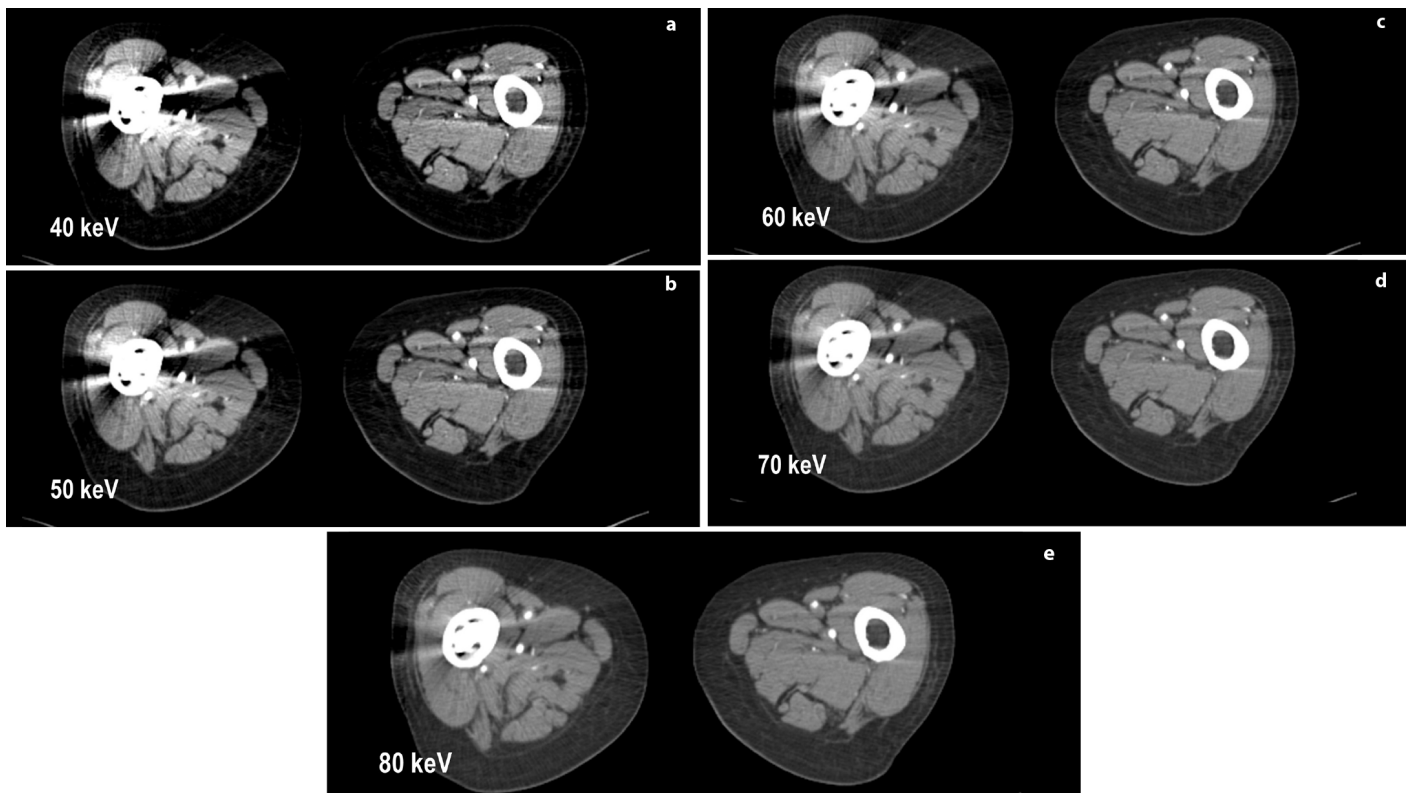


**Figure 4.** (a-e) The LE-CTA using MEI plus in an 80-year-old woman (body mass index: 23.8 kg/m<sup>2</sup>; CTDIvol: 7.8 mGy; DLP: 956 mGy-cm) with PAD in both SFAs, both PAs, and both PTAs as well as grade 3 stenosis. Metal artifacts caused by total hip replacement affect the right SFA evaluation, and their effect gradually decreases in images from 40 to 80 keV. The diagnostic value scores of segmented image quality were 1, 2, 3 and 4 at 40, 50, 60–70, and 80 keV, respectively. LE-CTA, lower extremity computed tomography angiography; MEIs, monoenergetic images; CTDI, CT volume dose index; DLP, dose-length product; PAD, peripheral arterial disease; SFA, superficial femoral artery; keV, kiloelectron volt.

**Table 4.** Quantitative analysis of MEI attenuation and noise in five image sets (*P* values)

Parameter (keV)	Noise			Attenuation		
	Ao	RCIA	LCIA	Ao	RCIA	LCIA
40	vs. 50	<0.001	<0.001	<0.001	<0.001	<0.001
	vs. 60	<0.001	<0.001	<0.001	<0.001	<0.001
	vs. 70	<0.001	<0.001	<0.001	<0.001	<0.001
	vs. 80	<0.001	<0.001	<0.001	<0.001	<0.001
50	vs. 60	<0.001	0.003	0.002	<0.001	<0.001
	vs. 70	<0.001	<0.001	<0.001	<0.001	<0.001
	vs. 80	<0.001	<0.001	<0.001	<0.001	<0.001
60	vs. 70	<0.001	0.320*	0.565*	<0.001	<0.001
	vs. 80	<0.001	0.009	0.014*	<0.001	<0.001
70	vs. 80	0.003	>0.999*	>0.999*	0.006	<0.001

\*Not statistically significant ( $P \geq 0.01$ ). MEIs, monoenergetic images; keV, kiloelectron volt; Ao, infrarenal aorta; RCIA, right common iliac artery; LCIA, left common iliac artery.

data corresponding to a level of >90 keV, MEIs with polyenergetic images, or other MEI blending factors were not compared. Further studies including polyenergetic images and various combinations of MEIs should be conducted.

In conclusion, among the MEIs at different keV levels, the 70–80 keV MEIs obtained higher diagnostic interpretation scores in the overall and segmental subjective image quality evaluations that also considered metal artifacts. The image quality at 60–80 keV was more acceptable in terms of venous contamination since the higher contrast in low-keV images may lead to the overestimation of small venous contamination.

### Acknowledgments

This research was supported by the Basic Science Research Program through the National Research Foundation of Korea and funded by the Ministry of Science ICT and Future Planning (2018R1C1B5044024).

### Conflict of interest disclosure

The authors declared no conflicts of interest.

### References

1. Fowkes FG, Rudan D, Rudan I, et al. Comparison of global estimates of prevalence and risk factors for peripheral artery disease in 2000 and 2010: a systematic review and analysis. *Lancet*. 2013;382(9901):1329-1340. [CrossRef]
2. Horehledova B, Mihal C, Milanese G, et al. CT Angiography in the lower extremity peripheral artery disease feasibility of an ultra-low volume contrast media protocol. *Cardiovasc Intervent Radiol*. 2018;41(11):1751-1764.









3. Aboyans V, Ricco JB, Bartelink MEL, et al. 2017 ESC Guidelines on the Diagnosis and Treatment of Peripheral Arterial Diseases, in collaboration with the European Society for Vascular Surgery (ESVS): document covering atherosclerotic disease of extracranial carotid and vertebral, mesenteric, renal, upper and lower extremity arteries Endorsed by: the European Stroke Organization (ESO) The Task Force for the Diagnosis and Treatment of Peripheral Arterial Diseases of the European Society of Cardiology (ESC) and of the European Society for Vascular Surgery (ESVS). *Eur Heart J*. 2018;39(9):763-816. [CrossRef]
4. Criqui MH, Aboyans V. Epidemiology of peripheral artery disease. *Circ Res*. 2015;116(9):1509-1526. [CrossRef]
5. May MS, Wiesmueller M, Heiss R, et al. Comparison of dual- and single-source dual-energy CT in head and neck imaging. *Eur Radiol*. 2019;29(8):4207-4214. [CrossRef]
6. Yamamoto S, McWilliams J, Arellano C, et al. Dual-energy CT angiography of pelvic and lower extremity arteries: dual-energy bone subtraction versus manual bone subtraction. *Clin Radiol*. 2009;64(11):1088-1096. [CrossRef]
7. Sommer WH, Johnson TR, Becker CR, et al. The value of dual-energy bone removal in maximum intensity projections of lower extremity computed tomography angiography. *Invest Radiol*. 2009;44(5):285-292. [CrossRef]
8. Symons R, Choi Y, Cork TE, et al. Optimized energy of spectral coronary CT angiography for coronary plaque detection and quantification. *J Cardiovasc Comput Tomogr*. 2018;12(2):108-114. [CrossRef]
9. Mocanu I, Van Wettere M, Absil J, Bruneau M, Lubicz B, Sadeghi N. Value of dual-energy CT angiography in patients with treated intracranial aneurysms. *Neuroradiology*. 2018;60(12):1287-1295. [CrossRef]

10. Albrecht MH, Vogl TJ, Martin SS, et al. Review of clinical applications for virtual monoenergetic dual-energy CT. *Radiology*. 2019;293(2):260-271. [CrossRef]
11. Horat L, Hamie MQ, Huber FA, Guggenberger R. Optimization of monoenergetic extrapolations in dual-energy CT for metal artifact reduction in different body regions and orthopedic implants. *Acad Radiol*. 2019;26(5):67-74. [CrossRef]
12. McNamara MM, Little MD, Alexander LF, Carroll LV, Beasley TM, Morgan DE. Multireader evaluation of lesion conspicuity in small pancreatic adenocarcinomas: complimentary value of iodine material density and low keV simulated monoenergetic images using multiphasic rapid kVp-switching dual energy CT. *Abdom Imaging*. 2015;40(5):1230-1240. [CrossRef]
13. Patino M, Prochowski A, Agrawal MD, et al. Material Separation Using Dual-Energy CT: current and emerging applications. *Radiographics*. 2016;36(4):1087-1105. [CrossRef]
14. Shinohara Y, Sakamoto M, Iwata N, et al. Usefulness of monochromatic imaging with metal artifact reduction software for computed tomography angiography after intracranial aneurysm coil embolization. *Acta Radiol*. 2014;55(8):1015-1023. [CrossRef]
15. Sudarski S, Apfaltrer P, Nance JW Jr, et al. Optimization of keV-settings in abdominal and lower extremity dual-source dual-energy CT angiography determined with virtual monoenergetic imaging. *Eur J Radiol*. 2013;82(10):574-581. [CrossRef]
16. Grant KL, Flohr TG, Krauss B, Sedlmair M, Thomas C, Schmidt B. Assessment of an advanced image-based technique to calculate virtual monoenergetic computed tomographic images from a dual-energy examination to improve contrast-to-noise ratio in examinations using iodinated contrast media. *Invest Radiol*. 2014;49(9):586-592. [CrossRef]
17. Albrecht MH, Scholtz JE, Hüsters K, et al. Advanced image-based virtual monoenergetic dual-energy CT angiography of the abdomen: optimization of kiloelectron volt settings to improve image contrast. *Eur Radiol*. 2016;26(6):1863-1870. [CrossRef]
18. Zhao L, Li F, Zhang Z, et al. Assessment of an advanced virtual monoenergetic reconstruction technique in cerebral and cervical angiography with third-generation dual-source CT: Feasibility of using low-concentration contrast medium. *Eur Radiol*. 2018;28(10):4379-4388. [CrossRef]
19. Al-Baldawi Y, Große Hokamp N, Haneder S, et al. Virtual mono-energetic images and iterative image reconstruction: abdominal vessel imaging in the era of spectral detector CT. *Clin Radiol*. 2020;75(8):641. [CrossRef]
20. Magarelli N, De Santis V, Marziali G, et al. Application and advantages of

- monoenergetic reconstruction images for the reduction of metallic artifacts using dual-energy CT in knee and hip prostheses. *Radiol Med*. 2018;123(8):593-600. [\[CrossRef\]](#)
21. Pagniez J, Legrand L, Khung S, et al. Metal artifact reduction on chest computed tomography examinations: comparison of the iterative metallic artefact reduction algorithm and the monoenergetic approach. *J Comput Assist Tomogr*. 2017;41(3):446-454. [\[CrossRef\]](#)
22. Pollak AW, Norton PT, Kramer CM. Multimodality imaging of lower extremity peripheral arterial disease: current role and future directions. *Circ Cardiovasc Imaging*. 2012;5(6):797-807. [\[CrossRef\]](#)
23. Lee KH, Shim YS, Park SH, et al. Comparison of standard-dose and half-dose dual-source abdominopelvic CT scans for evaluation of acute abdominal pain. *Acta Radiol*. 2019;60(8):946-954. [\[CrossRef\]](#)
24. Beeres M, Trommer J, Frellesen C, et al. Evaluation of different keV-settings in dual-energy CT angiography of the aorta using advanced image-based virtual monoenergetic imaging. *Int J Cardiovasc Imaging*. 2016;32(1):137-144. [\[CrossRef\]](#)



# Role of T2 mapping of magnetic resonance imaging in the differentiation of endometrial cancer and benign endometrial lesions

Han Xu   
 Jie Zhang   
 Yuqing Han   
 Qingwei Liu   
 Jinlai Liu   
 Xianshun Yuan   
 Jiamei Li   
 Jinye Li   
 Ximing Wang 

From the Department of Radiology (H.X., J.Z. ✉ zhangjie1219@163.com, Y.H., Q.L.), Shandong Provincial Hospital, Cheeloo College of Medicine, Shandong University, Shandong, China; Department of Radiology (J.Z., Q.L., X.Y., X.W.), Shandong Provincial Hospital Affiliated to Shandong First Medical University, Shandong, China; Department of Radiology (J.L.), The Second People's Hospital of Jiaozuo (First Affiliated Hospital of Henan Polytechnic University), Jiaozuo, China; Department of Radiology (Jia.L.), Shandong Provincial Hospital Affiliated to Shandong First Medical University, Jinan, China; Department of Radiology (Jin.L.), Shandong Provincial ENT Hospital Affiliated to Shandong University, Shandong Provincial ENT Hospital, Jinan, China.

Received 24 August 2021; revision requested 25 September 2021; last revision received 28 March 2022; accepted 22 April 2022.



Epub: 28.12.2022

Publication date: 31.01.2023

DOI: 10.4274/dir.2021.21884

## PURPOSE

The T2 mapping of magnetic resonance imaging (MRI) in endometrial cancer (EC), benign endometrial lesions (BELs), and normal endometrium (NE) has rarely been reported. This study aimed to determine the T2 values of MRI in EC, BELs, and NE to investigate whether the T2 values can differentiate them and to assess the aggressiveness of EC.

## METHODS

In total, 73 patients [EC, 51 (age,  $57.4 \pm 5.4$  years); BELs, 22 (age,  $57.8 \pm 11.8$  years)] and 23 normal volunteers (age,  $56.1 \pm 6.6$  years) were included. The T2 values of MRI of the EC (type I and II), BEL, and NE groups were described and compared. The relationships between the T2 values of MRI in EC and the pathological characteristics [International Federation of Gynecology and Obstetrics (FIGO) stage and grade] were analyzed.

## RESULTS

The median T2 values of NE, BEL, and EC were 197.5 (142.9–324.0) ms, 131.1 (103.2–247.9) ms, and 103.0 (71.6–243.5) ms ( $P < 0.001$ ), respectively. The median T2 values of type I and type II EC were 100.8 (71.62–130.44) ms and 125.7 (119.7–243.5) ms, respectively. There were significant differences in the T2 values among the NE, BEL, type I EC, and type II EC groups ( $P < 0.001$ ) except for between the type II EC and BEL groups ( $P = 0.938$ ). The T2 value of MRI in type I EC was significantly lower than that in type II EC ( $P = 0.001$ ). There were no significant differences in patients with type I EC having different FIGO stages ( $P = 0.273$ ) or tumor grades ( $P = 0.686$ ).

## CONCLUSION

T2 mapping of MRI has the potential to quantitatively differentiate between EC, BELs, and NE as well as between type I and type II EC.

## KEYWORDS

Benign, benign endometrium lesions, endometrial cancer, MRI, T2 mapping, T2 value

Endometrial cancer (EC) is a common gynecologic malignancy and the sixth most prevalent cancer among women worldwide.<sup>1</sup> The risk factors for EC include conditions promoting increased estrogen exposure, such as hormonal replacement therapy, obesity, tamoxifen use, early menarche, late menopause, nulliparity, history of polycystic ovary disease, and hereditary no-polyposis colorectal cancer (Lynch syndrome).<sup>2,3</sup> An accurate diagnosis of EC and an assessment of its aggressiveness are crucial for determining the treatment plan and prognosis of patients. Sampling is not always sufficient and not always possible (e.g., cervical stenosis after cervical radiation therapy).<sup>4</sup> Psychologically, patients are more likely to accept non-invasive examinations. The pathologic type, stage, and grade of EC are important biological manifestations of its aggressiveness. Type II EC (non-estrogen-dependent EC) is closely linked with lymph node metastasis and poor prognosis. Many studies based on magnetic resonance imaging (MRI) have reported on the preoperative diagnosis and as-



assessment methods of EC.<sup>5-13</sup> Techniques such as T2-weighted imaging (T2WI), dynamic contrast-enhanced (DCE) imaging, and diffusion-weighted imaging (DWI) are widely accepted, with high accuracy for the staging of EC.<sup>5-9</sup> Other emerging techniques such as amide proton transfer (APT) imaging, magnetic resonance spectroscopy (MRS), and diffusion kurtosis imaging are also reported to have produced promising results regarding the type and grade of EC.<sup>10-13</sup>

Most of the studies on EC have focused on the application of qualitative MRI data. Meanwhile, quantitative MRI data could provide more unique and direct information regarding EC. The T2 value from MRI T2 mapping, which describes the decay of the magnetic vector (M) in the xy plane  $[(M)_{xy}]$ , a component of the total M, is an essential parameter in quantitative MRI. The T2 value reflects the absolute transversal relaxation time of the protons in the tissue. T2 mapping is mainly applicable for the musculoskeletal system, heart, and prostate because these tissues are composed of water compartments of different sizes, whose relative percentages vary between abnormal and normal tissues and between different pathologic grades of cancers.<sup>14-19</sup>

Few studies have reported on the application of T2 mapping in cases of normal uterine structure and uterine lesions. A short article reported that T2 mapping demonstrated a new layer, namely the linear submucosal myometrium of the uterine architecture, in one patient with adenomyosis and two patients with EC.<sup>20</sup> The difference in the myometrial architecture could partly be attributed to the difference in water content in the endometrium;<sup>21</sup> the T2 value was related to the water content. To the best of our knowledge, no study focusing on T2 mapping for the differentiation of EC has been reported. This would require knowledge of the T2 values of MRI of the normal endometrium (NE) and benign endometrial lesions (BELs),

which have rarely been reported. This study aimed to determine the T2 values of MRI in EC, BELs, and NE to investigate whether the T2 values can differentiate them and to assess the aggressiveness of EC based on the T2 values.

## Methods

### Subjects

The Institutional Review Board of Shandong Provincial Hospital approved this prospective study (approval number: SWYX2020-051). Written informed consent was obtained from all subjects before enrollment.

Patients with a confirmed or suspected diagnosis of EC by diagnostic curettage, those who showed intrauterine lesions on ultrasound but had contraindications to curettage, and those who did not receive any surgical treatment other than curettage were included. Patients with lesions that could not be clearly visualized upon MRI were excluded. From March 2012 to September 2015, 51 patients with EC and 22 patients with BELs confirmed by histopathology were included in this study.

The T2 values of the endometrium may vary depending on the menstrual cycle, and as the majority of patients with EC and BELs were post-menopausal women, the volunteers with NE that were included in this study were also post-menopausal women;<sup>22</sup> hence, the influence of menstrual cycle was not a consideration in the T2 values of MRI in the volunteers with NE. These volunteers were required to have no clinical symptoms, no submucous myoma on MRI, and no other gynecological diseases. Any volunteers with gynecological abnormalities after five years of follow-up were excluded. Finally, 23 volunteers with NE were included in this study.

### Image acquisition

MRI was performed using a 3T scanner (Magnetom Verio, Siemens Healthineers, Erlangen, Germany). Built-in integrated spine coils and an eight-channel pelvic phased array surface coil were used to receive signals. Patients were advised to fast for 4 h and were administered a raceanisodamine hydrochloride injection (Hangzhou Minsheng Pharma, Hangzhou, China) before MRI to reduce intestinal peristalsis, and their bladder was required to be partially full.

For anatomical scans, oblique sagittal, oblique coronal and oblique axial T2W turbo spin-echo (TSE) imaging, oblique axial and oblique sagittal DWI, and oblique sagittal DCE imaging were performed using the following parameters: oblique axial, sagittal, and coronal T2WI, repetition time (TR)/echo time (TE), 2,950–3,670/97–101 ms; slice thickness (ST)/gap, 3–4 (0.6–0.8) mm; average, 2; matrix, 320 × 256 or 320 × 310; field of view (FOV), 20 × 20 cm; oblique axial and sagittal DWI, TR/TE, 6,200/93 ms; ST/gap, 3–4 (0.6–0.8) mm; average, 6; matrix, 160 × 120; FOV, 20 × 20 cm; oblique sagittal DCE imaging, TR/TE, 5.21/1.8 ms; ST/gap, 3–4 (0.6–0.8) mm; average, 1; matrix, 224 × 161; FOV, 20 × 20 cm.

Oblique sagittal T2 mapping was performed using multi-echo TSE prior to DCE imaging, with the following parameters: TR, 1,500 ms; TE, 20, 40, 60, 80 and 100 ms; FOV, 20 × 20 cm; matrix, 256 × 256; ST, 3 mm; slice gap, 0.6 mm; 12 slices. The saturated band was placed on the anterior abdominal wall with an acquisition time of 4 m and 8 s.

### Image analysis

The T2 map was analyzed using the vendor's workstation (Syngo, Siemens Healthineers, Erlangen, Germany). The T2 mappings from the 23 normal volunteers and 73 patients were reviewed in consensus by two senior gynecologic radiologists (Zhang J and Xu H) who had 8 and 10 years of experience in clinical practice, respectively. On oblique sagittal T2 maps, the region of interest (ROI) was manually delineated along the edge of a lesion in consensus by the two radiologists according to the morphology and size of a lesion to avoid cystic and necrotic areas (Figure 1). A larger lesion contained more than one ROI. The ROI was drawn on each slice containing the lesion. The three-dimensional volume of interest (VOI) was constructed by the multiple two-dimensional ROIs. The ROI and VOI of NE were manually drawn in the same manner (Figure 2). The multi-parametric MR images, including DWI, DCE, and T2W images, were used as references to avoid cystic or necrotic areas. The ROI of EC and BELs were drawn with DCE images as the main reference, while the ROI of NE was drawn with T2W images as the main reference. The VOI of NE often contained more than one ROI. The mean T2 value of a VOI was calculated by averaging the T2 values of all voxels in a VOI

$$\text{mean T2} = (\sum_{i=1}^n T2_i S_i) / \sum_{i=1}^n S_i, \text{ equation 1}$$

### Main points

- The T2 mapping of magnetic resonance imaging in endometrial cancer (EC), benign endometrial lesions (BELs), and normal endometrium (NE) has rarely been reported.
- T2 mapping can help differentiate between EC, BELs, and NE.
- T2 mapping cannot differentiate between type II EC and BELs.
- T2 mapping cannot differentiate between the different stages or grades of EC.

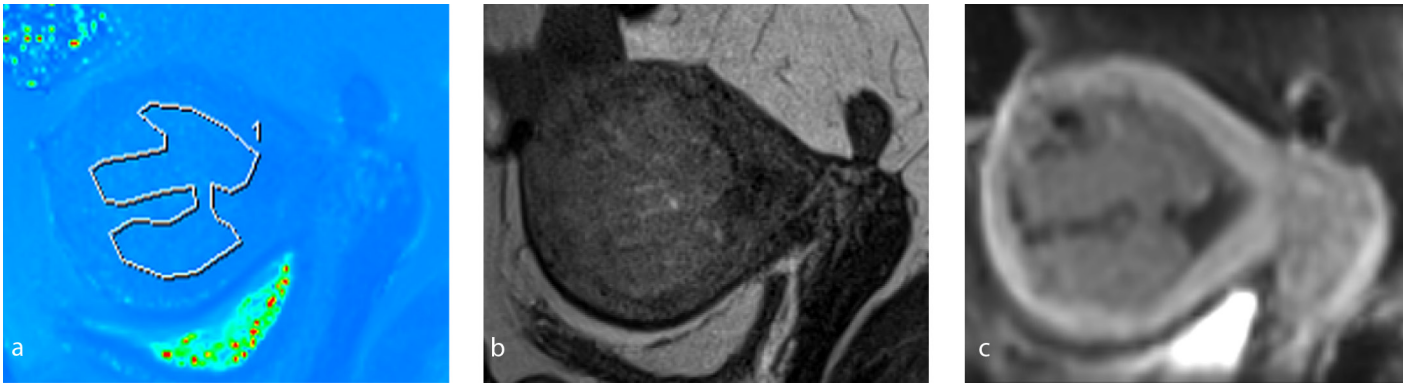


**Figure 1.** The ROI in a 65-year-old woman with type II endometrial cancer. (a) The ROI was manually placed in the lesions on the sagittal T2 map according to the morphology and size of the lesions to avoid the cystic and necrotic areas; (b) sagittal T2-weighted image and (c) sagittal enhanced image were used as the reference images. ROI, region of interest.

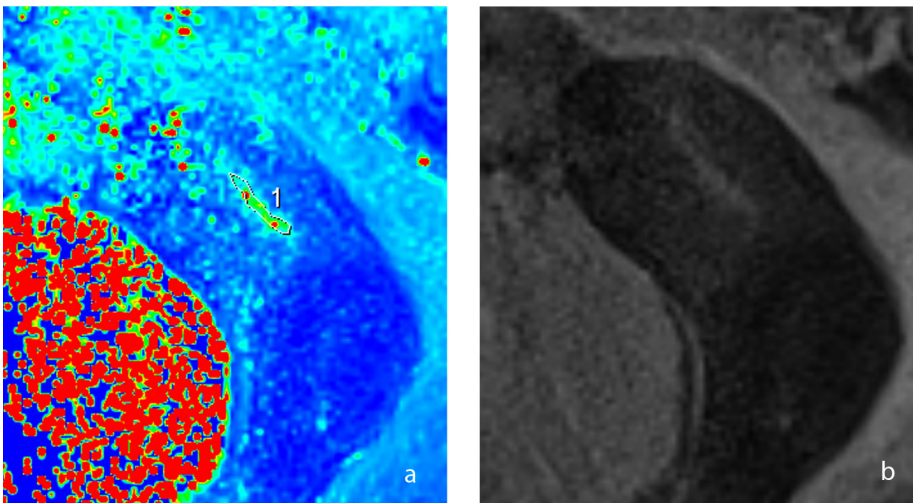


**Figure 2.** The ROI of normal endometrium in one slice in a 70-year-old volunteer. (a) T2 map of normal endometrium "1" was the ROI. (b) T2-weighted image was used as the reference image. ROI, region of interest.

where  $n$  was the number of ROIs for a lesion/NE (that is a VOI),  $T_{2_i}$  was the mean T2 value of the  $i$ th ROI, and  $S_i$  was the area of the  $i$ th ROI. As the area between each ROI in a lesion/NE is different, the area  $S_i$  was the weighting of the  $T_{2_i}$  to robustly calculate the mean T2 values.

After the measurement of the T2 values (in consensus by the two radiologists) for more than six months, the values were independently measured by a manually placed ROI by the two radiologists for interclass reliability analysis. Two weeks later, the T2 values were repeatedly measured by one of the two radiologists for intraclass reliability analysis.

### Histopathological analysis

The median interval between MRI and surgery was 3 (1–10) days. In total, 51 patients with EC underwent total hysterectomy and bilateral salpingo-oophorectomy and pelvic lymph node dissection, 19 patients with BELs underwent total hysterec-

tomy and bilateral salpingo-oophorectomy, and 3 patients with BELs (2 with complex hyperplasia and 1 with simple hyperplasia) underwent resection of the lesions. The lesions were histopathologically analyzed by a senior pathologist (Li J). Following the International Federation of Gynecology and Obstetrics (FIGO) 2009 revised FIGO staging criteria,<sup>23</sup> the stage, histologically differentiated degree (grade 1, well differentiated; grade 2, moderate differentiation; grade 3, poor differentiation), and type (type I, estrogen-dependent; type II, non-estrogen-dependent) of EC were reported.

### Statistical analysis

The Kolmogorov–Smirnov test was used to check the data normality. If the distribution was normal, values were represented as the mean  $\pm$  standard deviation; otherwise, the median and minimum–maximum values were given. Descriptive statistics of categorical variables were expressed as fre-

quency and percentage [ $n$  (%)]. Intra- and interobserver agreements of T2 values were analyzed by reliability analysis. If the data fit the normal distribution and the homogeneity of variance (Levene test), a one way analysis of variance (ANOVA) was used for the intergroup comparisons; otherwise, the Kruskal–Wallis H test was used. If the Kruskal–Wallis H test was statistically significant, the Dunn–Bonferroni post hoc test was used for pairwise comparisons. The corrected  $P < 0.05$  was considered statistically significant.

The receiver operating characteristic (ROC) curve analysis was performed, and the optimal threshold of the T2 value to distinguish between the two types of EC was obtained from the ROC curve analysis, according to the Youden index. The area under the curve (AUC) was of great significance in the comprehensive evaluation of diagnostic accuracy. In general,  $0.5 < AUC \leq 0.7$  indicated a low diagnostic value,  $0.7 < AUC \leq 0.9$  indicated an intermediate diagnostic value, and  $AUC > 0.9$  indicated a high diagnostic value.<sup>11</sup>

Few patients had type II EC in this study, which included multiple pathological types. Therefore, the following statistical analysis was only performed for type I EC. The T2 values of MRI in the different FIGO stages of EC as well as for the different grades of EC were compared. Spearman's correlation coefficient was used in the analysis of the relationship between the FIGO stage of type I EC and the T2 value as well as between the grade of type I EC and the T2 value. For all statistical analyses,  $P < 0.05$  was considered significant. The statistical analysis was performed using IBM SPSS statistics 22.0 for Windows (IBM Corp, Armonk, NY, USA).

## Results

The mean ages of the 51 patients with EC, 22 patients with BELs, and 23 normal volunteers (NE) were  $57.4 \pm 5.4$  years,  $57.8 \pm 11.8$  years, and  $56.1 \pm 6.6$  years, respectively. There were no significant differences between the ages of patients with EC, BELs, and NE ( $P = 0.743$ ). The cases of EC included 4 (7.8%) premenopausal patients (mean age,  $49.8 \pm 1.3$  years) and 47 (92.2%) post-menopausal patients (mean age,  $58.0 \pm 5.2$  years). The cases of BEL included 4 (18.2%) premenopausal patients (mean age,  $39.8 \pm 8.8$  years) and 18 (81.8%) post-menopausal patients (mean age,  $61.8 \pm 8.1$  years).

The characteristics of the patients and volunteers are summarized in Table 1. The intra- and interclass correlation coefficients of the T2 values were 0.981 [ $P < 0.001$ , 95% confidence interval (CI), 0.971, 0.987] and 0.949 ( $P < 0.001$ , 95% CI, 0.894, 0.972), respectively. The T2 values of MRI in patients with EC, BELs, and NE are shown in Table 2. There were statistically significant differences in the T2 values between EC, BELs, and NE ( $P < 0.001$ ; EC vs. BEL,  $P = 0.001$ ; EC vs. NE,  $P < 0.001$ ; BEL vs. NE,  $P = 0.005$ ) (Table 2, Figure 3a).

The T2 values of MRI in patients with type I and type II EC are also shown in Table 2. There were significant differences in the T2 values

Table 1. Patient characteristics	
Variable	n (%)
<b>Lesions</b>	
EC	51/96 (53.1)
BELs	22/96 (22.9)
NE	23/96 (24.0)
<b>Type of EC</b>	
Type I (estrogen-dependent)	41/51 (80.4)
Type II (non-estrogen-dependent)	10/51 (19.6)
<b>Subtype of type II EC</b>	
Adenosquamous	2/10 (20.0)
Squamous cell	2/10 (20.0)
Endometrioid	2/10 (20.0)
Serous	2/10 (20.0)
Mucinous	1/10 (10.0)
Mixed endometrioid/clear cell	1/10 (10.0)
<b>Subtype of BELs</b>	
Polyp	7/22 (31.8)
Complex hyperplasia with or without atypia	9/22 (40.9)
Simple hyperplasia	6/22 (27.3)
nN, number; EC, endometrial cancer; BELs, benign endometrial lesions; NE, normal endometrium.	

between patients with type I EC, type II EC, BELs, and the volunteers with NE ( $P < 0.001$ ). There was no significant difference in the T2 values between type II EC and BELs ( $P = 0.938$ ); however, there were statistically significant differences in the T2 values between all other pairs of groups (NE vs. BEL,  $P = 0.006$ ; NE vs. type I EC,  $P < 0.001$ ; NE vs. type II EC,  $P = 0.006$ ; BEL vs. type I EC,  $P < 0.001$ ; type I EC vs. type II EC,  $P = 0.001$ ) (Figure 3b). The AUC of differentiation between the two types of EC was 0.959 ( $P < 0.001$ ), i.e., a high diagnostic value (Figure 4a, Table 3). The threshold of the T2 value was 119.3 ms. The Youden index, specificity, and sensitivity were 0.902, 0.902, and 1.000, respectively. The AUC of differentiation between type I EC and BEL was 0.920 ( $P < 0.001$ ) (Figure 4b, Table 3). The threshold of the T2 value was 119.3 ms. The Youden index, specificity, and sensitivity were 0.675, 0.773, and 0.902, respectively.

The clinical information and results of the T2 mapping analysis of patients with type I EC are shown in Table 4. There were no significant differences in the patients with type I EC having different FIGO stages ( $P = 0.273$

or different tumor grades ( $P = 0.686$ ) (Table 4). Because there was only one case of EC in FIGO stage II, the EC cases in FIGO stages II and III were combined for statistical analysis. There was no significant correlation between the T2 value and FIGO stage of EC (Spearman coefficient  $r_1 = 0.176$ ,  $P = 0.271$ ) or between the T2 value and grade of EC (Spearman coefficient  $r_2 = 0.228$ ,  $P = 0.152$ ). No patient with type II EC had cancer of FIGO stage Ia. The mean T2 values for type II EC with the FIGO stage Ib (two patients) and stage II (two patients) were 123.4 ms and 125.7 ms, respectively. Six patients with type II EC had cancer of FIGO stage III; the median (minimum–maximum) value was 134.8 (119.7–243.5) ms. As very few patients had type II EC, statistical analysis of the different FIGO stages was not performed.

## Discussion

This study demonstrated that the T2 values of MRI in patients with NE, BELs, and EC were significantly different. The T2 value of MRI in patients with BELs was significantly lower than in those with NE, while the T2 val-

**Table 2.** T2 values of MRI in volunteers with NE and patients with BELs and EC

Cases	Median (min–max)	Kruskal–Wallis test <i>P</i> -value	Pairwise <i>P</i> -value
NE	197.5 (142.9–324.0)	<0.001	NE vs. BEL, 0.005
BEL	131.1 (103.2–247.9)		BEL vs. EC, 0.001
EC	103.0 (71.6–243.5)		EC vs. NE, <0.001
NE	197.5 (142.9–324.0)	<0.001	NE vs. BEL, 0.006
BEL	131.1 (103.2–247.9)		NE vs. type I EC, <0.001
Type I EC	100.8 (71.62–130.44)		NE vs. type II EC, 0.006
Type II EC	125.7 (119.7–243.5)		BEL vs. type I EC, <0.001
			BEL vs. type II EC, 0.938
			Type I vs. type II EC, 0.001

MRI, magnetic resonance imaging; NE, normal endometrium; BELs, benign endometrial lesions; EC, endometrial cancer; min, minimum value; max, maximum value.

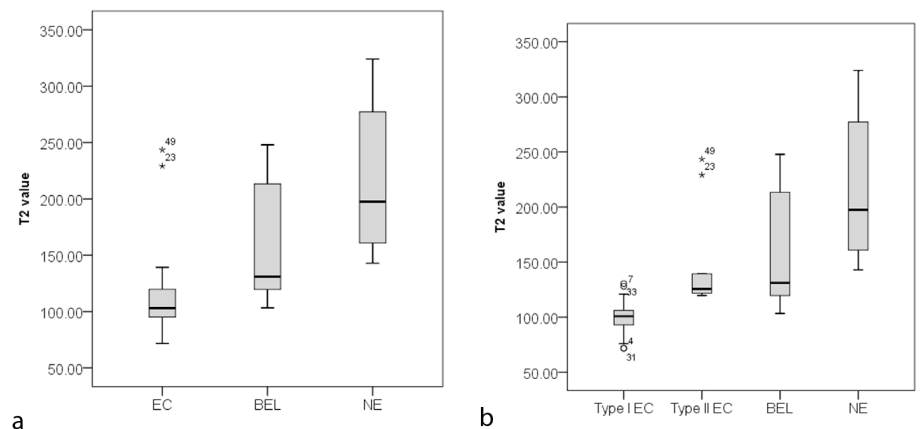


**Figure 3.** Box plot of the T2 value of MRI in patients with EC, BELs, and NE. (a) There were statistically significant differences between the T2 values in patients with EC, BEL, and NE. (b) There were statistically significant differences between all pairs of groups, except for between patients with type II EC and BELs. Two patients had serous cancer with a relatively high T2 value (\*). MRI, magnetic resonance imaging; EC, endometrial cancer; BELs, benign endometrial lesions; NE, normal endometrium.

ue in patients with EC, specifically type I EC, was significantly lower than in patients with BELs. Women with NE have normal secretion function and their glands are arranged in proper order. The acinar cavity and tissue space of the NE are relatively large, thereby accommodating more secretions and interstitial fluids. Hence, the T2 value of MRI is highest for those with NE. Patients with EC and BELs have different degrees of gland heteromorphism, especially those with EC. The EC has a high nucleus: plasma ratio, obvious nucleolus, and irregular glandular lumen.<sup>24,25</sup>

Hence, the T2 values of MRI in patients with EC and BELs are reduced to different degrees.

Furthermore, the T2 value of MRI in patients with type II EC was higher than that in patients with type I EC. However, the T2 values of MRI at different FIGO stages of EC were not significantly different; a similar finding was noted in patients with different grades of EC. Unfortunately, there was no significant difference in the T2 values of MRI between patients with type II EC and BELs. Type II EC has many pathological types, in-

cluding serous cancer, which is characterized by the secretion of more serous fluid. In this study, only two patients with type II EC had serous cancer (Figure 3), and they had relatively high T2 values of MRI. In such cases, benign and malignant lesions should be distinguished first using other MRI sequences such as DWI and contrast-enhanced imaging.<sup>26</sup> A previous study has shown that the apparent diffusion coefficient (ADC) of EC is lower than that of BEL, the b1000q of EC was higher than that of BEL, and the Cq of EC was lower than that of BEL (b1000q = DWI signal-intensity lesion/DWI signal-intensity myometrium; Cq = postcontrast signal-intensity lesion/postcontrast signal-intensity myometrium).<sup>26</sup>

It is vital to distinguish EC from BELs before initiation of treatment. Fractional dilatation and curettage (D & C) is the most commonly used method for preoperative diagnosis of EC; however, it does not always yield reliable results because of the limited number of samples.<sup>4</sup> About 16.7% to 62.5% of patients diagnosed with atypical hyperplasia during D & C were diagnosed as having EC based on the hysterectomy specimens.<sup>11</sup> Occasionally, the results of D & C are inconsistent with those of the hysterectomy specimens, and a certain rate of false negative results with D & C has also been observed.<sup>27</sup> Further, hysteroscopic fractional D & C may cause the spread of tumor cells within the peritoneal cavity.<sup>28</sup> Conventional qualitative MRI may some-

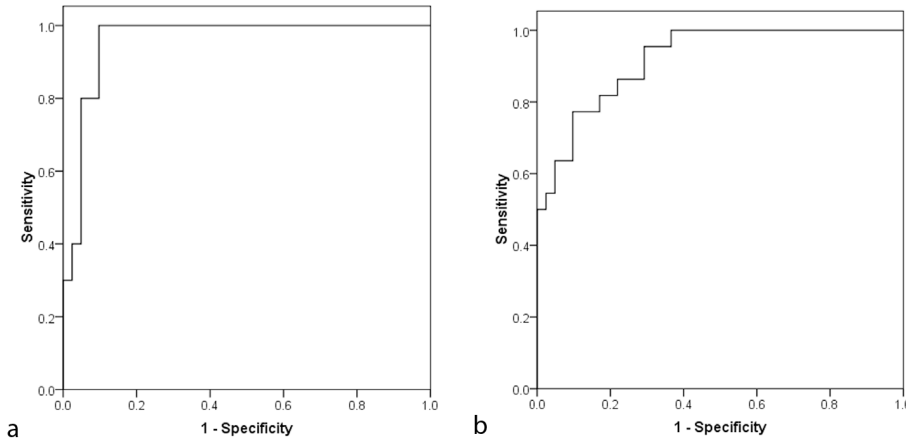


**Figure 4.** (a) The ROC curve to differentiate type II EC from type I EC. The area under the curve was 0.959, with a high diagnostic value. The Youden index was 0.902, with a sensitivity of 1 and a specificity of 0.902. (b) The ROC curve to differentiate type I EC from BELs. The area under the curve was 0.920, with a high diagnostic value. The Youden index was 0.675, with a sensitivity of 0.902 and a specificity of 0.773. ROC, receiver operating characteristic; EC, endometrial cancer; BELs, benign endometrial lesions.

	T2 value cut-off (ms)	Sensitivity	Specificity	AUC	SE	P value
Type I - II	119.3	1	0.902	0.959	0.026	<0.001
Type I - BELs	119.3	0.773	0.902	0.920	0.033	<0.001

EC, endometrial cancer; BELs, benign endometrial lesions; AUC, area under the curve; SE, standard error.

Variable	T2 value (ms)		n (%)
	Mean ± SD	Median (min-max)	
Type I EC			41/51 (80.4)
<b>FIGO stage</b>			
Ia	-	98.7 (75.8-120.4)	24/41 (58.5)
Ib	-	105.5 (90.1-130.4)	10/41 (24.4)
≥II	-	103.0 (71.6-120.8)	7/41 (17.1)
P-value	0.273		
<b>Grade</b>			
Grade 1	98.0 ± 7.2	-	8/41 (19.5)
Grade 2	99.9 ± 16.2	-	27/41 (65.9)
Grade 3	104.4 ± 7.4	-	6/41 (14.6)
P value	0.686		

EC, endometrial cancer; SD, standard deviation; n, number; min, minimum value; max, maximum value; FIGO, International Federation of Gynecology and Obstetrics.

times render the differentiation of EC from BELs difficult.<sup>22</sup> In this study, the T2 values of MRI in patients with EC were significantly lower than those in patients with BELs. Thus, this quantitative MRI parameter might be a supplement to preoperative pathological examination and routine MRI.

Considerable differences exist between the different types of EC in terms of histology, risk factors, and clinical features as well as in terms of therapeutic schedule, risk of surgery, and recurrence rate.<sup>29</sup> Type I EC is the most common, accounting for 80% to 85% of all EC, and it has a favorable prognosis, whereas type II EC is characterized by rapid tumor progression and a poor prognosis. Typically, the diagnosis of the different types of EC (estrogen-dependent or non-estrogen-dependent) depends on postoperative immunohistochemical examination rather than preoperative and intraoperative pathological examinations.<sup>30</sup> In the current study, the T2 value of MRI in type I EC was significantly lower than that in type II EC, which might help to distinguish between the two types of EC before surgery.

Recent studies have reported that some quantitative parameters could distinguish EC from benign lesions and identify the different types of EC and different FIGO stages of EC. A previous study by Zhang et al.<sup>11</sup> reported that the mean [choline-containing compounds (Cho)]/water obtained from MRS could distinguish EC from benign lesions and identify the different types of EC; they found that Cho/water was positively correlated with the FIGO stage of EC. Takayama et al.<sup>10</sup> found that the APT signal intensity was positively correlated with the histologic grade of EC. Nougaret et al.<sup>9</sup> reported that a combination of the volume and ADC of a tumor can be used to predict tumor grade, lymphovascular invasion, and depth of myometrial invasion. Some studies have reported on the MRI findings of type I to type II EC differentiation.<sup>31,32</sup> Chen et al.<sup>31</sup> reported that type II EC has a lower ADC and larger size than type I EC. Meng et al.<sup>32</sup> reported that the magnetization transfer ratio asymmetry (3.5 ppm) and apparent kurtosis coefficient values were higher and the non-Gaussian diffusion coefficient was lower in type II EC than in type I EC. Most endometrial polyp lesions were iso/hypointense in the DWI sequence ( $b = 1.000 \text{ s/mm}^2$ ), while the endometrium (endometrial physiological thickening) and endometrial hyperplasia lesions were hyperintense in the DWI sequence; there was no statistically significant difference between the endome-

trium (endometrial physiological thickening) and endometrial hyperplasia and polyp in ADC and Cq.<sup>26</sup> On T2WI, endometrial hyperplasia appeared iso/hypointense to the NE; however, T2WI appearance is non-specific.<sup>33</sup> The T2 value of NE was significantly higher than that of BELs in this study.

Ghosh et al.<sup>20</sup> reported that the T2 map can show the uterus with four layers. The thin fourth layer was more hypointense than the junctional zone and was observed between the endometrium and the junctional zone. T2\* mapping can also show the fourth layer.<sup>34</sup> Quantitative T2 values seem to be suitable for distinguishing between prostate cancer and normal gland tissue or benign prostate hyperplasia nodes, and they offer an indication of the aggressiveness of the prostate cancer.<sup>14,18</sup> To the best of our knowledge, no study has reported on the association between the invasiveness of EC and the T2 values of MRI. The T2 mapping techniques help to overcome the relatively insensitive visual inspection of differences in signal intensities. They allow direct measurement of T2 relaxation time in milliseconds and quantify the voxel-wise signal on a standardized scale, thereby enabling more direct investigation of the water content in the tissue and further tissue characterization. In this study, we investigated EC using T2 mapping and obtained some significant results.

This study has some limitations. First, the number of patients in this study was small, especially patients with type II EC, which included mostly uncommon histological types of EC, such as serous EC; therefore, more patients with type II EC are required for further research. Second, the normality of the endometrium of the healthy volunteers could only be assumed based on their clinical manifestations, imaging manifestations, and disease history; it could not be confirmed by histological examination as this was not considered ethical. Third, the T2 mapping was very sensitive to the water content in the endometrium. The area of interest could not be completely removed in case of slight endometrial secretions, which increase the T2 value, influencing the results. Fourth, the control group included only post-menopausal women; the same was not true for the patient group, which could have introduced some variation in the results. Fifth, T2 mapping is a difficult technique to reproduce, and a lot of variation exists in the parameters used to obtain T2 maps; in addition, there are no recommendations or standard values to achieve uniformity between studies. Last,

there was a high proportion of grade 2 lesions in patients with type I EC.

In conclusion, the present study shows that the differences in the T2 values between BELs and type II EC are not statistically significant. However, the T2 mapping of MRI has the potential to quantitatively differentiate between EC, BELs, and NE as well as between type I and type II EC.

## Funding

The study was funded by Primary Research & Development Plan of Shandong Province (no. 2016GSF201095).

## Conflict of interest disclosure

The authors declared no conflicts of interest.


## References

1. Lortet-Tieulent J, Ferlay J, Bray F, Jemal A. International patterns and trends in endometrial cancer incidence, 1978-2013. *J Natl Cancer Inst.* 2018;110(4):354-361. [\[CrossRef\]](#)
2. Otero-García MM, Mesa-Álvarez A, Nikolic O, et al. Role of MRI in staging and follow-up of endometrial and cervical cancer: pitfalls and mimickers. *Insights Into Imaging.* 2019;10(1):19. [\[CrossRef\]](#)
3. Rizzo S, Femia M, Buscarino V, et al. Endometrial cancer: an overview of novelties in treatment and related imaging keypoints for local staging. *Cancer Imaging.* 2018;18(1):45. [\[CrossRef\]](#)
4. Zhu HL, Liang XD, Wang JL, Cui H, Wei LH. Hysteroscopy and directed biopsy in the diagnosis of endometrial carcinoma. *Chin Med J (Engl).* 2010;123(24):3524-3528. [\[CrossRef\]](#)
5. Beddy P, O'Neill AC, Yamamoto AK, Addley HC, Reinhold C, Sala E. FIGO staging system for endometrial cancer: added benefits of MR imaging. *Radiographics.* 2012;32(1):241-254. [\[CrossRef\]](#)
6. Nougaret S, Lakhman Y, Vargas HA, et al. From staging to prognostication: achievements and challenges of MR imaging in the assessment of endometrial cancer. *Magn Reson Imaging Clin N Am.* 2017;25(3):611-633. [\[CrossRef\]](#)
7. Park SB, Moon MH, Sung CK, Oh S, Lee YH. Dynamic contrast-enhanced MR imaging of endometrial cancer: optimizing the imaging delay for tumour-myometrium contrast. *Eur Radiol.* 2014;24(11):2795-2799. [\[CrossRef\]](#)
8. Wu LM, Xu JR, Gu HY, Hua J, Haacke EM, Hu J. Predictive value of T2-weighted imaging and contrast-enhanced MR imaging in assessing myometrial invasion in endometrial cancer: a pooled analysis of prospective studies. *Eur Radiol.* 2013;23(2):435-449. [\[CrossRef\]](#)

9. Nougaret S, Reinhold C, Alsharif SS, et al. Endometrial Cancer: Combined MR volumetry and diffusion-weighted imaging for assessment of myometrial and lymphovascular invasion and tumor grade. *Radiology*. 2015;276(3):797-808. [\[CrossRef\]](#)
10. Takayama Y, Nishie A, Togao O, et al. Amide proton transfer MR imaging of endometrioid endometrial adenocarcinoma: association with histologic grade. *Radiology*. 2018;286(3):909-917. [\[CrossRef\]](#)
11. Zhang J, Cai S, Li C, et al. Can magnetic resonance spectroscopy differentiate endometrial cancer? *Eur Radiol*. 2014;24(10):2552-2560. [\[CrossRef\]](#)
12. Yue W, Meng N, Wang J, et al. Comparative analysis of the value of diffusion kurtosis imaging and diffusion-weighted imaging in evaluating the histological features of endometrial cancer. *Cancer Imaging*. 2019;19(1):9. [\[CrossRef\]](#)
13. Hori M, Kim T, Onishi H, et al. Endometrial cancer: preoperative staging using three-dimensional T2-weighted turbo spin-echo and diffusion-weighted MR imaging at 3.0 T: a prospective comparative study. *Eur Radiol*. 2013;23(8):2296-2305. [\[CrossRef\]](#)
14. Mai J, Abubrig M, Lehmann T, et al. T2 Mapping in prostate cancer. *Invest Radiol*. 2019;54(3):146-152. [\[CrossRef\]](#)
15. Kijowski R, Blankenbaker DG, Munoz Del Rio A, Baer GS, Graf BK. Evaluation of the articular cartilage of the knee joint: value of adding a T2 mapping sequence to a routine MR imaging protocol. *Radiology*. 2013;267(2):503-513. [\[CrossRef\]](#)
16. Nebelung S, Sondern B, Oehrl S, et al. Functional MR imaging mapping of human articular cartilage response to loading. *Radiology*. 2017;282(2):464-474. [\[CrossRef\]](#)
17. Puntmann VO, Isted A, Hinojar R, Foote L, Carr-White G, Nagel E. T1 and T2 mapping in recognition of early cardiac involvement in systemic sarcoidosis. *Radiology*. 2017;285(1):63-72. [\[CrossRef\]](#)
18. Sabouri S, Chang SD, Savdie R, et al. Luminal water imaging: a new MR imaging T2 mapping technique for prostate cancer diagnosis. *Radiology*. 2017;284(2):451-459. [\[CrossRef\]](#)
19. Hoang Dinh A, Melodelima C, Souchon R, et al. Quantitative analysis of prostate multiparametric MR images for detection of aggressive prostate cancer in the peripheral zone: a multiple imager study. *Radiology*. 2016;280(1):117-127. [\[CrossRef\]](#)
20. Ghosh A, Singh T, Bagga R, Srinivasan R, Singla V, Khandelwal N. T2 relaxometry mapping in demonstrating layered uterine architecture: parameter optimization and utility in endometrial carcinoma and adenomyosis: a feasibility study. *Br J Radiol*. 2018;91(1081):20170377. [\[CrossRef\]](#)
21. McCarthy S, Scott G, Majumdar S, et al. Uterine junctional zone: MR study of water content and relaxation properties. *Radiology*. 1989;171(1):241-243. [\[CrossRef\]](#)
22. Shitano F, Kido A, Kataoka M, et al. MR appearance of normal uterine endometrium considering menstrual cycle: differentiation with benign and malignant endometrial lesions. *Acta Radiol*. 2016;57(12):1540-1548. [\[CrossRef\]](#)
23. Creasman W. Revised FIGO staging for carcinoma of the endometrium. *Int J Gynaecol Obstet* 2009;105(2):109. [\[CrossRef\]](#)
24. Hendrickson M, Ross J, Eifel P, Martinez A, Kempson R. Uterine papillary serous carcinoma: a highly malignant form of endometrial adenocarcinoma. *Am J Surg Pathol*. 1982;6(2):93-108. [\[CrossRef\]](#)
25. Le Gallo M, O'Hara AJ, Rudd ML, et al. Exome sequencing of serous endometrial tumors identifies recurrent somatic mutations in chromatin-remodeling and ubiquitin ligase complex genes. *Nat Genet*. 2012;44(12):1310-1315. [\[CrossRef\]](#)
26. Bakir B, Sanli S, Bakir VL, et al. Role of diffusion weighted MRI in the differential diagnosis of endometrial cancer, polyp, hyperplasia, and physiological thickening. *Clin Imaging*. 2017;41:86-94. [\[CrossRef\]](#)
27. Eddib A, Allaf B, Lee J, Yeh J. Risk for advanced-stage endometrial cancer in surgical specimens from patients with complex endometrial hyperplasia with atypia. *Gynecol Obstet Invest*. 2012;73(1):38-42. [\[CrossRef\]](#)
28. Polyzos NP, Mauri D, Tsioras S, Messini CI, Valachis A, Messinis IE. Intraperitoneal dissemination of endometrial cancer cells after hysteroscopy: a systematic review and meta-analysis. *Int J Gynecol Cancer*. 2010;20(2):261-267. [\[CrossRef\]](#)
29. Huss A, Ihorst G, Timme-Bronsert S, Hasenburg A, Oehler MK, Klar M. The Memorial Sloan Kettering Cancer Center Nomogram is More Accurate than the 2009 FIGO Staging System in the Prediction of Overall Survival in a German Endometrial Cancer Patient Cohort. *Ann Surg Oncol*. 2018;25(13):3966-3973. [\[CrossRef\]](#)
30. Phelippeau J, Canlorbe G, Bendifallah S, et al. Preoperative diagnosis of tumor grade and type in endometrial cancer by pipelle sampling and hysteroscopy: Results of a French study. *Surg Oncol*. 2016;25(4):370-377. [\[CrossRef\]](#)
31. Chen J, Fan W, Gu H, et al. The value of the apparent diffusion coefficient in differentiating type II from type I endometrial carcinoma. *Acta Radiol*. 2021;62(7):959-965. [\[CrossRef\]](#)
32. Meng N, Wang X, Sun J, et al. Evaluation of amide proton transfer-weighted imaging for endometrial carcinoma histological features: a comparative study with diffusion kurtosis imaging. *Eur Radiol*. 2021;31(11):8388-8398. [\[CrossRef\]](#)
33. Pintican R, Bura V, Zerunian M, et al. MRI of the endometrium - from normal appearances to rare pathology. *Br J Radiol*. 2021;94(1125):20201347. [\[CrossRef\]](#)
34. Imaoka I, Nakatsuka T, Araki T, et al. T2\* relaxometry mapping of the uterine zones. *Acta Radiol*. 2012;53(4):473-477. [\[CrossRef\]](#)



# A computer program to assess the bone scan index for Tc-99m hydroxymethylene diphosphonate: evaluation of jaw pathologies of patients with bone metastases using SPECT/CT

Ruri Ogawa   
Ichiro Ogura 

## PURPOSE

This study aimed to evaluate the jaw pathologies of patients with bone metastases using a computer program to assess the bone scan index (BSI) for Tc-99m hydroxymethylene diphosphonate (HMDP) with single-photon emission computed tomography/computed tomography (SPECT/CT).

## METHODS

Ninety-seven patients with jaw pathologies (24 with bone metastases and 73 without) were evaluated. High-risk hot spots and BSI in the patients were evaluated using the VSBONE BSI (ver.1.1) analysis software for Tc-99m HMDP that scanned SPECT/CT and automatically defined the data. The two groups were compared using the Pearson chi-square test and Mann-Whitney U test for high-risk hot spots and BSI, respectively. A *P* value of <0.05 was considered statistically significant.

## RESULTS

High-risk hot spot occurrence was significantly correlated to bone metastases [sensitivity, 21/24 (87.5%); specificity, 40/73 (54.8%); accuracy, 61/97 (62.9%); *P* < 0.001]. The number of high-risk hot spots was higher in patients with bone metastases ( $5.96 \pm 10.30$ ) than in those without ( $0.90 \pm 1.50$ ; *P* < 0.001). Furthermore, the BSI for patients with bone metastases ( $1.44 \pm 2.18\%$ ) was significantly higher than for those without ( $0.22 \pm 0.44\%$ ; *P* < 0.001).

## CONCLUSION

A computer program that assessed BSI for Tc-99m HMDP may be useful in the evaluation of patients with bone metastases using SPECT/CT.

## KEYWORDS

Bone, diagnosis, metastatic tumor, scintigraphy, single-photon emission-computed tomography

From the Quantitative Diagnostic Imaging, Field of Oral and Maxillofacial Imaging and Histopathological Diagnostics, Course of Applied Science (R.O., I.O. [ogura@ngt.ndu.ac.jp](mailto:ogura@ngt.ndu.ac.jp)), The Nippon Dental University Graduate School of Life Dentistry at Niigata, Niigata, Japan; Department of Oral and Maxillofacial Radiology (I.O.) The Nippon Dental University School of Life Dentistry at Niigata, Niigata, Japan.

Received 14 June 2021; revision requested 2 November 2021; last revision received 3 December 2021; accepted 6 December 2021.



Epub: 29.11.2022

Publication date: 31.01.2023

DOI: 10.5152/dir.2022.21999

**B**isphosphonates are inhibitors of osteoclastic bone resorption and are useful in the treatment of osteoporosis and bone metastases of cancer. However, they are also implicated in the onset of medication-related osteonecrosis of the jaw (MRONJ).<sup>1-4</sup> Bone scintigraphy can demonstrate physiological changes in the bone and is useful for detecting MRONJ.<sup>5,6</sup> Furthermore, multimodal imaging techniques, such as scintigraphy, computed tomography (CT), and magnetic resonance imaging, are useful for the detection of MRONJ.<sup>7-10</sup>

The bone scan index (BSI) is based on a review of the bone scan, visually estimating the fraction of each bone involved, and summing this across all bones to determine the percentage of total skeletal involvement.<sup>11,12</sup> BSI can be used as a bone management tool to evaluate bone scintigraphy, e.g., by providing baseline-BSI<sup>13,14</sup> and response-BSI.<sup>15,16</sup>

Recently, a computer program called VSBONE BSI was developed that could scan bone scintigraphy and automatically define the BSI for Tc-99m hydroxymethylene diphosphonate

You may cite this article as: Ogawa R, Ogura I. A computer program to assess the bone scan index for Tc-99m hydroxymethylene diphosphonate: evaluation of jaw pathologies of patients with bone metastases using SPECT/CT. *Diagn Interv Radiol.* 2023;29(1):190-194.

(HMDP).<sup>17,18</sup> The VSBONE BSI software is a deep learning-based image interpretation system that performs skeletal segmentation and the extraction of hot spots of the bone metastatic lesion from a whole-body bone scintigram, followed by automated measurement of the BSI. This program is a computer-aided detection system for scintigraphy and is useful for screening bone metastases in prostate cancer. Furthermore, in recent years, single-photon emission CT/CT (SPECT/CT) has been applied for the evaluation of oral and maxillofacial lesions.<sup>19-26</sup> However, to the best of our knowledge, no reports have been published on BSI analysis aided by software for the jaw pathologies of patients with bone metastases using SPECT/CT. This study was performed to evaluate the jaw pathologies of patients with bone metastases using a computer program to assess BSI for Tc-99m HMDP with SPECT/CT.

## Methods

The protocol was approved by the Ethics Committee of The Nippon Dental University (ECNG-R-400). After providing written informed consent, 97 patients with jaw pathologies [35 men and 62 women; mean age, 74.5 years (range, 43–92 years)] underwent SPECT/CT at our university hospital from October 2018 to July 2021. Informed consent was obtained from patients who participated in the clinical investigations. Among the jaw pathology patients, 24 patients with different cancers (eight with breast, six with lung, six with prostate, two with rectal, one with thyroid, and one with kidney cancers) and bone metastases had MRONJ with bone metastases of cancer; 73 patients were without bone metastases, including 46 with MRONJ with osteoporosis, 17 with chronic osteomyelitis, and 10 with osteoradionecrosis (Table 1). MRONJ patients were diagnosed in accordance with the 2014 American Association of Oral and

Maxillofacial Surgeons position paper.<sup>1</sup> The histopathological diagnoses of jaw pathologies were obtained after sampling during surgery or biopsy performed in all cases at our university hospital, whereas osteoporosis and bone metastases were diagnosed and treated in another hospital.

Whole-body bone SPECT/CT scans were obtained using a SPECT/CT scanner (Optima NM/CT 640, GE Healthcare, Tokyo, Japan) following our hospital's protocol.<sup>19,20</sup> Patients were administered an intravenous injection of 740 MBq of Tc-99m HMDP (Clear Bone Injectible; Nihon Medi-Physics, Tokyo, Japan) prior to the scan acquisitions. Anterior and posterior-view bone scans were acquired using a low-energy high-resolution collimator, the 140 keV photoenergy peak for Tc-99m, a scanning speed of 10 cm/min, and a 256 × 1024 matrix of 2.1 mm pixel size.

The SPECT/CT data were obtained using the MI software and workstation (Q. Volumetrix and Xeleris 4DR, GE Healthcare Japan, Tokyo, Japan). The evaluation of high-risk hot spots and BSI in the patients was performed using commercially available software for Tc-99m HMDP (VSBONE BSI v.1.0; Nihon Medi-Physics, Tokyo, Japan), which scanned SPECT/CT and defined the data automatically. We defined the high-risk hot spots as suspected bone metastases. Furthermore, true positives for osseous metastatic diseases

were obtained by biopsy/pathologically in another hospital.

## Statistical analysis

The high-risk hot spots and BSI of patients with/without bone metastases were compared using the Pearson chi-square test and Mann-Whitney U test, respectively. Statistical analyses employed the SPSS Statistics (v.26) software package (IBM Japan, Tokyo, Japan). A *P* value of <0.05 was considered statistically significant.

## Results

The BSI for the jaw pathologies of patients with bone metastases evaluated by SPECT/CT is presented in Table 2. High-risk hot spots were significantly correlated to bone metastases [sensitivity, 21/24 (87.5%); specificity, 40/73 (54.8%); accuracy, 61/97 (62.9%); *P* < 0.001]. High-risk hot spot numbers in patients with bone metastases (5.96 ± 10.30) were significantly higher than in patients without bone metastases (0.90 ± 1.50, *P* < 0.001). Furthermore, the BSI of patients with bone metastases (1.44 ± 2.18%) was significantly higher than that of patients without bone metastases (0.22 ± 0.44%, *P* < 0.001). Figures 1 and 2 show MRONJ patients with and without bone metastases, respectively.

**Table 1.** The characteristics of jaw pathologies of patients, derived using a computer program to assess the bone scan index

Parameters	Bone metastases	
	With	Without
Number of patients	24	73
Age (years)		
Mean ± SD (range)	70.6 ± 7.1 (55 – 84)	75.8 ± 10.1 (43 – 92)
Sex		
Men	13	22
Women	11	51
Underlying disease		
MRONJ with bone metastases		
Breast cancer	8	
Lung cancer	6	
Prostate cancer	6	
Rectal cancer	2	
Thyroid cancer	1	
Kidney cancer	1	
MRONJ with osteoporosis		46
Chronic osteomyelitis of the jaw		17
Osteoradionecrosis of the jaw		10

SD, standard deviation; MRONJ, medication-related osteonecrosis of the jaw.

### Main points

- We evaluated the jaw pathologies of patients with bone metastases using a computer program to assess their bone scan index (BSI) for Tc-99m hydroxymethylene diphosphonate with single-photon emission computed tomography/computed tomography (SPECT/CT).
- Patients with bone metastases had a significantly higher BSI than those without bone metastases.
- The computer program could be useful for the evaluation of patients with bone metastases using SPECT/CT.



**Table 2.** The bone scan index of the jaw pathologies of patients with bone metastases, derived using single-photon emission computed tomography/ computed tomography

Parameters	Bone metastases		Total	P value
	With (n = 24)	Without (n = 73)	(n = 97)	
High-risk hot spots				< 0.001
Positive	21 (87.5%)	33 (45.2%)	54 (55.7%)	
Negative	3 (12.5%)	40 (54.8%)	43 (44.3%)	
High-risk hot spot numbers				< 0.001
Mean ± SD	5.96 ± 10.30	0.90 ± 1.50	2.15 ± 5.65	
Range	0 – 46	0 – 8	0 – 46	
Bone scan index (%)				< 0.001
Mean ± SD	1.44 ± 2.18	0.22 ± 0.44	0.52 ± 1.25	
Range	0.00 – 8.26	0.00 – 2.12	0.00 – 8.26	

SD, standard deviation.

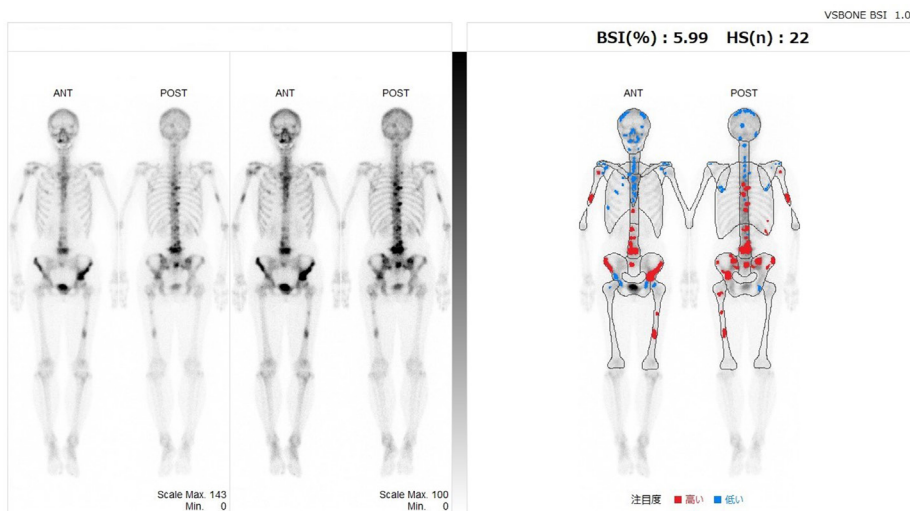


**Figure 1.** Medication-related osteonecrosis of the jaw of the right side of the maxilla in a 68-year-old woman with breast cancer and multiple bone metastases. The bone scan index and high-risk hot spot number (n) are 5.99% and 22, respectively. The red and blue areas indicate high-risk and low-risk hot spots, respectively.

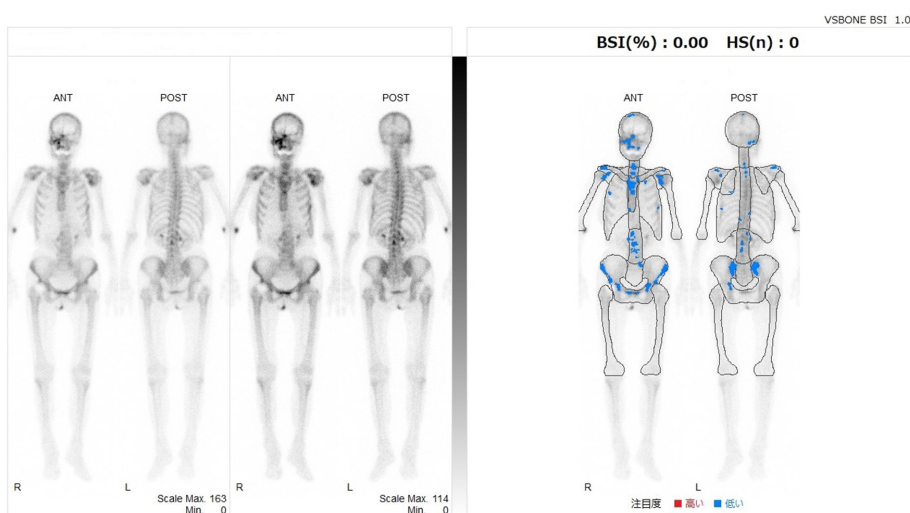


**Figure 2.** Medication-related osteonecrosis of the jaw of the right side of the maxilla in a 90-year-old woman with osteoporosis without bone metastases. The bone scan index and high-risk hot spot number (n) are 0.00% and 0, respectively. The red and blue areas indicate high-risk and low-risk hot spots, respectively.

## Discussion

We investigated the performance of a computer program to assess BSI for Tc-99m HMDP in the jaw pathologies of patients with bone metastases via SPECT/CT. The results showed that high-risk hot spots were significantly correlated to bone metastases, and the BSI of patients with bone metastases was significantly higher than of those without. Planar bone scintigraphy is a standard radiological technique used to detect skeletal metastases in patients with prostate cancer.<sup>27</sup> Petersen et al.<sup>28</sup> evaluated the response of bone metastasis in prostate cancer, particularly the correlation between computer-assisted BSI responses and clinical response classification. The findings indicated that the BSI software should be useful for the evaluation of bone metastases.

Sabbatini et al.<sup>13</sup> showed that the BSI quantifies the extent of skeletal involvement caused by the tumor and allowed for the stratification of patients with a distinct prognosis for clinical trials. Kaboteh et al.<sup>14</sup> developed an automated method for calculating BSI that could be used to calculate the number of new lesions and changes in BSI of serial bone scans. Dennis et al.<sup>15</sup> retrospectively examined the serial bone scans of patients with castration-resistant metastatic prostate cancer enrolled in four clinical trials. Mitsui et al.<sup>16</sup> showed that the BSI reflected bone metastasis' response to chemotherapy. However, to the best of our knowledge, little has been published regarding the usefulness of BSI for the jaw pathologies of patients using SPECT/CT. Our results showed that high-risk hot spots were significantly correlated to bone metastases [sensitivity, 21/24 (87.5%); specificity, 40/73 (54.8%); accuracy, 61/97 (62.9%);  $P < 0.001$ ]. Furthermore, the BSI of patients with bone metastases ( $1.44 \pm 2.18\%$ ) was significantly higher than that of patients without bone metastases ( $0.22 \pm 0.44\%$ ,  $P < 0.001$ ). We found that the BSI analysis software for Tc-99m HMDP could be useful for the evaluation of patients with bone metastases using SPECT/CT.

This study has several limitations. The sample was relatively small. The most interesting feature of BSI in cancer patients is the ability to detect and diagnose bone metastases early and perform follow-up procedures. However, the bone scan are not specific for malignant lesions or metastasis. There are numerous benign etiologies with a similar scintigraphic appearance as malignant lesions.<sup>29,30</sup> Therefore, diagnoses for malignant lesions or metastasis should be performed using multimodal imag-

ing. SPECT and SPECT/CT bone scans are at least twice as sensitive in detecting bone abnormalities, for malignant and benign etiologies. Based on scintigraphic appearance alone, it is not possible to differentiate between malignant and benign jaw pathologies.<sup>29,30</sup> A standardized uptake value (SUV) for the evaluation of jaw pathologies has been reported for Tc-99m HMDP SPECT/CT,<sup>19,20,23-25</sup> but further research in the jaw pathologies of patients is necessary to validate these results, particularly the relationship between BSI and SUV.

In conclusion, we evaluated the jaw pathologies of patients with bone metastases using a computer program to assess BSI for Tc-99m HMDP with SPECT/CT. The BSI of patients with bone metastases was significantly higher than that of patients without bone metastases. This computer program could be useful for the evaluation of patients with bone metastases using SPECT/CT.

### Acknowledgment

We thank Edanz (<https://jp.edanz.com/ac>) for editing a draft of this manuscript.

### Conflict of interest disclosure

The authors declared no conflicts of interest.

### References

- Ruggiero SL, Dodson TB, Fantasia J, et al. American Association of Oral and Maxillofacial Surgeons position paper on medication-related osteonecrosis of the jaw--2014 update. *J Oral Maxillofac Surg.* 2014;72(10):1938-1956. [Crossref]
- Ogura I, Kobayashi E, Nakahara K, Haga-Tsujimura M, Igarashi K, Katsumata A. Computer programme to assess mandibular cortex morphology in cases of medication-related osteonecrosis of the jaw with osteoporosis or bone metastases. *Imaging Sci Dent.* 2019;49(4):281-286. [Crossref]
- Ogura I, Minami Y, Ono J, et al. CBCT imaging and histopathological characteristics of osteoradionecrosis and medication-related osteonecrosis of the jaw. *Imaging Sci Dent.* 2021;51(1):73-80. [Crossref]
- Ogawa R, Minami Y, Ono J, et al. Medication-related osteonecrosis of the jaw in a patient with multiple myeloma: an unusual case with tumor in the surgical specimen. *Oral Radiol.* 2021;38(2):288-291. [Crossref]
- O'Ryan FS, Khoury S, Liao W, et al. Intravenous bisphosphonate-related osteonecrosis of the jaw: bone scintigraphy as an early indicator. *J Oral Maxillofac Surg.* 2009;67(7):1363-1372. [Crossref]
- Morag Y, Morag-Hezroni M, Jamadar DA, et al. Bisphosphonate-related osteonecrosis of the jaw: a pictorial review. *Radiographics.* 2009;29(7):1971-1984. [Crossref]
- Bisdas S, Chambron Pinho N, Smolarz A, Sader R, Vogl TJ, Mack MG. Bisphosphonate-induced osteonecrosis of the jaws: CT and MRI spectrum of findings in 32 patients. *Clin Radiol.* 2008;63(1):71-77. [Crossref]
- Ogura I, Sasaki Y, Kameta A, Sue M, Oda T. Characteristic multimodal imaging of medication-related osteonecrosis of the jaw: comparison between oral and parenteral routes of medication administration. *Pol J Radiol.* 2017;82:551-560. [Crossref]
- Ogura I, Oda T, Sue M, Sasaki Y, Hayama K. Comparison between squamous cell carcinoma and inflammatory diseases of the oral and maxillofacial region using gallium-67 scintigraphy with computed tomography and magnetic resonance imaging. *Pol J Radiol.* 2018;83:452-458. [Crossref]
- Ogura I, Sasaki Y, Sue M, Oda T, Kameta A, Hayama K. Tc-99m hydroxymethylene diphosphonate scintigraphy, computed tomography, and magnetic resonance imaging of osteonecrosis in the mandible: osteoradionecrosis versus medication-related osteonecrosis of the jaw. *Imaging Sci Dent.* 2019;49(1):53-58. [Crossref]
- Erdi YE, Humm JL, Imbriaco M, Yeung H, Larson SM. Quantitative bone metastases analysis based on image segmentation. *J Nucl Med.* 1997;38(9):1401-1406. [Crossref]
- Imbriaco M, Larson SM, Yeung HW, et al. A new parameter for measuring metastatic bone involvement by prostate cancer: the bone scan index. *Clin Cancer Res.* 1998;4(7):1765-1772. [Crossref]
- Sabbatini P, Larson SM, Kremer A, et al. Prognostic significance of extent of disease in bone in patients with androgen-independent prostate cancer. *J Clin Oncol.* 1999;17(3):948-957. [Crossref]
- Kaboteh R, Damber JE, Gjertsson P, et al. Bone scan index: a prognostic imaging biomarker for high-risk prostate cancer patients receiving primary hormonal therapy. *EJNMMI Res.* 2013;3(1):9. [Crossref]
- Dennis ER, Jia X, Mezheritskiy IS, et al. Bone scan index: a quantitative treatment response biomarker for castration-resistant metastatic prostate cancer. *J Clin Oncol.* 2012;30(5):519-524. [Crossref]
- Mitsui Y, Shiina H, Yamamoto Y, et al. Prediction of survival benefit using an automated bone scan index in patients with castration-resistant prostate cancer. *BJU Int.* 2012;110(11 Pt B):628-634. [Crossref]
- Shimizu A, Wakabayashi H, Kanamori T, et al. Automated measurement of bone scan index from a whole-body bone scintigram. *Int J Comput Assist Radiol Surg.* 2020;15(3):389-400. [Crossref]
- Yoshida A, Higashiyama S, Kawabe J. Assessment of a software for semi-automatically calculating the bone scan index on bone scintigraphy scans. *Clin Imaging.* 2021;78:14-18. [Crossref]
- Ogura I, Kobayashi E, Nakahara K, Igarashi K, Haga-Tsujimura M, Toshima H. Quantitative SPECT/CT imaging for medication-related osteonecrosis of the jaw: a preliminary study using volume-based parameters, comparison with chronic osteomyelitis. *Ann Nucl Med.* 2019;33(10):776-782. [Crossref]
- Ogura I, Sasaki Y, Sue M, Oda T, Kameta A, Hayama K. Tc-99m hydroxymethylene diphosphonate SPECT/CT for the evaluation of osteonecrosis of the jaw: preliminary study on diagnostic ability of maximum standardized uptake value. *Clin Radiol.* 2020;75(1):46-50. [Crossref]
- Ninomiya K, Toya S, Ogura I. Single-photon emission computed tomography/computed tomography for evaluation of salivary gland dysfunction: preliminary study on diagnostic ability of maximum standardized uptake value. *Oral Radiol.* 2020;36(2):163-167. [Crossref]
- Oohashi M, Toshima H, Hayama K, Ogura I. Gallium-67 SPECT-CT for the evaluation of head and neck: preliminary study on maximum standardized uptake value in lesions, and in the parotid and submandibular glands. *Pol J Radiol.* 2020;85:224-229. [Crossref]
- Toshima H, Ogura I. Assessment of inflammatory jaw pathologies using bone SPECT/CT maximum standardized uptake value. *Dentomaxillofac Radiol.* 2020;49(8):20200043. [Crossref]
- Minami Y, Ogura I. Bone single-photon emission computed tomography-CT peak standardized uptake value for chronic osteomyelitis, osteoradionecrosis and medication-related osteonecrosis of the jaw. *J Med Imaging Radiat Oncol.* 2021;65(2):160-165. [Crossref]
- Ogawa R, Ogura I. Analysis of medication-related osteonecrosis of the jaw with bone SPECT/CT: relationship between patient characteristics and maximum standardized uptake value. *Dentomaxillofac Radiol.* 2021;50(8):20200516. [Crossref]
- Minami Y, Ogura I. A clinical pilot study of salivary gland secretion for xerostomia patients with Sjögren's syndrome using SPECT/CT. *Gerodontology.* 2021;39(3):297-301. [Crossref]
- McLoughlin LC, O'Kelly F, O'Brien C, et al. The improved accuracy of planar bone scintigraphy by adding single photon emission computed tomography (SPECT-CT) to detect skeletal metastases from prostate cancer. *Ir J Med Sci.* 2016;185(1):101-105. [Crossref]

28. Petersen LJ, Gade M, Fonager RF, et al. Response evaluation of bone metastasis in prostate cancer: preliminary comparison of computerized bone scan index versus standardized clinical criteria. *Hell J Nucl Med.* 2021;24(1):2-9. [\[Crossref\]](#)
29. Joshi JK, Kushner GM, Bhatt G, Bhatt AD, Civelek AC. Role of nuclear medicine imaging in recognizing different causes of osteonecrosis of the jaw. *Clin Nucl Med.* 2013;38(1):40-43. [\[Crossref\]](#)
30. Bhatt G, Bhatt A, Dragun AE, Li XF, Civelek AC. Bisphosphonate-related osteonecrosis of the jaw mimicking bone metastasis. *Case Rep Oncol Med.* 2014;2014:281812. [\[Crossref\]](#)



# Sacral injury and influencing factors after ultrasonic ablation of uterine fibroids $\leq 30$ mm from the sacrum

An-Qi Zheng

Jin-Yun Chen

Zhi-Bo Xiao

Rong Zhang

Jin Bai

## PURPOSE

To study sacral injuries and influencing factors after ultrasonic ablation of uterine fibroids no more than 30 mm from the sacrum.

## METHODS

A total of 406 patients with uterine fibroids who underwent percutaneous ultrasound ablation were analyzed retrospectively. All patients underwent contrast-enhanced magnetic resonance imaging (MRI) scans before and after high-intensity focused ultrasound. The abnormal signal intensity (low signal intensity on T1WI and high signal intensity on T2WI) on the postoperative MRIs was indicative of a sacral injury. The patients were divided into a sacrum injury group and a sacrum non-injury group. The relationship between fibroid characteristics, ultrasound ablation parameters, and injury was analyzed using univariate and multivariate analyses.

## RESULTS

There were 139 cases of sacral injury (34.24%). When the distance from the fibroid's dorsal side to the sacrum was 0–10 mm, the risk assessment showed that the danger of sacral injury increased by 1.85 times and 3.03 times compared with that at a distance of 11–20 or 21–30 mm. Furthermore, the risk of sacral injury increased by 1.89 times and 3.23 times when the therapeutic dose (TD) of a fibroid was >500 KJ compared with that of a fibroid with TD= 250–500 KJ and <250 KJ.

## CONCLUSION

A distance of 10 mm or less and a TD of >500 KJ were significantly correlated with sacral injury. The distance from the fibroid's dorsal side to the sacrum and the TD were the main causes of injury to the sacrum. A distance of 10 mm or less and a TD of >500 KJ carried higher injury risks, while a distance of 21–30 mm and a TD of <250 KJ were the most appropriate circumstances to reduce the risk of sacral injury.

## KEYWORDS

High-intensity focused ultrasound (HIFU), magnetic resonance imaging, sacrum injury, ultrasound ablation, uterine fibroids

From the Ultrasound in Medicine and Engineering (A.-Q.Z, J.-Y.C. ✉ chenjy@cqmu.edu.cn, R.Z., J.B.), State Key Laboratory, Chongqing, China; Therapeutic Center of Ultrasound Ablation (J.-Y.C., R.Z.), The First Affiliated Hospital of Chongqing Medical University, Chongqing, China; Department of Radiology (Z.-B.X.), The First Affiliated Hospital of Chongqing Medical University, Chongqing, China.

Received 16 April 2021; revision requested 19 June 2021; last revision received 19 October 2021; accepted 22 October 2021.



Epub: 29.11.2022

Publication date: 31.01.2023

DOI: 10.5152/dir.2022.21407

With an incidence of 20%–40%,<sup>1,2</sup> uterine fibroids are the most common benign tumors found in the female reproductive system. As a non-invasive emerging technology, high-intensity focused ultrasound (HIFU) has been widely recognized in clinical practice.<sup>3-5</sup> However, due to its physical characteristics (refraction, reflection, etc.) and biological effects (cavitation effect and thermal effect),<sup>6</sup> its ultrasonic waves may cause varying degrees of thermal damage to surrounding tissues, resulting in abdominal wall damage,<sup>7</sup> sacrum and nerve pain,<sup>8,9</sup> abnormal vaginal discharge,<sup>10</sup> and other adverse effects. The greater the transmission distance from the transducer's ultrasound beam to the fibroids, the more complex the interaction between the ultrasound and the tissue. In addition, the incidence of adverse reactions increases.<sup>11</sup>

Magnetic resonance imaging (MRI) is characterized by its high-resolution imaging of soft tissue. The technique can be used to show the differences between tissue characteristics be-

fore and after HIFU and is often utilized to evaluate an injury after HIFU. Cun et al.<sup>8</sup> reported that 135 of 346 patients with single fibroids (39.0%) suffered a sacral injury after HIFU. Moreover, Li et al.<sup>9</sup> stated that 87 of 267 patients (32.6%) developed MRI signal intensity changes in the sacrum. After analyzing the factors of sacral injury, they found that the distance from the dorsal side of the fibroid to the sacrum was significantly correlated with MRI signal intensity changes in the sacrum. The shorter the distance, the higher the risk of sacral injury. Although the correlation between abnormal sacral signal intensity and clinical adverse events has not been reported, the long-term effects still require further attention, as minimizing secondary injury is an important strategy to avoid long-term complications in clinical practice. Therefore, a safe distance between fibroids and the sacrum should be ensured to avoid sacral injury.<sup>12</sup> A previous study suggested that >25 mm would be a safe distance.<sup>13</sup> However, Li et al.<sup>9</sup> believed that the transducer's focus should be kept at least 30 mm away from the sacrum. Such a case-screening strategy would result in the exclusion of too many patients with uterine fibroids. Therefore, it is necessary to further study sacral injuries and the influencing factors after the ultrasonic ablation of uterine fibroids adjacent to the sacrococcygeal region to provide a basis for a more accurate clinical selection of cases.

This study aimed to use MRI to evaluate sacral injuries after the ultrasonic ablation of uterine fibroids adjacent to the sacrococcygeal region and to analyze the risk factors. It provides the basis for a selection of ultrasonic ablation indicators, the formulation of an ablation surgical plan, and the adjustment of the therapeutic dose (TD) for uterine fibroids adjacent to the sacrococcygeal region.

#### Main points

- Ultrasonic ablation of uterine fibroids adjacent to the sacrococcygeal region can produce satisfactory ablation.
- Sacral injury will occur after the ultrasonic ablation of uterine fibroids adjacent to the sacrococcygeal region. The incidence remained similar to that of previous studies on undefined uterine fibroids adjacent to the sacrococcygeal region.
- A distance no greater than 10 mm and a TD greater than 500 KJ carried higher risks of injury. A distance of 21–30 mm and a TD less than 250 KJ were the most appropriate parameters for focused ultrasound ablation of uterine fibroids.

## Methods

### General data

Before HIFU treatment, the details were discussed with all patients, who then signed a consent form. This retrospective study was approved by our institutional review board (Ethics approval number: 2013–16), and informed consent was waived because the data were anonymized. All procedures followed were in accordance with ethical standards of the hospital and the Declaration of Helsinki.

The data from 406 patients who received ablation therapy in the First Affiliated Hospital of Chongqing Medical University between January 2014 to December 2018 were collected and analyzed. The inclusion criteria were: 1) patients over 18 years of age, married, and with no recent fertility requirements, 2) patients with fibroids ranging in size from 4–10 cm, and 3) patients with uterine fibroids adjacent to the sacrococcygeal region, with the distance between the fibroids' dorsal sides and the sacrum being no more than 30 mm. The exclusion criteria were: 1) patients with preoperative fibroid degeneration and contrast-enhanced MRIs showing no perfusion area presence, 2) patients with a preoperative history of HIFU, uterine artery embolization, or myomectomy, and 3) patients with a MRI contraindication or MRI contrast agent allergy.

### HIFU ablation

Before HIFU ablation, all patients underwent bowel and skin preparation. A Model-JC Focused Ultrasound Tumor Therapeutic System (Chongqing Haifu Medical Technology Co., Ltd, Chongqing, China) was used for ablation. The working frequency of the ultrasonic transducer used in this study was 0.8 MHz, and the physical focal area was  $1.5 \times 1.5 \times 10$  mm. Each patient was placed on the treatment table in a prone position so that the skin of the abdomen was immersed in low-temperature degassed water. In addition, for conscious sedation, they were intravenously administered with fentanyl citrate (Yichang Renfu Pharmaceutical Co., Ltd, Yichang, China) and midazolam (Jiangsu Enhua Pharmaceutical Co., Ltd, Jiangsu, China). Ablation was performed under the real-time guidance of the ultrasonographic device. The starting point was 10 mm from the boundary of the fibroid's (sacral side) deep surface, and the distance from the focal point to the surface of the sacrum had to be greater than 15 mm. During the procedure, the acoustic power, sonication

time, and cooling time were adjusted until the patient was comfortable. The acoustic power was maintained within 300–400 W, with a sonication time above 700 s per hour. When the monitoring ultrasound observed a significant increase in the target area's grayscale, the treatment could be terminated if the scope covered the planned treatment area completely. The perfusion in the fibroid was further observed by contrast-enhanced ultrasound. If there was almost no blood perfusion in the fibroid, the ablation was considered satisfactory. If the ablation was unsatisfactory, supplementary treatment was performed after 10 min. If the imaging was unsatisfactory due to the deep location of the fibroid, the treatment was ended at the planned dose calculated per unit volume. All the treatment parameters were recorded immediately after HIFU, including average power, treatment time, sonication time, TD, and post-treatment adverse effects. The dose–time intensity, energy efficiency factor (EEF) [i.e., the energy required for tissue ablation per unit volume ( $J/cm^3$ )] were calculated.

### MRI examination

All patients underwent MRI examinations within 1 week before HIFU and within 3 days following HIFU. An HDxt 3.0-T MRI scanner (Signa HD Excite, GE Healthcare, USA) and 8-channel phased-array abdominal coils were used. The patient was asked to lie in the supine position, and the scanning range was the iliac crest to the lower edge of the symphysis pubis. The scanning sequence and parameters were as follows: 1) plain scanning: T1 weighted image (T1WI) FSE (TR 270 ms, TE 2.1 ms, slice thickness 5 mm, slice spacing 1 mm), 2) plain scanning: T2 weighted image (T2WI) FRFSE (TR 3400 ms, TE 110 ms, slice thickness 5 mm, slice spacing 1.5 mm), and 3) enhanced scanning of LAVA (TR 4.2 ms, TE 2.0 ms, slice thickness 2.5 mm, slice spacing 0.5 mm). A gadolinium bisamine injection was used as the contrast-enhancing agent (Omniscan, General Electric Pharmaceutical Co., Ltd, Shanghai, China) (0.5 mmol/mL, 15–20 mL).

### MRI evaluation

The uterine position, fibroid position, and fibroid type were observed on the preoperative T2WI. The thickness of the abdominal wall, the long diameter, anteroposterior diameter, transverse diameter of the uterine and fibroid, the shortest distance from the ventral side of the fibroid to the skin, the shortest distance from the center of the fibroid to the sacrum, and the shortest dis-

tance from the dorsal side of the fibroid to the sacrum were measured. On the postoperative contrast-enhanced MRI, the long diameter, anteroposterior diameter, and transverse diameter of the non-perfusion area were determined. The uterine, fibroid, and non-perfusion area volumes were calculated. The volume calculation formula was  $V = 0.5233 \times D_1 \times D_2 \times D_3$ , and non-perfused volume rate (NPVR) = non-perfused volume (NPV)/fibroid volume  $\times 100\%$ . Compared with the preoperative MR images, the postoperative MR images showed the following: the sacrum displayed varying degrees of strip signal intensity changes, a low signal intensity on T1WI, a high signal intensity on T2WI, and a high signal intensity or non-enhanced area on the contrast-enhanced MRI.<sup>8</sup> The analyses and measurements of the imaging data were performed by two experienced radiologists. In the event of a discrepancy, there were consultations and discussions with senior radiologists.

### Statistical analysis

Statistical analyses were performed using SPSS 23.0 (IBM, USA) software. Measurement data that conformed to a normal distribution were expressed as mean  $\pm$  standard deviation. Skewed distribution data were expressed as median and interquartile ranges, and categorical data were expressed as percentages. With the sacral injury as a dependent variable, the clinical characteristics of patients and ultrasonic ablation parameters were considered covariates. The different influencing factors were subjected to univariate analysis. An independent-sample t-test was used for the normally distributed data measured, and the Mann-Whitney U test was used for skewed distribution data. In addition,

the  $\chi^2$  test or Fisher's exact test was used to compare count data. The significant independent variables in the univariate analysis were included in the multivariate analysis and were analyzed in a binary logistic regression analysis. The Hosmer-Lemeshow test was used to evaluate the fit of the model, while multicollinearity diagnosis was performed for all the independent variables. Furthermore, the linear relationship between the independent variables and the outcome variables was analyzed, and an assessment was conducted on the extreme values that might have affected the model's construction. The results of the multivariate analysis were set as dummy variables, and a logistic regression model was used for risk assessment. A value of  $P < 0.05$  was statistically different.

## Results

### The general situation

A total of 406 patients were included, with an average age of  $39 \pm 6.54$  years (range: 21–53 years). There were 406 fibroids, including 123 (30.3%) on the anterior wall, 138 (34.0%) on the posterior wall, 114 (28.8%) on the lateral wall, and 31 (7.6%) on the fundus. In addition, there were 279 intramural fibroids (68.7%), 92 subserosal fibroids (22.7%), and 35 submucosal fibroids (8.6%). The distance from the fibroid's dorsal side to the sacrum was 0–30 mm, with an average distance of  $14.6 \pm 8.6$  mm. The NPVR was 25.1%–100.0%, with an average of  $71.5 \pm 18.4\%$ .

### Sacral injury

Among the 406 patients, 139 (34.24%) developed sacral injuries. The MRIs of the sacrum injuries showed normal sacrum morphologies and structures. Areas with signal

intensity changes were strip-shaped and often noticed via high signal intensity or high-low mixed signal intensity on the T2WIs, with slightly enhanced or non-enhanced areas on contrast-enhanced MRIs (Figures 1, 2).

### Relationship between sacral injury and clinical features

The 406 patients were divided into two groups: 139 in the sacrum injury group and 267 in the sacrum non-injury group. There were statistically significant differences between the two groups in fibroid location and the distance from the dorsal side of the fibroid to the sacrum ( $P < 0.05$ ). The incidence of sacral injury for fibroids on the posterior wall was 42.8% (ranking the highest). The incidences of sacral injury on patients with fibroid on the anterior wall, lateral wall, and the fundus were 27.6%, 29.85%, and 38.7%, respectively. In the sacrum injury group, the distance from the dorsal side of the fibroid to the sacrum was shorter than that of the non-injury group (Table 1).

### Relationship between sacral injury and ultrasonic ablation parameters

There were statistically significant differences between the two groups in treatment time, sonication time, TD, dose-time intensity, NPVR, and EEF (all  $P < 0.017$ ). The NPVR of the sacrum injury group was lower than that of the non-injury group. Moreover, the treatment time, sonication time, TD, dose-time intensity, and EEF of the injury group were all higher than those of the non-injury group (Table 2).

### Risk assessment of sacral injury

The univariate analysis revealed all the factors related to the sacral injury, including

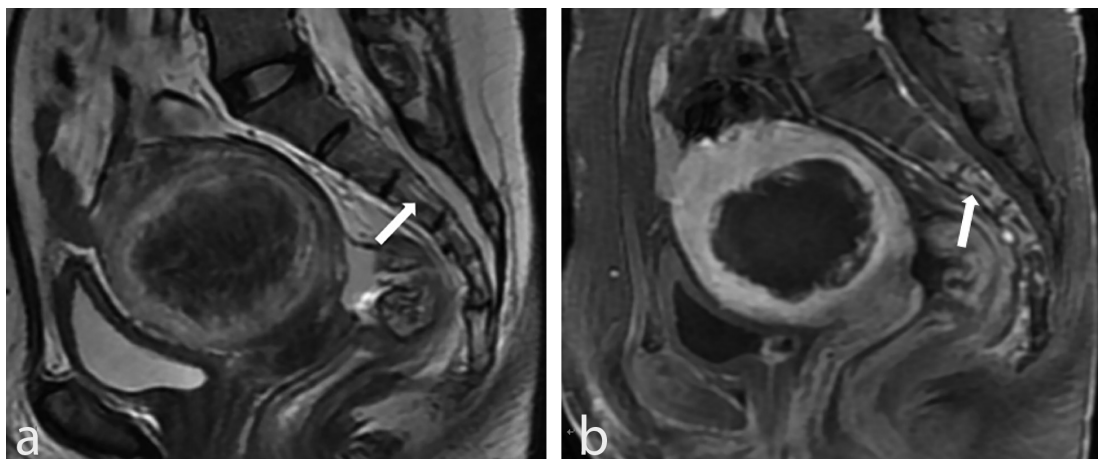


**Figure 1.** Sacral injury: sagittal view of MRI results obtained from a 44-year-old patient with uterine fibroids after high-intensity focused ultrasound showed normal morphology and structure in the sacrum. (a) The postoperative T2WI showed a strip-shaped high signal intensity of the 2<sup>nd</sup>–4<sup>th</sup> cones in the sacrum (arrow). (b) The postoperative contrast-enhanced MRI showed a slightly enhanced strip-shaped high signal intensity (arrow). MRI, magnetic resonance imaging.

the fibroid location, distance from the dorsal side of the fibroid to the sacrum, treatment time, sonication time, TD, dose–time intensity, NPVR, and EEF. These variables were included in the multivariate analysis, and the binary logistic regression analysis revealed that the distance from the dorsal side of the fibroid to the sacrum and TD were independent influencing factors on sacral injury. The shorter the distance from the dorsal side of the fibroid to the sacrum, the more easily the sacrum could be damaged. The higher the TD, the higher the incidence of sacral injury. The distances from the dorsal sides of the fibroids to the sacrum were 0–10, 11–20, and 21–30 mm. Meanwhile, the incidence rates of sacral injury were 51.1% (71/139), 31.7% (44/139), and 17.3% (24/139), respectively. The incidences of sacral injury at TD > 500 KJ, 250–500 KJ, and <250 KJ were 44.6% (62/139), 38.1% (53/139), and 17.3% (24/139), respectively. The risk of sacral in-

jury increased by 1.85 and 3.03 times when the distance from the dorsal side of a fibroid to the sacrum was 0–10 mm, compared with 11–20 or 21–30 mm. The risk of sacral injury in fibroids with a dose of >500 KJ was 1.89 times and 3.23 times higher, respectively, than with a dose of 250–500 KJ and <250 KJ (Table 3).

#### Adverse events after HIFU

Among the 406 patients, 95 (23.40%) developed adverse effects after HIFU. A total of 118 adverse effects were observed. Of these, 84.74% (100/118) were classified as Class A, 14.41% (17/118) were classified as Class B, and 0.85% (1/118) were classified as Class C. However, no Class D, E, or F adverse effects were observed in this study. The major adverse events were abdominal discomfort, sacrococcygeal pain, abnormal vaginal discharge, and pain or numbness of the lower limbs. The incidence of sacrococcygeal pain

was 8.6% in the sacrum injury group and 9% in the non-injury group, which were similar at  $P = 1.000$ . However, in the sacrum injury group, two patients experienced obvious pain, which disappeared 3 and 7 days, respectively, after NSAIDs were administered for pain relief. With Class B adverse effects, there was no statistical significance in incidence between either group ( $P > 0.05$ ). In the non-injury group, one patient (0.4%) experienced pain and numbness in their lower limbs. The pain disappeared 3 months after using NSAIDs (Table 4).

#### Discussion

The principle of HIFU ablation for uterine fibroids is to focus the *in vitro* ultrasonic waves on the *in vivo* tumor tissues so that the temperature of the target area can be instantaneously increased to 60°C–100°C, leading to coagulative necrosis of tissues and tumor

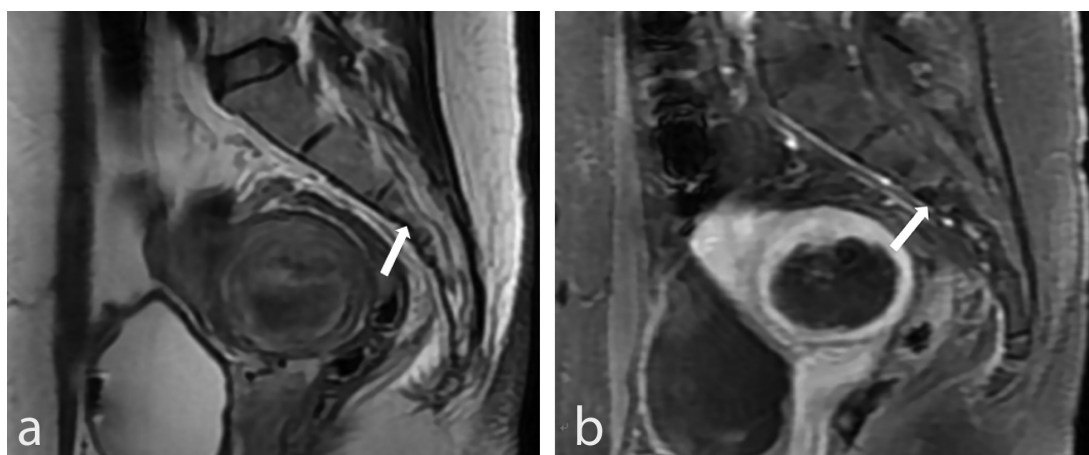


**Figure 2.** Sacral injury: sagittal view of MRI obtained from a 36-year-old patient with uterine fibroids after high-intensity focused ultrasound showed normal morphology and structure in the sacrum. (a) The postoperative T2WI showed a strip-shaped high–low mixed signal intensity of the 2<sup>nd</sup>–4<sup>th</sup> cones in the sacrum (arrow). (b) The postoperative contrast-enhanced MRI showed a non-enhanced area (arrow). MRI, magnetic resonance imaging.

Table 1. A comparison between the clinical features of the sacrum injury group and the sacrum non-injury group			
	Injury group (n = 139)	Non-injury group (n = 267)	P
Age (years)	41 (21–52)	41 (21–53)	0.86
Height (cm)	158 (146–173)	158 (144–178)	0.78
Weight (kg)	55 (39–80)	55 (40–87)	0.10
BMI (kg/cm <sup>2</sup> )	22.6 (15.8–30.5)	22.3 (15.4–35.7)	0.72
Thickness of abdominal wall (mm)	22 (9–38)	22 (8–52)	0.098
Position of the uterus (anteverted, mid-position, retroverted)	88/17/34	149/40/78	0.35
Volume of fibroid (cm <sup>3</sup> )	282.4 (42.1–1121.3)	268.6 (64.6–862.4)	0.12
Location of fibroids (adjacent, posterior wall, lateral wall, fundus)	34/59/34/12	89/79/80/19	0.044
Type of fibroid (intramural, subserosal, submucosal)	103/22/14	170/70/21	0.056
Volume of fibroid (cm <sup>3</sup> )	93.4 (33.9–549.2)	85.4 (34–584)	0.21
Fibroid ventral side to the skin (mm)	48 (14–117)	42 (11–119)	0.34
Fibroid center to the sacrum (mm)	42 (9–70)	42 (21–75)	0.11
Fibroid dorsal side to the sacrum (mm)	10 (0–30)	14 (0–30)	<0.001

BMI, body mass index.

death.<sup>14,15</sup> Previous studies have confirmed that HIFU ablation of uterine fibroids is safe and effective.<sup>3,16-18</sup> However, in the process of ultrasonic transmission, tissues along the acoustic pathway absorb energy and cause thermal damage. Also, thermal diffusion during the heating of the target tissue may cause thermal damage to the surrounding tissues. Previous studies have found that changes in signal intensity in the sacrum can be observed on MRIs after HIFU.<sup>8,9</sup> Therefore, a safe distance from the fibroid to the sacrum should be maintained during treatment. Some scholars believe that a distance above 25 mm is appropriate.<sup>13</sup> In this study, real-world data were used to focus on the sacral injury after the ultrasonic ablation of

uterine fibroids  $\leq 30$  mm from the sacrum. This was to study its influencing factors and investigate whether the uterine fibroid adjacent to the sacrococcygeal region was an indicator for ultrasonic ablation. This study provides the basis of the ablation scheme for the uterine fibroid adjacent to the sacrococcygeal region.

In this study, the distance from the focus to the surface of the sacrum was controlled by more than 15 mm during ultrasonic ablation, and the safety of the ablation was controlled based on patient tolerance. Among the 406 patients with uterine fibroids, the distance from the dorsal side of the fibroid to the sacrum was 0–30 mm, with an average

distance of  $15.4 \pm 8.7$  mm. The average NPVR was  $71.5 \pm 18.4\%$ , which is slightly lower than the results of other studies on HIFU therapy for undefined fibroids adjacent to the sacrococcygeal region.<sup>16,19</sup>

The effect of ultrasonic ablation depends on the energy deposition in the acoustic pathway. In this study, the lesion was adjacent to the sacrococcygeal region and located deep in the pelvic cavity. On the one hand, when focused ultrasound ablates deep lesions, the acoustic pathway is more complex than that of superficial lesions. Each tissue and interface will absorb, reflect, and scatter ultrasound, which results in energy loss. Therefore, tissue ablation requires high-

**Table 2.** A comparison between the ultrasonic ablation parameters of the sacrum injury group and the sacrum non-injury group

	Injury group (n = 139)	Non-injury group (n = 267)	P
Average power (w)	400 (300–400)	400 (269–401)	0.67
Treatment time (mins)	98 (16–247)	73 (10–233)	<0.001
Sonication time (s)	1200 (156–3803)	858 (95–7085)	<0.001
TD (KJ)	465.280 (52.2–1500)	324.8 (20–1400)	<0.001
Dose-time intensity (KJ/h)	290.909 (44.6–681.48)	271.629 (17.14–468.51)	0.043
NPV (cm <sup>3</sup> )	66.6 (15.3–388.6)	63.5 (15.5–307)	0.97
NPVR (%)	69.4 (25.1–100)	74 (28.8–100)	0.016
EEF (J/mm <sup>3</sup> )	4.6 (0.8–52.5)	3.7 (0.6–27.6)	0.002

NPV, non-perfusion volume; NPVR, non-perfusion volume rate; EEF, energy efficiency factor; TD, therapeutic dose.

**Table 3.** Risk assessment of the distance from the fibroid's dorsal side to the sacrum and TD on sacral injury

	OR	95% CI		P	
		Lower	Upper		
Fibroid dorsal side to the sacrum (mm)	Relative distance (mm)				
0–10	11–20	1.854	1.041	3.302	0.035
11–20	21–30	3.026	1.749	5.235	<0.001
	21–30	1.632	1.012	2.631	0.044
TD (KJ)	Relative TD (J)				
<500	250–500	1.893	1.083	3.308	0.024
250–500	<250	3.229	1.837	5.676	<0.001
	<250	1.706	1.062	2.740	0.027

CI, confidence interval; OR, Odds ratio; TD, therapeutic dose.

**Table 4.** Postoperative adverse effects

SIR classification	Adverse event	Injury group (n = 139)	Non-injury group (n = 267)	P
Class A	Abdominal discomfort	12 (8.6%)	47 (17.6%)	0.017
	Sacrococcygeal pain	10 (7.2%)	24 (9%)	0.58
	Abnormal vaginal discharge	5 (3.6%)	2 (0.7%)	0.049
Class B	Abdominal pain	0	2 (0.7%)	0.55
	Sacrococcygeal pain	2 (1.4%)	0	0.18
	Abnormal vaginal discharge	4 (2.9%)	6 (2.2%)	0.74
	Lower limb pain or numbness	1 (0.7%)	2 (0.7%)	1.00
Class C	Lower limb pain or numbness	0	1 (0.4%)	1.00
Class D–F	-	0	0	-

SIR, Society of Interventional Radiology.



er energy, which increases the difficulty of destroying tissue through thermal diffusion. On the other hand, due to the influence of lesion depth, ultrasonography is sometimes not clear enough for deep imaging to accurately determine the ablation range. Furthermore, as the lesion is close to the sacrococcygeal region, the posterior field energy decay decreases. This results in energy deposition in the sacrococcygeal region. During the ultrasound ablation procedure, the sacral discomfort of patients was aggravated, and the dose–time intensity (the total dose per unit treatment time) needed to be reduced, which affected the ablation effects. In this study, the NPVR of 55% (224/406) of patients was more than 70%. Therefore, the uterine fibroid adjacent to the sacrococcygeal region could be satisfactorily ablated; however, the depth of the lesion and the distance from the fibroid from the sacrum are still the influencing factors on the ablation effect.

In this study, 34.24% of patients developed abnormal signal intensity in the sacrum. Although the distance of uterine fibroids from the sacrum was  $\leq 30$  mm in all patients, the incidence was still similar to that of previous studies on undefined uterine fibroids adjacent to the sacrococcygeal region.<sup>8,9,20</sup> This study's NPVR was within 20%–100%, which was less than the NPVR reported by Li et al.<sup>9</sup> This may be a protective factor. Compared with Cun et al.'s<sup>8</sup> results, the TD of this study was lower. This suggests that this study's surgical ablation procedure for fibroids adjacent to the sacrococcygeal region was beneficial to the protection of the sacrum.

However, the incidence of sacral injury was still high after HIFU, and effective measures should be taken to reduce the incidence of injury after further clarification of its influencing factors, which remain the focus of attention in HIFU ablation. The MRIs of sacral injuries showed normal sacral morphology and structure. The injuries mostly occurred in the 2<sup>nd</sup>–4<sup>th</sup> cones of the sacrum. Striped high signal intensity or high–low mixed signal intensity was seen on T2WI. In addition, a slightly high signal intensity or non-enhanced region was seen on the contrast-enhanced MRIs. Changes in signal intensity in the sacrum are often associated with increased water content due to acute edema of the bone marrow. However, the non-enhanced area observed in the contrast-enhanced MRIs may be related to a thermal deposition injury, obstruction of blood vessels during the sonication, or compression of blood vessels due to edema.<sup>8</sup>

The reason for sacral injuries is that the bone has a strong ability to absorb ultrasound energy, and the acoustic impedance at the interface between the fibroid and the bone is quite different. When ultrasonic waves pass through two media that possess a great difference in acoustic impedance, obvious reflection and refraction will occur, and the bone will absorb a large amount of thermal energy, resulting in sacral injury. In addition, the blood supply to the sacrum mainly emanates from the distal vessels, and the relatively slow blood flow may induce an increased probability of thermal injury to the sacrum because the energy cannot dissipate easily through the circulation.<sup>8</sup> However, there was no pathological evidence of coagulative necrosis in the non-enhanced area shown on the contrast-enhanced MRIs, which requires further clarification via imaging and pathological studies.

In the univariate analysis, the location of uterine fibroids and the distance from the dorsal side of the fibroid to the sacrum were related to sacral injuries. The incidence of sacral injury was the highest in the posterior wall fibroid (42.3%). When the same ablation effect is achieved due to the posterior wall fibroid coming closer to the sacrum, more energy is needed than in the anterior wall, lateral wall, and fundus fibroids.<sup>21</sup> The posterior field energy attenuation lessens, leading to the sacrum becoming more vulnerable to injury. Further use of the multivariate logistic regression analysis concluded that the distance from the dorsal side of the fibroid to the sacrum was a protective factor for sacral injury. The incidence of sacral injury in fibroids 21–30 mm from the sacrum was only 17.3%. According to the risk assessment, the threat of sacral injury was 1.85 and 3.03 times higher for fibroids 0–10 mm from the sacrum than for fibroids at 11–20 and 21–30 mm, respectively. The closer the fibroid is to the sacrum, the less ultrasonic attenuation it will be. Moreover, the more ultrasonic energy absorbed by the sacrum, the higher the chance of sacral injury. Therefore, to avoid sacral injury during the ablation of fibroids adjacent to the sacrococcygeal region, an oblique angle ultrasound path can be considered to avoid the far-field sacrum. The initial treatment target can also be targeted at the anterior part of the fibroid, which is not close to the bone. After a few months, subsequent treatment can be conducted after fibroid shrinkage has increased the distance between the tumor and the sacrum.<sup>13</sup>

The energy required for the ablation of uterine fibroids of identical volume is posi-

tively correlated with focal depth.<sup>22</sup> The myoma requires more energy the deeper it is, so clinical long-term, high-dose treatments are generally used to ablate uterine fibroids adjacent to the sacral coccyx. The EEF, which is used to indicate the energy for ultrasound ablation of fibroid tissue per unit volume, reflects the relationship between dose and ablation efficiency.<sup>21</sup> The larger the EEF, the more energy a unit volume of a fibroid requires, and the more difficult it becomes to ablate. The univariate analysis showed that among the factors affecting sacral injury, the NPVR of the sacrum injury group was smaller than that of the non-sacrum injury group. Furthermore, the treatment time, sonication time, TD, dose–time intensity, and EEF of the injured group were all higher than those of the non-injury group. This suggests that the more difficult it is to ablate a fibroid, the more likely it is to cause injury to the sacrum. These indicators were incorporated into the multifactor logistic regression analysis to further identify TD as a risk factor for sacral injury. The larger the TD, the easier it is for the sacrum to be injured. In this study, it was concluded that the risk of sacral injury from TD >500 KJ was 1.89 times and 3.23 times higher than TD= 250–500 KJ and <250 KJ, respectively. Therefore, TD reduction is necessary. In clinical practice, the TD of a single procedure should be limited, and a divided session strategy should be considered if necessary. Researchers have also investigated other methods of TD reduction by changing the tissue's acoustic environment and enhancing local energy deposition.<sup>23</sup> However, the safety impacts caused by increased intervention factors still need to be examined.

In this study, 95 of 406 patients (23.40%) developed postoperative adverse effects, with a total of 118 adverse effects. According to the classification standard of the International Association of Interventional Radiology,<sup>24</sup> 84.74% of them were classified as Class A and spontaneously recovered within 1 week without treatment. Although the distance of fibroids from the sacrum in this group was 30 mm, the incidence and study degree of sacrococcygeal pain and lower limb pain did not increase compared with studies on the large sample.<sup>10,25</sup> In the sacrum injury group, two patients developed sacrococcygeal pain, which was completely relieved within 1 week after symptomatic treatment with NSAIDs. One patient (0.2%) developed lower limb pain in the sacrum non-injury group, which may have been caused by nerve stimulation. The pain disappeared within 3 months after treatment with NSAIDs and a vitamin agent.

The results revealed that MRI showing sacral injury does not increase the incidence and severity of clinically adverse effects; however, its long-term impact on patients needs to be explored.

In conclusion, the MRI results revealed the likelihood of sacral injury after ultrasonic ablation of uterine fibroids, and the incidence remained similar to that of previous studies on undefined uterine fibroids adjacent to the sacrococcygeal region. The location of fibroids, the distance from the fibroid's dorsal side to the sacrum, TD, and EEF showed significant associations with sacral injury. Among these, the distance from the fibroid's dorsal side to the sacrum and TD were the main causes of sacral injury. A distance of 10 mm or less and a TD greater than 500 KJ carried higher injury risks. Moreover, a 21–30-mm distance and TD <250 KJ were the most appropriate parameters for ultrasonic ablation of fibroids. Although subjects did not develop serious complications, these influencing factors should be carefully considered in uterine fibroids ≤30 mm to optimize the scheme for the focused ultrasound ablation of uterine fibroids.

### Acknowledgement

Thanks to the radiologist for performing specification MR scanning in this study and Yingying Feng for language editing.

### Conflict of interest disclosure

The authors declared no conflicts of interest.

### References

- Trefoux Bourdet A, Luton D, Koskas M. Clinical utility of ulipristal acetate for the treatment of uterine fibroids: current evidence. *Int J Womens Health*. 2015;7:321-330. [\[CrossRef\]](#)
- Borah BJ, Nicholson WK, Bradley L, Stewart EA. The impact of uterine leiomyomas: a national survey of affected women. *Am J Obstet Gynecol*. 2013;209(4):319. [\[CrossRef\]](#)
- Zhang L, Chen WZ, Liu YJ, et al. Feasibility of magnetic resonance imaging-guided high intensity focused ultrasound therapy for ablating uterine fibroids in patients with bowel lies anterior to uterus. *Eur J Radiol*. 2010;73(2):396-403. [\[CrossRef\]](#)
- Peng S, Xiong Y, Li K, et al. Clinical utility of a microbubble-enhancing contrast ("SonoVue") in treatment of uterine fibroids with high intensity focused ultrasound: a retrospective study. *Eur J Radiol*. 2012;81(12):3832-3838. [\[CrossRef\]](#)
- Wang ZB, Wu J, Fang LQ, et al. Preliminary ex vivo feasibility study on targeted cell surgery by high intensity focused ultrasound (HIFU). *Ultrasonics*. 2011;51(3):369-375. [\[CrossRef\]](#)
- Hassanuddin A, Choi JH, Seo DW, et al. Factors affecting tumor ablation during high intensity focused ultrasound treatment. *Gut Liver*. 2014;8(4):433-437. [\[CrossRef\]](#)
- Yin N, Hu L, Xiao ZB, et al. Factors influencing thermal injury to skin and abdominal wall structures in HIFU ablation of uterine fibroids. *Int J Hyperthermia*. 2018;34(8):1298-1303. [\[CrossRef\]](#)
- Cun JP, Fan HJ, Zhao W, Yi GF, Jiang YN, Xie XC. Factors influencing MR changes associated with sacral injury after high-intensity focused ultrasound ablation of uterine fibroids. *Int J Hyperthermia*. 2019;36(1):21-28. [\[CrossRef\]](#)
- Li D, Gong C, Bai J, Zhang L. Analysis of magnetic resonance signal intensity changes in the sacrococcygeal region of patients with uterine fibroids treated with high intensity focused ultrasound ablation. *Int J Hyperthermia*. 2020;37(1):404-413. [\[CrossRef\]](#)
- Liu Y, Zhang WW, He M, et al. Adverse effect analysis of high-intensity focused ultrasound in the treatment of benign uterine diseases. *Int J Hyperthermia*. 2018;35(1):56-61. [\[CrossRef\]](#)
- Yu T, Luo J. Adverse events of extracorporeal ultrasound-guided high intensity focused ultrasound therapy. *PLoS One*. 2011;6(12):e26110. [\[CrossRef\]](#)
- Rueff LE, Raman SS. Clinical and technical aspects of MR-guided high intensity focused ultrasound for treatment of symptomatic uterine fibroids. *Semin Intervent Radiol*. 2013;30(4):347-353. [\[CrossRef\]](#)
- Yoon SW, Lee C, Cha SH, et al. Patient selection guidelines in MR-guided focused ultrasound surgery of uterine fibroids: a pictorial guide to relevant findings in screening pelvic MRI. *Eur Radiol*. 2008;18(12):2997-3006. [\[CrossRef\]](#)
- Wang Z, Bai J, Li F, et al. Study of a "biological focal region" of high-intensity focused ultrasound. *Ultrasound Med Biol*. 2003;29(5):749-754. [\[CrossRef\]](#)
- Wijlemans JW, de Greef M, Schubert G, et al. A clinically feasible treatment protocol for magnetic resonance-guided high-intensity focused ultrasound ablation in the liver. *Invest Radiol*. 2015;50(1):24-31. [\[CrossRef\]](#)
- Chen J, Li Y, Wang Z, et al. Evaluation of high-intensity focused ultrasound ablation for uterine fibroids: an IDEAL prospective exploration study. *BJOG*. 2018;125(3):354-364. [\[CrossRef\]](#)
- Duc NM, Keserci B. Emerging clinical applications of high-intensity focused ultrasound. *Diagn Interv Radiol*. 2019;25(5):398-409. [\[CrossRef\]](#)
- Wang Y, Liu X, Wang W, Tang J, Song L. Long-term clinical outcomes of US-guided high-intensity focused ultrasound ablation for symptomatic submucosal fibroids: a retrospective comparison with uterus-sparing surgery. *Acad Radiol*. 2021;28(8):1102-1107. [\[CrossRef\]](#)
- Zhang YJ, Xiao ZB, Lv FR, et al. MRI evaluation of endopelvic fascial swelling and analysis of influencing factors in patients with uterine fibroids after high-intensity focused ultrasound ablation. *Int J Hyperthermia*. 2020;37(1):175-181. [\[CrossRef\]](#)
- Cheng CQ, Zhang RT, Xiong Y, et al. Contrast-enhanced ultrasound for evaluation of high-intensity focused ultrasound treatment of benign uterine diseases: retrospective analysis of contrast safety. *Medicine (Baltimore)*. 2015;94(16):e729. [\[CrossRef\]](#)
- Peng S, Zhang L, Hu L, et al. Factors influencing the dosimetry for high-intensity focused ultrasound ablation of uterine fibroids: a retrospective study. *Medicine (Baltimore)*. 2015;94(13):e650. [\[CrossRef\]](#)
- Ismail SZ, Bilgen M. Use of depth dependent attenuation characteristics of thermal energy deposition to increase spatial uniformity of HIFU ablation in large uterine fibroids. *Medical Instrumentation*. 2013. [\[CrossRef\]](#)
- Yang Z, Zhang Y, Zhang R, et al. A case-control study of high-intensity focused ultrasound combined with sonographically guided intratumoral ethanol injection in the treatment of uterine fibroids. *J Ultrasound Med*. 2014;33(4):657-665. [\[CrossRef\]](#)
- Cardella JF, Kundu S, Miller DL, Millward SF, Sacks D; Society of Interventional Radiology. Society of Interventional Radiology clinical practice guidelines. *J Vasc Interv Radiol*. 2009;20(suppl 7):189-191. [\[CrossRef\]](#)
- Chen J, Chen W, Zhang L, et al. Safety of ultrasound-guided ultrasound ablation for uterine fibroids and adenomyosis: A review of 9988 cases. *Ultrason Sonochem*. 2015;27:671-676. [\[CrossRef\]](#)



# Questions about “Intra-atrial right coronary artery on dual-source CT”

Furkan Ufuk

Dear Editor,

I read with great interest the article by P Ganga et al.<sup>1</sup>, “Intra-atrial right coronary artery on dual-source CT: prevalence and characteristics,” published in *Diagnostic and Interventional Radiology* in the September–October 2021 issue. The authors described the prevalence and radiological features of the intra-atrial course of the right coronary artery (IA-RCA) in adults on coronary computed tomography angiography (CCTA).<sup>1</sup> The IA-RCA is a rare anomaly of the right coronary artery course; recognition of IA-RCA is important before carrying out ablative procedures for arrhythmias, catheterization of the right heart chambers, and pacemaker implantation.<sup>1,2</sup> I congratulate the authors for this interesting and instructive retrospective study. I suggest some points that need to be clarified in this article that could significantly contribute to the literature.

In the methods section, the authors stated that CCTA images were evaluated independently by two cardiothoracic radiologists.<sup>1</sup> However, I could not find any statements in the text indicating the observers’ agreement or differences. In what situations were there differences in the assessment of IA-RCA between observers? How were these differences resolved by “discussion”? For example, which observer’s measurements were taken as a basis for quantitative evaluations, such as the length of the intra-atrial segment of RCA and the distance of the RCA from the atrial wall? In how many cases with IA-RCA did the RCA partially pass through the right atrium, and how many did it pass completely? What were the symptoms of patients with IA-RCA, and what were the CCTA indications? What were the coronary artery disease-reporting and data-system (CAD-RADS) scores of patients with IA-RCA? I suggest that the answers to these questions will make a significant contribution to the literature.

## References

1. P Ganga K, Ojha V, Goyal A, Deepti S, Kumar S. Intra-atrial right coronary artery on dual-source CT: prevalence and characteristics. *Diagn Interv Radiol.* 2021;27(5):595-598. [\[CrossRef\]](#)
2. Opolski MP, Pregowski J, Kruk M, et al. The prevalence and characteristics of intra-atrial right coronary artery anomaly in 9,284 patients referred for coronary computed tomography angiography. *Eur J Radiol.* 2014;83(7):1129-1134. [\[CrossRef\]](#)

## KEYWORDS

Cardiology, coronary artery, coronary artery disease, CT angiography, diagnosis

From the Department of Radiology (F.U. ✉ furkan.ufuk@hotmail.com), Pamukkale University Faculty of Medicine, Denizli, Turkey.

Received 29 September 2021; accepted 31 October 2021.



Epub: 07.12.2022

Publication date: 31.01.2023

DOI: 10.5152/dir.2022.211049

You may cite this article as: Ufuk F. Questions about “Intra-atrial right coronary artery on dual-source CT”. *Diagn Interv Radiol.* 2023;29(1):202.